Structure et hétérogénéité d'une plate-forme récifale Miocène (Majorque) ; implication pour les intrusions d'eau salée en zone côtière

Yves Maria-Sube

UNIVERSITE MONTPELLIER II
SCIENCES ET TECHNIQUES DU LANGUEDOC

THESE

pour obtenir le grade de

DOCTEUR DE L'UNIVERSITE MONTPELLIER II

Discipline : Géosciences
Formation doctorale : Dynamique de la lithosphère et du manteau terrestre
Ecole doctorale : Terre, Eau, Espace

présentée et soutenue publiquement

par

YVES MARIA-SUBE

le 13 décembre 2007

Titre :

Structure et hétérogénéité d'une plate-forme récifale Miocène (Majorque) ; implication pour les intrusions d'eau salée en zone côtière

_____

JURY

M. Marc Daignères	Professeur Université Montpellier II	Président
M. Gilbert Camoin	Directeur de recherche CNRS, Aix-en-Provence	Rapporteur
M. Modesto Montoto	Professeur, Université d'Oviedo	Rapporteur
M. Philippe Lapointe	Senior carbonate sedimentologist, Total, Pau	Examinateur
M. David Mainprice	Directeur de recherche CNRS, Montpellier	Examinateur
M. Oberto Serra	Consultant industrie pétrolière, Mery-Corbon	Invité
M. Philippe Pezard	Directeur de recherche CNRS, Montpellier	Directeur de thèse

A mon épouse,
A mes enfants,
A mes amis qui m’ont soutenu dans cette nouvelle aventure.

Remerciements

A MM. Les membres du jury qui me font l'honneur de juger ce travail, j'exprime ma reconnaissance.

« L'interprétation des diagraphies consiste en une « traduction » des données à partir des paramètres de *diagraphies* vers les données *géologiques*. Pour effectuer ceci, nous avons besoin d'un bon « dictionnaire » ou d'un « interprète » *qui connaisse bien les deux langages* », (Serra, 1986).

« La capacité potentielle des seniors, comme celle de tous les êtres humains, est sans limite » [a dit] Yuichiro Miura, alpiniste de 70 ans, après son ascension de l'Everest le 22 mai. (Challenges, 12 juin 2003).

Ma démarche est légèrement inhabituelle en ce sens qu'au lieu de commencer ma vie professionnelle avec en prélude une thèse, c'est plutôt sur sa fin que cette ambition m'est venue.

Mon intérêt pour la géologie n'est pas non plus arrivé précocement_ disons au milieu de ma vie professionnelle. Qu'il me soit permis de remercier Claude Boyeldieu (ancien élève de l'Ecole Centrale Lille, Ingénieur ENSPM, ancien vice-président de Schlumberger, ancien secrétaire de la SAID, malheureusement décédé en 2003) qui m'a permis au début des années 1980, d'aller dans cette voie, et Oberto Serra (Docteur es Sciences, Ingénieur ENSPM, ancien chef du service diagraphies de la SNEA(P), ancien géologue en chef de Services Techniques Schlumberger), qui au cours de la même période m'a patiemment et avec toute sa science inoculé le virus de la géologie.

Mes remerciements vont aux membres du CREUFOP (Mmes Laurence Pochard, Martine Frayssinet, M. Louis Pappalardo) qui m'ont patiemment guidé à travers les arcanes des lois et procédures de la Formation Continue et m'ont mis en premier contact avec le personnel enseignant de l'Université Montpellier II, ISTEEM (Institut des Sciences de la Terre, de l'Eau et de l'Espace, Montpellier).

A M. le professeur Marc Daignères, responsable de l'Ecole Doctorale Sciences de la Terre et de l'Eau, qui m'a fait confiance et m'a soutenu dans ma démarche doctorale.
A M. le Professeur Serge Lallemand, responsable du DEA Structure et Evolution de la Lithosphère (ISTEEM), directeur du laboratoire Dynamique de la Lithosphère, qui m'a écouté et a eu la bonté de m'orienter vers MM. Louis Briqueu et David Mainprice.
A M. le Professeur Louis Briqueu, responsable de l'option DEA Diagraphies : outils, traitement et interprétation, qui m'a reçu et m'a proposé un sujet de thèse.
A M. le Professeur David Mainprice, responsable de l'option DEA Pétrophysique des milieux poreux : roches et sols, qui m'a reçu, m'a encouragé dans ma démarche de rencontre de la pétrophysique et de la géologie, m'a proposé un sujet de thèse, et m'a introduit auprès de M. Philippe Pezard.
A M. le Professeur Jean-Louis Bodinier, directeur du Laboratoire de Tectonophysique (ISTEEM).
A M. le Professeur Philippe Pezard, Directeur du projet ALIANCE (Advance Logging Investigations of Aquifers iN Coastal Environments) au sein du laboratoire de Tectonophysique, mon Directeur de Thèse, qui m'a tout de suite proposé un sujet de thèse que

je ne pouvais pas refuser : dans le cadre de deux grands projets (ALIANCE et ISES-Industrie), auxquels une dizaine d'Universités européennes sont associées, projets dans lesquels sont entremêlés géologie, géophysique, pétrophysique, hydrologie, et ingénierie du réservoir. Il a ensuite eu la patience de me guider à travers le long périple d'une thèse, en dépit de mon profil inhabituel.

A toute l'équipe qui a travaillé sur le projet ALIANCE au sein du laboratoire de Tectonophysique (ISTEEM) et qui, à un moment ou un autre, m'a procuré aide et soutien avec enthousiasme : Philippe Gouze, Didier Loggia, Patrick Pinettes, Florence Einaudi, Gérard Lods, Hendrik Braaksma, Akram Belghoul, Gilles Henry, Arnaud Sandouly, Pierre Azaïs, Richard Leprovost, Joëlle Gastambide.

Au Professeur Modesto Montoto, de l'Université d'Oviedo, au Professeur Luis Pomar de l'Université des Iles Baléares, à toute l'équipe de l'Institut de Technologie de Zurich (Simon Löw, David Jaegghi, Nathalie Van Meir, Martin Herfort), au Professeur Gilbert Camoin de l'Université d'Aix (CEREGE), et à son étudiant Benjamin Bonnier, au Professeur Jeroen A.M. Kenter de l'Université Libre d'Amsterdam, et son étudiant Klaas Verwert.

A Gilbert Camoin, Didier Loggia, Philippe Gaillot, qui ont accepté la rude tâche de relire un ou plusieurs de mes quatre manuscrits avant de les soumettre à l'éditeur.

Aux Professeurs Michel Séranne, et Michel Lopez du laboratoire de Dynamique de la Lithosphère ; Bernard Célérier, du laboratoire de Tectonophysique ; Lionel Hautier et Dominique Jolly, du Laboratoire de Sciences de la Terre et de l'Environnement, qui m'ont transmis une petite partie de leur savoir en bassins, sédimentologie, et micro-paléontologie.

Table des matières

Introduction

Les aquifères côtiers sont menacés de façon croissante par des intrusions d'eau salée, et ceci pour des raisons climatiques ou anthropiques, qu'elles fassent suite à des sollicitations agricoles, urbaines ou touristiques. Dans un environnement souvent hétérogène, comprendre la dynamique des écoulements souterrains nécessite de développer une approche prenant en compte la structure géologique dans sa complexité. Nous proposons ici de traiter le cas des structures carbonatées d'origine récifale rencontrées sur le pourtour méditerranéen.

Dans le cadre de cette thèse, nous étudions le récif Miocène de l'île de Majorque (Espagne) qui constitue un laboratoire naturel d'une centaine de mètres d'épaisseur et à l'échelle horizontale de quelques dizaines de kilomètres de large. Cette structure fait l'objet d'études multi- disciplinaires dans le cadre des projets européens comme ALIANCE pour l'hydrodynamique en zone côtière, ou ISES-Industrie pour la structure des réservoirs analogues étudiés dans le cadre de l'exploration pétrolière.

Advanced Logging Investigations of Aquifers iN Coastal Environments (ALIANCE) est un projet «Energy, Environment and Sustainable Development », Water Key Action, Contract n° EKV-2001-00039, financé par la Commission Européenne de 2002 à 2006. Le but de ce projet de recherche est d'améliorer la production durable et la qualité de l'eau des nappes phréatiques en environnements côtiers et semi-arides. L'Union Européenne inclut un grand nombre d'aquifères côtiers potentiellement exposés en raison de sur-exploitation et/ou de sécheresse naturelle (et dans le futur, de plus en plus, en raison du réchauffement climatique global), spécialement dans la région Méditerranéenne. La pollution par eau salée est donc devenue un sujet majeur, d'autant plus que la salinité de l'eau souterraine excède souvent les minima de l'eau potable, et éventuellement menace les besoins agriculturaux à long terme.

Deux sites avaient été choisis pour mettre en œuvre ce projet : Stang Er Brune en Bretagne, Maguelone en Languedoc- Roussillon, et Ses Sitjoles à Majorque. Ce sont les résultats obtenus à Ses Sitjoles qui sont décrits dans cette thèse.

Le site de Ses Sitjoles (Maria-Sube et al., soumis), situé à 6km à l'intérieur des terres, est particulièrement intéressant pour étudier l'intrusion d'un biseau salé en zone côtière semi-aride, sujette à un une exploitation agricole avec pompage d'eau pour l'arrosage.

Les Universités suivantes ont participé à ce projet :

- Université Montpellier 2, Institut des Sciences de la Terre, de l'eau et de l'Espace de Montpellier (ISTEEM)
- Université de Birmingham, Hydrology Research Group (R-U)
- Eidgenössische Technische Hochschule (ETH), Engineering Geology (Suisse)
- Universidad de Oviedo, Departamento de Geologia, Area de Petrologia y Geoquimica, (Espagne)
- Université de Aix-Marseille, Centre Européen de Recherche et d'Enseignement des Géosciences de l'Environnement (CEREGE), Laboratoire de Géochimie/ Diagénèse, (France)

Le Centre de recherche Integrated Solid Earth Science (ISES), avec support de l'industrie pétrolière, a mis sur pied le projet ISES – Industrie, dans le but de rechercher la relation de la propagation des ondes acoustiques dans les séquences de roches sédimentaires avec la distribution spatiale des propriétés géologiques, géophysiques et pétrophysiques. Dans ce but, le projet a choisi deux laboratoires naturels, et a combiné des moyens de composants sismiques haute résolution 2D- 3D, géophysique et pétrophysique de forage, et quantification de propriétés de structure géologique. Deux sites ont été choisis pour ce projet : Cap Blanc à Majorque (Espagne), et Gargano en Italie.

Les directions des projets d'ALIANCE et d'ISES- Industrie ont décidé de combiner et partager une partie de leurs moyens sur les sites de Ses Sijoles (Maria-Sube et al., soumis) et Cap Blanc (Maria-Sube[1], soumis) à Majorque.
Les Universités suivantes ont participé au projet d'ISES- Industrie:

- Vrieje Universiteit Amsterdam, Petrophysics and Sedimentology Department, (Pays-Bas)
- Technische Universiteit Delt, Geophysics Department, (Pays-Bas)
- Universidad de las Baleares Islas, Sedimentology Department, (Espagne)
- University of Miami, (USA)

Université de Aix-Marseille, Centre Européen de Recherche et d'Enseignement des Géosciences de l'Environnement (CEREGE), Laboratoire de Géochimie/ Diagénèse, (France)

Dans le cadre de méthodes à la fois multi- scalaires (échelle du micron_ pour les analyses microscopiques, en passant par l'échelle du millimètre pour les diagraphies d'imagerie de la paroi du trou, et l'échelle du mètre pour les diagraphies conventionnelles mono-puit, jusqu'à une dizaine de kilomètres pour l'analyse à l'échelle du complexe récifal, englobant une douzaine de puits) et multi- disciplinaires, l'approche mise en œuvre sera à la fois géologique, géophysique, pétrophysique, géochimique et hydrogéologique. Plus particulièrement, cette thèse consistera à:

1. Examiner les connaissances géologiques et biologiques générales sur les coraux et réservoirs récifaux
2. Détailler les programmes associés et le complexe récifal du Sud-Est de Majorque
3. Examiner les moyens d'étude
4. Reproduire les quatre documents en cours de publication
5. Etudier l'hydrogéologie et le biseau salé sur le complexe récifal
6. Faire une synthèse, une conclusion et examiner les perspectives
7. Citer les références.

Le récif Miocène de Majorque (voir les cartes dans les publication, paragraphe 4) est visible au Cap Blanc (Sud-Est de l'île) par trois côtés : la plate-forme de surface et deux parois verticales à 90°. Sa géologie de surface a été décrite de façon extensive (Pomar, 1991 ; Pomar et al., 1994 ; Pomar et Ward, 1995 ; Pomar et al., 1996 ; Pomar, et Ward, 1999 ; Pomar, 2001). Les plates-formes récifales de Majorque ont progradé autour d'îles résultant de l'orogénie alpine (Miocène Moyen). Les bassins de Palma jusqu'à Alcudia résultent de failles créées du Miocène Inférieur jusqu'au Pleistocène, tandis que le bassin de Campos s'est effondré au cours du début du Pleistocène (Pomar et al., 1996).

1 Coraux et les réservoirs récifaux

Dans ce chapitre les connaissances sur les coraux actuels et anciens sont passées en revue, puis plusieurs complexes récifaux (Grande Barrière de Corail d'Australie, Grand Banc des Bahamas, Tahiti) comparables au complexe récifal du Sud-Est de Majorque sont introduits.

1.1 Les coraux

Les coraux sont des sortes de polypes avec un support calcaire blanc, rouge, ou noir, vivant dans des eaux peu profondes (habituellement moins de 20m), chaudes (en moyenne 25°C), tropicales. Les polypes vivent ensemble dans d'immenses colonies (Fig. 1A). Comme le polype croît, la coupe qu'il construit en temps qu'habitat est agrandie. Les polypes extraient du carbonate de calcium (moins soluble dans l'eau chaude, et donc aisément disponible) de l'eau de mer, secrétant leur propre solide maison, en forme de rocher.

1.1.1 Anatomie et reproduction des coraux modernes

Bien que le corail apparaisse comme un seul organisme, la colonie est en fait composée de nombreux individus génétiquement identiques, les polypes. Les polypes sont des organismes multicellulaires qui se nourrissent d'une variété de petits organismes, allant du plancton microscopique à des petits poissons.

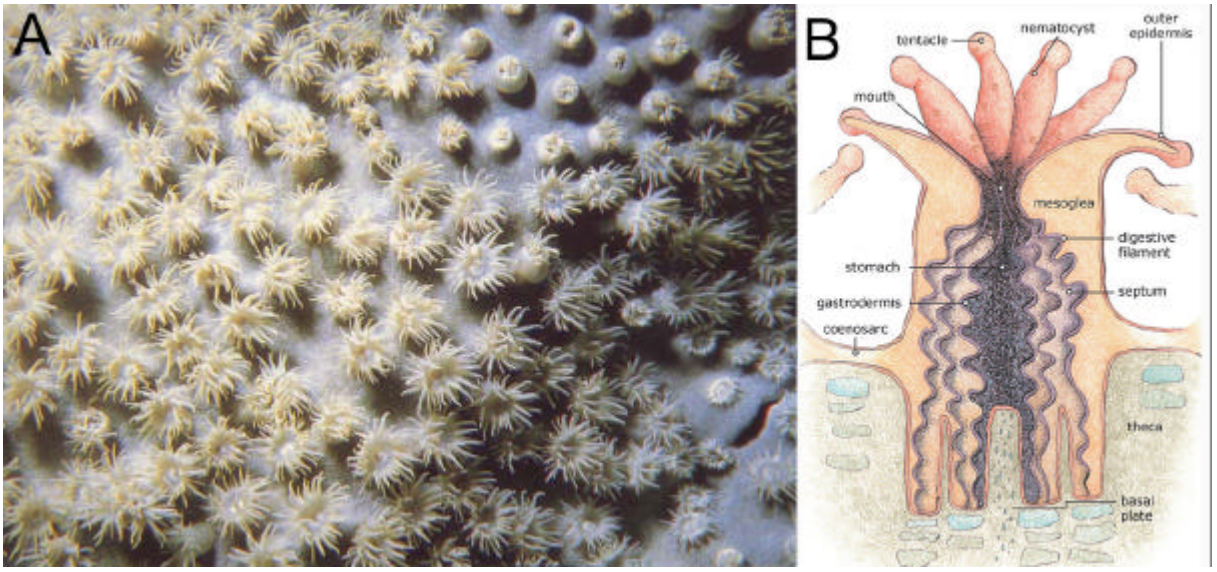

Figure 1. (A) Fonctionnant comme les anémones auxquelles ils ressemblent, ces coraux brassent l'eau à la recherche de proies microscopiques. Certaines des espèces les plus larges capturent même des poissons. Brown et Morgan, 1990. (B) Anatomie d'un polype de corail.

Les polypes ont une taille qui varie de 2,5 mm jusqu'à une dizaine de cm de diamètre, et sont formés par une couche extérieure appelée épithélium, et un tissu interne gélatineux appelé mésoglea (Fig.1B). Ils ont une symétrie radiale, avec des tentacules (plus de huit et en pultiple de six, d'ou leur nom d'hexacorallia) entourant une bouche centrale, le seul orifice conduisant à l'estomac (coelentéron), à travers lequel à la fois la nourriture est ingérée, et les résidus sont expulsés. L'estomac se ferme à la base du polype, où l'épithélium produit un exosquelette appelé le plateau de base, ou calicle. Celui-ci est formé par un anneau calcaire épais avec six arêtes radiales. Ces structures croissent verticalement et permettent au polype de se retirer dans l'exosquelette pour se protéger. Le polype croît par extension de calices verticaux qui sont occasionnellement septatés pour former un nouveau, plus haut plateau de base. Après que

le polype se soit ancré au substrat, il croît et s'élève au-dessus du fond de la mer, vivant dans la partie haute du tube de corail. A cet endroit, les tentacules sont mieux positionnées pour attraper la nourriture. Après plusieurs générations, cette extension forme de grandes calcifères structures de coraux et finalement des récifs de coraux. La formation d'un exosquelette calcifère comprend la déposition d'aragonite par les polypes à partir des ions de calcium qu'ils obtiennent à partir de l'eau de mer. Le taux de déposition, qui varie largement entre les différentes espèces et dépend des conditions d'environnement, peut atteindre 10g/m^2 de polype/jour. Ceci dépend de la lumière, avec une production de nuit 90% plus faible que durant le jour.

Les tentacules du polype capturent des proies en utilisant des cellules piquantes appelées nématocystes. Ce sont des cellules modifiées pour capturer et immobiliser les proies, comme le plancton, en injectant des poisons, déclenchant très rapidement en réponse à un contact. Ces poisons sont en général faibles, mais chez les coraux de feu ils sont suffisamment puissants pour blesser des êtres humains. Les nématocystes peuvent aussi exister chez les méduses et les anémones de mer. Les toxines injectées par les nématocystes immobilisent ou tuent la proie, qui peut alors être acheminée vers l'estomac du polype par les tentacules grâce à une bande contractive de l'épithélium appelée le pharynx.

Les polypes sont interconnectés par un système complexe et bien développé de canaux gastro-vasculaires permettant un partage important de nutriments et de symbiotes. Chez les coraux mous, ces canaux ont un diamètre de 50 à 500µm de façon à permettre le transport à la fois de métabolites et de composants cellulaires.

Les coraux présentent deux modes de reproduction différents : la reproduction sexuelle est également un essaimage, tandis que l'autre mode de reproduction, par bourgeonnement ou par division est un mode d'agrandissement de la colonie, sur place.

Les coraux se reproduisent d'une manière prédominante sexuellement, avec 25% des coraux hermatypiques formants des colonies unisexes, tandis que le reste sont hermaphrodites. Environ 75% de tous les coraux hermaphrodites émettent du frai en relâchant des gamètes (œufs et du sperme) dans l'eau pour diffuser des colonies à travers de grandes distances. Les gamètes fusionnent durant la fertilisation pour former une larve microscopique appelée planula, typiquement rose et de forme elliptique. Une colonie de taille moyenne peut former plusieurs milliers de ces larves par an, pour surmonter l'énorme sort défavorable contre la formation d'une nouvelle colonie.

La planula nage vers la lumière, démontrant ainsi une phototaxie positive, jusqu'à atteindre les eaux de surface, et grossissent pendant un certain temps avant de nager à nouveau vers le bas pour localiser une surface sur laquelle elle puisse s'attacher et établir une nouvelle colonie. A de nombreuses étapes de ce processus il y a un fort taux d'échec, et bien que des millions de gamètes soient émis par chaque colonie, bien peu de nouvelles colonies sont formées. Le temps entre le frai et l'établissement est souvent de deux à trois jours, mais peut atteindre jusqu'à deux mois. La larve croît en un polype corallien et éventuellement devient une tête de corail par bourgeonnement asexué et croissance, créant de nouveaux polypes.

Les coraux qui n'émettent pas de frai sont appelés couveuses, avec la majorité des coraux ahermatypiques présentant cette caractéristique. Ces coraux émettent du sperme, mais protègent les œufs, permettant à de plus grandes, non flottantes, planulae de se former ; elles sont ensuite relâchées, prêtes à s'établir. La larve croît en un polype corallien et

éventuellement devient une tête de corail par bourgeonnement asexué et croissance, créant de nouveaux polypes.

Le frayement synchronisé est très typique sur un récif corallien, et souvent, même quand il y a de multiples espèces présentes, tous le coraux du récif lâchent des gamètes durant la même nuit. Cette synchronisation est essentielle pour que les gamètes mâles et femelles puissent se rencontrer et former des planulae. Les raisons qui guident le lâcher sont complexes, mais incluent les changement de lune, l'heure de coucher de soleil, et peut-être un signal chimique. Le frayement synchronisé peut avoir comme résultat de former des coraux hybrides, peut-être impliqué dans la spéciation des coraux. Dans certains endroits, le frai corallien peut être spectaculaire, en général la nuit, l'eau claire devenant nuageuse avec les gamètes.

A l'intérieur d'une tête de corail les polypes génétiquement identiques de reproduisent asexuellement pour permettre la croissance de la colonie. Ceci se produit ou bien par gemmation ou bourgeonnement, ou par division. Le bourgeonnement signifie qu'un nouveau polype croît à partir d'un adulte, tandis que la division forme deux polypes aussi grands que l'original.

Des colonies entières peuvent se reproduire asexsuellement par fragmentation, lorsqu'une partie cassée de la tête de corail et emportée par l'action des vagues peut continuer à croître dans un nouvel emplacement.

1.1.2 Ecologie

1.1.2.1 Les coraux ahermatypiques

Freiwald, 2003, indique qu'il existe depuis au moins 240 millions d'années des coraux vivants en mer profonde (ahermatypiques, jusqu'à mille mètres de profondeur). Les coraux profonds intéressent les compagnies pétrolières, qui forent de plus en plus de gisements pétroliers en eaux profondes. Les coraux profonds ont besoin des conditions suivantes :

- Eaux de profondeur comprise entre 100 et 1000m,
- Température de 4 à 12°C
- Salinité élevée (les eaux salines contiennent beaucoup de calcaire dissous, que les coraux utilisent pour construire leur squelette)
- Zones de fort courants, où se forment aussi des ondes de marée, à proximité des talus continentaux escarpés, avec grande concentration de nutriments et de plancton
- Les hydrocarbures, qui suintent des sources sous-marines de pétrole, et les nutriments libérés par les sources hydrothermales, entretiennent des communautés florissantes ; mais les coraux profonds tirent l'essentiel de leur nourriture du plancton de surface qui sédimente.

L'espèce de corail profond la plus répandue est le Lophelia. Les Lophelia fossiles les plus anciens datent d'environ 50 millions d'années.
Bien que l'existence des coraux ahermatypiques est connue depuis longtemps, ils n'ont été étudiés en détail que récemment. Leur présence fossile est moins grande et moins étendue que celle des coraux hermatypiques. Leurs conséquence pour les réservoirs pétroliers est incertaine au mieux. Ils ne sont pas le sujet de cette thèse, et sont simplement mentionnés par soucis d'information.

1.1.2.2 Les coraux hermatypiques

Pour les espèces en eau peu profonde (hermatypiques), auxquelles nous nous intéressons ici, Chamley, 1987 indique les conditions suivantes :

- Nourriture zooplanctonique appropriée ; les coraux tropicaux se nourrissent principalement grâce à l'apport de zooxanthelles, des algues unicellulaires avec lesquelles ils vivent en symbiose, Freiwald, 2003. Les zooxanthelles se développent en absorbant le dioxyde de carbone libéré par les coraux, et fournissent en retour divers nutriments à leur hôte (glycérol, glucose, acides aminés, peptides), et fournit un apport d'oxygène pour la respiration d'oxygène du polype pendant le jour. Ceci entraîne les conditions suivantes :
  - Bon éclairement
  - Eaux peu profondes < 100m, généralement < 30m
- Chaudes (18 à 36°C) pendant toutes les saisons
- Normalement salées (de 27 à 43g/l)
- Présence d'un substrat dur et relativement stable, permettant la fixation des espèces.

Actuellement, on trouve des récifs coralliens vivants dans les zones tropicales et équatoriales :

- Aux Bahamas,
- En Floride,
- En Australie,
- A Madagascar,
- Dans la Mer Rouge,
- Etc…

1.1.2.3 Environnement, morphologie et bathymétrie des coraux hermatypiques modernes

Scholle et al., 1983, ont observé sur les coraux modernes que leur morphologie est adaptée à l'énergie des vagues correspondant à la bathymétrie où ils sont installés (Fig. 2). Ainsi, entre 0 et 10m de profondeur, où l'énergie des vagues, ainsi que la lumière, sont maximum correspondent les formes compactes des coraux encroûtants et massifs les plus aptes à une forte résistance mécanique, sans soucis de captation excessif d'une lumière naturellement abondante. Entre 10 et 20m de profondeur, où l'énergie des vagues est moindre, mais où la lumière est moins abondante, on trouve des formes plus fragiles et plus élargies des coraux branchus, en forme de doigts, et tabulaires. Entre 20 et 30m de profondeur, où l'énergie des vagues et la lumière sont minima, se trouvent les formes les plus fragiles et les plus étendues des fins coraux plateaux.

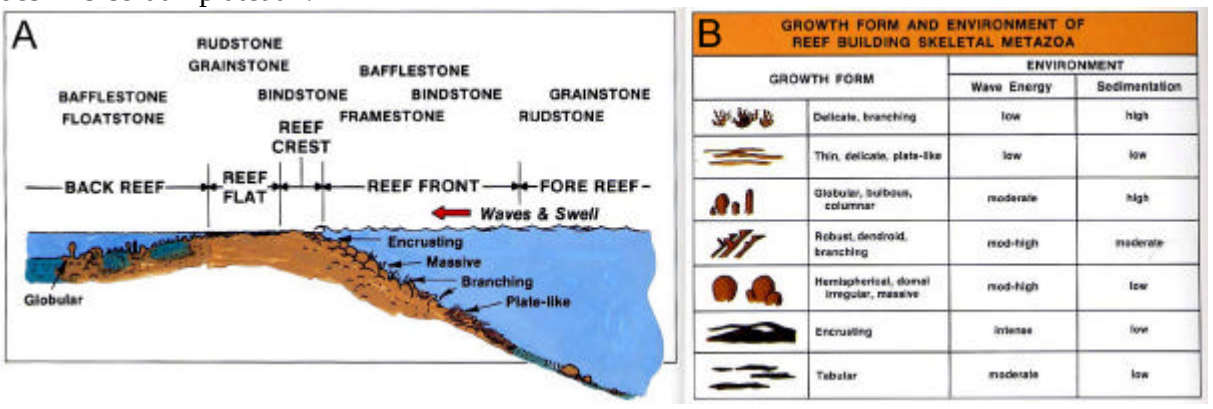

Figure 2. (A) Schéma des zones d'un récif, indiquant la morphologie des coraux correspondant à leur bathymétrie ainsi qu'à l'énergie correspondante des vagues, et les structures des sédiments carbonatés (Scholle et al., 1983). (B) Formes et environnement de coraux (Scholle et al., 1983).

Scholle et al. indiquent aussi la structure de sédiments carbonatés qui peuvent correspondre aux différentes zones du récif (Fig. 2A) : grainstone (Dunham, 1962), floatstone ou rudstone (Embry et Klovan, 1971) dépositionnels ; framestone, bindstone ou bafflestone (Wright, 1992) biologiques.

1.1.3 Histoire géologique

Les coraux actuels descendent de coelentérés primitifs, un groupe qui inclut des méduses, des anémones (actinides) et d'autres invertébrés colorés. La classe qui construit la structure familière de corail est l'Anthozoa. L'animal possède un corps mous qui est pratiquement inconnu parmi les fossiles, mais lorsque le polype croît, il construit un tube de corail calcaire, que l'on trouve fréquemment parmi les fossiles.
Leur histoire est longue (Fig. 3), et parsemée de différentes apparitions et extinctions, que nous allons détailler.

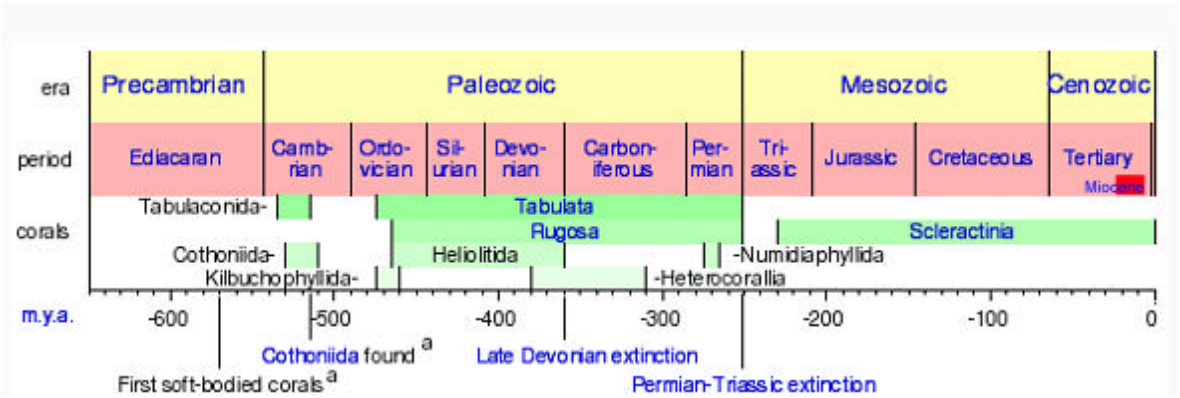

Figure 3. Les différents types de coraux suivants les périodes géologiques. Les coraux du Sud-Est de Majorque sont des Scléracténides (ou Madréporaires) du Miocène.

1.1.3.1 Les premiers coraux

Les premiers coraux apparurent au début du Paléozoïque, au Cambrien, il y a 542m.a. C'étaient des constructeurs de récifs. Les anciens tertres calcaires qui forment les coraux calcaires du Dévonien et du Carbonifère contiennent des récifs de coraux, mais sont construits et cimentés par des algues et des stromatoporoïdes, des organismes en forme de natte et de filet, qui sont apparentés aux coraux. Les fossiles sont extrêmement rares jusqu'à l'Ordovicien, 100m.a. plus tard, quand les coraux rugueux et tabulés se répandirent.

1.1.3.2 Les coraux tabulés

Les coraux tabulés prospèrent au fond de la mer depuis l'Ordovicien jusqu'au Paléozoïque Supérieur. Descendant des Métazoaires Pré- Cambriens, ces coraux construisent un simple tube de calcite creux divisé horizontalement par des « tabulae » plats, comme les étages dans un immeuble miniature. Ces tubes sont toujours en colonies et sont fossilisés en grand nombre dans les calcaires. Ils sont souvent arrondis, mais peuvent être anguleux et polygonaux (comme dans les *Favosites* du Silurien), ou ovales et liés ensemble comme une chaîne, comme dans les *Halysites*. Au moment où ces masses de tubes se développent, une boue calcaire emplit les espaces entre eux, produisant un calcaire tout prêt. Ils sont nombreux à l'Ordovicien et au Silurien ; leurs nombres commencent à décroître au milieu du Silurien et disparurent à la fin du Permien, il y a 250M.A..

1.1.3.3 Les coraux rugueux

Après avoir apprécié une vie en colonie pendant un certain temps, beaucoup de coraux s'établirent dans une vie solitaire. Les coraux rugueux (ainsi dénommés en raison de leur crêtes le long de leur parois externes) peuvent être soit solitaires, soit vivre en colonie. Depuis leur première apparence comme fossiles à l'Ordovicien Supérieur, ils ont proliféré et ont été communs tout au long du Paléozoïque Supérieur. N'ayant pas été aussi exigeants dans leurs besoins d'environnement que les coraux modernes, les coraux rugueux ont habité une variété d'environnements depuis le plateau continental peu profond jusqu'aux régions sous-marines

plus profondes. *Lithostrotion* et *Lonsdalia* vivaient avec des brachiopodes et autres organismes du fond marin peu profond de ce qui est aujourd'hui l'Europe du Nord au moment de la période Carbonifère. *Zaphrentis*, pendant ce temps, vivait dans les eaux sous-marines plus profondes.
Il y a des différences structurelles importantes entre les types tabulaires et rugueux. Les coraux rugueux sont plus complexes avec des partitions internes radiales, ou « septe », un élargissement de leur parois, appelés « dissipement », et des tabules courbes coupant leurs tubes de calcites horizontalement. Les septes sont groupés par quatre (Tétracoralliaires), et comme les coraux rugueux croissent vers le haut, ils construisent plus de septe pour accroître leur force et préserver sa base étroite d'origine, maintenant dessous une structure qui va en s'élargissant. Certains coraux rugueux peuvent atteindre 15cm ou plus haut. Les coraux rugeux devinrent dominant au milieu du Silurien, et disparurent au début du Trias. Les squelettes des coraux rugueux comme des coraux tabulés sont composés de calcite.

1.1.3.4 Les coraux Scléracténides

Les coraux *scléractinides ou Madréporaires*, ou *héxacoralliaires* (en fait, les héxacoralliaires sont un ensemble comprenant huit ordres dont un entièrement fossiles (Tétracoralliaires), les Actinides et les Scléracténides) , sont les représentants modernes, construisant les colorés récifs en eaux peu profondes. Leur histoire commence au Mésozoïque, quand ils commencèrent à prendre le dessus sur les formes tabulés et rugueuses ; ils devinrent relativement communs dans les roches à partir du Jurassique et dans les périodes suivantes. Leurs polypes peuvent être solitaires ou peut s'étendre et se joindre au corps mou dans le théca (la coupe en haut du corail, Fig. 1B) du voisin., devenant lié par des tissus mous. Les polypes, semblables à des anémones de mer, sont en forme de sacs avec des anneaux de tentacules autour de la bouche centrale. Ils diffèrent des coraux rugueux en ce qu'il ont leurs septes groupés en six.
Les paléontologistes ont l'habitude de considérer que ces fossiles dans le calcaire indiquent des conditions de mer chaude et peu profonde au moment où les animaux étaient en vie (Pellant et al., 1985) ; il n'y a pas lieu d supposer que leur système écologique était fondamentalement différent de celui des coraux modernes. Ceci entraîne des conséquences importantes sur les informations potentielles que les Madréporaires peuvent fournir sur les conditions climatiques (Brachert, et al., 2001), et de bathymétrie (Pomar et al., 1996) des temps géologiques.
Les squelettes des scléracténides sont composés d'une forme de carbonate de calcium de composition chimique identique à celle de la calcite, mais de structure cristalline différente nommée aragonite. Cette forme cristalline est plus instable que celle de la calcite, et lorsque les squelettes sont fossilisés ; l'aragonite se transforme relativement rapidement en calcite.

1.1.3.5 Environnement des coraux anciens

A certaines époques géologiques, les coraux étaient très abondants (Fig. 4), tout comme les coraux modernes le sont aujourd'hui dans les eaux chaudes tropicales des certaines parties du monde aujourd'hui. Comme les coraux modernes, leurs lointains ancêtres construisaient des récifs, certains maintenant reposent en tant que larges structures dans les roches sédimentaires.

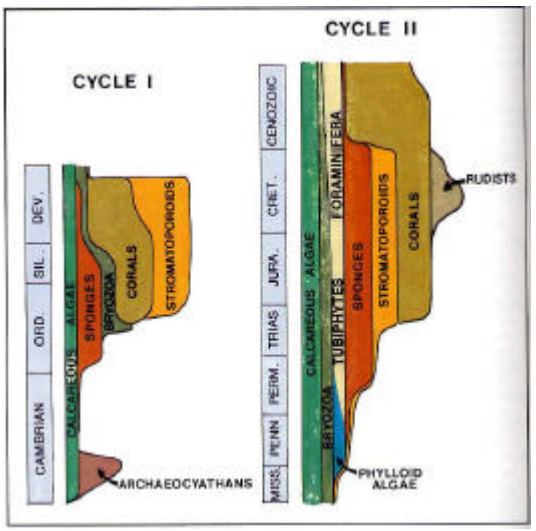

Figure 4. Les principaux composants biotiques des constructions carbonatées au cours des périodes géologiques (Scholle et al., 1983).

Ces anciens récifs ne sont pas composés uniquement de coraux. Des algues, des éponges, et les restes de nombreux échinoïdes, brachiopodes, lamellibranches, gastropodes, bryozoaires, foraminifères, qui vivaient sur les récifs, sont préservés parmi eux (Fig. 4). Ceci fait que certains coraux sont des marqueurs fossiles utiles.

1.1.4 Les genres de coraux du Sud-Est de Majorque

Un nombre relativement restreint de genres de madréporaires a été observé sur les coraux du Sud-Est de Majorque. Le genre le plus souvent représenté est de loin les Porites. Les autres genres ne sont observés qu'en très petits nombres, et sont composés de Sidérastraea, Tarbellastraea, et Montastraea (Fig. 5).

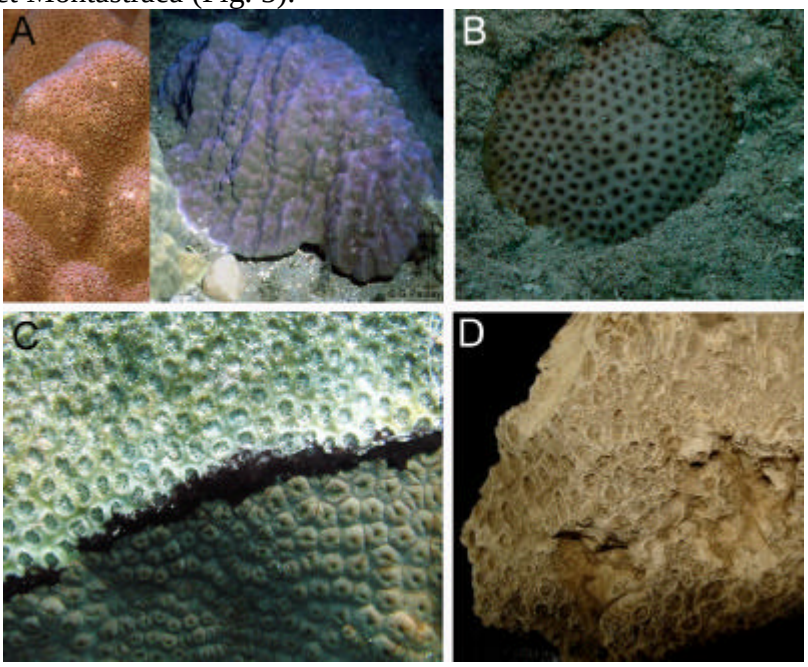

Figure 5. Ces genres de madréporaires ont été retrouvés dans les coraux du SE de Majorque. (A) Corail vivant de Porites Lutea. (B) Corail vivant de Sidérastraea Radians. (C) Corail vivant de Montastraea Cavernosa. (D) Fossile de Tarbellastraea.

1.1.5 La croissance des coraux

Les géologues se sont intéressés à la croissance des coraux depuis très longtemps. Lyells, 1830, a d'abord pensé que la forme en anneau des atolls (Fig. 6C) s'expliquait parce que les coraux avaient crû au-dessus du sommet d'un cratère volcanique submergé. Darwin, 1842, toujours intéressé par la croissance des coraux sur les îles volcaniques (qu'il avait observé de près lors de son voyage sur le Beagle), suggéra que l'effet d'une subsidence supposée pouvait expliquer le remplacement de la déposition continue des sédiments par la croissance vers le haut des coraux, et expliquer la formation de récifs barrières (Fig. 6B et 7) et d'atolls (Fig. 6C). Puis Daly, 1915, proposa que plutôt que la subsidence d'un volcan, la croissance des coraux s'expliquait mieux par l'élévation du niveau de la mer, comme après la fonte des glaciers lors des périodes inter-glacières, les coraux croissants pour garder le rythme d'élévation du niveau de la mer, et rester ainsi dans la zone de profondeur qui leur convenait le mieux (voir § 1.1.2.3 ci-dessus).

On remarquera que cette théorie a l'avantage d'expliquer la croissance des coraux, même lorsqu'ils ne se trouvent pas au voisinage d'îles volcaniques, et c'est plutôt cette théorie qui a été retenue. Aujourd'hui, on considère que les coraux tendent à rester à leur profondeur optimale : de 0 à 30m. Si :

1. le niveau relatif de la mer monte, on obtient soit :
   - une croissance verticale des coraux
   - une inondation, et la mort des coraux
2. le niveau relatif de la mer descend, on obtient soit :
   - une croissance horizontale des coraux et une progradation
   - une exposition, et la mort des coraux

Elle permet ainsi de considérer que les coraux enregistrent dans leurs fossiles les mouvement verticaux eustatiques du niveau marin dans les temps géologiques, qualité exploitée dans Camoin et al., 2001.

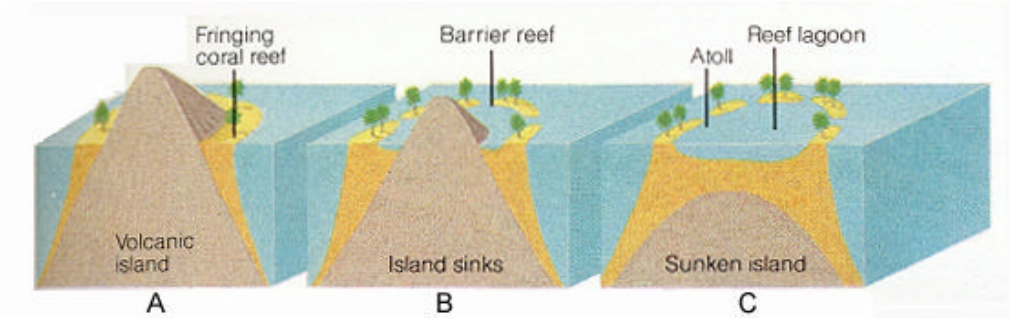

Figure 6. De nombreuses îles volcaniques se trouvent dans des endroits suffisamment chauds pour que les récifs coraux puissent croître. Les pentes douces du volcan sont des sites idéaux pour ces coraux, qui ont besoin d'une profondeur particulière d'eau. Au fur et à mesure que le récif de corail croît, le cône volcanique peut s'effondrer et le niveau d'eau de mer peut s'élever (peut-être dû aussi à la fonte de glaces) ou même les deux à la fois. Le corail continue à croître à la même profondeur et, l'on passe du récif frangeant (A), à la barrière de corail (B), et enfin des atolls classiques se développent (C). Pellant et al., 1985.

Figure 7. A l'île de Bora Bora, une des Iles sous-le-vent, en Polynésie française et dans l'Archipel de laSociété, le récif barrière entoure un lagon tranquille autour du volcan. Pellant et al., 1985.

1.2 Les réservoirs récifaux

La porosité totale dans les sédiments carbonatés a la propriété de ne pas être uniquement une porosité intergranulaire, qui dépend largement de la forme et de la taille des éléments solides, ainsi que de leur classement. Elle est en effet composée également de la porosité vacuolaire, acquise par dissolution, et de la porosité de fissures et de fractures, acquise mécaniquement (Serra, 2000). Les récifs coralliens fossiles forment des sédiments carbonatés, dont la porosité totale près de la surface peut atteindre jusqu'à 70%, et décroît progressivement avec la profondeur d'enfouissement. Ces récifs coralliens fossiles peuvent atteindre des surfaces et des épaisseurs très importantes ; ils peuvent donc former des réservoirs de volume très important. Ces réservoirs contiennent des fluides tels que eau (douce ou salée) et/ ou hydrocarbures (huile ou gaz). Plusieurs champs pétroliers géants ont été découverts dans ce type de réservoirs.

Nous avons étudié des réservoir à eau, tel que le complexe récifal du Sud-Est de Majorque, sujet de cette thèse. D'autre part plusieurs missions Ocean Drilling Program (ODP) ou Integrated Ocean Drilling Program (IODP) ont ciblé des plates-formes carbonatées récifales ; nous avons utilisé les données enregistrées au cours de ces missions comme exemples et comparaison dans plusieurs document en cours de publication qui sont cités en totalité dans cette thèse :

- La Grande Barrière de corail d'Australie (Davies et al., 1990, exemple utilisé dans Maria-Sube et al., sous presse)
- Le Grand Banc des Bahamas (Eberli et al., exemple utilisé dans Maria-Sube et al., sous presse)
- Tahiti (Camoin et al., 2005, exemple utilisé dans Maria-Sube[1] et al., sous presse)

Nous allons maintenant introduire ces sites ci-dessous, d'une manière plus complète qu'elle ne l'a été faite dans les document cités.

1.2.1 La Grande Barrière de Corail d'Australie

La Grande Barrière de Corail (Fig. 8) est le plus grand système de récif corallien du monde. La Grande Barrière est situé dans la Mer de Corail au large du Queensland, au Nord-Est de l'Australie. Elle est composée d'environ 3600 récifs individuels et de 900 îles qui s'étendent sur 2600 kilomètres, de Bundaberg à la pointe du Cape York. Elle couvre une superficie de 350000 km² ; à titre de comparaison, l'Allemagne a une superficie de 357000 km².

Figure 8. Grande barrière de corail, côte Est de l'Australie,. La Grande Barrière, située à environ 300km de la côte, s'étend sur des milliers de kilomètres.

La structure présente de récif corallien vivant est considérée comme ayant commencé à croître sur une plate-forme plus ancienne il y a environ 20000 ans. Le début de la croissance du récif présent aurait ainsi eu lieu au cours du maximum de la dernière glaciation. A ce moment, le niveau de la mer était d'environ 120m plus bas qu'aujourd'hui. La terre qui formait le socle de la Grande Barrière de Corail était une plaine côtière, avec quelques grandes collines (dont certaines étaient elles-mêmes des vestiges de récifs plus anciens).

De 20000 ans jusqu'à il y a 6000 ans, le niveau de la mer est monté régulièrement. Au fur et à mesure qu'il montait, les coraux ont poussé plus haut sur les collines de la plaine côtière. Il y a environ 13000 ans , le niveau de la mer était environ 60m plus bas qu'aujourd'hui, et les coraux commencèrent à croître autour des collines de la plaine côtière, qui étaient alors des îles continentales. Comme le niveau d'eau montait plus haut encore, la plupart des îles continentales furent submergées. Les coraux pouvaient alors envahir les collines de la plaine côtière, pour former les présents cayes (îles d'origine corallienne) et récifs. Le niveau de la mer n'a pas monté d'une manière significative depuis les derniers 6000 ans. L'age de la présente structure de récif vivant est estimé à de 6000 à 8000 ans. Ces précisions sur les variations de niveau marin et de climat ont pu être apportées grâce à l'étude des coraux (Davies et al, 1990).

Les restes d'un ancien récif barrière similaire à la Grande Barrière de Corail peuvent être trouvés dans le Kimberley, une région au Nord de l'Australie de l'Ouest.

1.2.2 Le Grand Banc des Bahamas

Les Bancs des Bahamas sont la plate-forme carbonatée submergée qui comprend une grande partie de l'Archipel des Bahamas. Le terme est utilisé d'habitude pour désigner soit le Grand Banc des Bahamas autour de l'île d'Andros, soit le Petit Banc des Bahamas des îles de Grand Bahama et de Grand Abaco, qui sont les plates-formes les plus grandes (Fig. 9). Les autres bancs sont le Banc Caicos des îles Caicos, et le Banc Cay Sal, au Nord de Cuba, et le banc totalement submergé Silver Bank au Nord de la République Dominicaine.

Figure 9. Photo satellite du Banc des Bahamas. Les nuages apparaissent en blanc. Les terres émergées apparaissent en brun ou vert ; au Sud-Ouest : Cuba ; au Nord-Ouest : la Floride ;au centre, la grande île d'Andros, avec à sa droite, la petite île de Nouvelle Providence ; au Nord, l'île de Grand Abaco, et à sa gauche, l'île de Grand Bahama ; au Sud-Est, les îles Acklins. Il faut compter environ 600km de gauche à droite de la photo. La République Dominicaine est à l'Est de Cuba, et n'est pas visible sur la photo. Le Banc des Bahamas apparaît en bleu pâle sur la photo.

Le calcaire que comprend les Bancs s'est accumulé depuis au moins le Crétacé, et peut-être aussi tôt que le Jurassique ; aujourd'hui, l'épaisseur totale sous le Grand Banc des Bahamas est de plus de 4500m. Comme son calcaire a été déposé en eau peu profonde, la seule manière d'expliquer une colonne aussi massive est d'estimer que toute la plate-forme s'est enfoncée sous son propre poids à un taux d'environ 3,6cm par 1000 ans.
Les eaux des Bancs des Bahamas sont très peu profondes ; au-dessus du Grand Banc des Bahamas, elle ne sont généralement pas profondes de plus de 25m. Les pentes à la périphérie des Bancs, telle que en bordure de la Langue de l'Océan dans le Grand Banc des Bahamas sont très vives. Les Bancs étaient exposés durant les dernières glaciations, quand le niveau de la mer était jusqu'à 120m plus bas qu'aujourd'hui ; la région autour des Bahamas aujourd'hui représente donc seulement une faible portion de leur étendue pré-historique. Quand ils étaient exposés à l'atmosphère, leur calcaire était soumis à l'érosion chimique qui créa les grottes et les avens couramment rencontrés en terrain karstique, et qui se retrouvent aujourd'hui sous l'eau.

1.2.3 Tahiti

Les îles de la Polynésie française, dont font partie les Iles du vent Tahiti et Moorea (Fig. 10B), résultent de l'activité des «points chauds » situés à l'intersection de failles sismiques. L'origine de ces îles est volcanique.

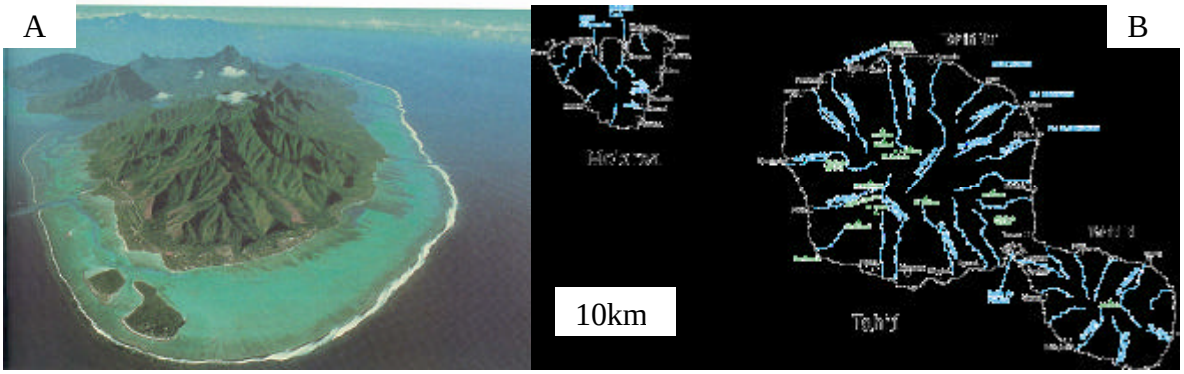

Figure 10. (A) L'île de Moorea, Tahiti, est une île volcanique bordée de récifs coralliens, qui forment une nappe côtière peut profonde, avec récif barrière, lagon, et récif frangeant, Pellant et al., 1985. (B) Carte des îles de Moorea et Tahiti.

Tahiti est longue de 45km à ses points les plus éloignés, et couvre environ 1043 km². L'île se compose de deux parties centrées sur des volcans éteints et reliées par un court bras de terre, l'isthme de Taravao. La plus grande de ces parties est nommée Tahiti Nui (Grand Tahiti) et l'autre Tahiti Iti (Petit Tahiti).

À 15km à l'ouest de Tahiti se situe l'île- sœur Moorea (Fig. 10A), centrée elle aussi sur un volcan éteint, qui représente, en modèle réduit, le même environnement qu'à Tahiti.

Les buts de l'expédition IODP 310, étaient d'établir l'évolution de l'élévation du niveau de la mer au cours de la dernière déglaciation (20000 à 10000 ans avant aujourd'hui), Camoin et al., 2005.

2 Complexe récifal du Sud-Est de Majorque

A l'Est des côtes de l'Espagne, à partir du Cap de la Nao sur la côte Est espagnole, s'étend l'Archipel des Baléares, qui comprend de l'Ouest à l'Est les îles de : Ibiza et Formentera, Majorque, et Minorque. Majorque est la plus grande des îles de l'Archipel. Le complexe récifal Miocène du Sud-Est de Majorque est localisé sur les cartes géologique simplifiées de tous les documents soumis à publication qui font partie de cette thèse (Maria-Sube et al., Maria-Sube[1] et al., Maria-Sube[2] et al., Maria-Sube[3] et al.).
Les îles de l'Archipel ont une histoire géologique commune, que nous allons maintenant présenter.

2.1 Histoire géologique de Majorque

2.1.1 Les roches de surface

Les roches les plus anciennes de la surface de Majorque (Fig. 11B) sont de la période Paléozoïque ; seulement quelques affleurements existent ; et ils sont de la période Carbonifère (-359 à –299m.a.). Les séquences mésozoïques commencent avec un Triassique (-251 à –200m.a.) de type Allemand (faciès Buntsandstein, Muschelkalk et Keuper), et une épaisse couche de calcaires Jurassiques (-200 à 145,5m.a..) le suit. Ils recouvrent la plupart des sommets de montagnes (Sierra de Tramuntana et Sierres de Llevante) et falaises, et de nombreux recouvrements sont constitués de récurrences de ces couches du Jurassique Inférieur. Des dépôts pélagiques constituent le reste de la séquence Mésozoïque. Les roches du Cénozoïque Inférieur sont inconnues dans l'île, probablement en raison de l'émergence de la région durant cette période. Le premier dépôt du Cénozoïque appartiennent à l'Eocène Moyen, et elles contiennent des calcaires à eau douce et des veines de charbon. Les dépôts de l'Oligocène contiennent des séquences d'éventails alluviaux venant du Nord-Ouest, et des sédiments côtiers. Les roches du Miocène Inférieur, du Pliocène et du Pléistocène sont déposées dans des bassins plus ou moins restreints, post- orogéniques, et correspondants à des environnements côtiers.

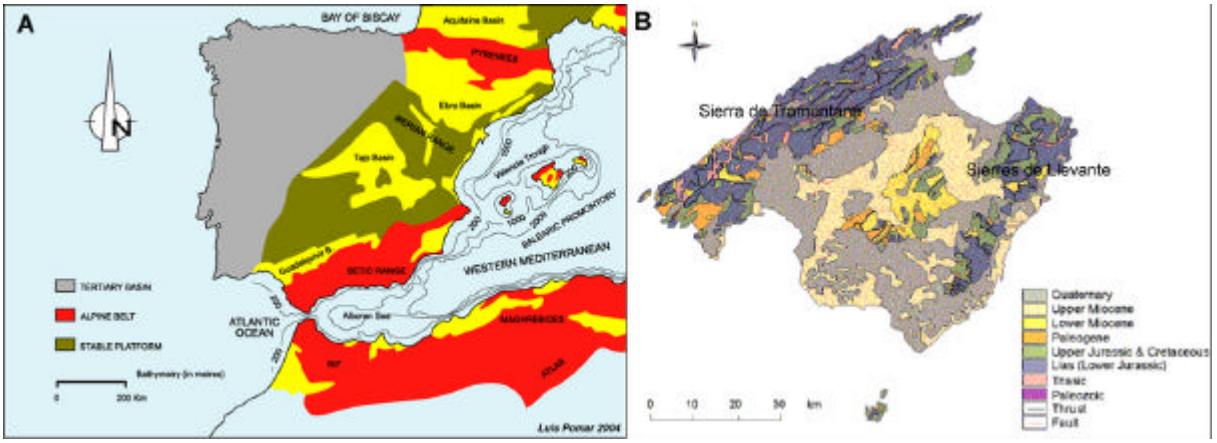

Figure 11. (A) Carte géologique du promontoire des Baléares et de la chaîne alpine Espagne- Afrique du Nord (Pomar, 2004). (B) Carte géologique de Majorque.

2.1.2 Synthèse géodynamique de la Méditerranée occidentale

Pour comprendre la géologie de surface de Majorque qui vient d'être évoquée, il est nécessaire de faire appel à la théorie de la tectonique des plaques à une échelle mondiale. Smith et Woodcock, 1982 ont décrit que l'évolution pendant le Mésozoïque et le Cénozoïque du géosynclinal de Téthys fut une conséquence des mouvements relatifs à partir du super-continent de la Pangée du Trias des continents d'Amérique, d'Afrique et d'Eurasie. A cette

époque, l'Ibérie était séparée de la France par une grande faille et décalée de 400km vers l'Ouest par rapport à sa position actuelle ; le bloc corso- sarde appartenait alors à la partie Est de l'Ibérie, et la Corse se trouvait au Sud de l'actuelle chaîne des Pyrénées (qui n'existaient pas encore), Mattauer, 2001. Cette évolution se traduisit par une translation lévogire de l'Afrique par rapport à l'Amérique et à l'Eurasie. Avec celle-ci, se crée d'abord un Atlantique Sud et aussi l'Océan Téthys entre Afrique et Eurasie.

Plus tard, au Crétacé Supérieur (Santonien, -85,8 à – 83,5m.a.), le mouvement entre ces deux derniers continents se fit dextrogire et compressif. L'ouverture de l'Atlantique Nord se produit, et, simultanément, le lent mouvement des plaques a fait coulisser l'Ibérie le long de la grande faille, ouvrant le Golfe de Gascogne, et la Corse s'est retrouvée plus à l'Est, avec la Sardaigne au Sud du Golfe du Lion.

Ensuite, il y a environ 40m.a., l'Ibérie, incluant la Corse et la Sardaigne après la dérive vers l'Est, s'est raprochée de l'Europe en se déplaçant vers le Nord. La compression résultant de ce déplacement a fait surgir la chaîne des Pyrénées (Fig. 11B), dont les reliefs allaient de l'Atlantique à la Côte d'Azur actuelle. Des montagnes se trouvaient alors dans le Golfe du Lion.

Il y a 30m.a., un très grand bouleversement a modifié le relief de l'Ouest de l'Europe et de la Méditerranée. En France, des fossés d'effondrement se sont ouverts, du fossé rhénan au Languedoc. Lors de cette extension, la chaîne des Pyrénées s'est effondrée à l'emplacement actuel du Golfe du Lion. Cette extension a continué doucement pendant une dizaine de m.a.

Il y a 20m.a., l'étirement s'est brusquement accéléré et a provoqué l'ouverture du petit océan méditerranéen, avec la rotation du continent corso- sarde, enfin indépendant, jusqu'à sa position actuelle. La Péninsule Italique, qui s'était fichée dans l'Afrique par un contact Sicile-Tunisie vers –160m.a., ensuite vers -20m.a., comme une microplaque autonome, crée les Alpes par collision et rotation.

Le Bassin Sud- Baléares – Mer de Alboran est entouré par le promontoire des Baléares, la Cordillère Bétique, le Riff et l'Atlas Tellien (Fig. 11B). Ce double système de polarité tectonique divergente est uni par le grand arc de Gibraltar (Riba et Arderiu, 1983).

Le promontoire des Baléares est considéré par tous les auteurs comme une prolongation subsidente de la Cordillère Bétique dont émergent les îles Baléares ; cette région s'est prolongée au Nord-Est avec le bloc Corso- Sarde adjacent à la marge Méditerranéenne Catalogne- Provence. Pour Ibiza et Majorque, les faciès méso- cénosoïques correspondraient à l'unité sub- Bétique andalouse.

Le système alpin, formé par les Cordillères Bétiques, tourne vers le Sud, enlacé par les Cordillères du Riff, l'Atlas Tellien, l'Arc de Sicile- Calabre et continue par les Apennins. Les Alpes, les Pyrénées, la Cordillère Bétique se forment simultanément en un intervalle de temps compris entre le Crétacé Supérieur et l'Oligocène, avec les ultimes phases situées dans le Miocène Moyen.

La paléo- géographie de la Méditerranée occidentale était encore très distincte de la géographie actuelle. Selon Mauffret, 1976, à l'Oligocène, la ligne de la côte passait par le Cap de la Nao, peut-être par le Sud de Formentera, et par le Sud de la Sierra de Tramuntana majorquine, et ensuite, très au Sud de Minorque.

Durant l'Oligocène Supérieur commence le détachement rotatoire du bloc Sardo- Corse adhéré à la Péninsule Ibérique, qui entraîne le charriage vers le Sud-Est de l'île de Minorque, selon des failles NO-SE, avec un déplacement relatif de 75km, et pour Majorque de 15km, dans la même direction. Ces déplacements, ou extensions, commencent l'ouverture de la fosse de Valence, ou Mer de Catalogne- Baléares, avec un enfoncement de l'écorce terrestre suivant une arête orientée parallèlement à la Catalogne, qui se prolonge par les fosses Rhodaniennes et Rhénanes.

Au Nord des Baléares, la phase de dérive du Bassin Baléarico- Provençal se produit en une courte période de temps comprise entre l'Aquitanien et le Burdigalien Inférieur, avec création d'écorce océanique. Une telle ouverture fut suivie d'une forte subsidence provoquée par le refroidissement de la lithosphère océanique, et à la surcharge d'eau et de sédiments (7 à 9km). Pour le bassin Sud des Baléares, entre les Baléares et la côte africaine, il est admis que l'extension du bassin, par translation des Massifs de Kabylie vers le Sud, est contemporain de la formation de l'arc de la Mer d'Alboran.
Dans le contexte de Majorque, les événement compressifs majeurs eurent lieu durant le Miocène Moyen, en même temps que la formation de la Cordillère Bétique et (Pomar et al., 1996) et des chaînes Maghrebines. Le Basin de Campos a subsidé seulement au début du Pléistocène (Jenkyns et al ., 1973).

2.2 Datation des coraux du Sud-Est de Majorque

Pomar et al., 1996, ont daté par plusieurs méthodes (micropaléontologie, isotopes Sr., K-Ar.) le complexe récifal du Sud-Est de Majorque, à l'affleurement de la falaise de Cap Blanc. Ils obtiennent –8m.a. (Tortonien Supérieur) dans la partie basse du récif (talus proximal) et –6m.a. (Messinien Moyen) dans la partie haute, identifiée comme un lagon interne par Pomar et al, 1996. Ces datations indiquent que la totalité du récif date du Miocène Supérieur, et confirme la progradation du récif décrite par ces auteurs. D'autre part, les complexes récifaux des autres îles Baléares (Fig. 12) sont également attribués à l'époque Tortonien Supérieur à Messinien (Bizon et al., 1973 ; Alvarro et al. 1984 ; Pomar et al., 1983). Tout ceci suggère donc un large ensemble récifal des îles Baléares datant du Tortonien Supérieur au Messinien.
Plus récemment, des datations de carottes ont été faites (Camoin, travail en cours) sur le site de Ses Sitjoles, situé dans le complexe récifal du Sud-Est de Majorque 16km au NE de Cap Blanc, par la méthode Sr. 87/86. Les résultats obtenus sont : -22m.a. (Aquitanien) pour la partie basse du récif (talus proximal), -17m.a. pour le cœur du récif (Burdigalien), soit pré-orogénique, et –6m.a. pour la partie haute, identifiée comme étant un Terminal Carbonate Complex (TCC, voir ci-dessous) coéval avec le « lagon interne » de Pomar et al., 1996 (voir Maria-Sube et al., sous presse), soit post-orogénique. Ainsi, pour la première fois dans l'Archipel des Baléares, des récifs coralliens du Miocène Inférieur ont été reconnus. D'autre part, Camoin a aussi daté des carottes provenant du récif des puits récemment forés S19 et S20, situés à mi-chemin entre Cap-Blanc et Ses Sitjoles ; ces mesures datent le récif au Tortonien. Ceci confirme une progradation de la construction récifale à Majorque orientée NE-SO, commençant au Miocène Inférieur (-23m.a.) et s'arrêtant au Miocène Supérieur (-5,3m.a.).

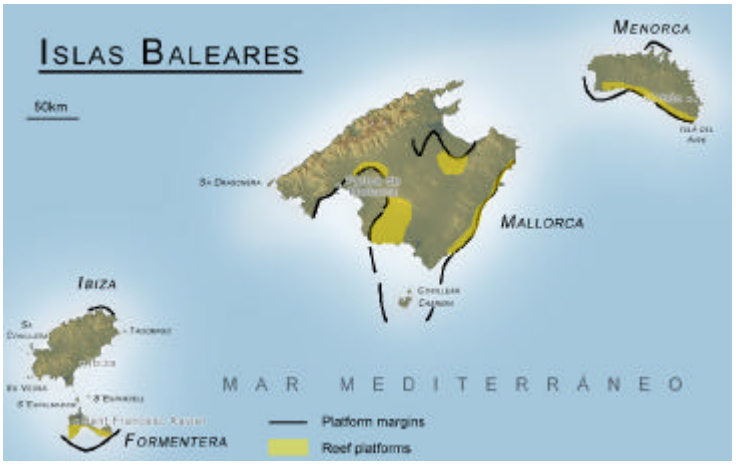

Figure 12. Plate-formes récifales Miocène dans l'archipel des Baléares (d'après Pomar et al., 1996).

2.3 Climat et niveau eustatique dans la Méditerranée occidentale au Miocène

Pomar et al., 1996, décrivent les variations de climat et de niveau de la mer en Méditerranée occidentale au cours de l'époque Miocène de la façon suivante (Tab. 1 et Fig. 13) :

- Les ages **Aquitanien** et **Burdigalien** sont chauds et humides. Le niveau de la Méditerranée est en moyenne environ 100m au-dessus du niveau actuel. La courbe du niveau de mer Néogène présente une pulsation transgressive de l'Aquitanien au Serravallien, durant laquelle une grande partie des Baléares furent inondées. A la frontière Aquitanien-Burdigalien commence l'orogénèse alpine qui va se poursuivre jusqu'au Serravallien Moyen
- Durant l'age **Langhien**, le climat commence à se refroidir
- Durant l'age **Serravallien**, le climat est généralement froid. Une régression se produit à la frontière Serravallien- Tortonien, qui coïncide avec la dernière phase de compression Baléares et le placement des couches supérieures de la Serra de Tramuntana
- A l'age **Tortonien**, le climat est sec et commence à se réchauffer durant le Tortonien Inférieur, et atteint un point haut durant le Tortonien Supérieur. Une seconde transgression post-tectonique commencée durant le Tortonien forme les plate-formes carbonatées qui couvrent une grande partie du Sud-Est de Majorque, le Migjorn minorquin, l'île de Formentera et une partie d'Ibiza (Riba y Arderiu, 1983)
- Au **Messinien** Inférieur, le climat sec commence une tendance refroidissante, qui atteindra son point le plus bas seulement dans le Pliocène Supérieur, au Plaisancien.

Durant toute la période Néogène (Du Miocène Inférieur à la période actuelle), les changements de température sont très lents (géologiquement parlant) comparés au changements de température beaucoup plus rapides et beaucoup plus froids qui se sont produits durant l'époque du Pléistocène, qui a vu se produire les seules glaciations de toute la période (Fig. 14). Ce fait est une des raisons majeures pour laquelle les coraux modernes ne présente pas les mêmes caractéristiques que les coraux du Miocène.

Période	Sous-période	Température	Niveau d'eau	Coraux
Miocène	Messinien	Refroidissement	Retour de la mer Episode Messinien Régression Haut	Disparition des Madréporaires hermatypiques Méditerranéens en raison de la haute salinité de l'eau ; formation d'un TCC stromatolitique.
	Tortonien	Chaud	Transgression	Explosion de la construction récifale Durant le Tortonien Supérieur, mais avec seulement deux genres de Madréporaires: *Porites* et *Sidérastraea*
	Serravallien	Froid	Haut	Hiatus dans la construction récifale
	Langhien	Refroidissement	Haut	Moins de variété dans les genres de Madréporaires
	Burdigalien	Chaud	Haut	Grande variété de genres dans les Madréporaires, mais faible construction récifale
	Aquitanien	Chaud	Haut	

Tableau 1. Température, niveau de la mer, et effet sur les coraux de Majorque, suivant les périodes géologiques.

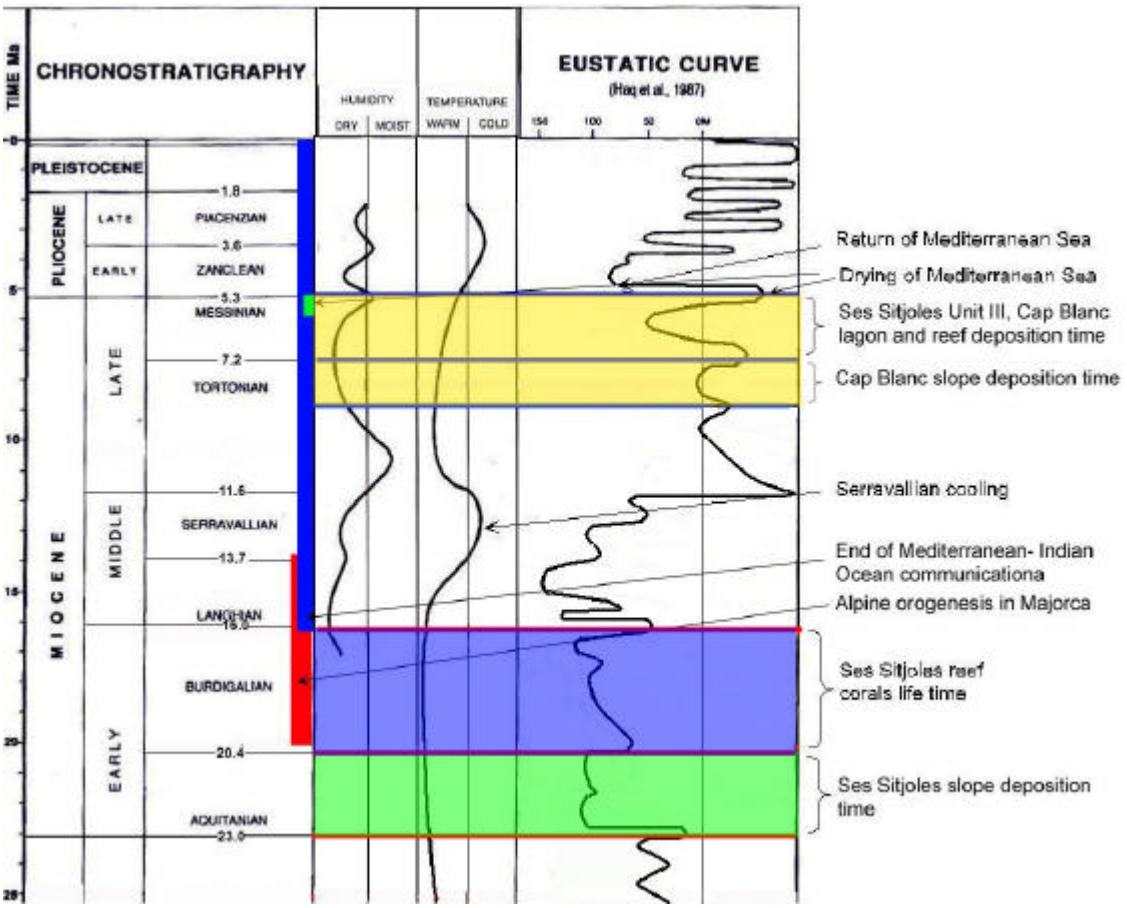

Figure 13. Humidité, temperature et niveau d'eau dans la méditerranée Durant les périodes Néogène et quaternaire (adapté de Pomar, 2001 ; courbe eustatique d'après Haq et al., 1987 : le niveau 0 correspond au niveau d'aujourd'hui, positif est au-dessus du niveau actuel). L'assèchement de la Méditerranée correspondit à un niveau bas eustatique de –60m, insuffisant en soi pour l'expliquer, le niveau de la Méditerranée atteignant à ce moment un niveau beaucoup plus bas que celui indique sur la figure. Datation de l'orogénèse alpine à Majorque selon Riba y Arderiu, 1983. Datation de la crise de salinité Messinienne (MSC) selon Cornée et al., 2002.

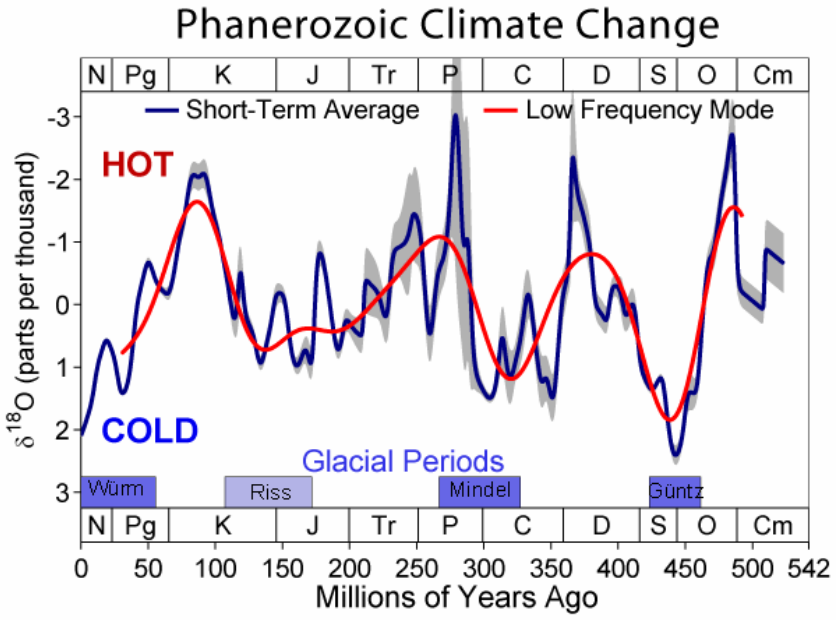

Figure 14. Les glaciations-déglaciations du Pléistocène, mesurées par le rapport $d^{18}O$ dans les glaces fossiles (Veizer et al., 1999).

2.4 Conséquence sur les coraux Miocène de la Méditerranée occidentale

Plusieurs auteurs (Sun et Esteban, 1994, Brachert et al., 2001) ont décrit de la façon suivante (Tab. 1) les conséquences des changements de climat du Miocène sur les coraux de la Méditerranée (Fig. 15) :

- **Aquitanien** et **Burdigalien** (Miocène Inférieur) : il y a une grande variété de genres de Madréporaires, mais une faible construction récifale (Chevalier, 1977 ; Saint Martin, 1990)
- **Langhien** : après la rupture de communications Méditerranée- Océan Indien, la salinité augmente, le nombre de genres de Madréporaires observé diminue (Chevalier, 1977 ; Saint Martin, 1990, voir aussi Lieske et Myers, 2004 : dans la Mer Rouge actuelle, où la salinité est de 42 g/l, les genres de Madréporaires représentés sont principalement *Acropora* et *Porites*)
- **Serravallien** : en raison du refroidissement du climat, un hiatus dans la construction récifale est observé dans toute la Méditerranée (Saint Martin, 1990). La rupture de communications entre la Méditerranée et l'Océan Indien à -14m.a. est estimée avoir contribué à l'évolution vers un refroidissement de l'eau, la Méditerranée devenant un bassin Atlantique marginal (Chevalier ; 1977, Hsü, et al., 1977 ; Rouchy et Saint Martin, 1992)
- **Tortonien** : Une transgression est observée. Une explosion dans la transgresion récifale correspond au Tortonien Supérieur, mais seulement avec deux genres : *Porites* et *Siderastraea* (Chevalier, 1977 ; Saint Martin, 1990). On pense que ceci est dû à la fermeture progressive des deux bras de mer (Fig. 15), par lesquels se faisait la communication Atlantique- Méditerranée, et de l'augmentation correspondante de salinité. L'existence de ces bras de mer est attestée par la présence de récifs coralliens fossiles, l'un au Nord, dans la Cordillère Bétique, l'autre au Sud, dans le Riff Maroquin et l'Atlas Tellien Algérien. Cette fermeture de communications était peut-être due à l'abaissement du niveau eustatique mondial, mais plus probablement à des évènement tectoniques locaux. L'augmentation de la salinité a quelquefois permis une spectaculaire et partielle re- colonisation des édifices coralliens, avec d'autres organismes, tels que des annélides, participants à cette dynamique (Saint Martin, 1990)
- **Messinien** : La température commence à baisser depuis le Messinien Inférieur. Au même moment, les communications Atlantique- Méditerranée sont momentanément interrompues, avec en conséquence un mouvement régressif, et une augmentation de salinité. C'est la « Messinian Salinity Crisis » (MSC), qui conduit finalement à l'assèchement de la Méditerranée ; d'où la présence dans le plancher profond de la Méditerranée d'évaporites (Hsü et al, 1973, 1877 ; Krijgsman et al., 1999), et de formations marginales évaporitiques Méditerranéennes (Saint Martin, 1990 ; Cunningham et al., 1994 ; Riding, et al., 1991 ; Braga et Aguirre, 2001 ; Cornée et al., 2002), similaires à l'unité Gypsum and Grey Marls du bassin de Palma à Mayorque (Pomar, 1991 ; Pomar et al., 1996), durant le Messinien Supérieur (de –5,96 à –5,33m.a. ; Hsü et al, 1973 et 1977 ; Saint Martin, 1990 et 2003 ; Krijgsman et al., 1999 ; Duggen et al., 2003). Les remplissages et évaporations récurrents se terminent par une inondation finale à la fin du Messinien, qui ; avec l'entrée d'eaux Atlantiques plus froides, est la perturbation environnementale majeure contrôlant les étapes finales (Esteban, 1979). Le Messinien correspond à la fin de la construction récifale en Méditerranée ; cette disparition se produit durant le Messinien, et elle est antérieure à l'épisode évaporitique principale (Saint Martin, 1990). Esteban, 1979 ; Saint Martin,

1990 ; Rouchy et Saint Martin, 1992 ; Cunningham et al., 1994 ; Pomar et al., 1996 ; Riding et al., 1991 et 1998 ; et Cornée et al., 2002, mentionnent un « Terminal Carbonate Complex » (TCC) stromatolitique, qui correspond à une extension des eaux résiduelles, et à un confinement plus accentué, avec des mouvements d'eau durant le Messinien.

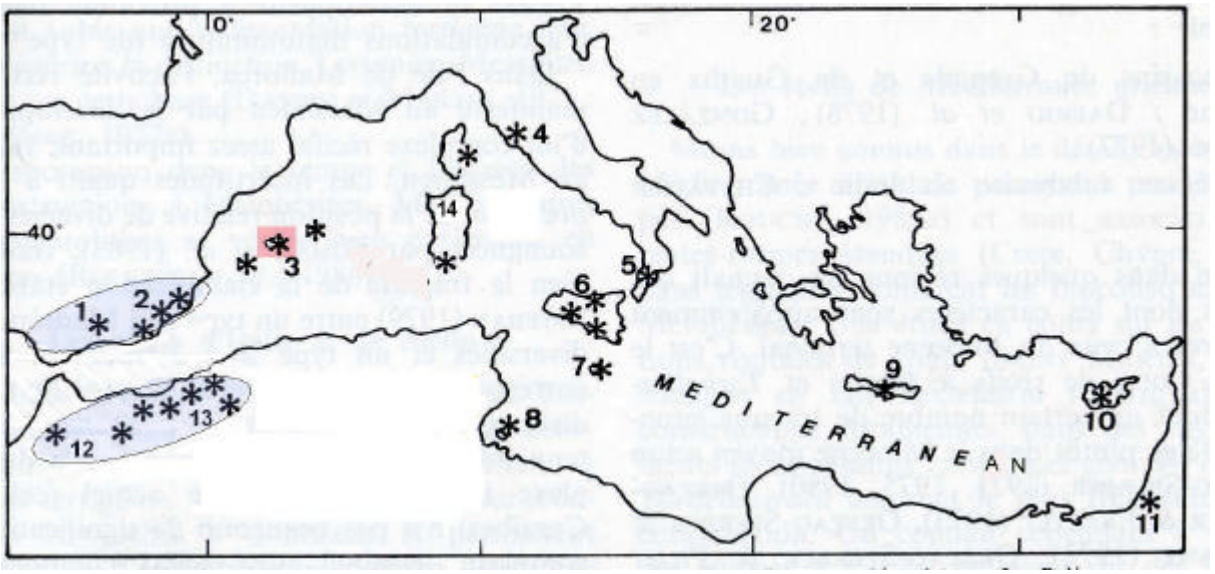

Figure 15. Localisation des principales zones de récifs coralliens (*) du Miocène Supérieur en Méditerranée. 1 : Bassin de Grenade ; 2 : Bassin du Levant Espagnol (entre Alicante et Almeria : Nijar, Purchena, Sorbas, Fortunas, Santa Pola) ; 3 : Baléares : Majorque (rectangle rose, aire d'étude), Minorque, Ibiza, Formentera ; 4 : Toscane : Livourne ; 5 : Calabre ; 6 : Sicile ; 7 : Malte ; 8 : Golfe de Gabes ; 9 : Crète ; 10 : Chypre ; 11 : Israël ; 12 : Maroc : Séfrou, Taza, Melilla ; 13 : Algérie : Tafna, Oran, Tessala ; 14 : Corse, Sardaigne. D'après Saint Martin, 1990, et Pomar et al., 1996. Les ellipses ombrées en bleu sont les bras de mer, Bétique au Nord et Riffain au Sud, pour la communication Atlantique à Méditerranée.

Pour toutes les raisons énoncées ci-dessus, Esteban, 1979, a dit: «les derniers coraux de la Méditerranée ne sont pas comparables aux coraux tropicaux modernes », tandis que Sun et Esteban, 1994, ont dit : « dans des milieux arides, confinés, sous-tropicaux à tempérés, des conditions environnementales peu favorables causées par une salinité augmentant périodiquement, et probablement par des températures relativement basses, ont restreint la pleine croissance des constructions carbonatées. En conséquence, des récifs coralliens frangeants, relativement minces et étroits, avec des lagons faiblement développés dans des rampes rhodalgales, forment les faciès les plus communs du Miocène Supérieur de la Méditerranée ». Ces affirmations seront vérifiées avec les comparaisons d'une part du complexe récifal du Sud-Est de Majorque, et d'autre part les complexes récifaux de la Brande Barrière de Corail, du Grand Banc des Bahamas (Maria-Sube et al., soumis), et de Tahiti (Maria-Sube[1] et al., soumis)

Saint Martin, 1990, décrit les quatre principaux groupes de récifs du Miocène suivants en Méditerranée :

- Groupe 1 : **récifs frangeants ou de hauts-fonds**, soumis à des apports terrigènes qui perturbent l'édification et montrant une stratification des constructions ; il en résulte un aspect étagé en escalier caractéristique ; il s'agit d'ailleurs de récifs qui développent le maximum de puissance (50 à 60m) et ne présentent pas nettement la différenciation structurale classique avec lagon, platier et front récifal ; enfin, le genre *Porites* y joue un rôle de pionnier et de stabilisateur, tandis que globalement les constructions sont plurigénériques

- Groupe 2 : **récifs frangeant avec un relief bien marqué** et soumis à des décharges détritiques importantes ; il s'agit de corniches assez étroites (ne dépassant pas 100 à 200 mètres) réalisées par plusieurs genres de Madréporaires
- Groupe 3 : **récifs de plates-formes** étroitement liés au développement des *Mélobésiées* et en général peu développés ; les genres *Porites* et *Tarbellastraea* y sont dominants
- Groupe 4 : **récifs monogénériques à Porites présentant des phénomènes de progradations** et une importante contribution des thalles d'*Halimeda* à la sédimentation

Dans les récifs d'Espagne et des Baléares, on retrouve tous ces groupes.

3 Les moyens d'étude

Dans ce chapitre, nous allons présenter les moyens d'étude utilisés pour cette thèse. D'une manière générale, deux moyens principaux d'étude ont été utilisés : 1) les affleurements sur site ; 2) les sites de forage.
Les sites de forages permettent d'utiliser deux moyens d'étude principaux : 1) les carottes ; 2) les diagraphies.
Les carottes permettent de : 1) faire des observations visuelles ; 2) obtenir des lames minces qui permettent de faire des observations au microscope optique ou électronique ; 3) obtenir des bouchons sur lesquels des mesures pétrophysiques peuvent être obtenues ; 4) obtenir des échantillons sur lesquels d'autres mesures en laboratoire, généralement destructives, peuvent être obtenues.
Les diagraphies utilisées dans cette étude sont principalement de deux sortes : 1) diagraphies d'images de la paroi du trou ; 2) diagraphies conventionnelles.
Ainsi, on voit donc qu'en utilisant l'ensemble de ces moyens, nous nous sommes donnés les moyens de faire une étude à la fois multi-scalaire, et multi-disciplinaire.
Ces moyens d'études sont détaillés dans chacun des quatre documents soumis à publication, chaque fois qu'ils sont utilisés. Nous allons simplement les présenter ci-dessous d'une manière synthétique.

3.1 Affleurements

Les affleurements de coraux Miocène du Sud-Est de Majorque sont spectaculaires et particulièrement observables sur les falaises le long de la côte. Ils ont été décrits de manière extensive par Pomar, 1991 ; Pomar et Ward, 1994, 1995 ; Pomar et al., 1996 ; et Pomar et Ward, 1999, particulièrement sur la côte entre Cap Blanc et Valgornera (voir aussi Maria-Sube[1] et al., sous presse).

3.2 Sites de forage

Le site de forage de Ses Sitjoles (12 forages de 100m de profondeur) a été soigneusement conçu dans un carré de 100m X 100m pour varier des distances d'un puit à l'autre allant de 2,30m à 100m (Maria-Sube et al., sous presse), avec des géométries variant du groupement concentré au grand carré, en passant par un alignement. Le puit MC2 de Ses Sitjoles a été considéré comme puit de référence.
13 autres forages, de profondeur pouvant atteindre jusqu'à 321m, disséminés sur l'ensemble du complexe récifal Miocène du Sud-Est de Majorque, permettent d'avoir une vision sur un domaine couvrant une étendue de 20km par 35km (Maria-Sube[1] et al., sous presse).
Certains des 25 forages utilisés (9 d'entre eux) étaient déjà pré-existant avant cette étude, et avaient été forés par les service d'hydrogéologie de Majorque, avec comme but l'étude et l'observation de la qualité de la nappe phréatique.

3.3 Carottes

Sur l'ensemble de ces 25 forages, 16 étaient des nouveaux puits, les autres étant des forages anciens. Parmi les nouveaux puits, 12 ont été carottés d'une manière continue.

3.3.1 Observation visuelle

Les carottes, généralement de 8cm de diamètre, sont sciées longitudinalement ; elles peuvent ainsi être observées et photographiées soit intérieurement, soit extérieurement (Voir Maria-Sube et al., et Maria-Sube[3] et al., sous presse).

3.3.2 Lames minces

A partir des carottes de MC2, des lames minces soit pour microscope optique, soit pour microscope électronique, ont été faites à ETH, Oviedo, et au CEREGE. Les résultats sont exposés dans Jaeggi, 2006, Mateos et al., sous presse, Bonnier, 2005, Maria-Sube et al., et Maria-Sube[2] et al., sous presse. D'autres lames minces sur les carottes des puits MC1, MC3 et MC5 ont été faites à ETH (Jaeggi, 2006). Les observations sur lames-minces conduisent à des résultats de sédimentologie, tels que micro-paléontologie, cimentation et diagénèse, et nature des cristaux.

3.3.3 Mesures pétrophysiques sur bouchons

116 bouchons de 2,5mm de diamètre et 22mm de long ont été taillés dans les carottes du puit MC2. Des mesures pétrophysiques statiques (porosité, densité de grain, propriétés électriques et vitesses acoustiques) et dynamiques (perméabilité, potentiel électrocinétique) ont été effectuées sur ces bouchons (Maria-Sube[2] et al., sous presse).

3.3.4 Autres mesures en laboratoire

Des échantillons supplémentaires ont été prélevés sur les carottes du puit MC2. Ces échantillons ont permis de faire d'autres mesures en laboratoire, généralement destructives : porosimétrie mercure, CEC, spectrométrie rayons-X.

3.4 Mesures et images en forage

L'équipe «subsurface » du département de Géosciences à l'Université Montpellier 2 dispose de facilités d'enseignement, de maintenance et d'expérimentation au site de Lavalette à Montpellier, qui possède trois forages de 100m de profondeur. De plus Lavalette dispose d'une série d'outils de diagraphies de faible diamètre extérieur pour mesures dans les forages à eau de faible profondeur (moins de 1000m, la principale limitation provenant de la température maximum, qui pour certains outils n'excède pas 50°C), avec deux véhicules équipés d'un câble de logging, permettent d'effectuer ces mesures partout en France, en Europe, et même dans le monde. Ainsi une campagne IODP de mesures a été effectuée en 2005 sur plate-forme de forage au large de Tahiti (Leg 310, Camoin et al., 2005).
Alors que les carottes permettent d'évaluer d'une manière aussi précise que possible, mais ponctuelle, les caractéristiques sédimentologiques, pétrophysiques, de composition minérale des roches du forage, les diagraphies permettent une évaluation continue de ces roches.
On distingue les diagraphies d'imagerie de la paroi du puit et les diagraphies dites conventionnelles.

3.4.1 Images de la paroi du puit

Parmi les outils de diagraphies de faible diamètre extérieur dont dispose l'équipe subsurface, les outils de diagraphies d'imagerie de la paroi du puit (Tab. 2) sont ceux qui supportent la comparaison avec les outils de diagraphies de large diamètre de l'industrie pétrolière avec le plus d'avantages. En effet, les outils d'imagerie de la paroi du puit de faible diamètre non seulement présentent une meilleure résolution que les outils correspondants de l'industrie pétrolière, mais en plus, ce sont des outils mandrin 360° complet, qui ne présentent pas les images coupées des outils à patins de l'industrie pétrolière, en raison des séparations entre les patins. Ces outils ont été utilisés dans tous les quatre articles sous presse reproduits plus loin, qui font partie de cette thèse.

Nom de l'outil	Nature	Constructeur/ Logiciel d'acquisition	Diamètre extérieur de l'outil (mm)	Mesures
FAC40, puis ABI40	Imagerie acoustique	ALT/ALT	40	Inclinométrie, imagerie acoustique amplitude et temps de parcours (diamètre des capteurs : 3 mm)
OBI40	Imagerie optique	ALT/ALT	40	Inclinométrie, imagerie optique (diamètre des capteurs : 1mm)

Tableau 2. Les outils d'imagerie de la paroi du puit de l'équipe subsurface.

3.4.2 Diagraphies conventionnelles

Les outils conventionnels de l'équipe subsurface offrent une panoplie assez complète des différents moyens possibles.

Nom de l'outil	Nature	Constructeur/ logiciel d'acquisition	Diamètre extérieur de l'outil (mm)	Mesures
SGR 1428	Spectral GR	Antares/ ALT	52	Uranium, Thorium, Potassium, GR total naturel
ELXG	Diagraphie électrique	Robertson-Geologging/ ALT ou RG	44	Gamma Ray total naturel, SP, Short Normal, Long Normal, Single point Resistance
GLOG	Latérolog 3	Robertson-Geologging/ ALT ou RG	42	Résistivité focalisée
DIL 45	Dual induction	ALT/ALT	40	Résistivité des formations
PNN	Neutron	Antares/ALT	40	Porosité neutron
	Sonic à un émetteur monopole ou dipôle et trois récepteurs	Mount Sopris Instrument Co/ ALT	39	Vélocité acoustique Vp, Vs et Stoneley, distance entre récepteurs, 1, 2 ou 3 pieds, fréquence réglable entre 1 et 30kHz
	Diamétreur à trois bras solidaires	Mount Sopris Instrument Co/ ALT	45	Diamètre du trou. Ouverture maximum des bras : 47cm
Idronaut	Hydrogéologie	ALT/ ALT	50	Propriétés du fluide dans le puit : Conductivité, Pression, température, pH, Eh, Oxygène dissous
Muset	Hydrogéologie	ALT/ ALT	50	Propriétés du fluide dans le puit : Conductivité, Pression, température, pH, Eh, Oxygène dissous ; et SP
IMPF	Débit-mètre à hélice	RG/ RG	45	Débit de fluide

Tableau 3. Les outils de diagraphie conventionnels de l'équipe subsurface.

Ainsi, les outils suivants (Tab. 3) sont disponibles, et ont été utilisés dans les documents sous presse cités ci-dessous :

- Un outil de spectrométrie du gamma-ray naturel (SGR), qui permet une investigation du contenu minéral radioactif des roches, ainsi qu'une investigation sédimentologique et environnementalle (Maria-Sube et al, Maria-Sube[1] et al., sous presse)
- Trois outils de mesure de résistivité (ELXG, GLOG, DIL), qui peuvent être utilisés alternativement en fonction de la gamme de résistivité à mesurer dans la formation (Maria-Sube[3] et al., sous presse)
- Deux outils de mesure de porosité (Neutron et Sonic), Maria-Sube[3] et al., sous presse
- Un diamétreur (Maria-Sube[3] et al., sous presse)

- Deux outils d'hydrogéologie (Idronaut et Muset), permettant de mesurer les propriétés de l'eau du forage (et dans notre cas, de l'eau de formation également), Maria-Sube[2] et al., Maria-Sube[3] et al., sous presse
- Un outil de mesure du débit dans le forage

4 Publications

Dans ce chapitre sont reproduits les quatre documents en cours de publication et cités en référence (Maria-Sube et al., Maria-Sube[1] et al., Maria-Sube[2] et al., et Maria-Sube[3] et al.). Les deux premiers documents ont trait à la sédimentologie et aux environnement de déposition, l'un au site de Ses Sitjoles, l'autre sur l'ensemble du complexe récifal, le troisième document présente les résultats de mesures pétrophysiques obtenus sur les carottes de Ses Sitjoles, et le quatrième traite de structure de porosité à Ses Sitjoles.

4.1 Sédimentologie et environnement de déposition à Ses Sitjoles

Résumé

Les environnements de déposition carbonatés sont étudiés dans la région de Ses Sitjoles, qui appartient au complexe récifal du Miocène du sud est de Majorque (Espagne), en utilisant des méthodes multi-scalaires et multi-disciplinaires. Douze puits de 100m de profondeur ont été forés dans cette région, et organisés dans un carré de 100m de côté.
Exploitant le travail sédimentologique intense précédemment accompli le long de la falaise de Cap Blanc (située à une distance de 20km) sur l'affleurement du complexe récifal, un modèle géologique et une stratigraphie détaillés sont déduits pour le site.
En utilisant des carottes, des images de la paroi du puits à haute résolution, et des diagraphies continues de spectral gamma-ray naturel (SGR), les 12 puits permettent d'obtenir un modèle géométrique 3D, documentant des variations stratigraphiques 3D à l'échelle de 100m. Profitant de la géométrie unique du site de mesures, des diagraphies SGR sont étudiées aux échelles 5m, 20m, et 100m, afin d'examiner l'hétérogénéité du site. Les données SGR sont comparées au lames minces de carottes et aux analyses géochimiques dans un puits référence carotté d'une manière continue (MC2). L'analyse de l'enregistrement thorium et du potassium du spectral gamma ray naturel dans tous les forages pour le contenu en minéraux radioactifs montre généralement un contenu de minéral radioactif extrêmement bas, sauf dans la couche supérieure, où des faibles contenus de minéraux argileux montmorillonite et d'illite sont notés. Les données d'uranium permettent l'analyse du contenu de matière organique : algues corallines abondantes dans toutes les sous-unités, sauf dans la supérieure, présence de racines de mangrove dans la sous-unité supérieure. Le rapport thorium/ uranium donne une indication sur les environnements de déposition. Comme dans d'autres récifs coralliens méditerranéens du Miocène Supérieur, la couche supérieure est identifiée comme un «Carbonate Complexe Terminal » en relation avec la Crise de Salinité Messinienne. L'unité récifale est divisée en trois sous-unités, qui contiennent toutes exclusivement des porites massives ; ceci indique que l'unité récifale s'est développée dans une bathymétrie à faible profondeur (de 0 à 10m), impliquant que ceci est un récif de type plate-forme à faible profondeur, différent du récif corallien massif-branchu-plateau exposé à Cap Blanc et entrainant une bathymétrie de 0 à 30m, avec des parois plus pentues qu'à Ses Sitjoles.
Les données SGR du programme de forage de l'océan (ODP) de la Grande Barrière de Corail australienne et du Grand Banc des Bahamas sont comparées à celles de Ses Sitjoles, soulignant les différences en paléo-bathymétrie de construction et en paléo-distances à la côte, et les similarités dans les excursions des trois types de paléo environnements marin-transitionnel- continental dans ces trois sites.

Multi-scalar study of depositional environments and heterogeneities in a Miocene reef sequence, Majorca (Balearic Islands), Spain.

YVES MARIA-SUBE[1], GILBERT CAMOIN[2], PHILIPPE PEZARD[1], SIMON LÖW[3], DAVID JAEGGI[3], MODESTO MONTOTO[4], and FELIX MATEOS[4].
[1]*Université Montpellier II, Géosciences Montpellier, UMR 5243, CC 60, Place Eugène Bataillon 34095 Montpellier Cedex 5, France ; (e-mail : adeuxpoints@infonie.fr)*
[2]*Université de Marseille-Aix-en-Provence, Centre Européen de Recherche et d'Enseignement des Géosciences de l'Environnement (CEREGE), Europôle de l'Arbois, BP 80, 13545 Aix-en-Provence, France*
[3]*Eidgenossische Technische Hochschule(ETH) Hönggerberg, Engineering Geology, Geologisches Institut ETH Zürich Wolfgang-Pauli-Str. 15. HIL D 21.3. CH-8093 Zurich, Switzerland*
[4]*University of Oviedo, Facultad de Geologia, Departomento de Geologia, Area de Petrologia y Geoquimica, Campus de Llamaquique, Jesús Arias de Velasco s/n, 33005 Oviedo, Spain.*

ABSTRACT

Carbonate depositional environments are studied in the Ses Sitjoles area, which belongs to the Miocene Reef Complex of SE Majorca (Spain), using multi-scalar and multi-disciplinary methods. Twelve 100m long holes have been drilled in this area, and organized in a 100m scale square.
Taking advantage of previous extensive sedimentological work along the Cap Blanc cliff (located 20km away), on the exposed reef complex, a detailed geological model and stratigraphy are derived from for the area.
Using cores, high resolution borehole images, and natural spectral gamma-ray (SGR) continuous logs, the 12 holes provide a 3D geometrical model, documenting spectacular 3D stratigraphic variations at 100m scale. Taking opportunity of the test site unique geometry, SGR logs are studied at 5m, 20m, and 100m scales, in view of examining the test site heterogeneity. SGR data are compared to core thin sections and to geochemical analyses in a cored reference well (MC2) that was cored continuously. The analysis of thorium and potassium natural spectral gamma-ray channel records in all boreholes for radioactive mineralogical content shows generally extremely low radioactive mineral content, except in the uppermost layer, where low contents of montmorillonite and illite clay minerals are noted. Uranium data allow the analysis of organic matter content: abundant coralline algae in all subunits except the top one, presence of mangrove roots in the top sub-unit. The thorium/ uranium ratio provides an indication on the depositional environments. As in other Upper Miocene Mediterranean coral reefs, the shallower strata are found to belong to a "Terminal Carbonate Complex" related to the Messinian Salinity Crisis. The reef unit is divided in three subunits, which are all containing exclusively massive porites; this indicates that the reef unit developed in a shallow bathymetry (0 to 10m), implying that this is a shallow water platform type reef, different from the massive-branching-dish coral reef exposed at Cap Blanc and involving a 0 to 30m bathymetry, with steeper walls than in Ses Sitjoles.
Ocean Drilling Program (ODP) SGR data from the Australian Great Barrier Reef and the Great Bahama Bank are compared to those of Ses Sitjoles, underlining the differences in

constructional paleo-bathymetry and paleo-distances to the shore line, and the similarities in excursions of all three marine- transitional- continental paleo environments types, at these three sites.

INTRODUCTION

Reefs and shallow-water carbonate platforms have been extensively studied by geologists since a long time because they store fundamental information about the Earth's response to changes in sea level, climate and tectonics, and are capable of monitoring climatic and environmental changes at a variety of time scales (Camoin, 2001, Camoin et al., 2001, Brachert et al., 2001). Furthermore, fossil shallow-water carbonate systems, including reef complexes, contain societally important resources (e.g. hydrocarbons and potable water). Carbonate reservoirs contain more than half the world's oil, including highly productive reservoirs in Cretaceous and Cenozoic carbonates from the Middle East and Southeastern Asia.

Reservoir rocks comprised of shallow-water carbonates are usually characterized by heterogeneities related to the complexity both of their internal architecture and of the distribution of their diagenetic fabrics that may hamper inter-well correlations at various scales and predictions regarding flow paths and volumes of fluids. In the past decades, the knowledge regarding the stratal architecture, depositional facies, as well as sedimentological, structural and petrophysical characteristics of outcrop analogs of subsurface carbonate reservoirs has increased sharply. It therefore led to a better understanding of sequence-stratigraphic and structural controls on reservoir quality, and of the internal architecture of reservoirs and the spatial distribution of geological, geophysical and petrophysical properties. However, the prediction of heterogeneities and the relationship between geological parameters and petrophysical properties within carbonate reservoirs are not yet fully understood, although they remain fundamental problems for field development and optimum production. Significant advances on those problems can be made through joint research in confined natural laboratories including outcrops plus shallow boreholes with maximum control on all geophysical, geological and petrophysical parameters involved. However, few studies of this type have been carried out so far.

Miocene platform carbonates and reef complexes in SE Spain, including the Balearic islands, offer an exceptional opportunity to study the depositional geometries and the distribution of carbonate reservoir facies in a variety of carbonate rocks, stratal patterns and depositional settings and have been extensively described in the literature (see review by Esteban, 1996). The southwestern part of the island of Majorca appears as a natural laboratory where direct comparisons between outcrop and shallow subsurface datasets can be obtained. It is characterized both by very spectacular outcrops in the Cabo Blanco area, that have been extensively studied (e.g. Esteban et al., 1978 ; Esteban, 1979 ; Pomar, 1991 ; Pomar and Ward, 1994, 1995, Pomar et al., 1996 ; Pomar and Ward, 1999), and by relatively shallow wells, up to 100 m deep, that have been carried out to improve groundwater sustainability and quality in that coastal semi-arid environment. The reef complexes that form the bulk of those carbonate platforms can be considered as analogs of subsurface hydrocarbon reservoirs and have been used as such for many active hydrocarbon exploration plays (Pomar et al., 1996 ; Pomar and Ward, 1999).

The subsurface dataset that we acquired in that area includes sedimentological, geochemical, geophysical and petrophysical data that have been partially described (Bonnier, 2005; Jaeggi, 2006). This paper focuses on the study of Miocene platform carbonates that were drilled in the geographically limited area of Ses Sitjoles with the aim of analyzing the distribution in space and time of the various carbonate facies and the heterogeneities identified over the

drilled area, a key to the knowledge of the transmissivity of platform carbonates. The overall coherence of the data acquisition has been accurately checked by various geophysical records. Those topics are of pivotal interest in problems of correlations in shallow-water carbonate rocks and predictions of the heterogeneous distribution of petrophysical properties.
The present paper is based on a sedimentological study coupled with the results obtained through a suite of wireline logs, run in twelve 100m deep boreholes drilled in a limited squared area of 100m by 100m. It is particularly focused on the methodological approach (slimhole logging tools calibration, validation and interpretation by comparison with core results) related to the different tools that were used for investigation. This drilling area therefore provides a unique opportunity to investigate the 3D internal architecture and composition of a Miocene reef from cores and logs, using a multi-scalar approach, ranging from the thin-section to the 100m scales. The data obtained on the Ses Sitjoles wells are then integrated to the existing data concerning the nearby Cabo Blanco outcrops and then compared to other carbonates complexes such as the Great Bahama Bank and the Great Barrier Reef. Furthermore, a separate paper will consider a larger scale encompassing the whole SE Majorca reef complex, using the same methodological approach as established in this document. Diagenetic and petrophysical patterns of the carbonate Ses Sitjoles sequence will be described in other papers.

GEOLOGICAL SETTING

The Majorca island is characterized by the extensive post-orogenic development of Miocene reef complexes that grew on shallow-marine shelves adjacent to basins (Pomar and Ward, 1999) and overlying deformed Early and Middle Miocene, Paleogene and Mesozoic rocks. The Llucmajor platform that occurs on the southeastern side of the Palma basin (Fig. P1-1) consists of a 20-km-wide carbonate platform thought to result from the progradation and aggradation of up to 100 m-thick reefal carbonates controlled by high-frequency sea-level fluctuations during late Tortonian to Messinian times, a period characterized by tectonic quiescence and low terrigenous fluxes. The platform has undergone only slight tilting and flexure associated with normal and strikeslip NE-SW faulting during Late Neogene to Middle Pleistocene times, so that most of the original geometries are retained; the Campos basin seems to have subsided only during Pleistocene time (Jenkyns et al., 1990). Minor burial compaction and scarcity of pervasive cementation has preserved much of the primary porosity (Pomar and Ward, 1999).
The facies architecture and the depositional sequences displayed by the spectacular sea-cliff outcrops along 16 km of the southern coast of Mallorca, between Cabo Blanco and Vallgornera, have been extensively described (Pomar 1991; Pomar et al., 1996, Pomar and Ward, 1994, 1995, 1999). Furthermore, some subsurface data obtained on 69 100-300m deep water wells drilled by the by the Hydrogeological Department of the Government of the Baleares have been used to delineate the three-dimensional architecture Llucmajor platform as a whole; however, it has been established that the lateral relationships of chronostratigraphic units are far from straightforward with highly complex lithofacies stacking patterns (Pomar and Ward, 1999).
The drilling area, described in this document, is located at Ses Sitjoles, near the city of Campos, in the Campos basin, 12 km to the northeast of the Cabo Blanco outcrops, in a zone which is thought to have slightly collapsed at the beginning of Pleistocene (Pomar et al., 1996). In that region, the Miocene platform carbonates form a fresh water reservoir.
The Llucmajor platform appears therefore as a model of progradational carbonate platform in which the distribution in space and time of the various carbonate facies and the pre-deep-burial stratigraphic and diagenetic heterogeneities can be studied in great details. The

comparison between the Ses Sitjoles area and the well-studied Cabo Blanco outcrops may bring valuable information, although some differences between the two sites are noted.

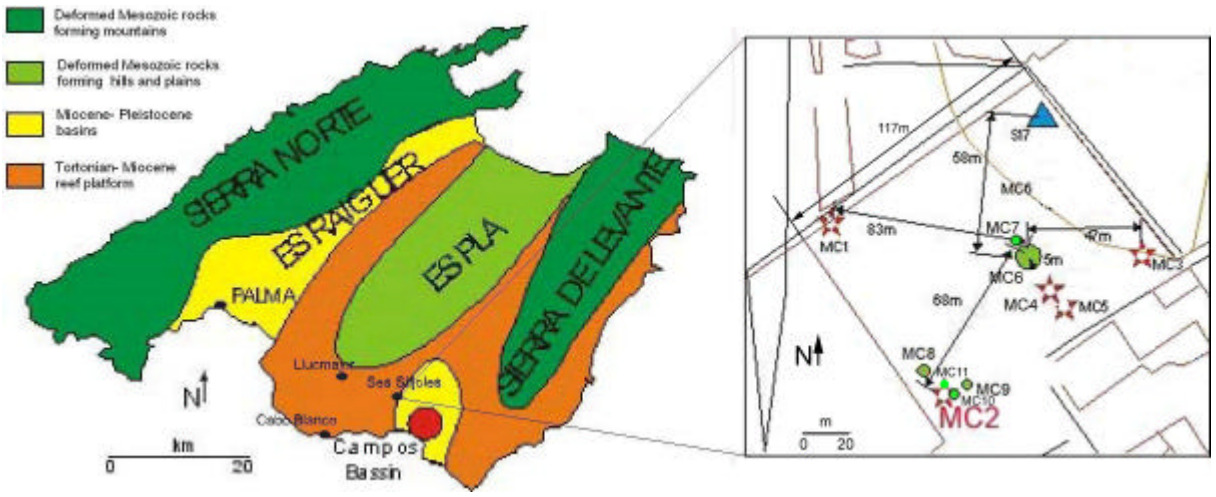

Figure P1- 1. Left: Simplified geological map of Majorca island, showing the distribution of the Miocene carbonate platform (from Pomar et al., 1996). Right: Ses Sitjoles drilling site in the Campos Basin; red star: cored wells, green circle: destructive wells, blue triangle: existing slot lined observation well.

MATERIAL AND METHODS

The drilling site has been carefully planned and designed for offering extraordinary research ground. Eleven shallow wells, of approximately 100m depth, MC1 to MC11, (Fig. P1-1) have been drilled from 2003 to 2006 for scientific purposes in the Ses Sitjoles area. The drilling area is located 6km North of the coast, at an altitude of about 40m above sea level (masl). Five wells, MC1 to MC5, were continuously cored, whereas the others were destructive. One previous well, S17, had been drilled and slot lined by the Government of the Balearic Islands several years ago. The twelve wells are located in a small square of about 100m by 100m, the shortest well-to-well distance being 2.3m. Four wells (MC1, MC2, MC3 and S17) are located at the corners of the drilled area, thus providing a 100m distance scale; four other wells (MC5, MC4, MC7 and MC7) are part of a 20m long alignment extending along the perpendicular bisector of a side to the center of the square; a cluster of five wells (MC2, MC8, MC9, MC10, MC11), not more than 5m apart, are located in a corner of the square, thus providing a 5m distance scale. Core recovery has been generally high, especially for the MC2 and MC5 wells (86 and 94% respectively). The only exception concerns MC1 with a core recovery of only 33% due to the use of an inadequate drilling technique. In all wells, low recovery is mostly related to the occurrence of karstic cavities or of poorly cemented intervals. The drill core diameter is of 8cm.

The sedimentological facies have been identified both by core observations (Fig. P1-2), and by standard petrographic analysis and techniques (Fig. P1-3). X-ray diffraction has been carried out on a Philip Pro X'Pert spectrometer. Thorium and uranium were measured by the Inductively Coupled Plasma- Mass Spectrometry method, at the Geoscience Labs, Ministry of Northern Development and Mines, Ontario, Canada) (Table P1-1). The MC2 well has been defined as the reference hole at that site.

A suite of slimhole logging tools have been used in Ses Sitjoles wells, including especially the spectral natural gamma-ray (SGR), high resolution imaging (OBI and ABI) tools, several types of resistivity tools (electrical log, laterolog and dual induction), neutron porosity, sonic, and the hydrogeolocical Idronaut tools. Other papers will describe results obtained from the logging tools other than SGR and borehole imaging.

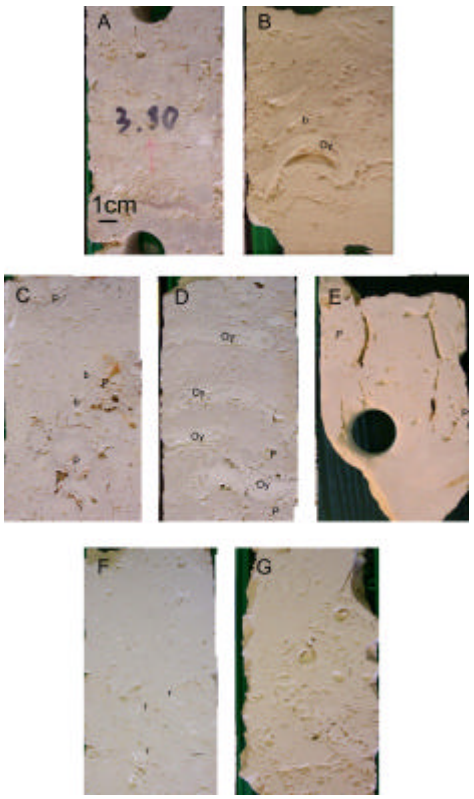

Figure P1- 2. MC2 photos of each unit and sub-unit characteristic core slab. ***Top row: Unit III: (*****A) Subunit IIIb, depth 3.80mbgl, yellow-grey grainstone-packstone limestone rich in bivalves and gastropods with abundant quartz grains, Porites fragments. (B) Subunit IIIa, depth 14.9mbgl, yellow-whitish grainstone limestone , large bivalves (b), oyster (Oy), molds.** ***Middle row: Unit II:*** **(C) Subunit IIc, depth 32.5mbgl, whitish framestone limestone, Porites (P), bivalves (b), some white small size (a few mm) rhodoliths, macropores,. (D) Subunit IIb, depth 41.7mbgl, whitish grainstone limestone, oysters (Oy), Porites fragments (P), macropores. (E) Subunit IIa, depth 59.4mbgl, yellow-whitish framestone dolomitized limestone Porites (P), megapores, the bottom part is showing signs of mineralisation. Bottom row: Unit I: (F) Subunit I top, depth 70.6mbgl, whitish grainstone limestone, rhodoliths (r), small size molds (a few mm), color. (G) Unit I bottom, depth 81.3mbgl, yellow whitish rudstone limestone, bivalve, gastropod and worm molds of centime tric size.**

The identified sedimentological facies have been analyzed on the borehole image log, and on the spectral natural gamma-ray log (SGR) in MC2. The image log, in conjunction with the SGR, is used for correlation purposes of twelve wells from the Ses Sitjoles area. Because, in contrast to the SGR, the image log is not available for all wells and depth intervals, the SGR alone is used for some depth intervals.

The borehole images were recorded by slimhole (40 mm diameter) tools OBI40 (optical) and ABI40 (acoustic) built by the Advanced Logic Technology (ALT) company in Luxembourg which also provides the acquisition software. The optical and acoustic images display a resolution of 1 and 3mm respectively, in 10cm diameter boreholes. Such resolutions are much higher than those currently obtained in the oil industry by larger diameter tools that are about 90mm in diameter. Furthermore, the optical tools are not used by the oil industry as they would not provide images through an opaque drilling mud; the electrical and acoustic images used in the oil industry exhibit resolutions of 2.5 and 5 to 10mm respectively. Both optical and acoustic images also have the advantage compared to the micro-scanner electrical images to present a 360° continuous image, as opposed to the gaps seen on the electrical images, due to the spacing between pads and flaps. The optical image log works also in an air-filled hole (i.e. the vadose zone), whereas the acoustic image log needs a liquid-filled hole. The optical image log has the advantage, compared to the acoustical and electrical image log, to present very close colors to the one observed either on outcrops or cores, which, facilitates the

comparison image log to core and outcrop. The acoustic image log presents two sets of images: one obtained from the travel time and the other one obtained from the amplitude of the acoustic signal. Those images are generally more contrasted than those obtained from the optical image log. To be able to transmit in time a large number of high definition image data, the slowest possible logging speed (0.5m/mn) has to be used.

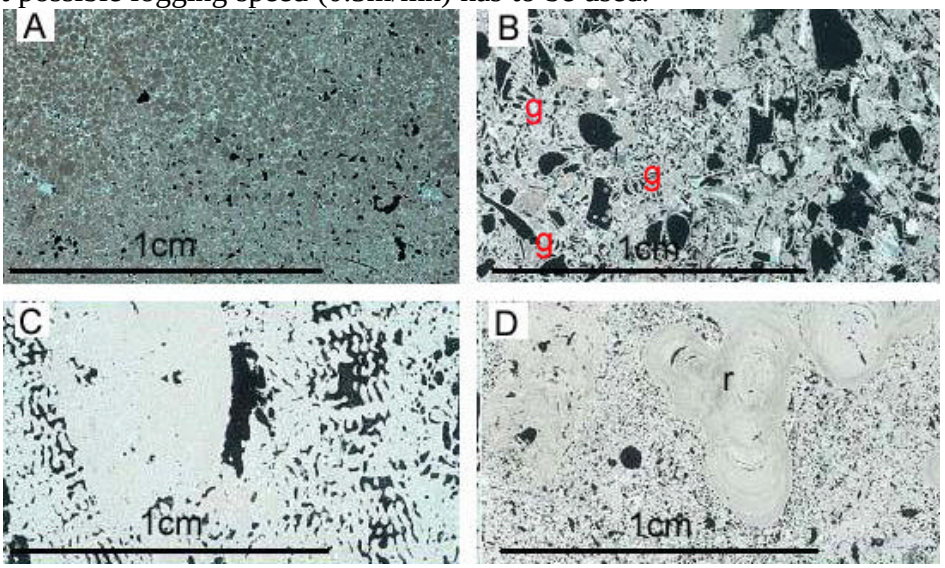

Figure P1- 3. Thin-sections microphotographs from MC2 well of characteristic facies: (A) Subunit IIIb, depth 3.8mbgl, oolithic grainstone with shale fragments. (B) Subunit IIIa, depth 14.4mbgl, skeletal grainstone, abundant coralline algae, benthic foraminifers, and gastropods (g), moldic and intergranular porosity. (C) Subunit IIc, depth 30.5mbgl, massive coral (Porites) framework. (D) Subunit I, depth 70.9mbgl, floatstone, consisting of encrusting red algae (rhodolith (r)) in a grainstone matrix, moldic porosity.

The basis for natural radioactive rocks' evaluation have been elaborated from 1954 to 1974. The spectral gamma-ray logging tool, appeared in 1976 in the oil industry larger diameter version, and has been since then widely used for its various applications. The slimhole tool version appeared much more recently (2000); this version is used in shallow slimhole wells for environmental and laboratory purposes. Spectral gamma ray instruments record the natural gamma radiations that originate from the decay of the three radio-isotopes found in rocks that have a sufficient life-time and whose disintegration produces an important number of gamma-rays: ^{40}K, ^{238}U, and ^{232}Th. The spectral natural gamma-ray slimhole logging tool SGR 1428 is manufactured by the Antares company in Germany. The outside diameter of the tool is 52mm. The detector is a bismuth germanate BGO scintillation crystal, 38mm in diameter and 150mm long, optically coupled to a photo-multiplier. The acquisition software is made by the ALT company. The behaviour of the detector as a function of the tool temperature is adjusted at surface by subjecting the tool to a potassium source of 1.46MeV ray and adjusting the detector high voltage until the detection of the gamma ray spectrum is appropriate. It is also automatically controlled by the acquisition software while logging and can be monitored from surface. Because of the low values of natural gamma-rays of Majorca carbonates, it is essential to use the proper logging speed to avoid an insufficient number of gamma ray counts per sample that would create excessive statistical variations. We have adopted a logging speed of 1m/mn and a sample stepping distance of 5cm, except in wells MC1, MC2, MC10 and MC11, where a logging speed of 0.5m/mn and a stepping distance of 10cm have been used, thus providing four times more gamma-ray counts per time unit on the detector. The tool records uranium, thorium (Th) and potassium (K) contents of the formation in Bq/Kg and total natural gamma-ray SGR in counts per second (CPS). The unit Bq/kg is the International System radiation unit and is not suited to analyze a mineral content in the formation. It has

then been necessary to convert this unit in volumetric units (ppm for uranium and thorium, and % for potassium); the conversion factors for this tool have been provided by the manufacturer. The SGR CPS unit corresponds roughly to 4 API GR units. In spite of the low logging speed and the relatively high sampling distance used, the tool statistical variations are still important, and it is necessary to submit the three elementary channels uranium, thorium and potassium to a filtering process (Gaussian weight, 10 samples above and 10 samples below the current depth) before processing them. The thorium/ potassium (Th/K) and thorium/uranium (TURA) ratios and the Computed gamma-ray (CGR, or the total gamma-ray without uranium influence) outputs are then calculated. Because slimhole logging tools are designed and manufactured primarily for shallow water wells, they do not benefit from the same research and development efforts as the one deployed in the oil and gas industry, and they are often considered more as qualitative than quantitative instruments; consequently, we have taken a particular care in validating our SGR records in calibration and repeatability.

Core depth (mbgl)	Log depth (mbgl)	CaO (wt %)	MgO (wt %)	SiO_2 (wt %)	Al_2O_3 (wt %)	Fe_2O_3 (wt %)	MnO (wt %)	Na_2O (wt %)	K_2O (wt %)	TiO_2 (wt %)	P_2O_5 (wt %)	Th (ppm)	U (ppm)
2.20	0.7											0.42	0.42
2.23	0.73	54.7	0.4	0.99	0.6	0.16	0,00	0.01	0.01	0.03	0.01	-	-
5.30	3.8											0.47	0.56
5.99	4.5	52.82	0.51	2.87	0.94	0.3	0.01	0.02	0.1	0.06	0.01	-	-
6.05	4.55											1.21	1.49
6.10	4.6											0.92	1.36
8.00	6.5											0.32	0.83
14.5	13	56.94	0.27	0.23	0.03	0.03	0,00	0.11	0.01	0.01	0.03	0.17	0.68
17.51	16	55.49	0.35	0.21	0.13	0.03	0,00	0.01	0,00	0.02	0.08	-	-
19.54	18	56.49	0.34	0.19	0.02	0.04	0.01	0,00	0.01	0.02	0.01	-	-
21.52	20	56.78	0.31	0.09	0.01	0.03	0,00	0.01	0.01	0.01	0.02	0.22	2.97
33.31	33.2	55.9	0.34	0.29	0.18	0.05	0.01	0.01	0.01	0.02	0.01	.06	0.44
34.53	34.4	55.79	0.31	0.27	0.19	0.04	0,00	0.01	0.01	0.02	0.01	0.07	0.64
42.08	40.1	55.62	0.3	0.12	0.18	0.03	0.01	0.01	0.01	0.01	0.01	0.05	1.16
48.12	46.1	52.99	0.38	0,00	0.05	0.03	0,00	0.01	0,00	0.02	0.01	0.14	0.32
48.32	46.3	35.01	17.12	1.1	0.49	0.14	0.01	0.06	0.05	0.15	0.04	0.31	4.06
50.78	48.8	55.73	0.34	0.37	0.33	0.05	0,00	0.01	0.01	0.02	0.01	0.18	0.78
56.83	55.9	55.8	0.31	0.16	0.12	0.04	0.01	0.01	0.01	0.02	0.01	0.07	0.7
60.96	61	34.02	18.93	0.66	0.35	0.12	0,00	0.04	0.02	0.03	0.03	0.28	3.52
70.03	70	54.49	0.38	1.13	0.23	0.07	0,00	0.02	0.01	0.03	0.02	0.3	1.65
81.15	81.15	55.96	0.3	0.11	0.12	0.03	0,00	0.03	0,00	0.02	0.02	0.18	0.48
85.6	85.6	51.04	4.35	0.28	0.15	0.04	0,00	0.01	0.01	0.022	0.02	-	-
88.92	88.9	41.83	11.25	1,00	0.37	0.11	0,00	0.06	0.01	0.03	0.02	-	-

Table P1- 1. Chemical composition of MC2 cores (Mateos et al., in prep.), Th and U from Geosciences Labs, Ontario, Canada.

RESULTS

The results detailed in that section concern all wells (called MCxx for the new wells, and S17 for the already existing well) drilled in the Ses Sitjoles area. MC2 has been chosen as reference hole for the area based on the high core recovery (103 cores for 100 m of drilling; average recovery: 86%), the drilling quality (smooth hole, no very large cavities), the quality

of the downhole measurements, and the existence of a four well cluster surrounding it, allowing to check the consistency of the measurements.

Sedimentological data

The carbonate sequence in MC2

Three distinctive sedimentological units comprise the carbonate sequence in MC2 well and have been identified based on visual core description (Fig. P1-2 ; Table P1-2) and thin section observation (Fig. P1-3 ; Table P1-3). They have been called I, II and III (Fig. P1-4) from base to top and have been locally subdivided in subunits based on their lithological characters and/or biological content.

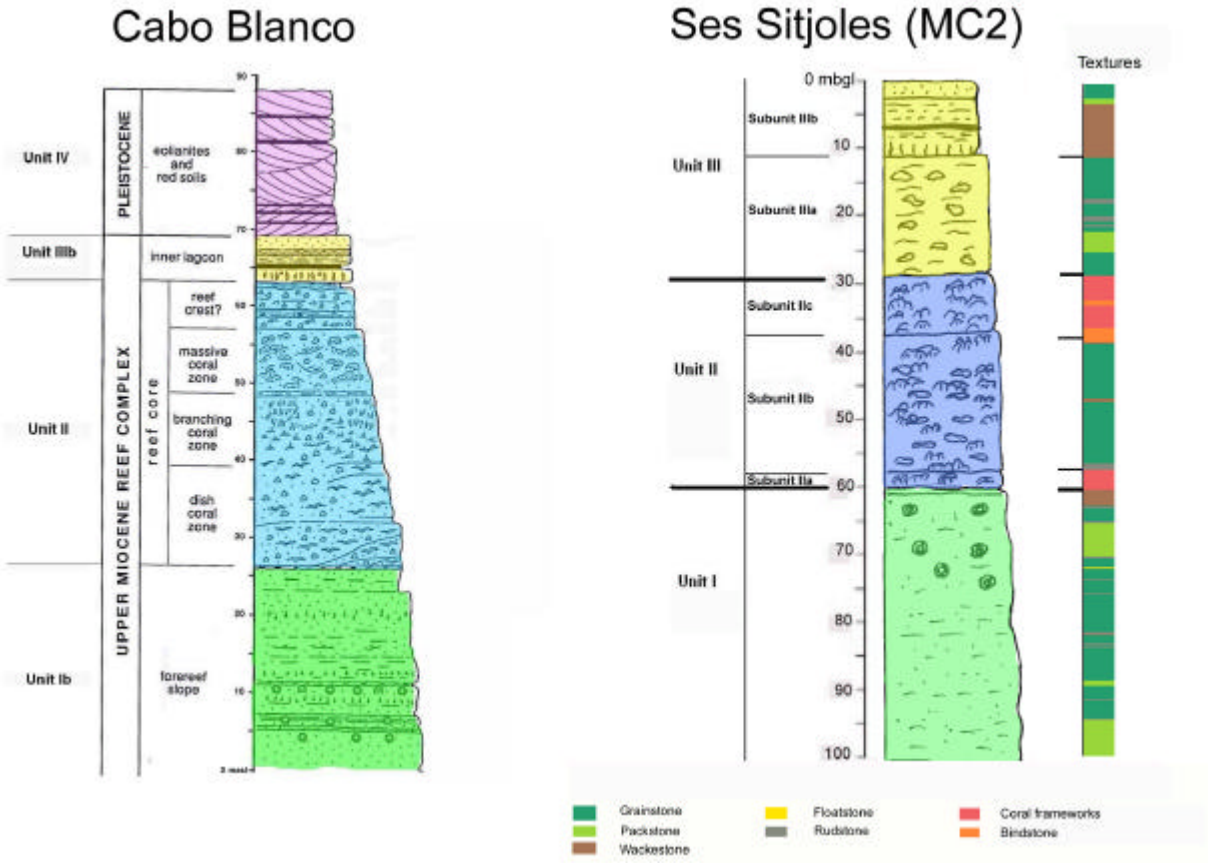

Figure P1- 4. Left: Stratigraphy from the Cabo Blanco outcrops, cores and thin sections (adapted from Pomar et al., 1996). Right: Ses Sitjoles MC2 well stratigraphy and depositional textures recognized from core and thin section observation. Stratigraphy color coding: green, slope deposits; blue: coral frameworks and associated facies; yellow: unit III- low energy shallow marine restricted environments; pink: eolianites.

Unit I is comprised of a white bioclastic limestone that is gently to steeply bedded (10-30°). It extends from 100 to 60m below ground level (mbgl) and grades from fine-grained skeletal packstones between 100 and 75mbgl to slightly coarser skeletal packstones to grainstones between 75 and 60mbgl (Table P1-3). Occurrences of wackestones, rudstones, and floatstones are noted locally in the upper part of the unit. The “chalky” appearance of those rocks is generally related to their good sorting and overall fine grain size coupled with extensive moldic and intergranular porosities. The degree of cementation increases from base to top; the lower part of the unit is generally poorly cemented whereas patchy blocky spars are common in the upper part.

Units	Subunits	Interval core depth (mbgl(m)	Lithology	Biota	**Mineralization**	**MC2 plugs average porosity (%)**	**Cap Blanc plugs average porosity (%)**
Unit III	Subunit IIIb	0-12	Shale (4.10-10.70m interval), otherwise calcareous	Rhodoliths, bivalves, molluscs, coral fragments		**23**	**22**
	Subunit IIIa	12-28	Calcareous	Molluscs (oysters), molds, coral debris, possible presence of mangrove roots at 12.2-12.8m; bivalves and gastropods, rhodoliths	At 25m	38	26
Unit II	Subunit IIc	28-37	Calcareous	Corals, vugs, molluscs, rhodoliths and encrusting coralline algae, bivalves, worms	At 36m	20	22 (massive corals)
	Subunit IIb	37-57	Calcareous	Molluscs (oysters), molds, some coral fragments, rhodoliths, bivalves, gastropods	**At 46 and 48m**	**30**	**28 (branching corals)**
	Subunit IIa	57-60	Calcareous	Coral, vugs, rhodoliths	At 56 and 58m	13	24 (dish corals)
Unit I		60-100.9	Calcareous, détrital	Molds, rhodoliths, small molluscs (1 mm) Molds, average size molluscs (1 cm), worms		40 44	42

Table P1- 2. MC2 visual core observations, and plug average porosity. Cap Blanc plugs average porosities from Van Berkel & Verhoef, 2005.

Units	Subunits	Interval core depth (mbgl)	Depositional texture	Biota	Cement type	Fabric	Porosity type
Unit III	Subunit IIIb	0-12	**Oolitic grainstone**	**Shell fragments**	**Important sparitic**	**Isotropic and homogeneous**	**Mainly intergranular, some intragranular porosity and a few vugs,**
	Subunit IIIa	12-28	Skeletal grainstone	Abundant coralline algae and forams	Micritic	Anisotropic but quite homogeneous	Moldic and intergranular
Unit II	Subunit IIc	28-37	Framestone	Built by massive corals (Porites); extensive borings	sparitic cement which partly occludes porosity	Highly heterogeneous	Growth-framework porosity with important vugs
	Subunit IIb	37-57					
	Subunit IIa	57-60					
Unit I		60-75.0 75.0-100.9	Floatstone Grainstone, fine grained	Encrusting coralline algae Molds of shells, only echinoids are preserved	Micritic Exclusively micritic	Isotropic and heterogeneous Anisotropic and homogeneous	Mainly intergranular and some moldic porosity Mainly intergranular porosity and some moldic porosity

Table P1- 3. MC2 lithology, biological content and diagenetic features after thin section observations (from Jaeggi, 2006). The thin section descriptions corresponds to the depths indicated in Figure 3 caption.

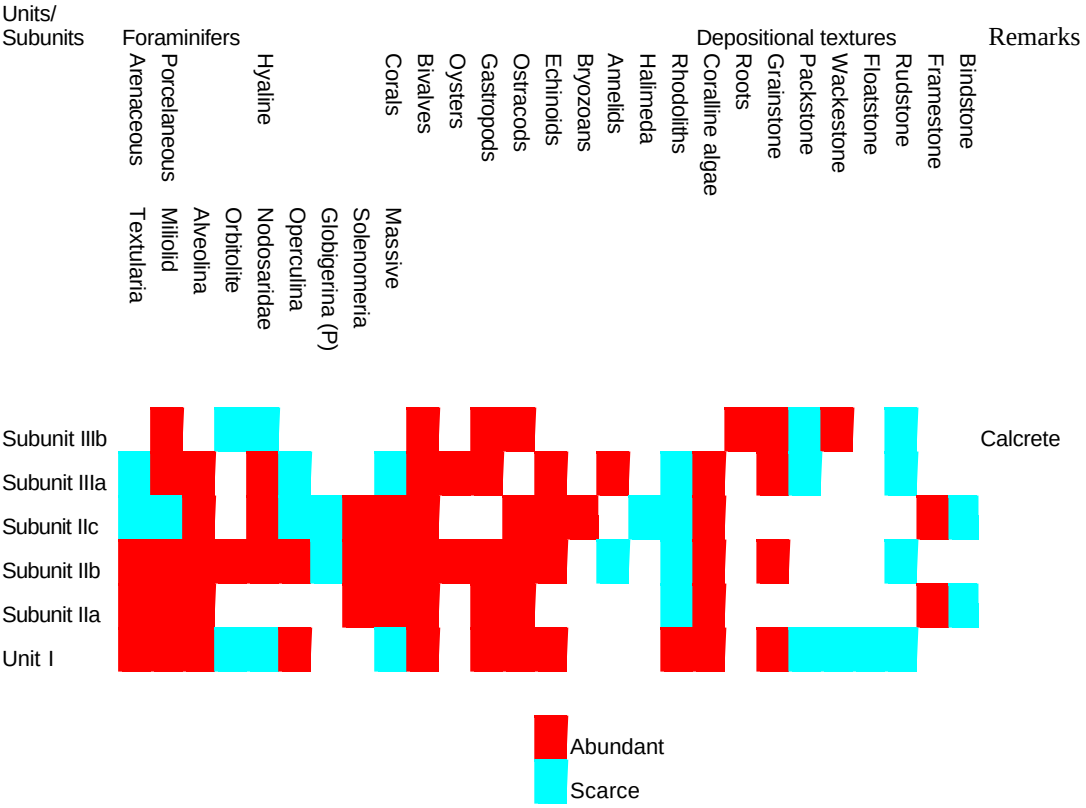

Table P1- 4. Fossil content and depositional textures of successive lithological subunits in MC2, based on thin-section observations. Data from Bonnier, 2005, (23 thin-sections), Jaeggi, 2006 (32 thin-sections), Mateos et al., in prep. (13 thin-sections).

The fabric grades from homogeneous at the base to slightly anisotropic at the top, due to the occurrence of steeply dipping beds and coarse grained layers in between, (Jaeggi, 2006). Porosity averages 40% in this unit; the highest values, up to 52% are related to the occurrence of larger cavities affecting both the matrix and larger skeletal pieces. Two dolomitic intervals occur between 88 and 85mbgl and between 61 and 60mbgl respectively.

The biological content is primarily composed of coralline algae (fragments and rhodoliths), echinoid plates and, to a less extent, fragments of molluscs (bivalves and gastropods), ostracods and corals in the lower part of the unit. Benthic foraminifers include textularids, miliolids, alveolinids, peneroplids (*Orbitolites*), nummulitids (*Operculina*) and a few nodosarids (Table P1-4).

The depositional environment is interpreted as a proximal carbonate slope environment characterized by moderate energy conditions.

Unit II, from 60 to 28mbgl, includes three subunits that are composed of *in situ* massive coral colonies (*Porites*) encrusted by coralline algae and foraminifers (framestone, with possibility of having bindstone; subunits IIa and IIc) and skeletal beds comprised of large pieces of corals (massive *Porites*) and coralline algae (rudstone, grainstone; subunit IIb).

The matrix of those coral frameworks is micritic and includes fragments of corals, coralline algae (both encrusting and branching) and molluscs (bivalves, including oysters in subunit IIb, and gastropods), echinoid plates, benthic foraminifers (textularids, miliolids, alveolinids, peneroplids, nodosarids, nummulitids); a few planktonic foraminifers (*Globigerina*) and ostracods (Table P1-4); worm tubes occur sporadically. *Halimeda* plates are rare and are recorded only at the top of the unit.

The fabric is highly heterogeneous. The total porosity is highly variable and ranges from 5 to 51%; it reflects the uneven distribution both of pore spaces and meteoric blocky and granular

calcite cements. Porosity mostly includes large primary pores that merely correspond to large open cavities between coral colonies and secondary pores (moldic pores and solution cavities). Karstification occurs at various levels and especially in the lower part of the unit where decimeter-to-meter scale cavities are partly filled by red-brown ankerite mineralizations; within those intervals, pore spaces are usually filled by blocky spars providing a denser structure to the rock. Dolomitization is conspicuous at 37 and 48mbgl.
This unit is interpreted as being deposited in a warm shallow-water environment characterized by moderate energy conditions.
Unit III, from 28mbgl to the surface, includes two successive subunits that are characterized by distinctive textures and grain contents.
Subunit IIIa occurs from 28 to 12mbgl and is mostly comprised of well-sorted skeletal packstones and grainstones with variable cementation and local occurrence of rudstones, rich in fragments of coralline algae and molluscs (including oysters), benthic foraminifers (textularids, miliolids, alveolinids, nodosarids, nummulitids); echinoid plates, fragments of gastropods and annelid worms are fewer. Some beds are characterized by the occurrence of small coral colonies (massive *Porites*). Calcite cements include isopachous crusts, especially between 15 and 40 mbgl, and patchy blocky spars.
Subunit IIIb forms the top of the unit, from 12mbgl to the surface, and corresponds to karstified oolitic grainstones and packstones, with local occurrence of rudstone, bearing very small benthic foraminifers (mostly miliolids, a few peneroplids, nodosarids, nummulitids), a few mollusks (bivalves, gastropods) and echinoids; traces of roots, attributed to the presence of mangroves, and calcretes are noted locally. Red clays commonly fill karstic cavities. Blocky cements occur in most intergranular pore spaces.
The overall average porosity throughout this unit ranges from 24% in subunit IIIb to 36% in subunit IIIa. It is merely related to dissolution processes affecting the skeletal grains and the ooids (moldic pores); solution cavities occur locally.
The depositional setting is interpreted as a very shallow warm water environment characterized by low energy conditions, probably locally and temporarily restricted, with fluctuating ecological conditions (e.g. temperatures, salinities and exposure) during the deposition of subunit IIIb as indicated by the composition of its poorly diversified biological content. Furthermore, the occurrence of calcretes indicates temporary periods of subaerial exposure.

Comparison with the Cabo Blanco outcrops

The lithological succession reported in the MC2 well displays similarities with the sequence described in the Cabo Blanco area where three Upper Miocene units ranging in ages from the late Tortonian to the middle Messinian, and capped by Pleistocene eolianites (Fig. P1-4), have been extensively described (e.g. Pomar 1991; Pomar and Ward, 1994, 1995, 1999, Pomar et al., 1996). Those units are thought to reflect a shallowing-upward sequence including successively slope deposits, a reef core and lagoonal beds that could be respectively compared, in a first approach, to the units I, II and III described in the MC2 well (Fig. P1-4). However, several differences in lithology and biological content between units I and II identified in Ses Sitjoles, and the slope and reef units described in the Cabo Blanco area suggest that the relevant Miocene units cannot be correlated straightforwardly. For instance, the coral assemblages that characterize the Unit II in the Ses Sitjoles area do not include dish nor branching corals like in Cabo Blanco, implying different depositional environments and/ or morphology of the carbonate platform. Furthermore, Sr. isotope dating results obtained on units I and II in MC2 well indicate that those units are older than the Cabo Blanco outcrops (Camoin et al., work in progress). In contrast, the Unit III from the Ses Sitjoles area displays striking similarities with the uppermost Miocene strata (“lagoonal beds”, Pomar et al., 1996)

cropping out in Cabo Blanco despite the lack of stromatolites in the studied drill cores; consistent Sr isotope dating results at both sites (Camoin et al., work in progress) indicate that those units are coeval. Subunit IIIb from Ses Sitjoles is also very similar to the "Santanyi Limestone" that forms extensive outcrops along the South-Eastern coast of Majorca, including miliolid packstones and grainstones bearing root traces, skeletal grainstones, stromatolites, and cross-bedded oolitic grainstones including giant thrombolites and stromatolites, (Pomar et al., 1983), thus implying that it can be correlated with the "Terminal Carbonate Complex (TCC)" (Esteban, 1979, 1996, Rouchy and Saint Martin, 1992), in relation with the "Messinian Salinity Crisis (MSC)" (Hsü et al., 1973, 1977, Krijgsman et al., 1999) as well as other Mediteranean peripheric TCCs (Esteban, 1979, 1996, Esteban et al., 1996, Rouchy and Saint Martin, 1992, Cunningham et al., 1994, Franseen et al., 1998, Pomar, 1991, Riding et al., 1991, 1998, Braga and Aguirre, 2001, Cornée, et al. 2002).

Image logging

There is a great number of applications for image logging (Serra and Serra, 2000, 2003). The sedimentological applications tend to analogically compare cores and outcrops to image logging to define: 1) the geometry and shape of beds, including their limits; 2) the internal organization of beds (i.e. texture, internal structure); 3) the organization of beds, including changes in their thickness); 4) the diagenetic features (i.e. cementation, nodular concretions, pressure- solution, dissolution); 5) the depositional environment based on facies, and facies sequences. The tectonic applications are more related to physical and mathematical computations and include the recognition of: 1) fractures (i.e. localization, nature, type, dip magnitude and azimuth, aperture, frequency); 2) structural dip (i.e. angle and azimuth); 3) structural dip evolution (i.e. identification and geometry of folds and faults, slumps, unconformities). The petrophysical properties applications include the study of pore types and permeability. Image logging can also be used for the quantitative interpretation of logs through the choice of equations (i.e. type of saturation equation, sonic equation) and of parameters (i.e. cementation parameter m), and the use of quantitative data (i.e. shale to sand ratio, shaliness, percentage of secondary porosity). Image logging is also used as a completion help (perforation localization, perforation density).

Some of the applications that are described above are more related to clastic sediments, and for the use by the oil and gas industry. In this document, we have selected more particularly two relevant applications: 1) facies description and identification, and to the geometry and shape of beds; 2) fracture identification and characterization, that are related to tectonic stress. Other applications of image logs (tectonics, petrophysics, diagenesis) will be addressed in other papers.

A characteristic optical imaging log *facies* was selected from the subunits defined in MC2 cores (Table P1-1, Fig. P1-5), similarly to the core slab photos that are illustrated on Fig. P1-2. The description of the image log for each subunit, reflecting some of the various facies is summarized in Table P1-5. However, it appears from Fig. P1-5, that, regardless of the presence or not of water in the hole that somehow affects the recorded colors, each subunit is characterized by high resolution, full 360° image displaying remarkable features that can be very helpful to define the various subunits (Fig. P1-5), especially in the wells that were not cored.

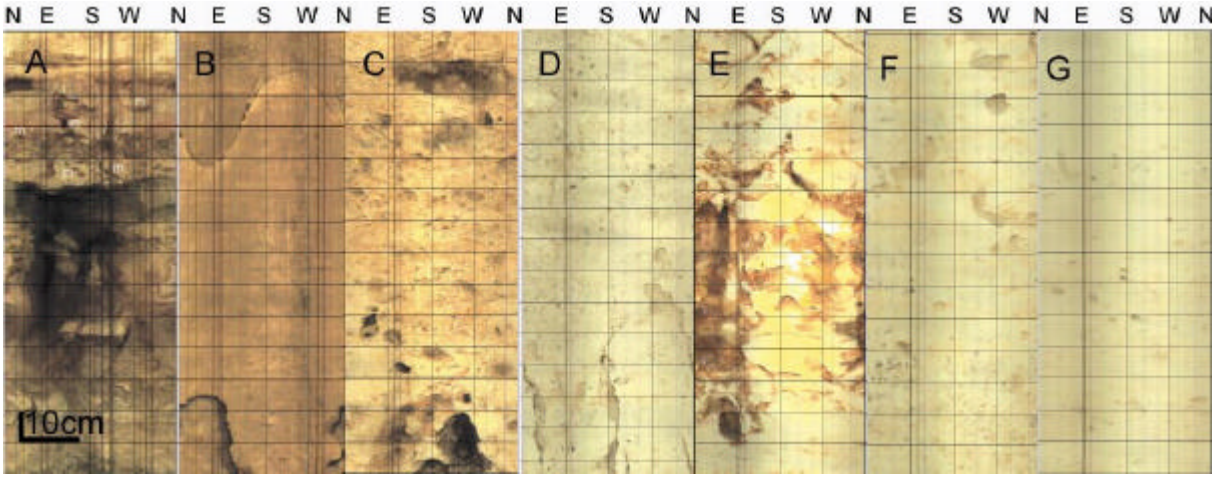

Figure P1- 5. Characteristic borehole optical high resolution full 360° images from MC2 well; A to C in air, D to G in water (greenish color, less contrast). (A) Subunit IIIb, depth 7.5-6.1mbgl, shale, cave, and possible mangrove roots (m). (B) Subunit IIIa; depth 18.1-16.7mbgl, closed fracture at 17.0mbgl of excellent planarity, NE oriented dip of 70° magnitude; closed to open fracture at 18.0mbgl, SW oriented dip, of 60° magnitude. (C) Subunit IIc, depth 32.6-31.2mbgl, this interval is characterized by abundant important megapores. (D) Subunit IIb, depth 39.4-38.0mbgl, abundant megapores; closed fracture at 39.5mbgl, East oriented, of 80° magnitude. (E) Subunit IIa, depth 57.6-56.2m, karstification, and mineralized (yellow) zones, closed fracture at 56.15mbgl, NE oriented dip, of 60° magnitude. (F) Unit I top, depth 64.4-63.0mbgl, interval characterized by average value of macroporosity. (G) Unit I bottom, depth 86.4-85.0mbgl, interval characterized by very low value of macroporosity.

Units/ subunits	Interval log depth (mbgl)	Observed facies characteristics	Fractures (see details in Table P1-6)	Color on the optical image
Subunit IIIb	0-9.5	Shale and caves, roots	Only one fracture	Grey shale and black caves
Subunit IIIa	9.5-26.8	Low macro-porosity	Eight 0 to 70° inclined fractures	Ochre, sometimes greyish
Subunit IIc	26.8-36.8	High macro-porosity, many 17-20cm diameter cavities between corals	Only one fracture	Ochre, sometimes greyish
Subunit IIb	36.8-56.3	Low to high macro-porosity, 15-20cm diameter cavities between corals	Two fractures	Ochre, black caves
Subunit IIa	56.3-59.3	Low to high macro-porosity, 15-20cm diameter karst cavities between corals	Two fractures	Ochre, black caves
Unit I	59.3-75	Low to high macro-porosity, 5-10 cm cavities (debris)	No fracture	Ochre, black caves
	75-100.9	Low macro-porosity	No fracture	Ochre, sometimes greenish

Table P1- 5. Imaging log observations, according to the lithological subunits.

Several planar (appearing in the form of horizontal axis sinusoids) or sub-planar features have been identified in MC2 (Fig. P1-5, Table P1-6). Computations on these sinusoids allows the evaluation of the dip magnitude and azimuth of those planar features (Table P1-6). Considerations regarding their frequency and their orientation imply that those features are *fractures*: they are planar or near-planar, no bedding is reported, they are absent in the only detrital bed of the depth interval, they are scarce and their orientation is not constant, and their magnitude is too high to represent beddings. Furthermore, fractures are likely to occur in carbonates. It is interesting to note that these fractures are mostly oriented NE-SW, i.e. parallel to general orientation the fault planes in this area, a fracture-fault relation that has been previously observed (Babcock, 1978; Bell and Gough, 1979; Cox, 1983).

Unit/ subunit	Log depth (mbgl)	Dip magnitude (0-90°)	Dip orientation	Aperture	Planarity quality	Uranium content relative to maximum over interval (%)
Subunit IIIb	1.75	30	SW	Closed	Average	19.8
Subunit IIIa	14.0	70	SW	Closed	Average	31.2
	16.3	0	-	Closed	Good	38.6
	17.0	60	NE	Closed	Excellent	41.3
	18.0	60	SW	Closed to open	Average	**74.8**
	18.8	60	SW	Closed	Good	**69.6**
	20.6	30	SW	Closed	Average	47.7
	23.4	15	W	Open	Average	**66.3**
	24.8	5	SE	Closed	Average	41.9
Subunit IIc	28.3	80	SE	Closed	Average	27.7
Subunit IIb	39.4	80	E	Closed	Average	36.2
Subunit IIa	56.15	60	NE	Closed	Excellent	23.4
	58.8 to 59.1	60	NE	30cm aperture	Good	**67.1**
		40				**54.7**

Table P1- 6. Identification and characterization (dip magnitude, orientation, aperture, and planarity quality) of fractures by image logs. Uranium content (bold characters if larger than 50%) of fractures provided by SGR log in MC2 well.

Stylolites are sedimentological features that could have been expected in this context, and would appear as saw-tooth shape, 3D linear, not necessarily NE-SW oriented, and not necessarily of high magnitude features. Although the features recorded at 24.8, 23.4 and 16.3mbgl fit with the two last criteria, they are not consistent with the two first conditions. Accordingly, we conclude that MC2 cores do not display any stylolite.
All logs are depth referenced to MC2 borehole optical image log.

Spectral natural gamma-ray log

Fig. P1-6 displays the recorded natural spectral gamma-ray, the associated borehole image logs, and the observed depositional textures in well MC2.
All scales have been selected to amplify the natural radioactive signals, because this carbonate formation displays generally very low radioactivity values.
Potassium, thorium and uranium laboratory measurements have been made on samples or MC2 cores and are reported on Table 1. These measurements compare well to the corresponding log measurements (Fig. P1-7).

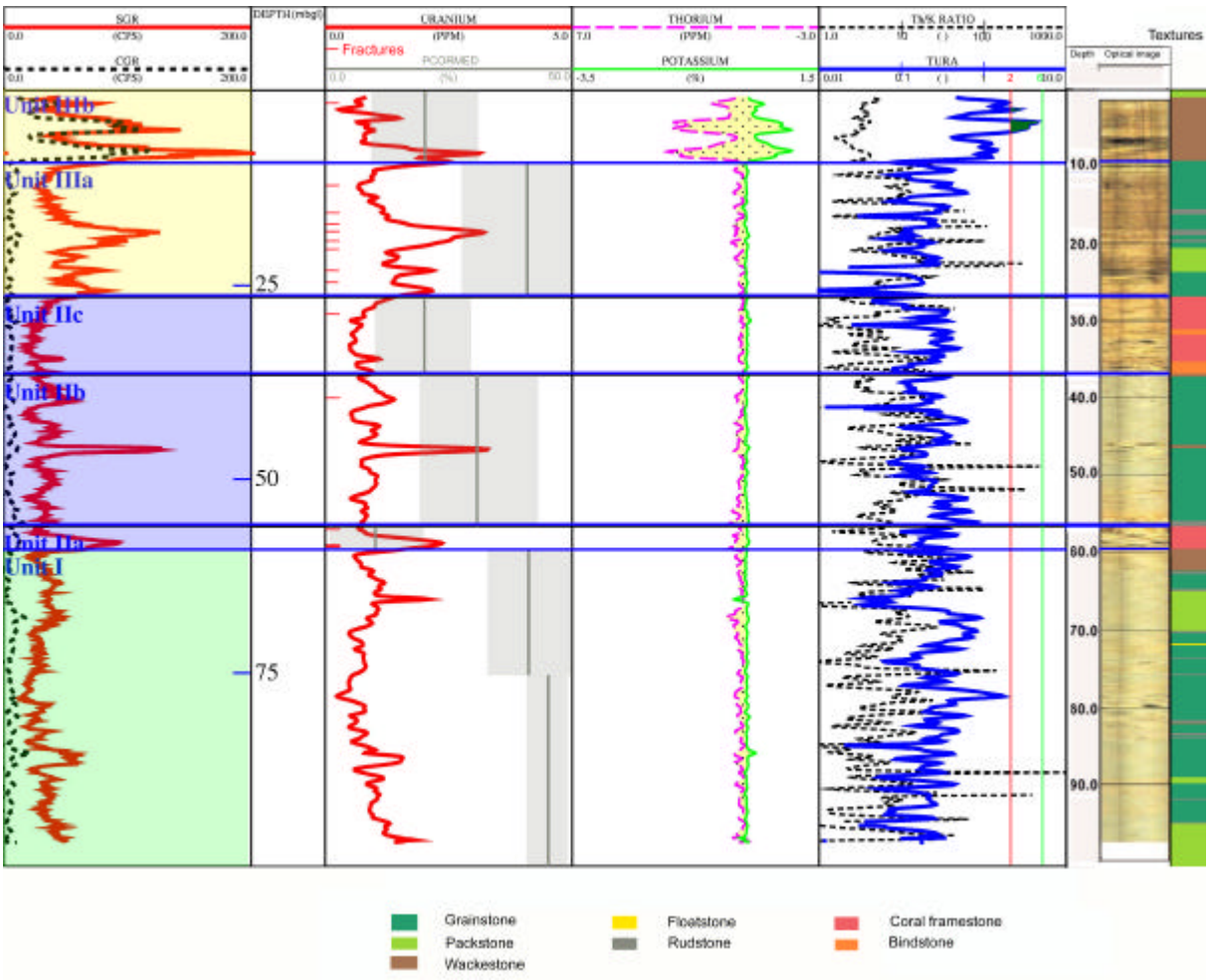

Figure P1- 6. Spectral natural gamma-ray log different channels in MC2 well (left) and optical image logs (right), and depositional texture column at the extreme right. PCORMED channel is the median value of measured core porosity for each sub-Unit, and the grey area around it represents the interval of standard deviation. The yellow-black dotted shading between the Thorium and Potassium curves highlights the presence of radioactive minerals; the green dark shading indicates that the Thorium/ Uranium (TURA) curve exceeds the value of 2. Unit color as per Fig. P1-4. Detected fractures (Table P1-5) are indicated by red pips on the left side of track 2).

Uranium

The *uranium* track is displayed in Fig. P1-6, track 2.

Exceeding a relatively high average background of about 1ppm, large uranium peaks are observed at 59.3-57mbgl, 46.5mbgl, 26.8-17mbgl, and 10-7mbgl. There is also a decreasing upward trend from the bottom of the well up to 70mbgl.

Uranium is easily soluble, under certain conditions, and can be transported from its source under the form of either solution or of particles. Organic matter has the property of adsorbing uranium by humic fractions, or by bacterial activity from uranyl UO_2^{++} solution. Organic matter has also the property of precipitating uranium. In an acid environment, humic and fulvic acids, and other components, facilitate uranium precipitation by reduction of U^{6+} in insoluble uranuous ion U^{4+}; organic matter acts as a reducer, and uranyl is transformed in U^{4+}. For these reasons, *uranium is an organic matter indicator*, either sapropelic or humic (Beers and Goodman, 1944; Russell, 1945; Swanson, 1960; Serra et al., 1980, Serra and Serra, 2000 and 2003). This uranium is then adsorbed or precipitated in sediments below the surface of deposition (Swanson, 1960).

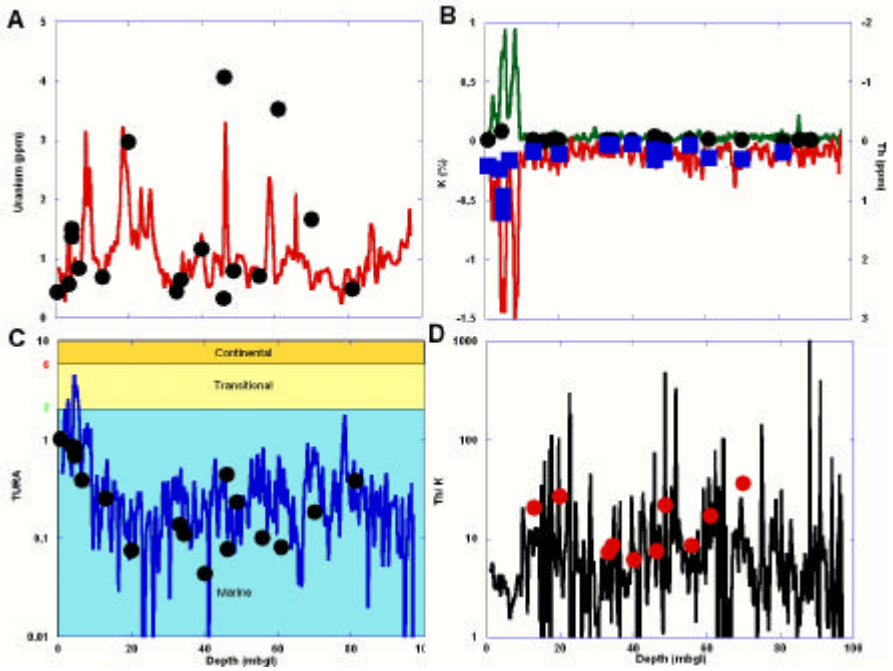

Figure P1- 7. Comparison between continuous log (lines) in MC2 well and discrete lab (dots) SGR measurements vs. depth (from Table 6). (A) Uranium. (B) Potassium (green line, black dots) and thorium (red line, blue full squares). (C) Thorium/ uranium. (D) Thorium/ potassium.

The trends displayed by the MC2 uranium curve are related to the occurrence of algae (marine and transitional environments) or roots (transitional environment) deduced from n the sedimentological observations. Coralline algae (especially rhodoliths) are noted in all units from MC2 well, but more particularly in Unit I. Scarce *Halimeda* are noted at the top of Unit II, whereas presence of mangrove roots are noted only in subunit IIIb (Table P1-3). The 1ppm average uranium background noted above throughout the three units, can be associated to the marine uranium content of dissolved uranium ions, with increasing algal density related to the different uranium peaks. The upward decreasing uranium trend noted between 70 and 100mbgl can be attributed to the decreasing abundance of coralline algae in this depth interval as a consequence of the changes in under water depth and light intensity.

Some authors (Wignall andNewton, 2001; Lüning et al., 2003) have also considered that a high uranium content is observed in anoxic waters (-400mV < Eh <0) and the complex ion uranyl UO_2^{++} precipitates in uranous ion $U4^{+}$ (Serra and Serra, 2000). The occurrence of these conditions being very unlikely in a coral reef environment, we will not consider them here.

Because the circulation of fluid may have contributed to the precipitation of uranium in the fracture system, *increased uranium content will be noticed in front of fractured zones* (Serra and Serra, 2003). MC2 fractures that were detected on the image logs (Table P1-6) are represented at their correct depth on the uranium log (Fig. 6), and the corresponding uranium content is recorded (Table P1-6). It therefore appears that uranium peaks at 59.1-58.8, 23.4 and 18.8-17.0mbgl may be due more to the occurrence of fractures and the related circulation of fluid than to the presence of algae.

Uranium can also be associated to stylolites, due to enrichment in uranium caused by concentration of insoluble materials such as clays, coal, lignite fragments, organic matter (Serra and Serra, 2003). However, since the MC2 cores or image logs analysis have not detected the existence of stylolites, we will not consider them here.

Thorium and potassium

In Fig. P1-6 track 3, Th and K curves are displayed in opposite scales, so that the separation between the two curves, highlighted by the shading, is indicative of the quantity of radioactive minerals in the formation (Hassan and Hossin, 1975). This is also indicated by the CGR curve on track 1. The separation between SGR and CGR curves indicates that most of the radioactivity is related to the uranium content of the formation and shows that the radioactive mineral content is very low, except in subunit IIIb. Thus, the SGR curves (CGR, SGR, uranium, Th, K) are not very useful tools to define the successive subunits, except in the case of subunit IIIb. In contrast, the median porosity value is a much more useful parameter as it confirms or strengthens the distinctions made between subunits IIb and IIIa and between subunits IIa and IIc respectively.

Thorium/ uranium ratio

The *thorium/ uranium ratio* (TURA) curve is displayed in Fig. P1-6 track 4 . Thorium has an extremely low solubility (10^{-14} g/g), while uranium is soluble in specific pH and rH (oxydo-reduction) conditions. This property and its consequences have been exploited under several forms by different authors. *TURA*, together with Th, are thought to be indicators of depositional environments (Adams and Weaver, 1958; Serra et al., 1980, Serra and Serra, 2000, 2003) or of distance of sediment transport (Andersson and Werden, 2004) to the shore line, therefore indirectly of water depth. In MC2 well, the TURA curve increases upward, from marine (units I to subunit IIIa, where TURA is less than 2) to transitional environments in subunit IIIb (2< TURA < 6; Fig. P1-6). A clear shallowing-upward trend is recorded at the transition between subunits IIIa and IIIb.

Thorium/ uranium and thorium/ potassium ratios

Uranium and potassium being both more soluble than thorium, high TURA associated to a high Th/K can reflect hot and humid paleoclimates when used in continental depositional environments (Mutterlose and Ruffell, 1999; Ruffell and Worden, 2000; Schnyder et al., 2005). In marine depositional environments, TURA variations cannot be interpreted as a change in humidity/dryness ratio. In our study site, we do observe parallel changes of TURA and Th/K curves from Unit I to subunit IIIa , if we neglect the high peaks of Th/K curve that are due to very low potassium values. At the boundary between subunits IIIa and IIIb, a sharp change is observed: while TURA increases sharply from ~0.2 to 1, Th/K decreases sharply from ~20 to ~4, providing a clear separation between the TURA and Th/K curves. A much larger separation between thorium and potassium, already noted above, occurs coevally, indicating therefore a larger amount of radioactive mineral content in subunit IIIb.

Based on the Th/U and Th/K data, we can therefore conclude that: 1) the depositional environments grade from normal marine (Unit I to subunit IIIa) to very shallow, closer to the shoreline, and temporarily restricted (subunit IIIb); 2) radioactive minerals in subunit IIIb, indicated by thorium and potassium higher values, are chemically immature (low values of Th/K, presence of clays and silts), typifying a short distance of transport from the source to land (Selley, 1976).

TURA may also reflect diagenetic changes. However, the facies changes that are coeval to significant changes of TURA (in Fig. P1-6) strongly suggest that this is not the case here. In the same way, most of the alteration and diagenetic processes concerning radioactive minerals are observed in micas, feldspaths and clay minerals (Hassan and Hossin, 1975) that are rare, or even lacking, in the studied carbonate sequence. In carbonate rocks, diagenetic alteration may influence both the uranium concentration and distribution (Hassan and Hossin, 1975) but there is no evidence for the occurrence of such a phenomenon in the Ses Sitjoles material.

The TURA and Th, K data confirm therefore conclusions based on sedimentological and borehole image observations to split Unit III in two subunits, IIIa and IIIb.

Correlation between Ses Sitjoles wells

Ses Sitjoles well unit correlation

The Ses Sitjoles area provides an exceptional opportunity to investigate the distribution in space and time of the various carbonate facies and their petrophysical properties at various scales, a key to the prediction of heterogeneities and the relationship between geological parameters and petrophysical properties within carbonate reservoirs.
MC2-MC8-MC9 and MC10 wells on one hand, and MC4-MC5-MC6 and MC7 wells on the other hand form respectively a cluster and an alignment of wells that are apart from only a few meters (Fig. P1-1 right). This distribution compensates either the lack of cores (wells MC6 to MC10 and S17) or of borehole image logs (partial in MC1 and MC4, total in MC6 and S17), thus allowing high-resolution correlations by assuming horizontal continuity of facies over such short distances. S17 is a particularly difficult case because located 58m apart from the nearest hole (MC7), it was not cored, and image logs were not recorded. Wells MC1, MC2, MC3 and S17 materialize the corners of the drilled area.
Correlations of the various carbonate units identified in the cored wells (MC1 to MC5) based on sedimentological data are illustrated in Fig. P1-8. MC3 well presents a special case: in this well, Unit II is not composed mainly of coral framestones and grainstones as in the other wells, but of coral framestones, grainstones and coral rudstones. This is asserted by core thin-sections, core slabs and borehole image logs.

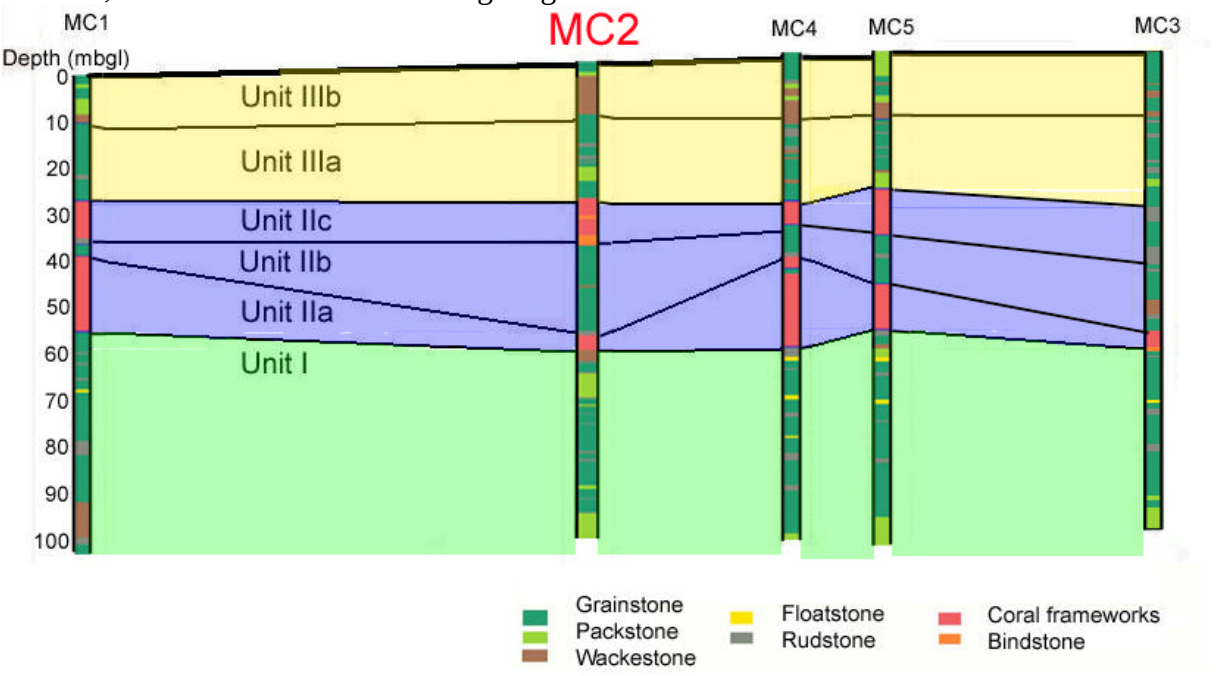

Figure P1- 8. Correlation between MC1 to MC5 cored wells, projected over a fictive plane passing through MC1 and MC3 wells. Modified from Jaeggi, 2006.

Table P1-7 summarizes the characteristic values acquired with the SGR tool in the various lithological units that comprise the carbonate sequence in the twelve Ses Sitjoles wells. The following information has been obtained from the downhole measurement datasets: 1) All subunits are clearly related to a marine depositional environment, except subunit IIIb in which some depth intervals are characterized by a transitional and restricted depositional

environment; 2) The occurrence of organic matter (algae, possibly mangrove roots in subunit IIIb) is noted in all units but is clearly scarcer in Unit II that is typified by the occurrence of coral frameworks; 3) Clay content that can be evaluated by removing the influence of uranium from the total natural gamma-ray SGR channel is low in all units except in subunit IIIb; 4) Subunit IIIb is clearly identified both by the CGR, SGR, Th and K channels; 5) Uranium is not very useful to delineate facies, with the possible exception for the top of Unit I, in most wells around MC2.

Unit/ subunit	CGR (CPS)	SGR (CPS)	Thorium (ppm)	Potassium (%)	Uranium (ppm)	Thorium/ Potassium	Thorium/ Uranium
Subunit IIIb	[0- 180], 61.6	[10- 190], 66.3	[0- 6.2], 1.8	[0- 4], 0.46	[1- 4.2], 1.28	[2- 100+], 4.0	[0.01- 6], 1.6
Subunit IIIa	[0- 120], 9.8	[18- 120], 46.5	[0- 1.6], 0.51	[0- 1.2], 0.03	[1- 8], 1.61	[1- 100+], 10.6	[0.01- 10], 0.38
Subunit IIc	[0-110], 7.2	[10- 120], 23.6	[0- 4], 0.36	[0- 0.5], 0.02	[1- 4.2], 0.78	[1- 100+], 8.8	[0.01- 4.0], 0.49
Subunit IIb	[0-90], 10.7	[10- 120], 31.5	[0- 3.5], 0.50	[0- 0.6], 0.04	[1- 4], 0.90	[1- 100+], 8.2	[0.01- 4.0], 0.67
Subunit IIa	[0-162], 11.7	[10- 210], 48.8	[0- 4], 0.53	[0- 2], 0.05	[1- 5.6], 1.69	[1- 100+], 11.0	[0.01- 5.0], 0.38
Upper Unit I	[0- 30], 8.0	[10 -80], 30.3	[0- 0.3], 0.38,	[0- 0.1], 0.03	[0.2- 3.0], 1.01	[1- 100+], 8.2	[0.01- 1.5], 0.43
Lower Unit I	[0- 30], 9.1	[10 -80], 38.0	[0- 0.3], 0.50	[0- 0.1], 0.02	[0.2- 3.0], 1.33	[1- 100+], 6.4	[0.01- 1.5], 0.45

Table P1- 7. SGR data characteristic values in successive unit/ subunits recovered in the 12 wells of the Ses Sitjoles site: [minimum- maximum values], average MC2 values (Th/K median).

Correlations between wells which were not cored have been based only on downhole measurement data. Image logs are a powerful tool as a consequence of their very good resolution, and because the optical image log, like the SGR log, is also available in the vadose zone and is not influenced by porosity. Thorium and potassium contents are low and are therefore not helpful for correlating the various units, except in the uppermost part of subunit IIIb where clastics are present; uranium can hardly be used for unit correlation. Accordingly, it has been necessary to design a specific correlation strategy. Tables P1-5 and P1-7 summarize the image and SGR log data that have been used for correlating the various lithological units and subunits, and applying the results obtained on MC1 to MC5 wells to correlate the remaining wells: MC6 to MC10 and S17 (Table P1-8). MC11 data has not been used for correlation, because it is too close and too similar to MC10 to be of interest.

SGR correlations for all Ses Sitjoles wells are illustrated in Fig. P1-9. Correlations based on SGR data allow a precise reconstruction of the 3D architecture of the successive carbonate units at various scales. The tops of Units I and II are flat. The top of subunit IIIa is flat, except in MC6 well where this surface defines a clear depression (Fig. P1-9B). Accordingly, the calculated thicknesses of Units I to III are 40m, 38m and 28m respectively (Table P1-8). The thickness of Unit II for each well has been indicated on Table 8; in this square area of 100m by 100m, this unit displays an average thickness of 37.8m with a standard deviation of 1.2m in ten wells, whereas it exhibits a thickness of 6m only in MC3 well, thus displaying a platform-like appearance over the Ses Sitjoles site area. No other well with a Unit II similar to MC3 has been found.

Unit/ subunit	MC1 (mbgl)	MC2 (mbgl)	MC3 (mbgl)	MC4 (mbgl)	MC5 (mbgl)	MC6 (mbgl)	MC7 (mbgl)	MC8 (mbgl)	MC9 (mbgl)	MC10 (mbgl)	S17 (mbgl)
Subunit IIIb	0-8.5	0-9.5	0-12.8	0-11.0	0-10.6	0-22.6	0-12.5	0-12.5	0-12.6	0-9.2	0-9.8
Subunit IIIa	8.5-30.8	9.5-26.8	12.8-31.5	11.0-30.3	10.6-25.6	22.6-28.5	12.5-25.1	12.5-33.8	12.6-29	9.2-27	9.8-26.8
Subunit IIc	30.8-38.8	26.8-36.8	31.5-43.0	30.3-33.4	25.6-36.8	28.5-41.2	25.1-36.9	33.8-37.7	29-36.8	27-37.8	26.8-36
Subunit IIb	38.8-42.8	36.8-56.3	43.0-60.0	33.4-41	36.8-42.05	41.2-45.1	36.9-47	37.7-59	36.8-57	37.8-55.4	36-45.6
Subunit IIa	42.8-58.8	56.3-59.3	60.0-65.6	41-60.0	42.05-59.4	45.1-58.2 TD	47-63.2	59-61.5	57-59.7	55.4-59.2	45.6-63.5
Unit I Upper	58.6-75.3	59.3-75	65.6-87.4	60.0-100.97	59.4-87	-	63.2-86.1	61.5-75	59.7-72.5	59.2-75.8	63.5-76.3
Lower	75.3-99	75-100.9	87.4-98		87-99	-	86.1-100.7	75-100.14	72.5-TD	75.8-96.6	76.3-99
Today water table depth ~ MSL	35.88	36.43	39.13	38.48	38.45	38.49	38.49	36.43	36.43	36.43	39.36
Distance top of coral unit to MSL	5.08	9.63	-20.47	8.18	12.85	9.99	13.39	2.63	7.43	9.43	12.56
Unit II thickness	28	32.5	34.1	29.7	33.8	29.7	38.1	27.7	30.7		36.7

Table P1- 8. Correlation of the various lithological units in the Ses Sitjoles wells. The last lines are estimates of the distance from the top of the coral unit to the Mean Sea Level (MSL), and of the thickness of the coral unit II.

SGR, Th, K, and generally TURA curves record accurately the top of subunit IIIa (Fig. P1-9). The precise location of the upper boundaries of other units needs to be defined on the basis of core observation and/ or borehole images due to the very little activity on the thorium and potassium channels; a slight change in activity does not automatically indicate a boundary between two successive units.

Unit II in MC4 well displays a spectacular succession of five beds bearing radioactive minerals and rich in organic matter. Those five beds are not seen in any other Ses Sitjoles well; a single occurrence of such beds in Unit II has been noticed in MC1, MC5 and MC6 wells (Fig. P1-9). It is also noteworthy that at the level of those beds, TURA value ranges from 1 to 2, close to the transitional environment area, and that no particular variations are noted regarding the depositional textures (Fig. P1-8). The origin of those radioactive mineral bearing beds is related to the occurrence of channels, with a minor influx of terrestrial clastic sediments.

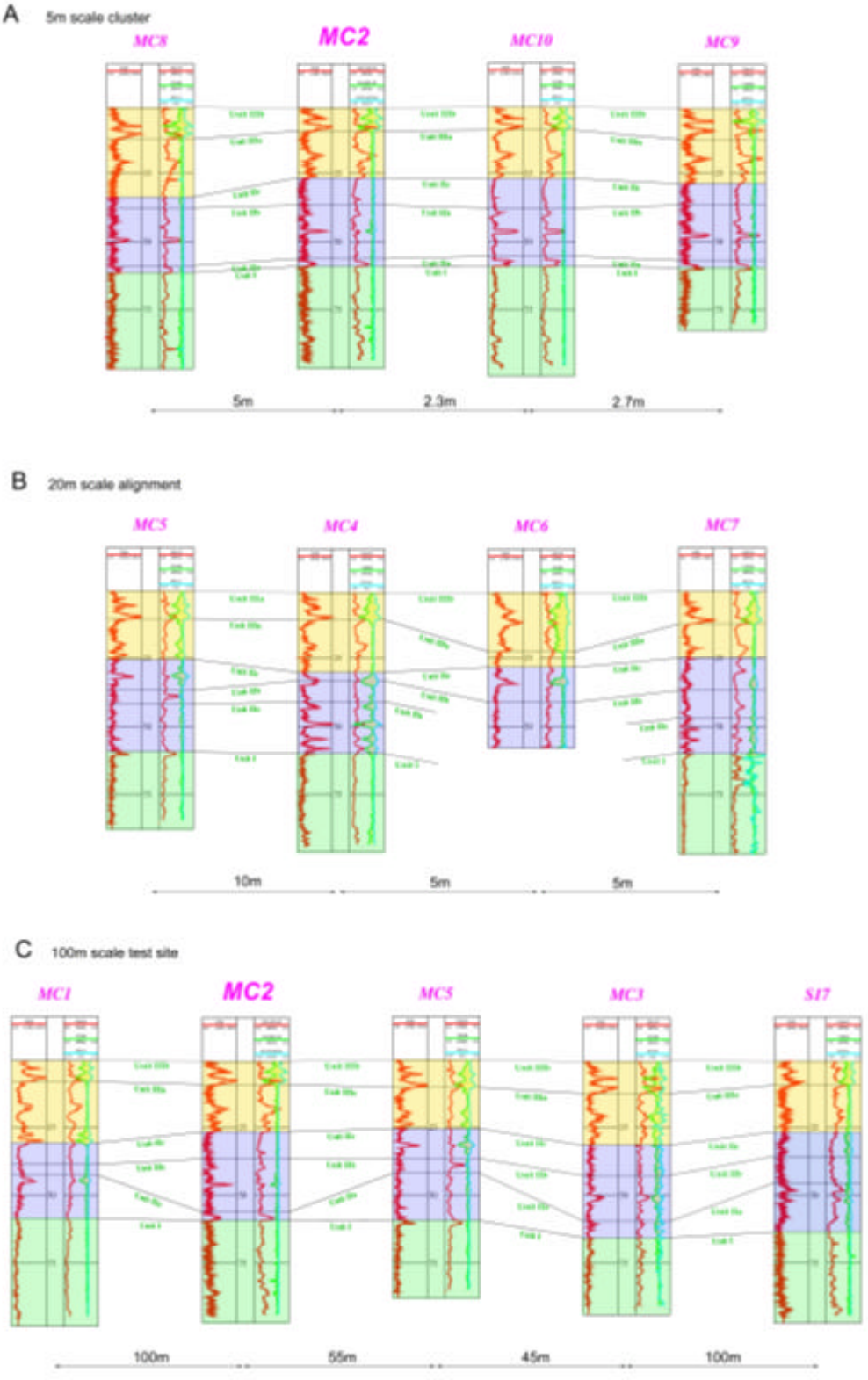

Figure P1- 9. SGR facies correlation over Ses Sitjoles site. On each well, the four represented curves include from left to right: SGR (track 1, red, scale 0 to 150 CPS), Uranium (track 2, red, scale 0 to 5 ppm), Thorium (track 2, green, scale 7 to –3 ppm), Potassium (track 2, blue, scale –3.5 to 1.5 %). The yellow-black dotted shading between the Thorium and Potassium curves highlights the presence of radioactive minerals. Below each figure, the distances between successive wells are indicated.

Ses Sitjoles overall coherence/ heterogeneity

The particular design of the Ses Sitjoles drilling site provides the opportunity to compare the evolution vs. depth both of uranium and of the couple thorium-potassium in each well by grouping the wells in 5m scale cluster, 20m scale alignment, and 100m scale test site respectively.

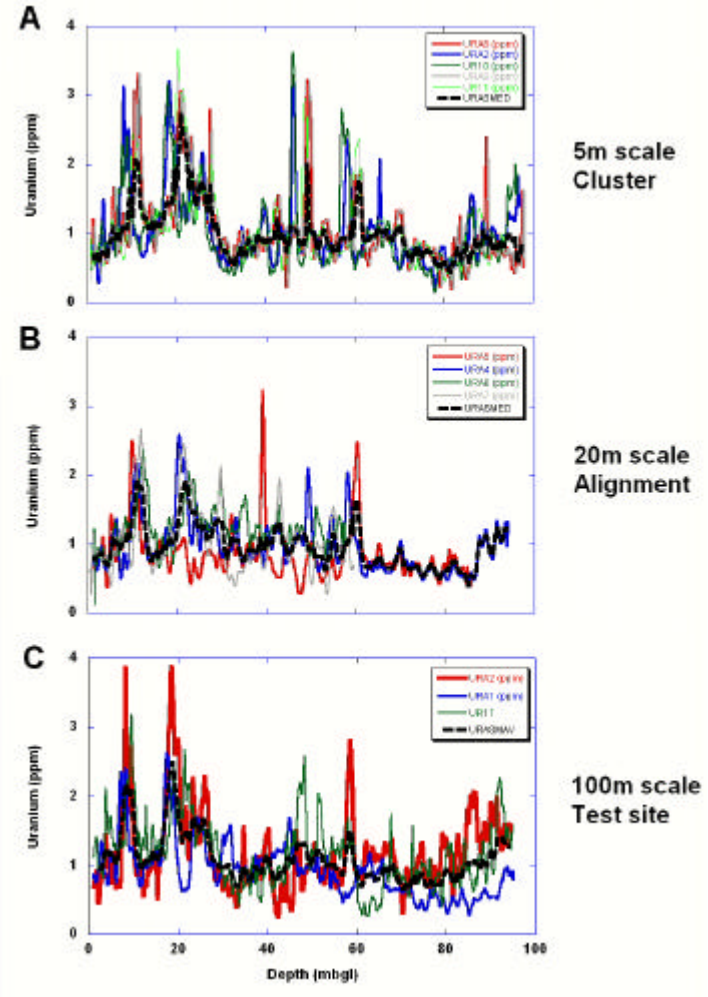

Figure P1- 10. Uranium curves vs. depth for different Ses Sitjoles wells; the URASMED channel is the smoothed median of the relative Uranium channels. (A) wells MC2, MC8, MC9, MC10 and MC11 are part of a 5m scale cluster. (B) wells MC4, MC5, MC6 and MC7 are part of a 20m scale alignment. (C) wells MC1, MC2 and S17 are at the corners of the 100m side test site.

Fig. P1-10 and Fig P1-11 illustrate the overall radioactive measurements lateral coherence ranging from a 5m to a 100m scale for the Ses Sitjoles site. As expected, the coherence is better observed on the 5m scale than on the 20 and 100m scales. In Fig. P1-10, the three plots display an upward decrease in uranium content between 100mbgl and 80mbgl (bottom of unit I) (already noted on MC2), and peaks at 60 (bottom of subunit IIa), 20 and 12mbgl (bottom of subunit IIIb) respectively, thus indicating favorable ecological conditions for the development of coralline algal encrustations and or accumulations at those levels.

In Fig. P1-11, five radioactive mineral peaks are clearly identified in Unit II from the well MC4 (Fig P1-11B), and a characteristic "double belly" pattern is observed at the bottom of subunit IIIb; this pattern occurs at a lower level in well MC6 than in any other well (Fig. P1-11B). This plot clearly demonstrates a larger heterogeneity of thorium- potassium on the 20m scale (Fig. P1-11B) than on the 100m scale (Fig. P1-11C).

It can also be noted that there is no particular correlation between the evolution of uranium and thorium- potassium curves, with the exception of the bottom part of subunit IIIb.

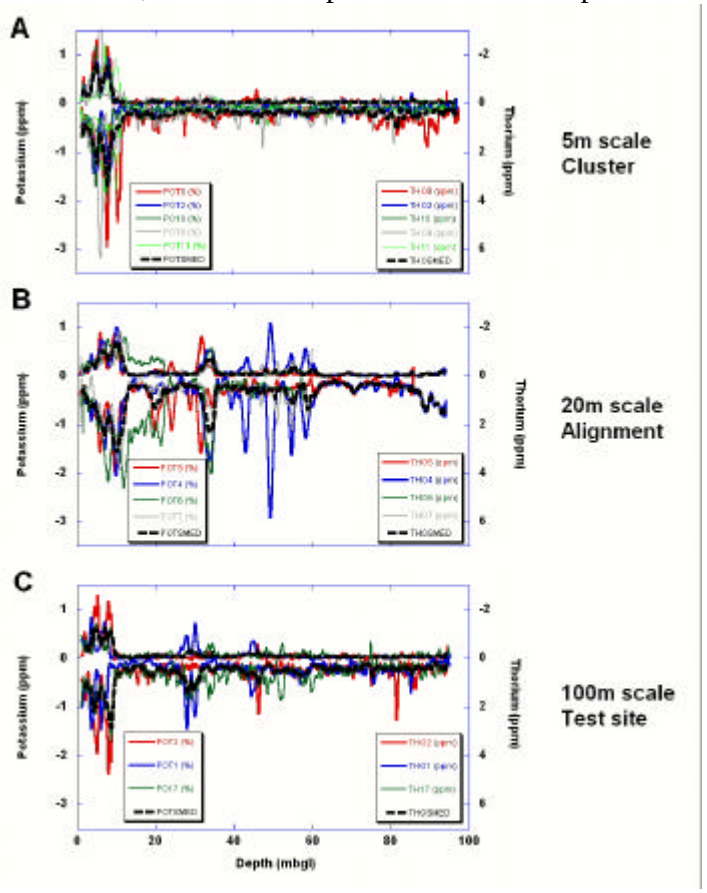

Figure P1- 11. Equivalent of Figure 10, for the Thorium-Potassium channels.

Clastics in Subunit IIIb

Subunit IIIb displays many more distinctive and varied features compared to the rest of the carbonate sequence drilled in Ses Sitjoles. It is also the only interval where the Th and K outputs of the SGR logging tool exhibit significant values, implying the presence of clastic sediments. Additional investigations are therefore needed both to delineate the facies changes and the relevant SGR log outputs variations vs. depth, and to analyze the crossplot thorium vs. potassium for radioactive mineral content.

Subunit IIIb SGR log vs. depth and facies

Fig. P1-12 illustrates an enlarged depth scale of SGR for subunit IIIb in MC2 well. The TURA curve in Fig. P1-6 shows that this subunit corresponds clearly to the shallowest depositional environment in the whole 100m interval. Facies vary extensively throughout this short depth interval (Tables P1-9 and P1-10; Fig. P1-12 and P1-13), while TURA varies from 0.03 to about 6, suggesting a change from a marine to a marine-continental transitional depositional environment. The highest TURA values correspond to the highest clay contents (separation thorium-potassium), indicating more terrigenous influence. The large separation Th-K noted on logs correspond to the l (clay, Fig. P1-13G and H) and o (siltstone, Fig. P1-13F, and J) thin section facies (Fig. P1-12). At 5m log depth, a calcrete is evidenced and coincides with a high TURA value (3.4) that typifies a continental depositional environment. Mangrove roots (thin section facies k; Fig. 12) are also apparent both on cores (Fig. P1-13E and P1-13I) and on borehole images (Fig. P1-5A).

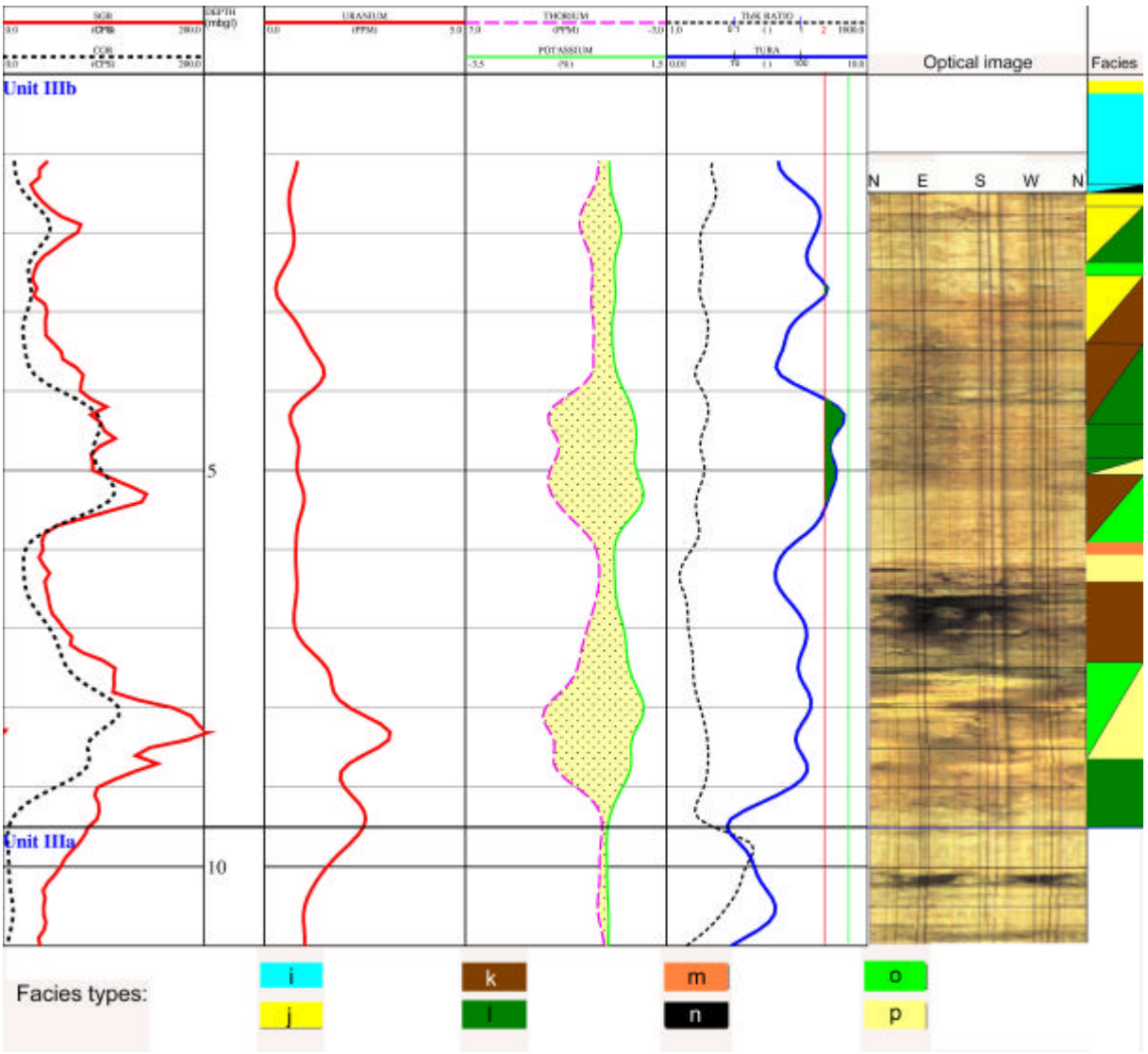

Figure P1- 12. Enlarged depth scale of SGR for subunit IIIb in MC2 well (left) and corresponding borehole optical images (right). The facies column is displayed at the extreme right, colours are coded according to the letters shown in the legend and described in Table P1-12.

The two clay peaks at the bottom of subunit IIIb are remarkable features that can be recognized over the whole study site (Fig. P1-9, P1-11). These peaks correspond to grey clay, or siltstone (Fig. P1-12, Tables P1-9 and P1-10, facies l and o). The small clay peak at 2.0mbgl corresponds to a small amount of clay (Table P1-11); the siltstone thin layer at 2.5mbgl, (Table P1-9 and Fig. P1-12), is probably too thin for having been detected properly by the SGR tool.

This comparison on an enlarged scale of facies and SGR log values on subunit IIIb strengthens, through complementary and consistent conclusions, and by the lateral extension observed on all wells by the use of the SGR tool, our attribution of this interval to the TCC. The features that usually typify this subunit include: 1) rapid changes in time of facies and depositional environments; 2) the coeval occurrence of characteristic facies identified on core (such as calcrete or peaks of radioactive minerals) and the corresponding indication by the TURA curve of continental environment. Moreover, this result confirms that the methodology used for that study is appropriate.

Thin section reference number on Table 6	Core depth (mbgl)	Core depth converted to log depth (mbgl)	Depositional texture	Porosity type	Facies	Remarks	Thorium/ Uranium ratio	Clay content evaluated from CGR (%)	Laboratory measured porosity (V/V)
-	0-0.2	-	-	-	Soil	-	-	-	-
-	0.2-0.3	-	-	-	m	-	-	-	-
-	1.3-1.4	-	Grainstone	Mainly intergranular	i	Restricted environment	-	-	0.165
-	1.7-1.8	0.2-0.3	Grainstone	Mainly intergranula	j	Well sorted, high wave energy, miliolids	-	-	0.15
-	3.0-3.1	1.5-1.6	-	-	I/n	Blackened grain, oolitic	1.1	2.5	0.18
1	3.1—3.2	1.6-1.7	Packstone	Mainly intergranular	j	Restricted environment, miliolids	1.1	4	0.18
-	3.2-3.5	1.7-2.0	-	-	j/l	Karstified with subvertical open fracture, with reddish brown clay cover	4.5	7.5	0.17
-	4.0	2.5	-	-	o	Clayey siltstone, grey, with marly pebbles	2	2.5	0.20
2	4.8-4.9	3.3-3.4	Packstone	Intragranular	j/k	Roots, restricted biota, sedimentological features and depositional environment, intraclasts, miliolids,grey-brown	1.5	4	0.22
3	5.8-5.9	4.3-4.4	Wackestone	Intragranular	k/l	Low wave energy, quartz, miliolids, roots	3	16	0.22
-	6.1-6.3	4.6-4.8	-	-	l	Claystone, plastic, brown	4	15	0.15
4	6.5-6.6	5.0-5.1	Calcrete	-	l/p	Calcrete, calcite precipitation, oxidation, clay	6	20	0.28
-	6.6-7.4	5.1-5.9	Wackestone	-	k/p	Wackestone, bright grey, with greenish and pink parts, mangrove roots	2	8	0.29
-	7.4-7.5	5.9-6.0	-	-	m	Calcrete hardpan	1	4	0.29
-	7.5-7.9	6.0-6.4	-	-	p	Chalky components in calcrete	1	3.8	0.32
-	7.9-9.0	6.4-7.5	-	-	k	-	3	10	0.32
-	9.0-10.2	7.5-8.7	-	-	o/p	Clayey siltstone, reddish beige, with coarse chalky components (paleo-calcrete), from 9.7m on marly limestone, chalky green is beige	1.5	20	0.18
-	10.2-11.1	8.7-9.6	-	-	l	Claystone, greenish, with thin intercalations of limestone	1	5	0.20
5	11.4-11.5	9.9-10.0	Grainstone	Intragranular		Open environment, quartz grains, miliolids	0.5	2	0.432

Table P1- 9. MC2 thin section and core visual descriptions (from Jaeggi, 2006) in subunit IIIb, in relation with SGR log displayed on Figure P1-12, and laboratory porosity measurements (three columns on the right). Thin section 5 belongs to subunit IIIa, and is given here for comparison.

Facies type	Thin section reference number	Facies descripton
i	-	Oolitic
j	1	Grainstone-packstone rich in bivalves and gastropods with abundant quartz grains
k	2	Rich in bivalves and gastropods with abundant quartz grains, mangrove roots,
l	3	Green brown and grey clays, different stages of subaerial oxidation and probably some altered volcanic ashes
m	4	Calcrete with hard pans and nodular chalky limestone, effect of shrinking, desiccation and calcite precipitation, no fossil
n	-	Thin layers of continental blackened horizon
o	-	Siltstone or marly limestones, poor in fossils
p	-	Calcrete

Table P1- 10. Description of the eight facies types indicated in Table P1-9. These facies are also observed in other wells (from Jaeggi, 2006).

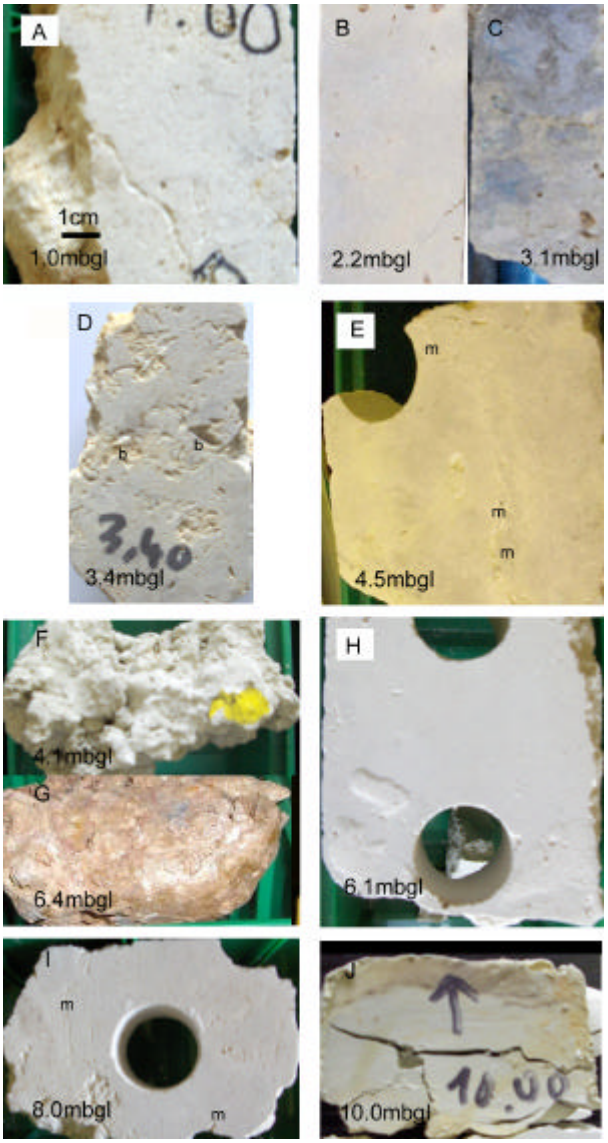

Figure P1- 13. Core photos from subunit IIIb in MC2 well. See description of facies in Table 10. (A) 1.0mbgl, facies i. (B) 2.2mbgl, facies j. (C) 3.1mbgl, facies j. (D) 3.4m, facies j/l, bivalves (b). (E) 4.5mbgl, facies j/k, mangrove root (m). (F) 4.1mbgl, facies o. (G) 6.4mbgl, facies l/p. (H) 6.1mbgl, facies l. (I) 8.0mbgl, facies k, mangrove root (m). (J) 10.0mbgl, facies o/p. Note that core G at 6.4mbgl (5m log depth) and core J at 10.0mbgl (8.5mbgl log depth) are very similar on the SGR log (Figure 12), but are in fact very different both in core, and in thin section facies (Tables 9 and 10); G is a caliche with clay content (facies l/ p), and J is a clayey silstone with coarse chalky components (paleo-calcrete) (facies o/p).

Core depth (mbgl)	Log depth (mbgl)	Calcite(%)	Dolomite (%)	Ankerite (%)	Montmorillonite + Illite (%)	Glauconite (%)	Total (%)
2.23	0.7	93.9	4.5	Traces	1.6	0	100
5.99	4.5	95.8	0	Traces	4.2	0	100
14.5	13	100	0	Traces	0	0	100
17.51	16	100	0	Traces	0	0	100
19.54	18	100	0	Traces	0	0	100
21.52	20	100	0	Traces	0	0	100
33.31	33.2	100	0	Traces	0	0	100
34.53	34.4	100	0	Traces	0	0	100
42.08	40.1	100	0	Traces	0	0	100
48.12	46.1	87.5	12.5	Traces	0	0	100
48.32	46.3	16.4	82.0	Traces	1.6	0	100
50.78	48.8	100	0	Traces	0	0	100
56.83	55.9	100	0	Traces	0	0	100
60.96	61	14.5	85.5	Traces	0	0	100
70.03	70	93.5	6.5	Traces	0	0	100
81.15	81.15	100	0	Traces	0	0	100
85.6	85.6	80.5	19.5	Traces	0	0	100
88.92	88.9	36.4	55.0	Traces	0	8.6	100

Table P1- 11. MC2 rocks mineralogical composition deduced from Table P1-1.

Subunit IIIb crossplots Th vs. K

We have seen before that the use of the separation between the Th and K curves, displayed on opposite scales (see Fig. P1-6, P1-9 and P1-12), is of interest to evaluate the radioactive mineral content in the formation. To be able to analyze the type of radioactive mineral(s), it is necessary to use a Th vs. K crossplot. The first studies of the Th vs. K crossplot (Hassan and Hossin, 1975; Serra et al., 1980) concluded that it is possible to identify the presence and type of radioactive minerals based on the Th/ K ratio, or the slope in the Th vs. K crosssplot. So far, this property has been mainly used in sandstones (Hurst and Milodowski, 1996) in which various radioactive minerals can occur in relatively large amounts. However, it is clear that more than two radioactive minerals occur in non negligible quantity in the rocks and even more within the surveyed interval. Later on, when more laboratory data were compiled, it was shown that, even in the simple case of occurrence of only two radioactive minerals, the slope of Th/K was not sufficient to identify clearly the minerals (Serra, 1990). Indeed, since thorium and potassium are rarely both present in the chemical formulae of the radioactive minerals such as clays, micas, and feldspars, it is clear that their occurrence is related to their adsorption by the mineral during its alteration, transport or diagenesis, and, accordingly, that the proportion of these chemical elements will be variable (Hurst and Milodowski, 1996). For this reason, Serra and Serra, 2000, 2003, decided, based on the previous data (Serra, 1990), to represent the 100% “pure” radioactive mineral by an elliptic domain (Fig. P1-14); it appears therefore that there is a clear overlap between the montmorillonite and the kaolinite ellipses. Furthermore, a line joining the origin (i.e. the quartz or any non radioactive matrix point) to the centre of the biotite mineral, would define a mixture of quartz- mixed layers- illite- biotite. In the Ses Sitjoles carbonate sequence, the plot of ten wells SGR data (Fig.P1-14B and C) defines an ellipse-shaped cloud of points spreading from the plot origin; it seemingly indicates an illite- biotite trend. However geochemical and mineralogical analyses of 18 samples from MC2 well (Tables. P1-1 and P1-11) demonstrate that those rocks are primarily made of calcite, with some levels displaying dolomitization processes; noticeable amounts of clay

(mostly montmorillonite and illite) are only apparent in subunit IIIb, and only traces of ankerite are observed . There is a good agreement between CGR data and the amount of clay deduced from geochemical and mineralogical analyses.

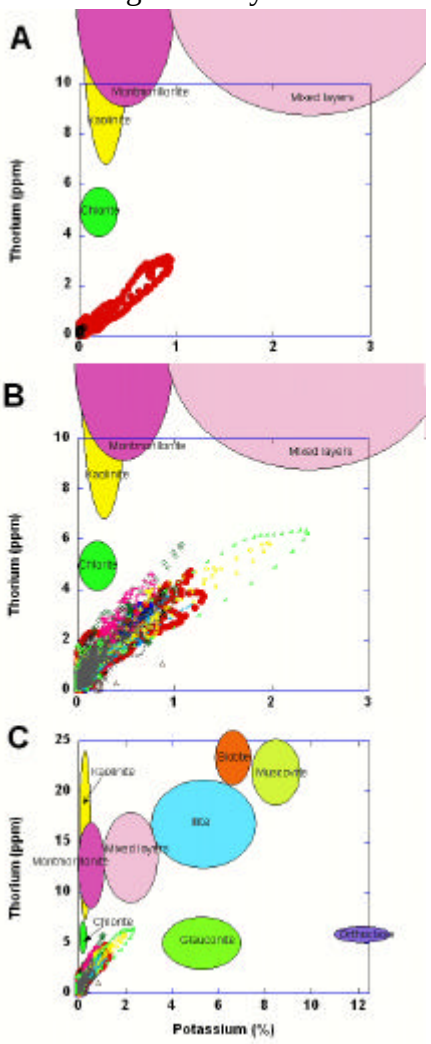

Figure P1- 14. Ses Sitjoles Thorium vs. Potassium crossplots. The colored ellipses that represent empirical radioactive mineral domains are adapted from Serra, (2000 and 2003). (A) MC2 well, 2000 data points, expanded scale. The black dots represent lab measurements (Table P1-1). (B) Ses Sitjoles ten wells, 22000 data points, expanded scale; MC2 data are plotted as red dots. (C) Ses Sitjoles ten wells, reduced scale, allowing to view a complete display of most representative radioactive mineral domains; MC2 data are plotted as red dots.

Because of the greater solubility of K compared to that of Th, Fig. P1-14 plots may also be used to evaluate the distance of transport of sediments, their diagenesis, their chemical maturity (increasing counterclock-wise) and to consider a general paleoclimatic aproach.
The presence of noticeable amounts of montmorillonite and illite in subunit IIIb of the Ses Sitjoles carbonate sequence, is an indication that this formation was close to land during deposition, and that the chemical maturity was relatively low.

Ses Sitjoles thorium vs. TURA crossplots

Fig. P1-15A illustrates the different depositional environments and boundaries in the Th vs. Th/ U axes for MC2 well. The general increase in clay content (see Th axis), reflects the environment changes from marine to transitional related to an increase in terrigenous supplies. Some wells display few data related to a continental depositional environment (Fig.P1-15C).

Fig. P1-15B and P1-15C show also a remarkable statistical overlapping of the different Ses Sitjoles wells data, which confirms the validity of the data.

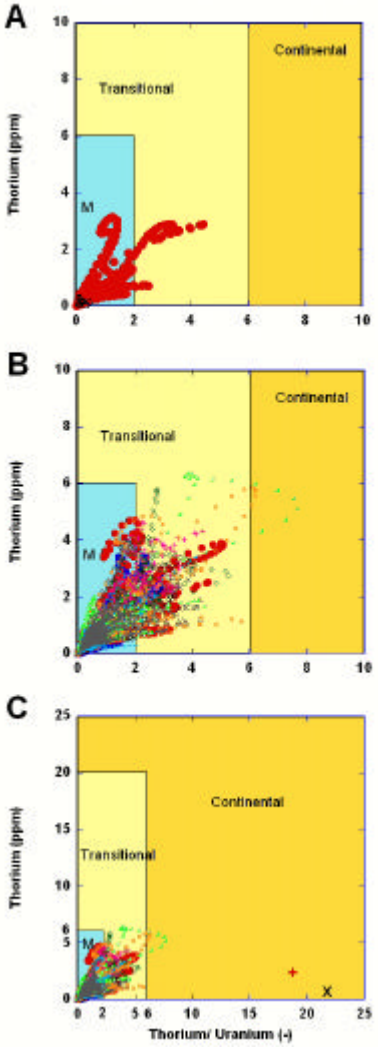

Figure P1- 15. Ses Sitjoles Thorium vs. Thorium/ Ur anium ratio crossplots, showing domains of marine (M, blue), transitional (yellow), and continental (ochre) environments (crossplot template after Adams, 1958). (A) MC2 well, 2000 data points, expanded scale. (B) Ses Sitjoles ten wells, 22000 data points, expanded scale; MC2 data are plotted as red dots. (C) Ses Sitjoles ten wells, 22000 data points, reduced scale, allowing to view a complete display of all data points; MC2 data are plotted as red dots.

Ses Sitjoles paleo-environments, TURA overall coherence and heterogeneity

Fig. P1-16 includes profiles of TURA vs. depth of different groups of Ses Sitjoles wells.
The TURA curves for the MC8-MC2-MC10-MC9-MC11 group of wells (i.e. a 5m scale cluster) are reasonably overlapping for the five well curves, and also with the smoothed median curve, as it would be expected for such a short distance cluster of wells (Fig. P1-16A). The smoothed TURA median curve increases upward from 0.1 at the bottom of the well (i.e. 97mbgl) to a maximum of 1 at 78mbgl. Between 78 and 34mbgl, a median TURA relative plateau is typified by a value of 0.3 and is bounded by the 78mbgl peak and a peak of 0.6 at 34mbgl. From 34mbgl upwards, median TURA decreases to 0.12 at 22mbgl before increasing up to 2 at 8mbgl and forming a plateau up to the surface, except for a short low of 0.7. Thus, in this cluster of wells, median TURA reaches a low of 0.1 in the bottom part of Unit I

(97mbgl), and of 0.13 in the middle part of subunit IIIa (22mbgl), seemingly coinciding with the deepest depositional environments. Unit II (30-60mbgl) that includes coral frameworks exhibits a relatively stable median TURA characterized by an average value of 0.3 (maximum of 0.6, minimum of 0.13), suggesting a rather limited and stable water depth. The highest median TURA values are recorded in the lowest part of Unit 1 (78mbgl, value 1) where they could be explained by the occurrence of terrigenous particles, and in subunit IIIb (0-8mbgl), where values as high as 2 indicate a marine to continental transitional environment.

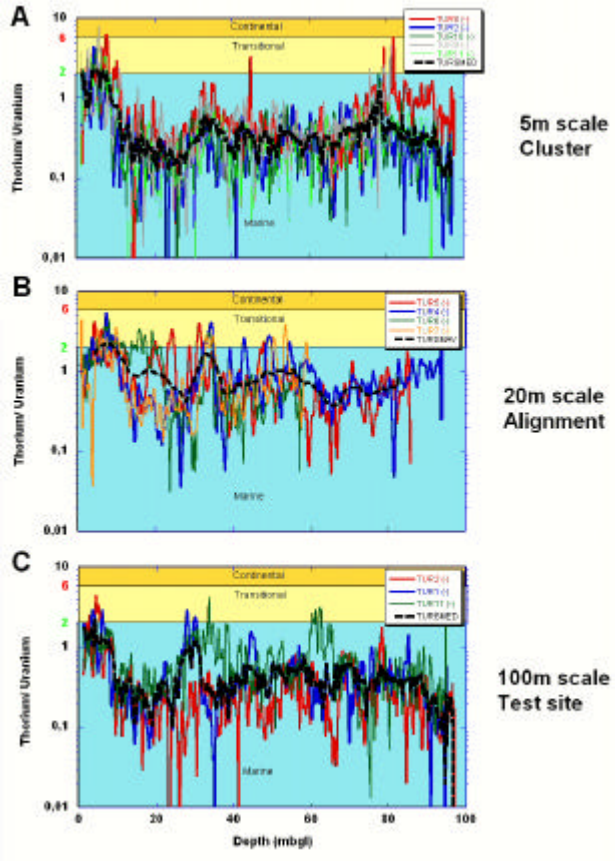

Figure P1- 16. Thorium/ Uranium ratio curves versus depth for cluster of wells MC8-MC2-MC9-MC10-MC11 (A), alignment of wells MC4-MC5-MC6-MC7 (B), and test site MC2-MC1-S17 (C). The thick dashed black line is the smoothed median of the other curves. Environments are color coded; blue means marine, light yellow means transitional, and dark yellow means continental.

TURA data concerning the four aligned wells MC5, MC4, MC6 and MC7 are illustrated in Fig. P1-16B. Compared to Fig. P1-16A, a larger scattering of data is related to the greater distance between wells (i.e. 20m between MC5 and MC7). Furthermore, those wells exhibit remarkable SGR features that have been summarized before: 1) MC6 displays a deeper than usual bottom for subunit IIIb (22.6mbgl vs. 10mbgl in average); 2) beds including noticeable amounts of radioactive minerals occur in Unit II in MC5, MC6,MC7 (one bed) and MC4 (four beds) wells (Fig. P1-9B). In those wells, median TURA starts at 97mbgl with a high value of 1.5 and decreases upward to a value of 0.4 at 66mbgl before increasing upward, with some oscillations, and reaching a maximum of 1.7 at 32mbgl; it then decreases upward to a value of 0.5 at 26mbgl, and increases upward to reach a plateau of 2 from 8mbgl up to the surface. The comparison between Fig. P1-16A and P1-16B shows that the top part of the relevant sequences (0 to 32 or 34mbgl) are quite similar in trend, while the lowermost part (below 32-34mbgl) exhibit significant differences.

Fig. P1-16C illustrates TURA for wells MC1-MC2 and S17, located at more than 100m distance from each other. Although the MC3 well should have been logically included in this

"100m scale site" display, it was not possible to get a good quality SGR data in this well, and, accordingly, TURA and Th/K curves were of insufficient quality to be useful. In spite of the greater distance between wells, the overlapping of the curves is striking (Fig. P1-16), in a similar way to what is displayed by the 5m scale cluster (Fig. P1-16A), but in clear contrast to what has been reported on the 20m scale alignment (Fig. P1-16B). On this 100m scale site plot, the median TURA curve increases upward from 0.2 at 96mbgl to a value of 0.6 at 80mbgl, and then forms a plateau up to 29mbgl where a peak of 1 is reached. From 29 to 18mbgl, median TURA decreases upward from 1 to a value of 0.2 and then increases upward to a value of 1.5 at 8mbgl, staying then more or less stable at that value up to the surface.
To summarize, the plots for the 5m scale cluster and the 100m scale test site are very similar and differ markedly from the 20m scale alignment, except for the top part of the carbonate sequence (i.e. 34m in Fig. P1-16A, 32m in Fig. P1-16B and 29m in Fig. P1-16C). This provides another example of the heterogeneities identified in the study site.
The shift between the three smoothed median TURA curves displayed on each graph of Fig. P1-15, more particularly for the case of Fig. P1-15B, suggests that the apparent change in bathymetry is probably related to the local topography of coral frameworks.

DISCUSSION

The use of combined core analysis, high resolution borehole image logs, and natural spectral gamma-ray logs data on twelve boreholes carefully located on a 100m by 100m square site in the Ses Sitjoles area, and their comparison with similar data recorded in two other carbonate complexes has allowed to assert the methodology, and obtain a large number of results that are discussed below.

Depositional environments of the Ses Sitjoles Miocene carbonate sequence (core analysis vs. borehole images and SGR)

MC2 reference well core data have been analyzed; units (I, II, and III) and subunits have been identified and described. Characteristic borehole images from this well have been selected and described for each subunit. Then, MC2 SGR log data (SGR, Uranium, Th, K) and computed data (CGR, TURA, Th/K) have been analyzed vs. depth or on crossplots.

TURA

TURA is used for identifying the general type of depositional environment (marine, transitional or continental), and for giving an indication on the distance with respect to the shore line, whether off-shore (where it might give information on the water depth) or on the continent where it may additionally provide paleoclimate information. In Ses Sitjoles, the thorium/ uranium ratio as well as the radioactive mineral analysis performed from the thorium and potassium channels suggests that the distance from the reef to the coast was short, therefore agreeing with what had been deduced already from the micro biota analysis.
The reef unit is thought to be of low angle platform type, uniformly low bathymetry (moderate TURA values of average value 0.3 to 0.6, no steps in variations), formed of exclusively massive morphology corals (0 to10m), mostly *Porites* (living depth: 10m), in contrast to what has been observed in Cabo Blanco outcrops where massive, branching, and dish corals growth forms suggest that those frameworks developed within a 0-30m depth interval.
Comparison and discussion of the core visual examination and thin sections analysis results, borehole images, and SGR interpretation, particularly in subunit IIIb, which is characterized

by a succession of distinctive facies in a short interval, lead to the conclusion that subunit Iib belongs to the TCC.

TURA and Th/K

The comparison of the evolution of the TURA and Th/K curves vs. depth, allows to describe paleoclimate changes in continental environments.
In Ses Sitjoles, we observe that the transition from Unit I to subunit IIIa characterizes a shallowing upward evolution from normal marine environment ending in a very shallow environment, closer to the shoreline. There is a sharp change in TURA and Th/K curve trends at the boundary between subunits IIIa and IIIb; subunit IIIb that indicates an abrupt evolution towards a very shallow, transitional depositional environment, which characterizes the TCC.
The low values of the Th/K ratio are indicative of sediment transport over a short distance.

Facies composition (core analysis vs. borehole images and SGR)

Uranium: Organic matter, fractures, stylolite

One of the main use of the uranium content in sediments in general and in Ses Sitjoles in particular is the detection of the presence of organic matter of either humic (mangrove roots) or sapropelic origin (algae).
14 fractures have been detected by borehole images in MC2, 8 of them occurring in subunit IIIa. Some fractures have been confirmed by the occurrence of high uranium content.
High uranium content occurrences have also been observed in stylolites; however it was not possible to detect stylolites either by cores or by borehole images in MC2.

Th and K: radioactive minerals

The separation either of the Th and K curves, when displayed in opposite scales, or of the SGR and CGR curves, are indicative of the amount of radioactive minerals in sediments or rocks. In Ses Sitjoles, most of the radioactivity derives from the uranium content of the formation, with a very low radioactive mineral content, except in subunit IIIb, where a Th-K "double belly" bottom of subunit IIIb pattern is a clear marker and delineator. MC1, MC5 and MC6 wells display the occurrence of a single bed bearing radioactive minerals in Unit II, while MC4 displays a succession of five those beds. Those beds are attributed to the existence of channels, with minor terrigenous supply, attested by TURA values ranging from 1 to 2.
Th vs. K crossplots allow the identification and quantification of sedimentary radioactive mineral content, including different types of clays. In Ses Sitjoles wells, illite and montmorillonite have been detected, and their occurrence has been confirmed by laboratory mineralogical analyses.
The detection of a particular mineral in sediments may have implications for the reconstruction of depositional environment and/ or diagenetic processes. In Ses Sitjoles, the occurrence of illite and montmorillonite implies that the sediment transport was short.

Heterogeneities in the Ses Sitjoles Miocene carbonate sequence

Other cored wells (MC1, MC3, MC4, MC5) have been investigated through core analysis, and corresponding borehole images and SGR data.
The remaining wells were not cored and have been therefore studied from borehole images (when available) and SGR data. These data and information obtained in surrounding wells,

when available, have been used to detect boundaries between the successive units and subunits in those wells.

Borehole images: lithological boundaries, fractures, stylolites

High resolution, 360° continuous borehole images, allow to identify distinctive facies fossils and features, such as shale layers, caves, cavities, karst, macro-porosity, corals, stylolites, etc. Fractures can be identified, quantified by their dip magnitude, orientation, and characterized by their planarity quality, their aperture. In contrast, stylolites were not detected.

SGR: lithological boundaries

The SGR, CGR, uranium, thorium and potassium continuous data are usually good tools for formation correlation. In this heterogeneous reef sequence comprised of complex, multi-facies subunits, distributed on 100m horizontal and vertical scales, the SGR slimhole tool is only helpful to define Unit boundaries, because of the generally very low level of the thorium and potassium channels. It is of limited help for characterizing the various subunits, although it has been used to define subunit IIIb, which is typified by high potassium and thorium content; it allowed to show that this subunit is thicker in well MC6 (28.5m), whereeas in the rest of the site, its thickness ranges from 8.5 to 12.8m. Such a use is of huge interest on greater scale (35km horizontal and 200m vertical) reconstructions concerning the whole Miocene carbonate platform in SE Majorca (Maria-Sube et al., in prep.), especially when the available datasets are limited.
The SGR tool also confirms the distinction between subunits IIb and IIIa already characterized by their respective biological content (Table P1-3): Table P1-7 displays very contrasted CGR, SGR, uranium, thorium/ potassium, and thorium/ uranium readings in those two subunits.

Comparison of Ses Sitjoles with the Great Bahama Bank and the Great Barrier Reef

Two Ocean Drilling Program (ODP) legs have concerned carbonate complexes covering a Miocene to modern time window, respectively the Great Barrier Reef (GBR), leg 133 (Davies et al., 1990), and the Great Bahama Bank (GBB), leg 166 (Eberli et al., 1996; Eberli et al., 1996a), on which core and SGR data were obtained. FMS electrical image logs are also available for the GBB sites. The comparison of those data and those collected on the Ses Sitjoles Miocene carbonate complex might allow the confirmation of the SGR methodology and of the slimhole SGR logging tool validity asserted for Ses Sitjoles. Furthermore, the general paleoceanographic and tectonic context related to the GBB and GBR sites, as well as detailed information (e.g.: radioactive mineral content, uranium vs. depth evolution) might bring a valuable comparative dataset to further interpret the Ses Sitjoles carbonate sequences (e.g. water depth, distance to land, and location of the drilling sites compared to the reef main body).
The Bahama Banks are the submerged carbonate platforms that form the basement of the modern Bahama Archipelago. The GBB is the carbonate bank that is located around Andros Island, extending on 600km from the Northwest to the Southeast. Four sites (1005C, 1003D 1007C, and 1006A), were drilled and logged in the North-West slope transect off the GBB, between Florida, Cuba and Andros Island, from the proximal to the drift, from 350 to 660m below sea level (mbsl) water depth during the ODP Leg 166 (Eberli et al., 1996, Table P1-12). The site is more than 200km away from the coasts of Florida, Cuba or Andros island; the biostratigraphic evidence suggests a depositional environment deeper than 200mbsl. The GBB

is a carbonate system that developed from the Jurassic up to modern time. The drilled formations range in ages from the Lower Miocene to the Pleistocene (Table P1-12).

Site	Location	Depth interval (mbsf)	Sea floor depth (mbsl)	Distance from GBB edge (km)	Interval (mbsf)	Uranium average (ppm)	Lithology	Lithoclasts (B.= benthic P.= planktonic)	Paleobathymetry (mbsl)	Age
1003D	Lower slope	82-1024	470	5	82-100	1	Mud to wackestone-packstone, turbidites, slumps	B. forams, coral fragments, halimeda debris	300-500	Pleistocene
					100-160	2		P. & B. forams	300-700	Late Pliocene
					160-300	1				Early Pliocene to late Miocene
					300-700	2.5	Marl/ limestone alternations and clay layers, turbidites, slumps	B. forams, halimeda debris	200-600	Late Miocene
					700-1024	4.5		P. & B. forams, halimeda debris		Late to early Miocene
1005C	Upper slope	0-684	350	1.6	0-200	2	Mud to wackestone-packstone, turbidites, slumps	B. forams, coral fragments, halimeda debris	200-400	Pleistocene to late Pliocene
					200-400	1		P. & B. forams	200-600	Early Pliocene to late Miocene
					400-684	3	Marl/ limestone alternations and clay layers, turbidites	P. & B. forams, halimeda debris		Late Miocene to middle Miocene
1006C	Drift	84-691	660	27	84-100	0.5	Ooze/ chalk	B. forams, coral fragments, halimeda debris	400-1000	Pleistocene
					100-450	0.5	Ooze/ chalk	P. & B. forams, coral fragments, halimeda debris		Late Pliocene to late Miocene
					450-691	2	Marl/ limestone alternations and clay layers, turbidites	P. & B. forams, halimeda debris		Late Miocene to middle Miocene
1007C	Toe of slope	0-1125	650	14	0-30	2.5	Ooze/ chalk, turbidites	B. forams, coral fragments, halimeda debris	400-1000	Pleistocene
					30-100	0.5	Mud to wackestone-packstone, turbidites, slumps	P. & B. forams		Early Pliocene to late Miocene
					100-350	2.5 to 3				
					350-1125		Marl/ limestone alternations and clay layers; highstand system track, turbidites, slumps	P. & B. forams, halimeda debris		Late to early Miocene

Table P1- 12. GBB sites characteristics (from Eberli et al., 1996).

Table 1. GBR sites characteristics (from Davies et al., 1990).

Site	Location	Depth interval (mbsf)	Sea floor depth (mbsl)	Interval (mbsf)	Uranium average (ppm)	Lithology	Lithoclasts (B.= benthic P.= planktonic)	Paleobathymetry (mbsl)	Age
812B	Queensland Plateau	12-270	405	12-30	0.3	Pelagic, hemipelagic and periplatform, micritic chalk	B. & P. forams, tropical fauna	200-600	Pleistocene
				30-70			B. forams, tropical fauna	30-100	Upper Pliocene
				70-160	2	floatstone & packstone		0-30	Middle Miocene to Late Pliocene
				160-270		Platform carbonate,	Coralline algae		
814A		6-268	405	6-60	0.3	Pelagic, hemipelagic and periplatform	B. & P. forams	200-600	Early Pliocene to Pleistocene
				60-130	3	Platform carbonate, micrite ooze	B. forams	0-30	Upper Miocene
				130-268		Pelagic, hemipelagic and periplatform, mudstone	-	200-600	Middle Miocene to upper Pliocene
815A	Marion Plateau	77-409	400	77-409	2	Nanno-ooze, nanno-chalk	B. & P forams	200-600	Late Miocene to Pleistocene
816C		0-218	400	0-180	0.3	Nanno-ooze	B. & P. forams	200-600	Early Pliocene to Pleistocene
				180-218	1.5	Dolomitized floatstone & rudstone	Coralline algae	< 50	Middle Miocene
817D	Townsville Trough	63-662	900	63-200	1	Pelagic, hemipelagic and periplatform, micrite and nanno ooze	B. & P. forams	600-1000	Middle Miocene to Pleistocene
				200-400		Pelagic, hemipelagic and periplatform	B. & P. forams	400-600	Middle to upper Miocene
				400-662		Chalk and micrite Platform carbonate	Coralline algae	0-200	Middle Miocene
819A	Modern GBR	0-355	620	0-65	0.3				Pleistocene
				65-355	2				
820B		77-360	340	77-150	2	Clayey wackestone with bioclastic wackestone/ packstone	B. forams	0-200	Pleistocene
				150-360		Upward coarsening cycles, mudstone to packstone	Nannofossils	200-600	
821A		0-365	212	0-65	0.3	Upward fining	Reef related	0-30	0-0.5MA
				65-140	2	cycles of sands	benthic fossils		
				140-365		Upward coarsening cycles of dolomitized calcareous sandstone and calcareous mudstone	Scattered forams and mollusks	0-60	0.5-1.8MA
822A		67-299	1010	67-80	2	Clayey bioclatic ooze, micrite	Nannofossils, B. & P forams	600-1000	Pleistocene
				80-299		Calcareous mud w. various amounts of terrigeneous clay	Nannofossils, B. & P forams		Pliocene
823C	Queensland Trough	0-960	1650	0-960	1.5	Pelagic, hemipelagic, slumps & turbidites	Nannofossils, B. & P. forams	1000-2000	Late Miocene to Pleistocene
				800-960		Chalks, turbidites, hemipelagic sediments	Nannofossils, B. & P. forams	600-1000	Upper Miocene

Table P1- 13. GBR sites characteristics (from Davies et al., 1990).

The GBR is the world's largest modern coral reef system, composed of roughly 3,000 individual reefs and 900 islands, that extend on about 2,600 kilometres, covering an area of

approximately 344,400km². The reef is located in the Coral Sea, off the coast of Queensland in North-East Australia. The North-Eastern Australian margin was investigated from the GBR to the landward side of the Queensland Plateau. During ODP Leg 133 (Davies et al., 1990), sites 819A, 820B, 821A, and 822A were drilled on the Eastern side of the modern barrier reef, from 212 to 1010mbsl, 10km offshore Cairns. Sites 812B, 814A and 823C were drilled on the Queensland Plateau (812A and 814A) or Through (823C) North-East of the GBR sites, 20 to 50km away from the coast line, at water depths ranging from 405 to 1650mbsl. Site 817D was drilled in the Townsville Through South-East of the GBR sites, 40km away from the coast, at 900mbsl water depth, while sites 815A, 816C were drilled on the Marion Plateau, South-East of the GBR sites, 30km away from the coast, at 400mbsl (Table P1-13). This carbonate complex has developed from the late Miocene to modern time (Table P1-13). The reef initiation is related to the Australian plate drift from the poles to the tropic and the consequent changes in sea surface temperature from temperate to tropical around 15m.a. Reefs were first seen on the Marion and Queensland Plateaus; they did not survive the mid Miocene (10.4m.a) sea level fall on the emerged Marion Plateau, while they developed continuously on the Queensland Plateau. However, the occurrence of non-tropical water conditions caused a dramatic decrease in production of shallow-water carbonate sediments, until the reappearance of tropical-water conditions (3m.a.) on the Queensland Plateau, while the Marion Plateau was drowned at that time and was therefore too deep to support coral reef growth. The rapid subsidence of the Australian continental shelf created conditions for the rise of the GBR at about 1.5m.a. The Queensland Plateau had been used as refuges for the corals, which migrated later towards to the modern GBR when environmental conditions became favorable at about 0.5m.a. (Davies et al., 1990).
Both GBB and GBR form carbonate complexes that are larger than the SE Majorca Miocene reef complex, even though the later belongs to a system more than 300km long and covering most of the Balearic archipelago, including Majorca, Menorca, Ibiza, Formentera and smaller islands, (Pomar and Ward, 1996). In contrast to the Ses Sitjoles site, both GBB and GBR legs are located off the reef main body (except for site 821A of the GBR, drilled trough a Pleistocene reef, much younger than the Ses Sitjoles reef) in the distal slope, or even in troughs.

Thorium vs. potassium comparison

The large hole Th and K data were plotted in Fig. P1-17A (GBB) and P1-17B (GBR), to be compared to the slimhole data from Ses Sitjoles wells, Fig. P1-17C.
The GBB Th vs. K plot data present a fan-like cloud of points spreading from the plot origin. The differences with the plot obtained in Ses Sitjoles concern the general distribution of the points, and a lower radioactive intensity, except for a few data that plot in the kaolinite area, implying long sediment transport distance. The scattering of points is larger, ranging from potassium evaporite to kaolinite, in relation to the very low intensity of the data, and therefore to large statistical variations. The low content in terrigenous material can be explained by the location of the four GBB sites more than 200km away from the present day coasts, and more than 1.6km from the GBB edge, on or down the slope, or away from the slope.
The GBR Th vs. K plot data displays an ellipse-shaped cloud of points spreading from the plot origin quite similar to the Ses Sitjoles data concerning the radioactive intensity, but are slightly more tilted toward the NNE, the majority of the data falling therefore into the kaolinite to montmorillonite zones, and a substantial number in the illite and chlorite zones. However, because we dealing with a system for which at least four data are unknown (i.e. the formation radioactive mineral content of each mineral on the plot) and two are known (i.e. Th and K), the system is undetermined. For instance, the apparent chlorite points on the diagram

could simply correspond to low content kaolinite points, and similarly, apparent montmorillonite points could be low content mixed layer clay.

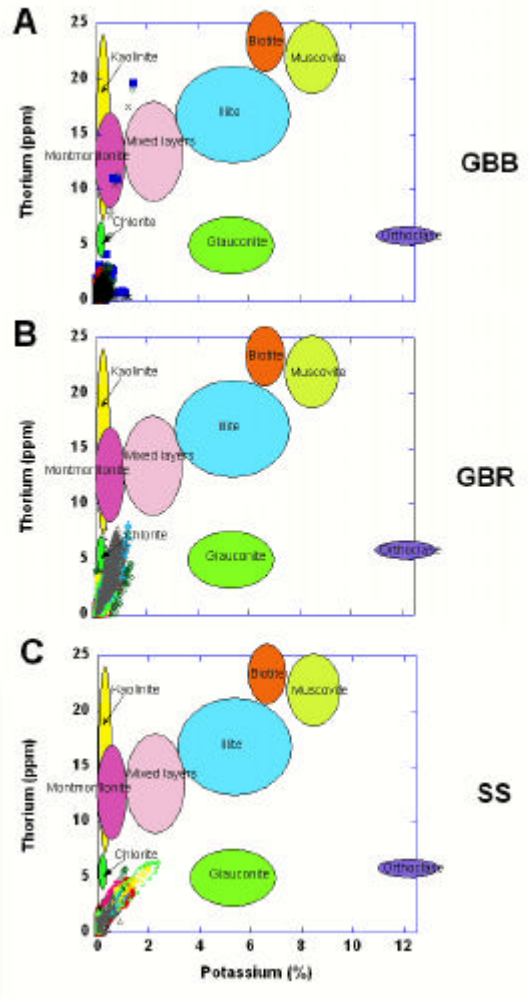

Figure P1- 17. Comparison of Thorium vs. Potassium crossplots reduced scale for three different carbonate complexes: (A) Great Bahama Bank (GBB) four sites (ODP Leg 166), 25000 data points. (B) Eastern Australia Great Barrier Reef (GBR) ten sites (ODP Leg 133), 17000 data points. (C) Ses Sitjoles ten wells, 22000 data points.

The clay content of 60 samples from site 823C includes: 45 to 85%, (mean 60%) smectite (or montmorillonite); 10 to 35%, (mean 25%) kaolinite; 3 to 18%, (mean 10%) illite; traces to 10%, (mean 5%) of mixed layers; 0 to 5% chlorite (Chamley et al., 1990). These analytical results therefore confirm borehole measurements data. Site 823C is located 20km away from the coast.

The GBR sediments and Ses Sitjoles rocks display very comparable contents in radioactive minerals, even though those sites are located nowadays respectively 20 to 50km and 6km away from the coast. The prevalent montmorillonite- kaolinite and montmorillonite- illite compositions for the GBR and Ses Sitjoles sites respectively indicate in both cases a short sediment transport and even a relatively shorter transport in Ses Sitjoles.

TURA vs depth and Thorium vs. TURA comparisons

In Fig. P1-18, TURA curves vs. depth for the Ses Sitjoles area (Fig. P1-18C), are compared to those obtained on the GBB (Fig. P1-18A) and four selected wells (for clarity of the plot) on the modern GBR slope (Fig. P1-18B).

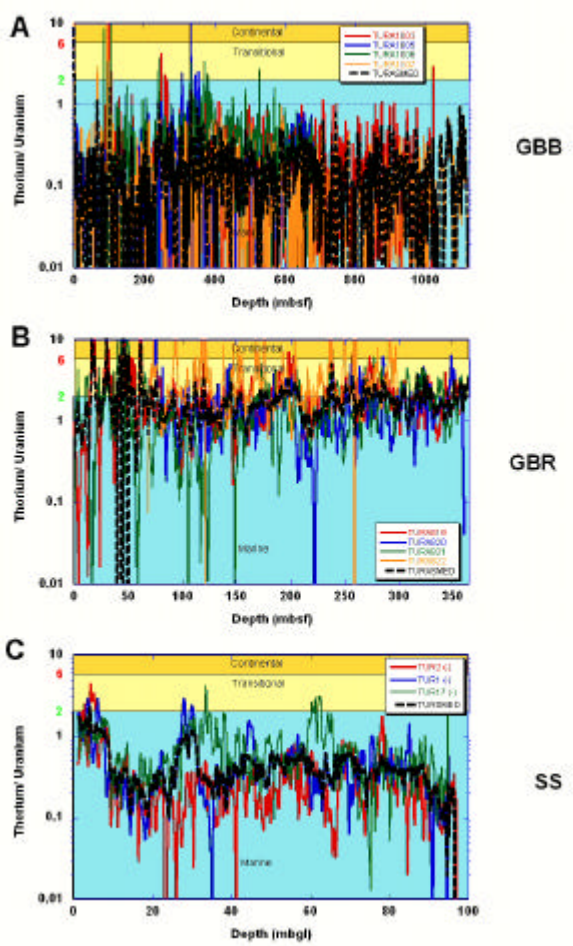

Figure P1- 18. Comparison of Thorium/ Uranium ratio curves versus depth for three different carbonate complexes: (A) Great Bahama Bank (GBB) four sites (ODP Leg 166). (B) Eastern Australia Great Barrier Reef (GBR) four sites (ODP Leg 133). (C) Ses Sitjoles three wells (MC1-MC2-S17) 100m distant from each other. The thick dashed black line is the smoothed median of the other curves. Environments are color coded; blue means marine, light yellow means transitional, and dark yellow means continental.

This comparison demonstrates that for the GBB, where the investigated interval ranges from 0 to 1125m below sea floor (mbsf), the involved depositional environments are deeper, more constantly marine (i.e. median TURA around or below 0.1, to compare with the paleobathymetry in Table 12) than in Ses Sitjoles (i.e. median TURA around 0.5). However, the GBB sites seemingly underwent several brief episodes of transitional and even continental environments (higher than respectively 2 or 6 TURA values, Fig. P1-18A), particularly during Pleistocene times, as also demonstrated by the few high kaolinite contents noted on the Th vs. K crossplot (Fig. P1-17A). Those apparent transitional or continental episodes could have been caused by turbiditic flows composed of bank material which was subaerially exposed during glaciation events. The average sedimentation rate is of 35m/m.a. at those sites.

The data concerning four GBR sites (819 to 821; Fig. P1-18B) and especially the interval ranging from 0 to 365mbsf comprised exclusively of Pleistocene sediments are indicative of a much closer transitional/ continental environment (i.e. median TURA around 2, to compare with the paleobathymetry ranging from 0 to 1000mbsl in Table 12) than in Ses Sitjoles. This explains the occurrence of several excursions of the TURA curves in the transitional or even the continental environment areas observed on the plot, in relation with the high amplitude and high frequency sea-level fluctuations recorded during Pleistocene times. The calculated average sedimentation rate is of 202m/m.a. and is much higher than that deduced from the

GBB record, probably as a consequence of the impact of rapid sea-level changes on reef accretion.

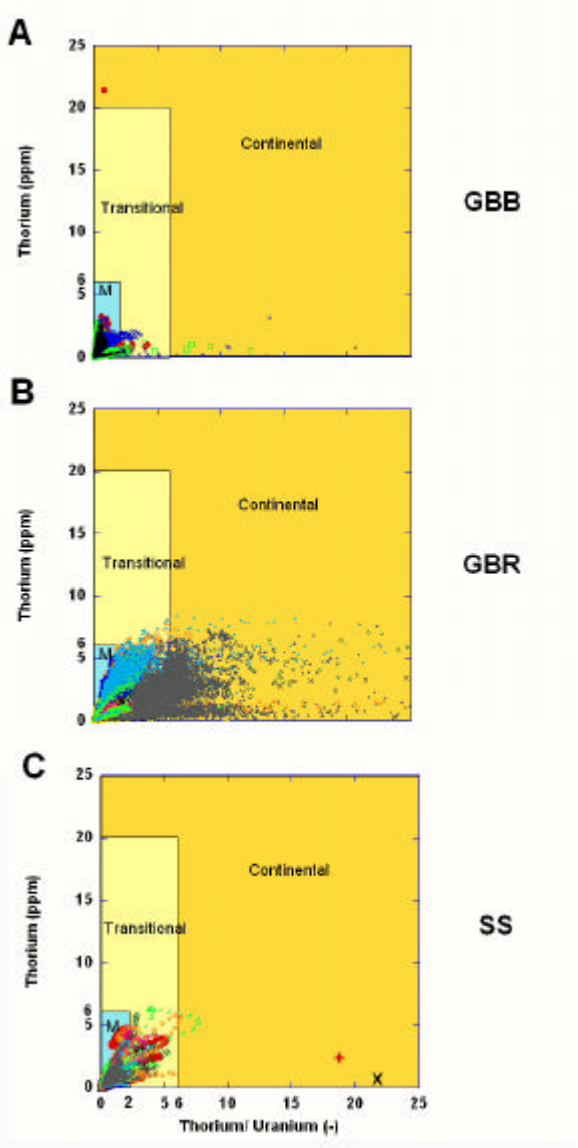

Figure P1- 19. Comparison of Thorium vs. Thorium/ Uranium ratio crossplots reduced scale for three different carbonate complexes: (A) Great Bahama Bank (GBB) four sites (ODP Leg 166), 25000 data points. (B) Eastern Australia Great Barrier Reef (GBR) ten sites (ODP Leg 133), 17000 data points. (C) Ses Sitjoles ten wells, 22000 data points, with the same crossplot template as on Figure 15C.

The comparison between Fig. P1-18B (GBR, Pleistocene reef) and Fig. P1-18C (Ses Sitjoles, Miocene reef) implies more reduced changes in bathymetry and carbonate production for Ses Sitjoles as a consequence of limited amplitude of sea-level changes during Miocene.
Comparisons between Ses Sitjoles Th vs Th/U plot data and corresponding data for the GBB and the GBR are displayed in Fig. P1-19.
The GBB data (Fig. P1-19A) are more concentrated in the marine zone than the Ses Sitjoles data (Fig. P1-19C), with Th highest values limited to 3.5ppm (compared to Th values up to 6ppm). Less data points plot in the transitional area than in Ses Sitjoles, and only a few data plot in the continental area, like in Ses Sitjoles. These results are in agreement with the observations made on Fig. P1-18A and P1-18C.
The GBR data (Fig. P1-19B) at all sites are more scattered and extend more toward the continental environment area than the corresponding Ses Sitjoles data (Fig. P1-19C). As already noted on Fig. P1-18B, concerning only four sites, and P1-18C, more points are falling

in the transitional and in the continental areas for the GBR than for Ses Sitjoles, as a consequence of larger sea-level fluctuations during the Pleistocene (GBR) than during Miocene times (Ses Sitjoles).
To summarize, the Ses Sitjoles SGR data display more similarities with the GBR sites than with the GBB sites, thus reflecting closer depositional conditions in terms of proximity to the coast and the reef edge between Ses Sitjoles and the GBR sites, despite higher frequency sea-level changes during Pleistocene than during Miocene times.

Uranium comparison

In Fig. P1-20, uranium curves vs. depth for the Ses Sitjoles area (Fig. P1-20C), are compared to those obtained for the GBB and GBR areas.

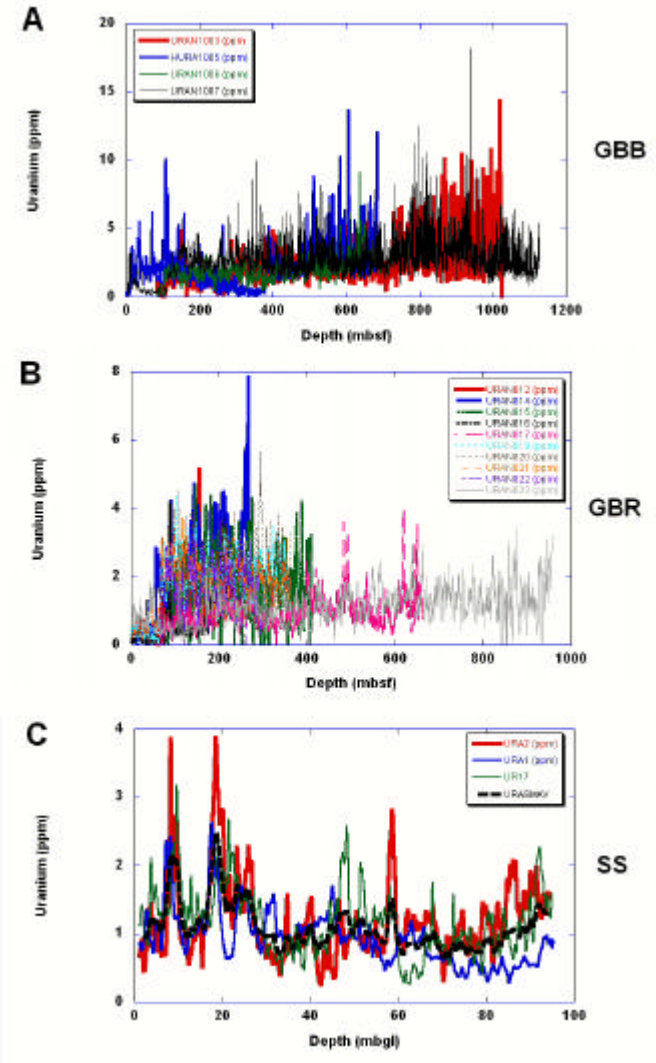

Figure P1- 20. Uranium vs. depth curves. (A) GBB, sites 1003, 1005, 1006, 1007 ; (B) GBR, sites 812, 814, 815, 816, 817, 819, 820, 821, 822, 823 ; (C) Ses Sitjoles, wells MC1, MC2, SS17 and the median uranium curve.

The GBB data (Fig. P1-20A) include the highest amounts of average uranium content (up to 2.5 and even 4.5ppm in site 1003D (Table P1-12); for comparison, maxima of 3ppm (Table P1-13), and of 1.7ppm for the GBR and Ses Sitjoles sites (Table P1-7), respectively. After site 1003D, the highest uranium contents have been recorded at site 1007C. Sites 1003D and 1007C correspond respectively to the lower slope and the toe of slope of the GBB transect, where the abundance of turbidites and slumps is maximum. In contrast, at the most offshore

site 1006C, that corresponds to the drift of the slope transect, turbidites and slumps are scarce, and the uranium content displays the lowest average values (Table P1-12). Although high uranium in deep marine sediments, (i.e. mostly below the photic zone) might appear remarkable, they could be explained both by organic matter supplies (e.g. planktonic algae) and bank sources through turbiditic flows, as indicated by the common occurrence of *Halimeda* fragments in turbidites (Table P1-12). High uranium values are typically recorded in the 700- 1024msbf interval at site 1003D, and are associated to marl/ limestone alternations and clay layers, related to gravity flow processes. The uranium peaks are mostly recorded in high porosity low resistivity packstone wackestone facies type characterized by the occurrence of clays (5 to 7% clay). They also occur close to the top facies type as a component of a calciturbidite-rich unit (Trevor & Pirmez, 1996) as shown by the comparison between FMS images and uranium peaks. The majority of the calciturbidites results from shedding during sea-level highstands, but calciturbidites produced during sea-level lowstands are also significant (Bernet et al., 1997). Other occurrences of uranium peaks at leg 166 sites are recorded at sequence boundaries, flooding surfaces, and unconformities. However, Colley & Thomson (1985), have demonstrated that the oxidation of organic carbon in turbidites mobilizes uranium originally adsorbed onto the organic matter as uranyl carbonate, which is then reduced and concentrated below the oxidation front in the pelagic sediment underlying the turbidite. These peaks therefore represent likely relict oxidation fronts. Below 740mbsf at site 1003D, organic carbon concentration is as high as 4% in uranium rich sediments, and is thought to result from hydrocarbon migration (Eberli et al., 1996), in clear contrast with the conditions that have been observed in Ses Sitjoles.

Fig. P1-20B summarizes uranium data vs. depth, from 10 GBR sites. These sites are representative of the various conditions in the area, from Queensland and Marion Plateaus, to Townsville and Queensland troughs, and from neritic to pelagic depositional environments (Table P1-13). Average uranium values range from a minimum of 0.3ppm to a maximum of 3ppm, regardless of the involved depth. It is interesting to separate the 10 GBR sites into two groups that will successively described: seven “shallow water” (i.e. 212 to 409mbsl) sites (812B, 814A, 815A, 816C, 819A, 820B, and 821A); and three “deep water” (i.e. 900 to 1650mbsl) sites (817D, 822A and 823C).

In the shallow water sites, the average uranium value is 3ppm. The depositional depth ranges from 0 to 600mbsl. Overall, the uranium curves follow a bell shaped curve, with a maximum of 5ppm around 150mbsf, and minima of 0.2ppm between 0 and 30mbsf and of 2 at 400mbsf. Among the shallow water sites, sites 821C (0-365mbsl) and 816C (specially between 0 and 180mbsl) are characterized by depositional conditions close to those described at Ses Sitjoles (Table P1-13), and the uranium values recorded at those sites are particularly comparable to those observed in Ses Sitjoles (Fig. P1-20B and P1-20C).

In the deep water sites, the average uranium value is 1.5ppm, notably lower than in the shallow water wells. The depositional depth ranges from 0 to 2000mbsl, generally much deeper than in the shallow water wells. Among the deep water sites, site 823C displays a relatively constant uranium level from 0 to 960mbsl averaging to 1.5ppm, however slightly decreasing upward; this site, at 1650mbsl water depth and with depositional depth ranging from 600 to 2000mbsl, i.e. constantly in the aphotic zone, is characterized by the occurrence of high uranium levels slumps and turbidites in a similar way to the GBB lower slope site 1003D. However, its location in the nearly flat bottom part of the Queensland trough, about 50 km away from the edge of the barrier reef, suggests that it should be better compared to the GBB drift site 1006C (Table P1-12), where the uranium values are quite comparable (Fig. P1-20A and P1-20B). In contrast, the deep water GBR sites uranium curves vs. depth are rather different from the curves obtained on the Ses Sitjoles sites (Fig. P1-20B and P1-20C) where the aphotic zone was never reached.

In summary, the GBB uranium vs. depth example displays environmental conditions that are very different from those recorded for the Ses Sitjoles carbonate sequence; the existence in some cases of unexpected very high uranium content has triggered the search for satisfactory explanations; this is a classical case of data confrontation, resulting, in this case, in an explanation of the apparent incoherence, or, in other cases, in either the correction or the abandon of some data.
The GBR uranium vs. depth example offers a large range of distinctive cases; with some environmental conditions and uranium values close either to the GBB or the Ses Sitjoles cases, while some of them are specific and cannot be directly compared to either the GBB or Ses Sitjoles.
In either case, it was interesting to compare the results for the three sites, and to see how the method is fruitful for such very different cases. This is very encouraging for applying the method on a larger scale, i.e. on the Miocene SE Majorca coral reef complex (Maria-Sube et al., in prep.).

Tectonics

The core- borehole images- SGR investigation method developed on the Ses Sitjoles site has also some tectonic applications.
The reef crest in Ses Sitjoles is generally 9m higher than the present day water table. It is known that during the Miocene time of reef creation, the mean sea level (MSL) was around 100m above the present day MSL. These observations are demonstrating that during the early Pleistocene evolution of the Campos basin (Pomar, 1996), the basement collapsed by several tens of meters.
A series of NE-SW wide faults have been identified by the SGR records carried out in wells within the entire reef complex (Maria-Sube et al., in prep.).
The SGR tool may also be used in some cases for identifying time unconformities (Serra and Serra, 2000). Sr. isotope dating results obtained on Units I, II and III in MC2 well indicate that there is a time unconformity between each of these units (Camoin et al., work in progress). Those are not detected on the SGR tool; however, we assume that those time unconformities are caused by reef prograding, as it is in Cabo Blanco, but with a different time scale (Pomar et al., 1996); those time unconformities are therefore local and not regional. In contrast, a regional time unconformity is detected by the SGR tool at the boundary between subunit IIIa and subunit IIIb, at the on-set of the TCC (which is thus a time-marker), within most of the reef complex (Maria-Sube et al., in prep.).

Diagenesis

The core sedimentological and petrophysical analysis has provided information on the composition (calcite, dolomite, ankerite, clay) and the diagenesis (cementation, mineralization) of the Ses Sitjoles carbonate sequence. The borehole images may also be used for diagenetic applications such as the identification of mineralization zones, like it was done on the Ses Sitjoles site. This property leads to the reconstruction of paleo- standstill and eustatic sea-level (Maria-Sube et al., in prep).

CONCLUSIONS AND PERSPECTIVES

The Ses Sitjoles site provided the opportunity to carry out a large number of downhole on-site measurements, due to the occurrence of a limited vadose zone (37m thick, as opposed to 80m in Cabo Blanco_ thus covering the entire zone of interest).

Within the multi-scalar and multi-disciplinary approach of the ALIANCE program, a 3D geological and geometrical model for the reef complex located within the 100m by 100m square site of Ses Sitjoles has been described. The drilling of cluster or alignment of wells a few meters apart was a unique opportunity to observe 3D facies variations in a reef complex over such a limited scale, with a coeval 100m scale.
The combination of core study, high definition borehole image records, and SGR log investigation that has been used and asserted on the Ses Sitjoles carbonate sequence provided information on: 1) *depositional environments*, as complements to the core study and borehole image analysis were provided by the TURA curve, and the comparison between TURA and Th/K; 2) *facies composition*, e.g. organic matter, fracture, stylolites, from core analysis, borehole images and SGR, and radioactive mineral composition from Th and K analysis; 3) *heterogeneities* (e.g. lithological boundaries, fractures, stylolites) from continuous borehole images and SGR log; 4) *tectonics* (e.g. faults, folds, slump, unconformities) from the borehole images and SGR data analysis; 5) *diagenesis*, *with* complements to the core analysis (e.g. mineralogy, porosity, cementation type) provided by the borehole image analysis (i.e. planar horizontality of the Ses Sitjoles wells mineralization zones, and consequences on the paleo sea-level standstills).
The quality of the borehole images (i.e. high definition, continuous 360°, natural color in the case of optical images) allowed to approach core and outcrop visual observation conditions, and thus enhancing the analytical results.
The comparison of the Ses Sitjoles SGR data with ODP data concerning the Great Bahama Bank and the Great Barrier Reef shows the same consistency of data, with local variations regarding the spread of concentration, or intensity of radioactive minerals, changes of depositional environments (i.e. continental- transitional- marine), and the occurrence of organic matter, that are related to the paleo-bathymetry and distances to the shoreline of the GBB and GBR sites compared to the Ses Sitjoles site.
We believe that the combined cores- high definition borehole images- SGR log study is very valuable, and should be used in all sedimentologic/ tectonic multi-well studies.

ACKNOWLEDGEMENTS

We are grateful for funding from the European Union Advanced Logging Investigations of Aquifer iN Coastal Environment (ALIANCE) project EKV-2001-0039 a three and half years duration program (2002-2005)
The authors wish to thanks specially Gilles Henry, Université Montpellier II, Institut des Sciences de la Terre, de l'Eau et de l'Espace de Montpellier (ISTEEM) France, who carried out most of the downhole logging on the well-site and maintenance of the downhole equipment, although several other persons participated as well.
ISES-Industry, an associated European project based in Amsterdam, provided help in the form of data originating from the Vrieje Universiteit (V.U.), Amsterdam (The Netherlands).
Oberto Serra provided very useful explanations and complementary information on his referenced documents, and more particularly on interpretation of the Thorium vs. Potassium crossplot.
We thank Crocker Data Corporation, Australia, for allowing us use of their software Petrolog for graphical purposes (SGR log curves vs. depth and site correlation of logs).
Ses Sitjoles log data are available at http://hplus.ore.fr.
The ODP Legs 133 and 166 log data were collected on-line from the Columbia Lamond Doherty Earth Observatory Internet site.
We also want to acknowledge the help provided by the Direccio General de Régim Hydraulic, from the Balearic Government, especially by hydro-geologists Concha and Alfredo Baron,

who, among other things, proposed the drilling site of Ses Sitjoles, arranged for the drilling and coring of two additional wells (MC10 and MC11), and smoothed relations with the Majorcan authorities.

REFERENCES

Adams, J.A.S. and Weaver, C.E. (1958) Thorium to uranium ratio as indicator of sedimentary processes; examples of concept of geochemical facies. *AAPG Bull*., 42, 2.

Andersson, P.D. and Werden, R.H. (2004) Mudstones of the Tonqua Basin South Africa: an anlysis of lateral and stratigraphic variations within mudstones and a comparison of mudstones within and between turbite fans. *Sedimentology*, 51, 3, 479-502.

Babcock, E.A. (1978) Measurements of subsurface fractures from dipmeter logs. *AAPG Bull*., 62, p. 1119-1126.

Beers, R.F. and Goodman, C. (1944) Distribution of radioactivity in ancient sediments. *Geol. Soc. America Bull*., 55.

Bell, J.S. and Gough, D.I. (1979) Northeast-south-west compressive stress in Alberta: evidence from oil wells. *Earth Planet Sci. Lett*., 45, p. 475-482.

Bernet, K., Eberli, G.P., Betzler, C. and Gill, A. (1997) Hihgstand versus lowstand shedding of carbonates – new data for an old controversy from the Western margin of Great Bahama Bank. EOS: Transactions, *American Geophysical Union*, 78 (46), F359.

Bonnier, B. (2005) Etude sédimentologique et géochimique des récifs Miocènes de Majorque (Baléares, Espagne). Influence des caractéristiques diagénétiques sur les propriétés physiques des roches carbonatées. Ms. Thesis, 31p. (unpublished), *Université Paul Cézanne, CEREGE, Aix-en-Provence.*

Braga, J.C. and Aguirre, J. (2001) Coralline algal assemblages in upper Neogene reef and temperate carbonates in Southern Spain. *Palaeogeogr. Palaeoclimatol. Palaeoecol.*, 175, 27-41.

Brachert, T.C., Hultz, N., Knoerich, A.C., Krauworst, U.M.R. and Stückrad O.M. (2001) Climatic signatures in shallow water carbonates: high resolution stratigraphic markers in structurally controlled carbonate buildups (Late Miocene, Southern Spain). *Palaeogeogr. Palaeoclimatol. Palaeoecol*., 175, 211-237.

Camoin, G. (2001) Palaeoceanology of reefs and carbonate platforms: Miocene to modern. *Palaeogeogr. Palaeoclimatol. Palaeoecol*. 175, 1-6.

Camoin, G.F., Ebren, P., Eisenhauer, A., Bard, E. and Faure, G. (2001) A 300 000-yr coral reef record of sea level changes, Mururoa atoll (Tuamotu archipelago, French Polynesia). *Palaeogeogr. Palaeoclimatol. Palaeoecol*., 175, 325-341.

Chamley, H., Robert, C. and Müller, D.W. (1990) The clay mineralogical record of the last 10 million years off Northeastern Australia. *ODP* Leg 133, *Proc. ODP*, 132/133, *Sci. results*, 461-470.

Colley, S. and Thomson, J. (1985) Recurrent uranium relocations in distal turbidites emplaced in pelagic conditions. *Geochim. Cosmochim. Acta*, 49, 2399-2348.

Cornée, J.J, Roger, S., Münch, P., Saint Martin, J.P., Féraud, G., Conesa, G. and Pestrea- Saint Martin, S. (2002) Messinian events: new constraints from sedimentological investigation and new AR40/AR39 ages in the Melilla-Nador Basin (Morocco). *Sedim. Geol.*, 151, 127-147.

Cox, J.W. (1983) Long axis orientation in elongated boreholes and its correlation with rock stress data. *SPWLA*, 24th Ann. Log. Symp. Trans. Paper J.

Cunningham, K.J., Farr, M.R. and Rakid-El Bied, K. (1994) Magnetostratigraphic dating of an Upper Miocene depositional shallow marine and continental sedimentary succession in northeastern Morocco. *Earth Planet. Sci. Lett*., vol. 127, Issues 1-4, p. 77-93.

Davies, P.J., McKenzie, J.A., Palmer-Julson, A.A. et al. (1990) Northeast Australian Margin. *Proc. ODP, Sci. Results*, Leg 133, 810p.

Duggen, S., Hoernie, K., Van den Bogaard, P., Rüpke, L. and Phipps M.J. (2003) Deep roots of the Messinian salinity crisis, *Nature* , 422, 602.

Eberli, G., Swart, P.K., and shipboard scientific party, (1996) Bahamas Transect, Init. Rep. *ODP*, vol. 166. 849p.

Eberli, G., Swart, P.K., and shipboard scientific party, (1996a) Bahamas Transect, Sci. Results, *ODP*, 166. 213p.

Esteban, M., Calvet, F., Dabrio, C., Baron, A., Giner, J., Pomar, L., Salas, R. and Permannyer, A. (1978) Aberrant features of the Messinian coral reefs, Spain. *Acta Geol. Hisp*., 13, 20-22.

Esteban, M. (1979) Significance of the Upper Miocene reefs of the Western Mediterranean. *Palaeogeogr. Palaeoclimatol. Palaeoecol.* 29, 169-188.

Esteban, M. (1996) An overview of Miocene reefs from Mediterranean areas : General trends and facies models, in Fransee E.K, Esteban M., Ward W.C., Rouchy J.-M., eds., Models for carbonate stratigraphy from Miocene reef complexes of Mediterranean regions. *SEPM Concepts in Sedimentology and Paleontology*, 5, 3-53.

Franseen, E. K., Goldstein, R.H. and Farr, M.R. (1998) Quantitative controls on location and architecture of carbonate depositional sequences: upper Miocene, Cabo de Gata region; SE Spain. *J. Sediments. Res.* 68 (2) 283-298.
Hassan, M. and Hossin, A. (1975) Contribution à l'étude des comportements du thorium et du potassium dans les roches sédimentaires. *C.R. Acad. Sci. Paris*, 280.
Hsü, K.J., Ryan, W.B.F. and Cita, M.B. (1973) Late Miocene desiccation of the Mediterranean. *Nature*, 242, 240-244.
Hsü, K.J., Montadert, L., Bernouilli, D., Cita, M.B., Erikson, A., Garrison, R.E., Kidd, R.G., Mélières, F., Müller, C. and Wright, R. (1977) History of the Messinian salinity crisis. *Nature*, 267, 399-403.
Hurst, A. and Milodowski, A. (1996) Thorium distribution in some North Sea sandstones: implications for petrophysical evaluation. *Petrol. Geosci*., 2, 59-68.
Jaeggi, D. (2006) Multiscalar porosity structure of a Miocene reefal carbonate complex. *PhD thesis*, Diss ETH nb. 16519.
Jenkyns, H.C., Sellwood, B.W. and Pomar, L. (1990) A field incursion guide to the island of Mallorca: Geologists' Association guide. *London, The Geologists' Association*, 93p.
Krijgsman, W., Hilgen, F.J., Raffi, I., Sierro, F.J. and Wilson D.S. (1999). Chronology, causes and progression of the Messinian crisis. *Nature*, 400.
Lüning, S., Wendt, J., Belka, Z., Kaufmann, B. (2004). Temporal-spatial reconstruction of the early Frasnian (Late Devonian) anoxia in NW Africa: new field data from the Ahnet Basin (Algeria). *Sedim. Geol.* 163, 237-264.
Mutterlose, J., Ruffell, A. (1999). Milankovitch-scale paleoclimate changes in pale-dark bedding rhythms from the early Cretaceous (Hauterivian and Barremian) of eastern England and northern Germany. *Palaeogeogr. Palaeoclimatol. Palaeoecol.* 154, 133-160.
Pomar, L., Esteban, M., Calvet F., Baron, A. (1983) La unidad arrecifal del Mioceno superior de Mallorca, El terciaro de la Baleares (Mallorca- Menorca). *Guia de las excursions del X Cong. Nac. Sedimentologia* (Ed. by L. Pomar, A. Obrador, J. Fornos & A. Rodriguez- Perea), pp. 139-175. Inst. Est. Balearics and Universidad de Palma de Mallorca, 256.
Pomar, L. (1991) Reef geometries, erosion surfaces and high frequency sea-level changes, upper Miocene reef complex, Mallorca, Spain. *Sedimentology*, 38, 2, 243-269.
Pomar, L., Ward, W.C. (1994) Response of a late Miocene Mediterranean reef platform to high-frequency eustasy. *Geology*, 2, 131-134.
Pomar, Luis, Ward, W.C. (1995) Sea-level changes, carbonate production and platform architecture: the Llucmajor platform, Mallorca, Spain. In *Sequence stratigraphy and depositional response to eustatic, tectonic and climatic forcing*, 87-112, B.U. Haq, Kluwer Academic Publishers,
Pomar, L., Ward, W.C., Green, D.G. (1996) Upper Miocene reef complex of the Llucmajor area, Majorca, Spain. *SEPM Concepts in Sedimentology and Paleontology*, 1-56576-033-6, 191-225.
Pomar, L., Ward, W.C. (1999) Reservoir-scale heterogeneity in depositional packages and diagenetic patterns on a reef-rimmed platform, Upper Miocene, Mallorca, Spain. *AAPG*, 83, 1759-1773.
Riding, R., Martin, J.M., Braga, J.C. (1991) Coral-stromatolite reef framework, Upper Miocene, Almeria, Spain. *Sedimentology*, 38, 799-818.
Riding, R., Braga, J.C., Martin, J.M., Sanchez-Almazo, I.M. (1998) Mediterranean Messinian Salinity Crisis: constraints from a coeval marginal basin, Sorbas, southeastern Spain. *Marine Geology*, 146, 1-20.
Rouchy, J.M., Saint Martin, J.P. (1992) Late Miocene event in the Mediterranean as recorded by carbonate-evaporite relations. *Geology*, v. 20, 629-632.
Ruffell, A., Worden, R. (2000) Palaeoclimate analysis using spectral gamma-ray data from the Aptian (Cretaceaous) of southern England and southern France. *Palaeogeogr. Palaeoclimatol. Palaeoecol.* 155, 265-283.
Russell, W.L. (1945) Relation of radioactivity, organic content and sedimentation. *AAPG Bull.* 29, 10.
Schnyder, J., Ruffell, A., Deconinck, J.F., Baudin, F. (2005) Conjunctive use of spectral gamma-ray logs ands clay mineralogy in defining late Jurassic-early Cretraceous paleoclimate change (Dorset, U.K.). *Palaeogeogr. Palaeoclimatol. Palaeoecol.* 229, 4, 303-320.
Selley, R.C. (1976) An introduction to sedimentology. *Academic Press*, London, 408 pp.
Serra, O., Baldwin, J., Quirein, J.A. (1980) Theory, interpretation and practical applications of Natural Gamma Ray spectroscopy. *SPWLA*, 21st Annual Log. Symp. Trans., paper G.
Serra, O. (1990) Element, Mineral , Rock Catalog, *Schlumberger*.
Serra, O., Serra, L. (2000) Diagraphies, *Serralog*.
Serra, O., Serra, L. (2003) Well logging and geology, *Serralog*.
Swanson, V.E. (1960) Oil yield and uranium content of black shales. *Geol. Surv, prof. Paper* 356-A.
Trevor, W., Pirmez C. (1996) FMS images from carbonates of the Bahama Bank slope, ODP leg 166: lithologial identification and cyclo- stratigraphy, Sci. Results. *ODP*, 166, 77-88.

Van Berkel, J., Verhoef, M. (2005) High resolution multi-component 2D-3D natural laboratory linking geology, geophysics and petrophysics: Mallorca, Spain, Ms. Thesis. *Vrieje Universiteit,* Amsterdam.
Wignall, P.B., Newton, R. (2001) Black shales on the basin margin: a model based on examples from the Upper Jurassic of the Boulonnais, northern France. *Sedim. Geol.* 144, 335-356.

4.2 Sédimentologie et environnement de déposition sur le complexe récifal Miocène du Sud-Est de Majorque

Résumé

Des paléo environnements de déposition sont étudiés dans le complexe récifal Miocène du sud-est de Majorque (Espagne), en utilisant des méthodes multi-scalaires et multi-disciplinaires. Quatre sites principaux (Cap Blanc, Llucmajor, Campos et Ses Salines) couvrant une aire de 35 par 20km, incluant 25 forages différents de 22 à 320 de profondeur, permettent une large investigation. Profitant du travail intense précédemment accompli sur le complexe récifal affleurant de Llucmajor/ Cap Blanc, et du nouveau travail fait sur les sites de Ses Sitjoles (12 forages dans un carré de 100m de côté) appartenant à Campos (deux forages supplémentaires ont été étudiés dans cette zone), Cap Blanc (trois forages), Llucmajor (quatre forages) et Ses Salines (quatre forages), un modèle géologique et une stratigraphie détaillés sont déduits pour la région. La même méthodologie (les informations obtenues par les carottes sont complétées par des enregistrements d'images de la paroi du puits et de Gamma-Ray Naturel Spectral (SGR)) que celle utilisée à Ses Sitjoles, est utilisée pour l'ensemble du complexe récifal. L'analyse des enregistrements de thorium et de potassium dans tous les forages pour le contenu minéral radioactif montre généralement un contenu minéral radioactif très bas, sauf dans les couches supérieures, où un faible pourcentage de minéraux argileux illite et montmorillonite est noté, et dans les couches profondes (talus distant et plate-forme externe) où des marnes sont trouvées. Les données d'uranium permettent l'analyse du contenu en matière organique : du moins abondant (1 sur une échelle de 5), éolianites de l'Unité IV, où aucun fossile n'est noté, et la sous-unité IIIa où des algues corallines sont trouvées, au plus abondant, talus distant (5 sur une échelle de 5), où des algues corallines et *Halimeda* sont particulièrement abondantes. Les algues corallines sont trouvées dans chaque unité, sauf dans les éolianites, *Halimeda* est trouvée uniquement dans le talus distant, tandis que *Dasycladacées* et racines de mangrove sont trouvés uniquement dans la sous-unité IIIb. Le rapport thorium/ uranium (TURA) procure une indication sur le type de paléo environnement de déposition ; Les unités stratigraphiques du complexe récifal de Majorque sont identifiées comme environement totalement marin dans les strates profondes (plate-forme externe, talus distant, talus proche, sous-unité IIIa) ; dans le sommet du récif, et dans la sous-unité IIIb, en eau moins profonde, elles peuvent devenir de type continental. En utilisant les carottes, les images de la paroi du puits, et les enregistrements SGR pour l'identification des unités du complexe récifal, les 25 forages procurent un modèle géométrique 3D, et documentent des variations stratigraphiques 3D spectaculaires. Par exemple, l'unité récifale peut varier entre 0 et 47m. Deux failles normales SE-NO et une faille inverse SE-NO ont été détectées. Les données de l'expédition Tahiti Sea Level du programme intégré de forage de l'océan (IODP), donnent l'opportunité de comparer les récifs coralliens Pléistocène et Holocène de Tahiti au complexe récifal du sud-est de Majorque. Les données de Tahiti procurent des preuves de rapide et nombreux changements de niveau océanique eustatique, et d'une beaucoup plus grande variété de genres de coraux que dans le complexe récifal de Majorque.

Depositional environment and structure in a Miocene reef complex, Majorca, Spain.

Yves Maria-Sube, Gilbert Camoin, Philippe Pezard, David Jaeggi, Hendrik Braaksma, Klaas Verwert.

ABSTRACT

Paleo-environments of deposition are studied in the Miocene Reef Complex of S.E. Majorca (Spain), using multi-scalar and multi-disciplinary methods. Four main sites (Cap Blanc, Llucmajor, Campos and Ses Salines) extending over an area of 35 by 20km, including 25 different boreholes from 22 to 320mbgl deep, allow a broad investigation. Taking advantage of previous extensive sedimentological work done on the Llucmajor/ Cap Blanc exposed reef complex, and of new work done in the Ses Sitjoles site (twelve boreholes in a 100m by 100m square) of Campos (two more boreholes were surveyed in this area), Cap Blanc (three boreholes), Llucmajor (four boreholes) and Ses Salines (four boreholes) sites, a detailed geological model and stratigraphy are inferred for the area. The same methodology (core information is complemented by borehole image and Natural Spectral Gamma-Ray (SGR) logs) as the one asserted in Ses Sitjoles, is used for the whole reef complex. The analysis of thorium and potassium records in all boreholes for radioactive mineralogical content shows generally extremely low radioactive mineral content, except in the uppermost layers, where low contents of illite and montmorillonite clay minerals are noted, and in the deep layers (distal slope and off reef open shelf) where marls are found. Uranium data allow the analysis of organic matter content: from the less abundant (1 over a scale of 5), Unit IV eolianites, where no fossil is reported, and subunit IIIa where coralline algae are found, to the most abundant, distal slope (5 over a scale of 5), where coralline algae and *Halimeda* are particularly abundant. Coralline algae is found in every unit except in the eolianites, *Halimeda* is found only in the distal slope, while *Dasyclad* and mangrove roots are found only in subunit IIIb. The thorium/ uranium ratio (TURA) provides an indication on the deposition paleo-environment type. The stratigraphic Units of the Majorca reef complex are identified as fully marine environment in the deep strata (off reef open shelf, distal slope, proximal slope, Unit IIIa); in the shallower reef crest Unit and in subunit IIIb, they may occasionally become transitional, while in the eolianites, they may even become of continental type. Using cores, borehole images and SGR logs for reef complex Unit identification, the 25 holes provide a 3D geometrical model, documenting spectacular 3D stratigraphic variations; for instance, the reef unit thickness may vary from 0 to 47m. Two SE-NW normal faults and one SE-NW reverse fault have been detected. Integrated Ocean Drilling Program (IODP) Tahiti Seal Level expedition data provide the opportunity to compare the Pleistocene and Holocene Tahiti coral reefs to the Miocene SE Majorca reef complex. The Tahiti data supply evidences for rapid and numerous eustatic sea level changes, and a much greater variety of coral generae than in the SE Majorca reef complex.

AUTHORS

Yves Maria-Sube, ~ *Laboratoire de Tectonophysique, University of Montpellier II, 34095 Montpellier; France ; yves.maria-sube@dstu.univ-montp2.fr*

Yves Maria-Sube is presently PhD student (Miocene reef complex of Majorca). He received his Engineering degree from Ecole Centrale de Nantes, France and worked for 18 years with Schlumberger Wireline as international staff.

Philippe Pezard, ~ *Laboratoire de Tectonophysique, University of Montpellier II, 34095 Montpellier; France*

Philippe Pezard is head scientist CNRS, Aliance project coordinator, received his engineering degree form ESIM, Marseille France, and his PhD in Borehole Geophysics from Lamont-Doherty Earth Observatory of Columbia University, New-York.

Gilbert Camoin, ~ *Centre Européen de Recherche et d'Enseignement des Géosciences de l'Environnement (CEREGE), University of Aix-Marseille, France*

Gilbert Camoin is head scientist CNRS, ESSAC Chair.

David Jaeggi, ~ *Swiss Federal Institute of Technology Zurich (ETH-Z), Institute of Geology, Engineering Geology*

Davis Jaeggi has been graduated PhD in 2006 (multi-scalar porosity and permeability structure of Ses Sitjoles site, Majorca).

Klaas Verwert, ~ Vrieje Universiteit, 1081 HV Amsterdam, The Netherlands; klaas.verwer@falw.vu.nl

Klaas Verwert is presently a PhD student (ISES- Industry Natural Laboratories, Majorca and Gargano_ Italy).

ACKNOWLEDGEMENTS

We are grateful for funding from the European Union Advanced
Logging Investigations of Aquifer iN Coastal Environment (ALIANCE) project EKV-2001-0039 a three and half years duration program (2002-2005)
The authors wish to thanks specially Gilles Henry, Université Montpellier II, Institut des Sciences de la Terre, de l'Eau et de l'Espace de Montpellier (ISTEEM) France, who carried out most of the downhole logging on the well-sites.
ISES-Industry, an associated European project based in Amsterdam, originating from the Vrieje Universiteit (VU), Amsterdam (The Netherlands), and headed by Dr. Jeroen A.M. Kenter, provided valuable help in the form of data and access for logging to their well sites of Cap Blanc. Drs. Philippe Pezard, Luis Pomar, Gilbert Camoin and Hendrik Braaksma were members of the ISES-Industry project. Drs. G. Camoin and H. Braaksma were latter associated to the Aliance project.
Oberto Serra provided very useful explanations and complementary information on his referenced documents, and more particularly on interpretation of the Thorium vs. Potassium crossplot.
We thank Crocker Data Corporation, Australia, for allowing us use their software Petrolog for graphical purposes (SGR log curves vs. depth and site correlation of logs).
We also want to acknowledge the help provided by the Direccio General de Régim Hydraulic, from the Balearic Government, in particular by hydro-geologists Concha and Alfredo Baron, smoothed relations with the Majorcan authorities, provided access to their well sites for logging, and obtained the cooperation from their management for drilling and coring four additional wells.
Reef complex log data are available on http://hplus.ore.fr Internet site.

INTRODUCTION

Because coral reefs and shallow water carbonates store information about sea level, climate, environment, ecology, tectonics, and age, geologists have been studying them for a long time (Camoin, 2001; Camoin et al, 2001; Brachert et al., 2001).

Coral reefs are natural reservoirs. The Miocene coral Reef Complex of SE Majorca is a fresh water reservoir for the island, with potential coastal salt water intrusion, that is surveyed by the Hydrogeological Department of the Government of the Baleares. It is also a prospect for an analogue (to a hydrocarbon reservoir) natural laboratory, easier and less costly to investigate thoroughly than a hydrocarbon reservoir, because of its very shallow depth and outcrop exposure. Several giant oil and gas fields have been recently found in coral reef reservoirs, and more than 60% of the oil and gas reservoirs are found in carbonate sediments.

Shallow water carbonate reservoir rocks are characterized by very contrasted and complex heterogeneities in terms of both depositional texture and diagenetic processes. During the last decades, a better understanding of these reservoirs' sequence stratigraphy, internal architecture, the spatial distribution of geological, geophysical and petrophysical properties has been acquired. The use of multi-disciplinary methods including natural laboratory, outcrops, shallow boreholes, with multi-scalar geological, geophysical and petrophysical data records, can greatly improve the knowledge about the prediction of heterogeneities, the relationship between geological parameters and petrophysical properties. Few studies of that sort have been made before.

Several SE Spain Miocene carbonate platforms and reef complexes, including the Balearic islands have been extensively described in the literature (see review by Esteban, 1996). The Miocene SE Majorca reef complex offers a well-known and spectacular outcrops in the Cabo Blanco area, and shallow wells (up to 300m deep) that have been drilled and surveyed by the Government of the Baleares; outcrops and wells have been comprehensively studied (e.g. Esteban et al., 1978 ; Esteban, 1979 ; Pomar, 1991 ; Pomar and Ward, 1994, 1995, Pomar et al., 1996 ; Pomar and Ward, 1999).

While our previous document (Maria-Sube et al., in press), focused on the study of the 100m by 100m square site of Ses Sitjoles in the Campos basin of the SE Majorca reef complex, this work studies the entire Miocene reef complex at a larger scale (35 by 20 km long). The previous document was particularly focused on the methodological approach (slimhole logging tools calibration, validation and interpretation by comparison with core results) related to the different tools that were used for investigation. In this document, the methodological approach will consequently refer to and rely on the previous document. Four different sites, spread over the entire reef complex, have been considered: Cabo Blanco, Llucmayor, Campos, and Ses Salines. In those sites, on top of using the previously existing outcrop and well materials, new wells were cored and drilled and new measurements were recorded. The results provide a unique opportunity to investigate the 3D architecture and stratigraphy of the reef complex on a scale ranging from the few meters to the tens of km scale. The data obtained in the Miocene SE Majorca reef complex are then compared to the Holocene and Upper Pliestocene Tahiti reef data. Diagenetic and petrophysical patterns of the carbonate Ses Sitjoles sequence will be described in other papers.

GEOLOGICAL SETTINGS

The Miocene reef of SE Majorca (Balearic Islands, Mediterranean, Spain; see Fig. P2-1 for Majorca simplified geological map and the Reef Complex) outcrops at Cap Blanc (or Cabo Blanco, South-East of the island) by three sides: the top platform on horizontal ground, and two 90° cliffs. Its surface geology has been described in an extensive way by Pomar, 1991 ; Pomar and Ward, 1994, 1995, Pomar et al., 1996 ; Pomar and Ward, 1999. The Majorca reef

platforms have prograded around islands resulting from the alpine orogeny (Middle Miocene). The Palma to Escudia basins result from Lower Miocene to Pleistocene faults, while the Campos basin slumped at the beginning of Pleistocene (Jenkyns et al., 1990).

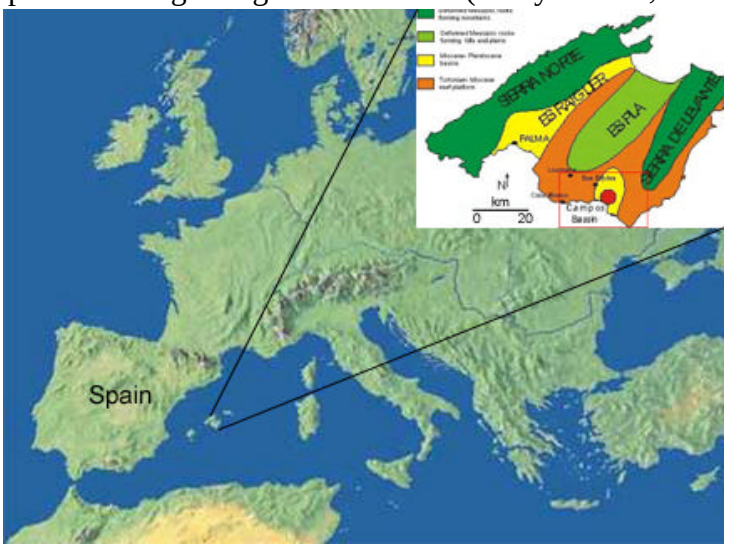

Figure P2- 1. Left: Western Europe map, showing Spain and the location of the Balearic islands, and in particular Majorca, in the Mediterranean. Top right: Simplified geological map of Majorca island, showing the paleo-geography of the Upper Miocene reef platforms (Upper Tortonian and Lower Messinian) (adapted from Pomar et al., 1996). The red frame part corresponds to the enlarged sketch of the SE Majorca reef complex represented on Figure P2-2.

Pomar, 1991 ; Pomar and Ward, 1994, 1995, Pomar et al., 1996 ; Pomar and Ward, 1999 have described the Upper Miocene reefs of the Balearic archipelago (Majorca, Menorca, Ibiza, Formentera and smaller islands), with a special emphasis on the Majorcan cliff outcropping between Cap Blanc and Vallgornera (Fig. P2-2), and even more particularly on the Cap Blanc cliff. According to these authors, the Llucmajor carbonate platform (which outcrops at Cap Blanc, and from there about 6km Northwest and 6 km East_ see Fig. P2-2) has prograded during late Tortonian and early Messinian periods over an area of about 15km by 20km, and with a thickness of up to 100m. The various environments encountered in the SE Majorca Reef Complex are from bottom to top: Off reef open slope (OROS); distal and proximal Reef slope; the Reef Core (where coral morphologies of dish, branching and massive corals were recognized); Outer and Inner Lagoon; and Pleistocene Eolianites.
In Pomar et al., 1996, several dating methods (micropaleontology, Sr isotopes, K-Ar) date Cap Blanc reef complex from late Tortonian (8 Ma) to Middle Messinian (6 Ma). The OROS is dated from Lower Tortonian (Pomar, 2001).

MATERIAL AND METHODS

Four different sites, spanning over an area of 35 by 20km wide, have been studied (Fig. P2-2, Table P2-1): **Llucmajor**, including observation wells S15, S16, S18 and S20 previously drilled by the Government of the Baleares Islands (except for S20 which was drilled in 2006); **Cabo Blanco**, including three wells CBA, CBB and CBC that have been drilled in 2003 by the team of ISES-Industry project; **Campos**, including observation wells S14, S17 and S19 previously drilled by the Government of the Baleares Islands (except for S19, which was drilled in 2006), and 11 experimental wells MC1 to MC11 which have been drilled by the team of ALIANCE project from 2003 to 2005 at the Ses Sitjoles site (see Maria-Sube et al., in press; MC10 and MC11 were drilled by the Government of the Baleares Islands in 2006); **Ses Salines** including observation wells S21, S22, S23, S24 previously drilled by the Government of the Baleares Islands. The depth of the wells ranges from 22 to 321mbgl, the majority of the

well depth being 100mbgl (Table P2-2). These sites thus provide a unique opportunity for the oil industry as well as for university laboratories for studying a Miocene Reef Complex from cores and logs, using multi-scalar methods (from micrometer to 35km scale).

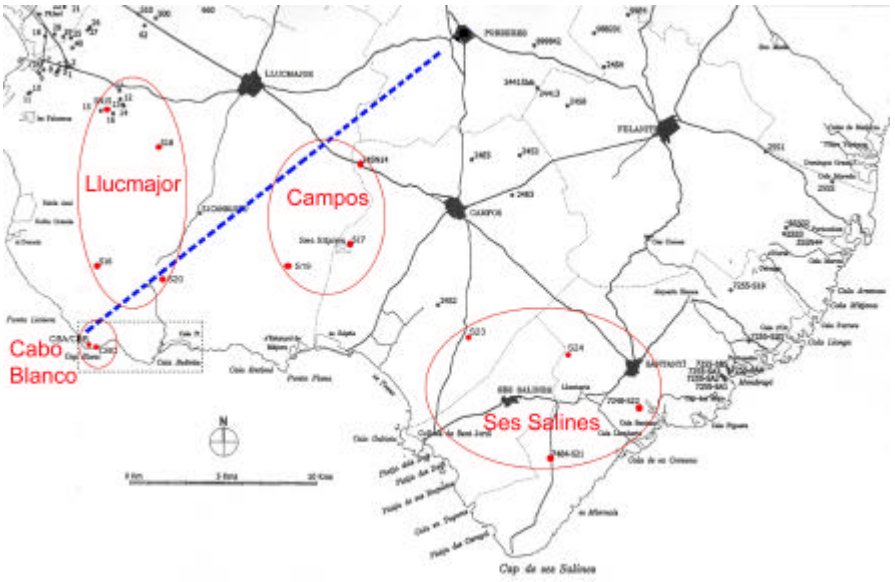

Figure P2- 2. SE Majorca Reef complex, surveyed sites and 25 boreholes, from West to East: S15, S16, S18, S20 (Llucmajor), CBA, CBB, CBC (Cabo Blanco), S17 and MC1 to 11 (in the 100m square site of Ses Sitjoles, represented by a crossed rectangle icon) and S14 and S19 (Campos), S21 to 24 (Ses Salines), from a modified Government of the Baleares Islands map. The area inside the dashed black rectangle corresponds to the area studied and described by Pomar et al., 1996. The thick dashed blue line represents a fault that outcrops at Cabo Blanco cliff (positioned after Pomar and Ward, 1995, 1999).

Cores have been obtained on most of the wells; the cores of Ses Sitjoles and Cabo Bianco have provided thin section observations, while the older wells, previously drilled by the Government of the Baleares, provided cores and core descriptions (Table P2-1). The core diameter was generally of 8cm, but could vary from 6.5 to 10cm. Examples of photographs of MC2 cores and thin sections were provided in Maria-Sube et al., in press. The sedimentological facies have been identified by core observations and by standard petrographic analysis.

A suite of slimhole logging tools have been used in the 25 SE Majorca reef complex surveyed wells, including especially the spectral natural gamma-ray (SGR) and high resolution imaging (OBI and ABI) tools, and several types of resistivity tools (electrical log, laterolog and dual induction), neutron porosity, sonic, and the hydrogeolocical Idronaut tools. Other papers will describe results obtained from the logging tools other than SGR and borehole imaging.

The identified sedimentological facies have been analyzed on the borehole image log, and on the spectral natural gamma-ray log (SGR) in wells where the core and thin section informations are available. The image log, in conjunction with the SGR, is used for correlation purposes of the wells where these informations are not available. Because, in contrast to the SGR, the image log is not available for all wells and depth intervals, the SGR alone is used for some depth intervals.

Optical and acoustic borehole images logs have been run in most of the Ses Sitjoles wells, and in particular in the reference well MC2, and in wells CBC of Cap Blanc, S19 of Campos and S20 of Llucmajor. These images come from slim hole (40mm diameter) tools OBI40 (optical) and ABI40 (acoustic) built by Advanced Logic Technology (ALT) company in Luxembourg, which also provides the acquisition software. The optical images have a 1mm resolution, whereas the acoustic images have a 3mm resolution. These resolutions are much higher than those currently obtained in the oil industry (where the optical images are non existent_ for

good reasons since they would not provide useful images through an opaque drilling mud_ but can be compared to electrical images_ 2.5mm resolution; acoustic images from the oil industry tool offers only 5 to 10mm resolution). Both optical and acoustic images also have the advantage compared to the micro-scanner electrical images to present a 360° continuous image, as opposed to the gaps seen on the electrical images, due to the spacing between pads and flaps.

Site	Boreloless	Data	Results
Cabo Blanco	CBA, CBB, CBC	3D surface geology	3D coral visual observation, 3D seismic by ISES → sedimentology, dating (CEREGE)
		Cores	Thin-sections, description, petrophysical measurements by ISES
		Borehole optical image log (CBC)	Complement to core visual observations
		SGR log	Mineralogy of radiactive minerals, study of paleo-environment
Llucmajor	S15, S16, S18, S20	SGR, resistivity, Neutron porosity logs (S16)	Mineralogy of radioactive minerals, study of paleo-environment, porosiy
		Borehole optical image log (S20)	Complement to core visual observations
		Cores (S15, S16, S18)	Description by Government of Baleares
		S20 Cores	Dating (CEREGE)
Ses Sitjoles (Campos)	MC1 to MC11, S17	Surface geology	Electrical tomography by ETH, electrical monitoring by Montpellier II → reservoir architecture
		Cores on MC1, MC2, MC3, MC4, MC5, MC10, MC11	Petrophysical laboratory measurements (porosity, acoustic, conductivity, permeability, electrokinetic potential), visual observation, thin-section observations (ETH, CEREGE, Oviedo), dating (CEREGE) → sedimentology, diagenesis
		Borehole optical and acoustic image logs	Complement to core visual observations
		Petrophysical logs (SGR, resistivity, porosity Neutron and Sonic)	Mineralogy of radioactive mineral, paleo-environment, porosity, mineralogy study
Other Campos	S14, S19	Electrical and total GR logs (S14), SGR, resitivity (S19)	Mineralogy of radioactive mineral, paleo-environment
		Borehole optical image log (S19)	Complement to core visual observations
		Cores (S14, S17)	Description by Government of Baleares
		S19 cores	Dating (CEREGE)
Ses Salines	S21, S22, S23, S24	SGR, resistivity logs	Mineralogy of radioactive minerals, study of paleo-environment, porosity
		Cores (S22, S23)	Description by Government of Baleares

Table P2- 1. Recapitulation of Miocene SE Majorca Reef Complex data and results.

The optical image log works also in an air-filled hole, whereas the acoustic image log needs a liquid-filled hole. Thus the optical log is very useful even in the vadose zone, something very appreciated in the Majorcan wells, where the vadose zone can be relatively long compared to the total depth.

The acoustic image log presents two sets of images: one obtained from the travel time and the other one obtained from the amplitude of the acoustic signal. Those images are generally more contrasted images than those obtained from the optical image log.

The spectral gamma ray instruments record the natural gamma radiations that originate from the decay of the three radio-isotopes found in rocks that have a sufficient life-time in comparison with the Earth age and whose desintegration produces an important number of gamma-rays: ^{40}K, ^{238}U, and ^{232}Th.

The SGR 1428 spectral natural gamma-ray slimhole logging tool is manufactured by the Antares company, in Germany. The tool outside diameter is 52mm. The detector is a bismuth germanate BGO scintillation crystal of 38mm diameter and 150mm long, optically coupled to a photo-multiplier. The acquisition software is made by ALT.

The detector behaviour in function of the tool temperature is adjusted on surface by submitting the tool to a potassium source of 1.46 MeV ray and adjusting the detector high voltage until the detection of the gamma ray spectrum is appropriate. It is also automatically

controlled by the acquisition software (from ALT, Luxembrourg) while logging, and can be monitored from surface.

Site	Cabo Blanco			Llucmajor				Campos			Ses Salines			
Stratigraphy\Well	CBA (mbgl)	CBB (mbgl)	CBC (mbgl)	S15 (mbgl)	S16 (mbgl)	S18 (mbgl)	S20 (mbgl)	S14 (mbgl)	S17 (mbgl)	S19 (mbgl)	S21 (mbgl)	S22 (mbgl)	S23 (mbgl)	S24 (mbgl)
Eolianites (Fig. 5) IV	0-22 (TD)	0-25.85	0-19.5	-	-	-	-	-	-	-	0-23	0-15	-	-
Subunit IIIb	-	25.85-35.24	19.5-29.7	0-13	-	0-13	-	-	0-9.8	0-11.5	23-49.8	15-75.6	-	-
Subunit IIIb1	-	-	-	-	-	-	-	-	-	-	49.8-56.5	75.6-88.0	-	-
Suubnit IIIa	-	-	29.7-40.9	-	0-40	-	-	-	9 .8-26.8	-	56.5-71	88.0-107 (TD log)	-	0-45
Reef crest Subunit IId	-	35.24-38.85	-	13-60	40-51	13-26	0-37	-	- 26.8-36	11.5-26	71-80	-	-	45-55
Massive coral Subunit IIc	-	38.85-44.86	40.9-53.2						36-45.6					
Massive and branching coral Subunit IIb	-	44.86-53 (TD log)-58.20	-						45.6-63.5					
Dish coral Subunit IIa	-	58.20-68.54	53.2-63.5 + dish corals with protuberances											
Proximal slope Subunit Ib	-	68.4-83.95	63.5-83.3 (TD)	60-70	-	26-63	37-60	0-22	63.5-99 (TD log)	-	80-110	107-141.8	0-13	55-72
Distal slope Subunit Ia	-	-	-	70-150	51-115	63-115	60-122	22-80	99-128	26-60	110-160	-	13-85 (TD log)	72-110
Off reef open shelf	-	-	-	150-171 (TD log)-235	115-200 (TD log)-241	115-179 (TD log)-299.7	-	80-145 (TD log)-321	128-266	60-101	-	141.8-211	85-155.5	-
Today water table depth ~MSL	94.25	94.04	83.25	125.42	86.16	118.46	74.46	82.54	41.25	61.35	63.87	42.09	5.92	48.13
Distance reef crest to MSL	-	58.8	42.35	112.42	46.16	105.46	74.46	-	14.45	49.85	-7.13	-	-	3.13
Distance to coast (km)	0.5	0.5	0.01	6	4	11	5	11	6	5	2.5	1.7	4.5	7
Reef II thickness	-	33.3	22.6	47	11	13	37	0	36.7	14.5	9	-	0	11

Table P2- 2. Unit stratigraphy on Cap Blanc, Llucmajor, Campos (including S17 from Ses Sitjoles), Ses Salines. CBA, CBB et CBC correlation according to core indications provided by ISES, and from borehole optical image and SGR logs. Other wells according to SGR (S14,S15 total GR only), and core indications provided by Government of Baleares; S19 and S20 according to SGR and borehole images. The last lines are indications of the distance reef crest- Mean Sea Level (MSL), the distance to coast, and of the reef thickness.

In the low values of natural gamma-rays of Majorca carbonates, it is essential to use the proper logging speed – sampling distance couple so that the number of gamma ray counts per acquisition sample is not too low (which would create excessive statistical variations). We have adopted a logging speed of 1m/mn and a sample stepping distance of 5cm, except in wells MC1, MC2, MC10 and MC11 of Ses Sitjoles, and S19 (Campos) and S20 (Llucmajor), where a logging speed of 0.5m/mn and a stepping distance of 10cm have been used, thus providing four times more gamma-ray counts per time unit on the detector.

The tool records the uranium, thorium (Th) and potassium (K) contents of the formation in Bq/Kg and the total natural gamma-ray SGR in counts per second (CPS). The unit Bq/kg is the International System radiation unit, and is improper to analyze a mineral content in the formation. It has then been necessary to convert this unit in volumetric units (ppm for

uranium and Th, and % for K); the conversion factors for this tool have been provided by the manufacturer.
The SGR CPS unit corresponds roughly to 4 API GR units.
In spite of the low logging speed and the relatively high sampling distance used, the tool statistical variations are still important, and it is necessary to submit the three elementary channels uranium, Th and K to a powerful filtering process (Gaussian weight, 10 samples above and 10 samples below the current depth) before processing them. The thorium/ potassium (Th/K) and thorium/uranium (TURA) ratios and the computed gamma-ray (CGR, or the total natural gamma-ray without uranium influence) outputs are then calculated.
The SGR log has been recorded in the 25 wells of this study, except for wells S14 and S15, whose inside diameter of 50mm only would not allow to run in the 52mm outside diameter SGR tool. In those two wells, the 40mm outside diameter Electrical log ELXG tool was used instead. Providing different spacing short normal SN and long normal LN resistivity measurements; the ELXG slimhole tool is manufactured by Robertson Geologing, U.K for hardware as well as acquisition software; the tool is combined with a total natural gamma ray measurement.

RESULTS

Sedimentological data

Fig. P2-2 displays the geographical location of the four different sites, and of the 25 surveyed wells. Table 1 demonstrates that the data and their results were unevenly distributed over the four different sites, Cap Blanc and Ses Sitjoles being the two sites where the most complete data were obtained. For this reason, we will start studying the Reef Complex sedimentological data on the Cap Blanc site, use the knowledge already acquired on the Ses Sitjoles site, and from there extend our observations to the two remaining sites.

Cap Blanc site carbonate sequence

Three wells (CBA, CBB and CBC_ this last well being located at less than 100m from the cliff_ Fig. P2-3) were drilled in 2003 at Cap Blanc by the team of ISES-Industry project. These wells benefit at the same time from: 1) 3D outcrop observations (top and two cliff sides_ Fig. P2-4) made during several years by the Baleares Islands University, and in particular by Pomar, 1991 ; Pomar and Ward, 1994, 1995, Pomar et al., 1996 ; Pomar and Ward, 1999. This is a difference with the observations made at Ses Sitjoles, which did not benefit from the coast proximity, located at about 6km; and, because of the Campos basin grabben, the closest coast to Ses Sitjoles (Sa Rapita beach_ Fig. P2-2) does not present a cliff. 2) Observations and measurements done by ISES-Industry during their 2003 to 2004 campaigns (Table P2-1). 3) Observations made by ALIANCE team on SGR and borehole optical image logs, recorded in 2004.
On an other hand, since the vadose zone is about as thick in the Cabo Blanco wells as the well total depth, the only available logs are the borehole optical image and the natural spectral gamma ray logs.
In the three wells, the carbonate sequence (described in Table P2-2 and Figure P2-6A) derives from the outcrop (Figure P2-5) and core observations made and communicated by the ISES-Industry team (Table P2-3). It can thus be noted that a similar carbonate sequence (from bottom to top: proximal slope, Fig. P2-5H_, reef, Fig. P2-5E, outer and inner lagoon, Fig. P2-5D, Fig. P2-5B) as in Ses Sitjoles are recognized on the sediments crossed by the wells, with on top the *eolianites,* Fig. P2-5A_, not seen in Ses Sitjoles (Figures P2-6A and P2-6C). We have called those layers Unit I to IV, with different subunits.

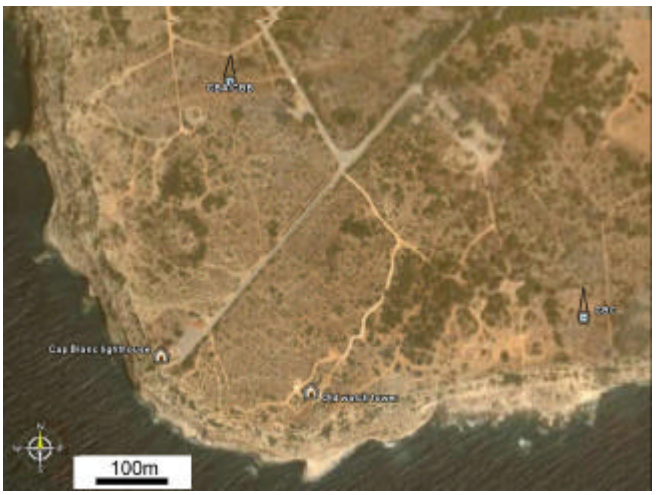

Figure P2- 3. Localization of CBA, CBB and CBC boreholes and constructions in Cabo Blanco. Satellite photo.

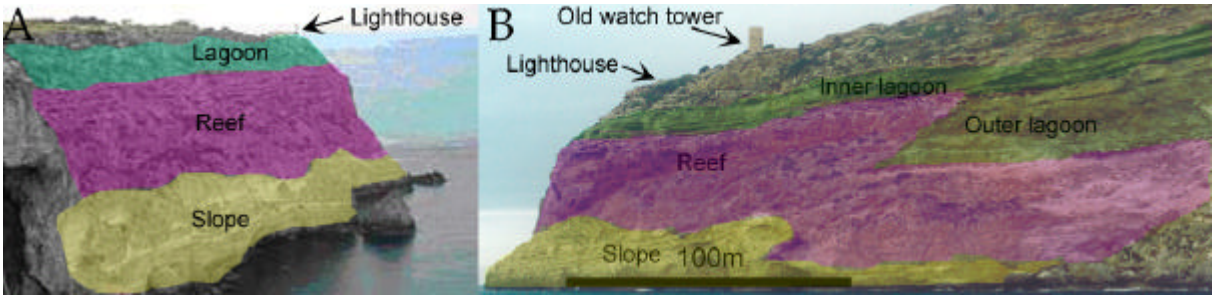

Figure P2- 4. (A): Southern side of Cabo Blanco cliff, schematization of environments. (B): Cabo Blanco cliff Eastern side: schematization of environments.

Other features are seen on Cabo Blanco cliff outcrop, such as stromatolites (Figure P2-5C), head-like columnar corals (Fig. P2-5F), and dish corals (Fig. P2-5G). These correspond to indications given by Pomar, 1991; Pomar et al., 1996.

Cabo Blanco, Llucmajor, Ses Sitjoles, and Ses Salines carbonate sequences

The elements described in the previous section allow to outline a stratigraphy. In Maria-Sube et al., in press, is described the stratigraphy found in the Ses Sitjoles site (see also Table P2-4), where twelve wells were drilled, and one well, S17, is used as reference in this document. A core description made after drilling boreholes was provided by the Government of the Baleares Islands on wells S14 to S18, S22 and S23 (see Table P2-5); although these core descriptions were much less elaborated than what was provided on Ses Sitjoles and Cap Blanc sites, it allowed us to complete and validate the stratigraphy of Majorca reef complex as displayed on Figure P2-6.

We observed Unit IV (S21) in Llucmajor and Ses Salines sites, as in Cap Blanc, and subunits IIIb/ IIIa, Unit II (S16 and S21), and subunit Ib (S21), as in Cap Blanc and Ses Sitjoles. We were also able to recognize Units or subunits that were not apparent neither in Ses Sitjoles , nor in Cap blanc: subunit Ia, (S16 and S21), and OROS (S16).

There are similarities between the carbonate sequences of the four different sites. However, Sr isotope dating results obtained on Units I and II in MC2 well indicate that those units are older than the Cabo Blanco outcrops (Camoin et al. work in progress), suggesting an older and longer than previously thought NE-SW progradation of the reef.

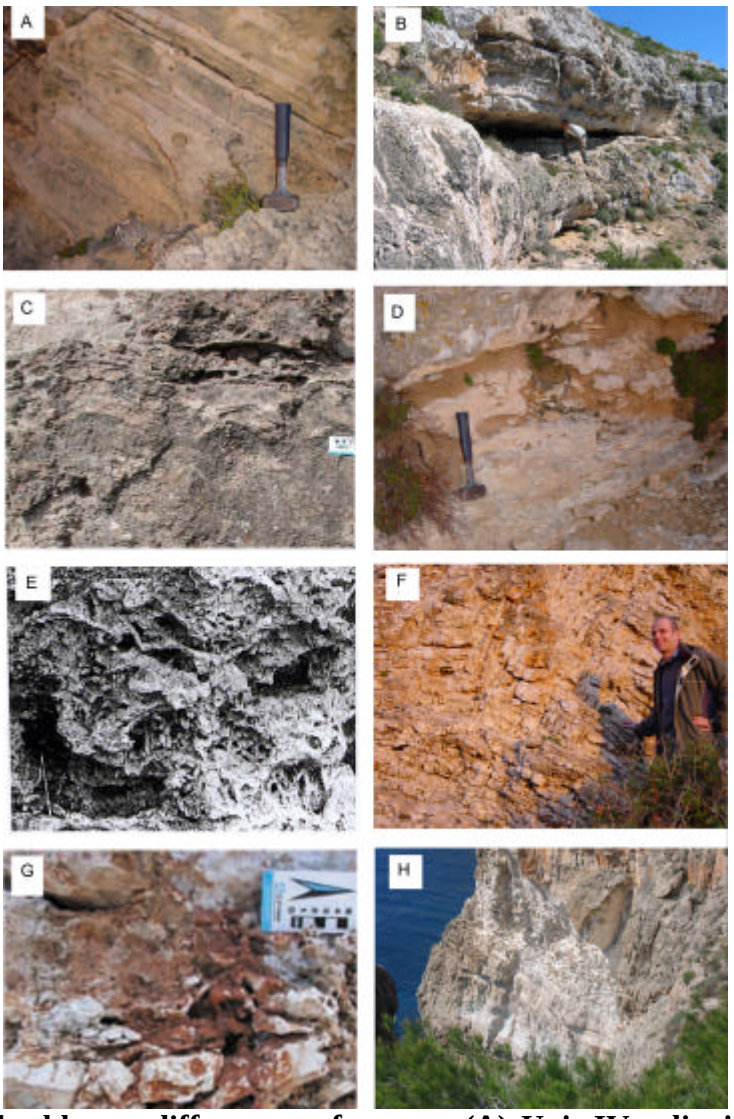

Figure P2- 5. Cabo blanco cliff outcrop features: (A) Unit IV eolianite. (B) Unit IIIb, with gray shale in the cave. (C) Subunit IIIb Stromatolite, from Van Berkel and Verhoef, 2005. (D) Subunit IIIa with orange shale. (E) Unit II massive coral, from Pomar, 1996. (F) Unit II head-like columnar coral. (G) dish coral, from Van Berkel and Verhoef, 2005. (H) this plunging view of Cabo Blanco cliff is showing bottom left the white slope, and top right the beige-orange part of the coral reef. Picture scales are indicated by either person or object on each picture.

Off reef open shelf (OROS) has been observed on cores in wells S14 to S18 and S23 by the Government of Baleares only. Pomar et al., 1996 describe this facies from outcrops as either grainstone-packstone with abundant red algae, or packstone-wackestone with planktonic foraminifers. It can start as high as from 60mbgl, and goes as deep as 320mbgl, perhaps even deeper. Note that the core observations are recorded, most of the time, from deeper than the logging tools. The only reported (in the Llucmajor platform by Pomar , 1996, and by the Government of Baleares in wells S14_ Llucmajor_ and S17_ Ses Sijoles, Campos), benthic foraminifers are *Heterostegina* (a large hyaline nummulitid). Coral debris, bivalves, oysters, echinoids, annelids, gastropods, fish scales and teeth are observed. Marls are the dominant lithology; coralline algae are found starting from 200m below the reef crest, in the photic zone (Table P2-5).

Unit I is composed of subunits Ia and Ib.

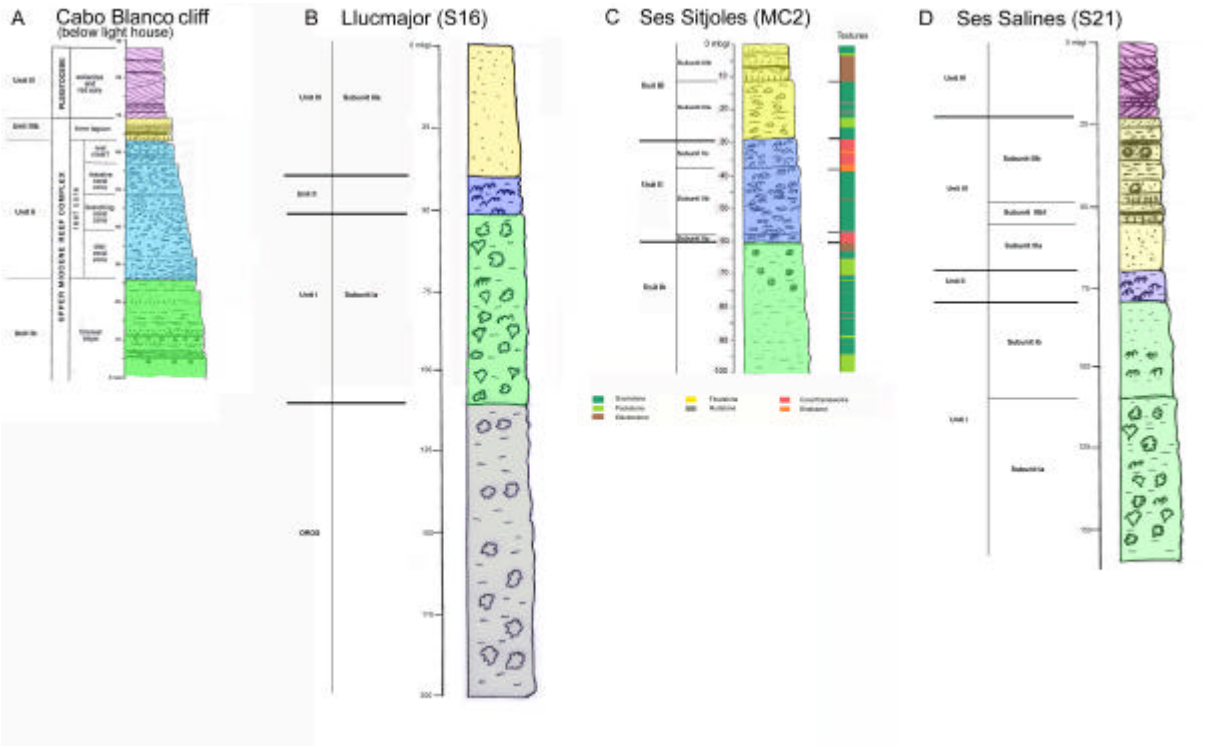

Figure P2- 6. (A) Cabo Blanco stratigraphy below the lighthouse, recognized from outcrops, cores and thin-sections (adapted from Pomar et al., 1996); see the very detailed description of the reef part. (B) Llucmajor S16 borehole borehole stratigraphy recognized from core descriptions (provided by the Government of the Baleares); two new units (described by Pomar et al., 1996) are appearing: distal slope and off reef open shelf. (C) Ses Sitjoles MC2 borehole stratigraphy recognized from thin-sections, and corresponding depositional texture column (from Jaeggi, 2006). (D) Ses Salines S21 borehole stratigraphy recognized from core descriptions (provided by the Government of the Baleares).

Subunit Ia has been observed on cores in wells S14 to S18 and S23 by the Government of Baleares, and also by Pomar, 1996 on outcrops in his zone of interest. The depositional texture is mainly packstone-wackestone. We do not have a description of the foraminifers in this sub-Unit. Coral debris, bivalves, oysters, gastropods, abundant coralline algae and *Halimeda* are reported (Table P2-5). The depositional environment is interpreted as a distal carbonate slope.

Subunit Ib has been observed in every site, however the most complete description is coming from Ses Sitjoles well MC2, reproduced from Maria-Sube et al., in press, as follows. Subunit Ib is comprised of a white bioclastic limestone that is gently to steeply bedded (10-30°). It grades from fine-grained skeletal packstones to slightly coarser skeletal packstones to grainstones. Occurrences of wackestone, rudstone, and floatstone are noted locally in the upper part of the unit. The "chalky" appearance of those rocks is generally related to their good sorting and overall fine grain size coupled with extensive moldic and intergranular porosities. The degree of cementation increases from base to top; the lower part of the unit is generally poorly cemented whereas patchy blocky spars are common in the upper part. The fabric grades from homogeneous at the base to slightly anisotropic, due to steeply dipping beds and coarse grained layers in between, at the top (Jaeggi, 2006). Porosity averages 40% in this unit; the highest values, up to 52% are related to the occurrence of larger cavities affecting both the matrix and larger skeletal pieces. The biological content is primarily composed of coralline algae (fragments and rhodoliths), echinoid plates and, to a less extent, pieces of molluscs (bivalves and gastropods), ostracods and corals in the lower part of the unit. Benthic foraminifers include textularids, miliolids, alveolinids, peneroplids (*Orbitolites*), nummulitids (*Operculina*) and a few nodosarids (Table P2-4). The depositional environment

is interpreted as a proximal carbonate slope environment characterized by moderate energy conditions. The mineral composition in Cap Blanc is calcite/ dolomite, while it is mostly calcite with very localized occurrences of dolomite in Ses Sitjoles.

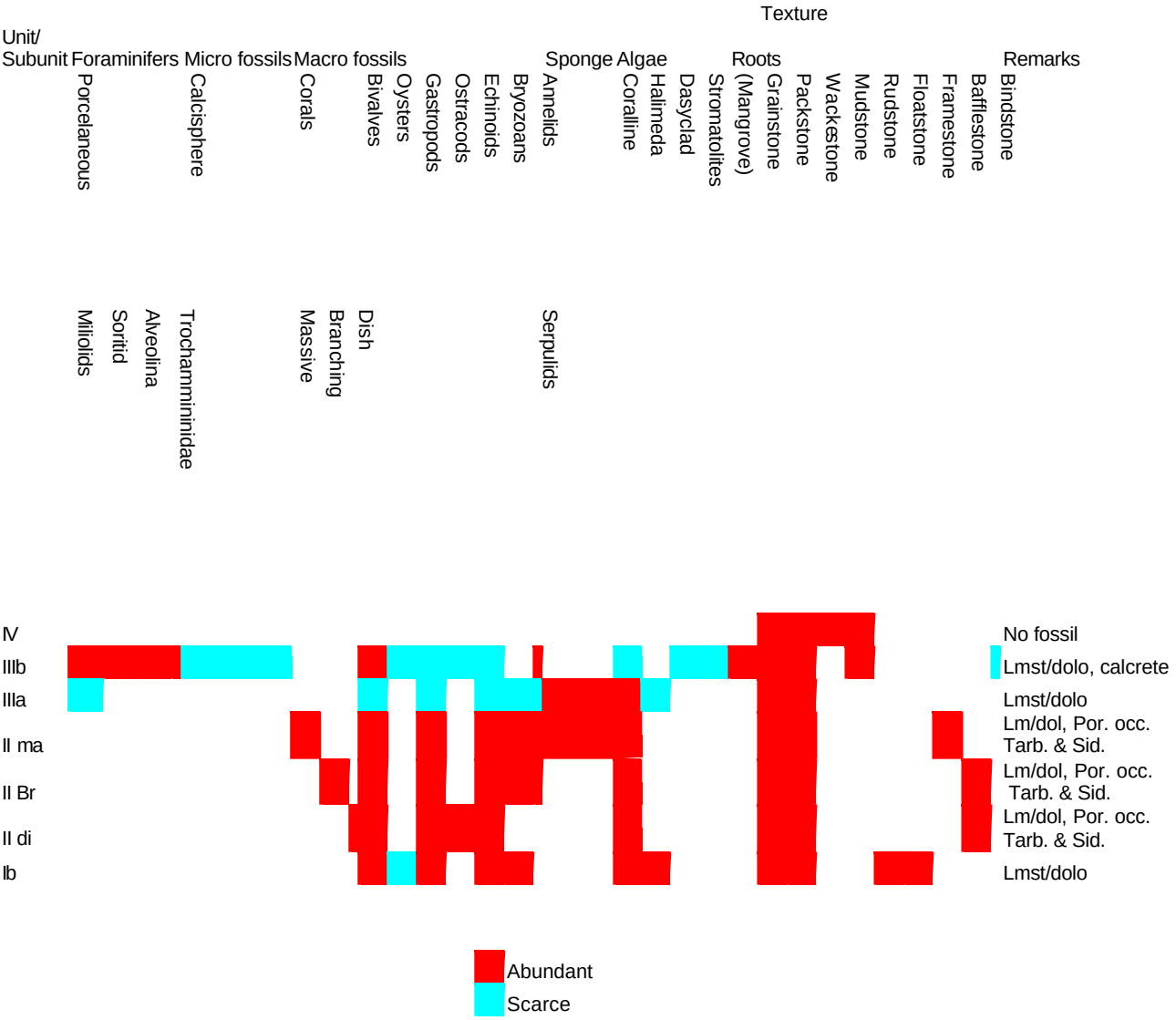

Table P2- 3. Fossil content and depositional texture in each Unit/ subunit in CBB/ CBC. Data from Verwert, in press, core thin section observations, and completed from Pomar et al., 1996.

Unit II has been observed in the four sites. In Ses Sitjoles as well as in Cap Blanc, Unit II could be subdivided into three subunits IIA, IIB, IIC; however, although a similarity was found between the average porosities of the three equivalent subunits of Ses Sitjoles and Cap Blanc (See Figures P2-10 and P2-11, track 2, channels PCORMED or PCORAV), the coral morphology occurring in Unit II from Ses Sitjoles do not include dish nor branching corals like in Cap Blanc, implying different depositional environments and bathymetry of the carbonate platform. In the other sites, the available information was not complete enough to allow a subdivision in three subunits. The coral generae diversity is very poor: mostly *Porites*, and a few *Tarbeslastraea*, *Siderastrea*, *Montastraea*. The dominant depositional texture is coral framework. The matrix of those coral frameworks is micritic and includes fragments of corals, coralline algae (both encrusting and branching) and molluscs (bivalves, including oysters in Ses Sitjoles subunit IIb, and gastropods), echinoid plates, benthic foraminifers (textularids, miliolids, alveolinids, peneroplids, nodosarids, nummulitids in Ses Sitjoles); a

few planktonic foraminifers (*Globigerina*) and ostracods (Table P2-4); worm tubes occur sporadically. *Halimeda* plates are rare and are recorded only at the top of the unit.

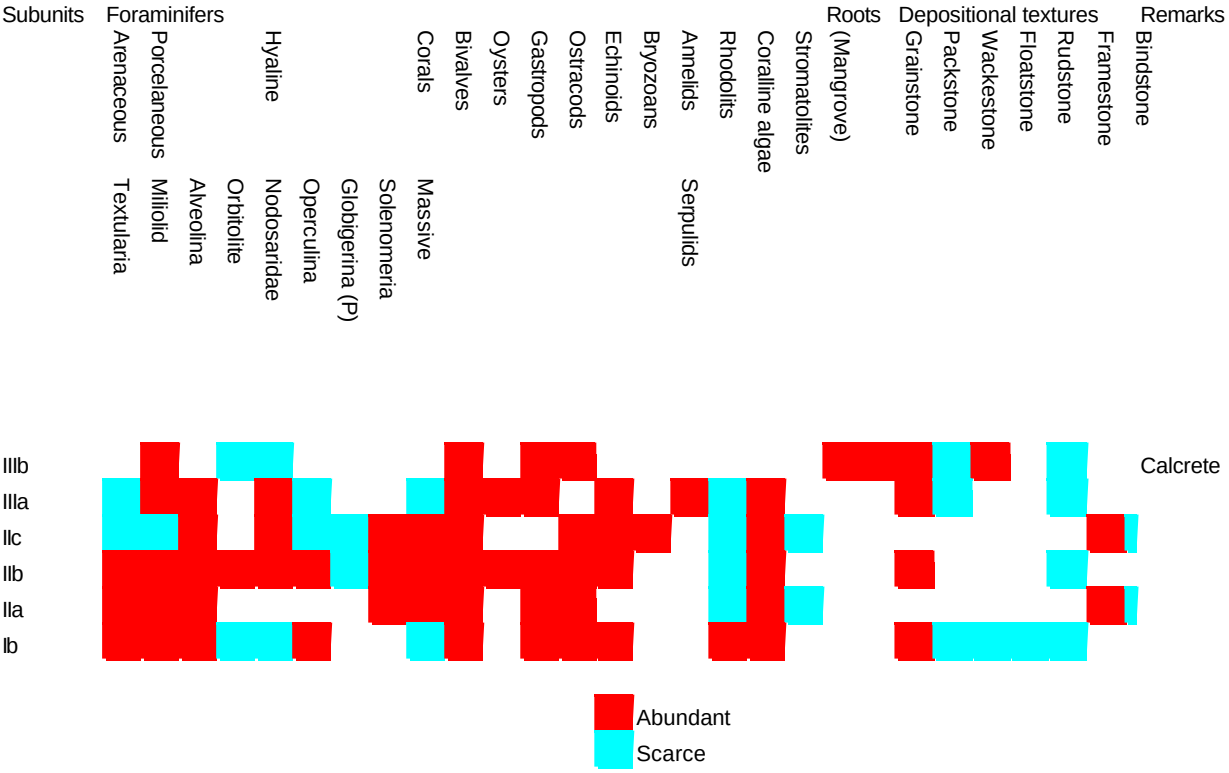

Table P2- 4. Fossil content and depositional textures in each Unit/ subunit in MC2. Data from Jaeggi, 2006, Mateos, in press, and Bonnier, 2005 core thin section observations.

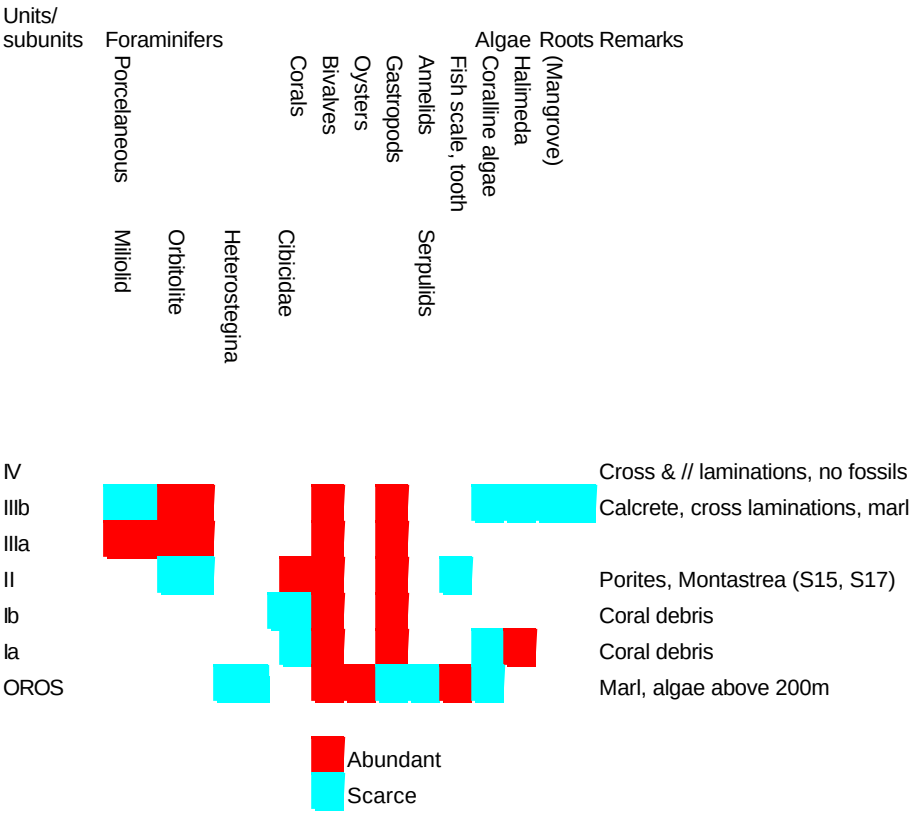

Table P2- 5. Fossil content in each Unit/ subunit in reef complex wells S14 to S24 (except S19 to S21, and S24). Data from Government of Baleares core reports. OROS: Off reef open shelf.

The fabric is highly heterogeneous. The total porosity is highly variable and ranges from 5 to 51% in MC2; it reflects by the uneven distribution both of pore spaces and of meteoric blocky and granular calcite cements. Porosity mostly includes both large primary pores that merely correspond to large open cavities between coral colonies, and secondary pores (moldic pores and solution cavities). Karstification occurs at various levels and especially in the lower part of the unit where decimeter-to-meter scale cavities are partly filled by red-brown ankerite; within those intervals, pore spaces are usually filled by blocky spars providing a denser structure to the rock. Dolomitization processes are omnipresent at Cap Blanc, while they are only occasional in Ses Sitjoles. This unit is interpreted as being deposited in a warm shallow-water environment characterized by moderate energy conditions.

Unit III is composed of subunits IIIa and IIIb, that are characterized by distinctive textures and grain contents, and have been observed in the four sites, the most complete description being provided by the Ses Sitjoles data.

Subunit IIIa is mostly comprised of well-sorted skeletal packstones and grainstones with variable cementation and local occurrence of rudstone, rich in fragments of coralline algae and molluscs (including oysters in Ses Sitjoles), benthic foraminifers (textularids, miliolids, alveolinids, nodosarids, nummulitids); echinoid plates, fragments of gastropods and annelid worms are fewer. Some beds are characterized by the occurrence of small coral colonies (massive *Porites*). Calcite cements include isopachous crusts, and patchy blocky spars.

Subunit IIIb forms the top of the unit, and corresponds to karstified oolitic grainstones and packstones, with local occurrence of rudstone, bearing very small benthic foraminifers (mostly miliolids, a few peneroplids, nodosarids, nummitulids), a few mollusks (bivalves, gastropods) and echinoids; traces of roots (attributed to presence of mangrove, because mangroves are nowadays often associated to very shallow depth warm salted water and in the vicinity of coral reefs) and calcretes are noted locally; stromatolites are noted in Cap Blanc outcrops (Figure 5C). Red clays commonly fill karstic cavities. Blocky cements occur in most intergranular pore spaces. The depositional setting is interpreted as a very shallow warm water environment characterized by low energy conditions, probably locally and temporarily restricted, with fluctuating ecological conditions (e.g. temperatures, salinities and exposure) during the deposition of subunit IIIb as indicated by the composition of its poorly diversified biological content. Furthermore, the occurrence of calcretes indicates temporary periods of subaerial exposure. Subunit IIIb is also very similar to the "Santanyi Limestone" that forms extensive outcrops along the South-Eastern coast of Majorca, including miliolid packstones and grainstones with vertical root traces, skeletal grainstones, stromatolites, and cross-bedded oolitic grainstones including giant thrombolites and stromatolites, and (Pomar et al., 1983), thus implying that it can be correlated with the "Terminal Carbonate Complex (TCC)" (Esteban, 1979, 1996, Rouchy and Saint Martin, 1992), in relation with the "Messinian Salinity Crisis (MSC)" (Hsü et al., 1973, 1977, Krijgsman et al., 1999) as well as other Mediteranean peripheric TCCs (Esteban, 1979, 1996, Esteban et al., 1996, Rouchy and Saint Martin, 1992, Cunningham et al., 1994, Franseen et al., 1998, Pomar, 1991, Riding et al., 1991, 1998, Braga and Aguirre, 2001, Cornée, et al. 2002).

Unit IV is observed only in Cap Blanc and in Ses Salines. It is not part of the reef complex, and consequently has not been described at length in Cap Blanc; the depositional environment is interpreted as eolianites. No fossil is reported in this Unit; the Unit features distinctive cross and parallel laminations (Fig. P2-5A, Tables P2-3 and P2-5).

Image Logging

The optical borehole image logs (Fig. P2-7) were used as reference and for comparison with the borehole image logs obtained at Ses Sitjoles (Fig. P2-8). Note that the image logs run in Ses Sitjoles do not allow to identify dish-corals as in Cap Blanc (Fig. P2-7E); and also, in Cap

Blanc a new image log facies was defined in Unit IV (Fig. P2-7A). On boreholes S19 and S20, borehole images could be obtained; Fig. 9 displays images from well S19. If subunit IIIb (Fig. P2-9A), and Unit II (Fig. P2-9B) present features that have already been seen in Ses Sitjoles and Cap Blanc, subunit Ia (Fig. P2-9C) and OROS (Fig. P2-9D and P2-9E) were not seen previously on borehole images. No core description was available on this well, but the Units were determined from SGR and image logs compared to the core descriptions and SGR available on other wells where these facies are encountered.

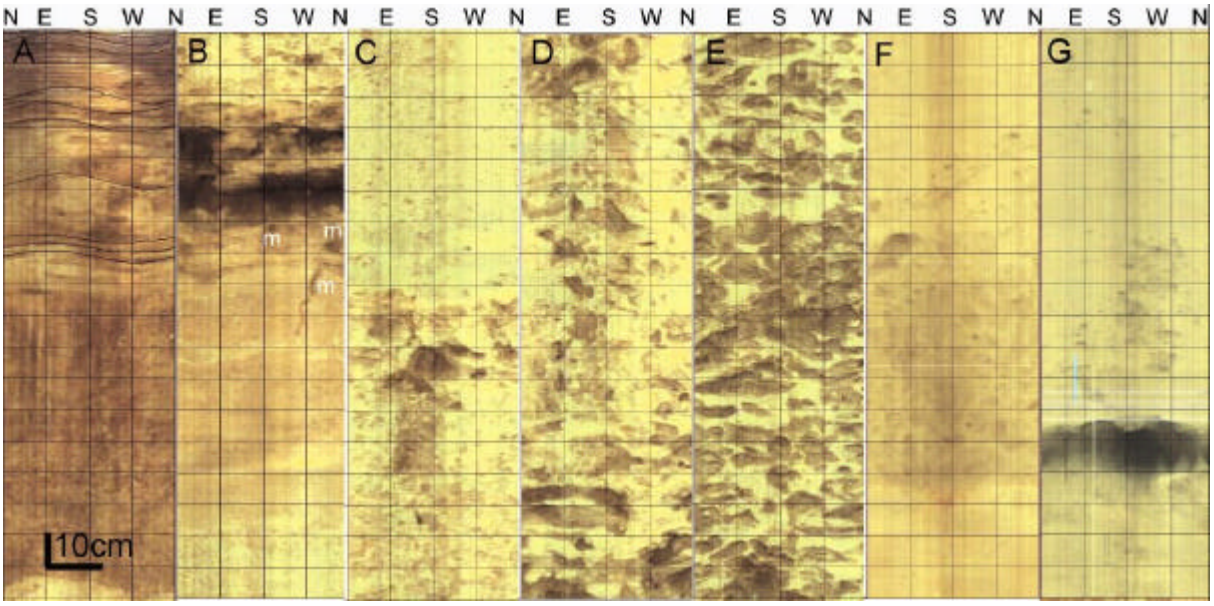

Figure P2- 7. Cabo Blanco CBC well characteristic borehole optical high resolution full 360° images; all images are in the vadose zone. (A) Unit IV eolianite, depth 0.3-2.1m, showing oriented West cross laminations (outlined by sinusoids, and of inclination 20 to 30°). (B) Subunit IIIb, depth 21.3-23.1m, shale, cave, possible presence of mangrove roots (m); note facies similarity with Fig. P2-8A and P2-9A. (C) Subunit IIIa, depth 40.0-41.8m; this facies is to be compared with the facies of Fig. 8B. (D) Unit II massive coral, depth 45.2-47.0m, compare with facies of Fig P2-8C , P2-8D, P2-8E, and P2-9B. (E) Unit II dish coral, depth 54.0-56.2m; this very characteristic facies has no comparable equivalent in Ses Sitjoles different boreholes, in Campos S19, or in Llucmajor S20.(F) Subunit Ib proximal slope, depth 74.8-76.6m, compare with Fig. P2-8F. (G) Subunit Ib proximal slope, depth 79.1-80.9m, compare with Fig. P2-8G.

Spectral natural gamma-ray

Fig. P2-10 and P2-11 display the recorded natural spectral gamma-ray, the associated borehole image logs, and the depositional structure column over the complete interval, respectively in wells MC2 and CBC. MC2's SGR log description was already made in Maria-Sube et al., in press, so, in this document, we will rather describe CBC's SGR, Fig. P2-10 being provided for comparison with Fig. P2-11. A more complete discussion of the SGR log channels interpretation is provided in Maria-Sube et al, in press, and we will not repeat it here. All scales have been selected to amplify the natural radioactive signals, because this carbonate formation displays generally very low radioactivity values.

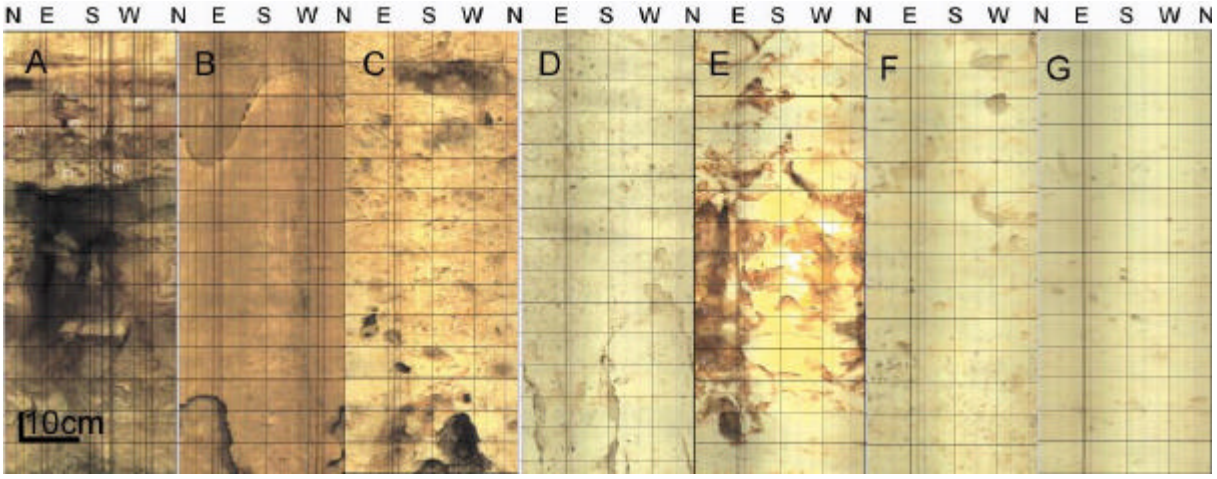

Figure P2- 8. Characteristic borehole optical high resolution full 360° images from MC2 well; A to C in air, D to G in water (greenish color, less contrast). (A) Subunit IIIb, depth 7.5-6.1mbgl, shale, cave, and possible mangrove roots (m), compare with Fig. P2-7B and P2-9A. (B) Subunit IIIa; depth 18.1-16.7mbgl, closed fracture at 17.0mbgl of excellent planarity, NE oriented dip of 70° magnitude; closed to open fracture at 18.0mbgl, SW oriented dip, of 60° magnitude; compare with Fig. P2-7C. (C) Subunit IIc, depth 32.6-31.2mbgl, this interval is characterized by abundant important megapores. (D) Subunit IIb, depth 39.4-38.0mbgl, abundant megapores; closed fracture at 39.5mbgl, East oriented, of 80° magnitude. (E) Subunit IIa, depth 57.6-56.2m, karstification, and mineralized (yellow) zones, closed fracture at 56.15mbgl, NE oriented dip, of 60° magnitude; Fig. P2-8C, P2-8D, and P2-8E are to be compared to Fig. P2-7D and P2-9B. (F) Subunit Ib top, depth 64.4-63.0mbgl, interval characterized by average value of macroporosity, compare with Fig. P2-7F. (G) Subunit Ib bottom, depth 86.4-85.0mbgl, interval characterized by very low value of macroporosity, compare with Fig. P2-7G.

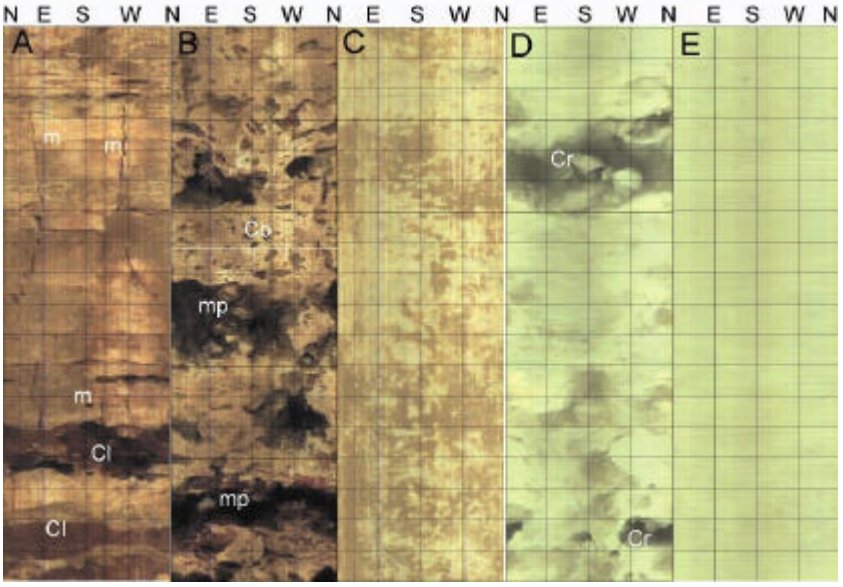

Figure P2- 9. Campos S19 well characteristic environment borehole high resolution full 360° optical images; A to C in air, D and E in water (greenish color, less contrast). (A) Subunit IIIb, depth 8.1-9.9m, presence of clay (Cl), possible presence of mangrove roots (m), compare with Fig. P2-7B and P2-8A. (B) Unit II Reef, depth 17.7-19.5m, megapores (mp), compare with Fig. 8C, coral (Co) compare with Fig. P2-7C, P2-7D, P2-7E, P2-8C, P2-8D, and P2-8E. (C) Subunit Ia distal slope, depth 49.3-51.1m; this the first borehole image of this subunit to be displayed in the SE Majorca reef complex; observe the characteristic red marbling. (D) Off reef open slope, depth 74.0-75.8m, with apparent coral debris (Cr) (E) Off reef open slope, depth 92.8-94.6m; 9D and 9E are the first Off reef open shelf borehole images to be displayed.

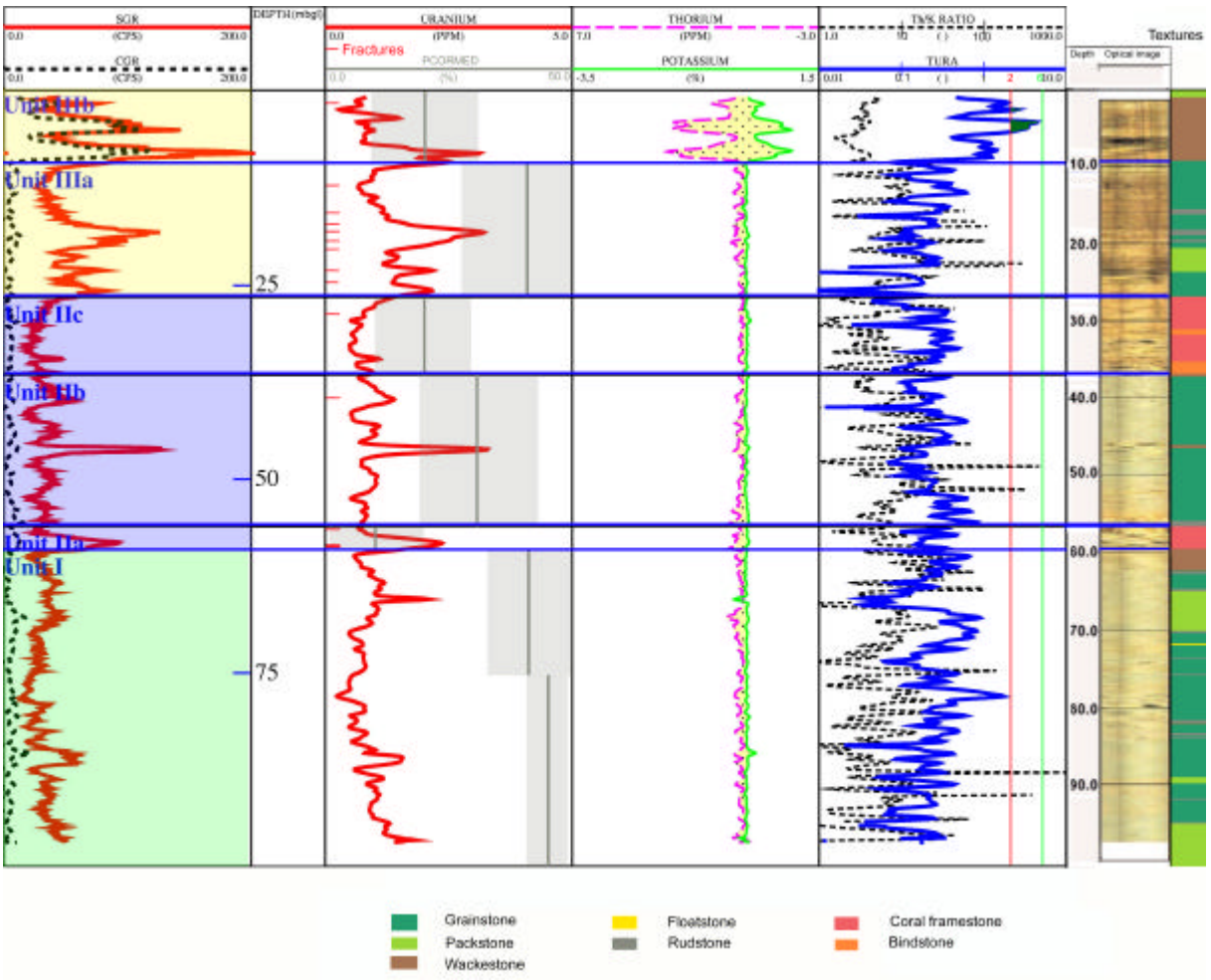

Figure P2- 10. Spectral natural gamma-ray log different channels (left) and optical image logs (right) in MC2, carbonate classification column at the extreme right. PCORMED channel is the median measured core porosity for each sub-Unit, and the grey area around it represents the interval of standard deviation. The yellow-black dotted shading between the Thorium and Potassium curves highlights the presence of radioactive minerals; the green dark shading indicates that the Thorium/ Uranium (TURA) curve exceeds the value of 2. Unit III is colour coded light yellow, Unit II is colour coded light blue, while Unit I is colour coded light green.

Uranium

On Fig. P2-11, the uranium track is displayed on track 2. Large uranium contents are encountered over subunit IIIa and more particularly over subunit IIIb. Low uranium contents are noted over Unit IV.

Because organic matter has the property of adsorbing or precipitating uranium, uranium is an organic matter indicator, either sapropelic (for marine environments) or humic (for continental environments) (Beers and Goodman, 1944; Russell, 1945; Swanson, 1960, Serra et al., 1980, Serra, 2000 and 2003). Coralline algae (from rhodolite traces, Table P2-3) is noted over all units of CBC, but more particularly in subunit Ib, *Halimeda* is noted over subunit IIIa, *Dasyclad* is noted over subunit IIIb, mangrove roots are noted only in subunit IIIb (Table P2-3).

Thorium and potassium

On Fig. P2-11 track 3, Th and K curves are displayed in opposite scales, so that the separation between the two curves, highlighted by the shading, is indicative of the volumetric quantity of radioactive minerals in the formation. This is also indicated by the CGR curve on track 1. On

top of that, the separation between SGR and CGR curves is indicating that, except in subunit IIIb, most of the radioactivity is coming from the uranium content of the formation, which shows that the radioactive mineral content is very low, except in subunit IIIb. In CBC subunit IIIb, we find once more the *"double belly"* on the thorium- potassium curves that we have seen in all Ses Sitjoles twelve wells (Maria-Sube et al., in press). Thus, the SGR curves (CGR, SGR, uranium, Th, K) are not very good subunit delimiters (except for Unit IIIb); compared to them, the average porosity value is a much better subunit delimiter.

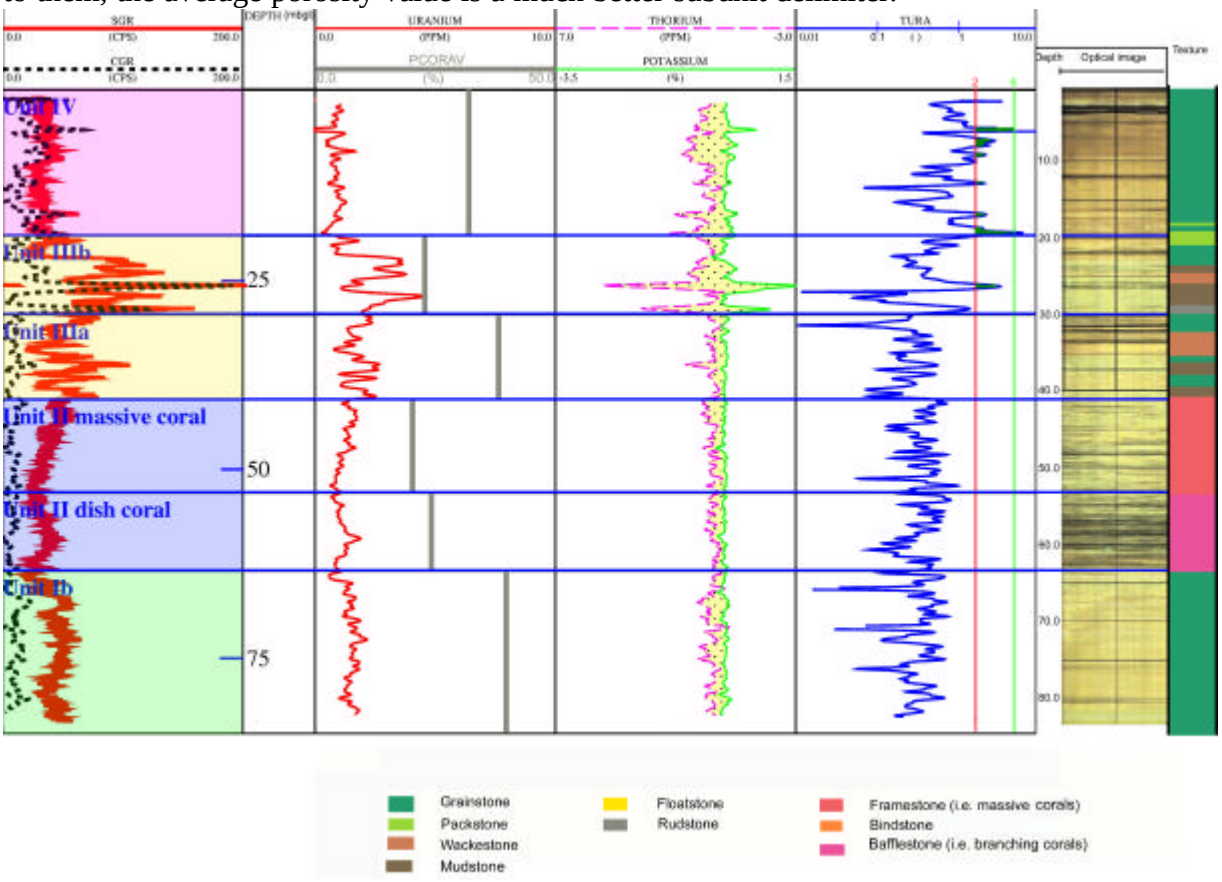

Figure P2- 11. Spectral natural gamma-ray log different channels (left) and optical image logs (right) in CBC well, carbonate classification column at the extreme right. PCORAV channel is the average measured core porosity for each sub-Unit. The yellow-black dotted shading between the thorium and potassium curves highlights the presence of radioactive minerals; the green dark shading indicates that the Thorium/ Uranium (TURA) curve exceeds the value of 2. Unit IV is color coded pink, Unit III is color coded light yellow, Unit II is colour coded light blue, while Unit I is color coded light green.

Thorium/ uranium and thorium/ uranium ratios

On Fig. P2-11 track 4 is displayed the thorium/ uranium ratio (TURA) curve. Thorium has an extremely low solubility (10^{-14} g/g), while uranium is soluble in certain conditions of pH and rH (oxydo-reduction). This property and its consequences have been exploited under several forms by different authors. For instance, TURA, together with Th are deposition paleo-environment type indicators (Adams and Weaver, 1958; Serra et al., 1980, Serra, 2000 and 2003) or of distance of sediment transport (Andersson and Werden, 2004) to the shore line, and hence in the sea, indirectly of bathymetry.

On Fig. P2-11, the TURA curve is increasing upward, from marine (subunits Ib to IIIa, where TURA is less than 2) to transitional environments in subunit IIIb (2< TURA < 6) and Unit IV where TURA reaches values larger than 6 (continental environment). Subunit IIIa displays a higher water level than subunit IIIb, a justification for separating these two subunits. Subunit IIIb case will be discussed more completely further down.

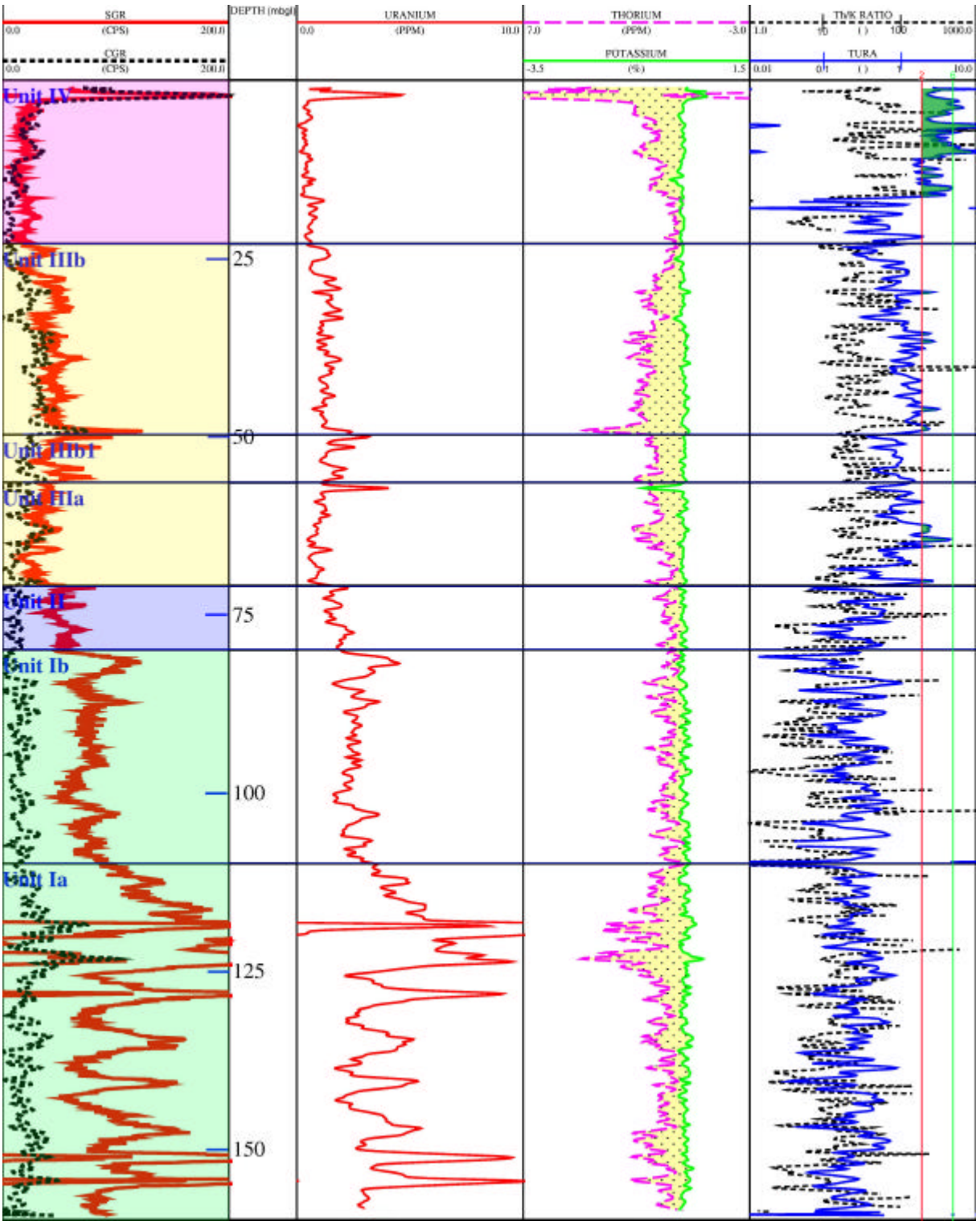

Figure P2- 12. SGR log in S21 well of Ses Salines site. Same color coding as for Fig. P2-10 and P2-11.

U and K being both more soluble than Th, high TURA associated to a high Th/K can reflect hot, humid climates and paleoclimates (Mutterlose and Ruffell, 1999; Ruffell and Worden, 2000; Schnyder et al., 2005). This property is preferably used when the paleo-environment of deposition is constantly of continental type, because then it is clear that TURA changes are not going to be significative of an environment type change; besides, if the environment type is marine, it is also clear that the variations of TURA cannot be interpreted as a change of paleoclimate humidity/ dryness. In Ses Salines well S21 (Figure P2-12), the paleoenvironment

was not of continental type; however, we do observe (subunits Ia to IIIa) parallel changes of TURA and Th/K curves (the high peaks of Th/K curve are due to very low values of K and should be neglected).
At the border between subunit IIIa and subunit IIIb, a brusque trend change is observed: while TURA increases sharply from ~0.2 to 2, Th/K stays rather constant around ~0.1, providing a clear separation between TURA and Th/K curves, that did not exist on Units I to subunit IIIa. At the same time, there is also a much larger separation between Th and K (already noted above), indicating a larger amount of radioactive mineral content in subunit IIIb (Fig. P2-10 and P2-12).
This is suggesting that: 1) the environment is changing from frankly marine (Unit I to subunit IIIa) to partly transitional (subunit IIIb), closer to the shoreline (as indicated by TURA value, and the presence of radioactive minerals, indicated by Th and K higher values); 2) these radioactive minerals in Unit IIIb are chemically immature (indicated by low Th/K value, and the presence of clays, silt), itself indicative of a short distance of transport from the source rock on land (Selley, 1976).
TURA may also reflect diagenesis changes. However, the changes of facies, simultaneous to significant changes of TURA, noted on Fig. P2-11, indicate that this is not the case here. In the same way, most of the alteration and diagenesis processes concerning radioactive minerals are observed in the micas, feldspaths and clay minerals (Hassan and Hossin, 1975), practically absent or in scarse quantity in the carbonate rocks of the reef complex. In carbonate rock, diagenetic alteration may influence concentration and distribution of uranium (Hassan and Hossin, 1975), but there is no evidence for the occurrence of such a phenomenon in the reef complex.
The TURA and Th, K data confirm our decision (made primarily from core indications, and also from borehole image observations) to split Unit III into subunits IIIa and IIIb. This decision had already been made in our Ses Sitjoles study (Maria-Sube et al., in press).

Correlation between reef complex wells

Reef Complex Unit identification

The 25 boreholes used for this study in the Miocene SE Majorca reef complex provide an exceptional opportunity to investigate the distribution in time and space of the various carbonate facies and their petrophysical properties, over a 20km by 35 km large area.
In the 100m by 100m square Ses Sitjoles site, we had already asserted our method of unit identification, based, by order of reliability and availability, on cores and thin sections, image log, SGR log (Maria-Sube et al., in press). This method benefited from the previous work made at Cap Blanc, a site located around 16km away from Ses Sitjoles, from 1979 or before to 2001 by other scientists, all Ses Sitjoles units and subunits recognized in Ses Sitjoles having been already identified in Cap Blanc. The new unit identification made by the Ises-Industry team in the three wells of Cap Blanc confirmed the previous outcrop data of Cap Blanc.
Starting from the reliable thin-section analyses and other observations of core and borehole images made in the sites of Ses Sitjoles and Cap Blanc, the unit correlations made on these sites to the wells where no such data was available was transported by using the recorded SGR logs, and when not available (wells S14 and S15), the total gamma-ray (GR) logs from the ELXG tool, and verified them with the well core observations provided on some wells by the Government of Baleares. Spectral gamma-ray markers (or signatures) were observed in three different environments, from bottom to top:
Subunit Ia, represented in wells S14 to S16, S18 to S21, and S23-S24 (Table P2-2), but not observed in the Ses Sitjoles nor Cap Blanc sites, is characterized by very large total natural

gamma-ray values (up to 410 CPS, see Figures P2-10 to P2-13; Table P2-6) with low but non negligible values of Th (average: 1.2ppm) and K (average 0.09%), and very large values of uranium (maximum 18ppm, average 4.6ppm, the largest value of any Unit). This zone is therefore a low energy zone (presence of shale, attested by the relatively large values of Th and K, means small particles) The presence of clay minerals of terrigeneous origin is explained by the decreasing of the limestone production compared to the inner platform, where are found the maximum number of living organisms. There is a strong presence of organic matter (coralline algae, *Halimeda*). Values of TURA are constantly below 0.8, hence largely and constantly in the marine environment area. This subunit is found below subunit Ib. These observations confirm our interpretation of subunit Ia depositional environment as a distal carbonate slope. A borehole image of that Unit coming from well S19 is shown on Figure 9C.

Data Unit/ subunit	CGR (CPS)	SGR (CPS)	Thorium (ppm)	Potassium (%)	Uranium (ppm)	Thorium/ Potassium	Thorium/ Uranium	Porosity (V/V)
Eolianites IV	[0-220] # 20	[15-220] # 40	[0-5] #1.5	[0-0.8] #.03	[0-5] #.6	[2-80], # 8	[0.2-25]	0.32
IIIb	[0-200]	[20-210]	[0-5] #1.4	[0-3] #.05	[1-10] #1.4	[1-100+], # 3-8	[0.01-6]	0.23
IIIa	[0-30]	[20-100]	[0-0.8] #1.1	[0-0.1] #.006	[1-4] #1	[2-100+]	[0.01-5]	0.38
Reef IIc massive coral	# 10 [0-10]	# 20 [20-60]	[0-0.5] [0-0.3]	[0-0.1] [0-0.1]	[1-5] [1-2]	[1-100+] [1-100+]	[0.07-3.0] [0.07-1]	0.20
Reef IIb branching coral	-	-	-	-	-	-	-	0.30
Reef IIa dish coral	[0-8]	[20-50]	[0-0.3]	[0-0.1]	[1-2]	[1-100+]	[0.08-0.6]	0.24
Proximal slope Ib	# 10	# 50	[0-0.3] #.7	[0-0.1] #.06	[1-2.1] #2.6	[1-100+]	[0.05-0.6]	0.40
Distal slope Ia	# 10	[40-410]	[0-2] #1.2	[0-0.1] #.09	[0.5-18] #4.6	[2-100+]	[0.01-0.8]	0.42
Off reef open shelf	# 10	[60-190]	[0-1] #.9	[0-0.1] #.06	[1-6.2] #3.8	[1-100+]	[0.02-0.7]	0.46

Table P2-6. SGR tool channels characteristics ([Min.-max] #Average) observed over the different Units/ subunits of the Reef Complex of Majorca. Porosity measurements on the right column : Units Ib to IV: from Cabo Blanco cliff core measurements Van Berkel and Verhoef, 2005; Units Ib to IIIb: Ses Sitjoles ALIANCE core measurements; Off reef open shelf and Unit Ia: neutron porosity measurement in S16 (Figure P2-13).

Subunit IIIb, characterized by a very remarkable "double belly" of shale (maximum value of Th: 5ppm; maximum value of K: 3%) whose bottom has been, in Maria-Sube et al., in press, determined as being the bottom layer of subunit IIIb, with possibly some important values of uranium (maximum 10 ppm, average 1.4 ppm). This unit is the shaliest of the reef complex (maximum total gamma-ray, 210 CPS, see Table P2-6 and Fig. P2-14), together with Unit IV. The "double belly" is found practically in every well of the reef complex (see Figures 10 to 13, and 15 to 16, and also Maria-Sube et al., in press, for Ses Sitjoles), at least in every well where subunit IIIb has been identified. In subunit IIIb_ CBB-CBC, S15, S18, S19, S17 and all the Ses Sitjoles wells, S19 to S21 (Table P2-6)_, TURA values vary from 0.01 to 6, or from marine to continental environments.

Unit IV, represented in wells CBA to CBC, and S21-S22 (Table P2-2) is characterized by a relatively large amounts of shaly materials (maximum value of Th: 5ppm; maximum value of K: 0.8%) and with possibly some important values of uranium (maximum 5 ppm, average 0.6ppm); it is thus easy (from the examination of the SGR data alone) to confuse subunit IIIb and Unit IV; however, the "double belly" is absent from Unit IV, and also, there is in Unit IV a sharp and high gamma-ray peak (Figures P2-12, P2-15A and P2-16B) with maximum value of 220 CPS, visible on wells S21 and S22 of Ses Salines, although not visible in other wells where Unit IV is present (Cap Blanc, Figures 11 and 15A). In Unit IV, TURA varies from 0.2 to 25, or from marine to continental environment, i.e. the whole range of environment types (Table P2-6).

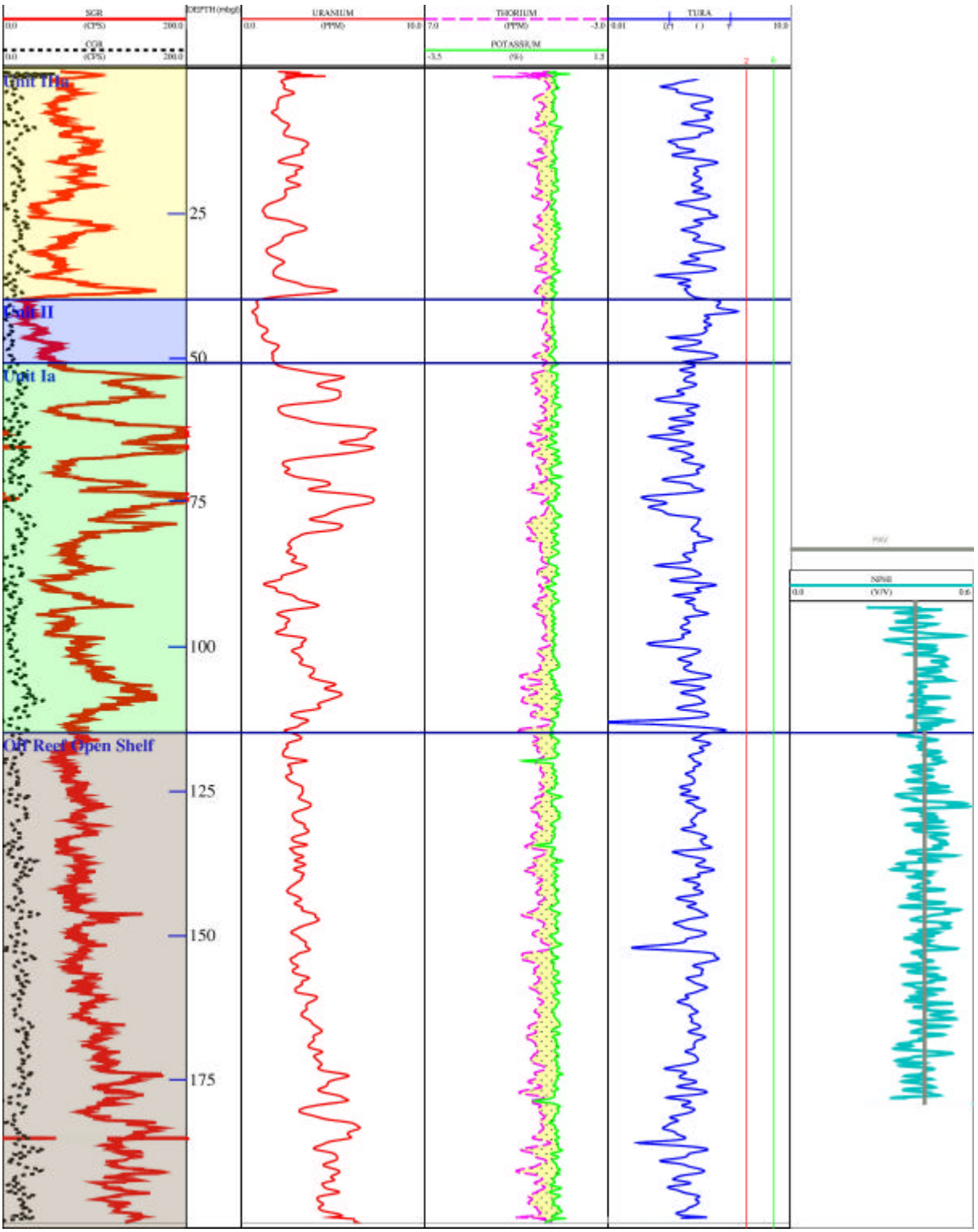

Figure P2- 13. SGR log in S16 well of Llucmajor site. Same color coding as for Fig. P2-10, P2-11 and P2-12, with Off reef open shelf color coded light gray. Neutron porosity log in the right track ; average porosity PAV (from neutron porosity log) is indicated with a thick grey line. Note the very high porosity in the off reef open shelf, even higher than in Unit Ia.

These three different markers allow to identify from their presence on the SGR data their corresponding unit, and from their absence, combined with the stratigraphic position, the possible occurrence of a different unit or subunit. Thus, the **OROS** (Figure 13), not represented in Cap Blanc nor Ses Sitjoles sites, was identified on wells S14 to S16, and S18 to S20 (Figures 13, 14B, 15B, 16A) because it is located right below subunit Ia, and has a facies

with a lower total natural GR, lower uranium (hence less algae presence than in subunit Ia), but as much clay content as in subunit Ia. Note also (Figure P2-13) the higher average porosity reading than on the distal slope. Figures P2-9D and P2-9E are displaying a borehole image of that facies in well S19. Thanks to the borehole images, we could identify on that facies coral debris (Figure P2-9D), that confirm our identification of that facies as OROS.

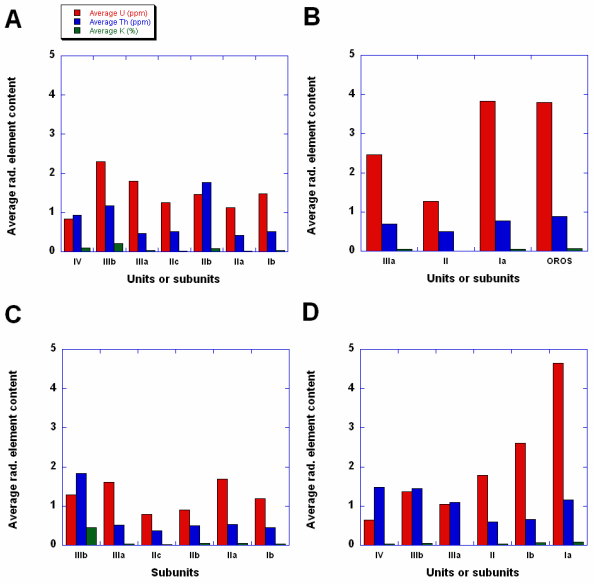

Figure P2- 14. (A) Histogram of uranium, thorium and potassium averages in well CBC of Cabo Blanco for each stratigraphic subunit. (B) Same histogram as in A for well S16 of Llucmajor.(C) Same histogram as in A and B for well MC2 of Ses Sitjoles. (D) Same histogram as in A, B, and C for well S21 of Ses Salines.

In between the markers, one can also note that TURA indicates constantly marine environment from OROS to subunit Ib, while the range of environment type varies from marine to transitional from Unit II to subunit IIIb (with the frequency of transitional occurrences increasing upward), and from marine to continental in Unit IV. The differentiation between subunit Ib, Unit II and subunit IIIa is made mainly on the basis that SGR and CGR channels are lower in Unit II (Table P2-6). Due to the relative lack of information in Llucmajor and Ses Salines sites, it was not possible in these sites to identify subunits in Unit II.

Average values of SGR channels in the different units

Fig. P2-14 is an illustration of the SGR channels subunits identification capacity as well as of their limitations: subunit Ia is clearly identified by the high value of uranium, Unit II is the lowest one in Th, subunit IIIb and Unit IV are the highest one in Th and K. The level of radioactivity is generally lower in Ses Sitjoles than in the other sites, on a subunit by subunit basis (compare Fig. P2-14C with P2-14A, P2-14B and P2-14D). The clay content generally decreases upward (see Th bar), from OROS to Unit II, and then increases upward from Unit II to subunit IIIb, and stays constant from subunit IIIb to Unit IV. The largest uranium content is found in subunit Ia, followed immediately by the OROS (Figures P2-14 B and P2-14D), while the lowest uranium content is found in Unit IV (Figures P2-14A and P2-14D).

Reef complex unit correlation

The reef complex unit identification made from cores and logs have allowed to build Tables P2-2 and P2-6.

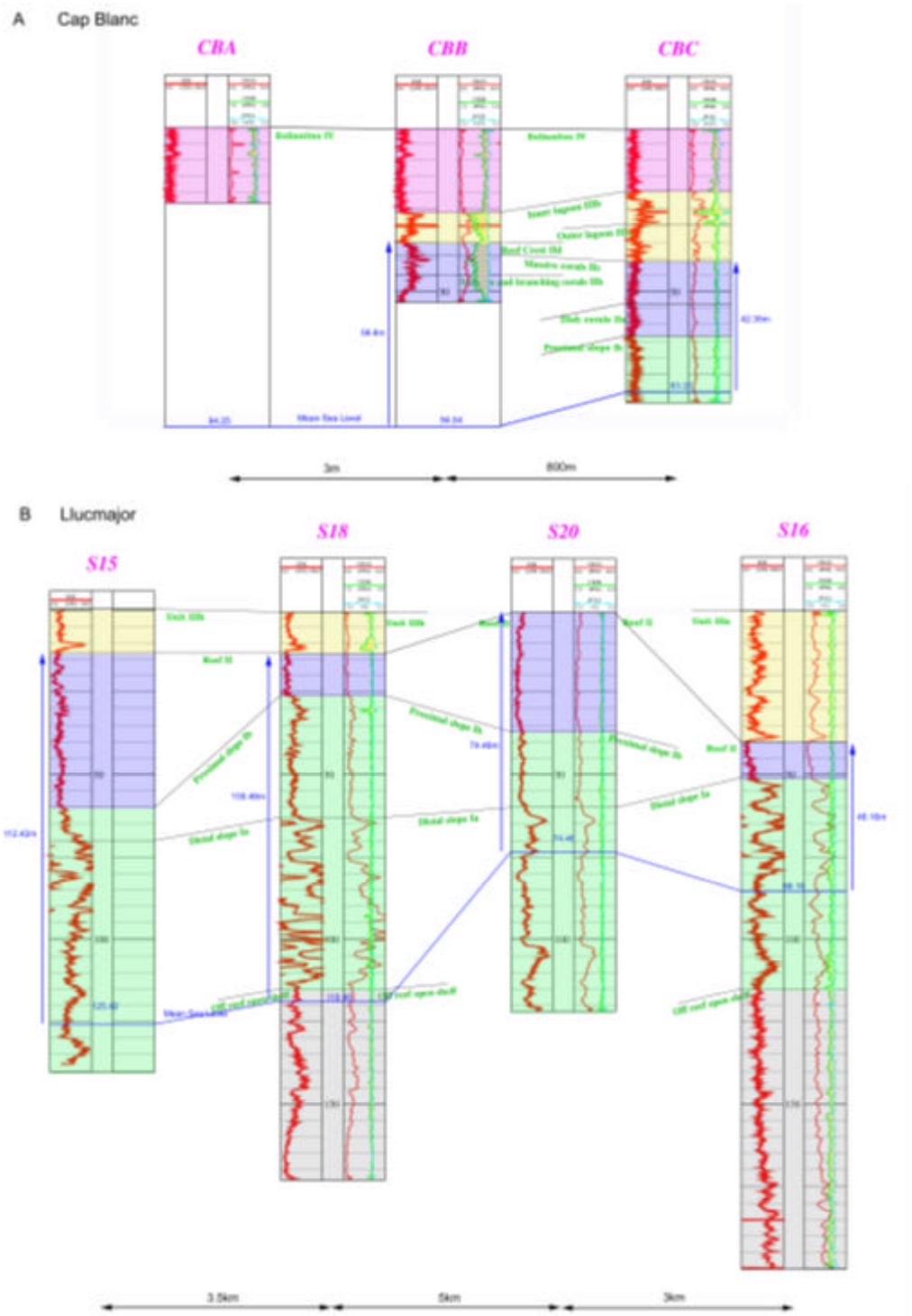

Figure P2- 15. SGR facies correlation over Cap Blanc and Llucmajor sites. On each well, the represented four curves are from left to right: SGR (track 1, red, scale 0 to 200 CPS), Uranium (track 2, red, scale 0 to 10 ppm), Thorium (track 2, green, scale 7 to –3 ppm), Potassium (track 2, blue, scale –3.5 to 1.5 %). The yellow-black dotted shading between the Thorium and Potassium curves highlight the presence of radioactive minerals. Unit IV is color coded green; Unit III is color coded light yellow; Unit II is color coded light blue; Unit I is color coded light green, while Off reef Open Shelf is color coded light gray. Below Figures (A) and (B), the distances between wells are indicated.(A) SGR Unit correlation over Cap Blanc site wells CBA, CBB and CBC. (B) SGR unit correlation over Llucmajor site wells S15, S16, S18, S20. No spectral GR tool could be run on S15, only a total natural GR with roughly four times less CPS than for the Spectral GR; for this reason, the display scale was divided by four, for comparison purposes with the other wells. Today Mean Sea Level (MSL), taken roughly from today water table depth, and the distance MSL to reef crest_ see Table P2-2_ are indicated in blue.

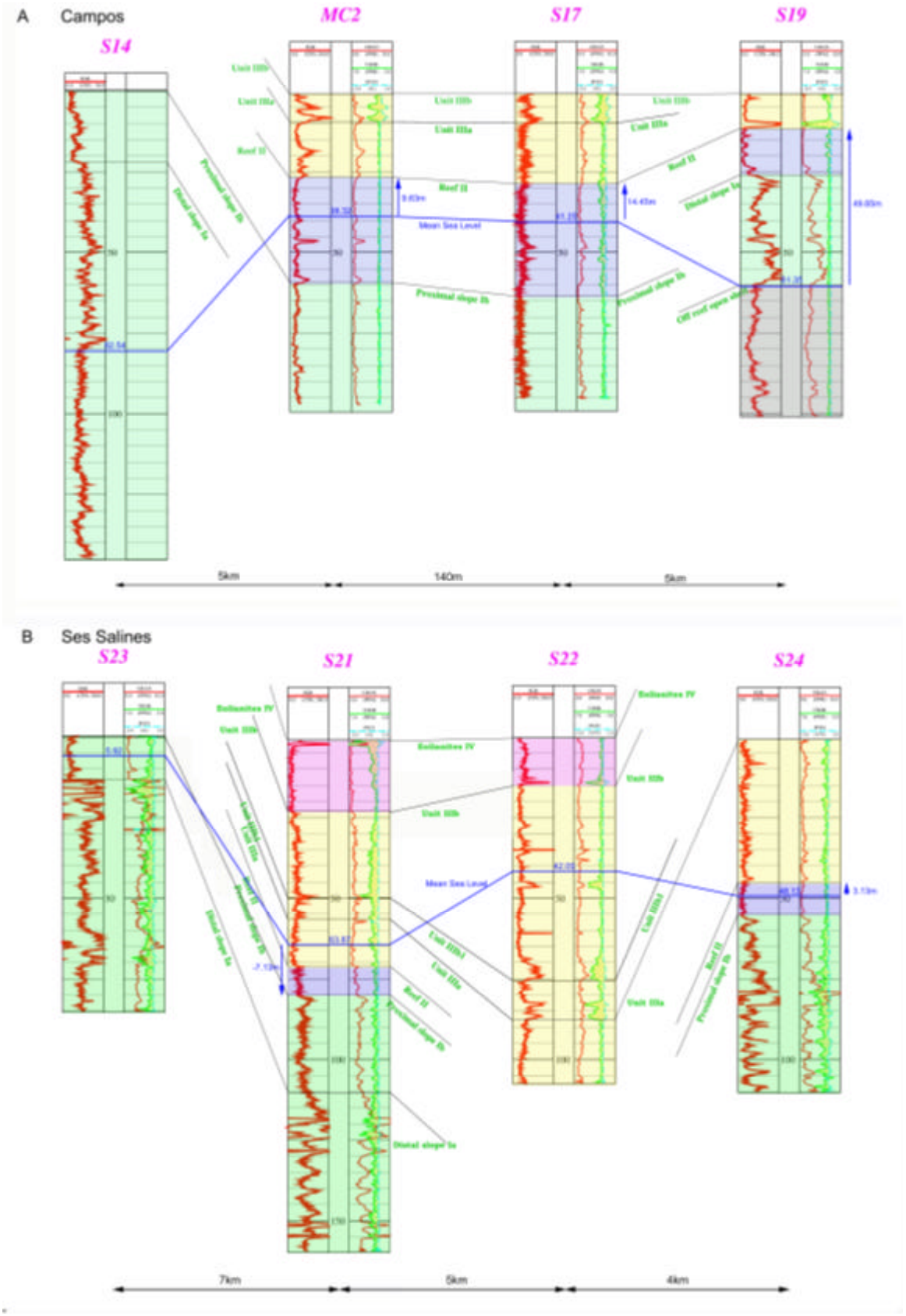

Figure P2- 16. SGR facies correlation over Campos and Ses Salines sites. Same scales and colour coding as on Fig. 15. (A) SGR Unit correlation over Campos site wells S14, MC2, S17and S19. No spectral GR tool could be run on S14, only a total natural GR with roughly four times less CPS that for the Spectral GR; for this reason, the display scale was divided by four, for comparison purposes with the other wells. (B) SGR Unit correlation over Ses Salines site wells S21 to S24.

Using the data from Table P2-2, Fig. P2-15 and P2-16, illustrating the Reef Complex Unit correlation in the wells of the four different sites, were constructed. On Figures P2-15 and P2-16, the Mean Sea Level (MSL) has been indicated, to take into account the topographic effect. Wells MC2 and S17 have been used as witnesses of the Ses Sitjoles site stratigraphy (Figure P2-16 A); for a more detailed Ses Sitjoles wells stratigraphy, see Maria-Sube et al., in press.
The last row of Table P2-2 indicates Unit II's thickness; two wells (S14 and S23) do not feature Unit II because their sequence starts from surface at subunit Ib, while two other one (CBA and S22) do not feature it because they were not drilled deep enough to reach it (in fact, the core report shows that this last well was drilled to 211m, to reach the slope, but no coral was noticed). When Unit II was represented, we distinguish a group of wells featuring thin reef layer (S16, S18, S19, S21, S24) with a layer thickness of 9 to 14.5m, and a group of wells with a thicker reef layer (CBB, CBC, S15, S20, S17) of thickness ranging from 22.6 to 47m. However, we have seen (Maria-Sube et al., in press) in Ses Sitjoles that out of twelve wells in a 100m side square, eleven had an average reef thickness of 31.9m with a standard deviation of 3.5m, but one well (MC3) had a reef thickness of 6m only; which is an other confirmation of the extreme heterogeneity of the Reef Complex, and also that even at a 100m scale, local reef thickness variations may occur.
Fig. P2-15 and P2-16 provide a spectacular and exceptional view of 3D evolution of facies in a coral reef platform covering an area of 20 by 35 km.

Clastics

We have seen higher up (Fig. P2-10 to P2-13) the use of the separation between the Th and K curves, displayed on opposite scales, for evaluating the quantity of radioactive mineral content in the formation. To be able to analyze the type of radioactive mineral(s), it is necessary to use a Th vs. K crossplot. The same method, derived from Serra 2000, 2003, of elliptic 100% pure radioactive mineral domain, as explained and used in Maria-Sube et al., in press, for the Ses Sitjoles sediments, was used for the reef complex (Fig. P2-17). In the carbonates of Ses Sitjoles, the plot of ten wells SGR data (Fig. P2-17A), as well as in the reef complex (Fig. P2-17B and C), seems to indicate a montmorillonite- illite- biotite trend.
Because of the greater solubility of K compared to that of Th, Fig. P2-17 plots may also be used to evaluate the sediments distance of transport, their diagenesis, the paleoclimates, the chemical maturity (increasing counterclock-wise).
In the case of the reef complex, the presence of these terrigeneous sediments is an indication that these formations, particularly subunit IIIb and Unit IV, were close to land at time of deposition, and that the chemical maturity was relatively low.

Majorca reef complex paleo-environments, TURA overall coherence and heterogeneity

Fig. P2-18A displays the different environmental domains and boundaries in the Th vs. TURA axes for ten wells in Ses Sitjoles. Fig. P2-18B and P2-18C display also a remarkable statistical overlapping of the different reef complex wells data, which confirms the validity of the data. A few wells even display a few data in the continental domain (Fig. P2-18C).

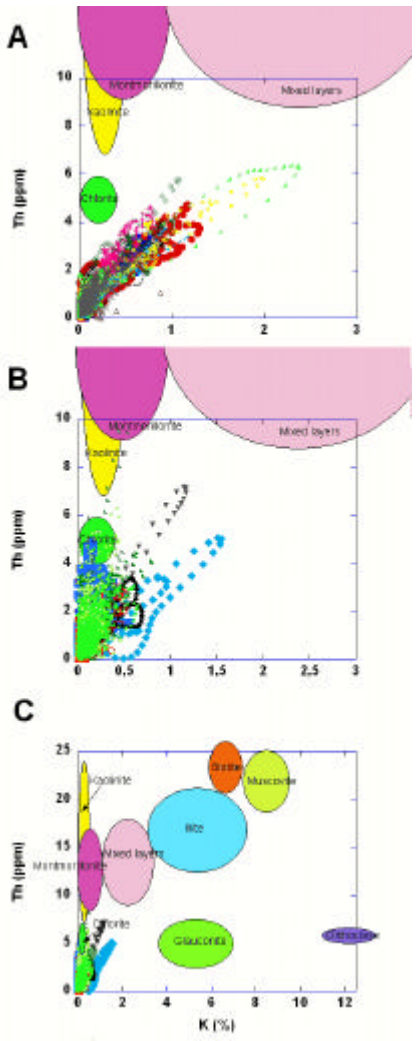

Figure P2- 17. Majorca Reef complex Thorium vs. Potassium crossplots. The colored ellipses representing empirical radioactive mineral domains are adapted from Serra, 2000, 2003. (A) Ses Sitjoles ten wells, 22000 data points, expanded scale; S17 data are plotted as grey triangles. (B) Reef Complex twelve wells, 12000 data points, expanded scale; Cap Blanc (CBA, CBB, CBC) data points are plotted as large blue full dot, square, diamond; Llucmajor (S16, S8, S20) data points are plotted as red open smaller dot, square, diamond; Campos (S17, S19) are plotted as tip up and tip down full even smaller black (S17, tip up) or grey (S19, tip down) triangles; Ses Salines (S21 to S24) data points are plotted as smallest green full or open triangles (C) Reef Complex twelve wells, 12000 data points, reduced scale, allowing to view a complete display of most representative radioactive mineral domains; the data points coding is the same as for (B).

Fig. P2-19 displays profiles of TURA vs. depth of different groups of wells in Majorca reef complex. The top P2-19A graph, displays TURA for Cap Blanc site. The TURA curves are reasonably overlapping for the three well curves in the first 22mbgl, mostly in Unit IV (this is very expected from CBA and CBB wells, which are only 3m away one from the other); most of the curve occurrences are in the marine paleoenvironment area, with many incursions in the transitional area, and some of them in the continental area. The CBA curve is not recorded below 22mbgl, and from 22 to 30mbgl, CBB and CBC curves are rather overlapping, in a facies corresponding predominantly to subunit IIIb (Table P2-2). From 30 to 53mbgl, we observe that the two CBB and CBC curves are separating, the CBB curve being in the range 1 to 2 (marine environment, but not far from transitional), while the CBC curve is in the range 0.1-1 (frankly marine environment); this is interesting, because we know that CBB is further away from the present shoreline than CBC (Fig. P2-3). In CBB we enter from 35.24 to 38.85mbgl in the reef crest (bathymetry 0-2mbsl), from 38.85 to 44.86mbgl in massive corals

(bathymetry 0-10mbsl), and then from 44.86 to 53.20mbgl in branching corals (bathymetry 10-20mbsl); in that well, dish corals (bathymetry 20-30m) are observed from 58.20 to 68.54m. A decreasing downward trend from 2 to 1 starting from 44mbgl is observed on the TURA curve from CBB, thus leaning toward CBC's TURA curve. Massive corals are observed in CBC, from 40.9 to 53.2mbgl. Therefore, we observe in both CBB and CBC wells between 38.85 and 44.86mbgl the same facies of massive corals, implying the same bathymetry, and different TURA curves. This observation, combined with the observation made above on the distance of wells CBB and CBC to the present day shore line, allows to conclude that the TURA curve is sensitive to both the distance to the shoreline and to the bathymetry. Globally, it can be said that the diagram of Figure P2-19A is very similar to the corresponding diagrams obtained in Ses Sitjoles (Fig. P2-19C), except of course that in Ses Sitjoles, Unit IV is not seen.

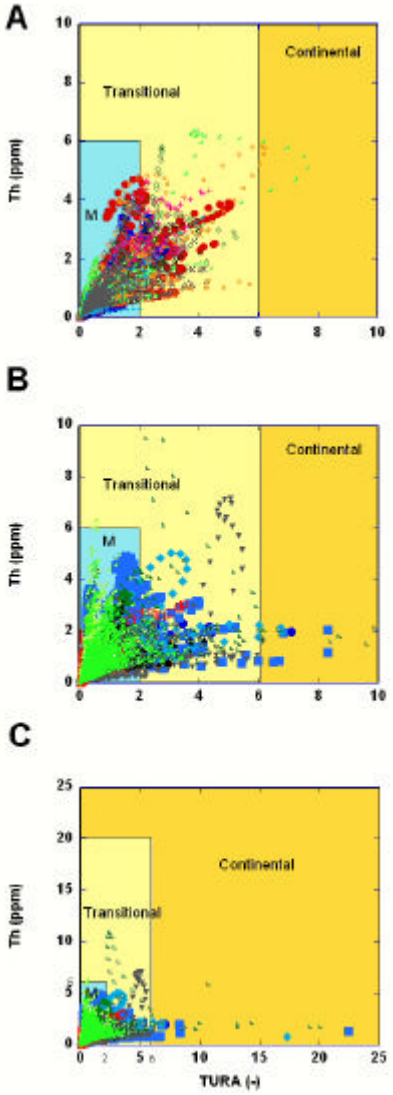

Figure P2- 18. Majorca reef complex Thorium vs. Thorium/ Uranium ratio crossplots, showing domains of marine (M, blue), transitional (yellow), and continental (ochre) environments (crossplot template after Adams and Weaver, 1958). (A) Ses Sitjoles ten wells, 22000 data points, expanded scale; S17 data are plotted as gray triangles. (B) Reef Complex twelve wells, 12000 data points, expanded scale; Cap Blanc (CBA, CBB, CBC) data points are plotted as large blue full dot, square, diamond; Llucmajor (S16, S8, S20) data points are plotted as red open smaller dot, square, diamond; Campos (S17, S19) are plotted as tip up and tip down full even smaller black (S17, tip up) or gray (S19, tip down) triangles; Ses Salines (S21 to S24) data points are plotted as smallest green full or open triangles (C) Reef Complex twelve wells, 12000 data points, large scale, allowing to view a complete display of most representative radioactive mineral domains; the data points coding is the same as for (B).

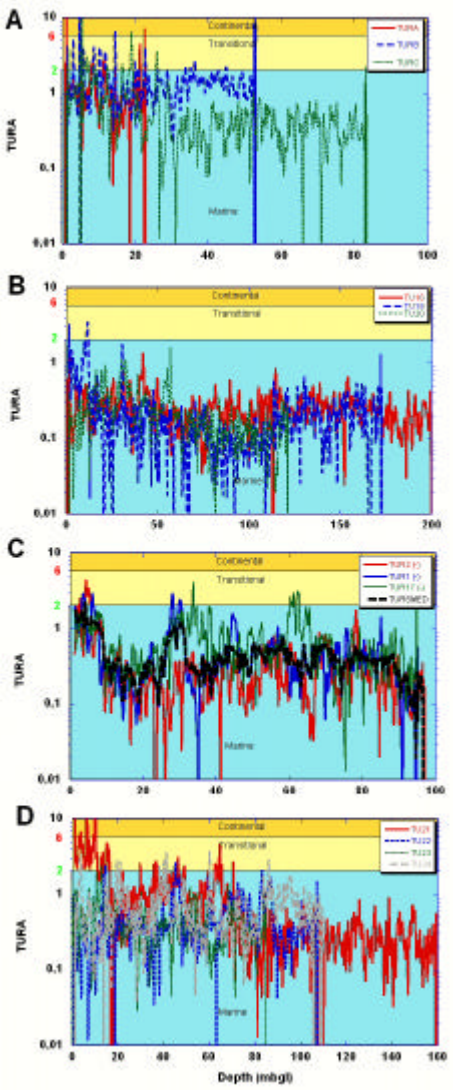

Figure P2- 19. Thorium/ Uranium ratio curves vs. depth in wells of (A) Cap Blanc, (B) Llucmajor (C) Ses Sitjoles and (D) Ses Salines sites. Similar plots are available for Ses Sitjoles wells of Campos site in Maria-Sube, submitted.

Figure P2-19B displays TURA of three wells in *Llucmajor site* (S16, S18, S20; of course, S15 TURA cannot be shown, since the SGR logging tool could not be run in that well, because of a too restricted inner diameter). The values of TURA overlap remarkably well. This diagram is very similar to the corresponding diagram that was obtained in Ses Sitjoles (Fig. 19C), except that, since the wells of Llucmajor are drilled through deeper and unknown in Ses Sitjoles formations (subunit Ia, OROS), TURA reaches lower values than in Ses Sitjoles (roughly 0.03 compare to 0.1); this is mainly due to subunit Ia very high values of uranium (Fig. P2-14B).

Fig. P2-19D displays TURA of four wells in *Ses Salines* (S21 to 24). Here again, we see a picture very similar to what was observed in Ses Sitjoles (Fig. P2-19C, and Maria-Sube et al., in press). The curve overlap is generally good; however, we observe a different behaviour of TURA in S21 and S22 in Unit IV: While for S21, TURA is almost constantly above 2 in Unit IV interval (0-23mbgl, identified by the large gamma-ray peak_ Fig. P2-12 and P2-16B), it has only a brief excursion above 2 in the Unit IV interval (0-15mbgl) of S22.

DISCUSSION

Methodology

The multi-scalar and multi-disciplinary methodology asserted in Maria-Sube et al., in press, at the limited scale of Ses Sitjoles site, worked well at the larger scale of the reef complex, in a similar, but more complex geological environment. This methodology, based on the use of outcrops and cores, completed by borehole images and SGR logs from a large number of either old or new boreholes.

Cores allow: core observation, petrophysical plug measurements and other laboratory measurement, thin section observations and measurements; they represent the most reliable sedimentological and petrophysical information, and lead to reliable deposition environment conclusions.

Continuous high resolution 360° slimhole borehole images, and in particular optical images, approach the resolution and the color of the core visual observations. They can only be recorded if the well is not cased, i.e. in new wells, and their resolution is best in a specific range of well diameter. In optimum conditions, they may allow the identification of coral morphology. They are a valuable complement to the core information, and may even allow facies identification in the absence of core. Their dip and fracture information has no competition from other measurements.

The slimhole natural spectral gamma-ray logging tool is an other complement to the core information. It can be recorded through casing (especially, in our case, if it is a plastic casing) and the only cases where we were not able of recording it in Majorca was because of excessively small inner diameter casing (in S14, and S15 wells). It provides information (from the uranium content) on the organic matter content of the formation, and, in our case, on the relative abundance of algae. It provides information (from the Th and K contents) on the radioactive mineral content and type of the formation, and hence on the distance of transport, and the chemical maturity of the sediments. It provides information (from the TURA, Th/K, and Th values) on the environment of deposition, the distance of transport, and eventually on the depositional bathymetry of the sediments. It is a very valuable complement to the core informations. In the absence of core, and even in the absence of borehole image log, it may allow the facies identification. In the SE Majorca reef complex, it allows a reliable identification of OROS, subunits Ia, Ib, IIIb, and Unit IV; the identification of Unit II and subunit IIIa is more difficult. The use of borehole images, combined to the SGR, helps the identification of Unit II and subunit IIIa.

Majorca reef complex sedimentology

Eolianites

The eolianites (Unit IV) are represented only in wells CBA/B/C, S21/ S22 (Fig. P2-15 and P2-16), which are all less than 2.5km away from the present day coast (Table P2-2, and Fig. P2-20A). All surveyed wells further away from the present day coast do not feature eolianite environment. Eolianites are also observed at different outcrops along SE Majorca seashore (Fig. P2-5A and P2-20A). Since it is generally observed that dunes occur quite often close to the coast line, it can be inferred that the present day coast line is probably not much different from what it was in the Pleistocene time of deposition of this environment. TURA in the eolianites of CBB (Figure P2-15A) and S21 wells (Figures P2-12 and P2-16D) reaches peak values of respectively 22.45 and 20.03, largely in the continental environment range.

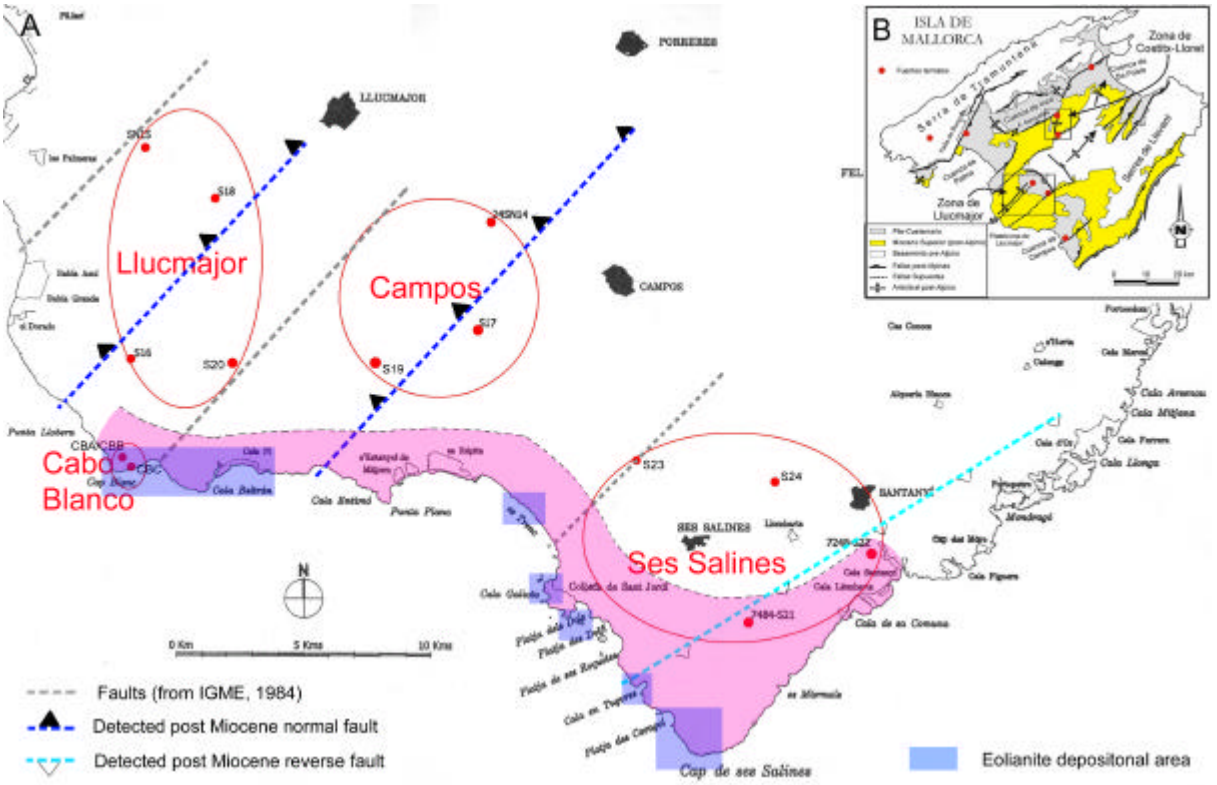

Figure P2- 20. (A) SE Majorca Reef Complex surveyed sites and 25 boreholes. The coastal pink strip represents the area where eolianites are visible on borehole SGR log. The blue shaded rectangles represent the coastal outcrops where eolianites have been identified by the authors. The blue dashed lines represent supposed normal faults (dark blue) identified in this document from comparison of today reef crest to water table distance on the different boreholes of the reef complex, and reverse fault (light blue) identified from repeat sections on the SGR logs of S21 and S22 boreholes; the gray dashed lines represent the IGME, 1984 supposed faults. (B) Structural Majorca map (IGME, 1984), with indications of supposed faults, identified from existence of thermal wells in the vicinity.

Santanyi Limestone and subunit IIIb

The extension of the Santanyi Limestone or TCC is represented on Fig. P2-21A, described originally by Fornos and Pomar, 1983, and corrected from the borehole data presented in this document: addition around wells S15 and S18, removal around wells S23 and S24.
From the SGR tool information it looks as if there is no difference between the Santanyi Limestone and subunit IIIb. This has been demonstrated in Maria-Sube et al., in press, for the Ses Sitjoles site, and the occurrence of stromatolites in Cap Blanc subunit IIIb outcrops is one more argument that subunit IIIb and the Santanyi limestone are coeval, because stromatolites are observed too in the Santanyi limestone.

Coral extension and morphology

The Miocene coral extension in Majorca is represented on Fig. P2-21B, originally from Pomar et al., 1983. The extension of Unit II observed in the borehole data presented in this document, overlaps Pomar et al., 1983 observations. The contours of subunit IIIb (Fig. P2-21A) and of Unit II (Fig. P2-21B), although offering some similitude, do not overlap exactly.
The coral morphology is only known from outcrops and core observation (Figure P2-4E/F/G), and sometimes from borehole images (massive corals: Figures P2-6D, P2-7C/D/E; dish corals: Fig. P2-6E); the SGR tool alone is not sufficient to analyze the coral morphology. Note that dish corals were detected from image logs only in CBC well, and not in the Ses

Sitjoles site, where cores clearly identify massive corals only, nor in S19/S20 where image logs were also recorded.

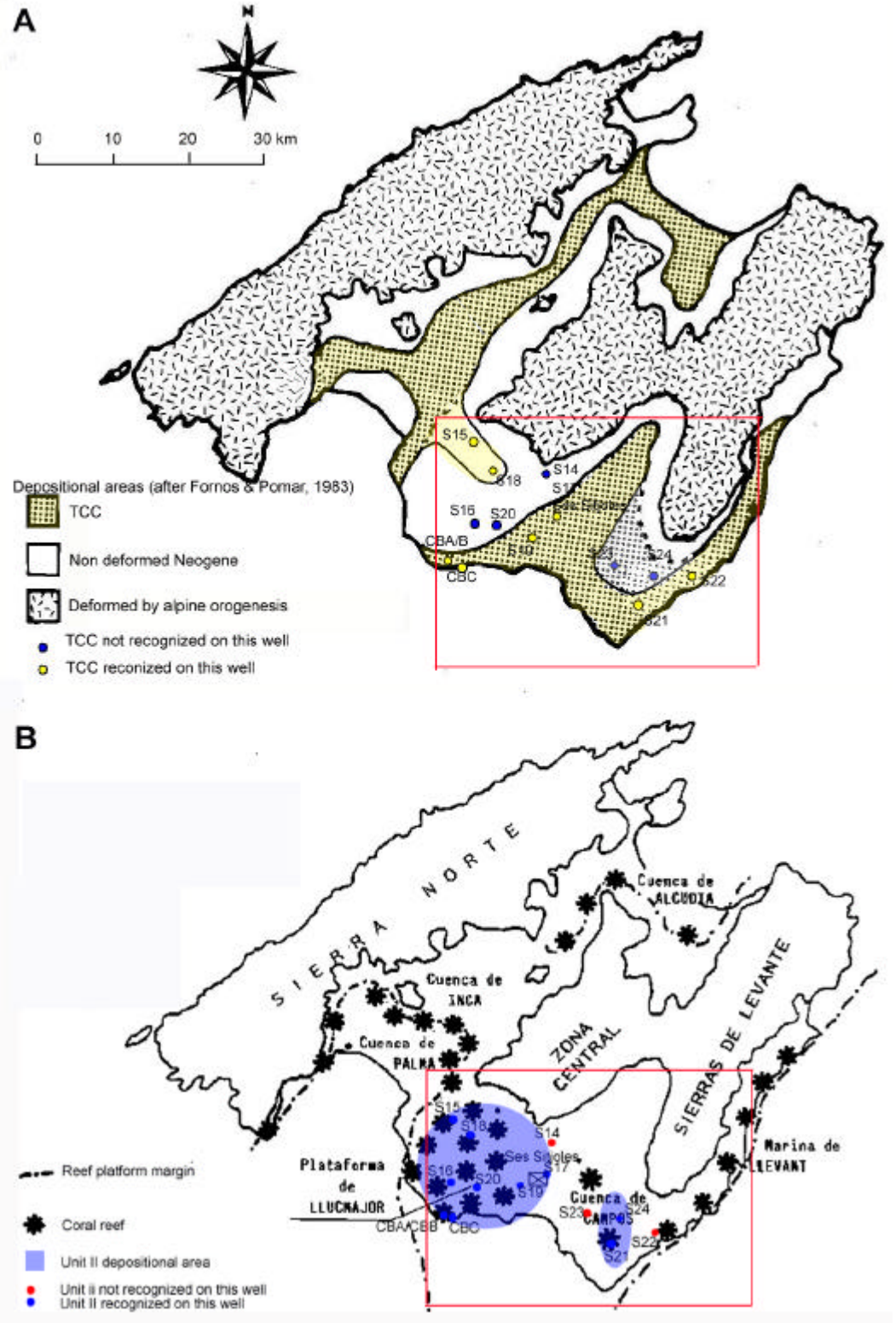

Figure P2- 21. Maps of Majorca, with the red rectangle representing the area displayed on Fig. P2-20, and displaying: (A) subunit IIIb (TCC) depositional area as described by Fornos and Pomar, 1983 (yellow with black dots shading), and as found in this document (plain yellow shading when additional area, plain white shading when removed area); (B) Unit II (coral reef) depositional area as described by Pomar et al., 1983 (black stars), and as found in this document (blue shading).

Carbonate factory and ecology

Table P2-7 is providing an analysis of the different environments in Majorca reef complex, with indications of the corresponding bathymetry, light intensity, main carbonate constructors, and energy level, thus showing the relationship between the carbonate factory bathymetric position, environment, lithofacies, ecology, biology, and energy level.

Unit/ subunit	Average water depth (mbsl)		Light intensity	Main carbonate constructors	Energy level
	Top	Bottom			
Eolianites IV	+30	0	Meteoric	Wind	High
IIIb	0	-10	High euphotic	Restricted, high salinity resistant, benthic organisms	Low
IIIa	-10	-25	Medium euphotic	Abundant mostly benthic organisms	Average
Reef IIc	0	-10	High euphotic	Massive corals, coralline algae, abundant mostly benthic organisms	Very high
Reef IIb	-10	-20	Medium euphotic	Branching corals, coralline algae, abundant mostly benthic organisms	High
Reef IIa	-20	-30	Low euphotic	Dish corals, coralline algae, abundant mostly benthic organisms	Average
Proximal slope Ib	-30	-50	High oligophotic	Coralline algae, coral breccia, mostly benthic organisms	Low
Distal slope Ia	-50	-110	Medium oligophotic	Abundant coralline algae and *Halimeda*, coral breccia, mostly benthic organisms	Low
Off reef open shelf	-110 -200	-200 -	Low oligophotic Aphotic	Coralline algae, benthic and possible planktonic organisms. As depth increases, ratios of areanaceous/limestone test and planktonic/ benthic foraminifers increase	Very low Very low

Table P2- 7. Bathymetry of the different environments in Majorca reef complex, with indication of the light intensity, main carbonate constructors, energy levels. The aphotic zone (-200m and below) has not been reached in any of the surveyed wells. The general frame of this table was inspired by an oral presentation of Luis Pomar at AAPG Convention May 2006 in Palma de Majorca "Architecture of carbonate systems through time": "Variability in carbonate platform architecture,…".

Comparison with Tahiti corals

In Maria-Sube et al., in press, the Ses Sitjoles site data were compared to the Great Barrier Reef (Davies et al., 1990), and the Great Bahama Bank (Eberli et al., 1996) data of ODP respectively legs 133 and 166, for confirmation of the SGR methodology and the slimhole SGR logging tool validity. In this document, we will compare the SE Majorca reef complex to the IODP Tahiti Sea Level, Expedition 310, (Camoin et al., 2005) data. Interestingly, Expedition 310 logging tools (SGR, image logs, and other tools) were exactly the same slimhole logging tools as the one used in the SE Majorca reef complex. We expect from this comparison an interesting discussion on the similitudes and differences (in age, paleobathymetry, distance to land, mineral composition, existence and nature of algae) between the two sites.

Two different locations have been surveyed in Tahiti Expedition 310: Maraa, SW less than 1 km offshore Tahiti, in water depths ranging from 44.45 to 72.15mbsf; Tiarei North less than 5km offshore Tahiti, in water depths ranging from 64.15 to 100.31mbsf (Table P2-8). The ages of the different surveyed formations have been temporarily dated respectively: Unit I: Last deglacial; Unit II: Older Pleistocene, pending dating confirmation, not yet available at the time of writing.

High resolution borehole optical images on site M0005D, interval 96.24 to 79.31mbsf are displayed in Fig. P2-22A to P2-22G, and compared to core photos taken at corresponding depths, but different scale (Fig. P2-22H to P2-22M). This interval corresponds to subunits IIG to IIE (Table P2-8), composed mainly of older Pleistocene coralgal frameworks. A large variety of coral generae is observed: *Porites*, *Montastrea*, *Acropora*, *Pocillopora*, *Pavona*, and so on (other corals have been observed on other cores of Tahiti Unit II, but are not mentioned here). Similarly, a large variety of coral morphologies are observed: massive, encrusting, branching, robust branching, tabular. The order of coral morphologies: top depth: massive; medium depth: branching; bottom depth: tabular, usually observed in present day

tropical corals, is not respected; this can possibly be attributed to the large and relatively rapid eustatic sea level changes during the Late Pleistocene glaciations and inter-glaciations episodes.

Site	Location	Depth interval (mbsf)	Water depth (mbsl)	Interval (mbsf)	Lithology Calcite: C	Lithoclasts	Subunit	Age
M005D	Maraa western transect seaward	23-98	59.63	23-33.5	C	Coralgal microbialite frameworks, Halimeda	IB	Last deglacial sequence
				33.5-37	C, volcanic grains	Coralgal frameworks, floatstone-rudstone, coralline algae, Halimeada	IIA	Older Pleistocene sequence
				37-50	C, volcanic grains	Skeletal floatstone-rudstone, corals, coralline algae, Halimeda	IIB	
				50-60	C, volcanoclastic silt to sand	Fragments of corals, coralline algae, Halimeda floatstone	IIC	
				60-75	C, volcanic grains	Coralgal frameworks, coralline algae, microbialites, skeletal packstone to grainstone	IID	
				75-82	C, Sandy skeletal, volcanic grains	Grainstone to packstone, corals, coralline algae	IIE	
				82-85	C, volcanic grains	Coralgal rudstone to floatstone, massive Porites	IIF	
				85-98	C, volcanic grains and sandstone abundance increasing downward	Coralgal frameworks, skeletal grainstone to packstone	IIG	
M0007A	Maraa western transect landward	0-43	44.45	1.5-20	C	Coralgal microbialite frameworks, coralline algae	IA	Last deglacial sequence
				20-42	C	Coralgal microbialite framworks, Halimeda, coralline algae	IB	
M0008A	Tiarei marginal landward	0-31	64.15	1.5-22	River deposit, volcanistic sand silt clay	Coralline algae	A	Last deglacial sequence
				22-27	River deposit, volcaniclastic silstone to sandstone, feldspars, feldspathoids, quartz, iron oxides and hydroxides	Skeletal grains, organic rich sediments	B	
				27-31	Skeletal sandy limestone	Coralgal boundstone, Halimeda, bryozoans	II	Older Pleistocene sequence
M0009B	Tiarei outer ridge	0-27	100.31	0-5	C, volcanic grains	Coralgal microbialite frameworks, coralline algae, Halimeda	IA	Last deglacial sequence
				5-9	C, silt to snd sied volcanic grains and basalt gravels	Coralgal microbialite framworks, coralline algae, Halimeda	IB	
				8.8-12.6	C, volcanic grains	Coralgal microbialite frameworks, coralline algae, Halimeda	IA	
				12.6-16.7	C, volcaniclastic sediments	Coral colonies, Halimeda	IC	
				16.7-17	C, silt to snd sied volcanic grains and basalt gravels	Coralgal microbialite framworks, coralline algae, Halimeda	IB	
				17-18.5	C	Coral colonies, microbialite coating, coralline algae	ID	
				18.5-20.5	C, volcaniclastic sediments	Coral colonies, Halimeda	IC	

Table P2- 8. Tahiti sites characteristics (from Camoin et al., 2006). Maraa is SW less than 1 km offshore Tahiti, Tiarei is North less than 5km offshore Tahiti.

Site	Location	Depth interval (mbsf)	Water depth (mbsl)	Interval (mbsf)	Lithology Calcite: C	Lithoclasts	Subunit	Age
M0009E	Tiarei outer ridge	0-20.61	93.0	1-11.2	C, volcanic grains	Coralgal microbialite frameworks, coralline algae, Halimeda	IA	Last deglacial sequence
				11.2-12.8	C, volcaniclastic sediments	Coral colonies, Halimeda	IC	
				12.8-13.8	C, silt to snd sied volcanic grains and basalt gravels	Coralgal microbialite framworks, coralline algae, Halimeda	IB	
				13.8-15.2	C, volcaniclastic sediments	Coral colonies, Halimeda	IC	
				15.2-17	C	Coral colonies, microbialite coating, coralline algae	ID	
M0010A	Tiarei outer ridge	0-46.0	89.53	1-12	C, volcaniclastic sediments	Coral colonies, Halimeda	IB	Last deglacial sequence
				12-21.4	C, volcanic grains	Coralgal microbialite frameworks, coralline algae, Halimeda	IC	
				21.4-34	Skeletal sandy limestone	Coralgal boundstone, Halimeda, bryozoans	II	Older Pleistocene sequence
M0015A	Maraa eastern transect seaward	0-42	72.15	1-8	C	Coralgal bindstone, microbialite, coralline algae	IA	Last deglacial sequence
				8-15.5	C	Coralgal microbialite frameworks, coralline algae, Halimeda	IB	
				15.5-36	C, volcanic silt and sand	Coralgal microbialite frameworks, coralline algae, Halimeda	IC	
				36-42	C, vomcanic grains	Skeletal limestone (grainstone to rudstone-floatstone), coralgal frameworks, Hamimeda, coralline algae	II	Older Pleistocene sequence
M0017A	Maraa eastern transect landward	0-41	56.5	4-12	C	Coralgal bindstone, microbialite, coralline algae	IA	Last deglacial sequence
				12-29	C	Coralgal microbialite frameworks, coralline algae, Halimeda	IB	
				29-38.5	C	Coralgal microbialite frameworks, coralline algae, Halimeda	IC	
				38.5-42	C, vomcanic grains	Skeletal limestone (grainstone to rudstone-floatstone), coralgal frameworks, Hamimeda, coralline algae	II	Older Pleistocene sequence
M0021B	Tiarei outer ridge	0-33	81.7	0.5-6	C, volcanic grains	Coralgal microbialite frameworks, coralline algae, Halimeda	IA	Last deglacial sequence
				6-16.3	C, silt to snd sied volcanic grains and basalt gravels	Coralgal microbialite framworks, coralline algae, Halimeda	IB	
M0023B	Tiarei inner ridge	0-29	67.0	4-9.5	C	Coralgal bindstone, coralline algae	IA	Last deglacial sequence
				9.5-29	C, volcanic clastics	Corals, rudstone, coralline algae Halimeda	IC	

Table P2-8 (Continued).

The M0005D and M0007A Maraa sites display a low uranium content in Unit I (around 0.3ppm), and a higher uranium content in Unit II (around 1ppm, and locally up to 3.5ppm) (Fig. P2-24A); these levels of uranium can be attributed to the presence of mostly coralline algae, and locally of Halimeda (in subunit IIC); they are of comparable intensity to the levels observed in the reef parts (Unit II) of SE Majorca reef complex (Fig. P2-14). The Uranium level of Tahiti sites never reaches the average or maximum values observed in the distal slope nor even in the OROS of the SE Majorca reef complex (Table P2-6); possibly, because the

depositional bathymetry of the Tahiti sites is shallower than the depositional bathymetry of the distal slope and OROS in the SE Majorca reef complex, and the optimum depth and light intensity for the development of coralline algae is not reached (Table P2-7).

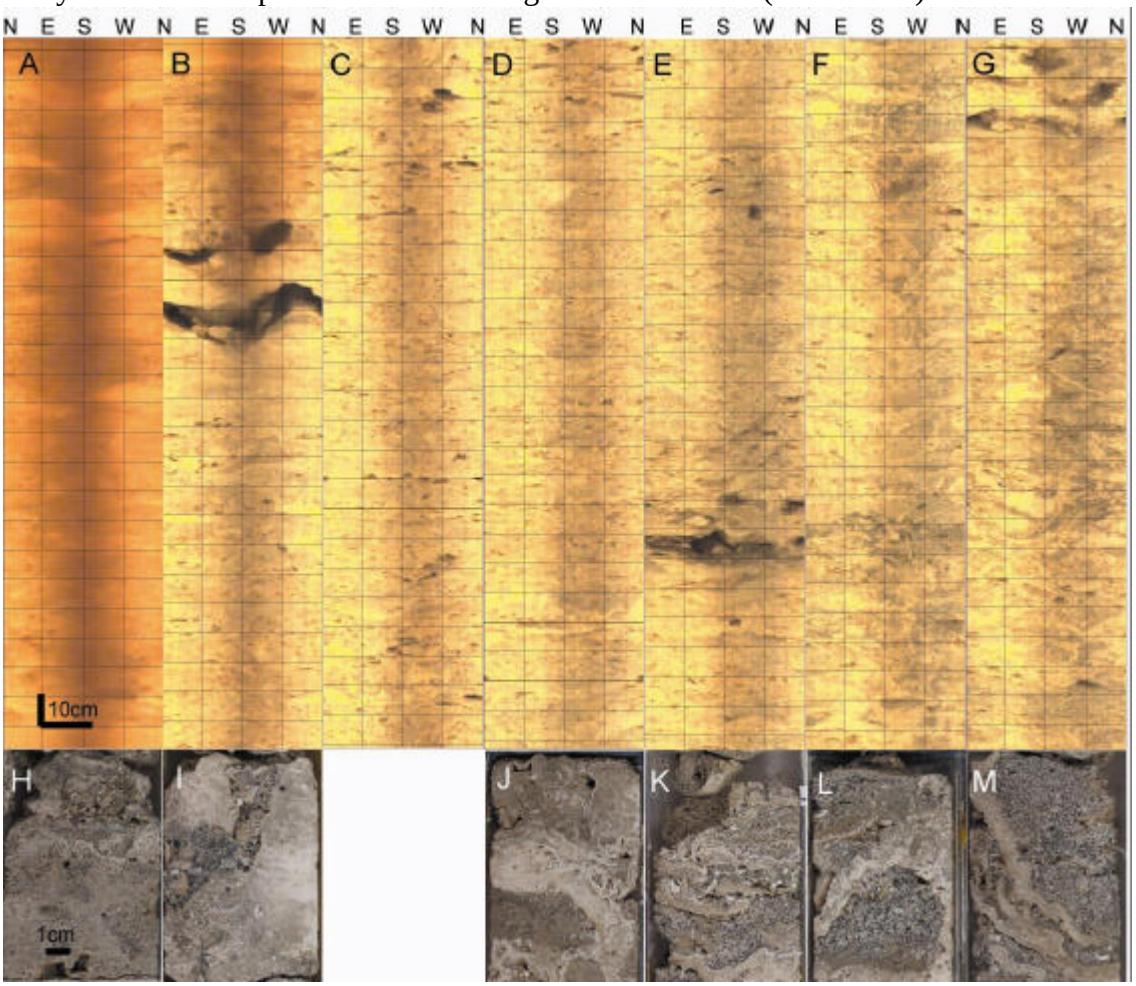

Figure P2- 22. Site MOOO5D borehole high resolution full 360° optical images (A to G) and interval corresponding core slab photos (H to M); image logs and core slab are presented one on top of the other, when the core depth is included in the image log interval. (A) optical image interval 81.71- 79.31mbsf, subunit IIE, sandy skeletal grainstone to packstone, large coral fragments of massive *Porites*, and skeletal fragments of nongeniculate coralline algae and corals. (B) optical image interval 84.16- 81.71mbsf, subunit IIF, coral and algal rudstone to floatstone composed of rhodoliths, lithoclasts and fragments of corals (massive, encrusting and branching corals), coralline algae, echinoids and mollusks in a coarse sandstone matrix; note at 91.0mbsf the open fracture (aperture 10cm, dip magnitude 20°, direction S). (C) optical image interval 86.58- 84.16mbsf, subunit IIG, coralgal frameworks interbedded with skeletal grainstone to packstone; included coral assemblages are dominated by massive colonies of *Porites* and *Montastraea* associated with tabular colonies of *Acropora*, robust branching colonies of *Pocillopora* and *Pavona*, and encrusting colonies of *Porites* and faviids; corals are diagenetically altered. (D) optical image interval 88.99- 86.58mbsf, subunits IIG (see Fig. 21C description). (E) optical image interval 91.41- 88.99mbsf, subunit IIG (see Fig. 21C description). (F) optical image interval 93.83- 91.41mbsf subunit IIG (see Fig. 21C description). (G) optical image interval 96.24- 93.83mbsf, subunit IIG (see Fig. 21C description). (H) Core 29R-1, subunit IIE, packstone, including volcanic grains and skeletal fragments (corals and nongeniculate coralline algae), note thin coralline algal crusts. (I) Core 30R-1, subunit IIF, coralgal rudstone, including fragments of massive *Porites* in a volcanic-rich sedimentary matrix. (J) Core 31R-2, subunit IIG, encrusting colonies of *Porites* in a volcanic-rich matrix, thinly encrusted with coralline algae, note bioerosion of corals. (K) Core 32R-3, subunit IIG, coralgal frameworks of encrusting colonies of *Porites* and tabular colonies of *Acropora* (?) interbedded with grainstone rich in volcanic grains and skeletal fragments. (L) Core 33R-3, subunit IIG, encrusting colony of *Montastraea* and tabular colony of *Acropora* in a volcanic sediment-rich matrix. (M) Core 34R-1, subunit IIG, encrusting colonies of *Porites* in a volcanic sediment-rich matrix. (Camoin et al., 2006).

The Th and K contents of the Maraa sites is generally low, lower than in the SE Majorca reef complex (compare Fig. P2-24D and P2-17B), even bwer in Unit I than in Unit II (Fig P2-24B). The higher content in Unit II can be attributed to the presence of volcanoclastics (absent from Unit I).

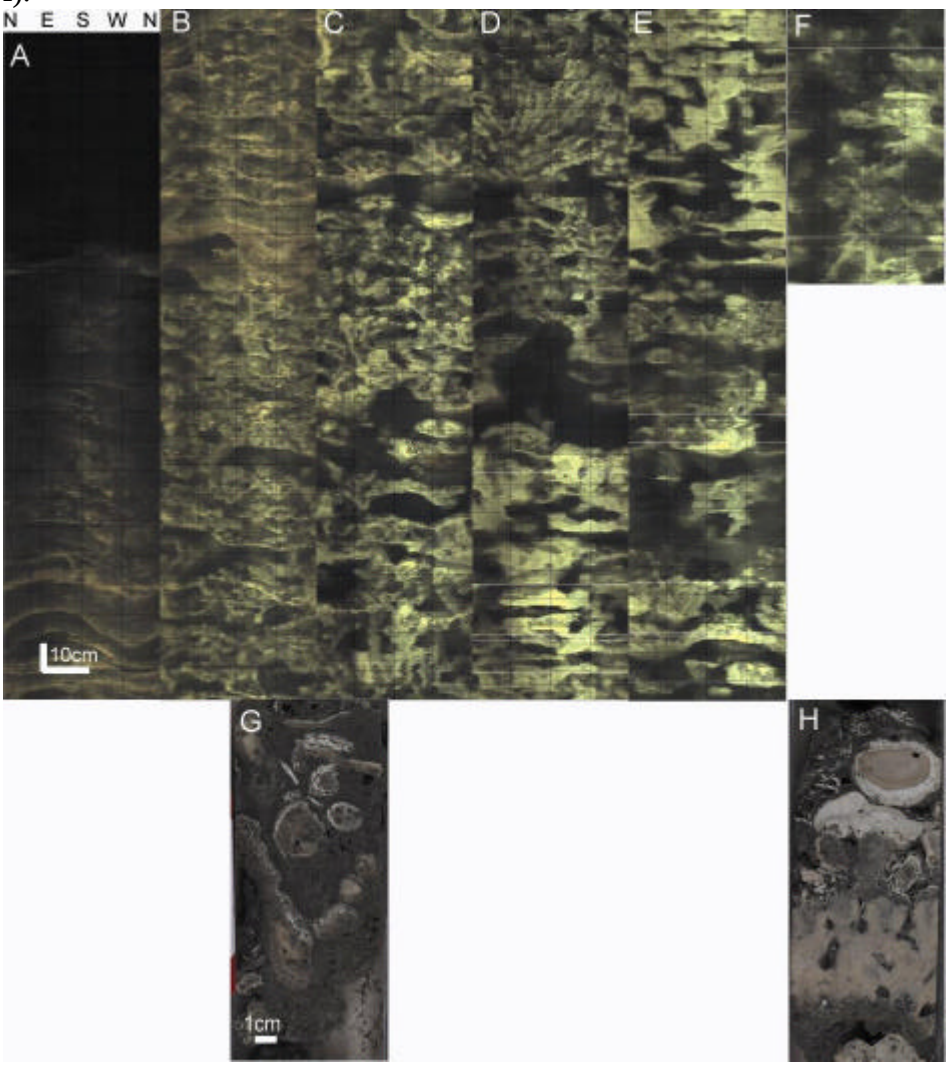

Figure P2- 23. Site MOOO9B borehole high resolution full 360° optical images (A to F) and interval corresponding core slab photos (G and H); image logs and core slab are presented one on top of the other, when the core depth is included in the image log interval. (A) Optical image interval 5.32- 7.62mbsf, subunit IB: coralgal - microbialite frameworks dominated by branching and encrusting colonies of *Porites* and *Montipora*; observe cross-stratifications in the bottom 50cm (channel?). (B) Optical image interval 7.62- 10.04mbsf, subunit IA, coralgal- microbialite frameworks (bindstone) dominated by encrusting colonies of *Montipora*, *Montastraea*, *Leptastrea*, *Pavona* and *Porites* and encrusting and foliaceous colonies of agariciids (*Pachyseris* and *Leptoseris*); other corals are less abundant and include branching colonies of *Porites* (see description Fig. 22G) and *Pocillopora*. (C) Optical image interval 10.04- 12.46mbsf, subunit IA (see description Fig. 22B). (D) Optical image interval 12.46- 14.87mbsf, subunit IC, coral assemblage dominated by massive colonies of *Porites*; associated coral colonies include encrusting and branching *Porites*, robust branching *Pocillopora*, and encrusting *Montipora*; branching corals are distinguished in the top 70cm. (E) Optical image interval 14.87- 17.29mbsf, subunits IC (14.87- 16.6mbsf, see description Fig. 22D) and IB (16.6- 17.29mbsf, see description Fig. 22A), massive corals. (F) Optical image interval 17.29-18.24mbsf, subunit IB, see description Fig. 22A; coral colonies are coated with crusts of nongeniculate coralline algae up to 2.5cm thick, nongeniculate coralline algae algal crusts are generally overlain by microbialites (see description Fig. 22H). (G) Core 9R-1, within interval 8.8-10.7mbsf, subunit IA, coral framework of branching *Porites* colonies with coralline algae and microbialites. (H) Core 13R-1, within interval 16.6- 18.5mbsf, subunit IB, tabular colony of *Acropora*, note thick crusts of coralline algae covering tips of coral branches; sediments matrix contains abundant *Halimeda* segments (Camoin et al., 2006).

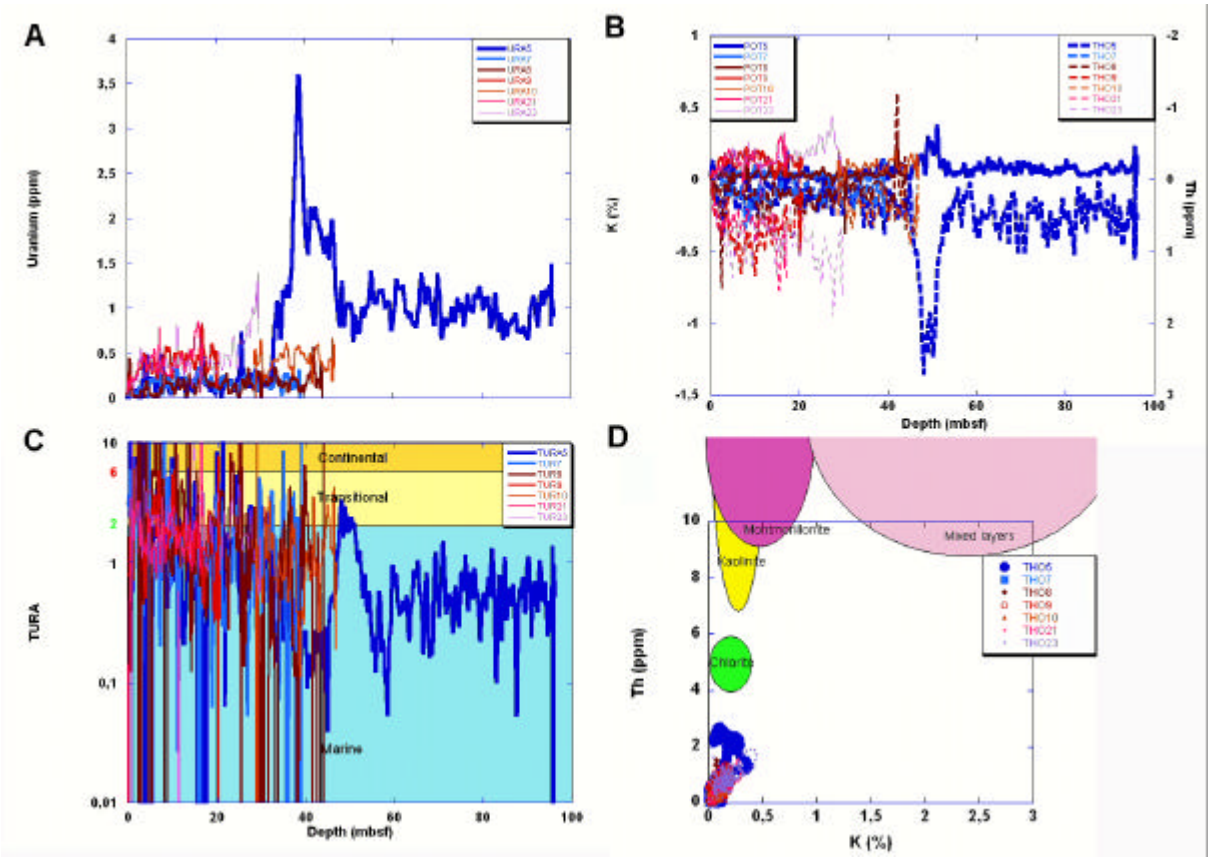

Figure P2- 24. SGR log measurements vs. depth for Tahiti sites M0005D, M0007A (Maraa, blue color), M0008A, M0009B, M0010A, M0021B, M0023B (Tiarei, maroon to violet color), Fig P2-23A, B and C. (A) Uranium. (B) Potassium (solid lines), and thorium (dashed lines). (C) Thorium/ uranium. (D) Thorium vs. potassium crossplot for the same sites.

In M0005D, it is observed that below 53mbsf the environment is frankly marine (Fig. P2-24C), between 53 and 45mbsf, the environment is transitional (while the Th and K contents increase to a Tahiti all sites maximum, Fig. P2-24B), and then becomes marine again up to 33mbsfl (the contact level between Unit II and Unit I); above 33mbsfl, the TURA curves oscillates between marine, transitional and continental levels, while the Th an K contents are very low. It becomes then apparent that in Tahiti, the periods of exposures of the last deglacial were not associated to terrigeneous sediment deposition, possibly due to the volcanic hard rock nature of Tahiti island. Nevertheless, the Tahiti data points orientation is more tilted toward NNE (Fig. P2-24D) than the SE Majorca reef complex data points (Fig. P2-17B), in the same way that the Great Barrier Reef data points (Maria-Sube et al., submited); this indicates a kaolinite- montmorillonite clay component, whereas the SE Majorca reef complex data points are more in the montmorillonite- illite zone.

High resolution borehole optical images on site M0009B, interval 18.24 to 5.32mbsf are displayed on Fig. P2-23A to P2-23F, and compared to core photos taken at corresponding depths, but different scales (Fig. P2-23G to P2-23H). This interval corresponds to subunits ID to IA (Table P2-8), composed mainly of coralgal microbialite frameworks. Here again, a large variety of coral generae (*Porites, Montipora, Montastrea, Leptastrea, Pavona, Pachyseris, Leptoseris, Pocillopora, Acropora*) and morphologies (encrusting, branching, massive, tabular) are observed. In this younger Unit I than Unit II, the coral morphology can sometimes be identified directly on the borehole optical image, probably because the sediments are so young (less than 20,000 years) that the diagenesis could not have been intense enough to hide the morphology. Here again, the order of coral morphology top: massive, medium: branching,

bottom: tabular, is not respected; this can possibly be attributed to the large and rapid eustatic sea level changes during the Holocene.
The M0008D, M0009B, M0010A, M0021B and M0023B Tiarei sites SGR logs have all been recorded through Unit I exclusively, except for site M0010A, which has been recorded in Unit II. They display a low uranium content: an average between 0.2 and 0.5ppm with a maximum never exceeding 1.5ppm (Fig. P2-24A). These levels of uranium can be attributed to the presence of mostly coralgal frameworks, and locally of *Halimeda* (in subunit IC). Contrarily to the Maraa sites, the presence of coralline algae is not observed. These levels of uranium are of comparable intensity to the levels observed in the reef parts (Unit II) of SE Majorca reef complex (Fig. P2-14).
The Th and K content of the Tiarei sites is generally lower than in the SE Majorca reef complex (compare Fig. P2-24D and P2-17B). The last deglacial sequence at Tiarei has a greater volcanoclastic component than the one at Maraa (from digital image scans and quantified by diffuse color reflectance spectro photometry and magnetic susceptibility core logs, Camoin, 2005); on Fig. P2-24B, it is possible to see that the Th and K values of the Tiarei sites are larger than the Th and K values of the Maraa sites, in Unit I. Actually, the Tiarei sediments of Unit I contain volcanoclastics, while the Tiarei sediments of Units II (as observed in site M0010A) contain no volcanoclastics (exactly the contrary of what has been observed in Maraa). M0008A site presents a special case of river deposits, with more than 50% volcanoclastic sediments; however, the Th and K content of this site is very low; this is explained by the fact that the volcanoclastic sediments at M0008A are low radioactive acid basalts, while other Tahiti sites contain high radioactive basic volcanoclastic sediments (See Serra, 2000 for radioactivity level of igneous rocks). There is no apparent difference between the Maraa and the Tiarei sites in terms of the Th-K plot data points orientation (Fig. P2-24D): the Tiarei data points indicate the same kaolinite- montmorillonite composition as the Maraa data points.
In the Tiarei sites, whether in Unit I, or in Unit II (M0010A), the TURA curve (Fig. P2-24C) oscillates between marine, transitional and continental levels, thus indicating that on the Northern part of Tahiti, from Older Pleistocene to last deglacial times, the sea water was never deep enough to prevent exposure during glaciation times.
We observe a much greater coral generae variety in the modern tropical coral reefs of Tahiti than in the Miocene Mediterranean coral reefs. The Miocene Mediterranean coral reefs lack of generae variety has been related to the high salinity in the Mediterranean after the Langhien Mediterranean- Indian Ocean communication break (Chevalier, 1977; Saint Martin, 1990), as observed in the present day Red Sea (Lieske and Myers, 2004).

Majorca reef complex tectonics

Normal faults

On Fig. P2-15 and P2-16, have been displayed, from Table P2-2, the vertical distances between reef crest and today Mean Sea Level (MSL). The reef crest corresponds roughly to the MSL at the time of reef deposition. Significant variations in the reef crest to today's MSL interval length may come from: 1) local reef thickness variations at the 100m scale (25m variation as seen on Ses Sitjoles MC3); 2) post reef creation vertical tectonic variations at the horizontal kilometer scale; 3) significant reef age differences at the kilometer scale. We will not consider the third reason for the time being.
We observe a West-East evolution trend and three well groups in the variations of the reef crest to today MSL interval length: 1) average 108.94m with a standard deviation of 3.48m for S15 and S18; 2) average 54.32m with a standard deviation of 11.45m for CBB, CBC, S16,

S20, S19; 3) average 8.23m with a standard deviation of 4.68m for S17 (and generally speaking, all Ses Sitjoles wells), S21 and S24.
The vertical distance between the reef crest and today's MSL for the first group of wells (S15, S18) is the highest observed over the reef complex. This distance appears to be in agreement with the Haq et al., 1987, eustatic curve, showing that the MSL decreased for more than 100m since Miocene times. For this reason, this western part of the reef is then considered as having sustained no vertical tectonic movement since Miocene times.
It has been demonstrated that the subsidence of the Campos basin has been of 100m since its creation during early to mid Pleistocene times (Jenkyns et al. 1990, Pomar et al, 1996). This subsidence is observed in two different steps materialized by the vertical distance between the reef crest and today's MSL which is intermediate for the second group of wells (CBB, CBC, S16, S20, S19), and lowest (and near 0) for the third group of wells (all Ses Sitjoles wells, S21 and S24). These variations can only be explained by the existence of two NE-SW faults (Fig. P2-20A) separating the first and second on one hand, and the second and third groups of wells on the other hand. These normal faults occurred in the early Pleistocene tectonic extension that created the Campos Basin. Many faults have been identified in the reef complex, notably thanks to the existence of warm thermal sources, (see Fig. P2-20B); in particular a warm water entrance has been found in S23 well between 17 and 11mbgl depth. The two normal faults identified on Figure P2-20A correspond remarkably well to the two NE-SW faults of the Llucmajor area identified by IGME, 1984 (Fig. P2-20B).

Santanyi reverse fault

The subunit IIIb of wells S21 and S22 in the Ses Salines site displays exceptional features. S21, 5km Southwest of Santanyi town, and S22, 22km South of Santanyi town, (Fig. P2-20A), feature both a subunit IIIb of exceptional thickness (respectively 33.5m and 73m, compared with other wells 10 to 13m_ Table P2-2, Fig. P2-12 and P2-16B). In these two wells, and especially in S21, we do not see the subunit IIIb "double belly" of Th-K as clearly as in S17 or S19 of Campos site (Figures P2-10 and P2-16A), CBC of Cap Blanc site (Figures P2-11 and P2-15A), and S18 of Llucmajor site (Fig. P2-15B). In these two wells, we observe a longer interval displaying a large separation of the Th and K channels than in the wells presenting the double- belly feature; this is more similar to what is observed in CBB (Fig. P2-15A). It looks like there is a double layer of subunits IIIb from the SGR log_ the second and bottom layer having been called subunit IIIb1 (Fig. P2-16B). No reef was detected in wells S22 and S23; there is a difference of 10m in the distance reef crest to MSL between S21 and S24, the reef crest being lower in S21 than in S24 (Table P2-2).
Although Pomar, 1991 has interpreted a similar depositional environment in the Cap Blanc to Vallgornera area as an inner lagoon overlaid by a Santanyi Limestone (or TCC) layer, and with an erosional surface separating them, it is also possible to interpret this double layer as a repeat section due to a reverse fault in the Santanyi area (Fig. P2-20A), the area containing S21's reef crest being pushed down compared to the area containing S24's reef crest. We find again a remarkable correspondence with the interrupted NE-SW fault localized by IGME, 1984, starting from Playa des Caragol, and bordering the Western side of the Serres de Llevant (Fig. P2-20B).

Fractures (Ses Sitjoles, Cap Blanc, S19, S20)

The optical image logs have allowed to identify and characterize (dip magnitude, orientation, aperture, planarity quality) fractures in the Cap Blanc (CBC well), Llucmajor (S20 well), and Campos (MC2, MC8, MC9, MC10, MC11, S19 wells) sites (Table 9). It appears that most of the fractures are oriented NE-SW, parallel to the general fault direction in SE Majorca (Fig. 20B). It has frequently been observed that the fracture system, or network in a given region

tends to have the same orientation as the fault system and is related to the stress orientation (Serra, 2003).

Well	Unit/ subunit	Log depth (mbgl)	Dip magnitude (0-90°)	Dip orientation	Aperture	Planarity quality
CBC	IV	4.1	0	-	Closed	Bad
		6.6	0	-	Closed	Bad
		6.95	5	SW	Closed	Bad
		8.5	15	E	Closed	Good
		11.8	10	W	10cm aperture	Average
	IIIb	20.2	15	SW	Closed	Average
		29.7	25	W	Closed	Good
	IIIa	31.4	35	S	10cm aperture	Average
		32.1	0	-	20cm aperture	Bad
		33.3	0	-	10cm aperture	Average
		33.8	2	E	Closed	Average
		37.0	3	S	Closed	Good
	IIc	48.4	20	W	Closed	Good
MC2	IIIb	1.75	30	SW	Closed	Average
	IIIa	14.0	70	SW	Closed	Average
		16.3	0	-	Closed	Good
		17.0	60	NE	Closed	Excellent
		18.0	60	SW	Closed to open	Average
		18.8	60	SW	Closed	Good
		20.6	30	SW	Closed	Average
		23.4	15	W	Open	Average
		24.8	5	SE	Closed	Average
	IIc	28.3	80	SE	Closed	Average
	IIb	39.4	80	E	Closed	Average
	IIa	56.15	60	NE	Closed	Excellent
		58.8 to 59.1	60	NE	30cm aperture	Good
			40			
MC8	IIIb	2.0	80	NE	Closed	Average
	IIIa	16.1	0	-	Closed	Average
	IIb	48.17	5	W	Closed	Good
MC9	IIIa	12.8	30	W	Closed	Good
	IIIa	13.1	30	NE	Closed	Good
	IIb	47.82	0	-	Closed	Average
	Unit I	61.85	70	E	Closed	Average
	Unit I	65.0	80	E	Closed	Average
MC10	IIIb	1.2	10	S	Closed	Average
	IIIa	17.4	30	NW	Closed	Average
	IIIa	19.9	20	E	Closed	Average
MC11	IIIb	3.0	0	-	Closed	Average
	IIIa	17.7	10	SE	Closed	Average
	IIIa	19.15	30	S	Closed	Average
	IIc	30.1	45	SW	Closed	Average
	IIc	33.4	20	S	Closed	Good
S19	IIIb	4.3	20	E	Closed	Good
		6.0	30	SW	Closed	Average
	Ia	26.5	20	SW	Closed	Average
		34.7	30	SW	Closed	Average
S20	II	7.75	20	N	4cm aperture	Average
		11.2	30	SE	Closed	Bad
		14.3	45	SE	Closed	Average

Table P2- 9. Identification and characterization (dip magnitude, orientation, aperture, and planarity quality) of fractures by image logs in CBC, MC2 (from Maria-Sube et al., in submitted), MC8, MC9, MC10, MC11, S19 and S20 wells.

CONCLUSIONS AND PERSPECTIVES

Within the multi-scalar and multi-disciplinary ALIANCE program, the methodology (cores, thin-sections, slimhole borehole image, and SGR logs) already asserted in Ses Sitjoles was used in 25 boreholes, distributed in four sites within the SE Majorca Miocene reef complex.

Using core thin-section analysis (Cap Blanc cliff and CBB, CBC wells, Ses Sitjoles' MC2), or core description (Llucmajor's S16, Ses Salines' S21), detailed carbonate sequences have been described and compared. Since the full range of data was not available in every well, the carbonate sequence analysis performed in a data rich reference well in each site was extended to the data poorer wells of the site, using slimhole high resolution borehole images, SGR and total gamma-ray logs.

The SGR survey of 25 boreholes completed with the optical and acoustical image survey of about half of them, ranging from a depth of 22 to 320mbgl over an area of 20 by 35km allowed to acquire an extraordinary Miocene coral reef data set. The intensity of thorium and potassium content is low, with maxima observed in subunit IIIb; they indicate an illite and montmorillonite radioactive mineral content, chemically mature sediments, a relatively long distance of transport. The particularly high uranium level in subunit Ia indicates the abundant presence of algae (coralline algae and *Halimeda*) under a 50 to 100mbsl water depth, medium oligophotic light intensity. Along the carbonate sequence of the different wells, TURA indicates from bottom (OROS) to top (Unit IV) frankly marine to oscillations transitional-continental. It appears that the TURA curve is sensitive to both the distance to shore line and the bathymetry.

The stratigraphic column inferred from the data in each well provided a unique opportunity to observe 3D facies variations within a reef complex over such a large scale; the previous SE Majorca reef complex detailed description was limited to the 5km cliff between Cap Blanc and Vallgornera (Pomar et al., 1996).

The full range of facies described by Pomar et al., 1996, is present from OROS to eolianites; however, we have not detected any occurrence of Gypsum nor Grey Marl formation, which Pomar et al., 1996 describes as being present only in the Palma basin (several kilometres away to the West of this study area). The eolianites are recognized only within a 2.5km band from the coast line. There is no apparent difference between the Santanyi limestone and subunit IIIb, and either of them is assimilated to a TCC. The lateral extension of subunit IIIb in the studied area corresponds roughly to the description of Fornos and Pomar, 1983, with however a few additions or omissions. The lateral extension of Unit II in the studied area corresponds exactly to the description of Pomar et al., 1983. The coral morphology recognized in Cap Blanc cliff and wells (massive, branching, dish) could not be identified elsewhere. The Miocene corals of SE Majorca are largely dominated by *Porites*, their generae variety is very poor and not comparable to the one observed in the modern tropical corals.

The carbonate factory fauna or algae components vary greatly in function of the bathymetry and hence of the light intensity and the energy level.

The analysis of the reef crest to today Mean Sea Level (MSL) distance variations lead to the conclusion of the existence of two NE-SW normal faults in the Campos Basin. The identification of repeat sections in subunit IIIb on the SGR logs of two wells in the Santanyi area, and the longer than usual interval of this subunit in these wells, leads to the hypothesis of a NE-SW reverse fault in this area; this identification is coherent with the analysis of the crest to today MSL distance in the fault surrounding wells. Most of the detected fractures are oriented in the same direction.

The Tahiti IODP data offer a good ground for comparison with the SE Majorca reef complex. The SGR thorium and uranium data suggest a kaolinite and montmorillonite radioactive mineral composition, indicating even more mature sediments than in Majorca, and a longer distance of transport. The level of radioactivity is lower than in Majorca, possibly due to the

volcanic hard rock nature of Tahiti. The uranium level is not so high as observed in Majorca Unit IIIa. The very good quality borehole images is probably due to the relatively low level of diagenesis in this mostly less than 20,000 years sediments. The great variety of coral generae observed, much larger than in the Majorca reef complex, confirms that the Miocene Majorca corals were subjected to high salinity conditions of the Mediterranean.
It would be interesting to drill holes in the NE part of the reef complex to possibly observe the birth conditions of the reef, and around the Santanyi area, the elucidate the Santanyi limestone question.

CITED REFERENCES

Adams, J.A.S. & Weaver, C.E., 1958, Thorium to uranium ratio as indicator of sedimentary processes; examples of concept of geochemical facies, Bull. Amer. Assoc. Petr. Geol., 42, 2.

Andersson P.D., Werden R.H., 2004, Mudstones of the Tonqua Basin South Africa: an anlysis of lateral and stratigraphic variations within mudstones and a comparison of mudstones within and between turbite fans, Sedimentology, vol. 51, issue 3, page 479-502.

Beers R.F., Goodman C., 1944, Distribution of radioactivity in ancient sediments, Bull. Geol. Soc. America, 55.

Brachert T.C, Hultz N., Knoerich A.C., Krauworst U.M.R., Stückrad O.M., 2001, Climatic signatures in shallow water carbonates: high resolution stratigraphic markers in structurally controlled carbonate buildups (Late Miocene, Southern Spain), Palaeogeog., Palaeoclimatol., Palaeoecol., 175 211-237.

Braga J.C., Aguirre, J., 2001, Coralline algal assemblages in upper Neogene reef and temperate carbonates in Southern Spain, Palaeogeog. Palaeoclimatol. Palaeoecol. 175 27-41.

Camoin G., 2001, Palaeoceanology of reefs and carbonate platforms: Miocene to modern. Palaeogeog. Palaeoclimatol. Palaeoecol. 175, 1-6.

Camoin G. F, Ph Ebren, A. Eisenhauer, E. Bard, G. Faure, 2001, A 300 000-yr coral reef record of sea level changes, Mururoa atoll (Tuamotu archipelago, French Polynesia), Palaeogeog. Palaeoclimatol. Palaeoecol., 175 325-341.

Camoin G.F., Iryu Y., McInroy D.B., and the Expedition 310 Scientists, 2005, Tahiti Sea Level, Proceedings of the Integrated Ocean Drilling Program, V. 310 Expedition reports.

Chevalier J.P., 1977, A glimpse of the Neogene corallian fauna, Second Symposium international sur les coraux et récifs coralliens fossiles, Paris, , BRGM Orléans France, 1977, p. 359-366, Mem. BRGM n° 89.

Cornée J.J, Roger S., Münch P., Saint Martin J.P., Féraud G., Conesa G., Pestrea- Saint Martin S., 2002, Messinian events: new constraints from sedimentological investigation and new AR^{40}/AR^{39} ages in the Melilla-Nador Basin (Morocco), Sedimentary Geology 151 127-147.

Cunningham, K. J., Farr M.R., Rakid-El Bied K., 1994, Magnetostratigraphic dating of an Upper Miocene depositional shallow marine and continental sedimentary succession in northeastern Morocco. *EPSL*, vol. 127, Issues 1-4, p. 77-93.

Davies, P., J., J.A. McKenzie, A. Palmer-Julson, et al., 1990, Proceed. ODP, Sci. Rep., 133, 810p

Eberli, G., Swart, P., and shipboard scientific party, 1996, Sci. Res., ODP, 166.

Esteban, M., Calvet, F., Dabrio, C., Baron, A., Giner, J., Pomar, L., Salas, R., & Permannyer, A., 1978, Aberrant features of the Messinian coral reefs, Spain. Acta geol.Hisp., 13, 20-22.

Esteban Mateu, July 1979, Significance of the upper Miocene coral reefs of the Western Mediterraneann, Palaeogeog. Palaeoclimatol. Palaeoecol. 29, 169-188.

Esteban, M., 1996, An overview of Miocene reefs from Mediterranean areas : General trends and facies models, in Fransee E.K, Esteban M., Ward W.C., Rouchy J.-M., eds., Models for carbonate stratigraphy from Miocene reef complexes of Mediterranean regions. SEPM Concepts in Sedimentology and Paleontology 5, 3-53.

Fornos J.J., Pomar L., 1983, Mioceno Superior de Mallorca: unidad calizas de Santanyi ("complexo terminal), Itinerario E., in: El Terciaro de la Baleares. Guia de la excursions des X Congreso Nacional de Sedimentologia, Menorca.

Franseen E.K., Goldstein, R.H., Farr M.R.,1998, Quantitative controls on location and architecture of carbonate depositional sequences: upper Miocene, Cabo de Gata region; SE Spain. J. Sediments. Res. 68 (2) 283-298.

Hassan M. and Hossin A., 1975, Contribution à l'étude des comportements du thorium et du potassium dans les roches sédimentaires. C.R. Acad. Sci. (Paris). 280.

Hsü, K.J., Ryan, W.B. F., Cita, M.B., 1973, Late Miocene desiccation of the Mediterranean . Nature 242, 240-244.

Hsü K.J., Montadert, L., Bernouilli D., Cita M.B., Erikson A., Garrison R.E., Kidd R.G., Mélières F. Müller, C., Wright, R., 1977, History of the Messinian salinity crisis, Nature 267, 399-403.

IGME, 1984, Proyecto de investigación preliminar del Pirineo Oriental, zona meridional prelitoral catalana e Islas Baleares. Vol. 3, Estudio Geotérmico preliminar de Baleares. Ministerio de Industria y Energía, 188 pp.

Jaeggi David, 2006. Multiscalar porosity structure of a Miocene reefal carbonate complex, thesis, Diss ETH nb. 16519.
Jenkyns, H.C., Sellwood B.W., Pomar L., 1973, A field incursion guide to the island of Mallorca: Geologists' Association guide, London, the Geologists' Association, 93 p.
Krijgsman W., Hilgen F.J., Raffi I., Sierro F.J., Wilson D.S., 1999, Chronology, causes and progression of the Messinian crisis, Nature, 400.
Lieske, E., Myers, R.F., 2004., Coral reef guide, Red Sea London, HarperCollins.
Maria-Sube Y., Camoin G., Pezard P., Löw S., Jaeggi D., Montoto M., Mateos F., in press, Multi-scalar study of depositional environments and heterogeneities in a Miocene reef sequence, Sedimentology, Blackwell.
Mutterlose J., Ruffell A., 1999, Milankovitch-scale paleoclimate changes in pale-dark bedding rhythms from the early Cretaceaous (Hauterivian and Barremian) of eastern England and northern Germany, Palaeogeog. Palaeoclimatol. Palaeoecol. 154 133-160.
Pomar L., Esteban M., Calvet F., Baron A., 1983, La unidad arrecifal del Mioceno Superior de Mallorca, in El Terciaro de la Baleares. Guia de la excursions del X Congreso Nacional de Sedimentologia, Menorca.
Pomar L., 1991, Reef geometries, erosion surfaces and high frequency sea-level changes, upper Miocene reef complex, Mallorca, Spain, Sedimentology, vol. 38, n° 2, pp. 243-269.
Pomar L., Ward W. C., 1994, Response of a late Miocene Mediterraneann reef platform to high-frequency eustasy, Geology, 2, 131-134.
Pomar L., Ward W. C., 1995, Sea-level changes, carbonate production and platform architecture: the Llucmajor platform, Mallorca, Spain, Kluwer Academic Publishers.
Pomar L., Ward W. C., Green D. G. , 1996, Upper Miocene reef complex of the Llucmajor area, Majorca, Spain, SEPM Concepts in Sedimentology and Paleontology.
Pomar L., Ward W.C., 1999, Reservoir-scale heterogeneity in depositional packages and diagenetic patterns on a reef-rimmed platform, Upper Miocene, Mallorca, Spain, The American Association of Petroleum Geologists.
Pomar L., 2001, Ecological control of sedimentary accommodation: evolution from a carbonate ramp to rimmed shelf, Upper Miocene, Balearic Islands, Palaeogeog. Palaeoclimatol. Palaeoecol. 175 249-272.
Riding R., Martin J. M., Braga J. C.,1991, Coral-stromatolite reef framework, Upper Miocene, Almeria, Spain, Sedimentology, 38, 799-818.
Riding R., Braga J. C., Martin J. M., Sanchez-Almazo I. M., 1998, Mediterranean Messinian Salinity Crisis: constraints from a coeval marginal basin, Sorbas, southeastern Spain, Marine Geology, 146, 1-20.
Rouchy J.-M., Saint Martin J.-P., 1992, Late Miocene events in the Mediterranean as recorded by carbonate-evaporite relations, Geology, V. 20, 629-632.
Ruffell A., Worden R., 2000, Palaeoclimate analysis using spectral gamma-ray data from the Aptian (Cretaceaous) of southern England and southern France, Palaeogeog. Palaeoclimatol. Palaeoecol., 155 265-283.
Russell, W.L., 1945, Re lation of radioactivity, organic content and sedimentation, Bull. AAPG, 29, 10.
Saint Martin J.P., 1990, Les formations récifales coralliennes du Miocène supérieur d'Algérie et du Maroc, Mémoire du Muséum National d'Histoire Naturelle.
Saint Martin J.P., Cornée J.J., Muller J., 1995, Nouvelles données sur le système de plate-forme carbonatée du Messinien des environs d'Oran. Conséquences, C.R. Acad. Sci. Paris t. 320, série IIa, p. 837 à 843.
Serra O., Baldwin, J., & Quirein, J.A., 1980, Theory, interpretation and practical applications of Natural Gamma Ray spectroscopy, SPWLA, 21st Annual Log. Symp. Trans., paper G.
Serra Oberto, Serra Lorenzo , 2000, Diagraphies, Serralog.
Serra Oberto, Serra Lorenzo, 2003, Well logging and geology, Serralog.
Selley, R.C. (1976) An introduction to sedimentology, Academic Press, London, P. 408.
Schnyder J., Ruffell A., Deconinck J.-F., Baudin F., 2006, Conjunctive use of spectral gamma-ray logs ands clay mineralogy in defining late Jurassic-early Cretraceous paleoclimate change (Dorset, U.K.), Palaeogeog. Palaeoclimatol. Palaeoecol., 229 4 303-320.
Swanson, V.E., 1960, Oil yield and uranium content of black shales, Geol. Surv, prof. Paper 356-A.
Van Berkel, J., Verhoef, M.,2005, High resolution multi-component 2D-3D natural laboratory linking geology, geophysics and petrophysics: Mallorca, Spain, Ms Thesis, Vrieje Universiteit, Amsterdam.

4.3 Mesures pétrophysiques statiques et dynamiques sur les carottes de Ses Sitjoles

Résumé

Ce document présente les propriétés pétrophysiques statiques et dynamiques d'échantillons de carottes extraits d'un récif corallien du site de Ses Sitjoles, Majorque, Espagne. Ce récif

exhibe de la surface à 100m de profondeur une séquence carbonatée composée de trois unités distinctes. Il représente un laboratoire naturel de réservoirs d'hydrocarbures analogues. Il offre l'opportunité unique d'étudier par la géologie de surface, les mesures en laboratoire, et l'extensif forage et carottage de puits peu profonds, les intrusions d'eau salée dans un environnement côtier. Douze puits peu profonds ont été forés dans ce site. Dans l'un ce ces puits, MC2, un carottage continu a procuré 116 bouchons calcaires sur lesquels des mesures en laboratoire de propriétés pétrophysiques ont été effectuées. Des mesures extensives non-destructives ont été effectuées en utilisant de l'eau en équilibre ionique.

Des propriétés pétrophysiques statiques ont été mesurées : porosité, électrique et acoustiques. Ces mesures fournissent des informations de porosité, densité de grain, diamètre de gorges de pore, conductivité d'échantillon saturé, conductivité de surface, facteurs de formation et de cimentation, et vélocités acoustiques, qui permettent la caractérisation de la composition minérale, la diagenèse, la structure interne et l'extraordinaire hétérogénéité verticale de cette particulière formation carbonatée. Les sédiments sont principalement calcitiques, avec une présence d'argile dans la partie supérieure. Plusieurs niveaux de minéralisation dus à des paléo et présents niveaux de nappe phréatique stationnaire ont été trouvés, généralement accompagnés de dolomitisation. Une relation entre le facteur de formation et la porosité, différente de la formule d'Archie, a été trouvée. Un autre résultat a été l'affaiblissement du cisaillement de la roche par humidification ; le degré d'affaiblissement est faiblement lié à la surface spécifique des grains de carbonate ; l'affaiblissement du cisaillement explique l'occurrence de certaines fractures.

Des propriétés pétrophysiques dynamiques, effectuées sur les mêmes bouchons utilisés pour les propriétés statiques, ont été mesurées, en utilisant une cellule de mesure originale : perméabilité et potentiel électrocinétique. Le potentiel électrocinétique procure le coefficient C de débit hydraulique au potentiel électrique, et le potentiel zêta. Les mesures de perméabilité et de potentiel électrocinétique permettent de confirmer et de compléter l'extrême hétérogénéité et les informations de caractère diagenétique (les niveaux de minéralisation) déjà trouvées avec l'étude des propriétés statique. Une relation de proportionnalité directe entre le potentiel électrocinétique et la perméabilité, et une relation poly-modale entre la perméabilité et la porosité ont été trouvées. Trois différents types de sédiments ont été clairement identifiés par leurs propriétés pétrophysiques : les sédiments A, ou sédiments de minéralisation, sont caractérisés par des faibles porosités/ perméabilités/ facteurs de cimentation et une forte solidité mécanique ; les sédiments B et C sont caractérisés par une forte porosité, et une faible solidité mécanique ; les sédiments B et C sont cependant différents, parce que les sédiments B montrent une faible perméabilité/ facteur de cimentation, tandis que les sédiments C ont une forte perméabilité/ facteur de cimentation. Les sédiments B sont affectés de traits diagenétiques et de différents types de ciments. Les sédiments C, qui offrent les meilleurs qualités de transmissivité hydraulique, sont caractéristiques des textures grainstone et framestone, avec peu ou pas de cimentation. Ces mesures sont primordiales pour évaluer la conductivité hydraulique de ce réservoir.

Les zones de minéralisation sont reliées en temps par ingénierie arrière aux périodes de nappe phréatiques stationnaires présente et paléo, et aux mouvements tectoniques du Pléistocène.

Ces résultats sont des pierres d'achoppement pour l'étude future sur une base multi-scalaire et multi-disciplinaire de la plate-forme récifale.

Core petrophysical properties of a Miocene coral reef, Ses Sitjoles site, Majorca, Spain.

Yves Maria-Sube*[1], Philippe Pezard[1], Didier Loggia[1], Gilbert Camoin[4], Hendrik Braaksma[1], Modesto Montoto[2], Felix Mateos[2], David Jaeggi[3], Simon Löw[3]

[1]*Laboratoire de Tectonophysique, ISTEEM, CNRS UMR5568, Université Montpellier II, 34090 Montpellier Cedex 5, France.*
[2]*University of Oviedo, Facultad de Geologia, Departomento de Geologia, Oviedo, Spain.*
[3]*ETH Hönggerberg, Engineering Geology, Zurich, Switzerland.*
[4]*Centre Européen de recherche et d'Enseignement des Géosciences de l'Environnement (CEREGE), University of Aix-Marseille, France.*

Abstract

This document presents static and dynamic petrophysical properties of core samples extracted from a Miocene coral reef of the Ses Sitjoles site, Majorca, Spain. This reef displays from surface to 100mbgl deep a carbonate sequence composed of three distinct units. It represents a natural laboratory of analogue oil or gas reservoirs. It offers the unique opportunity to study through surface geology, laboratory measurements, and extensive shallow boreholes drilling and coring, the intrusion of salted water in a coastal environment. Twelve shallow wells have been drilled in this site. In one of these wells, MC2, a continuous coring has provided 116 limestone plugs on which laboratory measurements of petrophysical properties were performed. Extensive non-destructive measurements were performed using equilibrium water. Static petrophysical properties were measured: porosity, electrical and acoustic properties. These measurements provide porosity, grain density, pore throat diameter, saturated sample conductivity, surface conductivity, formation and cementation factors, and acoustic velocities insights which allow characterization of the mineral composition, the diagenesis, the inner structure and the extraordinary vertical heterogeneity of this particular carbonate formation. The sediments are mainly calcitic, with presence of clay in the top part. Several mineralization levels due to paleo and present water-table standstills, often accompanied by dolomitization were found. A relation between the formation factor and the porosity, different from the Archie formula, was found. Another finding was the shear weakening of the rocks by water wetting; the degree of weakening is loosely related to the specific area of the carbonate grains; the shear weakening explains the occurrence of some fractures.

Dynamic petrophysical properties, performed on the same plugs used for static properties, were measured, using an original measurement cell: permeability and electrokinetic potential. Electrokinetic potential measurements provide hydraulic flow to electrical potential coefficient C and zeta potential. Permeability and electrokinetic potential measurements allow to confirm and complete the extreme heterogeneity and the diagenetic feature information (mineralization levels) already found with the static property study. A direct proportional relationship between electrokinetic potential and permeability and a poly-modal relationship between permeability and porosity were found. Three different types of sediments were clearly identified by their petrophysical properties: sediments A, or mineralization sediments, are characterized by low porosity/ permeability/ cementation factor and high mechanical strength; sediments B and C are characterized by high porosity, and low mechanical strength; sediments B and C are however different, because sediments B exhibit low permeability/ cementation factor, while sediments C have high permeability/ cementation factor. Sediments B are affected by diagenetic features and different types of cements. Sediments C, which offer the best hydraulic transmissivity quality, are characteristic of grainstone and framestone textures, with little or no cementation. These measurements are key to evaluate the hydraulic conductivity of this reservoir.

Zones of mineralization are related in time by backward engineering to present and paleo water-table standstills of interglacial periods, and to tectonic movements of the Pleistocene.
These results are building stones for further study on a multi-scalar and multi-disciplinary basis of the reef platform.

1 Introduction

This document addresses two of the most acute problems of our time: water, and energy (under the form of hydrocarbon fossil fuel), through the study of key parameters for the transmissivity of water and hydrocarbons through carbonate reservoirs.
Seventy percent of the earth's surface is covered by water. Ninety-seven percent of this water is contained in oceans, hence salty and unsuitable for drinking or irrigation. Of the remaining 3% of freshwater, only 0,3% is found in rivers and lakes, the rest being frozen. This water runs off in rivers and refills our aquifers. While the world's population tripled in the 20th century, the use of renewable water resources has grown six-fold. Within the next fifty years, the world population will increase by another 40 to 50%. This population growth, coupled with industrialization and urbanization, will result in an increasing demand for water and will have serious consequences on the environment. Coastal aquifers, such as in the island of Majorca, are particularly vulnerable to salt water intrusion.
Carbonate rocks represent more than 50% of the world oil and gas reservoirs, notably in the Middle-East. With continued worldwide production, this fraction will increase, and the giant Middle East reservoirs are expected to dominate production in the mid to long-term future. It is in the interest of the oil and gas industry to understand carbonate reservoirs. Carbonate rocks have the particularity, compared to siliclastic rocks, to present high heterogeneities in terms of both static and dynamic petrophysical properties; heterogeneities imply accrued difficulty in continuous evaluation of petrophysical properties. Static petrophysical properties such as porosity and cementation factor m are of paramount importance for the evaluation of oil and gas reserves; dynamic petrophysical property such as permeability is of primary importance for the production of oil and gas reservoirs. Permeability in carbonate rocks is highly related not only to the primary deposition, but also to the diagenesis and different dissolution or cementation processes.
The Miocene coral reef complex of SE Majorca is a fresh water reservoir that is surveyed by the Hydrogeological Department of the Government of the Baleares for groundwater sustainability in that coastal semi-arid environment. It also offers a unique shallow depth laboratory of analogue oil and gas producing reservoirs, that are existing and have been identified at much greater depths. It is outcropping along the coast and notably at Cabo Blanco, where it has been studied for many years (Esteban et al., 1978 ; Esteban, 1979 ; Pomar, 1991 ; Pomar and Ward, 1994, 1995, Pomar et al., 1996 ; Pomar and Ward, 1999).
In the reef complex, the Ses Sijoles site, located 12km to the North East of Cabo Blanco, has been selected for drilling 12 research wells, in which cores have been extracted, and borehole images and conventional logs have been recorded. The cores provided slabs (for visual examination), thin-sections (for sedimentological study) and plugs (for petrophysical measurements). The core and log data provided materials for a multi-scalar and multi-disciplinary method of investigation. The sedimentological results have been detailed in Maria-Sube et al., submitted, for Ses Sitjoles, and in Maria-Sube et al., submitted a, for the reef complex. This document focuses on the petrophysical measurements that have been performed on the plugs.
Static and dynamic petrophysical properties are key parameters concerning 1) the characterization and monitoring of coastal aquifers for vulnerability assessment, and 2) the investigation of pre-selected and tested natural laboratories that are analogue of oil or gas reservoirs; these two subjects are the goals of respectively 1) Aliance (Campos site) and 2)

Ises-Industry (Cabo Blanco site) research projects, on which this study relies. So far, these laboratory measurements were mostly carried out on siliciclastic sediments .
The involved phenomena are much more complex in carbonates than in siliclastic rocks, and as a result, for instance, the law relating permeability to porosity is generally multi-modal in carbonates, while it is generally uni-modal and of power type over a relatively short depth interval in siliclastic rocks. Similarly, the cementation factor m, and the saturation exponent n are usually fairly constant in siliclastic rocks, while they are highly variable in carbonates. This is why extensive non-destructive static and dynamic petrophysical measurements were carried out on the same set of more than one hundred core samples of a 100m interval in a single well. The results were completed with pore throat size evaluations from mercury porosimetry, mineralogical determination from laboratory measurements, and information on depositional texture and diagenesis deduced from thin-section analyses.
Static core laboratory measurements of porosity, electrical and acoustic velocity properties allow to: 1) derive values (grain density, pore throat diameter, formation electrical factor, cementation factor, surface conductivity, mechanical elastic moduli) and draw conclusions on their evolution vs. porosity or depth, the relative value of the surface conductivity, and on consequences such as the hardening or softening of the rocks by water wetting; 2) investigate the heterogeneity and the diagenesis of the rocks; 3) evaluate the hydraulic transmissivity of the formations, in combination with dynamic core laboratory measurements; 4) validate and calibrate shallow logging measurements that have been conducted in-situ (in Maria-Sube et al, in prep.).
Dynamic petrophysical properties have been investigated through permeability and electrokinetic potential measurements.
The comparison of the static and dynamic measurement results allows to complete the analysis and classify the plugs according to their porosity, permeability and different other petrophysical or geological parameters, thus identifying good and bad transmissivity rocks, in terms of texture and diagenesis.
Additional analysis has been made on the detected mineralization zones, by checking their occurrence and horizontal planarity in the other boreholes of the site with the help of borehole image logs; a backward engineering brings some light on the possible origin of these five mineralization zones.

2 Geological setting

The Llucmajor Miocene carbonate platform occurs on the southeastern side of the Palma basin (Fig. P3-1) and consists of a 20km-wide and up to 100m-thick carbonate platform that is thought to result from progradation and aggradation processes controlled by high-frequency sea-level fluctuations during late Tortonian to Messinian times. The facies architecture and the depositional sequences displayed by the spectacular sea-cliff outcrops along 16km of the southern coast of Majorca, between Cabo Blanco and Vallgornera, have been extensively described in the literature (Pomar, 1991; Pomar and Ward, 1994 , 1995; Pomar et al., 1996; Pomar and Ward, 1999). The platform has undergone only slight tilting and flexure associated with normal and strikeslip NE-SW faulting during Late Neogene to Middle Pleistocene times, so that most of the original geometries are retained; the Campos basin seems to have subsided only during Pleistocene time (Jenkyns et al., 1990). Minor burial compaction and scarcity of pervasive cementation has preserved much of the primary porosity (Pomar and Ward, 1999).
In that region, the Miocene platform carbonates form a fresh water reservoir that is surveyed by the Hydrogeological Department of the Government of the Balearic islands. Subsurface data have been obtained on water wells (100 to 300m deep) and have been used to delineate the three-dimensional architecture of the whole Llucmajor platform. The twelve shallow wells which support this study have been drilled between 2003 and 2006 in the Ses Sitjoles area that

is located in the Campos basin, 12km to the northeast of the Cabo Blanco outcrops (Fig. P3-1C and P3-1D).

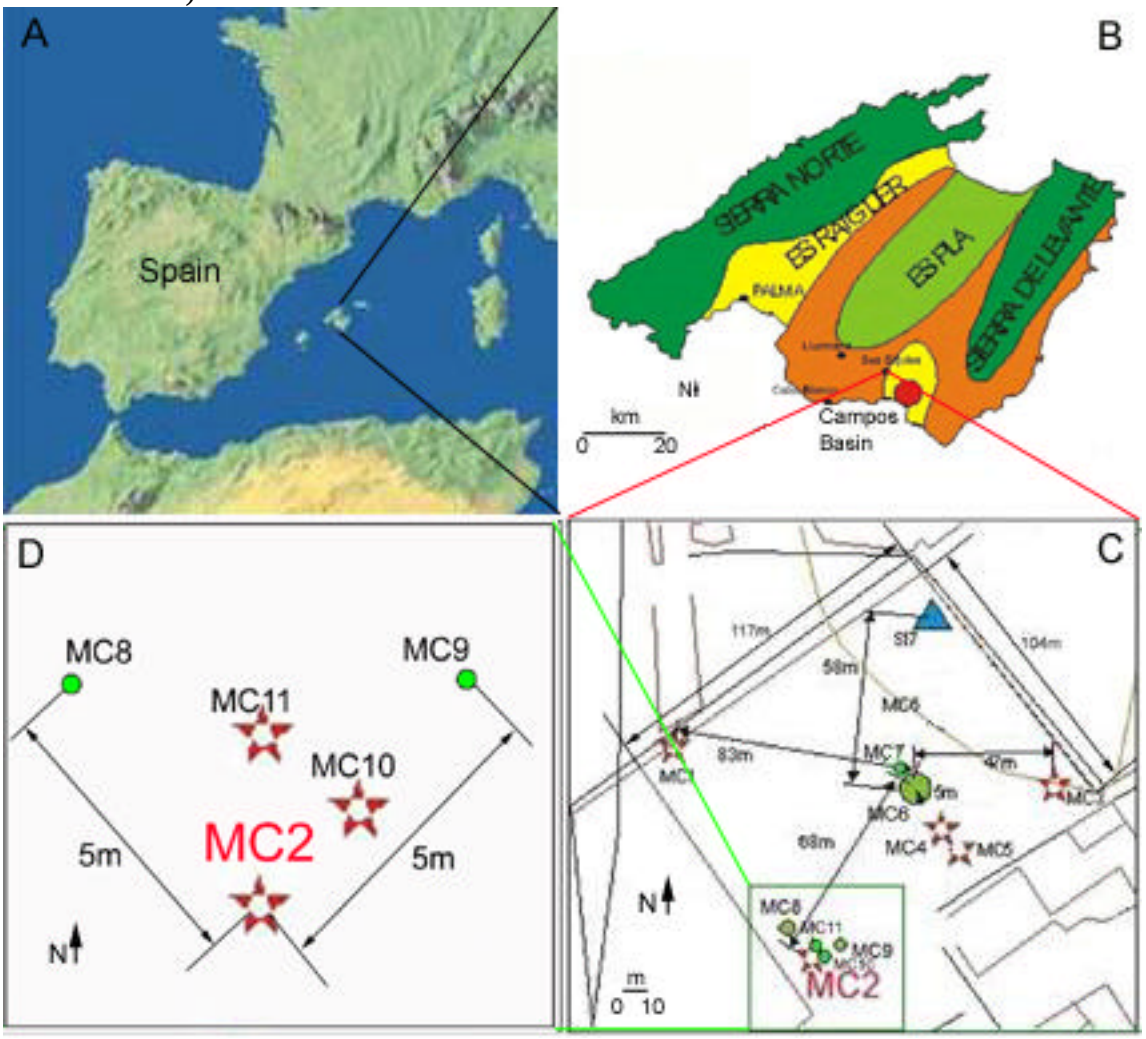

Figure P3- 1. (A) Map of Western Mediterranean Sea, showing Spain and the Balearic Islands, including Majorca. (B) Simplified geological map of Majorca island, showing the paleo-geographic setting of the Upper Miocene carbonate platforms (Upper Tortonian and Lower Messinian) (from Pomar et al., 1996). (C) Ses Sitjoles drilling site in the Campos Basin; red star: cored well, green circle: destructive well, blue triangle: existing slot lined observation well. (D) enlarged cluster of five Ses Sitjoles wells (MC2, MC8-11) located in a 5m square.

3 Material and methods

3.1 Cores and samples

Among the twelve wells that have been drilled in the Ses Sitjoles area, the MC2 well has been chosen as the reference hole. This well is 100m deep and has been continuously cored from top to bottom; the core diameter is 8cm. 116 plugs, 22mm long and 25mm in diameter, have been prepared for physical laboratory measurements. The axis of all plugs is oriented horizontally, except for 16 of them which are oriented vertically; the later samples were taken at the following depths, by groups of four plugs, in close proximity: 12.13, 12.15, 12.25, and 12.27m below ground level (mbgl); 71.53, 71.55, 71.65, and 71.67mbgl; 90.78, 90.80, 90.90, and 90.92mbgl; 98.33, 98.35, 98.45, and 98.47mbgl.

3.2 Methods

Because calcite equilibrium water was used for all petrophysical measurements on these plugs, various successive non-destructive measurements could be carried out on the same plug, i.e. exactly at the same depth. This provides an exceptionally coherent set of measurements on each particular plug, which is of great importance in such highly heterogeneous rocks.

Other destructive measurements (Hg porosimetry, CEC, spectrometry, thin-sections) have been carried out on some small-sized MC2 rock samples, generally on a smaller number of samples than the plugs, sometimes taken at the same depth than the corresponding plug, sometimes without any correspondence in depth.

3.2.1 Porosity measurements

The total porosity (Φ_T) of a porous material is the ratio of the pore volume to the total volume of the material. In a sedimentary rock, it is necessary to distinguish in this total porosity, the porosity that can be effectively used by fluid transport or effective porosity (Φ_e), from the closed porosity (Φ_c) or the porosity of the closed pores, and the porosity that is accessible only under a certain fluid pressure and where the fluid becomes trapped, because of the capillary forces, or trapped porosity (Φ_t). The following formula relates these different porosities:

$$F_T = F_e + F_t + F_c \quad (1)$$

Porosity and grain density were obtained from triple weighting. For these samples that are characterized by high porosity values, a thin teflon tape was wrapped around each sample to reduce the effect of water evaporation, or of water film accumulation around the sample. For each sample, three different measurements of each weighting method was made, and the average kept as the most representative measurement. Through the combination of this process and the use of a precision electronic balance Precisa 410 AM-FR, it was possible to lower the calculated relative error to 1.5% in porosity, and 2% in density, which represents an absolute error of 0.75% in porosity, and of 0.05g/cm^3 in grain density. The porosity that we have measured with the triple weighting method is an effective porosity Φ_e. However we have assumed that Φ_t and Φ_c were generally either negligible or nil in the considered plugs, and that consequently we were measuring Φ_T (applying Formula (1)).

To validate the triple weighting porosity and grain density measurements, and to provide pore throat diameter information, 28 small size (about 1cm^3) cutting samples were submitted to mercury porosimetry measurements on either an automated Micromeritics Autopore II 9215 (15 samples), or a later Micromeritics machine (13 samples). The mercury capillary pressure was varied between 1 and 4000 bars (400MPa), and the measurement of the mercury volume intrusion provided the pore throat diameter distribution using the Washburn equation (1921):

$$r_p = \frac{-2g\cos q}{p} \quad (2)$$

with r_p (µm): pore throat radius; g of mercury: surface tension of the liquid-vapor interface (480 dyne/cm); q: contact angle of mercury in air (140°); P (dyne/cm^2): external pressure required to force mercury into the pore.

The Hg porosimetry method allows also to estimate Φ_t, because it allows to monitor the cumulative intrusion and extrusion of the mercury into the sample pores.

3.2.2 Electrical properties

3.2.2.1 Principle

In a porous media composed of a matrix media considered as infinitely resistive and a connected pore space saturated with a conductive electrolyte, there is a linear relation between the sample conductivity σ_o, and the electrolyte conductivity σ_w (Archie, 1942):

$$s_o = \frac{s_w}{F} \quad (3)$$

The formation factor F of the rock is dimensionless and reflects the electrolytic conduction mechanism in pore volumes. F depends on the microstructure of the rock, it increases as the fluid conductivity pathways are more complex. It is an interesting parameter to delineate different lithology patterns.

The electrical tortuosity factor α,

$$a = FF \quad (4)$$

is a parameter related to the formation factor. The porous tube model shows that α represents the complexity of the current path through the pore volume of the porous media.

However, the pore volume electrolytic conduction is not always the prevalent phenomena, and surface electrical conduction can be sometimes dominant; this is generally the case when clays are present in the rock, or in the presence of fluids of very low conductivity. When surface processes cannot be neglected with respect to electrolytic volume conduction, Waxman and Smits (WS, 1968) proposed a modified empirical model to take into account the excess or surface conductivity (σ_s), with:

$$s_o = \frac{s_w}{F} + s_s \quad (5)$$

$$\text{with } s_s = \frac{BQ_v}{Ft_s^2} \quad (6)$$

$$\text{and } Q_v = CEC\, r_{ma} \frac{(1-f)}{f} \quad (7)$$

The surface conductivity depends on the CEC (cation exchange capacity) of the clays which represents the number of cations that might be adsorbed by the surface grains of the rock. For carbonate rocks, the surface conductivity depends on the chemistry of the surfaces, which can be represented by a complex equilibrium between the solubility and adsorption of ionic species, the pH, and the partial pressure of CO_2. The CEC can be measured per unit weight of rock matrix, and is expressed in meq/100g (or in Cmol/kg). When expressed in meq/ml, the CEC is noted Q_v. ρ_{ma} is the matrix grain density, and Φ the porosity; B represents the mobility of the cations in the diffuse layer, and τ_s^2 represents the added tortuosity of pore surfaces with respect to pore volumes.

Equations (3) and (5) were introduced in the first studies of rock conductivity (Archie, 1942, Waxman and Smits, 1968) through the use of empirical measurements. Using rigorous arguments and base state equations, Johnson et al., 1986, demonstrated them later. Equation (5) describes the conductivity of the rock as a function of the fluid conductivity, and is generally successful in most of the cases.

Another more sophisticated approach based on the pore space micro-geometry and mixing law theory has been proposed by Revil and Glover (RG, 1998). This leads to a nearly similar but more complex relation. However, the comparison of F and σ_s values from RG vs. values from WS for MC2 samples leads to the conclusion that the RG method does not bring significant changes in this case; as a consequence, throughout the rest of this document, we will abandon RG and use only WS.

Kan and Sen, 1987, have also shown that:

$$\sigma_s \approx \frac{2}{3} b_s \rho_{ma} CEC \quad (8)$$

where b_s is the equivalent ionic mobility of the adsorbed ions in the Stern layer. β_s seems to be independent of the clay mineralogy (Revil et al., 1998).

Another problem of wide interest is to find and study the relation between the microstructural parameters. A great number of core measurements have demonstrated (Archie, 1942) that the formation factor F of Formula (3) of a clay-less porous rock can be related with a rather good accuracy to porosity by a relation of the type:

$$F = \frac{a}{\phi^m} \quad (9)$$

m is referred to as the cementation factor, or cementation exponent. Its value depends on the sediment types, the pore shapes, the connections between pores, hence on the porosity type and its repartition mode, lastly, in a certain way, on compaction. Actually, m is a parameter characterizing the porous space. *a* is a lithology dependent coefficient; empirical values have been reported to be included between less than one to greater than 8 (Gomes-Rivero, 1976) or between 0.6 and 2.15 (Serra and Serra, 2000).

In carbonated formations, a value is often close to 1. In the case of a=1, Formula (9) may be written:

$$F = \phi^{-m} \quad (10)$$

This simplification allows to calculate locally the cementation factor as a function of the porosity , by taking the logarithm of Formula (10):

$$m = \frac{Log(F)}{Log(\phi)} \quad (11)$$

The a and m parameters are of the outmost importance for the evaluation of the water saturation S_w in the oil and gas reservoirs for well log interpretation.

3.2.2.2 Measurement procedures

After being desiccated in an oven, the core samples are degasified and saturated successively in ten different salt concentration solutions (2, 1, 0.5, 0.1, 0.05, 0.01, 0.005, 0.001, 0.0005, 0.0001 Mole/l.

The complex electrical conductivity (real and imaginary part, from which the module and the phase measurements are deduced) of each sample is measured for each fluid salt concentration, at sweeping electrical frequencies varying from 1 to 10^6 Hz. The electrical signal is generated by a Solartron SI 1260 device, which provides a high accuracy measurement of the impedance (less than 1%). Finally, the σ_o conductivity is measured at 1000Hz, to avoid polarization phenomena at low frequency, and dielectric phenomena at high frequency. This measurement procedure has been described in Glover et al. (1994). $1cm^3$ pieces of samples were submitted to CEC measurements by cobaltexaline titration of the extracted fraction, with 0.1 meq/100g accuracy.

Plotting σ_o vs. σ_w (Fig. P3-2A) in natural logarithm axes and then using a WS equation best fit curve provides values for F and for σ_s from Formula (5).

Downhole σ_w measurements have been made with the Idronaut logging tool. This tool has a sensor set composed of downhole fluid measurements of: conductivity, temperature, pressure, dissolved oxygen, pH and Redox (Eh), made by Idronaut SRL of Brugherio, Italy, and packaged by Advanced Logic Technology (ALT) company in Luxemburg, which also provides the software.

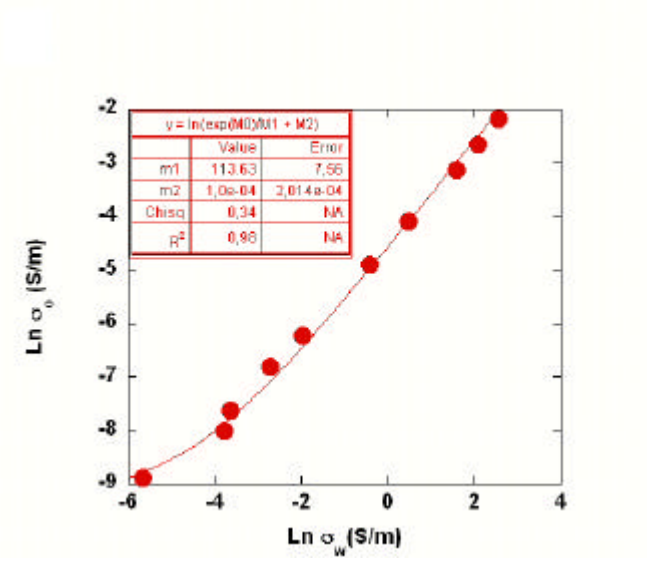

Figure P3- 2. Natural logarithm of s_o conductivity of the saturated sample vs. natural logarithm of s_w fluid conductivity for the sample at 1mbgl, in MC2, with a WS equation best fit curve, allowing to determine F (= m1 value) and s_s (= m2 value) from Equation (5).

3.2.3 Acoustic velocity

3.2.3.1 Acoustic velocity and mechanical elastic moduli principles

We consider the velocities of compressional and shear ultrasonic acoustic waves (respectively V_p and V_s) propagating through a medium of volumetric mass ρ. The mechanical elastic moduli (bulk incompressibility volume modulus K, shear modulus μ, longitudinal elasticity or Young modulus E, Poisson coefficient, or unit transversal contraction/ unit axial extension ratio ν) of this medium are related to V_p, V_s and ρ:

$$K = r(V_p^2 - 4/3V_s^2) \quad (12)$$

$$\mu = rV_s^2 \quad (13)$$

$$E = 9K\mu/(3K+\mu) \quad (14)$$

$$n = \frac{0.5\left(\frac{V_p}{V_s}\right)^2 - 1}{\left(\frac{V_p}{V_s}\right)^2 - 1} \quad (15)$$

The following inequalities result from equation (15):

$$0 < n < 0.5 \quad (16)$$

In a porous medium like a sedimentary rock of porosity Φ filled with a fluid (index f), and matrix density ρ_{ma}, one has to consider the cases of dry (index d) and wet (index w) rocks (Table 1, which includes formulae (17) to (26)). Equation (18) is known as the Gassmann's equation (Gassmann, 1951). One important assumption of Gassmann's equation is that the rock frame properties are not altered by the fluid, with the exception from the additional stiffening of the rock frame by the fluid (Mavko et al., 1998). Under this assumption, the shear modulus μ should not change during saturation (equation (20)).

In carbonates, the Poisson coefficient varies generally between 0,2 and 0,4; the Young and shear moduli can also vary considerably, depending on the lithology and the microstructure of the rock. The study of the mechanical moduli is then an important tool for geological and

petrophysical characterization of the reservoirs, especially in carbonate formations, where the heterogeneity is high, and very different types of diagenesis can be observed.

	Dry porous medium	Wet porous medium
K	$K_d = K_{ma}(1-\beta\Phi/A)$ (17)	$K_w = K_d + \dfrac{K_f\left(1-\frac{K_d}{K_{ma}}\right)^2}{\Phi+\left(1-\frac{K_d}{K_{ma}}-\Phi\right)\frac{K_f}{K_{ma}}}$ (18)
μ	$\mu_d = \mu_{ma}(1-\beta'\Phi/A)$ (19)	$\mu_w = \mu_d$ (20)
Bulk density ρ	$\rho_d = \rho_{ma}(1-\Phi)$ (21)	$\rho_w = \rho_{ma}(1-\Phi) + \rho_f\Phi$ (22)
P wave	$(Vp)_d = \left[\dfrac{\left(K_d + \frac{4}{3}\mu_d\right)}{r_d}\right]^{1/2}$ (23)	$(Vp)_w = \left[\dfrac{\left(K_w + \frac{4}{3}\mu_w\right)}{r_w}\right]^{1/2}$ (24)
S wave	$(Vs)_d = (\mu_d/\rho_d)^{1/2}$ (25)	$(Vs)_w = (\mu_w/\rho_w)^{1/2}$ (26)

Table P3- 1. K, μ, E,a nd n **Elastic moduli, density, P ans S waves in a porous dry and wet medium.**

3.2.3.2 Measurement procedures

Laboratory acoustic compressional and shear velocity measurements are carried out on 113 dry then water-saturated plugs; a set of 500 kHz Valpey Fisher compressional and a set of shear emitters-receivers, hooked-up to a Sofranel 5072PR Pulser/ Receiver; measurements are made with a Techtronix TDS 3032 Oscilloscope, using a stacking mode to stabilize the waveform on the scope. All measurements were made under atmospheric pressure. The acoustic contact between emitter, plug and receiver is made by applying moderate pressure with a plier. An acoustic gel is applied between the rock and the transducer for the compressional waves, while honey is used for a best shear wave transducers coupling. The different acoustic measurements on the same plug are used for quality control, and making sure that the time measurements on the oscilloscope are performed on the right waveform cycle, taking into account the following relations:

$V_p < \sqrt{2}V_s$, $(V_p)_w > (V_p)_d$, $(V_s)_w < (V_s)_d$, and $\left(\dfrac{V_p}{V_s}\right)_w > \left(\dfrac{V_p}{V_s}\right)_d$.

On site acoustic measurements have been carried out using a 2S AA-1000/F 39mm outside diameter sonic wireline log tool built by Mount Sopris Instrument Co. Inc., USA. This tool includes acoustic emitters and receivers operated at a 0 to 30kHz frequency; we have used a 15kHz frequency in our case. The compressional wave emitter is a monopole type transducer, while the shear wave emitter is a dipole type transceiver, with two points vibrating in opposite phase. The dipole type emitter generates a vibration which is transmitted into the mud and into the borehole wall; this creates in the formation a shear mode which propagates along the hole axis. The movements of particles are transversal, like for the shear wave propagation process, and the propagation speed of the flexure wave is very close to the shear wave velocity in the formation (Serra and Serra, 2000). This way of emitting a kind of shear wave has to be used, because true shear waves do not propagate in fluid, and the sonic logging tool emitter cannot be applied to the formation, like the shear wave emitter is applied to the plug in a laboratory. The receiver 1-receiver 2 span is 30cm. The sonic log tool does not work in the vadose zone of the borehole. Data processing (V_p and V_s extraction from the sonic waveforms data acquisition record) was made using the LogCruncher software from Mercury Geophysics, USA.

3.2.4 Permeability measurements

3.2.4.1 Principle

The principle of the permeability measurement is to use the Darcy formula (Darcy, 1856) in a continuous flow; a stabilizing delay is allowing to reach continuous flow between each flow level:

$$\frac{Q}{S}=\frac{K}{\mu}\frac{\Delta P}{l} \quad (27)$$

with Q: flow through the sample; S: surface through which the fluid is injected; K: intrinsic permeability of the sample; μ: dynamic viscosity of the fluid; DP: pressure difference between fluid inlet and outlet; l: length of the sample.

Different porous rock permeability models have been proposed; in particular, geometrical and statistical models (with an random assembly of tubes or fractures) can be used (Guéguen and Dienes, 1989). In most of the theoretical studies, the results always lead to a K-ϕ relationship, such as:

$$K \mu d^2 f^n \quad (28)$$

where d represents a characteristic length of the porous media (such as the mean radius of the tubes, or the mean aperture of the fractures), and n is an integer with values varying between 1 and 3 (e.g. Wyllie and Rose, 1950).

Empirical K-Φ laws, similar to Formula (28), but with n being a decimal number as high as 4.4 (Timur, 1968), have been found in clastic rocks. For practical purposes, the value of n is variable, and has to be determined on a case by case level, over a relatively short interval, through plug measurements of K and Φ.

The K-Φ power relationship of Formula (28) works relatively well in clastic formations. But, because permeability is not actually determined by porosity, but by the microstructure of porosity (Guéguen, and Palciauskas, 1992), the power type K-Φ relation is much more illusory to define for carbonate sediments, where permeability depends on rock texture and pore type.

Recent studies have focused on the permeability of carbonate sediments. The studies are based on empirical models to describe experimental results, and show that the problem is still widely opened from a theoretical point of view.

Some authors have attempted to use a third dimension such as r_{35} (H.D. Winland from Amoco Production Company, reported in Kolodzie, 1980) or r_{p35} (Aguilera, and Aguilera, 2002) (both r_{35} and r_{p35} are equal and defined as the plug pore radius corresponding to a mercury saturation of 35%, determined during Hg porosimetry measurements). These authors have found empirical relationships relating r_{35} (or r_{p35}) to K and Φ:

$$r_{35}=5.395\left[\frac{K^{0.588}}{100\Phi}\right]^{0.864} \quad (29)$$

$$r_{p35}=2.665\left[\frac{K}{100\Phi}\right]^{0.45} \quad (30)$$

The Winland relation was found for a data set of 82 samples including 56 sandstones and 26 carbonates with low permeabilities that were corrected for gas slippage, and 240 other samples with uncorrected permeabilities. Winland ran regressions for other percentiles (30, 40, and 50), but the best correlation (highest R) was the 35th percentile.

More recently, Lønøy (2006), developed another method for the carbonate reservoirs, based on pore type classification, by using 3000 carbonate plug samples from a wide range of

sedimentary basins (North Sea, Russia, Barents Sea, western Iran, southeastern Asia, Libya, Italy, southeastern Spain, offshore Namibia), and geological ages (from Devonian to Miocene). Lønøy started from the existing Choquette and Pray (1970), and Lucia (1983, 1995, 1999)'s classification systems, each using five different pore type classes, and observed that it was possible through a regression within each class, to find a K-Φ power law with R^2 coefficients of determination ranging from 0.45 to 0.88. He then improved the Choquette and Pray and Lucia's classification system by introducing pore type, pore size, pore distribution, and pore fabric classification and reach 20 pore type classes; by this method, R^2, on the different pore type classes was ranging only from 0.79 to 0.96 (except for the vuggy class where the value R^2 is of 0.5). Therefore, Lønøy, 2006, using his method of pore type classification, shows a predictable, power type, relation between porosity and permeability, within each class. However, it should be noted that, even when $R^2 > 0.9$, the Lønøy regressions can lead to very large (with a factor 10 or even 100) errors. Thus, the K-ϕ power law relation can be a useful tool for the reservoirs characterization, but it should be used with caution, taking into account the statistical errors that are mainly associated to the heterogeneity of the carbonates.

3.2.4.2 Measurement procedures

After being desiccated in an oven (1 week at a temperature of 60°C), the samples are maintained 3 days under a 1mBar vacuum, and saturated with a degasified equilibrium water, which has been filtrated at 0.2µm (to eliminate the presence of the smallest bacteria bodies); living bacteria are eliminated by addition of formol drops. The samples are cleaned in a Sonorex Bondelin RK 510S ultrasonic cell, during a few hours. Both permeability and electrokinetic potential measurements use the same measurement cell (Fig. P3-3), in which the plug to analyze is inserted. This measurement cell is a quick assembly, improved safety (the PVC pressure vessel is 15bar guaranteed for a maximum 5bar confining air pressure), improved seal permeability measurement device for sedimentary plugs. A Pharmacia Biotech pump P-500 allows injecting fluid with a constant flow rate (adjustable from 1 to 500ml/hr, by increments of 1ml/hr). The fluid is not recycled before being filtrated again.
The Keller pressure sensors, for upstream and downstream water pressure measurement, are limited by a maximum pressure of 10bars. The confining air pressure is set at 4bars. The pressure measurements are made using a Kethley 2001 multimeter to read the pressure gages output voltage.
Several measurements (generally more than ten) are done using different flow levels by increasing and then decreasing values.

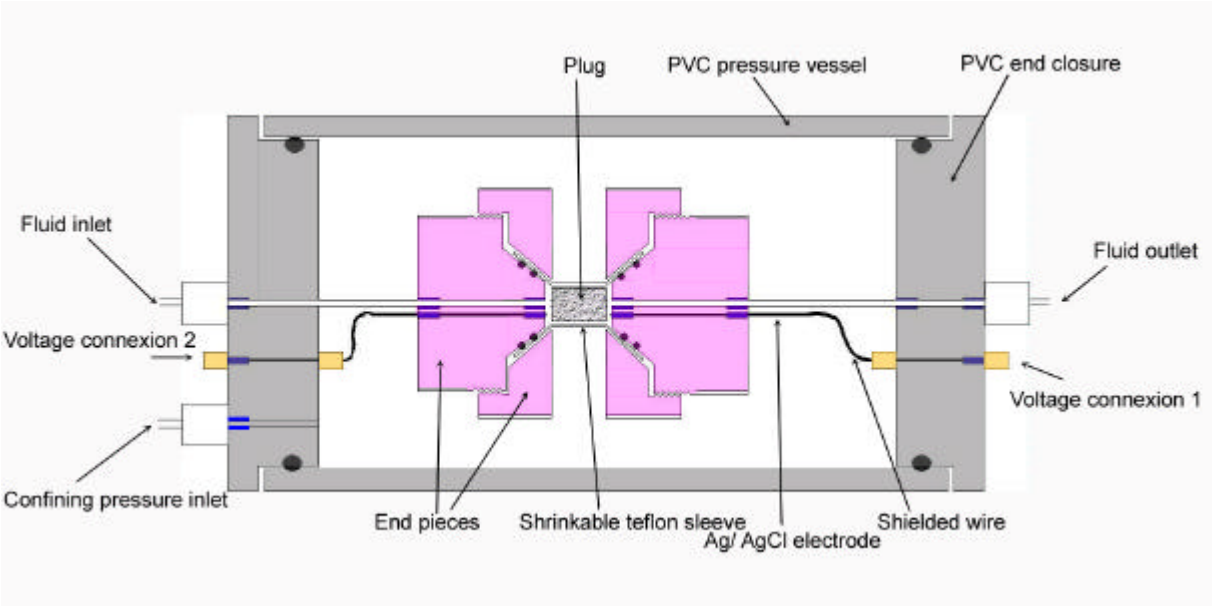

Figure P3- 3. Permeability and electrokinetic potential measurement cell.

3.2.5 Electrokinetic potential

3.2.5.1 Principle

Forcing a fluid through a capillary or porous rock induces a difference of electric potential called streaming potential or electrokinetic potential. In permanent regime, a laminar flow in saturated porous media creates an electric differential potential DV at the boundaries of the capillary which is proportional to the pore pressure gradient DP. The ratio between the applied pressure and the measured voltage is called the coupling coefficient C between hydraulic flow and electrical potential:

$$C=\frac{\Delta V}{\Delta P}=\frac{ez}{\mu s_f} \qquad (31)$$

e is the fluid dielectric constant, z is the zeta potential of the fluid/ rock interface, μ is the fluid dynamic viscosity (as in formula 27), s_f is the fluid electrical conductivity.

This effect is due to the excess of charges at the surface of minerals, generally negative with clays, combined with their high specific surfaces, which generates a coupling between the transport (of water and charges) and the macroscopic forces (pressure gradient and potential gradient). Consequently electrokinetic potential laboratory measurements give information on the electrical surface properties of the rock, particularly with the zeta potential z, defined as the electric potential at the shear plane or slipping plane in the electrolyte-rock interface. This parameter has not been studied extensively in carbonate rocks, because it depends complexly on the physicochemical conditions including many parameters: temperature, pH, partial pressure of CO_2, etc…

3.2.5.2 Measurement procedures

Since ζ is proportional to C, C is measured directly by ΔV and ΔP measurements, and ζ is deduced from measurements. The used set-up is similar to the one used to measure permeability and both measurements are simultaneous. The measurement cell is equipped with special Ag/ AgCl (preventing electrode polarization) electrical measurement electrodes (for ΔV measurement, see Fig. P3-3). Special caution must be taken for measuring low value DC voltages (electrical shielding, high impedance differential amplifier), with several flow

levels and maximum flow values as large as possible. To help taking care of the electrode polarization, measurements without flow were made between each measurement with flow, and the electrode drift with flow was corrected by the drift observed without flow (see Lorne et al., 1999).

3.2.6 Borehole images

Optical and acoustic borehole image logs have been obtained in most of the Campos wells, and especially in MC2. These images were acquired with slim hole tools (i.e. 40mm in diameter) OBI40 (optical) and ABI40 (acoustic) built by the Advanced Logic Technology (ALT) company in Luxembourg. The optical and acoustic images have a 1 and a 3mm resolution respectively. These resolutions are much higher than those currently obtained with larger diameter tools (i.e. about 90mm in diameter) for oil exploration as the oil industry tool offers a resolution ranging from 5 to 10mm; furthermore, the optical tools are not used for oil exploration because they would not provide images through an opaque drilling mud.
Both optical and acoustical images display also the advantage to present a 360° continuous image compared to the micro-scanner electrical images where gaps are due to the spacing between pads and flaps.
The acoustical image log needs a liquid-filled hole whereas the optical image log works also in an air-filled hole. The optical log is therefore very useful even in the vadose zone which is quite important in the studied wells where the vadose zone can be relatively long compared to the total depth.
The acoustic image log presents two sets of images: one obtained from the travel time and the other one obtained from the amplitude of the acoustic signal. Those images are generally more contrasted images than those obtained from the optical image log.

4 Results

4.1 Sedimentological data

The composition of the three units (units I to III) that comprise the carbonate sequence in MC2 well has been described in Bonnier (2005) and Maria-Sube et al. (submitted).
The mineralogical composition of these cores is primarily calcitic, although some clays occur in the upper part of the well, 0-12m below ground level (mbgl), as observed on the gamma-ray log (Fig. P3-4).
The texture, biological content, porosity and connection types of the various facies observed in the MC2 well are summarized in Table P3-2 and show that the Miocene carbonate sequence is very heterogeneous in that well. Selected characteristic facies of each lithological unit are displayed in Fig. P3-5A to P3-5D. The various diagenetic features observed in MC2 carbonate rocks are illustrated in Fig. P3-5E to P3-5G with fringes of granular calcite cements (P3-5E), micrite (P3-5F) and dog tooth calcite cements (P3-5G), and in Fig. P3-5H to P3-5J with drusy calcite cements (P3-5H), equant spars (P3-5I) and dolomitization (P3-5J). Fig. P3-5K to P3-5L are examples of ooids (P3-5K) with closed porosity and intergranular porosity (P3-5L).
The upper part of the MC2 well (0-37mbgl) is dry (vadose zone), while the lower part of the well is filled with brackish (37-62mbgl), transition (62-78mbgl) or sea (78-100mbgl) waters, as observed on the water conductivity log (Fig. P3-4).

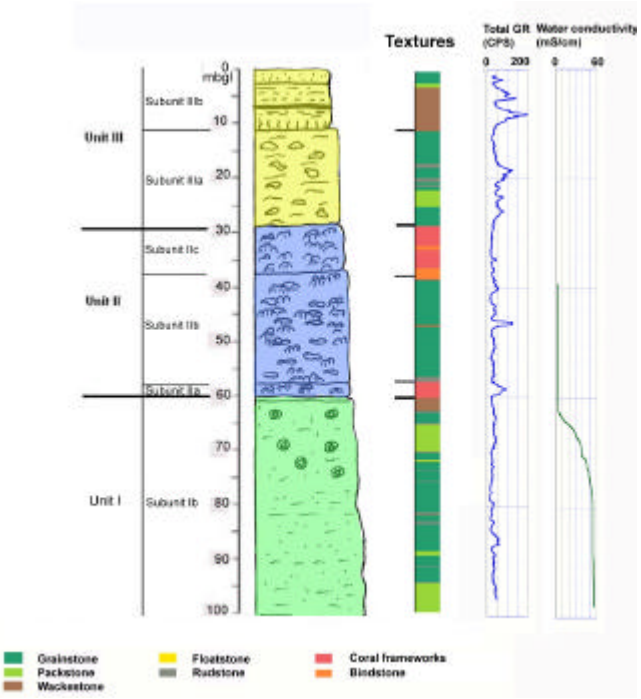

Figure P3- 4. Lithology of Ses Sitjoles MC2 well (Bonnier, 2005, Camoin et al., work in progress), corresponding depositional textures (from Bonnier, 2005, and Jaeggi, 2006), total natural gamma-ray and water conductivity logs. Stratigraphy color coding: green, slope facies; blue: frameworks; yellow: lagoonal to restricted facies.

Units	Subunits	Interval core depth (mbgl)	Depositional texture	Biota	Cement type	Fabric	Porosity type
Unit III	Subunit IIIb	0-12	Oolitic grainstone	Shell fragments	Important sparitic	Isotropic and homogeneous	Mainly intergranular, some intragranular porosity and a few vugs,
	Subunit IIIa	12-28	Skeletal grainstone	Abundant coralline algae and forams	Micritic	Anisotropic but quite homogeneous	Moldic and intergranular
Unit II	Subunit IIc	28-37	Framestone	Built by massive corals (Porites); extensive borings	sparitic cement which partly occludes porosity	Highly heterogeneous	Growth-framework porosity with important vugs
	Subunit IIb	37-57					
	Subunit IIa	57-60					
Unit I		60-75.0 75.0-100.9	Floatstone Grainstone, fine grained	Encrusting coralline algae Molds of shells, only echinoids are preserved	Micritic Exclusively micritic	Isotropic and heterogeneous Anisotropic and homogeneous	Mainly intergranular and some moldic porosity Mainly intergranular porosity and some moldic porosity

Table P3- 2. MC2 lithology, biological content and diagenetic features after thin section observations (from Jaeggi, 2006). The thin section descriptions corresponds to the depths indicated in Figures 5A to 5D caption.

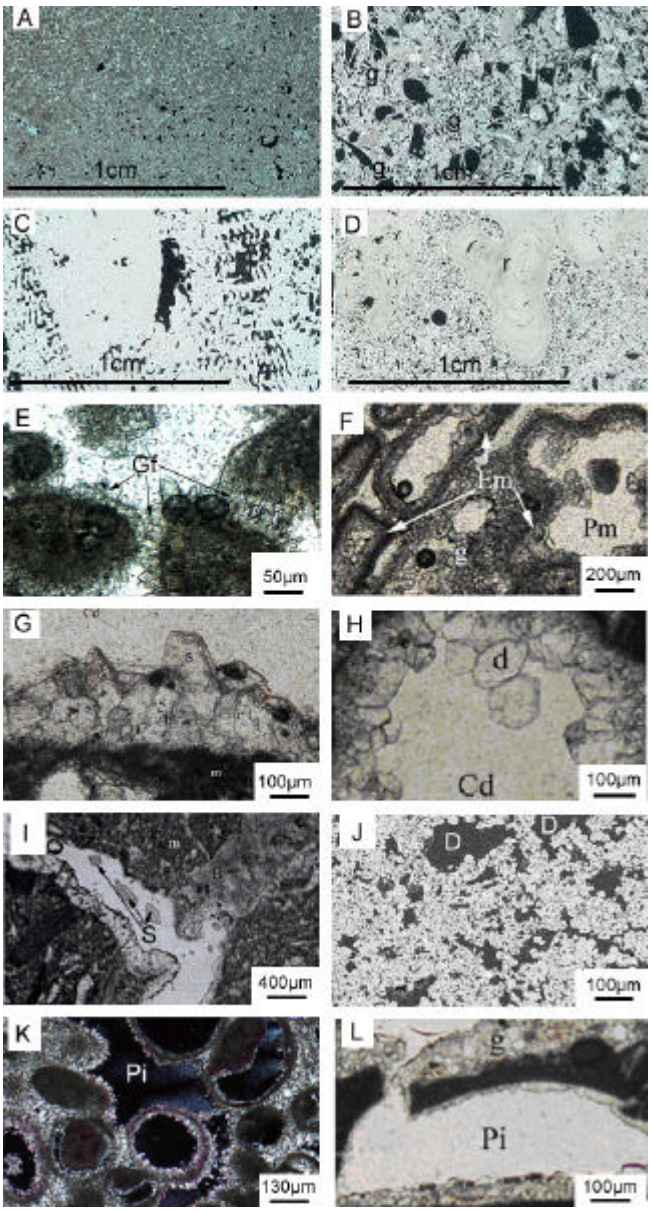

Figure P3- 5. MC2 thin sections photomicrographs. *Characteristic facies*: (A) Subunit IIIb, depth 3.8mbgl, oolitic *grainstone* with shale fragments. (B) Subunit IIIa, depth 14.4mbgl, skeletal *grainstone*, with abundant fragments of red algae, benthic foraminifers, and gastropods (g), moldic and intergranular porosity. (C) Subunit IIc, depth 30.5mbgl, *massive coral (Porites) framework*. (D) Unit I, depth 70.9mbgl, *floatstone*, consisting of rhodolites (r) in a grainstone matrix; moldic porosity. *Diagenetic features*: (E) Subunit IIIa, depth 17.47mbgl, *fringes of calcitic granular cement* (Gf) in a grain-supported grainstone. (F) Subunit IIc, depth 30.0mbgl, *micritic envelopes* (Em), associated to granular cement (g) and moldic porosity (Pm), in a skeletal limestone. (G) Subunit IIb, depth 39.20mbgl, *dog tooth cements* (s), fringing a solution cavity (Cd) and matrice (m) in a grain-supported grainstone. (H) Subunit IIb, depth 52.20mbgl, *drusy calcite cement* (d) in a solution cavity, occuring in a grain-supported grainstone, with moldic porosity. (I) Subunit IIc, 36.9mbgl, *equant spar cement* (S); micritic matrice (m). (J) Subunit Ib, depth 60.92mbgl, *dolomitization of a micritic limestone* (wackestone) (D). (K) subunit IIIb, depth 1.95mbgl, oolitic grainstone with leached *ooids*; intergranular porosity (Pi). (L) Subunit IIc, depth 33.60mbgl, *intragranular pores* (Pi) lined by granular cement (g).

Depth (m)	Porosity (V/V) from triple weighting	Grain density from triple weighting (g/cm^3)	Hg Porosity (V/V)	Grain density from Hg porosimetry (g/cm^3)	Hg porosimetry main pore throat diameter (μm)	Borehole image observations	Spectrometer Philips Pro X'Pert Observations, from Table 4
1.00	0.199	2.713					
1.30	0.165	2.705					
1.96*	0.158	2.703	0.067	2.671	Main peak:60, other: 17, 7, .15, .008		1.6% Clay
2.20	0.130	2.730					
2.21	0.207	2.690					
3.80	0.133	2.707					
3.95	0.196	2.691					
4.50	0.146	2.715					
5.20	0.290	2.731	0.271	2.743	Main peak : 10, secondary peak : .02		
5.30	0.250	2.716					
6.05	0.184	2.719					4.2% Clay
6.10	0.269	2.739					4.2% Clay
8.00	0.328	2.720					
9.90	0.188	2.325				Clay!	
11.30	0.456	2.712					
11.35	0.432	2.717					
12.13	0.442	2.727					
12.15	0.423	2.730					
12.25	0.431	2.734					
12.27	0.407	2.718					
15.30	0.455	2.710					
16.40	0.420	2.712					
17.48*	0.430	2.654	0.405	2.763	Main peak: 16, other: 13, 9, 7,.9, .4		100% calcite
17.68	0.467	2.733	0.425	2.95	Monomodal : 20		
17.70	0.492	2.710					
18.60	0.383	2.724					
18.80	0.360	2.760					
19.43*	0.421	2.778	0.362	2.832	Main peak: 6, other: 70, .4		100% calcite
21.10	0.420	2.693					
21.40*	0.322	2.639	-	-	Main peak: 20, secondary peak: 2		100% calcite
21.60	0.373	2.727					
24.86	0.048	2.845	0.051	2.74	Bimodal : .9 & .01	Mineralization	
24.88	0.020	2.720				Mineralization	
24.90	0.140	2.750				Mineralization	
24.95	0.390	2.720					
25.00	0.350	2.710					
26.8	0.421	2.725					
27	0.429	2.744					
28.5	0.332	2.714					
28.6	0.347	2.717					
30.9	0.334	2.766					
31.05	0.302	2.749					
32.4	0.212	2.722					
32.5	0.196	2.711	0.172	2.681	Main peak : 3 ; secondary peak : 200		
33.48*	0.228	2.703	0.281	2.732	Main peak: 40, secondary peak: 1.2		100% calcite
33.8	0.244	2.720					
34.45*	0.155	2.703	0.188	2.755	Monomodal: 50		100% calcite
34.6	0.154	2.722					
34.7	0.102	2.720					
34.8	0.159	2.719	0.089	2.695	Main peak: 100, secondary peak: .04		
35.9	0.130	2.730					
36.0	0.130	2.710					
36.7			0.075	2.659	Bimodal : 100 & .03	Mineralization	
36.9	0.052	2.752					
37.05	0.378	2.722					
39.7	0.424	2.719					
41.6	0.233	2.724					
41.7	0.180	2.710					
42.27*	0.214	2.709	0.217	2.734	Monomodal: 40		100% calcite
43.48	0.400	2.710	0.358	2.88	Monomodal : 20		
43.5	0.513	2.719					
46.3	0.255	2.732					

Table P3- 3. MC2 laboratory porosity, grain density measurements. Spectrometer observations extracted from Table 4. Sample depths marked * indicates measurements from Mateos et al., in prep.

Depth (m)	Porosity from triple weighting (V/V)	Grain density from triple weighting (g/cm^3)	Hg Porosity	Grain density from Hg porosimetry (g/cm^3)	Hg porosimetry main pore throat diameter (µm)	Borehole image observations	Spectrometer Philips Pro X'Pert Observations from Table 4
46.31	0.236	2.727					
46.4	0.220	2.719					
48.5	0.401	2.848	0.350	2.686	Monomodal : 8	Mineralization	82% Dolomite, 1.6% clay
48.55	0.120	2.800				Mineralization	Id.
48.57	0.120	2.790				Mineralization	Id.
48.60	0.190	2.720				Mineralization	Id.
49.00	0.280	2.760				Mineralization	
49.79	0.377	2.735				Mineralization	
49.80	0.32	2.730				Mineralization	
50.6*	0.418	2.744	-	-	Main peak: 10; other: 100, 0.8		
52	0.251	2.730					
52.02	0.225	2.728	0.219	2.80	Flat maximum between 2 and 60		
52.3	0.431	2.730					
52.75	0.347	2.728					
52.8	0.429	2.725					
53.8	0.467	2.734					
54.4	0.500	2.728					
55.2	0.370	2.721					
55.3	0.301	2.734					
56.2	0.05	2.710				Mineralization	
56.64*	0.120	2.715	0.235	2.666	Main peak: 1.8, other; 50, 8, 4, .6		100% calcite
57.2	0.075	2.717					
57.3	0.170	2.723					
58	0.091	2.719					
59.35	0.115	2.725					
59.4	0.11	2.750	0.126	2.678	Main peak: 5, secondary peak: .6	Mineralization	
59.55	0.10	2.710					
59.60	0.29	2.760					
59.7	0.347	2.771					
60.5	0.369	2.839					
60.6	0.35	2.830	0.344	2.87	Bimodal : .5 & 7		
60.9	0.268	2.811					
60.93*	0.383	2.803	0.358	2.937	Main peak : 4, other: 60, 2		85.5% Dolomite
61	0.224	2.796					
64.6	0.447	2.719					
68.1	0.495	2.729	0.508	3.03	Monomodal : 10		
69.7	0.512	2.691					
69.95*	0.419	2.703	-	-	Main: 5, other: 100, 0.8		93.5% calcite
70.5	0.439	2.698					
70.6	0.401	2.721					
71.53	0.411	2.698					
71.55	0.448	2.692					
71.65	0.400	2.697					
71.67	0.458	2.698					
75.2	0.449	2.690					
75.3	0.516	2.710					
77.4	0.457	2.724					
81.3	0.376	2.724	0.285	2.799	Bimodal : 1.2 & 30		
83.15	0.449	2.711					
85.2	0.389	2.746	0.258	2.448	Monomodal : 7		
85.55*	0.4219	2.736	-	-	Monomodal: 2		19.5% Dolomite
88.1	0.43	2.740					
88.59*	0.417	2.781	0.417	3.023	Main peak : .7, other : 60, 3		55% Dolomite, 8.6% glauconite
89.9	0.488	2.696					
90.78	0.419	2.674					
90.8	0.499	2.694					
90.9	0.478	2.695					
90.92	0.491	2.697					
93.4	0.448	2.744					
95.7	0.407	2.708					
97.6	0.457	2.706					
98.33	0.451	2.690					
98.35	0.455	2.699					
98.45	0.438	2.697					

Table P3-3 (Continued)

Depth (m)	Porosity from triple weighting (V/V)	Grain density from triple weighting (g/cm^3)	Hg Porosity	Grain density from Hg porosimetry (g/cm^3)	Hg porosimetry main pore throat diameter (µm)	Borehole image observations	Spectrometer Philips Pro X'Pert observations
98.47	0.412	2.695					
100.91	0.458	2.761	0.410	2.474	Monomodal: .8		

Table P3-3 (Continued)

4.2 Static petrophysical properties

4.2.1 Porosity, grain density and pore throat diameter

4.2.1.1 Triple weighting data

Grain density and porosity measurements obtained from triple weighting measurements are listed in Table P3-3, and presented on Figure P3-6A and P3-6B.

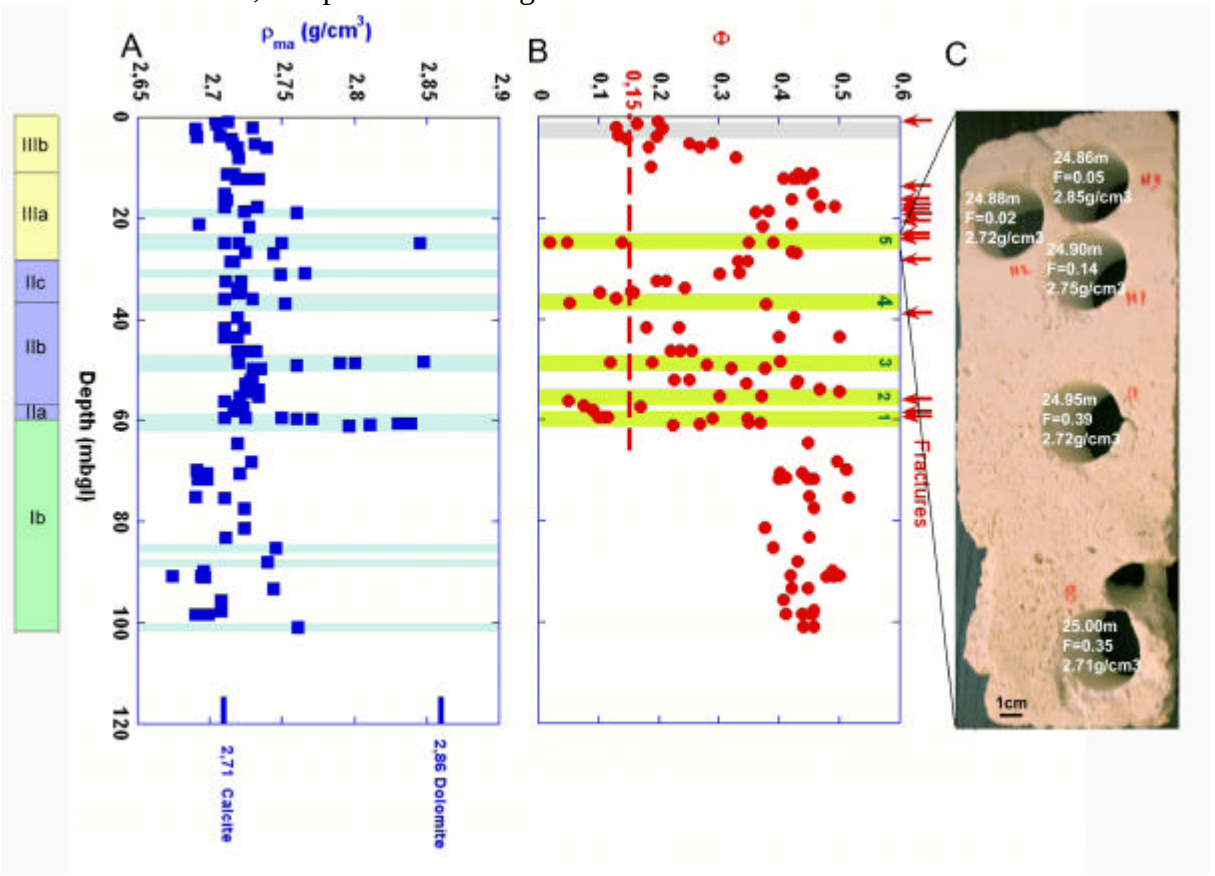

Figure P3- 6. Stratigraphic subunits are indicated on the left side. (A) Grain density r_{ma} vs. depth in MC2 well (116 plugs), with light blue shadings showing zones of dolomitization, recognized from grain density comprised between 2.74 and 2.86 g/cm^3 (thinner shading bands indicate grain density closer to 2.74g/cm^3) (B) Triple weighting porosity F vs. depth in MC2 well (116 plugs) with light green shadows showing five zones of mineralization recognized from porosity below 0.15 (the thick long dash red line indicates F = 0.15); an other zone of low porosity (at 2mbgl) is indicated by a light gray shading; red arrows indicate the depth at which fractures have been recognized from image logs (C) Core slab photo at 25mbgl; in plug holes are indicated values of: depth, porosity, and grain density (from top to bottom), illustrating a zone of both mineralization and dolomitization.

Fig. P3-6 illustrates the extreme vertical heterogeneity of the Miocene carbonate sequence in the MC2 well. However, the porosity range is much reduced below 60mbgl; within the 60-101mbgl interval that corresponds to the reef proximal slope (subunit Ib), the porosity

standard deviation is of 0.061 (as opposed to 0.13 on the whole interval), and the average porosity value is of 0.424. Several zones of very low porosity ($0.02 < \Phi < 0.15$, see for instance Fig. 6C at depth 25mbgl), are observed (Fig. 6B) at 25mbgl (zone 5), 36mbgl (zone 4), 48mbgl (zone 3), 56mbgl (zone 2) and 60mbgl (zone 1). We observe that zone 4 at 36mbgl corresponds to the present day water table, and that zones 1, 3, 4, and 5 correspond as well to zones characterized by high grain density ρ_{ma} (Fig. 6A), hence probably to dolomitic zones that are called here "zones of mineralizations", and will be better characterized later on. At this stage, no name is given to the zone occurring at 2mbgl.

Core depth (mbgl)	Log depth (mbgl)	CaO (wt %)	MgO (wt %)	SiO_2 (wt %)	Al_2O_3 (wt %)	Fe_2O_3 (wt %)	MnO (wt %)	Na_2O (wt %)	K_2O (wt %)	TiO_2 (wt %)	P_2O_5 (wt %)	Th (ppm)	U (ppm)
2.23	0.7	54.7	0.4	0.99	0.6	0.16	0,00	0.01	0.01	0.03	0.01	-	-
5.99	4.5	52.82	0.51	2.87	0.94	0.3	0.01	0.02	0.1	0.06	0.01	-	-
14.5	13	56.94	0.27	0.23	0.03	0.03	0,00	0.11	0.01	0.01	0.03	0.17	0.68
17.51	16	55.49	0.35	0.21	0.13	0.03	0,00	0.01	0,00	0.02	0.08	-	-
19.54	18	56.49	0.34	0.19	0.02	0.04	0.01	0,00	0.01	0.02	0.01	-	-
21.52	20	56.78	0.31	0.09	0.01	0.03	0,00	0.01	0.01	0.01	0.02	0.22	2.97
33.31	33.2	55.9	0.34	0.29	0.18	0.05	0.01	0.01	0.01	0.02	0.01	.06	0.44
34.53	34.4	55.79	0.31	0.27	0.19	0.04	0,00	0.01	0.01	0.02	0.01	0.07	0.64
42.08	40.1	55.62	0.3	0.12	0.18	0.03	0.01	0.01	0.01	0.01	0.01	0.05	1.16
48.12	46.1	52.99	0.38	0,00	0.05	0.03	0,00	0.01	0,00	0.02	0.01	0.14	0.32
48.32	46.3	35.01	17.12	1.1	0.49	0.14	0.01	0.06	0.05	0.15	0.04	0.31	4.06
50.78	48.8	55.73	0.34	0.37	0.33	0.05	0,00	0.01	0.01	0.02	0.01	0.18	0.78
56.83	55.9	55.8	0.31	0.16	0.12	0.04	0.01	0.01	0.01	0.02	0.01	0.07	0.7
60.96	61	34.02	18.93	0.66	0.35	0.12	0,00	0.04	0.02	0.03	0.03	0.28	3.52
70.03	70	54.49	0.38	1.13	0.23	0.07	0,00	0.02	0.01	0.03	0.02	0.3	1.65
81.15	81.15	55.96	0.3	0.11	0.12	0.03	0,00	0.03	0,00	0.02	0.02	0.18	0.48
85.6	85.6	51.04	4.35	0.28	0.15	0.04	0,00	0.01	0.01	0.022	0.02	-	-
88.92	88.9	41.83	11.25	1,00	0.37	0.11	0,00	0.06	0.01	0.03	0.02	-	-

Table P3- 4. Chemical composition of MC2 cores (from Mateos et al., in prep.) from spectrometer Philip Pro X'Pert. Th and U were measured by the Inductively Coupled Plasma- Mass Spectrometry method, at the Geoscience Labs, Ministry of Northern Development and Mines, Ontario, Canada.

Table P3-6 summarizes the presence in MC2 well of dolomite, deduced from grain density (Table P3-3), spectrometry (Tables P3-4 and P3-5), and Hg porosimetry (Table P3-3) data. A clear occurrence of dolomite at 25mbgl, 37mbgl, 48mbgl and 60.5mbgl is demonstrated by grain density data. This presence is confirmed by the results of spectrometry and Hg porosimetry (see below), respectively at 48.32 and 60.96mbgl, and at 24.86mbgl, 36.7mbgl, 59.4mbgl and 60.6mbgl. Spectrometry and Hg porosimetry are also detecting dolomite respectively at 88.92 and 88.59mbgl, where dolomite is hardly detected by ρ_{ma}; in contrast, ρ_{ma} measurement indicates also the occurrence of dolomite in the 30.9-31.05mbgl interval. High values of ρ_{ma} within the first six meters of the MC2 well are probably due to the occurrence of clay and calcretes. At 18.8/ 19.43mbgl, the apparent mismatch between spectrometry data and other laboratory measurements, is possibly related to a depth difference between the samples used for spectrometry and the corresponding plugs.

The 116 sample measurements display a wide range of porosity values, from 2 to 52 %, the average porosity being 32%, and the standard deviation 13.4%.

Clay-bearing samples may display a grain density as low as 2.325g/cm^3, while other samples are characterized by a grain density ranging from 2.69 to 2.85g/cm^3, with an average of 2.72g/cm^3, and a standard deviation of 0.05g/cm^3. However, this indicates the uncertainty that

characterizes grain density measurements in mostly calcitic formations, with low percentages of dolomite and ankerite. The interval 0-12mbgl can be slightly shaly (Table P3-5).

Core depth (mbgl)	Calcite(%)	Dolomite (%)	Ankerite (%)	Montmorillonite + Illite (%)	Glauconite (%)	Total (%)
2.23	93.9	4.5	Traces	1.6	0	100
5.99	95.8	0	Traces	4.2	0	100
14.5	100	0	Traces	0	0	100
17.51	100	0	Traces	0	0	100
19.54	100	0	Traces	0	0	100
21.52	100	0	Traces	0	0	100
33.31	100	0	Traces	0	0	100
34.53	100	0	Traces	0	0	100
42.08	100	0	Traces	0	0	100
48.12	87.5	12.5	Traces	0	0	100
48.32	16.4	82.0	Traces	1.6	0	100
50.78	100	0	Traces	0	0	100
56.83	100	0	Traces	0	0	100
60.96	14.5	85.5	Traces	0	0	100
70.03	93.5	6.5	Traces	0	0	100
81.15	100	0	Traces	0	0	100
85.6	80.5	19.5	Traces	0	0	100
88.92	36.4	55.0	Traces	0	8.6	100

Table P3- 5. MC2 rocks chemical composition deducted from Table P3-4.

Depth (mbgl)	ρ_{ma}	Spectrometry	Hg Φ	Conclusion
18.80/ 19.43	2.76/ 2.78	100% calcite	Multimodal	100% calcite
24.86	2.845	-	Bimodal	Pres. of dolomite
30.9/31.05	2.766/ 2.749	-	-	Pres. of dolomite
36.7/ 36.9	2.752	-	Bimodal	Pres. of dolomite
48.5/ 48.57	2.848	82% domomite	Monomodal	82% dolomite
49.0/ 52.0	2.76/ 2.73	-	Multimodal	Pres. of dolomite
59.4/ 59.6	2.75/ 2.76	-	Bimodal	Pres. of dolomite
60.5/ 61.0	2.839/ 2.796	85.5% dolomite	Bimodal	85.5% dolomite
85.2/ 85.55	2.746-2.736	19.5% dolomite	Monomodal	19.5% dolomite
88.1/ 88.59	2.74/ 2.78	55% dolomite	Bimodal	55% dolomite
100.91	2.761	-	Monomodal	Pres. of dolomite

Table P3- 6. Presence of dolomite based on grain density, spectrometry, and Hg porosimetry indications, in MC2 well.

The analysis of borehole image log has allowed to identify and characterize 14 different fractures in MC2 well (Maria-Sube et al., submitted; Table 7; Fig. 6B). It is interesting to note that no fracture was detected in Unit I, while 57% of the fractures are located in subunit IIIa. Fractures at 24.8, 56.15, 58.8 and 59.1mgbl correspond to zones 5, 2 and 1 of mineralization; fracture at 1.75mbgl corresponds to the low porosity zone at 1.30, 1.96, and 2.20mbgl.

Unit/ subunit	Log depth (mbgl)	Dip magnitude (0-90°)	Dip orientation	Aperture	Planarity quality
Subunit IIIb	1.75	30	SW	Closed	Average
Subunit IIIa	14.0	70	SW	Closed	Average
	16.3	0	-	Closed	Good
	17.0	60	NE	Closed	Excellent
	18.0	60	SW	Closed to open	Average
	18.8	60	SW	Closed	Good
	20.6	30	SW	Closed	Average
	23.4	15	W	Open	Average
	24.8	5	SE	Closed	Average
Subunit IIc	28.3	80	SE	Closed	Average
Subunit IIb	39.4	80	E	Closed	Average
Subunit IIa	56.15	60	NE	Closed	Excellent
	58.8 to 59.1	60	NE	30cm aperture	Good
		40			

Table P3- 7. Identification and characterization (dip magnitude, orientation, aperture, and planarity quality) of fractures by image logs in MC2 well from Maria-Sube et al., submitted.

4.2.1.2 Mercury porosimetry data

Porosity, grain density and pore throat diameter results are listed in Table P3-3.

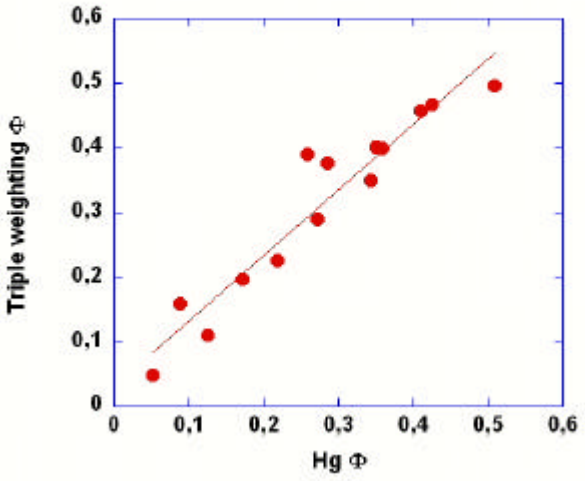

Figure P3- 7. Comparison between triple weight porosity and porosity from Hg porosimetry in MC2 well. Regression line equation: y= 0.032 + 1.01x, R^2= 0.91.

Triple weighting and mercury porosimetry porosity measurements match relatively well (Fig. P3-7), but the grain density obtained by the Hg porosimetry method often provides anomalous results. This can be explained by wrong results of the grain density based on mercury porosimetry either because total porous volume measured at atmospheric pressure is underestimated due either to the lack of penetration of mercury into samples characterized by high surface roughness as a consequence of its high curvature radius, or because the mercury volume in the measure stem was below 25% of the total stem volume on some measurements,

which is known to lead to inaccurate measurements. For these reasons, we will use only both porosity and grain density measurements based on the triple weighting method.

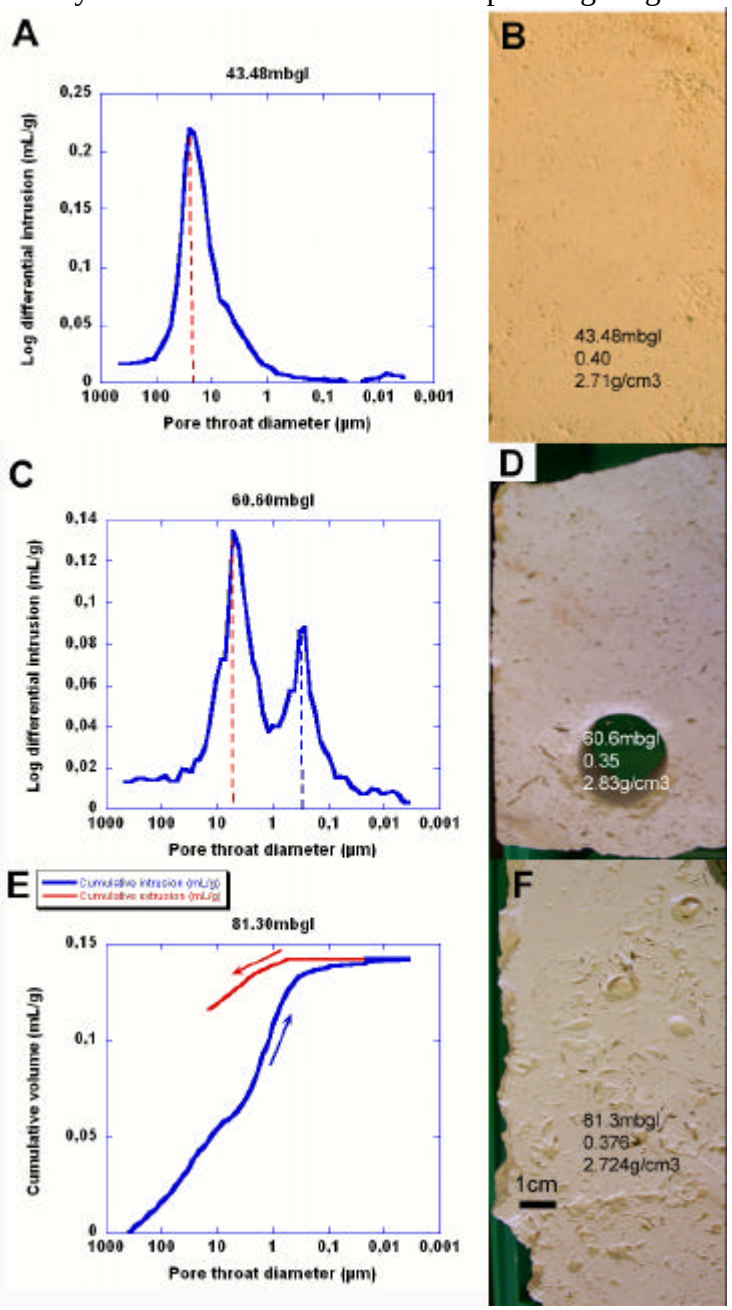

Figure P3- 8. Examples of Hg porosimetry results on MC2 samples. (A) Differential intrusion vs. pore throat diameter, at 43.48mbgl showing a monomodal distribution of pore throats. (B) core slab photo at 43.48mbgl (depth, porosity and grain density are indicated); the grain density value suggests that this rock is mostly pure calcite. (C) Differential intrusion vs. pore throat diameter, at 60.6mbgl, showing a bimodal distribution of pore throats, with dominant pore throat diameters at 7 and 0.5µm. (D) Core slab photo at 60.6mbgl; the grain density value suggests that there is a high percentage of dolomite in this calcitic rock; compare with Fig. 5J at 60.92mbgl thin section showing dolomitic cement. (E) Cumulative intrusion (increasing pressure, blue curve) and extrusion (decreasing pressure, red curve) at 81.3mbgl showing trapped porosity. (F) Core slab photo at 81.3mbgl, displaying moldic porosity.

However, one strong interest of mercury porosimetry is to give access to the mercury intrusion and extrusion, and the pore throat diameter data. Pore throat main peak diameter (27 samples) averages 18.4µm, with a minimum of 1.2µm and a maximum of 100µm (Table P3-3). Secondary peak diameter averages 23.33µm (33 measurements), with a minimum of

0.008µm and a maximum of 200µm. These results are indicative of different types of porosity, resulting from subsequent diagenetic processes.
Some results show monomodal differential intrusion vs. pore throat diameter (Fig. P3-8A); for instance at 43.48mbgl, the dominant pore throat diameter is 20µm, with a porosity of 40% and a grain density of 2.71g/cm^3 (Fig. P3-8B), indicating possibly a pure calcite mineral.
Several samples present on the differential intrusion curve vs. pore throat diameter plot a bimodal curve (Fig. P3-8C) at 60.60mbgl, where measured grain density is 2.83g/cm^3 (Fig. P3-8D), suggesting a high content of dolomite in this plug; this is confirmed by the occurrence of dolomite cements in thin section at 60.92mbgl (Fig. P3-5J). Guéguen and Palciauskas (1992) cited a very similar example initially described by Pittman (1984) as a dolomitized calcite, where dolomitization has induced the development of micropores between the dolomite rhombohedra. Samples at 5.2, 24.86, 32.5, 33.48, 34.8, 36.7, 59.4, 60.6, 81.3 and 88.59mbgl are therefore bimodal and could include dolomite. The occurrence of a substantial amount of dolomite at depths 48.5, 60.93, 85.2 and 88.92mbgl (Tables P3-4 and P3-5, only 18 samples were measured) is demonstrated by spectrometer measurements.
The mercury porosimetry also allows to study the extrusion curve (at decreasing pressure), and particularly the volume of mercury which remains trapped after the extrusion process. Trapped porosity was observed on all the samples (Fig. P3-8E), the highest one being recorded at 81.30mbgl (Fig. P3-8F). This demonstrates that there is generally trapped porosity Φ_t in the MC2 plugs; however, since, on one hand the mercury capillary forces are much larger than the water capillary forces, and, on the other hand we have seen that the Hg porosity matches relatively well the triple weighting porosity results, we will nevertheless consider that the trapped porosity is generally negligible in the relevant plugs.

4.2.2 Electrical properties

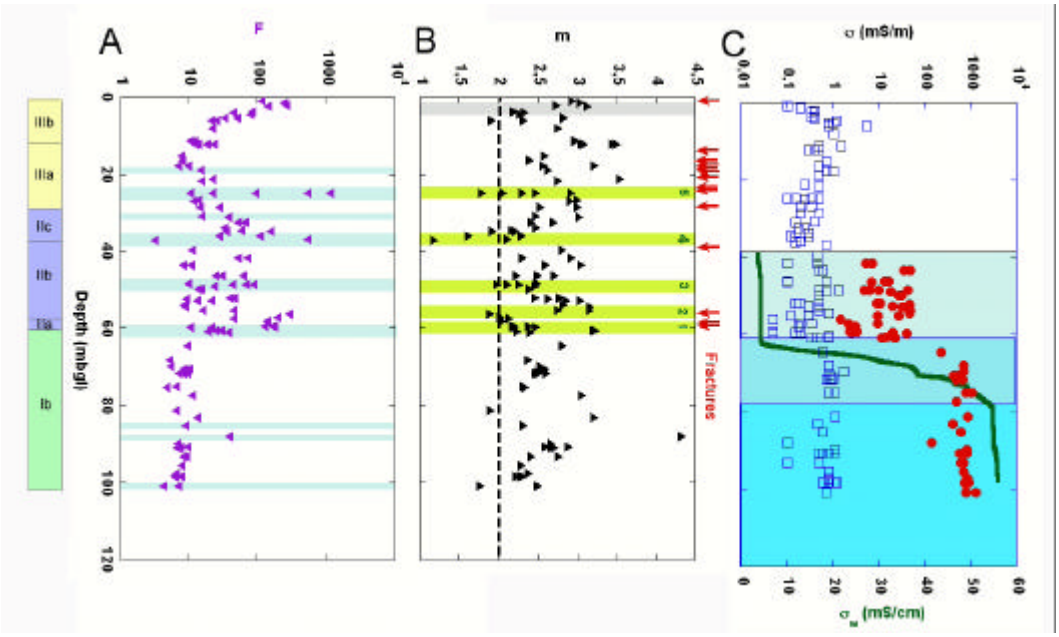

Figure P3- 9. Stratigraphic subunits, mineralization/ cementation and dolomitization zones, and fractures are indicated as on Fig. 6. (A) Formation factor F vs. depth in MC2 well (114plugs). (B) Cementation factor m vs. depth in MC2 well (114 plugs). Note that in the mineralization zones, F increases above a value of 100, m decreases below a value of 2 (black thick dashed line), while in the cementation zone F increases above 100, and m increases above 2. (C) Graphical representation of plug measured σ_s and σ_w/F, and σ_w measured from Idronaut log vs. depth in well MC2, showing that in the brackish water filled part of the well (σ_w~ 4mS/cm, pale blue shading), the surface conductivity σ_s is not negligible compared to the volumetric conductivity σ_w/F. The air-filled interval is represented in white, the transition zone is blue shaded, the sea water filled part of the well (σ_w~ 55mS/cm) is indicated by a dark blue shading.

Depth (mbgl)	Porosity	F	m	CEC (Cmol+/Kg)	Measured σ_s (S/m)	σ_s calculated by CEC (S/m)
1	0.199	113.63	2.93		0.0001	
1.3	0.165	238.10	3.04		0.0002	
2.2	0.13	262.85	2.73	2.1	0.0004	0.0189
2.21	0.207	138.88	3.13		0.00035	
3.8	0.133	83.33	2.19		0.00035	
3.95	0.196	44.44	2.33		0.0004	
4.5	0.146	78.74	2.27		0.0012	
5.2	0.29	33.22	2.83	2.4	0.001	0.0216
5.3	0.25	50.51	2.83	1.03	0.0008	0.0092
6.05	0.184	25.32	1.91	2.52	0.0008	0.0226
6.1	0.269	21.01	2.32	1.51	0.0055	0.0137
8	0.328	21.51	2.75		0.001	
9.9	0.188			7.47		0.0573
11.3	0.456	10.33	2.97		0.0015	
11.35	0.432	12.20	2.98		0.0005	
12.13	0.442	12.44	3.09		0.0005	
12.15	0.423	13.76	3.05		0.0004	
12.25	0.431	18.25	3.45		0.0005	
12.27	0.407	23.15	3.50		0.0003	
15.3	0.455	7.67	2.59		0.0007	
16.4	0.42	7.99	2.40		0.0005	
17.68	0.467	7.08	2.57		0.0007	
17.7	0.492	9.81	3.22	0.6	0.001	0.0054
18.6	0.383					
18.8	0.36	14.75	2.63	0.8	0.0005	0.0073
21.1	0.42	21.55	3.54		0.00025	
21.6	0.373	15.22	2.76		0.0005	
24.86	0.048	526.32	2.06		0.00035	
24.88	0.02	1111.10	1.79	1.1	0.00015	0.0099
24.9	0.14	93.46	2.31	0.8	0.0001	0.0073
24.95	0.39	10.33	2.48	0.8	0.0005	0.0072
25	0.35	21.51	2.92	0.7	0.00025	0.0063
26.8	0.421	13.50	3.01		0.00035	
27	0.429	11.79	2.92	0.4	0.0002	0.0036
28.5	0.332	27.55	3.01	0.5	0.0002	0.0045
28.6	0.347	14.60	2.53		0.0005	
30.9	0.334	15.08	2.47	0.5	0.0004	0.0046
31.05	0.302	37.31	3.02		0.00015	
32.4	0.212	65.79	2.70		0.00018	
32.5	0.196	51.81	2.42		0.00025	
33.8	0.244	32.68	2.47		0.0003	
34.6	0.154	57.80	2.17		0.00012	
34.7	0.102	156.25	2.21		0.00015	
34.8	0.159	34.60	1.93		0.0003	
35.9	0.13	27.55	1.63	0.8	0.0002	0.0072
36	0.13	107.53	2.29	0.7	0.00015	0.0063
36.9	0.052	526.32	2.12	1.3	0.0007	0.0118
37.05	0.378	3.17	1.19			
39.7	0.424	11.20	2.82		0.00045	
41.6	0.233	70.42	2.92		0.00045	
41.7	0.18	52.08	2.31	0.4	0.0001	0.0036
43.48	0.4	10.86	2.60		0.0006	
43.5	0.5	8.26	3.05	0.4	0.0005	0.0036
46.3	0.255	30.49	2.50	0.5	0.0001	0.0045
46.31	0.236	24.81	2.22		0.0007	
46.4	0.22	60.98	2.71		0.0001	
48.5	0.401	9.68	2.48	1	0.0013	0.0094
48.55	0.12	88.50	2.11		0.0005	
48.57	0.12	67.11	1.98	0.9	0.0005	0.0083
48.6	0.19	42.55	2.26	1.1	0.0005	0.0099
49	0.28	22.99	2.46	0.9	0.0007	0.0082
49.79	0.377	13.70				
49.8	0.32	15.43	2.40	0.8	0.0005	0.0072
52	0.251	46.30	2.77		0.00015	
52.02	0.225	39.37	2.46		0.00019	

Table P3- 8. MC2 core measurements of porosity, F, m, CEC, measured s_s, calculated s_s.

Depth (mbgl)	Porosity	F	m	CEC (Cmol+/Kg)	Measured σ_s (S/m)	σ_s calculated by CEC (S/m)
52.3	0.431	9.14	2.63		0.0005	
52.8	0.429	13.04	3.03		0.0005	
53.8	0.467	8.56	2.82		0.0005	
54.4	0.5	8.98	3.17		0.0008	
55.2	0.37	15.55	2.76		0.0003	
55.3	0.301	44.25	3.16		0.00012	
56.2	0.05	285.71	1.89	0.6	0.00005	0.0054
57.2	0.075	192.31	2.03		0.00035	
57.3	0.17	44.05	2.14		0.0002	
58	0.091	136.99	2.05		0.00018	
59.35	0.115	175.44	2.39		0.00005	
59.4	0.11	123.46	2.18	0.6	0.00005	0.0054
59.55	0.1	161.29	2.21	0.6	0.00015	0.0054
59.6	0.29	21.28	2.47	0.8	0.0002	0.0073
59.7	0.347	10.31	2.20		0.00005	
60.5	0.369	24.39	3.20		0.0008	
60.6	0.35	29.50	3.22	0.8	0.0008	0.0075
60.9	0.268	19.01	2.24		0.00045	
61	0.224	36.76	2.41		0.00035	
64.6	0.447	9.62	2.81		0.0006	
68.1	0.495	5.32	2.38	0.3	0.0008	0.0027
69.7	0.512	5.43	2.53		0.0017	
70.5	0.439	8.44	2.59		0.00085	
70.6	0.401	10.11	2.53		0.00085	
71.53	0.411	9.25	2.50		0.00085	
71.55	0.448	8.14	2.61		0.001	
71.65	0.4	9.56	2.46		0.0007	
71.67	0.458	7.08	2.51		0.00095	
75.2	0.449	6.39	2.32		0.0011	
75.3	0.516	4.70	2.34	0.2	0.0008	0.0018
77.4	0.457	10.95	3.06	0.4	1.00E-12	0.0036
81.3	0.376	6.39	1.90		0.0011	
83.15	0.449	13.12	3.22		0.00045	
85.2	0.389	8.93	2.32		0.0006	
88.1	0.43	38.61	4.33	0.6	0.0001	0.0054
89.9	0.488	6.79	2.67		0.0011	
90.78	0.419	9.55	2.59		0.0005	
90.8	0.499	7.44	2.89		0.0006	
90.9	0.478	7.38	2.71		0.0008	
90.92	0.491	6.68	2.67		0.0011	
93.35	0.42	8.13	2.42	0.4	0.0001	0.0034
93.4	0.448	9.21	2.77		0.0005	
95.7	0.407	7.83	2.29		0.0008	
97.6	0.457	6.49	2.39		0.0008	
98.33	0.451	6.17	2.29		0.0012	
98.35	0.455	6.02	2.28		0.001	
98.45	0.438	6.29	2.23		0.0006	
98.47	0.412	7.76	2.31		0.0008	
100.9	0.44	4.27	1.77	0.5	0.000001	0.0044
100.91	0.458	7.06	2.50		0.0007	

Table P3-8 (continued).

Table P3-8 lists the values of F for the 114 measured samples. The average value for F is 57 with a minimum and maximum values of 3.17 and 1111 respectively, the standard deviation being of 130. The accuracy of F measurements is estimated to 1% in relative value. For the 114 measured samples, the average σ_s is 0.55mS/m with a minimum and maximum values of 10^{-9}mS/m and 5.5mS/m respectively, the standard deviation being of 0.59mS/m. The accuracy of σ_s measurements is estimated to less than 1% in relative value. σ_s values reported for Berea and Darley Dale shaly sandstones are close to 1mS/m (Glover et al., 1994); the σ_s values obtained on MC2 "clean" carbonate samples are notably lower than this value.

F results vs. depth are plotted on Fig. P3-9A. Zones of mineralization and dolomite found on Fig. P3-6 are indicated on Fig. P3-9 for reference and comparison; F follows Φ in a mirror way (refer to Formula (9)).

Formula (11) provides the punctual m values listed in Table P3-8. The values of m vs. depth are plotted on Fig. P3-9B.

4.2.2.1 a coefficient and cementation factor m

Theoretical considerations have led to the conclusion that the cementation factor m value is included between 1 and a higher value directly related to the contrast in cross sectional area of pore and pore throat (Adisoemarta et al., 2000). Empirical values have been found to be included between less than 1 and greater than 6 (Gomez-Rivero, 1976), or between 1 and 5.5 (Serra and Serra, 2000). Wyllie and Gregory (1953) have shown that m increases with cementation, through experiments with spheres that are artificially cemented with a silica gel.
The measured values of m average 2.56. When porosity is below 0.15, the value of m is lower, around 1.32. The standard deviation is 0.44, the minimum and maximum values are of 1.10 and 4.32 respectively, i.e. within the empirical values indicated above.

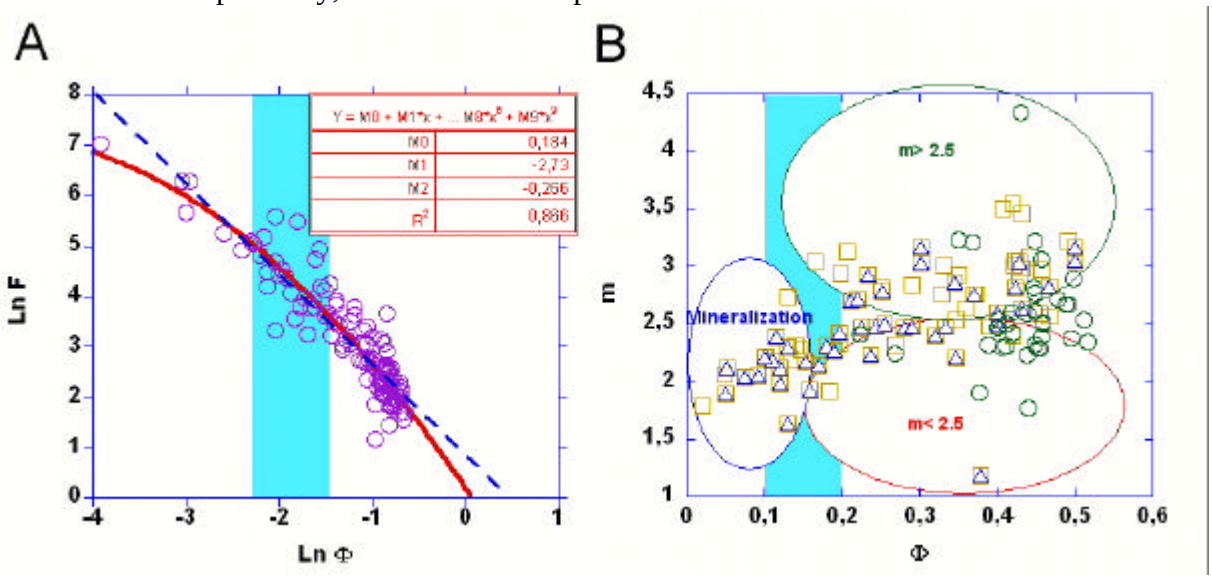

Figure P3- 10. The 0.1< F < 0.2 zone is marked by blue shading (A) Natural logarithm of formation factor F calculated from 114 plugs conductivity measurements vs. natural logarithm of triple weighting porosity on well MC2; the red curve is the polynomial regression curve whose parameters are indicated on the plot. (B) Cementation index m calculated from 114 plugs vs. triple weighting porosity plot showing a loose tendency for m to increase with porosity in MC2; the blue ellipse represents the mineralization zone (F < 15%), the red and green ellipses circle the points where F > 0.15 and, respectively, m< 2.5 and m> 2.5. The Unit III data are represented by yellow squares, the Unit II data are represented by blue triangles, the Unit I data are represented by green circles.

A plot of Ln(F) vs. Ln(Φ) (Fig. P3-10A) should lead to a linear regression line if relation (9) was observed; this linear regression line would have for equation:

$y = 0.842 - 1.8x, R^2 = 0.85$ (32)

Equation (32) leads to values of coefficient a= 2.32 (i.e. the value of F when Φ= 1, LnΦ= 0,or in water), and m= 1.8. This constant value of m is in conflict with the measured values average 2.56.
Instead of a linear regression line, we have plotted a polynomial regression curve of equation:

$y = 0.184 - 2.73x\ 6 - 2.266x^2 + \ldots, R^2 = 0.87$ (33)

Equation (33) leads to values of coefficient a= 1.2, m= 3.26 when F= 1, m= 2.12 at the average value of Φ=0.32, and m= 0.60 when Φ= 0.018 (i.e. LnΦ=-4). This value of a is close to 1, thus justifying Formula (10) and the local computation of m (Formula 11)) that results from it. There is a loose tendency for m to be proportional to the porosity (Fig. P3-10B). If we had plotted a linear regression line, the equation would have been:

$y = -0.028 + 0.14x, R^2 = 0.20$ (34)

This is in clear contrast with the so-called "Shell" industrial formula: m= 1.87 + 0.019/Φ, provided by Hilchie, 1982. Besides the value of m deduced from Formula (33) for the average value of Φ= 0.32 is much closer to the average measured values of m than is the value of

constant m deduced from Formula (32). The previous considerations justify the choice of a polynomial regression curve, instead of a linear regression line.
On Fig. 10B, three zones, delineated by ellipses, can be distinguished: 1) a mineralized zone, with $\Phi < 0.15$ and $1.6 < m < 2.6$, this zone is composed of sediments belonging to Unit II and III exclusively; 2) a zone characterized by high porosity and low cementation factor ($\Phi > 0.15$ and $1.2 < m < 2.5$), this zone is composed of sediments belonging to all three Units; and 3) a zone characterized by high porosity and a high cementation factor ($\Phi > 0.15$ and $2.5 < m < 4.3$, this zone is composed of sediments belonging to all three Units. In shallow water carbonates, well connected intergranular porosity coincides with m values close to 2, whereas vuggy, moldic porosity corresponds to $2.5 < m < 5$, according to Focke and Munn, 1987.
Mineralizations occur at five levels (Fig. P3-9B) characterized by low cementation index ($1.2 < m < 2$).
Cementation characterizes the 2mbgl level associated with low porosity and with m values reaching 3.2, showing therefore that it is different from mineralization processes.
The depth interval 60-100mbgl (Unit Ib) displays large variations of m, even if porosity is remarkably constant throughout that interval.
Detected fractures have also been represented on Fig. P3-9B.

4.2.2.2 Surface conductivity

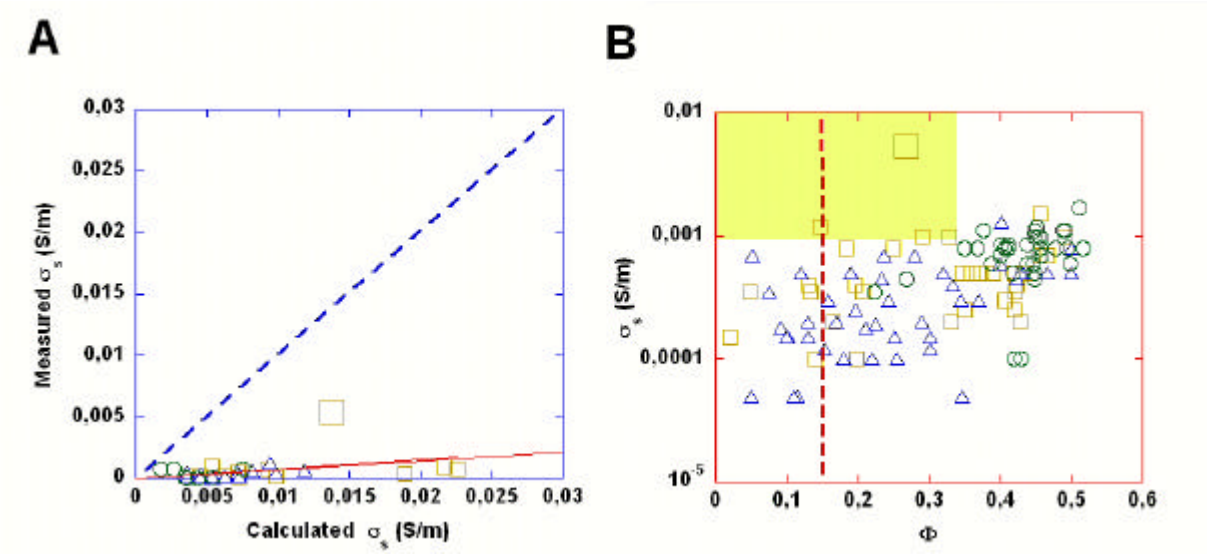

Figure P3- 11. Data symbols distinguishing Unit belonging are the same as for Fig. P3-10B. The highest measured s_s (5.5mS/m) is a clay point at 6.1mbgl and is indicated on the plots by a larger square. (A) Measured s_s vs. calculated s_s from Formula (7) ($s_{sc} \sim 2/3\ b_s\ r_m$ CEC) on 36 MC2 plugs; the dashed blue line is the line y= x. the red linear regression line equation is: y= 0.071x, R^2= 0.12; (B) Illustration of measured surface conductivity s_s vs. porosity for 114 MC2 plugs. Most of the measured surface conductivities larger than 1 mS/m are located in subunit IIIb (0-12m interval, yellow shading) (see Table P3-2); the dashed red line is the line $F = 0.15$.

A value for σ_s can be also obtained through Formula (8) and the value for β_s provided for a monovalent solute with Na^+ ions, at 25°C. Results of CEC measurements (1 $Cmol^+/Kg$ = 1 meq/ 100g) are listed in Table 8. σ_s can be calculated with the grain densities (Table P3-3), with ρ_{ma} expressed in kg/m^3, and knowing that $1meqg^{-1}$ = (eN) Ckg^{-1}= $96320Ckg^{-1}$. Fig. P3-11A illustrates calculated σ_s vs. measured σ_s values. A ratio of 0.071 exists between measured and calculated σ_s, suggesting that the sediments generally display 7% of either clay (in subunit IIIb) or of micritic matrix (Fig. P3-5F). Moreover, the linearity degree between calculated and measured σ_s is rather low (R^2 = 0.12).

CEC values of different clays and micas are shown in Table P3-9. This table shows that clays are not the only minerals to have a significant CEC. The CEC is directly related to the specific surface of the mineral (Patchett, 1975); clay minerals are made of several angströms thickness sheet pilings, and are characterized by very large specific surfaces. This explains why their CECs are larger than CECs from other minerals. However, minerals like calcite also have a certain specific surface, inversely proportional to their grain size, and a CEC, even if it is low. The measured CEC values for MC2 samples listed in Table P3-8 are much lower than those from Table P3-9. This demonstrates that: 1) MC2 rocks or cements are often of micritic nature; 2) That σ_s is not necessarily negligible, even though the clay content is very low, (Table P3-5).

Type	Mineral	CEC (meq/100g)
Clay	Kaolinite	3-25
	Illite	10-40
	Montmorillonite	80-150
	Chlorite	10-40
Mica	Glauconite	10-40
	Vermiculite	100-260

Table P3- 9. CECs of phyllistic minerals (Serra and Serra, 2000).

Measured surface conductivity vs. porosity is plotted in Fig. P3-10B and defines two specific areas: the low porosity area (Φ< 15%), and the high σ_s area ,mostly located in subunit IIIb where the clayey levels occur).

4.2.2.3 Consequences for in-situ electrical measurements

In MC2 well, the depth interval 0-36.4mbgl is vadose (Fig. P3-9C). The depth interval 36.4-62mbgl is filled up of brackish water characterized by *in-situ* measured conductivity (σ_w) values of 4 mS/cm; the depth interval 62-79mbgl is filled up of transitional water, while the bottom interval (79-100mbgl) is filled up of salt water displaying a conductivity (σ_w) of 55 mS/cm. Using the values reported in Fig. P3-9C and Table P3-8, the brackish water interval, σ_w/F> 1 mS/m, while σ_s < 1.2mS/m (Formula (5)): σ_s is not negligible compared to σ_w/F. In the sea water interval, σ_w/F> 100mS/m, and σ_s< 1.1mS/m: σ_s is generally negligible compared to σ_w/F. In this well, the surface conductivity measurements are not negligible compared to the volumetric conductivity in the fresh water zone. This has implications in the case of log hydrocarbon interpretation: there is no shale, and yet, the Archie Formula (3) is not valid and it is necessary to use a Waxman-Smits type saturation equation (Formula (5).

4.2.3 Acoustic velocity

Results of dry and wet acoustic velocity measurements are listed in Table P3-10, and Table P3-11 provides statistics on the measurements and derived values. The relative accuracy of velocity measurements is estimated to 1.5%, which provides relative accuracy measurements of μ, ν, K, and E of respectively: 5, 12, 10 and 45%.

Depth (mbgl)	Φ_T (V/V)	ρ_{ma} (g/cm^3)	Dry V_p (m/s)	Dry V_s (m/s)	Dry V_p/V_s	wet V_p (m/s)	wet V_s (m/s)
1,000	0,199	2,713	5123,27	2701,87	1,896	5128,08	2476,39
1,300	0,165	2,705	6115,16	3110,76	1,966	6191,19	2254,28
2,200	0,130	2,730	5340,03	2777,60	1,923	5370,99	2744,68
2,210	0,207	2,690	5097,01	2597,79	1,962	5125,74	2283,64
3,800	0,133	2,707	5248,74	2600,17	2,019	5519,21	2329,60
3,950	0,196	2,691	4704,35	2572,61	1,829	4985,40	2369,00
4,500	0,146	2,715	5526,26	3006,88	1,838	5704,76	2570,63
5,200	0,290	2,731	4430,88	2641,98	1,677	4434,45	2305,20
5,300	0,250	2,716	4501,42	2462,26	1,828	4618,22	2013,81
6,050	0,184	2,719	4151,30	2270,84	1,828	4185,77	2161,94
6,100	0,269	2,739	3790,77	2159,02	1,756	3804,02	1632,02
8,000	0,328	2,720	4252,45	2295,04	1,853	4255,73	1887,10
11,300	0,456	2,712	3057,58	1777,45	1,720	3740,43	1516,74
11,350	0,432	2,717	3490,40	1993,93	1,751	3501,58	1881,35
12,130	0,442	2,727	3754,11	1978,73	1,897	3782,50	1436,75
12,150	0,423	2,730	3636,12	1927,26	1,887	3826,73	1589,34
12,250	0,431	2,734	3742,18	2125,29	1,761	3744,73	1690,38
12,270	0,407	2,718	3667,12	2061,39	1,779	3669,57	1828,44
15,300	0,455	2,710	3561,84	1885,67	1,889	3671,82	1658,42
16,400	0,420	2,712	3493,67	1923,06	1,817	3657,43	1666,25
17,680	0,467	2,733	2882,89	1688,88	1,707	3071,18	1451,75
17,700	0,492	2,710	2350,69	1365,98	1,721	2712,66	1237,51
18,600	0,383	2,724	3366,19	1912,24	1,760	3661,21	1776,89
18,800	0,360	2,760	3535,56	1978,76	1,787	3549,34	1713,26
21,100	0,420	2,693	3972,65	2148,86	1,849	4235,51	1588,37
21,600	0,373	2,727	3985,17	2227,01	1,789	3999,71	1887,38
24,860	0,048	2,845	6069,72	3034,23	2,000	6076,43	2762,81
24,880	0,020	2,720	6485,73	3186,31	2,035	6455,55	2803,28
24,900	0,140	2,750	5572,04	2918,71	1,909	5577,70	2914,06
24,950	0,390	2,720	3920,33	2197,77	1,784	3923,16	1997,37
25,000	0,350	2,710	4044,29	2294,65	1,762	4108,40	1896,46
26,800	0,421	2,725	3976,09	2195,18	1,811	3990,59	1826,48
27,000	0,429	2,744	3759,36	2244,18	1,675	3772,41	1814,80
28,500	0,332	2,714	4452,47	2272,23	1,960	4456,10	1769,14
28,600	0,347	2,717	4079,59	2239,15	1,822	4389,45	2204,97
30,900	0,334	2,766	4522,18	2499,05	1,810	4563,81	2360,57
31,050	0,302	2,749	4565,72	2500,20	1,826	4569,51	2180,35
32,400	0,212	2,722	5005,77	2513,82	1,991	5028,50	2510,40
32,500	0,196	2,711	5281,03	2640,04	2,000	5286,08	2330,34
33,800	0,244	2,720	4571,94	2437,19	1,876	4629,53	2455,65
34,600	0,154	2,722	5655,74	2717,09	2,082	5690,37	2500,20
34,700	0,102	2,720	6016,91	2868,44	2,098	6023,41	2778,30
34,800	0,159	2,719	5538,29	2588,50	2,140	5599,54	2406,23
35,900	0,130	2,730	5559,36	2807,63	1,980	5709,97	2463,12
36,000	0,130	2,710	5456,26	2598,46	2,100	5483,52	2380,87
36,900	0,052	2,752	5925,09	2978,02	1,990	5996,34	2770,45
39,700	0,424	2,719	3884,12	2165,10	1,794	4030,34	1769,95
41,600	0,233	2,724	5235,74	2443,82	2,142	5240,70	2085,99
41,700	0,180	2,710	5387,78	2654,20	2,030	5414,43	2624,92
43,480	0,400	2,710	3755,90	2087,00	1,800	3758,50	1908,73
43,500	0,513	2,719	2566,36	1513,75	1,695	2841,19	1324,58
46,300	0,255	2,732	4539,09	2570,05	1,766	4757,94	2495,60
46,310	0,236	2,727	4811,90	2563,53	1,877	4816,14	2473,05
46,400	0,220	2,719	4925,05	2626,89	1,875	4992,16	2492,26
48,500	0,401	2,848	2583,04	1601,78	1,613	2639,17	1591,06
48,550	0,120	2,800	5233,21	2628,70	1,991	5309,37	2395,15
48,570	0,120	2,790	5385,32	2861,14	1,882	5390,62	2352,87
48,600	0,190	2,720	4685,93	2784,40	1,683	4730,56	2329,60
49,000	0,280	2,760	4217,72	2482,03	1,699	4234,05	1927,81

Table P3- 10. Acoustic velocity results (113 plugs) in MC2 well.

Depth (mbgl)	Φ_T (V/V)	ρ_{ma} (g/cm^3)	Dry V_p (m/s)	Dry V_s (m/s)	Dry V_p/V_s	wet V_p (m/s)	wet V_s (m/s)
49,790	0,377	2,735	3877,00	2204,85	1,758	3879,76	1810,74
49,800	0,320	2,730	4068,95	2301,19	1,768	4165,63	2024,34
52,000	0,251	2,730	5401,06	2562,65	2,108	5535,99	2546,16
52,020	0,225	2,728	4978,44	2632,94	1,891	5171,96	2142,72
52,300	0,431	2,730	3094,16	1891,65	1,636	3525,94	1405,26
52,750	0,347	2,728	4128,90	2197,77	1,879	4132,04	1957,08
52,800	0,429	2,725	4137,54	2385,31	1,735	4165,20	2086,53
53,800	0,467	2,734	3731,82	2056,34	1,815	3799,68	1710,58
54,400	0,500	2,728	3256,84	1783,47	1,826	3268,61	1496,21
55,200	0,370	2,721	4149,04	2333,29	1,778	4511,86	2002,16
55,300	0,301	2,734	4641,82	2536,22	1,830	4742,66	1962,55
56,200	0,050	2,710	6126,32	2979,38	2,056	6195,49	2695,47
57,200	0,075	2,717	6260,41	3147,30	1,989	6260,41	3070,62
57,300	0,170	2,723	5664,14	2802,51	2,021	5664,14	2754,52
58,000	0,091	2,719	6075,24	2848,34	2,133	6075,24	2588,41
59,350	0,115	2,725	5894,95	2798,94	2,106	5926,28	2793,33
59,400	0,110	2,750	5791,85	3056,94	1,895	5822,64	2758,30
59,550	0,100	2,710	5606,09	2831,52	1,980	5606,09	2331,80
59,600	0,290	2,760	3804,70	2123,98	1,791	3970,63	1498,29
59,700	0,347	2,771	3078,58	1611,31	1,911	3320,30	1141,55
60,500	0,369	2,839	4269,81	2414,02	1,769	4273,11	2000,31
60,600	0,350	2,830	4287,76	2429,14	1,765	4287,76	2403,52
60,900	0,268	2,811	3345,97	1935,83	1,728	3493,67	1846,16
61,000	0,224	2,796	4325,58	2289,05	1,890	4503,49	1446,18
64,600	0,447	2,719	3714,59	1929,85	1,925	3715,85	1585,98
68,100	0,495	2,729	2779,02	1579,10	1,760	2838,53	1317,31
69,700	0,512	2,691	2662,01	1549,87	1,718	2723,86	1252,37
70,500	0,439	2,698	3385,48	1708,40	1,982	3440,85	1534,01
70,600	0,401	2,721	3499,97	1851,30	1,891	3781,57	1740,18
71,530	0,411	2,698	3373,88	1883,70	1,791	3537,06	1538,21
71,550	0,448	2,692	3083,25	1753,78	1,758	3221,11	1518,38
71,650	0,400	2,697	3838,40	2018,01	1,902	3854,62	1691,22
71,670	0,458	2,698	2824,14	1669,29	1,692	2970,71	1466,97
75,200	0,449	2,690	2943,59	1624,86	1,812	3086,64	1439,08
75,300	0,516	2,710	2669,59	1396,96	1,911	2833,12	1295,91
77,400	0,457	2,724	3062,13	1753,00	1,747	3141,75	1516,39
81,300	0,376	2,724	4079,59	1816,78	2,245	4141,13	1811,39
83,150	0,389	2,711	3294,10	1802,85	1,827	3303,95	1640,01
85,200	0,389	2,746	3495,19	1613,44	2,166	3497,42	1501,03
88,100	0,430	2,740	3970,63	2123,98	1,869	4302,11	1736,43
89,900	0,488	2,696	3085,58	1500,62	2,056	3095,98	1478,87
90,780	0,499	2,694	3136,23	1854,78	1,691	3221,11	1548,44
90,800	0,478	2,695	2857,93	1737,09	1,645	2959,90	1485,42
90,900	0,491	2,697	2771,03	1692,13	1,638	2896,47	1360,04
90,920	0,473	2,680	2592,93	1586,37	1,635	2814,83	1446,04
93,400	0,448	2,744	3304,01	1926,94	1,715	3304,01	1664,97
95,700	0,407	2,708	3141,96	1845,67	1,702	3189,46	1573,52
97,600	0,457	2,706	2839,66	1652,58	1,718	2931,47	1475,92
98,330	0,451	2,690	2757,18	1688,86	1,633	2851,97	1477,40
98,350	0,455	2,699	2786,32	1657,22	1,681	2897,79	1493,56
98,450	0,438	2,697	2879,48	1682,34	1,712	3032,23	1565,25
98,470	0,412	2,695	3061,78	1815,34	1,687	3124,78	1614,82
100,910	0,410	2,761	2878,20	1689,85	1,703	2997,42	1543,51

Table P3-10 (Continued).

Measurement	Minimum value	Average value	Median value	Maximum value	Standard deviation	Sample population
Φ(V/V)	.02	.32	.37	.52	.13	116
ρ_{ma} (g/cm^3)	2.325	2.72	2.72	2.85	.05	116
F	3.17	57	15.49	1111	130	114
m	1.19	2.56	2.50	4.32	.44	116
σ_s (S/m)	10^{-12}	.00056	.0005	.0055	.00059	112
Dry V_p (m/s)	2350.69	4153.68	3990.63	6485.73	1057.78	113
Dry V_s (m/s)	1365.98	2227.35	2201.31	3186.31	461.65	113
Dry V_p/V_s	1.61	1.85	1.83	2.25	0.14	113
Dry K (GPa)	4.18	23.38	16.09	79.47	17.84	113
Dry μ (GPa)	2.56	10.29	8.54	27.06	6.11	113
Dry E (GPa)	6.4	26.76	21.87	72.31	16.45	113
Dry ν	0.19	0.29	0.29	0.38	0.04	113
Wet V_p (m/s)	2639.17	4246.78	4120.22	6455.55	1025.79	113
Wet V_s (m/s)	1141.55	1961.02	1863.76	3070.62	468.34	113
Wet V_p/V_s	1.66	2.17	2.15	3.11	0.22	113
Wet K (GPa)	13.54	43.46	35.51	111.91	25.51	113
Wet μ (GPa)	2.81	9.23	7.19	24.4	5.35	113
Wet E (GPa)	8.02	25.82	19.8	67.68	14.84	113
Wet ν	0.21	0.36	0.36	0.44	0.03	113

Table P3- 11. Statistics on porosity, grain density F, m, s_s, and acoustic measurements in MC2 well.

Figure P3-12A is displaying V_p measurements vs. depth, with 113 $(V_p)_d$ and $(V_p)_w$, measurements on MC2 plugs (with $(V_p)_w > (V_p)_d$), and $(V_p)_w$ continuous measurements from the sonic log. Lab. and log measurements fit generally fairly well, except in some spots, probably as a consequence of three factors: 1) the difference of acoustic frequency used for lab. (500kHz) and log (15kHz) measurements, 2) the difference between sample size for lab (2.5cm plug size), and log (30cm receivers span) measurements, 3) the fact that log measurement is oriented in the direction of the hole axis (i.e. vertically), while most of the plugs were oriented horizontally. Because compressional acoustic waves propagate faster in a low porosity than in a high porosity formation, a picture similar to Fig. P3-6B is observed, with clearly identified tight zones, and the large, constant porosity zone of subunit Ib.

Figure P3-12B displays V_s measurements vs. depth, with 113 $(V_s)_d$ and $(V_s)_w$ measurements on MC2 plugs (with $(V_s)_w < (V_s)_d$), and with $(V_s)_w$ measurements from the sonic log. Lab. and log measurements do not fit as well as for compressional waves. The reasons for those differences are similar to those explained above and, moreover, lab.- log differences for shear waves are probably also related to the fact that "some sort" of shear waves are generated by the sonic log (see "Material and methods" section). Because acoustic shear waves propagate faster in a tight formation, a picture similar to Fig. P3-6B is observed, with clearly identified tight zones, and the large, constant porosity zone of subunit Ib. Fractures are also represented on Fig. P3-12B.

In contrast to earlier conclusions (Pickett, 1963), we do not confirm that dry nor wet V_p/V_s are useful to identify the lithology in such carbonate rocks.

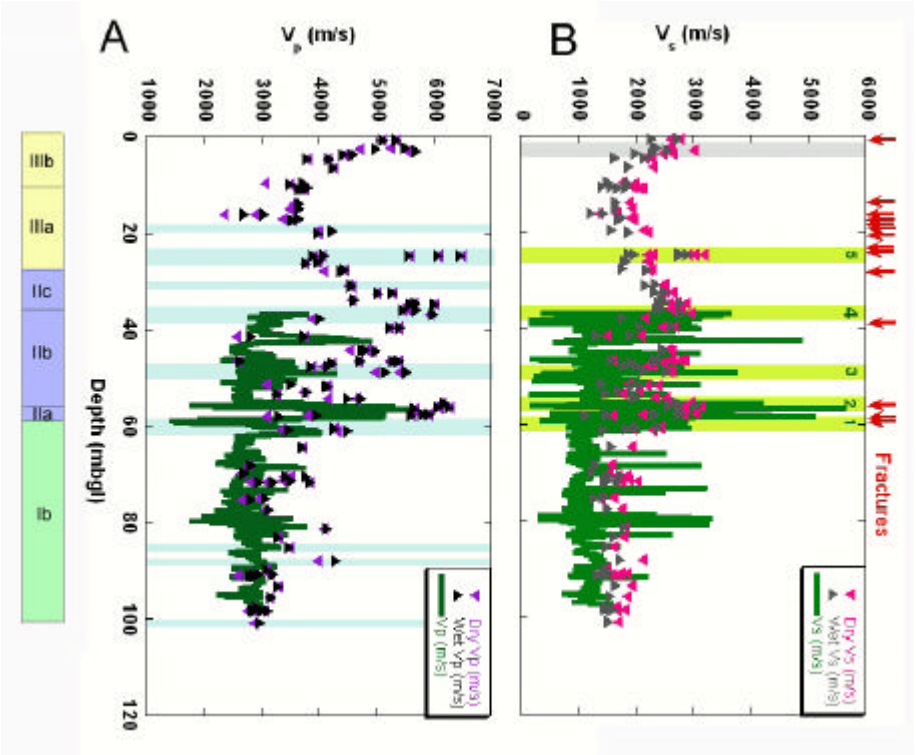

Figure P3- 12. Acoustic measurements vs. depth on 113 MC2 plugs. Stratigraphic subunits, mineralization/ cementation and dolomitization zones, and fractures are indicated as on Fig. P3-6. (A) V_p from dry and wet plugs, and from sonic log. (B) V_s from dry and wet plugs, and from sonic log.

4.2.3.1 Samples wetting and weakening or hardening

The four elastic moduli (μ, ν, K, E) evaluated from the acoustic velocity measurements (Formulae (12) to (15)) and comparisons between the wet (vertical axis) and the dry (horizontal axis) values are illustrated on Fig. P3-13. If the wet and dry values were equal, the data would fall on the 45° line passing through the plot origin. It is clear that this is not the case for any of the four elastic moduli, and in particular not for μ, implying that Relation (20) is not valid in this case (Fig. P3-13A). In contrast, the relation $K_w > K_d$, deduced from Formulae (17) and (18), is clearly confirmed as water saturation increases the rock incompressibility by filling the pores (water being incompressible), (Fig. P3-13C). In the same way, the relation $\nu_w > \nu_d$, deduced from Formula (15), is also verified, as water saturation increases the Poisson coefficient (Fig. P3-13B). The occurrence of μ and E data, and ν data, mostly below and above the 45° line respectively indicates that the wetting of the sample has the effect of weakening the rock frame, and that the Gassmann assumption is therefore not valid for our carbonate samples. However, E measurements are seemingly not very accurate, but results on μ, ν and K are good enough to demonstrate that the error on E is probably overestimated (Fig. P3-13D). This specific property has already been observed in carbonates (Baechle et al., unpublished; Mavko et al., 1998; Risnes et al., 2003 for the North Sea chalk), but also in sandstones, due to cement softening. Four wet plugs were destroyed (two dolomitic samples at 93.5 and 100.90mbgl by excessive applied mechanical pressure, a clay sample at 9.9mbgl, and a dolomitic sample at 37.05mbgl by simple washing) during laboratory measurements, while this never happened with dry plugs. The wetting results were found reversible: if the dry samples are saturated, and then dried and saturated again, the same dry and wet measurements, within the measurement accuracy, are obtained.

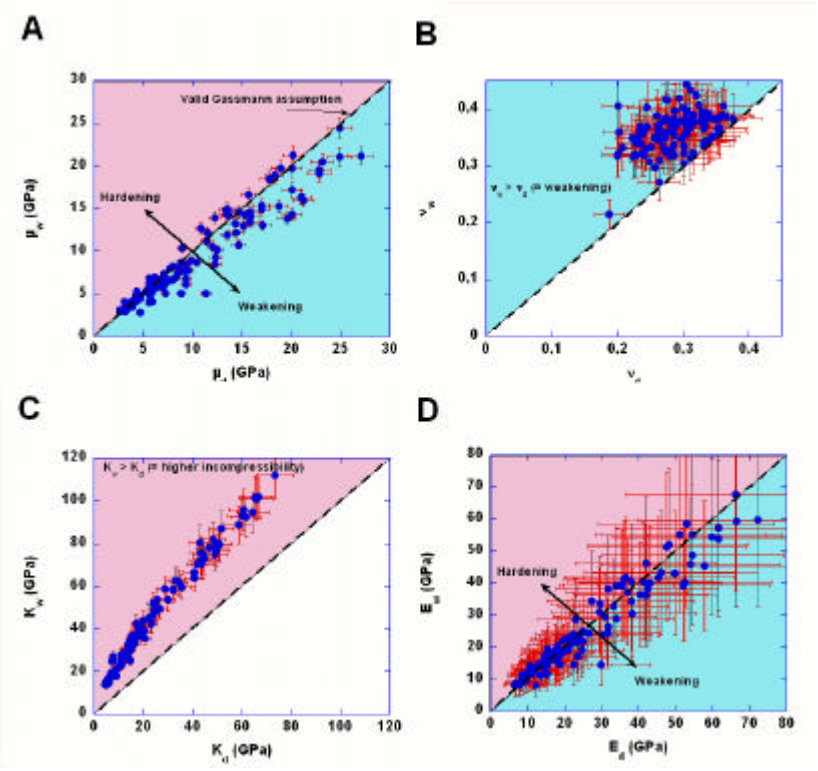

Figure P3- 13. Wet vs. dry elastic moduli on 113 MC2 plugs: (A) shear modulus μ; (B) Poisson's coefficient n; (C) bulk incompressibility modulus K; (D) longitudinal elasticity or Young modulus E. The black 45° line shows on all four plots where the data should fall for a relation wet modulus= dry modulus; error bars are indicated in red.

The Gassmann assumption is not confirmed by our measurements, and probably not in carbonates in general, because we did not find the equality $\mu_d = \mu_w$ (Formula (20)). The general trend reflects more a weakening of the samples under the action of the carbonate equilibrium water used for measurements. Risnes et al. (2003) indicate that carbonate mechanical weakening is due either to the type of fluid and water activity, or to the strength of adsorption of the fluid molecules onto the carbonate surface (i.e. the specific area of the carbonate). Three distinctive zones are clearly defined in Fig. P3-14D: 1) the low porosity/ low σ_s zone of cementation, which corresponds to core weakening, with a similar trend of both σ_s and μ_w/μ_d to decrease in the mineralized zones; 2) the high porosity/ low σ_s zone (including as well a clay point), which also corresponds to core weakening; 3) the high porosity/ high σ_s zone, which may correspond either to core weakening or core hardening. There are similarities between Fig. P3-10B and P3-14D where a clear low porosity mineralization zone, and two high porosity zones occur, in both cases, and are distinguished by the m values, and the μ_w/μ_d and σ_s values respectively.

Fig. P3-15B illustrates the μ_w/μ_d ratio vs. depth with a specific weakening in the mineralized zones. Furthermore, a clear weakening occurs at 60mbgl.

Fig. P3-14D shows that there is a loose proportionality between μ_w/μ_d and σ_s. Because σ_s is proportional to CEC (see Formulae (5) and (6)) and because CEC is directly related to the specific area of the mineral (Patchett, 1975), a loose relationship between μ_w/μ_d and the specific area of the carbonate can be deduced, and shear weakening appears larger with larger grain size (i.e. lower specific surface), while shear hardening is larger with smaller grain size (i.e. larger specific surface).

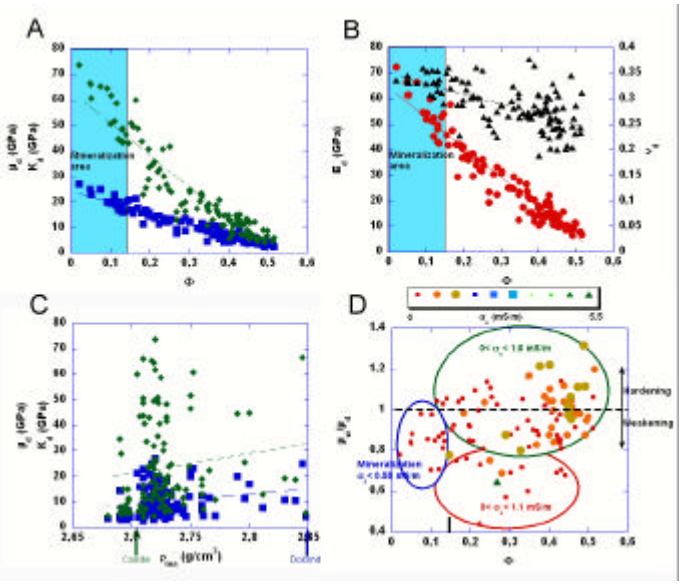

Figure P3- 14. Plots of 113 MC2 core dry μ_d (regression line equation: y= 24- 43x, R^2= 0.92, blue squares) and K_d moduli (regression line equation: y= 64 – 1.2e+0.2x, R^2= 0.89, green diamonds) (A) and E_d (regression line equation: y= 64 – 1.2e+0.2x, R^2= 0.93, red circles) and Poisson coefficient n_d (regression line equation: y= 0.35 – 0.2x, R^2= 0.39, black triangles) (B) vs. porosity F, and μ_d and K_d vs. grain density (C), showing the mineralization area blue shading in (A) and (B), and (C) the calcite (green arrow) and dolomite (blue arrow) zones respectively on the left and on the right of the plot. (D) Crossplot of μ_w/μ_d vs. porosity, the F = 15% value is indicated a black segment on the F axis; in z axis the intensity of the surface conductivity s_s is indicated by 10 degrees between the minimum value (0) and the maximum value (5.5 mS/m). The blue ellipse represents the mineralization zone (F < 15%), the red and green ellipses circle the points where F > 0.15 and, respectively, 0< s_s< 1.1mS/m and 0< s_s< 1.6mS/m. The clay point at 6.1mbgl (s_s= 5.5mS/m, green triangle) plots in the red ellipse.

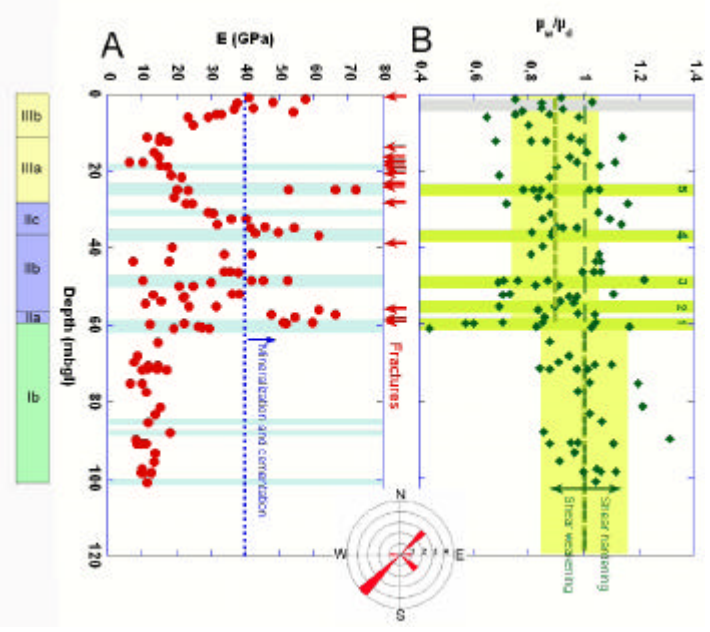

Figure P3- 15. Stratigraphic subunits, mineralization/ cementation and dolomitization zones, and fractures are indicated as on Fig. 6. (A) Dry E vs. depth in 113 MC2 plugs; the blue vertical dotted line indicates E= 40GPa. (B) μ_w/μ_d vs. depth in MC2; the light green long dash vertical line indicates μ_w/μ_d= 1; the thick light green dash vertical segments indicate the data median value of μ_w/μ_d= 0.89 over the 0-60mbgl depth interval, and μ_w/μ_d= 1 over the 60-100mbgl depth interval; the light yellow shaded area around these segments indicates μ_w/μ_d standard deviation around the median value for the corresponding depth intervals. An azimuth frequency rosace of the fracture is provided at the bottom of the fracture arrows column. Frequency.

4.2.3.2 Relations of elastic moduli with porosity and grain density

The three elastic moduli E, μ and K are well approximated as a linear function of porosity and are displaying the mineralization area ($\Phi < 15\%$), where $40GPa < E < 80GPa$ (Fig. P3-14A and P3-14B); those results regarding dry E are incorporated in Fig. P3-15A; we have privileged E compared to μ and K, because E results vs. porosity present both a better coherence and a better amplitude than for μ and K. Moreover, it is clear that ν is not a linear function of porosity (Fig. P3-14B).

The elastic moduli are not good indicators of carbonate types because it does not seem to be possible to decipher a calcite point from a dolomite one (Fig. P3-14C). However, values of elastic moduli μ and K appear generally relatively higher in dolomite than in calcite (see the best fit lines on Fig. P3-14C); this result can be compared with the fact that dolomite displays a Mohs hardness ranging from 3.5 to 5, compared to a value of 3 in calcite.

Fig. P3-15A illustrates dry E of samples vs. depth and must be compared to Fig. P3-9B. It demonstrates the extreme heterogeneity of the carbonate sequence. The mineralized and cemented levels already detected on Fig. P3-6B are confirmed on Fig. P3-15A. A trend toward weaker ($E < 20GPa$) and more porous (see Fig. P3-6B) material is clear below 60mbgl in subunit Ib that corresponds to a slope facies, mostly calcitic, characterized by a relatively high and constant porosity of about 40%.

Fractures have been represented on Fig. P3-15A. The occurrence of fractures is related to two different types of intervals: 1) low porosity, high E values, cementation and mineralization zone (1.75, 24.8, possibly 39.4, and 56.15, 58.8 to 59.1mbgl) on, and 2) high porosity, low E values zone in subunits IIIa and IIc (14.0, 16.3, 17.0, 18.0, 18.8, 20.6, 23.4, 28.3mbgl).

4.3 Dynamic petrophysical properties

4.3.1 Permeability

The permeability values obtained on 112 plugs are listed in Table P3-12. The average permeability is of 725mD (median of 22mD), with lowest and highest values of 0.06 and 26000mD, respectively (standard deviation: 3300mD); (see Table P3-13). The relative accuracy of the permeability measurement is estimated to 2%. Fig. P3-16A illustrates permeability values vs. depth in MC2 well with the occurrence of five mineralized levels that have already been noted (large green arrows) in Fig. P3-6B (i.e. porosity vs. depth), and a cemented level at 2.0m (thin gray arrow). Furthermore, four additional secondary mineralized levels (thin gray arrows) are identified at 8, 17.7, 41.6, and 85.2mbgl. All plugs except 16 of them, were horizontally oriented; the 16 plugs that were vertically oriented do not exhibit striking lower permeability values than the one horizontally oriented, thus implying that the carbonate sequence displays a permeability anisotropy coefficient close to 1. Furthermore, the 16 vertically oriented samples were selected by four groups of close proximity plugs (at 2.0cm depth difference). One 8cm diameter and 12cm long plug vertical permeability was measured 17.96mD at 90.95mbgl (Jacqmin, 2004). This value plots close to the average permeability of the four short vertical plugs that were measured at the near-by depth. The scattering of the permeability data on these plugs demonstrates again the high heterogeneity of the formation.

Fig. P3-16A also shows that the slope facies occurring within the 60-100mbgl depth interval displays heterogeneous permeability values, in clear contrast to their relatively homogeneous porosity. Fractures are also represented on Fig. P3-16A. Naturally, open fractures are not observed on plugs that are used for petrophysical measurements, otherwise, the plugs would be partitioned. The high permeability related to open fractures cannot be therefore quantified by plug measurements and would be only reflected by larger scale on-site measurements.

Depth (mbgl)	Subunit	Porosity (V/V)	rp_{35} (µm)	K (mD)	C (mV/bar)	ζ (mV)	Zone	Texture	Mineral	Porosity type	Diagenesis
1	IIIb	0.199		0.28	0.00	-0.00060	*B*	Grainstone	Calcite		
1.3		0.165		0.78	0.30	0.15280	*B*	Grainstone	Calcite	M	M,O
2.2		0.13		18.26			**A**	Grainstone	Clay		
2.21		0.207		0.87	0.55	0.41103	*B*	Grainstone	Clay		
3.8		0.133		1.01	0.02	0.01155	**A**	Mudstone	Calcite		O
3.95		0.196		3134.24			C	Mudstone	Calcite		
4.5		0.196		8.68	-0.30	-0.13604	*B*	Packstone	Calcite		
5.2		0.29	35.99	345.26	-1.79	-0.96685	C	Wackestone	Calcite		
5.3		0.25		4.87	0.98	0.43854	*B*	Wackestone	Calcite		
6.05		0.184		7.90	0.12	0.05201	*B*	Wackestone	Clay		
6.1		0.269		0.89	0.16	0.11629	*B*	Mudstone	Clay		
8		0.328		0.33	0.00	0.00024	*B*	Wackestone	Calcite		
9.9		0.188		2.19	-0.31	-0.13943	*B*	Mudstone	Calcite		
11.3	IIIa	0.456		51.31	3.14	2.34383	*B*	Grainstone	Calcite	Ia,M	P,S
11.35		0.432		369.01	-44.60	-22.60176	C	Grainstone	Calcite	Ia,M	P,S
12.13		0.442		30.69	5.35	3.98457	C	Grainstone	Calcite		
12.15		0.423		267.13			C	Grainstone	Calcite		
12.25		0.431		82.07			C	Grainstone	Calcite		
12.27		0.407		28.55	1.44	1.07396	C	Grainstone	Calcite		
15.3		0.407		649.29	-176.55	-89.47901	C	Grainstone	Calcite		
16.4		0.42		61.69			C	Grainstone	Calcite		
17.68		0.467	29.93	222.49			C	Grainstone	Calcite		
17.7		0.462		0.14	0.00	0.00069	*B*	Grainstone	Calcite		
18.6		0.383		9.48	-0.47	-0.25574	*B*	Grainstone	Calcite		
18.8		0.383		16.29	0.84	0.37594	C	Grainstone	Calcite		
21.1		0.42		36.29	-15.28	-7.74498	C	Rudstone	Calcite		
21.6		0.373		21.14	-2.38	-3.42474	C	Grainstone	Calcite		
24.86		0.048	0.63	0.06			**A**	Grainstone	Dolomite		
24.88		0.02		0.82	-0.15	-0.06904	**A**	Grainstone	Calcite		
24.9		0.14		2.89	-0.71	-0.31809	**A**	Grainstone	Calcite		
24.95		0.39		0.13	1.07	0.47813	*B*	Grainstone	Calcite		
25		0.35		50.36	-15.72	-7.05881	C	Grainstone	Calcite	Ia	
26.8		0.421		0.30			*B*	Grainstone	Calcite		
27		0.421		82.33			C	Grainstone	Calcite		
28.5	IIc	0.429		1042.34	22.57	10.13288	C	Framestone	Calcite	Fr	
28.6		0.347		355.54	-13.89	-6.23670	C	Framestone	Calcite	Fr	
30.9		0.334		112.26	6.33	85.55402	C	Framestone	Dolomite	Fr	
31.05		0.302		1613.33	-14.17	-6.36037	C	Framestone	Dolomite	Fr	
32.4		0.212		2.51	0.10	0.04688	*B*	Bindstone	Calcite		
32.5		0.196	3.60	4109.36	93.71	50.53694	C	Bindstone	Calcite		
33.8		0.196		2.54	2.25	1.68026	*B*	Framestone	Calcite	Fr,Ia	
34.6		0.154		11235.13	36.18	18.33601	C	Framestone	Calcite	Fr	
34.7		0.102		0.86	-0.18	-0.13230	**A**	Framestone	Calcite	Fr	
34.8		0.159	106.39	25.14	1.34	0.60063	C	Framestone	Calcite	Fr	
35.9		0.13		152.11	9.47	7.05806	**A**	Bindstone	Calcite		
36		0.13		0.22	-0.28	-0.20844	**A**	Bindstone	Calcite		
36.9		0.052		0.88	0.01	0.00458	**A**	Bindstone	Dolomite	M	M,S,Dr
37.05	Unit IIb	0.378		0.74	-0.52	-0.26421	*B*	Wackestone	Calcite		
39.7		0.424		2503.96	79.89	35.86696	C	Grainstone	Calcite		
41.6		0.233		8.21	0.37	0.27214	*B*	Grainstone	Calcite		
41.7		0.18		553.39	-29.59	-13.28296	C	Grainstone	Calcite		
43.48		0.4	25.49	83.85	-2.33	-1.04450	C	Grainstone	Calcite		
43.5		0.513		1401.62			C	Grainstone	Calcite		
46.3		0.255		0.55	0.08	0.04171	*B*	Grainstone	Calcite	M,V	S
46.31		0.236		133.65			C	Grainstone	Calcite	M,V	S
46.4		0.22		11.17			C	Grainstone	Calcite		
48.5		0.401	7.11	39.64			C	Grainstone	Dolomite		
48.55		0.12		10.50	0.41	0.18554	**A**	Wackestone	Dolomite		
48.57		0.12		8.58	-0.56	-0.30054	**A**	Wackestone	Dolomite		
48.6		0.19		7.94	0.50	0.22497	*B*	Wackestone	Dolomite	M	Ie
49		0.28		1.12	0.60	0.44817	*B*	Wackestone	Dolomite	M	Ie
49.79		0.377		13.01	0.13	0.05626	C	Grainstone	Calcite		
49.8		0.28		20349.32	518.92	232.96293	C	Grainstone	Calcite		
52		0.251		60.85			C	Grainstone	Dolomite	M,Fr	M,S

Table P3- 12. MC2 well laboratory porosity, rp_{35}, permeability (1mD= $10^{-15}m^2$), hydraulic to electrical coupling coefficient C, zeta potential ζ measurements, zone, dominant depositional texture (from Jaeggi, in press), mineral (from Tables P3-4 and P3-5), porosity type (Fr: framework, Ia: intraparticle, Ie: interparticle, M: moldic, V: vuggy), and diagenesis (O: ooids, P: peloïds, M: micrite, S: sparite, Dr: druze) from thin-section (not more than +/- 10cm depth difference with plug depth) results collected from Jaeggi, 2006, Mateos et al., in prep., Bonnier, 2005.

Depth (mbgl)	Subunit	Porosity (V/V)	rp_{35} (µm)	K (mD)	C (mV/bar)	ζ (mV)	Zone	Texture	Mineral	Porosity type	Diagenesis
52.02	IIb	0.225	18.00	304.93	-16.30	-7.31742	C	Grainstone	Dolomite	M,Fr	M,S
52.3		0.431		0.20	-0.02	-0.00882	*B*	Grainstone	Calcite		
52.75		0.347		66.97	-1.47	-0.65991	C	Grainstone	Calcite		
52.8		0.429		90.17	-2.43	-1.80763	C	Grainstone	Calcite		
53.8		0.467		1309.45	70.73	52.72530	C	Grainstone	Calcite		
54.4		0.467		7.31	0.58	0.43532	*B*	Grainstone	Calcite		
55.2		0.301		36.79	-3.40	-2.53533	C	Grainstone	Calcite		
55.3		0.301		11.85	-1.45	-0.78433	C	Grainstone	Calcite	V, Fr	S
56.2		0.05		0.25	0.01	0.00591	**A**	Grainstone	Calcite	V, Fr	S
57.2	IIa	0.075		0.24	0.00	-0.00020	**A**	Framestone	Calcite		
57.3		0.17		1156.91			C	Framestone	Calcite		
58		0.091		136.83	17.70	8.97104	**A**	Framestone	Calcite		
59.35		0.115		0.53	-0.40	-0.30113	**A**	Framestone	Dolomite	Ie, M	S
59.4		0.11	7.45	1.13	-0.12	-0.05193	**A**	Framestone	Dolomite	Ie, M	S
59.55		0.1		8.38	-0.47	-0.21090	**A**	Framestone	Dolomite		
59.6		0.29		9.08	-0.06	-0.02913	*B*	Framestone	Dolomite		
59.7		0.35		17.94			C	Framestone	Calcite		
60.5	Ib	0.369		0.75	0.19	0.08306	*B*	Wackestone	Dolomite	Ie,M	M
60.6		0.35	5.00	8.65	-0.21	-0.09328	*B*	Wackestone	Dolomite		
60.9		0.268	4.00	5.04	-1.24	-0.55554	*B*	Wackestone	Dolomite		M
61		0.224		8.39	-0.26	-0.11794	*B*	Wackestone	Dolomite		
64.6		0.447		30.87			C	Rudstone	Calcite		
68.1		0.495	12.00	150.18			C	Packstone	Calcite	Ie,M	S
69.7		0.51		47.63			C	Packstone	Calcite		
70.5		0.423		11.12	0.19	0.08652	C	Grainstone	Calcite		
70.6		0.401		6.85	0.49	0.21804	*B*	Grainstone	Calcite		
71.53		0.395		188.20			C	Grainstone	Calcite		
71.55		0.431		15.25	0.15	0.06824	C	Grainstone	Calcite		
71.65		0.389		31.02	-0.38	-0.17246	C	Floatstone	Calcite		
71.67		0.448		495.34	-40.50	-21.83876	C	Floatstone	Calcite		
75.2		0.449		141.66	-10.49	-5.65872	C	Grainstone	Calcite		
75.3		0.516		0.67	0.00	0.00008	*B*	Grainstone	Calcite		
77.4		0.457		0.32	-0.40	-0.20075	*B*	Grainstone	Calcite		
81.3		0.376	13.48	2043.93			C	Grainstone	Calcite	Ia,M	S
83.15		0.449		23.67			C	Rudstone	Calcite		
85.2		0.389	4.00	0.22	-0.02	-0.00981	*B*	Grainstone	Dolomite		
88.1		0.43		26410.41	-3398.83	-2058.64867	C	Grainstone	Dolomite	Ie,M	M,S
89.9		0.301		102.74	3.96	2.95330	C	Grainstone	Calcite		
90.78		0.419		9.47	-0.01	-0.00432	*B*	Grainstone	Calcite		
90.8		0.486		34.85	0.46	0.20510	C	Grainstone	Calcite		
90.9		0.463		18.33	-2.76	-2.05453	C	Grainstone	Calcite		
90.92		0.473		23.11	1.26	0.93680	C	Grainstone	Calcite		
93.4		0.448		24.80	0.65	0.29158	C	Grainstone	Calcite		
95.7		0.407		30.81	-1.78	-0.79953	C	Packstone	Calcite		
97.6		0.457		104.59	2.15	1.15860	C	Packstone	Calcite		
98.33		0.43		34.27			C	Packstone	Calcite		
98.35		0.44		31.89	8.67	4.39340	C	Packstone	Calcite		
98.45		0.418		58.39	255.45	236.93513	C	Packstone	Calcite		
98.47		0.396		8.21	-0.02	-0.01775	*B*	Packstone	Calcite		
100.91		0.458	6.3	39.79	3.59	1.81728	C	Packstone	Dolomite		

Table P3-12 (Continued)

Measurement	rp_{35}	K (mD)	C (mV/bar)	ζ (mV)
Minimum	0.63	0.06	-3398.83	-2058.65
Average	18.62	724.99	-29.12	-16.47
Median	7.44	22.12	0.00048	0.00024
Maximum	106.39	26410.41	518.92	236.94
Standard deviation	26.48	3293.32	363.15	219.79
Sample population	15	112	92	92

Table P3- 13. MC2 well statistics on rp_{35}, permeability, coupling coefficient and z potential.

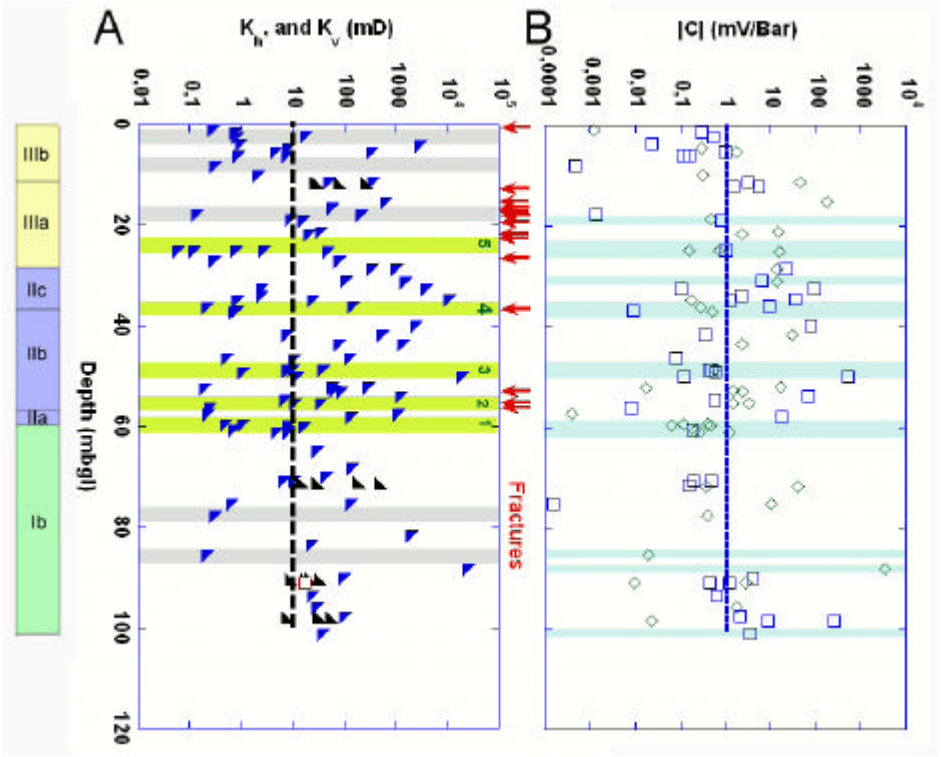

Figure P3-16. Stratigraphic subunits are indicated on the left side. (A) 112 plugs permeability vs. depth in MC2 well. Note that permeability is split between vertical (K_v, black triangle with left oriented spike, red square: 8cm diameter, 12cm long core, Jaqmin, 2004) and horizontal (K_h, blue triangle with right oriented spike) permeability. The black vertical dashed thick line highlights the permeability value of 10 mD, which distinguishes zones B and C on Figure 17A. Green shadows showing five zones of mineralization recognized from porosity below 0.15, an other zone of low porosity (at 2mbgl) is indicated by a grey shading, and when K< 10mD, grey cementation shadings have been added; red arrows indicate fractures recognized from image logs as on Fig. P3-6B. (B) 92 plugs coupling coefficient |C| vs. depth in well MC2. Blue shadings showing zones of dolomitization have been indicated as on Fig. P3-6A. The thick blue dotted vertical line highlights the |C| value of 1mV/bar that predominantly separates zones B and C on Fig. P3-18B.

A crossplot of permeability vs. porosity, with m in z axis, in MC2 well (Fig. P3-17A) indicates that there is no uni-modal relationship between permeability and porosity in this well; a single value of porosity may correspond to a wide range of permeability values. However, distinctive zones are apparent in Fig. P3-17A, to be compared to Fig. P3-10B (i.e. cementation factor vs. porosity) and P3-14D (i.e. μ_w/μ_d vs. porosity with σ_s in z axis): a low porosity/ low permeability/ low cementation factor mineralization zone (zone A) with $0.02< \Phi< 0.15$, $1.5< m< 1.82$, $0.05mD< K< 200mD$, a high porosity/ low permeability/ low cementation factor zone with $\Phi> 0.15$, $2.13< m< 3.38$, $0.1mD< K< 10mD$ (zone B), and a zone C, characterized by a high porosity, a high permeability and a high cementation factor with $\Phi> 0.15$, $2.13< m< 4.32$ and $K> 10mD$. These two last zones are clearly distinguished, because of the permeability gap between them, mostly apparent when Φ is larger than 0.30.

Thus, the multi-modal law between permeability and porosity is more related to the large variety of diagenetic modes of the sediments than to the various depositional environments, because the rocks that comprise the distinctive zones correspond to different depositional environments.

Another plot of K vs. Φ is displayed on Fig. P3-17B, featuring only the 15 plugs on which r_{p35} was measured at the same depth (Table P3-12), and the r_{p35} templates, calculated from Formula (30). Fig. P3-17B clearly demonstrates that the r_{p35} MC2 measurements do not fit with Formula (30).

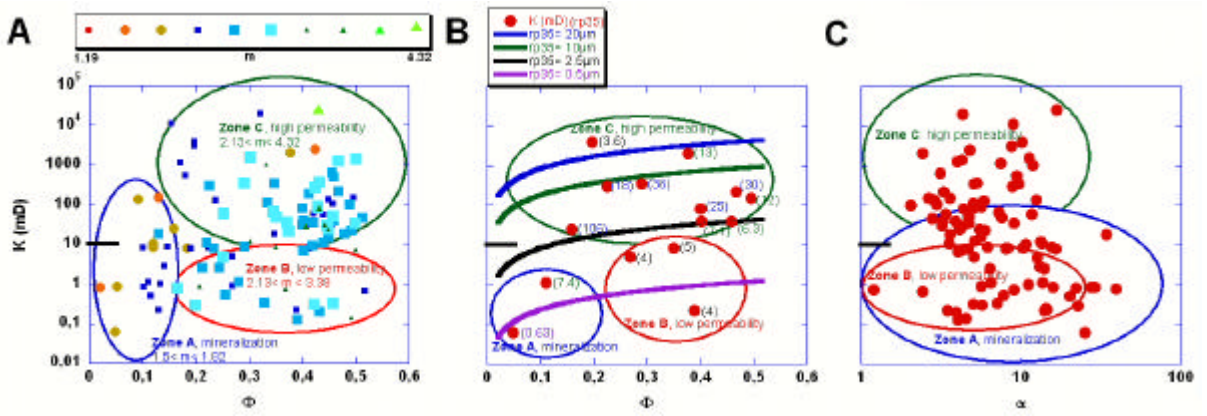

Figure P3- 17. Zone A (defined by F < 15%), zone B (defined by K< 10mD) and zone C (defined by K> 10mD) of MC2 plugs are indicated by respectively blue, red and green color coded ellipses on the three plots. The value K= 10mD is indicated by a thick segment on the K axis (A) Crossplot permeability vs. porosity in MC2 well for 112 plugs. In z axis the intensity of the cementation factor m is indicated by 10 degrees between the minimum value (1.19) and the maximum value (4.32, green triangle located at 88.1mbgl and in zone C on the plot). (B) Crossplot permeability vs. porosity in MC2 well for 15 plugs, on which Hg porosimetry has been performed, thus providing pore-throat apertures (r_{p35}) at a cumulative pore volume equal to 35%; r_{p35} values are indicated on the plot within brackets in µm on the right side of the measurement point with the same color as the closest value constant r_{p35} curve; the curves of constant r_{p35} follow formula (47). (C) Crossplot of permeability vs. electrical tortuosity a=FF in MC2 well for 112 plugs.

Fig. P3-17C demonstrates that it is not possible to relate permeability to either geometrical tortuosity τ (τ= L'/L, where L is the apparent path and L' is the path really followed by the fluid), or to the electrical tortuosity α as expressed by Formula (4). There is no clear trend between permeability and electrical tortuosity (obtained from porosity and formation factor measurements). On this 2D plot, that includes porosity, electrical and permeability measurements, zone A appears as a simple subset of zone B, while zone C is clearly separated from the two other zones.

Several conclusions arise form permeability measurements: 1) the range of permeability measurements is extraordinarily large and covers seven decades; 2) the relationship between permeability and porosity is multi-modal; 3) the rocks can be classified in three distinctive zones of low porosity/ low permeability/ low cementation factor mineralization, high porosity/ low permeability/ low cementation factor, and high porosity/ high permeability/ high cementation factor; 4) four additional cemented levels have been identified in addition to the five levels already revealed by static measurements.

4.3.2 Electrokinetic potential

Results of the coupling coefficient C and ζ potential measurements are listed in Table P3-12. Measurements have been carried out using an equilibrium water of pH ranging between 7.34 and 8.44. ζ is extracted from measured C values through Formula (31); accordingly, there is a linear relationship between ζ and C (ζ(mv)~ 0.6C(mV/bar)), and we will concentrate below on C results only.

C values range from –3400 to 520mV/bar, with a median value close to 0 (Table P3-13). The accuracy of the measurements is of 0.1% for C in relative value, and of 1% in relative value for ζ. This large range of negative to positive C values leads to a representation of the absolute value in a logarithmic scale, or separately in two different series: the negative and the positive values.

The cementation trends based on permeability data and illustrated in Fig. P3-16A are confirmed by |C| (Fig. P3-16B) and porosity (Fig. P3-6B) vs. depth plots, as it could be

expected from a certain linear relationship between Ln |C| and Ln (K) that appears in Fig. P3-18B.

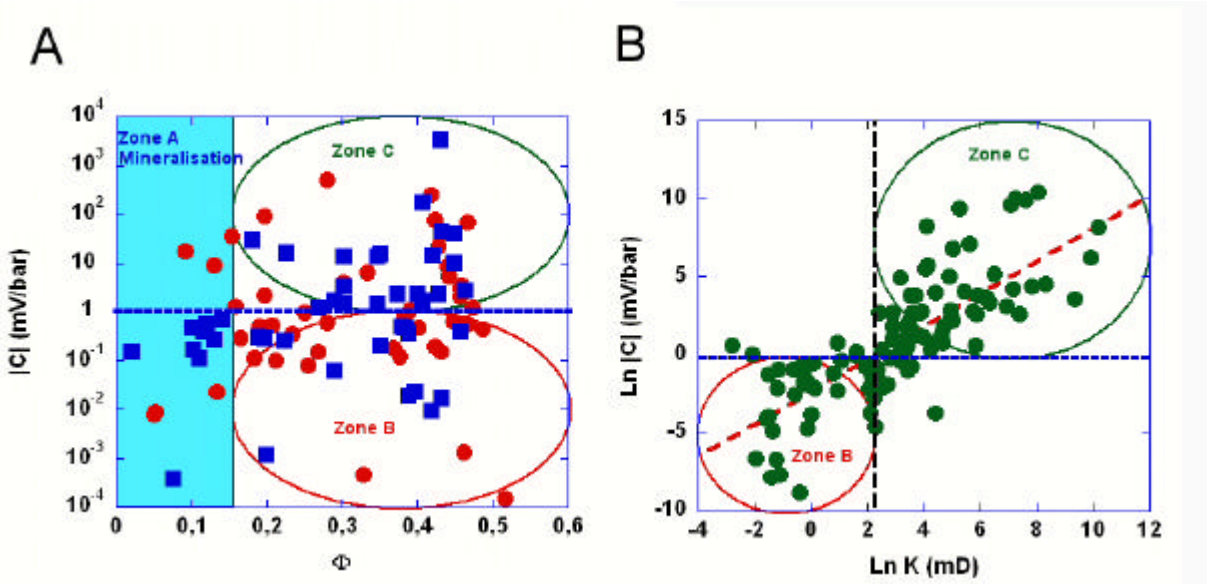

Figure P3- 18. Zone A (defined by Φ < 15%), zone B (defined by K< 10mD, |C|< 1mV/bar) and zone C (defined by K> 10mD, |C|> 1 mV/bar) of MC2 plugs are indicated by color coded rectangle or ellipses on the two plots. The thick dotted blue horizontal line is set at |C|= 1 mV/bar (or Ln|C|= 0). (A) |C| vs. porosity, represented by red circles when C> 0, and by blue squares when C< 0. (B) Ln|C| vs. LnK for 92 MC2 plugs. The thick black vertical line is set at K= 10mD (or LnK= 2.3). The linear regression dashed red line equation is: y= -2.3 + 1.05x, R^2= 0.60.

A crossplot of |C| vs. porosity shows that there is no clear relationship between those two parameters (Fig. P3-18A), in a similar way to what has been demonstrated for permeability and porosity (Fig. P3-17A). |C| values are generally lower than 10mV/bar, with most of the values being in the 0.1 to 10mV/bar range.

A plot of Ln |C| vs. Ln (K) (Fig. P3-18B) provides a linear regression line of equation:

$$y = -2.30 + 1.05x,\ R^2 = 0.60 \quad (35)$$

Equation (35) provides a power relation between |C| and K:

$$|C| = 10K^{1.05} \quad (36)$$

Actually, Equation (36) has an exponent so close to 1, that it is possible to write:

$$|C| \sim 10K \quad (37)$$

Equation (37) provides a correspondence between K and |C|, and in particular for the K=10mD border between zones B and C (|C|= 1mV/bar), allowing to distinguish zones B and C on Fig. P3-18A.

The polynomial regression curve would provide the following equation:

$$y = -2.27 + 0.99x + 0.00091x^2 + \ldots,\ R^2 = 0.60 \quad (38)$$

Equation (38) is very close to Equation (35), and has the same R^2: it is better and more simple to keep a linear regression line in this case.

5 Discussion

Complex, multi-modal, non-linear petrophysical phenomena characterize complex and very heterogeneous rock types such as those studied here, and that are typified by a great variety of facies, and depositional and diagenetic processes. It was therefore necessary to carry out a full array of non destructive static and dynamic petrophysical measurements used on a complete set of plugs collected on well MC2 from bottom to top, to be able to extract a comprehensive and nearly continuous characterization of depositional and diagenetic properties in order to help to better understand the studied Miocene carbonate sequence. These non-destructive

measurements were completed by other destructive measurements made on samples taken close to the plugs, including thin-sections, Hg porosimetry, CEC and spectrometry.

5.1 Mineral composition

The MC2 cores are mostly composed of calcite although minor amounts of clay are reported at the top of the well, at depths ranging from 0 to 12mbgl. It has been demonstrated that this low clay content results from terrigeneous fluxes during the transitional to continental episodes related to the deposition of subunit IIIb (Maria-sube et al., submitted). In other carbonate complexes like the Great Bahama Bank, the Great Barrier Reef, and Tahiti, comparable zones of low clay content have been related either to transitional to continental episodes or to terrigeneous debris carried by turbidites from shallow water or emerged areas to deeper marine zones (Maria-Sube et al., submitted, submitted a).
Calcite has been partially and locally transformed into dolomite or, to a less extent, ankerite, through diagenetic processes. The Ses Sitjoles carbonate sequence therefore differs markedly from the Cabo Blanco outcrops that are extensively dolomitized (Pomar et al. 1996, Pomar and Ward, 1999).

5.2 Texture, diagenesis

The Ses sitjoles Miocene carbonates are characterized by a great textural variety, including depositional mudstone, wackestone, packstone, grainstone, floatstone, rudstone, framestone, and bindstone. The anisotropy is quite low.
Diagenetic effects are conspicuous in this sequence, especially cementation; that includes a large variety of cements. In interganular pores, they mostly include granular fringes, micritic envelopes, and dog tooth cements. In intragranular pores they include drusy mosaic fabrics, equant spares, and dolomite (Fig. P3-5).
Some diagenetic processes also include mineralization characterized by decreasing porosity_ $0.02 < \Phi < 0.15$_ reduced cementation factor_ $1.6 < m < 2.6$), and dolomitization locally up to 80%. Traces of ankerite are conspicuous in some intervals.
Our results demonstrate that the diagenetic processes have a significant impact both on static and even more on the dynamic petrophysical properties of the relevant carbonate rocks, probably more important than the lithological characters that are related to the depositional environments (see below the paragraph on K to Φ relation).
The pore throat diameter (mono, bi, multi) modality implies the occurrence of diagenetic processes supported by the changes in grain density, and trapped porosity.

5.3 Surface conductivity

Surface conductivity is generally low within this carbonate sequence including a low clay content. The total clay or micritic cement content has been estimated to 7% from the ratio between measured σ_s and calculated (from CEC measurement) σ_s. Because of the micritic nature of some low clay sediments in the MC2 carbonate sequence, σ_s is not necessarily negligible.
However, the surface conductivity level σ_s is high enough in the interval filled with brackish water to be generally within the same order of magnitude as the conductivity volumetric term σ_w/F, while it is negligible in the interval filled with sea water. The fact that σ_s is not negligible in the brackish water interval of this low clay carbonate interval has important implications in the log interpretation and will be discussed in Maria-Sube et al., in prep.
CEC and σ_s are related with a low degree of linearity.

5.4 F to F relation

In such a carbonate sequence displaying a large range of porosity (from 2 to 52%) over a short depth interval, the cementation factor m (even if considered as a general trend and defined as the slope of a regression curve on Fig. P3-10A, and not as a local computation from Formula (11)) is not a constant, as previously observed in carbonates (see e.g. , Archie, 1942; Sen, 1997). It is however the current practice in well log interpretation for the oil and gas industry evaluation of water saturation to consider that m is constant over the interval of evaluation. In first approximation, when the core measurements are not available, it is possible to consider in MC2 that, when Φ is lower than 0.15, m values are close to 1.32, while when Φ is higher than 0.15, m values are close to 2.56. m displays a tendency to increase with porosity, in clear contrast with the "Shell" industrial empirical formula. Formula (10) is only an approximation over a limited range of porosity in this carbonate sequence. Fig. P3-17A demonstrates that in this carbonate sequence, the name of "cementation factor" traditionally given to m is a misnomer, since for zones B and C of higher than 0.15 porosity: 1) m does not separate zones of high and low permeability; 2) m can be higher for zone of high permeability than it is for zones of low permeability.

The coefficient a is measured with a relatively good accuracy. In siliclastic sequences over the same range of depth interval, the porosity range would be much reduced (typically a porosity range of 10 or 20% instead of 50%), and consequently, even though m could be relatively constant over that interval, the accuracy for measuring both m and a is not as good; this could provide an explanation for the large range of empirically determined values provided for those parameters in the oil and gas industry research documents.

m measurements are routine laboratory measurements, but field continuous measurements would be also useful for carbonates. The only existing step in this direction is through the use of NMR logging tool recording (Sen, 1997), which allows an analysis of the pore size distribution (Serra and Serra, 2000).

5.5 Wetting

The MC2 carbonate plugs measurements do not follow the Gassmann's assumption assuming that rock frame properties are not altered by the saturating fluid. The matrix frame is weakened by the carbonate equilibrium water used to saturate the samples during tests. There is a loose relationship between the water weakening and the specific area of the carbonate grains, related to surface conductivity.

This phenomenon, already noticed in the chalk reservoirs of the Southern North Sea (Risnes et al., 2003), has an important application in carbonate oil and gas reservoirs, where water injection is an important secondary recovery method. The weakening influence of water on the rock frame may lead to general reservoir frame crushing, consequent loss of porosity and permeability, and therefore decrease of hydrocarbon production.

5.6 Mechanical moduli characteristics

The mechanical strength of the samples is generally lower in the slope facies that comprises Unit I. This can be explained by the detrital nature of the slope facies, as opposed to the constructed nature of the overlaying facies.

The three elastic mechanical moduli E, μ and K are conversely proportional to porosity. This linearity trend is very unusual in carbonate rocks. In contrast, the Poisson coefficient ν is not a linear function of porosity. There is no linearity trend between the elastic moduli and the grain density.

In contrast to earlier conclusions, neither the elastic moduli, nor the V_p/V_s ratio, Pickett, (1963), are good indicators of carbonate types.

5.7 Fractures

The occurrence of fractures is observed in two distinct domains of the MC2 well (Table P3-7, Fig. P3-15A): low porosity, high E values, cementation and mineralization zone (1.75, 24.8, possibly 39.4, and 56.15, 58.8 to 59.1mbgl); and 2) high porosity, low E values zone in subunits IIIa and IIc (14.0, 16.3, 17.0, 18.0, 18.8, 20.6, 23.4, 28.3mbgl). No fracture has been detected in subunit Ib of low E value, while 57% of the fractures are located in subunit IIIa. Most of the fractures are oriented NE-SW (Fig. P3-15), parallel to the general fault direction in the southeastern part of Majorca (Jenkins et al. 1990).

Well	Unit/ subunit	Log depth (mbgl)	Dip magnitude (0-90°)	Dip orientation	Aperture	Planarity quality
MC8	Subunit IIIb	2.0	80	NE	Closed	Average
	Subunit IIIa	16.1	0	-	Closed	Average
	Subunit IIb	48.17	5	W	Closed	Good
MC9	Subunit IIIa	12.8	30	W	Closed	Good
	Subunit IIIa	13.1	30	NE	Closed	Good
	Subunit IIb	47.82	0	-	Closed	Average
	Unit I	61.85	70	E	Closed	Average
	Unit I	65.0	80	E	Closed	Average
MC10	Subunit IIIb	1.2	10	S	Closed	Average
	Subunit IIIa	17.4	30	NW	Closed	Average
	Subunit IIIa	19.9	20	E	Closed	Average
MC11	Subunit IIIb	3.0	0	-	Closed	Average
	Subunit IIIa	17.7	10	SE	Closed	Average
	Subunit IIIa	19.15	30	S	Closed	Average
	Subunit IIc	30.1	45	SW	Closed	Average
	Subunit IIc	33.4	20	S	Closed	Good

Table P3- 14. Identification and characterization (dip magnitude, orientation, aperture, and planarity quality) of fractures by image logs on MC8, MC9, MC10 and MC11 wells.

For comparison, the borehole images of wells MC8, MC9, MC10, and MC11, adjacent to MC2, were also analyzed for fractures (Table P3-14). In those wells, only 4 fractures in average were detected, compared to 14 in MC2; no open fracture has been observed, compared to three in MC2; only 19% of the fractures display a NE-SW orientation, compared to 57% in MC2. In contrast, in wells MC8 to MC11 and similarly to well MC2, a great number (44%) of the fractures are located in subunit IIIa and more particularly in the 13 to 19mbgl interval. Two fractures are located in a mineralized zone (see Table P3-17), three fractures are located in the low porosity, high E, high m top part (0 to 3mbgl) of subunit IIIb (compared to one in MC2), and very few fractures occur in Unit I very close to the top of it.

Fractures may be caused by a variety of causes: tectonic stress (tension, compression or torsion), expansion of rocks upon release of overburden load (i.e. erosion), unequal pressure, excessive pressure and compression, changes of temperature (i.e. dessication), leaching in the plane of stratification (e.g. schistosity), and by drilling (Serra and Serra, 2003). The most obvious cause of fractures in the Ses Sitjoles area is seemingly related to be formation of the Campos Basin by its extension during Early Pleistocene, associated to NE-SW faults (Jenkins et al., 1990), and creating both tensional and shear stresses.

Fractures appear predominantly in brittle rocks, hence in consolidated formations. The rock in which fractures are the most abundant are, in decreasing order: quartzites, dolostones, quartz, calcite cemented sandstone, and limestones. Very often, fractures disappear when entering formations which are more plastic (e.g. clays or halite), or friable (e.g. sands), (Serra and

Serra, 2003). Therefore, the occurrence of fractures in the low porosity, high E, dolomitized, mineralized or cemented zones of Ses Sitjoles wells, and the absence of fracture in the high porosity, low E, calcite zone of Unit I, are not surprising. In contrast, the occurrence of fractures in the high porosity, low E, calcite zone of subunits IIc and IIIa are more difficult to explain. An explanation to this last question is provided by Fig. P3-15B: contrarily to subunit Ib which displays a median $\mu_w/\mu_d = 1$, with a standard deviation of 0.15, subunits IIc and IIIa present a lower median shear modulus ratio $\mu_w/\mu_d = 0.89$, with a standard deviation of 0.14, with more frequent and deeper incursions in the $\mu_w/\mu_d < 1$ domain of shear weakening. This would mean that at the time of fracturation: 1) the rocks of subunits IIc and IIIa were wet; 2) the cause of subunits IIc and IIIa fractures was either brittleness of the rocks in the low porosity, high E mineralized or cemented zones, or shear stress in the high porosity low E zones (Fig. P3-15A).

5.8 K to F relation

It was not possible to relate permeability to electrical tortuosity α. This result implies that the electrical current does not follow the same path as the hydraulic flow.

The r_{p35} method is interesting because based on the dynamic process of mercury injection in the measurement cell. However, the Aguilera and Aguilera's, 2002, K to Φ relation template method did not give satisfactory r_{p35} results on the Ses Sitjoles plugs. We explain this result by the fact that the Aguilera and Aguilera's, 2002 empirical template does not apply to the Ses Sitjoles plugs, possibly because the samples on which it was established were too much different in terms of texture and diagenetic features; another reason could be that the Hg porosimetry maximum pressure of 4000bar (lower to that value at 35% cumulative volume, but nevertheless very high) on the generally unconsolidated MC2 samples is, at least in some cases, destructive of the pore system.

In contrast, we have privileged a method of texture and cementation classification inspired from the Lønøy's, 2006 method, with added control of the static and dynamic petrophysical parameters.

Zone	Porosity (%)	m	F	α	Dry E (GPa)	rp_{35} (µm)	Dry K (GPa)	Dry µ (GPa)	Permeability K (mD)	Electrokinetic potential |C| (mV/bar)
A cementation	$F <$ **15**	1.5< m< 3	45< F< 1100	0.9< α< 165	40< E< 80	rp_{35} < 7.45	40< K< 80	15< µ< 30	0.01< K< 200	0.00015<|C|< 60
B	15< Φ< 52	2.13< m< 3.39	3.2< F< 45	0.5< α< 23.5	E< 42	4< rp_{35} <5	K< 42	µ< 20	0.1< **K< 10**	0.00015< |C|< 1
C	15< Φ< 52	2.13< m< 4.32	3.2< F< 45	0.5< α< 23.5	E< 42	3.6< rp_{35} < 106.39	K< 42	µ< 20	**10< K**< 10^5	1< |C|< 10^4

Table P3- 15. MC2 sediments characterisation in three zones, according to their static and dynamic petrophysical properties.

We have classified the sediments in three separate zones (Table P3-15) of low porosity/ low permeability/ low cementation factor/ high mechanical strength/ high formation factor/ high electrical tortuosity/ low r_{p35} (zone A, or mineralization zone), high porosity/ low permeability/ low cementation factor/ low mechanical strength/ low formation factor/ low electrical tortuosity zone/ average r_{p35} (zone B), high porosity/ high permeability/ high cementation factor/ low mechanical strength/ low formation factor/ low electrical tortuosity zone/ high r_{p35} (zone C). Zone A is clearly distinguished by both static (Φ, m, F, mechanical acoustic moduli) and dynamic (permeability) petrophysical properties; in particular, $\Phi < 0.15$ clearly identifies the levels belonging to zone A. Zones B and C are not distinguished by their static petrophysical properties, but only by their dynamic petrophysical properties, the boundary being either K= 10mD, or |C|= 1mV/bar. r_{p35} has a tendency to be lower in Zone A, average in zone B, and higher in zone C, but there are no clear boundaries. This confirms that

this interesting parameter is not powerful enough for the Ses Sitjoles carbonate rocks. The full sediments classification was therefore only possible with the complete set of static and dynamic petrophysical measurements. Zone C displays the best hydraulic transmissivity quality. r_{p35} is not a good delimiter for any zone (Fig. P3-17B, Table P3-14).

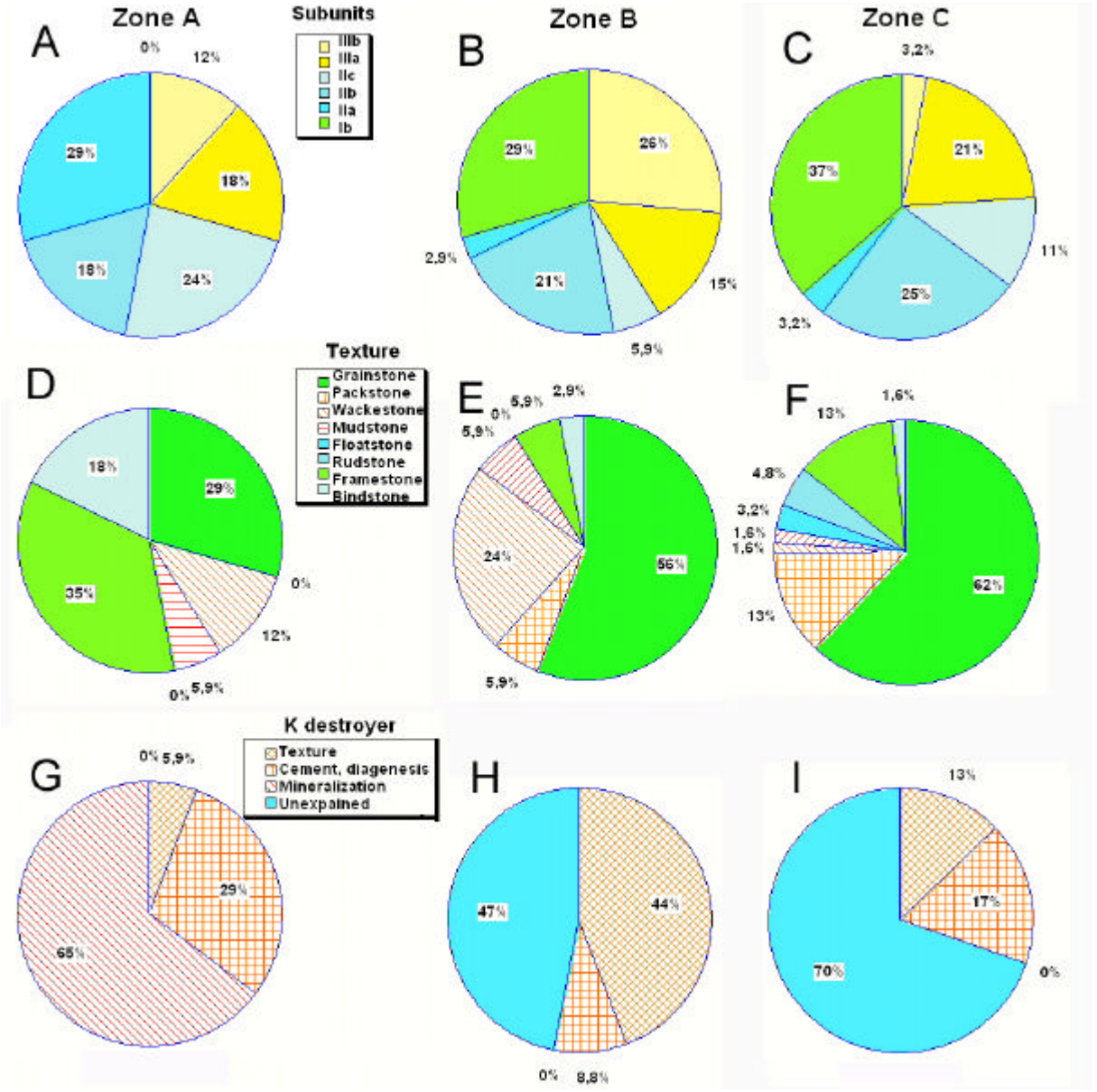

Figure P3- 19. This figure presents subunits, texture and permeability destroyer statistics on zones A, B, and C respectively; zones A, B and C are defined on Figure P3-17A. Percentages of occurrences of subunits Ib (green color code), IIa, IIb,, IIc (blue color codings), IIIa, and IIIb (yellow color codings) for zone A 17 plugs (A), zone B 34 plugs (B), and zone C 63 plugs (C). Percentages of occurrences of texture type for zone A 17 plugs (D), zone B 34 plugs (E) and zone C 63 plugs (F); permeability favorable textures (grainstone, framestone) are green color coded, permeability unfavorable textures (packstone, wackestone, mudstone) are different red pattern color coded, permeability indifferent textures (floatstone, rudtone, bindstone) are blue color coded. Percentages of occurrences of permeability destroyers (texture, cement/ diagenesis, mineralization, red patterns, unexplained, blue) for zone A 17 plugs (G), zone B 34 plugs (H) and zone C 63 plugs (I); in zone B, if no permeability destroyer was found (unexplained), this means that there was absence of thin section data within +/- 10cm depth of the plug; in zone C, if no permeability destroyer was found (unexplained), it means that there was either absence of thin section data within +/- 10cm depth of the plug, or there was thin section data, but this data did not exhibit any permeability destroyer.

It is also possible to characterize the three zones by their sedimentological properties (Table P3-12 and Fig. P3-19A to P3-19C): Zone A is found mostly in Unit II, and also in Unit III, it is completely absent from Unit I. Zone B is found mostly in Unit I and is also present in Units II and III. Zone C is found mostly in subunits Ib, IIb and IIc; and is also found in Unit III.
Bad transmissivity (zones B and A) is caused by: 1) textural factors: *clay, mudstone, wackestone, packstone* in Unit IIIb (Table P3-5) from 0 to 12mbgl; *non connected porosity* is also observed from 0 to 6mbgl (Fig. P3-5K), for instance, at 2.07mbgl, non connected porosity is equal to 7.67% compared to a total porosity of 15.44% (Mateos et al., in prep.), these two reasons are causing low effective porosity and permeability; 2) *paleo or modern standstills of water-table: mineralization often associated to dolomitic mud cement* (Fig. P3-5J and P3-5A), inducing low porosity and cementation factor, high mechanical hardness, bimodal (or multi-modal) pore throat diameter distribution, hence low permeability; 3) *diagenesis and creation of different types of cements*: micrite (Fig. P3-5F), sparite (Fig. P3-5I), drusy spar (Fig. P3-5H), the cementation factor is high with little effect on porosity, but inducing a decrease in permeability. This is summarized in Fig. P3-19D, P3-19E, P3-19G and P3-19H, where unfavorable textural or diagenesis (or both) features are predominant in zones A and B sediments.
Good transmissivity (zone C) is associated to: 1) *detrital deposition* (Unit I, Fig. P3-5D); 2) *grainstone* (Fig. P3-5B) and *framestone* textures (Unit II, Fig. P3-5C), implying high porosity and permeability; 3) Absence or low degree of cementation. This is summarized in Fig. P3-19F and P3-19I: depositional textural or diagenesis permeability destroyers are mostly absent from zone C sediments.

5.9 Zones of mineralization

Five mineralized intervals have been identified based on laboratory measurements at 25, 36, 48, 56 and 60mbgl; the present day water table is at 36.4mbgl. They exhibit low porosity ($\Phi < 15\%$), low cementation factor ($1.6 < m < 2.6$), high mechanical moduli E, K, μ, low permeability, and correspond generally to a dolomitization. At 2.20mbgl there is a cementation level where, in contrast to what has been observed in the mineralization levels, m and Φ vary in opposite ways; it corresponds to oolites, and will not be considered in this paragraph. In MC2, dolomitization is often accompanied by reduced porosity; this is unusual for dolomitization, since dolomite is denser than calcite, an increased porosity is generally observed. The dolomitization-low porosity association is therefore an evidence that carbonate precipitation occurs in the considered zones. The horizontal correlation of these mineralization intervals over at least eight other wells of the Ses Sitjoles area demonstrates that the mineralization of those intervals corresponds to paleo or present standstills of the watertable at the vadose-phreatic interface. The daily as well as seasonal tide movements of the water-table measured by pressure gauge measurements in Ses Sitjoles wells have demonstrated that even 6km inland, a tide amplitude of 30cm, and a seasonal amplitude of more than a meter, are noticed and may induce carbonate precipitation or dolomitization processes if the water contains enough magnesium concentration.
Those post-depositional mineralizations appear to have more impact on the porosity average values than the lithological changes. The more stable porosity range below 60mbgl is seemingly related to the lack of any mineralized level in that depth interval.
Accurate correlations, between all logs on one hand, and between MC2 core measurements and logs on the other hand, allowed the identification of mineralized intervals 1 to 4 on the acoustic amplitude image logs (Fig. P3-20A to P3-20D); the mineralized interval 5 could not be observed on acoustic images because it occurs in the vadose zone.

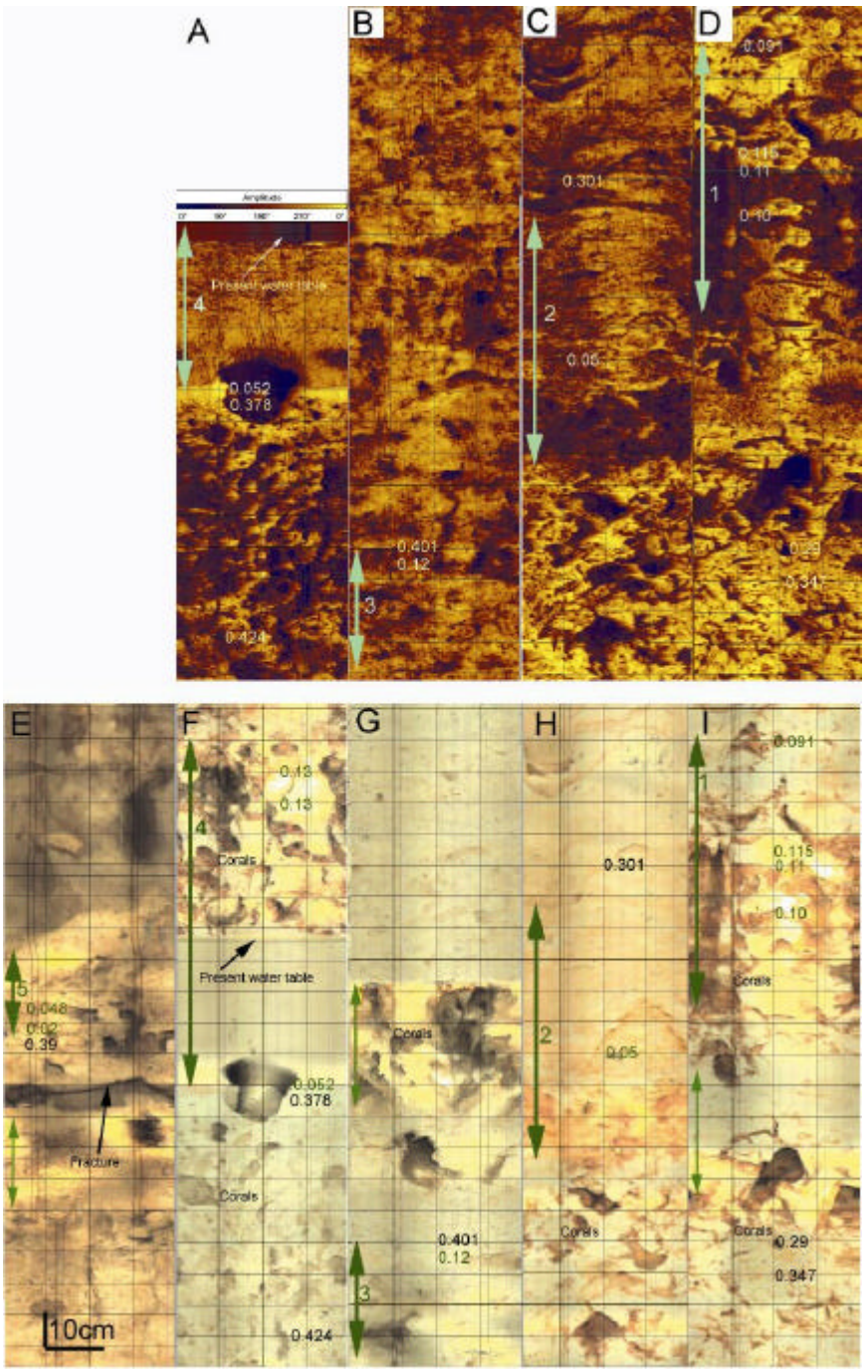

Figure P3- 20. MC2 Acoustic amplitude (A to D) and optical (E to I) image logging showing the five zones of mineralization; porosity values, measured on plugs, are indicated in green when below 0.15, and in black when above 0.15, at their corresponding depth; vertical green arrows are underlining zones of mineralizations, a zone identification number corresponding to the number indicated on Fig. 16C is indicated where it applies; (E) depth 23.6-25.7mbgl, zone 5; (A and F) depth 35.7-37.8mbgl, zone 4, corresponding to the present day water table; (B and G) depth 42.5-44.6mbgl, zone 3; (C and H) depth 53.9-56.0mbgl, zone 2; (D and I) depth 56.1-58.2mbgl, zone 1.

For all identified mineralized intervals, and for the plugs located in the same area, the wet bulk density (calculated from Formula (22)), the wet rock acoustic impedance and the wet rock acoustic reflection coefficient have been calculated (Table P3-16). For less than 0.15 porosity plugs, the wet rock acoustic impedance is higher than 13Mkg/m^2/s, and the reflection coefficient is more than 0.8, while for more than 0.15 porosity plugs, the wet rock acoustic impedance is lower than 13Mkg/m^2/s and the reflection coefficient is less than 0.8, implying

that acoustic amplitude image log is a good identifier of tight zones (see Fig. P3-21A and P3-21B).

Mineralization zone number	Core depth (mbgl)	Log depth (mbgl)	PHIT (V/V)	Wet bulk density (g/cm^3)	wet V_p (m/s)	Z_R (10^6 $Kg/m^2/s$)	R_A
5	24.86	24.58	0.048				
5	24.88	24.6	0.02				
5	24.9	24.62	0.014				
4	36.9	36.89	0.052	2.660	5996.33	15.95	0.82
3	48.5	46.5	0.401	2.106	2639.17	5.56	0.57
3	48.55	46.55	0.12	2.584	5309.36	13.71	0.80
3	48.57	46.57	0.12	2.575	5390.62	13.88	0.80
2	56.2	55.3	0.05	2.624	6195.48	16.26	0.83
2	57.2	56.3	0.075	2.588	6260.40	16.20	0.83
1	58	56.3	0.091	2.562	6075.24	15.56	0.82
1	59.35	57.65	0.115	2.526	5926.28	14.97	0.81
1	59.4	57.7	0.11	2.557	5822.63	14.89	0.81
1	59.55	57.85	0.1	2.539	5606.08	14.23	0.80
1	59.6	57.9	0.29	2.249	3970.63	8.93	0.71
1	59.7	58	0.347	2.156	3320.29	7.16	0.65

Table P3- 16. Mineralization zones on MC2 borehole. Rock acoustic impedance Z_R, and acoustic amplitude reflection coffeficient R_A, calculated from measured plug values of wet V_p, wet bulk density, and porosity.

Similarly to what was done for acoustic amplitude image logs, optical image logs have been correlated to the available core porosity measurements (Fig P3-20E to P3-20I) and led to the identification of all the mineralized intervals. All these intervals display a yellow color on the optical image logs, corresponding to a good optical reflection (these low porosity carbonates offer after drilling a smooth, mirror-like, borehole surface). The optical imagery appears therefore as a quite efficient tool for identifying mineralized intervals in wells where no plug porosity measurement is available. Correlations between those intervals was possible for several wells drilled in the Ses Sitjoles area (Table P3-17).

Well/ Mineralization nbr.	MC1 (mbgl)	**MC2 (mbgl)**	MC3 (mbgl)	MC4 (mbgl)	MC5 (mbgl)	MC6 (mbgl)	MC7 (mbgl)	MC8 (mbgl)	MC9 (mbgl)	MC10 (mbgl)	MC11 (mbgl)	S17 (mbgl)
5	N.A.	*24.3-24.62*	-	-	25.6-26.8	N.A.	27.0-28.0	-	24.0-24.7	24.16-24.71	24.3-25.0	N.A.
4	N.A.	*34.6-36.9*	38.2-39.2	N.A.	*38.4-39.4*	N.A.	36.9-39.8	37.2-37.6	36.8-37.8	36.43-38.91	36.2-37.1	N.A.
3	N.A.	*45.7-46.9*	50.8-51.8	N.A.	43.2-47.0	N.A.	48.0-49.1	47.5-48.6	45.6-47.8	47.91-49.61	-	N.A.
2	54.8-55.7	*54.8-55.9*	59.7-*62.1*	N.A.	57.0-57.8	N.A.	52.8-54.6	54.0-55.8	55.2-57.2	55.11-57.01	55.8-58.7	N.A.
1	58.6-59.7	*57.8-58.2*	*65.2-*66.4	N.A.	*58.4-59.6*	N.A.	56.4-58.5	58.4-60.4	58.0-59.4	57.51-59.01	-	N.A.
Well head elevation (masl)	37.77	**38.32**	41.02	40.37	40.34	40.38	40.38	38.32	38.32	38.32	38.32	41.25

Table P3- 17. Ses Sitjoles boreholes mineralization zones, seen on borehole images. Well head elevations allow to make depth corrections for Fig. 21, with MC2 well as reference. Italics: zones confirmed by porosity measurements, MC3 and MC5 porosity measurements made by Jaeggi, 2006.

In wells MC3 and MC5, the occurrence of some mineralized intervals could be checked based on plug porosity measurements (Jaeggi, 2006), although those measurements did not allow to check all mineralized intervals because they were not carried out in a sufficient number compared to the MC2 well (40 vs. 116).

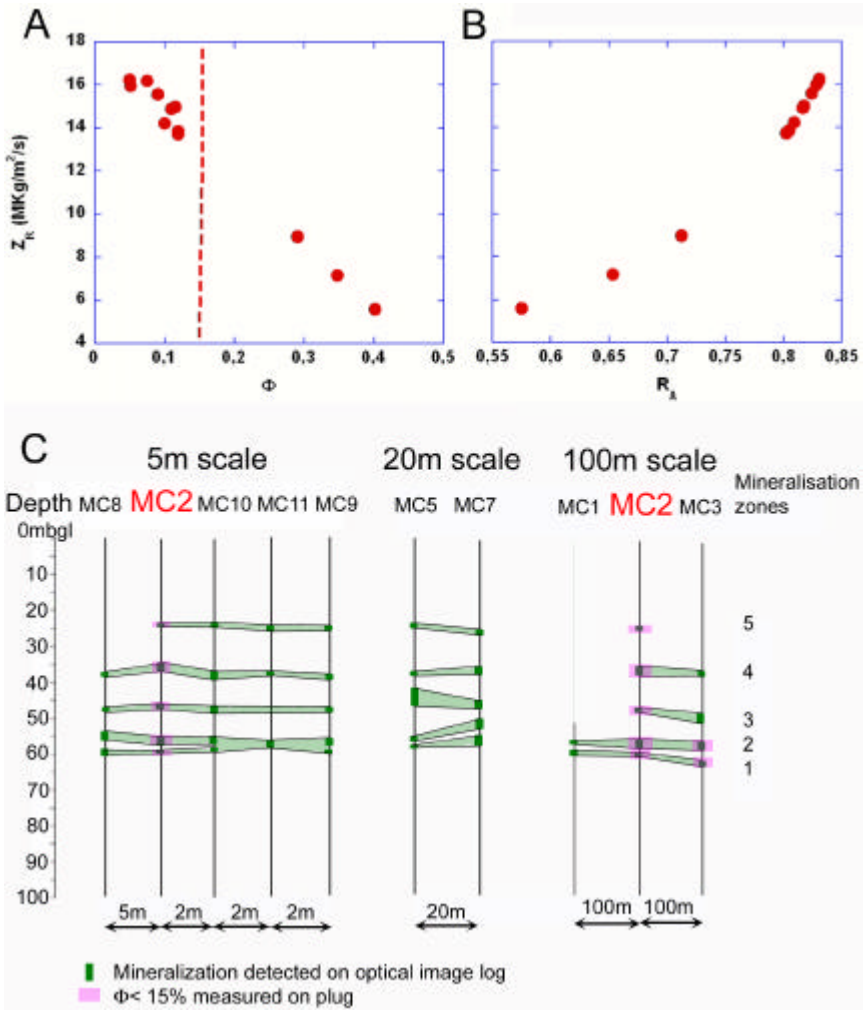

Figure P3- 21. (A) MC2 wet rock acoustic impedance $Z_R = r_b V_p$ (from Table 11) vs. porosity; the dashed vertical red line indicates F = 15%. (B) MC2 wet rock acoustic impedance vs. wet rock acoustic reflection coefficient $R_A = (Z_R - Z_F)/(Z_R + Z_F)$ (from Table 11). (C) 5m, 20m and 100m scale correlation of the five mineralization zones in wells of the Ses Sitjoles site (from Table 12); green thick lines indicate mineralization seen on optical image log, pink rectangular shading indicates that F < 15% has been measured on plugs; MC1 images are available only below 52.0mbgl (this well has been lined in its upper part), MC8 displays a spiky caliper log around 25m explaining that this uneven hole prevents from finding a reflective zone at that depth on the optical borehole image log.

The occurrence and horizontal planarity of the five mineralized intervals throughout the Ses Sitjoles area has been checked after making depth corrections for well head elevation (Fig. 21C), implying that the occurrence of those intervals is related to present (at 36.4mbgl) and paleo Mean Sea Level (MSL) standstills. This planarity is almost perfect at the 5m scale and good at the 100m scale, while it is more difficult to check at the 20m scale (Fig. P3-21C), probably as a consequence of the occurrence of more karstic zones in the 20m scale alignment of the Ses Sitjoles area. It seems likely that some mineralized intervals might not have been detected on the optical image log.

Several sea-level standstills are documented as epiphreatic calcite cements in Majorca caves (Gines and Gines, 1995). The youngest record of Upper Pleistocene to Holocene sea-level changes is documented in infralittoral sedimentary prisms, which have been recorded on the continental shelf (Hernandez-Molina et al., 1994).

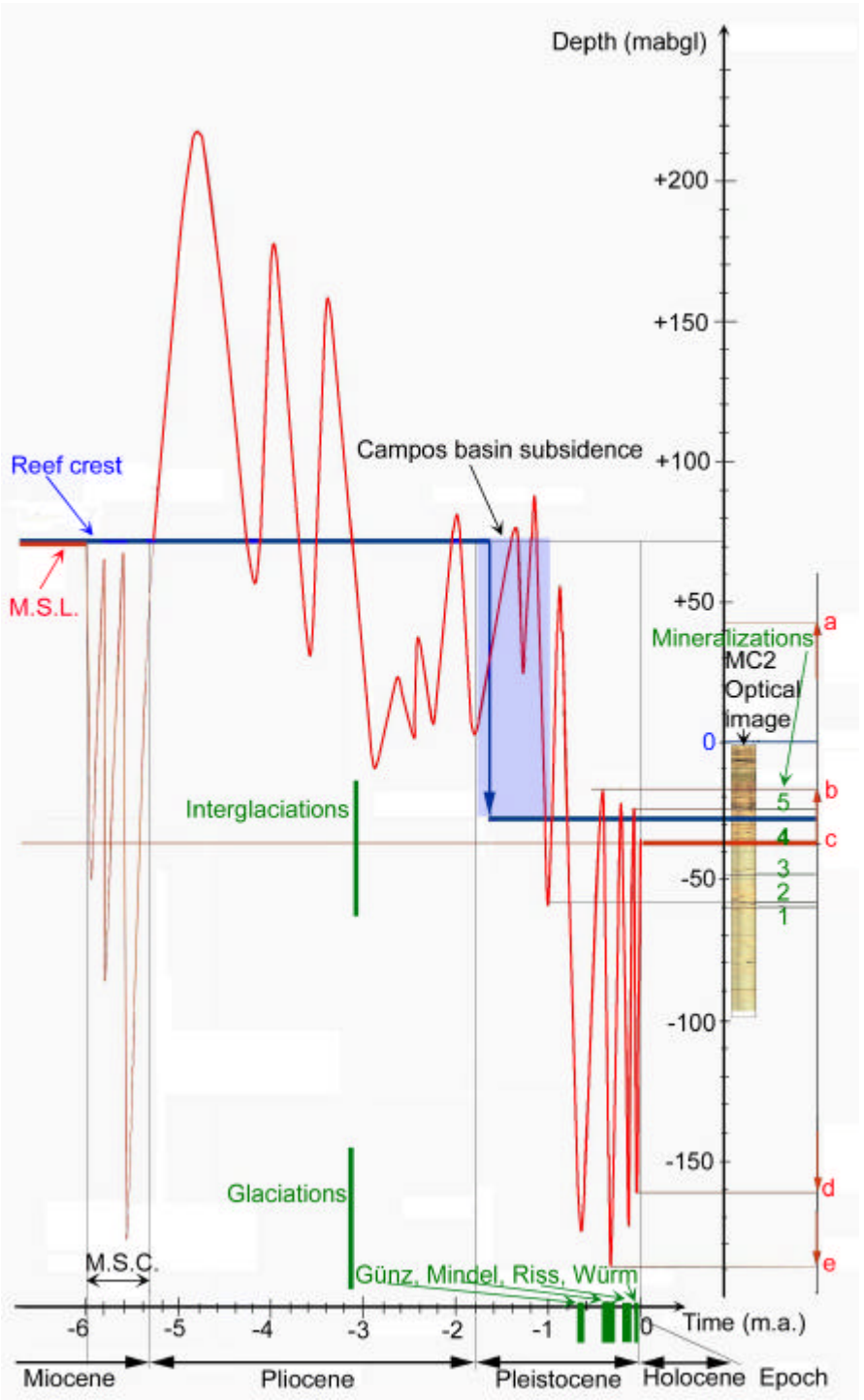

Figure P3- 22. This figure summarizes the vertical tectonic movement of the reef crest (blue thick line), and the vertical movement of the mean sea level (M.S.L., red curve), adapted from the eustatic curve of Wornardt and Vail, 1991; the relative thickness of this curve reflects the degree of confidence in the curve) from end of Miocene time to present. The MC2 borehole optical image column, with the five mineralization zones is represented next to a vertical black depth line; mineralizations are thus directly compared in depth with sea level standstills (minima or maxima of M.S.L. curve). A black horizontal timeline allows to represent the various geological events: M.S.C., Campos Basin creation (within the time window indicated by the blue shaded rectangle), Quaternary glaciations and interglaciations, vs. time. Remarkable sea levels are referenced on the rightmost column: (a) if total melting of present day glaciers occurred; (b) maximum during previous Quaternary glacial; (c) today water table, close to the M.S.L.; (d) last glacial maximum (-20,000 years, Würm); (e) Mindel glacial maximum.

The timing of the formation of the mineralized intervals based on the reconstruction of the fluctuations of the water table must take into account the sea-level fluctuations and the tectonic events that occurred between the Miocene and the modern times (see Fig. P3-22). It has been demonstrated that the subsidence of the Campos Basin has been of 100m since its creation during early to mid Pleistocene times (Jenkyns et al., 1990, Pomar et al., 1996, Maria-Sube et al., submitted a). The MSL decreased for more than 100m since Miocene times as shown by the height of the western part of the Llucmajor platform and in agreement with the Haq et al. 's curve (1987). Significant sea-level changes have affected the MSL-water table since Miocene times. During the Messinian Salinity Crisis (MSC) that occurred between 5.96 and 5.33m.a., an abrupt sea-level drop of about 100m was observed as a consequence of the interruption of communication between the Atlantic and the Mediterranean (Hsü et al., 1973, 1977; Krijgsman et al., 1999; Duggen et al., 2003). In the studied area, the end of this period is characterized by the deposition of the subunit IIIb that has been referred-to as the Terminal Carbonate complex (TCC; Maria-Sube et al., submitted). Sea-level variations from Pliocene to Holocene times are best described by the Wornardt and Vail (1991) eustatic sea-level curve. During Quaternary times, the amplitude of sea-level fluctuations driven by glacial-interglacial cycles has been in the order of 100-120m; among the successive glacial events (Günz, 680 to 620k.a. b.p., Mindel, 455 to 300k.a. b.p., Riss, 200 to 130k.a. b.p., and Würm, 110 to -12k.a. b.p.), the Mindel glacial stage is thought to have coincided with a maximum sea-level drop of 150m, while during the Last Glacial Maximum (23 to 26k.a. b.p.) the sea-level drop was at least of 120m (Fairbanks, 1989; Camoin et al., 2001; Yokoyama et al., 2001).

Standstills are likely to occur during maxima or minima of the eustatic curve, i.e. when the second derivative of the curve is nil.

Keeping in mind the relative uncertainties associated to the abolute depth amplitudes of the MSL curve displayed on Fig. P3-22, the following conclusions are drawn from the comparison between time variations of reef crest and MSL levels: 1) there are probably four mineralization levels, corresponding to the Pleistocene glaciations maxima, to be found deeper in MC2, somewhere between 150 and 200mbgl in the distal slope or the Off reef open shelf (as referenced by Pomar et al., 1996) facies, and exploring this (by drilling deeper boreholes and surveying them) would be a way to measure the paleo MSL associated with those glaciations; 2) mineralization 5 could correspond to a previous interglacial MSL highstand, possibly the last one, (i.e. Riss-Würm); 3) mineralizations 1 and 2 could correspond to the −1m.a. lowstand. 4) Our assumption made during fracture discussion that the fractures observed in MC2 well were created during the Campos Basin extension, and that subunits IIc and IIIa sediments were at that time under water, is verified on Fig. P3-22.

Also some questions are raised: 1) Is mineralization 3 intermediate Pleistocene or even Pliocene glaciation MSL standstill? 2) where are the two other Pleistocene interglaciation highstands? 3) Are there other MSC water table standstill to be found even deeper? To answer these questions, an accurate dating of the mineralization levels would be necessary.

5.10 Heterogeneity

The extreme heterogeneity of the carbonate sequence is illustrated on Tables P3-11 and P3-13 (i.e. large measurement standard deviations), and Fig. P3-6, P3-9A and P3-9B, P3-12, P3-15, P3-16, displaying important variations of the different measured parameters vs. depth.

The range of measured porosities is very large, from 2 to 52% (Table P3-11), except in the 60-101mbgl interval, where the range reduces to 22.4-52%, leading to an average porosity of 40% and an average formation factor of 2.25. This interval of reef proximal slope is also characterized by a lighter, weaker rock frame than the above interval.

Other carbonate complexes display porosity ranges of the same order, or even larger: the Cabo Blanco in Majorca (depth 0 to 70mbgl) with a porosity range of 8 to 43.4% (Van Berkel, and Verhoef, 2005; the Great Bahama Bank, Sites 1003 to 1009, (depth 0 to 1200m below sea floor (mbsf)) in which the porosity ranges from 0 (at 1200mbsf) to 80% (at 0mbsf) (Eberli et al., 1996); the Great Barrier Reef, Sites 819 to 821 (depth 0 to 400mbsf), with porosity ranging from 10 (at 400mbsf) to 80% (at 0mbsf) (Ladd et al., 1993); and Tahiti, Sites M0005, M0007 to M0026, (depth 0 to 100mbsf), with porosity ranging from 10 to 70% (Camoin et al., 2005). Considering the few hundred meters below the sea floor where larger porosities are found, the Great Bahama Bank, the Great Barrier Reef and Tahiti investigated sites are of modern to Pleistocene age; this explains the relative lack of low porosity cementation observed at shallow depth in these sites, compared to the Miocene Majorca carbonate sequences.
The ranges of permeability (7 decades) and of electrokinetic potential measurements (8 decades) are very large (Table P3-13) throughout the carbonate sequence, including the slope facies (60-100mbgl depth interval) that is characterized by a reduction in the range of porosity values. The permeability anisotropy is close to 1.

5.11 Electrokinetic potential

Several relationships have been demonstrated: 1) $\zeta \sim 0.6C$; 2) $|C|$ is generally lower to 10mV/bar, with most of the values being in the 0.1- 10mV/bar range; 3) Relation (37) directly relates $|C|$ to K, thus providing a way to measure permeability in a borehole, through the measurement of the spontaneous potential (SP).
Laboratory dynamic properties measurements are keys to different *in-situ* measurements and results regarding hydraulic conductivity and spontaneous potential. There are three possibilities of SP existence in a borehole: 1) a differential pressure creating a fluid movement (i.e. electrokinetic potential); 2) presence of clay (i.e. membrane potential); 3) salinity gradient (i.e. liquid junction). Because there is no clay in the wet zone of the MC2 well, possibility 2) can be eliminated. It has been possible to observe either possibility 1) or 3). Thus the SP becomes, in case of electrokinetic potential observation, and in the case of salinity gradient absence, an “electrical flowmeter”.

Conclusions and perspectives

In this complex, very heterogeneous type of carbonate rocks, with multiple facies, depositional, and diagenetic processes, complex, multi-modal, non-linear petrophysical phenomena can be observed. It was then necessary to use a complete set of plugs collected on well MC2 from bottom to top, and to perform on each plug a complete set of non destructive static and dynamic petrophysical measurements to be able to extract a complete, nearly continuous characterization of the well depositional and diagenetic properties, leading to a better knowledge of structure of the Miocene sequence at Ses Sitjoles. These non-destructive measurements were completed by other destructive measurements made on samples taken at short distance of the plugs: thin-sections, Hg porosimetry, CEC, spectrometry.
This method, used on the MC2 well carbonate sequence, has allowed to provide information on:
the mineral composition: mainly calcitic, with minor clay content in subunit IIIb, several local occurrences of dolomite, and some traces of ankerite,
the large range of texture and diagenetic features (great variety of cements; mineralization often associated to dolomitization, traces of ankerite),

the surface conductivity: low in this carbonate sequence characterized by a low clay content, except in subunit IIIb, but not necessarily negligible compared to the volumetric conductivity, especially in the brackish water interval,
the m to Φ relation: the cementation factor m is varying between 1.19 and 4.32, with a standard deviation of .44, it cannot be considered as constant, it displays a tendency to increase with porosity. The coefficient a has been determined as close to 1, the law relating F to Φ is more complex than indicated by the Archie Formula (9),
the wetting of the plugs alters the rock frame properties, contrarily to the Gassmann's assumption, either weakening or hardening them, in a loose relation to surface conductivity,
the mechanical moduli characteristics: the mechanical strength of the samples is generally lower in Unit I, E, μ and K are conversely proportional to Φ,
the fractures: the Ses Sitjoles carbonate sequence displays a moderate number of fractures, generally in the NE-SW direction, parallel to the general SE Majorca fault direction, appearing either in the low porosity, high E, dolomitized, mineralized or cemented zones, or in the high porosity, low E, shear weakening by sediment wetting zones,
the K to Φ relation: the MC2 plugs were classified in three zones: zone A (mineralization and non connected porosity, Φ< 15%, F> 45, E> 40Gpa, K> 40Gpa, zone A plugs are mostly found in Unit II, sometimes in Unit III, never in Unit I; texture is mostly grainstone and framestone, but clay and mudstone are found in Unit IIIb, porosity is hampered by mineralization or non-connection, and permeability by cements; zone B (Φ> 15%, F< 45, E< 42GPa, K< 42GPa, K< 10mD, zone B plugs are found mostly in Unit I, but are also present in Units II and III, the most common texture is grainstone, permeability is hampered by cements; zone C plugs (Φ> 15%, F< 45, E< 42GPa, K< 42GPa, K> 10mD, zone C plugs are found mostly in subunits Ib, IIb and IIc and in Unit III, the most common texture is grainstone, followed by framestone and packstone in equal percentages, the good permeability due to these favourable textures is not hampered by cementation,
the five zones of mineralization are caused by modern (mineralization 4) or paleo standstills of sea water (mineralization 5, possibly the Riss-Würm interglacial, mineralizations 1 and 2 the –1m.a. lowstill),
the vertical heterogeneity has been observed for every measured petrophysical property, the anisotropy coefficient is close to 1,
the electrokinetic potential absolute value has been found to be directly proportional to permeability; it allows, in the absence of clay, and in case of salinity gradient absence, to observe even low level hydraulic flow. Thus, the petrophysical method that has been used has greatly increased our knowledge on the MC2 carbonate sequence in particular, and on the reef reservoir hydraulic properties in general.
This petrophysical method, coupled with the advantages of the drilling site design (12 wells in a 100mx100m square, a cluster of four wells, not more than 5m away, around MC2) and of the high resolution borehole image logging, has allowed to investigate further in the problems of fractures and mineralization zones.
For future steps, it would be interesting to drill and core in the Ses Sitjoles site a 300mbgl depth well (or to deepen one of the already existing wells) for explorating the existence of Pleistocene glaciations maxima. At the same time, it would allow to study the unexplored carbonate facies of Ses Sitjoles (distal slope, Off reef open shelf).

Acknowledgements

This document was written within the framework of ALIANCE (Advanced Logging Investigations of Aquifer iN Coastal Environments), a European Union funded research project EKV-2001-0039, with aim "to improve the investigation. characterization and

monitoring of coastal aquifers for vulnerability assessment". We gratefully acknowledge the generous support of the EU.
The authors wish to thanks especially Pierre Azais, University of Montpellier II, Geosciences Department, who was very instrumental in getting significant petrophysical measurements.

References

Adisoemarta, P.S., Anderson, G.A., Frailey, S.M. Asquith, G.B., 2000. Historical Use of *m* and *a* in well log interpretation: is conventional wisdom backwards? SPE 59699, p. 7.

Aguilera R., Aguilera M.S., 2002. The integration of capillary pressures and Pickett plots for determination of flow units and reservoir containers. Soc. of Petrol. Eng. Reser. Eval. and Engineering 5, n° 6, p. 465-471.

Archie, G.E., 1942.The electrical resistivity log as aid in determining some reservoir characteristics, Trans. Americ. Inst. Mineral. Eng. 146, pp. 54-62.

Baechle, G. T., Weger, R. J., Eberli, G. P., Massafero, J.-L., Sun Y.-F., Changes of shear moduli in carbonate rocks: implications for Gassmann applicability, unpublished.

Bonnier, B., 2005. Etude sédimentologique et géochimique des récifs Miocènes de Majorque (Baléares, Espagne). Influence des caractéristiques diagénétiques sur les propriétés physiques des roches carbonatées. Ms Thesis, 31p. (unpublished), Université Paul Cézanne, CEREGE, Aix-en Provence.

Camoin, G.F., Ebren, P., Eisenhauer, A., Bard, E., Faure, G., 2001. A 300 000-yr coral reef record of sea level changes, Mururoa atoll (Tuamoto archipelago, French Polynesia). Palaeogeogr., Palaeoclimatol., Palaeoecol., 175 1-6.

Camoin G.F., Iryu Y., McInroy D.B., and the Expedition 310 Scientists, 2005, Tahiti Sea Level, Proceedings of the Integrated Ocean Drilling Program, V. 310 Expedition reports.

Choquette, P.W., Pray, L.C., 1970. Geologic nomenclature and classification of porosity in sedimentary carbonates. AAPG Bull., 54, n° 2, p. 207-250.

Darcy, H., 1856. Les fontaines publiques de la ville de Dijon, Appendice, Note D : détermination des lois d'écoulement de l'eau à travers le sable, Librairie des corps impériaux des Ponts et Chaussées et des Mines, Paris.

Duggen, S., Hoernie, K., Van den Bogaard, P., Rüpke, L., Phipps, M. J., 2003. Deep roots of the Messinian salinity crisis, Nature , 422, 602.

Eberli, G., Swart, P., and ship board scientific party, 1996. Bahamas Transect, Init. Rep., ODP, 166, p. 649.

Esteban, M., Calvet, F., Dabrio, C., Baron, A., Giner, J., Pomar, L., Salas, R., Permannyer, A., 1978. Aberrant features of the Messinian coral reefs, Spain. Acta geol.Hisp., 13, 20-22.

Esteban, M., 1979. Significance of the Upper Miocene reefs of the Western Mediterranean. Palaeogeogr. Palaeoclimatol. Palaeoecol. 29, 169-188.

Fairbanks, R.G., 1989. A 17000 year glacial eustatic sea-level record, influence of glacial melting rates on the Younger Dryas event and deep ocean circulation. Nature v 342 n 6250, p 637-642.

Focke, J.W., Munn, D., 1987. Cementation exponents in Middle Eastern carbonate reservoirs, SPE Form. Eval. 2, pp 155-167.

Gassmann, F., 1951. Über die Elastizität poröser Medien: Viertejahrschrift der Naturforschenden Gesellschaft in Zürich, 96, 1.

Gines, J. and Gines A., 1995. Speleochronological aspects of karst in Mallorca, in A. Gines and J. Gines, eds., Karst and caves in Mallorca; ENDINS federacio Balear d'espeleologia, 20: Palma de Mallorca, p. 216.

Glover, P.W.J., Meredith, G.P., Sammonds, P.R., Murrell S.A.F., 1994. Ionic surface conductivity in sandstone, Journal of Geophysical Research, 99, No B11, Pages 21,635-21,650.

Gomes-Rivero, O., 1976. A practical method for determining cementation exponents and some other parameters as an aid in well log analysis. The Log Analyst, p. 8-24.

Guéguen, Y., Dienes, J., 1989. Transport properties of rocks from statistics and percolation. Mathematical Geology. 21, 1-13.

Guéguen Y., Palciauskas V., 1992. Introduction à la physique des roches, Hermann.

Haq, B. U., Hardenbol, J., Vail, P. R., 1987: Chronology of fluctuating sea levels since the Triassic, Science, 235, p. 1156-1167, 1987.

Hernandez-Molina, F.J., Somoza, L., Rey, J., Pomar, L., 1994. Late Pleistocene-Holocene sediments on the Spanish continental shelves: Model for very high resolution sequence stratigraphy: Marine Geology, 120, 3-4, p. 129-174.

Hilchie D.W., 1982, Advanced Well Log Interpretation. D.W. Hichie Inc, Golden, Colorado.

Hsü, K.J., Ryan, W.B.F., Cita, M.B., 1973. Late Miocene desiccation of the Mediterranean. Nature 242, 240-244.

Hsü, K.J., Montadert, L., Bernouilli, D., Cita, M.B., Erikson, A., Garrison, R.E., Kidd, R.G., Mélières, F. Müller, C., Wright, R, 1977. History of the Messinian salinity crisis. Nature 267, 399-403.

Jacqmin, F., 2004 Mise en oeuvre d'expériences de perméamétrie en laboratoire et contribution au traitement d'images de roches fissurées. (Unpublished) Ms. training course report, Labo ratoire de Tectonophysique, Université Montpellier II.

Jaeggi, D., 2006. Multiscalar porosity structure of a Miocene reefal carbonate complex, PhD. thesis, Diss ETH nb. 16519.

Jenkyns, H.C., Sellwood, B.W., Pomar, L., 1990. A field excursion guide to the island of Mallorca: Geologists' association Guide: London, the geologists' association, p. 93.

Johnson, D.L., Koplik, J., Swart, M.L., 1986. New pore-size parameter characterizing transport in porous media, Physical Review Letters, 57, n° 20, pp2564-2567.

Kan, R., Sen, P.N., 1987. Electrolytic conduction in periodic arrays of insulators with charges. J. chem.. Phys., 86, 5748-5756.

Kolodzie, S., Jr., 1980. Analysis of porosity of pore throat size and use of the Waxman-Smits equation to determine OOIP in Spin dle Field, Colorado. SPE, 55th Annual Fall Technical Conference, Paper SPE-9382, 10p.

Krijgsman, W., Hilgen, F.J., Raffi, I., Sierro, F.J., Wilson, D.S., 1999. Chronology, causes and progression of the Messininan crisis, Nature, 400, 652-655.

Ladd, J., Moran, K., Kroon, D., Jarrad, R., Chen, M.-P., Palmer-Julson, A., Glenn, C., 1993. Porosity variation and consolidation on the Northeastern Australian margin, ODP, Sci. Results, 133, pp. 617-623.

Lønøy, A., 2006. Making sense of carbonate pore system, AAPG Bull., 90, n° 9, pp. 1381-1405.

Lorne, B., Perrier, F., Avouac, J.-P., 1999. Streaming potential measurements, Journal of Geophysical Research, 104, NO. B8, pages 17,857-17,877.

Lucia, F.J., 1983. Petrophysical parameters estimated from visual descriptions of carbonate rocks, A field classification of carbonate pore space. Journal of Petrol. Technol. 216, p. 221-224.

Lucia, F.J., 1995. Rock-fabric/ petrophysical classification of carbonate pore space for reservoir characterisation: AAPG Bul. V. 79, n° 9, p. 1275-1300.

Lucia, F.J., 1999. Carbonate reservoir characterization: Berlin, Springer-Verlag, 226 p.
Maria-Sube, Camoin, G., Y., Pezard, P., Löw, S., Jaeggi, D., Montoto, M., Mateos, F., submitted. Multi-scalar study of depositional environments and heterogeneities in a Miocene reef sequence, Majorca (Balearic Islands), Spain, Sedimentology.
Maria-Sube, Y., Camoin, G., Pezard, P., Jaeggi, D., Braaksma, H., Verwert, K., submitted a. Depositional environments and structure in a Miocene reef complex, Majorca, Spain, AAPG.
Mavko, G., Mukerji, T., Dvorkin, J., 1998. The rock physics handbook, Tools for seismic analysis in porous media. Cambridge University Press.
Patchett, J.G., 1975. An investigation of shale conductivity. SPWLA, 16th Ann. Log. Symp. Trans. , Paper V.
Pickett, G.R., 1963. Acoustic character logs and their applications in formation evaluation. J. Petrol. Technol., 15, 6.
Pittmann, E., 1984. The pore geometries of reservoir rocks, in Physics and chemistry of Porous Media, AIP, Conference Proceeding 107, Johnson D.L. and P.N. Sen Eds, N.Y.
Pomar, L., 1991. Reef geometries, erosion surfaces and high frequency sea-level changes, upper Miocene reef complex, Mallorca, Spain, Sedimentology. 38, 2, 243-269.
Pomar, L., Ward, W.C., 1994. Response of a late Miocene Mediterranean reef platform to high-frequency eustasy. Geology, 2, 243-269.
Pomar, L., Ward, W.C., 1995. Sea-level changes, carbonate production and platform architecture: the Llucmajor platform, Mallorca, Spain, In Sequence stratigraphy and depositional response to eustatic, tectonic and climatic forcing, 87-112, B.U. Haq, Kluwer Academic Publishers.
Pomar, L., Ward, W.C., Green, D.G., 1996. Upper Miocene reef complex of the Llucmajor area, Majorca, Spain. SEPM Concepts in Sedimentology and Paleontology, 1-56576-033-6, 191-225.
Pomar, L., Ward, W.C., 1999. Reservoir-scale heterogeneity in depositional packages and diagenetic patterns on a reef-rimmed platform, Upper Miocene, Mallorca, Spain. AAPG., 83, 1759-1779.
Revil, A., Cathles, III L.M., Losh, S., Nunn, J.A., 1998. Electrical conductivity in shaly sands with geophysical applications, Journal of Geophysical Research, vol. 103, n° B10, pp 23925-23936.
Revil, A., Glover, P.W.J., 1998. Nature of surface electrical conductivity in natural sands, sandstones and clays. Geophys. Res. Lett., 25: 691-694.
Revil, A., Pezard, P.A., Glover, P.W.J., 1999. Streaming potential in porous media, Theory of the Zeta Potential. J. Geophys. 104; 20, 021-20,031.
Risnes, R., Haghighi, H. Korsnes, R.I., Natvik, O., 2003, Chalk-fluid interactions with glycol and brines. Tectonophysics, 370 213-226.
Sen, P.N., 1997. Resistivity of partially saturated carbonate rocks with microresistivity. Geophysics, 62, n°2, 415-425.
Serra, O., Serra, L., 2000. Diagraphies, Serralog.
Serra, O., Serra, L., 2003. Well logging and geology, Serralog, pp. 436.
Timur, A., 1968. An investigation of permeability, porosity and residual water saturation relationship for sandstone reservoirs. SPWLA, 9th Ann. Log. Symp. Trans. Paper.
Van Berkel, J., Verhoef, M., 2005. High resolution multi-component 2D-3D natural laboratory linking geology, geophysics and petrophysics: Mallorca, Spain, Ms. Thesis, Vrieje Universiteit, Amsterdam.
Washburn, E.W., 1921. Note on a method of determining the distribution of pore sizes in a porous material: Proceedings of the National Academy of Science, v. 7, p. 115-116.
Waxman, M. H., Smits, L.J.M., 1968. Electrical conductivity in oil-bearing shaly sands. SPE, 8, 2.
Wornardt, W.W., Vail, P.R., 1991. Revision of the Plio-Pleistocene cycles and their application to sequence stratigraphy and shelf and slope sediments in the gulf of Mexico. Trans. Gulf Coast Assoc. Geol. Soc., 41: 719-744.
Wyllie, M.J.R., Rose, W.D., 1950. Theoretical considerations related to the quantitative evaluation of the physical characteristic of reservoirs. J. Petroleum Technol., 189.
Wyllie, M.J.R., Gregory, A.R., 1953. Formation factors of unconsolidated porous media: influence of particle shapes and effect of cementation. Petroleum Transactions of AIME, 198, p 103-110.
Yokoyama, Y., De Deckker, P., Lambeck, K., Johnston, P., Fifield, L. K., 2001. Sea-level at the glacial maximum: evidence from northwestern Australia to constrain ice volumes for oxygen isotope stage 2, Palaeogeogr., Palaeoclimatol., Palaeoecol., Vol 165, 3-4, p. 281-297.

4.4 Structure de porosité à Ses Sitjoles

Résumé

Ce document présente la structure de porosité déduite d'échantillon de carottes et de diagraphies d'un récif corallien Miocène du site de Ses Sitjoles, Majorque, Espagne. Ce récif présente de la surface à 100m de profondeur une séquence carbonatée composée de trois unités distinctes. Il offre l'opportunité unique d'étudier à l'aide de géologie de surface, de mesures de laboratoire, et de forage et de carottage extensifs de puits à faible profondeur, l'intrusion d'eau salée dans un environnement côtier et un laboratoire naturel de réservoirs d'hydrocarbures analogues. Douze puits à faible profondeur ont été forés dans ce site. Dans l'un de ces puits, MC2, un carottage continu a procuré 116 bouchons de carbonate sur lesquels des mesures de propriétés pétrophysiques en laboratoire extensives et non-destructives ont été exécutées, en utilisant de l'eau en équilibre ionique. Simultanément, plus de 150 diagraphies ont été enregistrées dans MC2 et les autres forages du site dans une série de campagnes étalée sur cinq ans.
Ce document présente des mesures de porosité et de densité de grain par la méthode de triple pesée en laboratoire exécutées sur les bouchons de MC2 ; plusieurs zones de minéralisation et

de dolomitisation ont été identifiées. La porosité de carotte Φ_{core} ainsi obtenue, est alors utilisée pour étalonner en porosité les mesures en laboratoire de vélocité acoustique compressionnelle V_p et de conductivité obtenues sur les mêmes bouchons. Un des remarquables résultats obtenus pour les mesures acoustiques, est que Φ_{core} est linéairement proportionnel à V_p sur la gamme complète de porosité (de 2 à 52%).
Les mesures de porosité triple pesée sont utilisées pour l'étalonnage des diagraphies neutron, sonique et électriques dans le forage MC2.
Ces trois diagraphies de porosité sont comparées et sont utilisées pour analyser la structure de porosité en termes de porosité primaire, secondaire et de cave.
Les données de porosité et de vélocité acoustique de carottes et de diagraphies du Programme de Forage de l'Océan (ODP) pour la Grande Barrière de Corail australienne et pour le Grand Banc des Bahamas sont comparées à celles du puits MC2, soulignant les différences dans la cohérence et la qualité de la méthode de mesure, dans la relation entre porosité et vitesse acoustique, et la comparaison avec les relations publiées dans la littérature de Wyllie et Raymer et al.
Les images de la paroi du puits haute résolution optique et acoustique (amplitude et temps de parcours) sont traitées par ordinateur pour l'extraction d'une macro porosité. Cette porosité est étalonnée par une méthode deux points, utilisant les diagraphies de diamétreur et d'images de la paroi. La macro porosité ainsi dérivée et étalonnée est alors comparée sur MC2, MC8 et MC9, trois puits distants de 5m. La macro porosité étalonnée est quantitativement et continuellement représentative d'à la fois la porosité de vacuole et de l'effet de cave. Les zones de minéralisation déjà observées à partir des mesures de porosité totale sont aussi clairement identifiées aux même niveaux par les mesures de macro porosité extraites des images de la paroi. Une zone de faible porosité de vacuole est observée en dessous de 83m dans la partie inférieure du talus proche du récif. L'analyse de la distribution azimutale des vacuoles dans MC2 identifie une tendance préférentielle NE-SO, compatible avec à la fois la distribution régionale NE-SO des failles, et la direction NE-SO préférentielle des fractures observée sur les images de la paroi du puits des sites de Ses Sitjoles, Cap Blanc et Llucmajor de Majorque.

Porosity structure of a Miocene coral reef, Ses Sitjoles site, Majorca, Spain.

Yves Maria-Sube*[1], Philippe Pezard[1], Didier Loggia[1], Hendrik Braaksma[1], Philippe Gaillot[5], Modesto Montoto[2], Felix Mateos[2], David Jaeggi[3], Simon Löw[3], Gilbert Camoin[4]

[1]*Laboratoire de Tectonophysique, ISTEEM, CNRS UMR5568, Université Montpellier II, 34090 Montpellier Cedex 5, France.*
[2]*University of Oviedo, Facultad de Geologia, Departomento de Geologia, Oviedo, Spain.*
[3]*ETH Hönggerberg, Engineering Geology, Zurich, Switzerland.*
[4]*Centre Européen de recherche et d'Enseignement des Géosciences de l'Environnement (CEREGE), University of Aix-Marseille, France.*
[5]*Center for Deep Earth Exploration CDEX, Japan Agency for Marine-Earth Science and Technolog,y Yokohama Institute for Earth Sciences, Yokohama Kanagawa, Japan.*

Abstract
This document presents porosity structure from core samples and logs from a Miocene coral reef of the Ses Sitjoles site, Majorca, Spain. This reef displays from surface to 100mbgl a carbonate sequence composed of three distinct units. It offers the unique opportunity to study through surface geology, laboratory measurements, and extensive shallow wells drilling and coring, the intrusion of salted water in a coastal environment and a natural laboratory of analogue oil or gas reservoirs. Twelve shallow boreholes have been drilled in this site. In one

of these wells, MC2, a continuous coring has provided 116 carbonate plugs on which extensive non- destructive laboratory measurements of petrophysical properties were performed, using equilibrium water. Simultaneously, more than 150 log runs were recorded in MC2 and the other boreholes of the site in a five years series of campaigns.
This document presents porosity and grain density measurements by laboratory triple weighting method performed on MC2 plugs; several zones of mineralization and dolomitization are identified. The core porosity Φ_{core} thus obtained, is then used for porosity calibration of the acoustic compressional velocity V_p and conductivity laboratory measurements obtained on the same plugs. One of the remarkable results obtained for acoustic measurements, is that Φ_{core} is linearly proportional to V_p over the complete range of porosities (from 2 to 52%).
The triple weighting porosity measurements are used for porosity calibration of the neutron, sonic and electrical logs measurements in MC2 borehole.
These three log porosities are compared and are used for analyzing the porosity structure in terms of primary, secondary and cave porosity.
Ocean Drilling Program (ODP) porosity and acoustic compressional velocity core and log data from the Australian Great Barrier Reef and the Great Bahama Bank are compared to those of MC2 well, underlining the differences in measurement method coherence and quality, in the relationship between porosity and acoustic velocity, and the comparison with the literature Wyllie and Raymer et al. relationships.
High resolution optical and acoustic (amplitude and transit time) borehole images are computer processed for extracting a macro porosity. This porosity is calibrated by a two points method, using the caliper and image logs. The macro porosity so extracted and calibrated is then compared on MC2, MC8 and MC9, three 5m distant boreholes. The calibrated macro porosity is quantitatively and continuously representative of both the vug porosity and the cave effect. The mineralization zones already observed from total porosity measurements are also clearly identified at the same levels by macro porosity measurements extracted from image logs. A zone of low vug porosity is observed below 83m in the bottom part of the reef proximal slope. Analysis of the azimuthal distribution of vugs in MC2 identifies a preferential NE-SW trend, compatible with both the NE-SW faulting regional distribution observed in the area, and the NE-SW fracture preferential direction observed on borehole images of Ses Sitjoles, Cabo Blanco and Llucmajor areas of Majorque.

1 INTRODUCTION

This document addresses two of the most acute problems of our time: water, and energy (under the form of hydrocarbon fossil fuel). It studies key parameters for the transmissivity of water and hydrocarbons through carbonate reservoirs.
Seventy percent of the earth's surface is covered by water. Ninety-seven percent of this water is contained in oceans, hence salty and unsuitable for drinking or irrigation. Of the remaining 3% of freshwater, only 0,3% is found in rivers and lakes, the rest being frozen. This water runs off in rivers and refills our aquifers. While the world's population tripled in the 20th century, the use of renewable water resources has grown six-fold. Within the next fifty years, the world population will increase by another 40 to 50%. This population growth _ coupled with industrialization and urbanization _ will result in an increasing demand for water and will have serious consequences on the environment. Coastal aquifers, such as in the island of Majorca, are particularly vulnerable to salt water intrusion.
Carbonate rocks represent more than 50% of the world oil and gas reservoirs, notably in the Middle-East. With continued worldwide production, this fraction will increase, and the giant Middle East reservoirs are expected to dominate production in the mid to long-term future. It

is in the interest of the oil and gas industry to understand carbonate reservoirs. Carbonate rocks have the particularity, compared to siliclastic rocks, to present high heterogeneities.
The Miocene coral reef complex of SE Majorca is a fresh water reservoir that is surveyed by the Hydrogeological Department of the Government of the Baleares for groundwater sustainability in that coastal semi-arid environment. It also offers a unique shallow depth laboratory of analogue oil and gas producing reservoirs, that are existing and have been identified at much greater depths. It is outcropping along the coast and notably at Cabo Blanco, where it has been studied for many years (Esteban et al., 1978 ; Esteban, 1979 ; Pomar, 1991 ; Pomar and Ward, 1994, 1995, Pomar et al., 1996 ; Pomar and Ward, 1999).
This document is the last one of a series of four devoted to the study of this reef complex, using multi-scalar and multi-disciplinary methods: well cores, image logs and conventional borehole logs. The two first documents were focusing on the sedimentological and environmental aspects in either a 100m by 100m scale (Maria-Sube et al., submitted), or a 20km by 35km scale (Maria-Sube et al., submitted a). The third paper was dedicated to the petrophysical (largely mono-well) study of core plugs (Maria-Sube et al., submitted b).
This document focuses on the porosity structure of the Ses Sitjoles site in the Campos Basin. Three different parts are considered: 1) MC2 reference well laboratory static core measurements with direct porosity and grain density measurements; these measurements, presented in Maria-Sube[2] et al., in press, are used to calibrate in porosity acoustic and electrical laboratory measurements; 2) MC2 well laboratory direct porosity measurements are also used to calibrate in porosity in-situ continuous logging tools: neutron porosity, sonic and resistivity tools; 3) processing and calibration of borehole (optical and acoustic) image logs to extract macro-porosity continuous measurements that are further compared to the continuous total porosity measurements previously obtained.

2 GEOLOGICAL SETTING

The Majorca island is characterized by the extensive post-orogenic development of Miocene reef complexes that grew on shallow-marine shelves adjacent to basins (Pomar and Ward, 1999) and overlying deformed Early and Middle Miocene, Paleogene and Mesozoic rocks. The Llucmajor platform that occurs on the southeastern side of the Palma basin (Fig. P4-1, left) consists of a 20km-wide carbonate platform thought to result from the progradation and aggradation of up to 100m-thick reefal carbonates controlled by high-frequency sea-level fluctuations during late Tortonian to Messinian times, a period characterized by tectonic quiescence and low terrigenous fluxes. The platform has undergone only slight tilting and flexure associated with normal and strikeslip NE-SW faulting during Late Neogene to Middle Pleistocene times, so that most of the original geometries are retained; the Campos basin seems to have subsided only during Pleistocene time (Jenkyns et al., 1990). Minor burial compaction and scarcity of pervasive cementation has preserved much of the primary porosity (Pomar and Ward, 1999).
The facies architecture and the depositional sequences displayed by the spectacular sea-cliff outcrops along 16 km of the southern coast of Mallorca, between Cabo Blanco and Vallgornera, have been extensively described (Pomar 1991; Pomar et al., 1996, Pomar and Ward, 1994, 1995, 1999). Furthermore, some subsurface data obtained on 69 100-150m deep water wells drilled by the by the Hydrogeological Department of the Government of the Baleares have been used to delineate the three-dimensional architecture of the whole Llucmajor platform; however, it has been established that the lateral relationships of chronostratigraphic units are far from straightforward with highly complex lithofacies stacking patterns (Pomar and Ward, 1999).

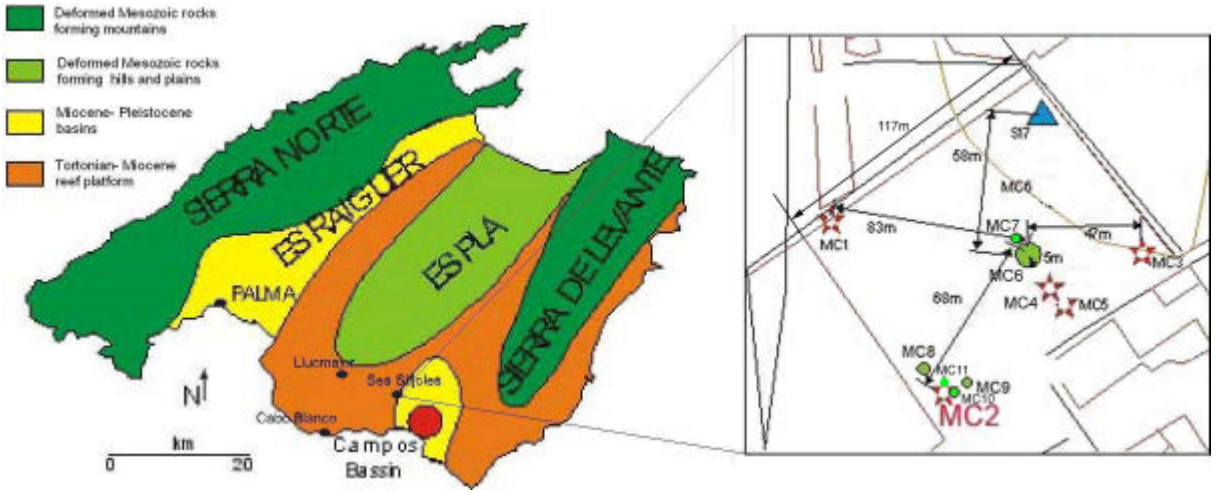

Figure P4- 1. Left: Simplified geological map of Majorca island, showing the paleo-geography of the Miocene reef complex. Right: Ses Sitjoles drilling site in the Campos Basin; red star: cored well, green circle: destructive well, blue triangle: existing slot lined observation well.

The drilling area, described in this document, is located at Ses Sitjoles, near the city of Campos, in the Campos basin, 12km to the northeast of the Cabo Blanco outcrops, in a zone which is thought to have slightly collapsed at the beginning of Pleistocene (Pomar et al., 1996). In that region, the Miocene platform carbonates form a fresh water reservoir.
The Llucmajor platform appears therefore as a model of progradational carbonate platform in which the distribution in space and time of the various carbonate facies and the pre-deep-burial stratigraphic and diagenetic heterogeneities can be studied in great details (Maria-Sube et al., submitted, and submitted a).

3 MATERIAL AND METHODS

3.1 Drilling site

The drilling site has been carefully planned and designed for offering extraordinary research ground. Eleven shallow wells MC1 to MC11 (of approximately 100m depth, Fig. P4-1, right) have been drilled from 2003 to 2006 for scientific purposes, in the Ses Sitjoles area. The drilling area is located around 6km North of the coast, at an altitude of about 40m above sea level (40masl). Five wells, MC1 to MC5, were continuously cored, whereas the others were destructive. One well, S17, had been drilled and slot lined by the Government of the Balearic Islands several years ago. The 12 wells are located in a small square of about 100m by 100m, the shortest well-to-well distance being 2.3m. Four wells (MC1, MC2, MC3 and S17) are located at the corners of the drilled area, thus providing a 100m distance scale; four other wells (MC5, MC4, MC7 and MC7) are part of a 20m long alignment extending along the perpendicular bisector of a side to the center of the square; a cluster of five wells (MC2, MC8, MC9, MC10, MC11), not more than 5m apart, are located in a corner of the square, thus providing a 5m distance scale. One of these wells, MC2, a 100m deep well, drilled with a 10cm diameter bit size, has been continuously cored from top to bottom, and has been designated as reference well.
The sedimentological facies have been identified both by core observation, and by standard petrographic analysis (Fig. P4-2A to P4-2D), X-ray diffraction from spectrometer Philip Pro X'Pert, and specific staining techniques. The MC2 well has been defined as the reference hole in that site.

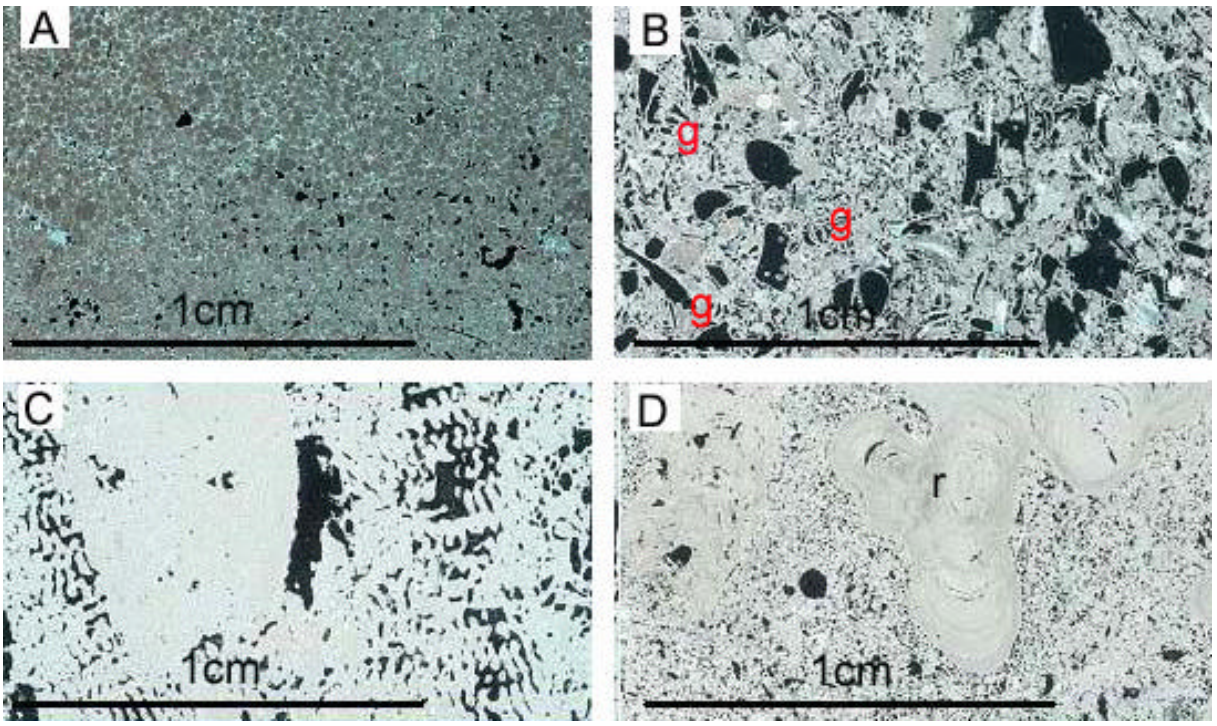

Figure P4- 2. MC2 thin sections photomicrographs, characteristic facies: (A) Subunit IIIb, depth 3.8mbgl, oolitic *grainstone* with shale fragments. (B) Subunit IIIa, depth 14.4mbgl, skeletal *grainstone*, with abundant fragments of red algae, benthic foraminifers, and gastropods (g), moldic and intergranular porosity. (C) Subunit IIc, depth 30.5mbgl, *massive coral (Porites) framework*. (D) Unit I, depth 70.9mbgl, *floatstone*, consisting of rhodolites (r) in a grainstone matrix; moldic porosity.

3.2 Core laboratory petrophysical measurements in MC2 well

From the 8cm diameter cores extracted from MC2 well, 116 22mm long, 25mm diameter plugs have been extracted for laboratory physical measurements. Because calcite equilibrium water was used for all petrophysical measurements on these plugs, various non-destructive measurements could be performed on the same plug, at the same depth. This provides an exceptionally coherent set of measurements on each particular plug, of great importance in these highly heterogeneous sediments.

These measurement principles have been presented in details in Maria-Sube, submitted b. We are going to focuse more particularly on the porosity structure.

3.2.1 Porosity structure

Porosity is the volumetric fraction of a rock that is not occupied by solid elements. There are different types of porosity.

Total porosity F_T, is equal to the ratio of total volume of empty spaces (pores, vacuoles, fractures, …) existing between the mineral elements of the rock, over the total volume or the rock.

$$\Phi_T = \frac{V_T - V_s}{V_T} = \frac{V_p}{V_T} \quad (1)$$

with V_p= pore volume (or void volume), generally occupied by fluids: water, oil, gas,

V_s= volume occupied by solid elements,

V_T= rock total volume.

Total porosity includes: *intergranular porosity*, which makes *primary porosity* F_1, and depends on form, size and sorting of the solid elements; this porosity is found mainly in

clastic rocks. It also includes *vuggy porosity*, from dissolution, and *fracture porosity*, from mechanical action, which makes *secondary porosity*, F_2; this porosity is found mainly in chemical or biochemical rocks (such as carbonates).
The previous definitions induce the following relation:

$$F_T = F_1 + F_2 \quad (2)$$

Open porosity F_o, is the volume percentage in the rock of void space connected between them. This porosity may be very inferior to total porosity if pores are not open (as in case of pumice, for which Φ_T is close to 50%, when Φ_o is zero). If the pores are not connected, then there is *closed porosity* F_c, such that:

$$F_T = F_o + F_c \quad (3)$$

Effective porosity, F_e, is porosity accessible to free fluids, excluding closed porosity and volume occupied by adsorbed water and water bound to the clays (Serra and Serra, 2000).
It is also possible to characterize the pores by their size: *macro porosity* refers to pores greater than 50µm in diameter; *meso porosity* refers to pores greater than 2µm and less than 50µm in diameter; *micro porosity* refers to pores smaller than 2µm in diameter.

3.2.2 Porosity to acoustic velocity relation

The acoustic compressional wave speed V_p in a rock is a function of many geological or environmental parameters: lithology, porosity, fluid nature, pressure, temperature, texture, structure (Serra and Serra, 2000).
The sound speed depends on the nature of *minerals* composing the rocks and their cement. For instance, in calcite of zero porosity, V_p= 6320m/s, while in dolomite, V_p= 7900m/s (Homand and Dufaud, 2000). If the mineralogy is complex, in case of laminations, it is generally accepted that the travel time in the rock Dt_{ma} is given by the relation:

$$\Delta t_{ma} = V_1\Delta t_{ma1} + V_2\Delta t_{ma2} + \ldots + V_n\Delta t_{man} \quad (4)$$

V_1… being the volumetric percentages of the laminations composed of $_{ma1}$ matrix. the travel time *Dt* has sometimes been called the slowness (that is to say the inverse of the speed).
In case of dispersion, if the dispersed material is isolated in the matrix, the fastest wave arrival is generally going to avoid and its effect is going to be nil.
The sound speed also depends on porosity, and on the nature of the fluid filling the pores. As porosity increases, speed decreases. In pure water, V_p= 1613m/s; in salt water, the speed increases slightly (1693m/s < V_p < 1847m/s), a lower speed than in most common minerals. The sound speed in water is also a function of temperature and pressure.
The sound speeds depends on the temperature and pressure in water, and also on the rock structure (Brie et al., 1985). However, in our conditions of measurement, with small variations of temperature and pressure, this effect is negligible.
The sound speed depends on texture. The grain arrangement, and the mode of porosity repartition have an influence on the sound speed. Sarmiento, 1961, has demonstrated that pore type, size and distribution (intergranular, vacuoles, fractures) also influence the sound speed. The cement nature also has an influence. However, grain form does not have influence (Brie et al., 1985). Anisotropy has an influence: the sound speed is not the same laterally or vertically. If the pore is isolated in the matrix, the fastest arrival ignores it: sonic measurement does not take into account secondary porosity of vuggy type.
The sound speed depends on structure. Homogeneity, beds thickness, laminations, their number and thickness, the dip, fracture presence, their inclination compared to the measurement, are parameters that also affect the sound speed, due to the anisotropy of formations.
For a given lithology, sound speed is a function of porosity. Wyllie et al., 1956, have proposed an empirical relation, based on many laboratory measurements. It allows to rely the

travel time Δt to porosity from acoustic measurement (Φ_s), by assuming that the total travel time is the sum of grain and fluid travel times, respectively Δt_{ma}, and Δt_f. This can be written, if one assumes a relation between travel time in the fluid and porosity:

$$\Delta t = \Phi \Delta t_f + (1 - \Phi)\Delta t_{ma} \quad (5)$$

From equation (5), it is possible to deduce porosity:

$$\Phi_S = \frac{\Delta t - \Delta t_{ma}}{\Delta t_f - \Delta t_{ma}} \quad (6)$$

The Wyllie equation (also called the "time-average porosity equation") establishes a linear equation between Φ_s and Δt not very much in accord with our remarks on texture (see above). However, it is satisfactory in the porosity range 10 to 25%, and for porosities corresponding to roughly spherical grains. In uncompacted formations, the Wyllie relation provides too high porosity values. In this case, a correction factor $100/c\Delta t_{sh}$ is introduced.

Raymer et al., 1980, proposed an other porosity to travel time relation. In that relation, the porosity to travel time curve is not any more a straight line, it is a curvy line with an inflexion point around $F = 0.42$, and a downward curvature before the inflexion point, an upward curvature after the inflexion point. Three equations (7) (for $F < 0.37$), (8) (for $0.37 < F < 0.47$, and (9) (for $F > 0.47$) of the compressional sound velocity V_p have to be used to express the relation:

$$V_p = (1-\Phi)2V_{ma} + \Phi V_f \quad (7)$$

$$\frac{1}{V_p} = \frac{0.47 - \Phi}{0.10}\frac{1}{V_{37}} + \frac{\Phi - 0.37}{0.10}\frac{1}{V_{47}} \quad (8)$$

$$\frac{1}{r_b V^2} = \frac{\Phi}{r_f V_f^2} + \frac{1-\Phi}{r_{ma} V_{ma}^2} \quad (9)$$

where V_{ma} and V_f are the sound velocity in grain and fluid respectively, V_{37} and V_{47} are the sound velocity in a saturated rock of 0.37 and 0.47 porosity respectively. ρ_b, ρ_{ma} and ρ_f are the volumetric mass of respectively a bulk rock, grain and fluid. Equation (8) represents a straight line joining the $\Phi = 0.37$ to the $\Phi = 0.47$ points on the Raymer et al. curve.

3.2.3 Porosity to electrical conductivity relation

In a porous media composed of a matrix media considered as infinitely resistive and a connected pore space saturated with a conductive electrolyte, there is a linear relation between the sample conductivity s_o, and the electrolyte conductivity s_w (Archie, 1942):

$$s_o = \frac{s_w}{F} \quad (10)$$

The formation factor F of the rock is dimensionless and reflects the electrolytic conduction mechanism in pore volumes.

When surface processes cannot be neglected with respect to electrolytic conduction, Waxman and Smits, (WS, 1968) proposed a modified empirical model to take into account the excess conductivity (σ_s), with:

$$s_o = \frac{s_w}{F} + s_s \quad (11)$$

A great number of core measurements have demonstrated (Archie, 1942) that the formation factor F of Formula (10) of a clay-less porous rock can be related with a rather good accuracy to porosity by a relation of the type:

$$F = \frac{a}{f^m} \quad (12)$$

a being a lithology dependent coefficient. m is the cementation factor, depending on the type of sediments, the pore's form, the connections between pores, hence on the porosity type and

its repartition mode, lastly, in a certain way, on compaction. Actually, m is a parameter characterizing the porous space.
a has often be found close to 1 in carbonates; if it is the case, then Formula (12) may be written:

$$F = f^{-m} \tag{13}$$

Which, by taking the logarithm of Formula (13), may be written:

$$m = -\frac{Log(F)}{Log(f)} \tag{14}$$

Making use of Formulae (11) and (13), it is then possible to extract a porosity value Φ_R from resistivity measurements:

$$\Phi_R = \left(\frac{S_O - S_S}{S_W} \right)^{\frac{1}{m}} \tag{15}$$

3.3 Downhole logging tools

It is understandable that no direct measurement of porosity such as the triple weighting or the mercury injection methods can be used for recording continuous downhole wireline logging porosity. However, with logging tools using neutron, acoustic or electrical physical effects (no downhole slimhole tool measuring density from gamma induced effect is available at the moment), it is possible to derive a continuous porosity measurement.
Because slimhole logging tools are designed and manufactured primarily for recording in shallow water wells, they do not benefit from as much research and development means as the oil and gas industry, and they are often considered more as qualitative than quantitative instruments. Consequently large efforts have to be made on tool validation, calibration and in a general way on quantitative measurements.
Water wells offer many differences, compared to oil and gas wells. They are generally shallower (in our case, only 100m depth), hence they present less drilling and operation costs, and this allows to take more time for measurements. Water (in our case brackish water) is used as drilling fluid, consequently, there is no mud invasion. There is no hydrocarbon, with its inherent tool reading corrections, in the formation. We have been able not to set casing in most of the cases, and to maintain the wells open for several years, with the possibility of repeating logs at time interval, in most of the cases. When not possible, a plastic liner was set, still allowing most of the logs to be recorded.
In water wells, most of the time, the logging sequence does not follow immediately the drilling operation; in such a way, the drilling fluid reaches equilibrium with the formation fluid, and there is no more salinity difference between them after a few days: this allows the hydrogeology Idronaut tool to actually measure continuously not only the borehole fluid, but at the same time the formation fluid conductivity, a feat completely unknown from the oil and gas people. A few days after the drilling operations, the drilling dust settles in the borehole column, thus allowing to run optical borehole imaging logs.
To be valid, the porosity measurements have to be calibrated during procedures using formations of known lithology and porosity (primary calibration) or against devices simulating known porosities (secondary calibration). We have performed calibrations using MC2 lab triple weighting porosity values against MC2 log values. Of course, this implies a correlation of MC2 core depths against MC2 log depth, which has been performed as carefully as possible, using the following principles: 1) optical image log is the reference log; 2) the water table is a depth marker; 3) the log order of correlation is the following: optical image log, acoustic image log, Idronaut, combined total gamma ray-electrical log, spectral

gamma-ray, induction log, porosity neutron, sonic, caliper. Then the cores are correlated to logs, using mainly porosity and spectral gamma ray logs (this method has some limitations: below 60m, the porosity contrast is insufficient, and core depth was assumed equal to log depth; also in the vadose zone, no porosity log is available).
For the other wells of Ses Sitjoles, the optical image logs are first correlated to MC2 image log, assuming that the water table is planar, and then the same correlation sequence as on MC2 is followed. The water table daily or seasonal movements were considered as negligible (of the order of +/- 30cm).
This task of log and core depth reconciliation may seem trivial, but it is actually of the utmost importance for core to log comparison. This is a long and tedious work to execute (more than 150 logs, were recorded in Ses Sitjoles). It was observed that log depth correction was far from negligible (+/- 3m).

3.3.1 Neutron

The PNN neutron logging tool is a 40 mm outside diameter device built by Antares, Germany, with acquisition software provided by Advanced Logic Technology (ALT), Luxemburg. It features a powerful electronic neutron source (neutron generator or minitron) providing a neutron energy of 14.1MeV. This source creates neutrons of fast initial speed (14,000km/s).
These fast neutrons have a great power of penetration, and due to this, they generate inelastic and elastic collisions with the formation atom nuclei, they loose progressively their energy and disappear. The life of these neutrons can be spread into four phases: fast neutron with inelastic collisions, neutron slowing down with elastic collisions, diffusion and capture. During the fast neutron phase, neutrons loose their kinetic energy. The neutron slowing down phase is important because hydrogen atoms have a great power of slowing down, because their mass is close to the neutron mass. The neutron reaches then the epithermal level of energy (between 100 and 0.2eV). After the diffusion phase, the neutrons reach the thermal level of energy (0.025eV), and are then absorbed during the capture phase. When a neutron is captured, it emits a gamma-ray which can be detected by the sonde gamma-ray detectors. It is possible to express the neutron flux in function of the slowing down length (the distance run by the neutron before its access to the thermal energy level), Tittman, 1986, Serra and Serra, 2000. Hence the neutron flux depends on the distance source to detector.
Because hydrogen is the greatest neutron slowing down atom, the neutron porosity tool has been called the hydrogen index measurement. But since hydrogen is mostly present in the sediments under the form of water or hydrocarbons, it can be seen than the number of gamma-rays received at the detector is an indication of the porosity of the formation.
As many modern neutron tools, the Antares tool uses two detectors: long spacing LSN and short spacing SSN, for compensating, and in a way eliminate, the influence of the closest to the hole zone. The measurements are recorded in counts per second (CPS), and the ratio of the two measurements is used to express the neutron porosity.
Antares provided the following neutron porosity F_N (V/V) relation in limestone:

$$\Phi_N = -0.1108 + 0.034405*(SSN/LSN) \quad (16)$$

Many parameters influence the neutron measure: elements composing the rocks or the fluids, parasitic and environmental effects (Serra and Serra, 2000).
The hydrogen index measurement depends on the elements composing the rocks or the fluids. The elements composing the minerals or fluids have each a neutron slowing down power and a more or less high capacity of thermal neutrons absorption. However, two elements have a particular role due to their properties and abundance. Those are hydrogen and chlorine. Hydrogen is the most powerful neutron slowing down element; as this element is present in many substances, the measurement is essentially the formation hydrogen concentration. The substances containing the most hydrogen are water and liquid hydrocarbons. In the shallow

formations of SE Majorca, hydrocarbons are excluded, so we can leave that question apart. When talking about the neutron porosity of a rock, the hypothesis is made that all hydrogen is contained in the water or oil of pores; however, this is not always true, and other substances, rich in hydrogen, exist in rocks; this is the case of clays, which contain hydrogen in their crystal and also in the pores; it is also the case of some rocks such as gypsum or carnallite. Chlorine may be a slowing down element, but it has a larger action in the capture of thermal neutrons, due to its large capture area. Chlorine is often part of the composition of formation water, or of the drilling fluid. Other substances as gadolinium, samarium, bore, lithium or iron also have an effect on thermal neutron measurement, due to their high capture area. The principal components of the rocks contribute more or less to the slowing down (C) or the capture (Ca, Si, Al, Mg, Fe, Cl…) of the neutrons. Neutron tools are calibrated in calcite. If the rock is composed of pure calcite, the response is directly a function of porosity (Formula (16)). If it is not the case, the other elements composing the rock having an other effect than calcite, the relation is not any more linear in porosity. It is then possible that the neutron porosity index has negative values (like in quartz).

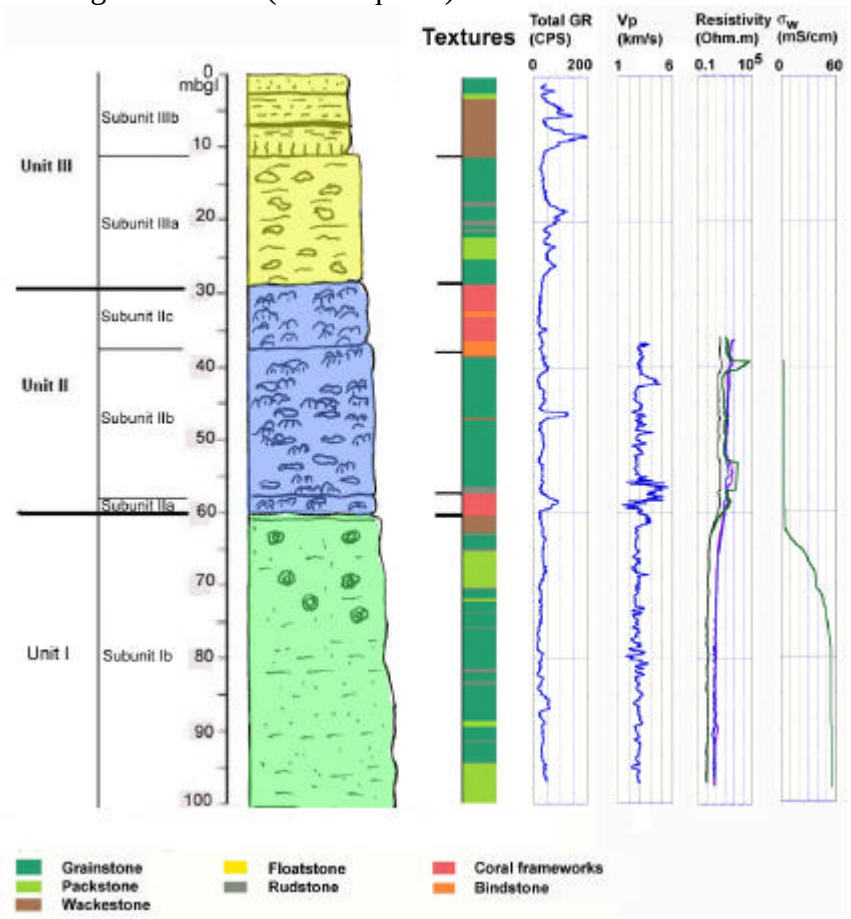

Figure P4- 3. Lithology of Ses Sitjoles MC2 well (Bonnier, 2005, Camoin et al., work in progress), corresponding depositional textures (from Bonnier, 2005, and Jaeggi, 2006), total natural gamma-ray, compressional acoustic velocity V_p, resistivity logs (electric log: thick violet line short normal, medium blue line long normal; and dual induction: thick dark green line deep, medium black line medium) and water conductivity s_w logs. Stratigraphy color coding: green, Unit I; blue: Unit II; yellow: Unit I.

Some parasitic and environmental effects have an influence on the neutron porosity measurement. In our case, the drilling fluid has no influence, since we have seen that the logging sequence is recorded days after drilling operations are completed, and then there is equilibrium between drilling water and formation water. So, the fluid in the hole has to be considered not as drilling fluid, but as formation fluid. In our case (Fig. P4-3): from 0 to

36.4mbgl: air; from 36.4 to 61mbgl: brackish water; from 61 to 78mbgl: transition water, and from 78 to 100mbgl: sea water. The PNN tool cannot be operated in air, for safety reasons. We have seen that chlorine is a great capturer of thermal neutrons, and hence the salt of the borehole fluid is going to affect the neutron measurement. The tool diameter has an influence: as it is larger, the volume of fluid in hole surrounding the tool is larger, and the more the neutrons are slowed down and absorbed by the hydrogen and chlorine contained in the borehole fluid. This effect is in part compensated by the two detector tools (as in the PNN). The neutrons counting rate increases as the tool is closer to the borehole wall. For this reason, an eccentralizer device is used for applying the tool against the borehole wall. For the above reasons, oil and gas service companies supply to their customers neutron correction charts for hole size, hole and formation fluid salinity, hole temperature (plus other parameters such as mudcake thicknes, mud density which are not relevant to us), contrarily to the water well service companies.

3.3.2 Sonic

Field measurements of acoustic measurement have been performed using 2S AA-1000/F 39mm outside diameter sonic wireline log tool designed by Mount Sopris Instrument Co. Inc., USA, featuring one acoustic emitter and three receivers operated at 15kHz frequency in MC2 case (actually, the tool frequency may be adjusted from 1 to 30kHz). The compressional emitter is a monopole type transducer. The tool is also capable of emitting a shear wave, but this property was not used for this document. The receiver-receiver span is 33cm; but it can also be 66 or 99cm. The sonic log does not work in the vadose zone of the borehole. Data processing (V_p extraction from the record of sonic waveforms) was made using the LogCruncher software from Mercury Geophysics, USA.
See above (paragraph 3.3.2 Core acoustic method) for the influence of geological or environmental parameters on the compressional wave sound speed.

3.3.3 Resistivity or conductivity measurements

The electrical logging tools measure as well the resistivity or the conductivity of the formation, since one is simply the inverse of the other. As the use in the oil and gas logging industry is to express the formation electrical properties in terms of resistivity, we will rather use that word.
It is not the aim of this document to review and explain the electricity and electromagnetism laws on which are based the different resistivity logging tools. This is done in Tittman, 1986, Ellis, 1987, and Serra and Serra, 2000.
We have used in Ses Sitjoles three different logging tools, using three different physical principles. 1) Electrical log, providing different spacing short normal SN and long normal LN resistivity measurements; the ELXG slimhole tool is designed by Robertson Geologing, U.K for hardware as well as acquisition software; the tool is combined with a total natural gamma ray measurement. 2) Laterolog 3 (LL3), providing an electrically focused (i.e. reading deeper in the formation) resistivity measurement; the GLOG slimhole tool is designed by Robertson Geologing for hardware as well as acquisition software. 3) dual induction slimhole tool, using the electromagnetic induction principle, providing deep (ILD) and medium (ILM) induction resistivity channels; the DIL 45 is designed by ALT for hardware as well as acquisition software.
The Ses Sitjoles wells offer a special medium for resistivity logging (Fig. 11A): from 0 to 36.4m, a vadose zone; from 36.4 to 62mbgl a brackish formation water zone of conductivity 4mS/cm; from 62 to 79mbgl, a transitional zone; from 79 to 100mbgl a salted formation water zone of conductivity 55mS/cm. In the top vadose zone, no resistivity tool is working. This large interval of 36.4m thickness has also caused to our GLOG tool a systematic failure: too

high and spurious resistivity readings; this had for consequence that we discarded the GLOG records made in Ses Sitjoles boreholes. An other problem is the formation water salinity contrast between top and bottom zones. The resistivity logging tools have a limited resistivity range of measurement. The focused LL3 GLOG tool would have been best for reading in the top zone low formation water salinity, the ELXG tool is the second best in that zone. The induction tool is best for recording in the formation water of higher salinity located in the bottom interval.
Since in our wells there is no difference between drilling fluid and formation water, no invasion, no mud cake nor mud filtrate, this eliminates many different causes for resistivity tool environmental corrections. In particular, the deep and shallow resistivity channels should read the same value.
Unfocused resistivity tools are poor bed delimiters: adjacent beds tend to influence thin bed reading. An other cause for recording distortion is that the LN reading is asymmetric compared to the bed median plan.
The DIL 45 tool measures the phase and the quadrature phase signals, thus allowing a better skin effect correction. ALT indicates a resistivity range of measurement between 0.2 and 200 Ohm.m for this tool.
Downhole continuous σ_w measurements have been made with the Idronaut logging tool. This tool has a sensor set composed of downhole fluid measurements of: conductivity, temperature, pressure, dissolved oxygen, pH and Redox (Eh). It is manufactured by Idronaut SRL of Brugherio, Italy, and packaged by ALT, which also provides the software.

3.3.4 Image logs

3.3.4.1 Logging tools

Optical and acoustic borehole image logs have been run in most of the Ses Sitjoles wells, and in particular in MC2. These images come from slimhole (40 mm diameter) tools OBI40 (optical) and ABI40 (acoustic) manufactured by ALT, which also provides the acquisition software. The optical images have a 1mm resolution, whereas the acoustic images have a 3mm resolution. These resolutions are much higher than those currently obtained in the oil industry by larger diameter (around 90mm) tools: thus, the optical imaging tool does not exist in the oil industry (it would not provide images through an opaque drilling mud), but can be compared with electrical image resolution (2.5mm); the acoustic imaging tool in the oil industry offers only 5 to 10mm resolution. Both optical and acoustic slimhole images have also the advantage compared to the FMI micro-scanner electrical images to present a 360° continuous image, as opposed to the observed gaps on the electrical images, due to the spacing between pads and flaps.
The optical image log works also in an air-filled hole, whereas the acoustical image log needs a liquid-filled hole. Thus the optical log is very useful even in the vadose zone, something very appreciated in the Majorcan wells, where the vadose zone can be relatively long compared to the total depth.
The acoustic image log presents two sets of images: one obtained from the travel time and the other one obtained from the amplitude of the acoustic signal. Those images are generally more contrasted images than those obtained from the optical image log.

3.3.4.2 Image log processing

Cunningham et al, 2004 developed and calibrated a method to estimate vuggy porosity from digital optical borehole images of the karstic Pleistocene limestone of the Biscayne aquifer (southern Florida). Basically, this method interprets vugs and background based on the grayscale color of the digital borehole images and calculates a percentage of vuggy porosity.

The development of the method was complicated because environmental conditions created an uneven grayscale contrast in the borehole images, in such a way that it is difficult to distinguish vugs from background. The irregular contrast was produced by unbalanced illumination of the borehole wall, which was a result of eccentering of the borehole-imaging tool. Experimentation showed that a simple, single grayscale threshold would not realistically differentiate between the grayscale contrast of vugs and background. Thus, they developed an equation for an effective subtraction of the changing grayscale contrast, due to uneven illumination, to produce a grayscale threshold that successfully identifies vugs. In this equation, a moving average calculated around the circumference of the borehole (1/8 of the borehole circumference) and expressed as the background grayscale intensity (BK) is defined as baseline from which to identify a grayscale threshold for vugs. For the carbonate rocks of the Biscayne aquifer a constant (P) was empirically derived by calibration with vuggy porosity values derived from digital images of slabbed-core samples and used to make the subtraction from the background baseline to derive the vuggy grayscale threshold [T = (1-P) BK] as a function of azimuth.

Gaillot et al., 2005, generalized the above described method to acoustic images. Even, if the proposed methodology applied to optical images should be effective in estimating vuggy porosity, its application to travel time acoustic images seems more appropriate. Indeed, porosity computation from optical images can be perturbed by dark colors not being generated by a hole in the borehole wall, but by a simple color change of the rock itself, whereas acoustic travel-time images are high-resolution 360° caliper views of the borehole wall roughness. So, macro-scale porosity (vuggy and fracture porosities) can be really identified as an excavation (cave or vug) in the borehole wall characterized by longer travel-times and not as a shadow (black) area like in the grayscale optical images. However, even if the physical foundations for using travel-time images are more obvious, travel time images suffer from the same tool eccentering and/or tool ovalization problems as the optical images. Thus, for travel time images, the 3-steps methodology that consists of: 1) computing BK, 2) derivating the calibration constant P, and 3) thresholding, is the same as in the work proposed by Cunningham et al., 2004, for optical images.

In addition to the travel time image, acoustic imaging tools generate an amplitude image of the borehole wall. The amplitude (A) of these reflections is representative for the properties of the rock surrounding the borehole, and can be somehow related to macro-scale porosity. Indeed, deep and high frequency rugosities (vug or karst) of the borehole wall are locally responsible for diffraction of ultrasound pulses. This local diffraction of the acoustic pulse is responsible for major losses of acoustic energy and result in low amplitude values, and also of apparent enlargement of the areas representing holes. Due to the important difference in amplitude values between rock and vugs, vugs can be simply detected by a threshold, A_0. Theoretically, this A_0 value varies with depth as it depends on the bulk reflexion coefficient of the formation. However, for a given depth, $A_0(z)$ can be automatically (or semi-automatically) derived from the image itself by looking at the distribution of the amplitude values over a given depth interval. Indeed, a slope-break in the histogram of amplitude values marks the limit between the low amplitude values resulting from the acoustic diffraction from the higher values associated to pulse reflection at the rock-fluid interface. The simplicity of this processing relies also on the fact that acoustic amplitude images are not sensitive to eccentering and ovalizing effects. Thus, the pre-computation of a background threshold is not necessary, reducing the processing into 2 steps that are: 1) the determination of A_0 for each depth (or each homogeneous depth interval), and 2) the identification of vug by simple thresholding.

3.3.4.3 Porosity from image log processing

Due to the logging tools resolution, the porosity derived from image log is necessarily a macro porosity (i. e. with pore diameter larger than 50µm). On top of perturbations on porosity derived from image log caused by different physical principles, other perturbations are caused by drilling effects. Thus, if the porosity derived from image log is called F_{image}, the macro porosity due to vugs or fracture is called F_{vug} (only three open fractures have been identified in MC2, Maria-Sube et al. in press, therefore, we will neglect the fracture porosity in this formation), the macro porosity due to caves is called F_{cave}, and the macro porosity artificially caused by drilling is called $F_{drilling}$, one can write the following relation:

$$\Phi_{image} = \Phi_{vug} + \Phi_{cave} + \Phi_{drilling} \quad (17)$$

We are not at all interested by $\Phi_{drilling}$, but image logs necessarily also record $\Phi_{drilling}$. Our interest lies in the formation macro porosity ($F_{formation\_macro}$) that can be defined by:

$$\Phi_{formation\_macro} = \Phi_{vug} + \Phi_{cave} \quad (18)$$

Φ_{cave} can be expressed in function of the hole caliper log measurement (*Cali*), the bit size (*BS*) and the maximum caliper measurement over the interval ($Cali_{max}$), in the following manner:

$$\Phi_{cave} = (Cali - BS)/(Cali_{max} - BS) \quad (19)$$

Through calibration of the results, we will show that it is possible to eliminate the $\Phi_{drilling}$ effect, and hence to estimate Φ_{vug} from the Φ_{image} processing.

3.3.5 Caliper log

The mechanical caliper log is an essential tool for accompanying the borehole image logs, for control and complementary information. The caliper we have used is a three joint arms tool manufactured by Mount Sopris Instrument Co. Inc.

4 RESULTS

4.1 The carbonate sequence in MC2 well

The carbonate sequence in the MC2 well has been detailed in Maria-Sube et al., submitted. A summary is provided below.

Three distinctive sedimentological units comprise the carbonate sequence in MC2 well and have been identified based on visual core description and thin section observation (Fig. P4-2A to P4-2D, Table P4-1, and Fig. P4-3). They have been called I, II and III (Fig. P4-3) from base to top and have been locally subdivided in subunits based on their lithological characters and/or biological content.

Unit I is comprised of a white bioclastic limestone that is gently to steeply bedded (10-30°). It extends from 100 to 60m below ground level (60mbgl) and grades from fine-grained skeletal packstones between 100 and 75mbgl to slightly coarser skeletal packstones to grainstones between 75 and 60mbgl (Fig. P4-2D). Occurrences of wackestone, rudstone, and floatstone are noted locally in the upper part of the unit. The "chalky" appearance of those rocks (Fig. 4, with a photo of Cabo Blanco cliff outcrop) is generally related to their good sorting and overall fine grain size coupled with extensive moldic and intergranular porosities. The degree of cementation increases from base to top; the lower part of the unit is generally poorly cemented whereas patchy blocky spars are common in the upper part.

The fabric grades from homogeneous at the base to slightly anisotropic, due to steeply dipping beds and coarse grained layers in between, at the top (Jaeggi, 2006). Porosity averages 40% in this unit; the highest values, up to 52% are related to the occurrence of larger cavities affecting both the matrix and larger skeletal pieces (Maria-Sube et al., submitted b). Two dolomitic intervals occur between 88 and 85mbgl and between 61 and 60mbgl respectively.

Units	Subunits	Interval core depth (mbgl)	Depositional texture	Biota	Cement type	Fabric	Porosity type
Unit III	Subunit IIIb	0-12	Oolitic grainstone	Shell fragments	Import ant sparitic	Isotropic and homogeneous	Mainly intergranular, some intragranular porosity and a few vugs,
	Subunit IIIa	12-28	Skeletal grainstone	Abundant coralline algae and forams	Micritic	Anisotropic but quite homogeneous	Moldic and intergranular
Unit II	Subunit IIc	28-37	Framestone	Built by massive corals (Porites); extensive borings	sparitic cement which partly occludes porosity	Highly heterogeneous	Growth-framework porosity with important vugs
	Subunit IIb	37-57					
	Subunit IIa	57-60					
Unit I		60-75.0 75.0-100.9	Floatstone Grainstone, fine grained	Encrusting coralline algae Molds of shells, only echinoids are preserved	Micritic Exclusively micritic	Isotropic and heterogeneous Anisotropic and homogeneous	Mainly intergranular and some moldic porosity Mainly intergranular porosity and some moldic porosity

Table P4- 1. MC2 lithology, biological content and diagenetic features after thin section observations (from Jaeggi, 2006). The thin section descriptions corresponds to the depths indicated in Figures P4-2A to P4-2D caption.

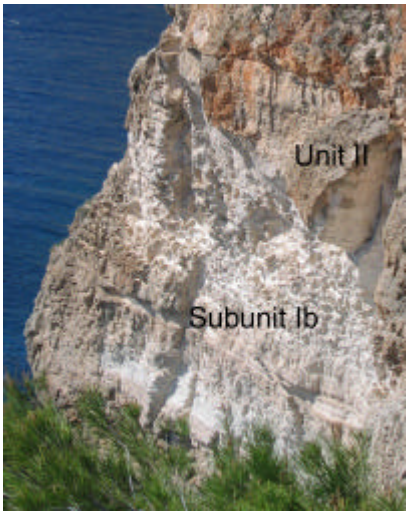

Figure P4- 4. Photography of Cap Blanc cliff, displaying white, chalk like, thin layered, detrital subunit Ib, and ochre, coral frameworks, Unit II.

The depositional environment is interpreted as a proximal carbonate slope environment characterized by moderate energy conditions.

Unit II, from 60 to 28mbgl, includes three subunits that are composed of *in situ* massive coral colonies (*Porites*) encrusted by coralline algae and foraminifers (framestone, with possibility of having bindstone; subunits IIa and IIc, Fig. P4-2C) and skeletal beds comprised of large pieces of corals (massive *Porites*) and coralline algae (rudstone, grainstone; subunit IIb).

The matrix of those coral frameworks is micritic and includes fragments of corals, and coralline algae (both encrusting and branching).

The fabric is highly heterogeneous. The total porosity is highly variable and ranges from 5 to 51% (Maria-Sube et al. submitted b); it reflects by the uneven distribution both of pore spaces and of meteoric blocky and granular calcite cements. Porosity mostly includes both large primary pores that merely correspond to large open cavities between coral colonies, and secondary pores (moldic pores and solution cavities). Karstification occurs at various levels and especially in the lower part of the unit where decimeter-to-meter scale cavities are partly filled by red-brown ankerite; within those intervals, pore spaces are usually filled by blocky

spars providing a denser structure to the rock. Dolomitization processes are conspicuous at 37 and 48mbgl.
This unit is interpreted as being deposited in a warm shallow-water environment characterized by moderate energy conditions.
Unit III, from 28mbgl to the surface, includes two successive subunits that are characterized by distinctive textures and grain contents.
Subunit IIIa occurs from 28 to 12mbgl and is mostly comprised of well-sorted skeletal packstones and grainstones with variable cementation and local occurrence of rudstone, rich in fragments of coralline algae (Fig. P4-2B). Some beds are characterized by the occurrence of small coral colonies (massive *Porites*). Calcite cements include isopachous crusts, especially between 15 and 40 mbgl, and patchy blocky spars.
Subunit IIIb forms the top of the unit, from 12mbgl to the surface, and corresponds to karstified oolitic grainstones and packstones (Fig. P4-2A), with local occurrence of rudstone, calcretes are noted locally. Red clays commonly fill karstic cavities. Blocky cements occur in most intergranular pore spaces.
The overall average porosity throughout this unit ranges from 24% in subunit IIIb to 36% in subunit IIIa. It is merely related to dissolution processes affecting the skeletal grains and the ooids (moldic pores); solution cavities occur locally.
The depositional setting is interpreted as a very shallow warm water environment characterized by low energy conditions, probably locally and temporarily restricted, with fluctuating ecological conditions (e.g. temperatures, salinities and exposure) during the deposition of subunit IIIb as indicated by the composition of its poorly diversified biological content. Furthermore, the occurrence of calcretes indicates temporary periods of subaerial exposure.

4.2 Core measurements

4.2.1 Porosity

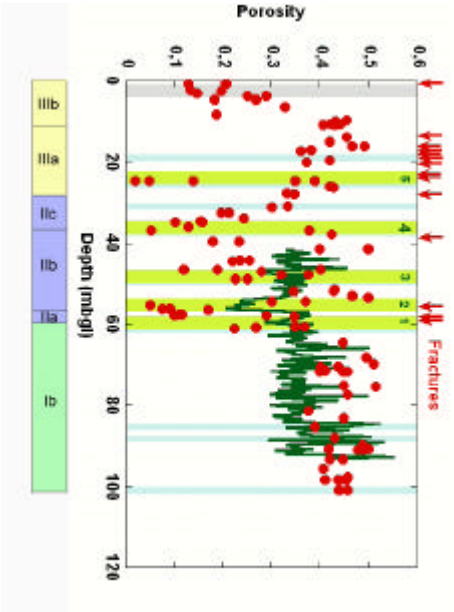

Figure P4- 5. Stratigraphic subunits are indicated on the left side of the figure. Calibrated porosity neutron log F_N green curve vs. depth, compared to triple porosity core F_{core} red full dots) measurements (116 plugs) in MC2 well. Light blue shadings are indicating zones of dolomitization, light green shadings are showing five zones of mineralization recognized from below 0.15 porosity; another zone of low porosity (at 2mbgl) is indicated by a light gray shading; red arrows indicate fractures, recognized from image logs (Maria-Sube et al., submitted, and submitted b).

Φ_{core} porosity and ρ_{ma} grain density measurements were obtained from plug triple weighting measurements. They are listed in Maria-Sube et al., submitted b, and Φ_{core} results are presented on Fig. P4-5.
The 116 sample measurements present a wide range of porosity: from 2 to 52%, the average porosity being 32%, while the standard deviation is 13.4%.
Apart from clay bearing samples, which may have a grain density as low as 2.325 g/cm^3 (at 9.9mbgl), the other samples present a grain density varying between 2.69 and 2.85g/cm^3, the average grain density being 2.72g/cm^3, and the standard deviation 0.05g/cm^3. This is indicative, nevertheless the uncertainty on grain density measurements, of a mainly calcitic formation, with low percentages of dolomite and ankerite; and is confirmed by spectrometry results (Maria-Sube et al. submitted b). The interval 0-12mbgl can be slightly shaly.
Fig. P4-5 is a dramatic visualisation of the extreme vertical heterogeneity of the formation in MC2. However, it can be noted that below 60mbgl, the porosity range is much reduced: on this interval, the porosity standard deviation is 0.061 (as opposed to 0.13 on the whole interval), and the average porosity value is 0.424; the interval 60-101mbgl geologically corresponds to the reef proximal slope, subunit Ib (this has been demonstrated in Maria-Sube et al. submitted a). Several zones of very low porosity (with $0.02 < \Phi < 0.15$), are observed (Fig. P4-5) at 25mbgl (zone 5), 36mbgl (zone 4), 48mbgl (zone 3), 56mbgl (zone 2), and 60mbgl (zone 1). We have observed that zone 4 at 36mbgl corresponds to the present day water table, and that zones 1, 3, 4, and 5 correspond as well to zones of high grain density, hence probably to dolomitic zones. We will call them zones of *mineralizations*, with a low cementation factor m. The zone at 2.2mbgl is a zone of cementation, with a high cementation factor (Maria-Sube et al. b).
Core laboratory wet V_p results are listed in Maria-Sube et al., submitted b.

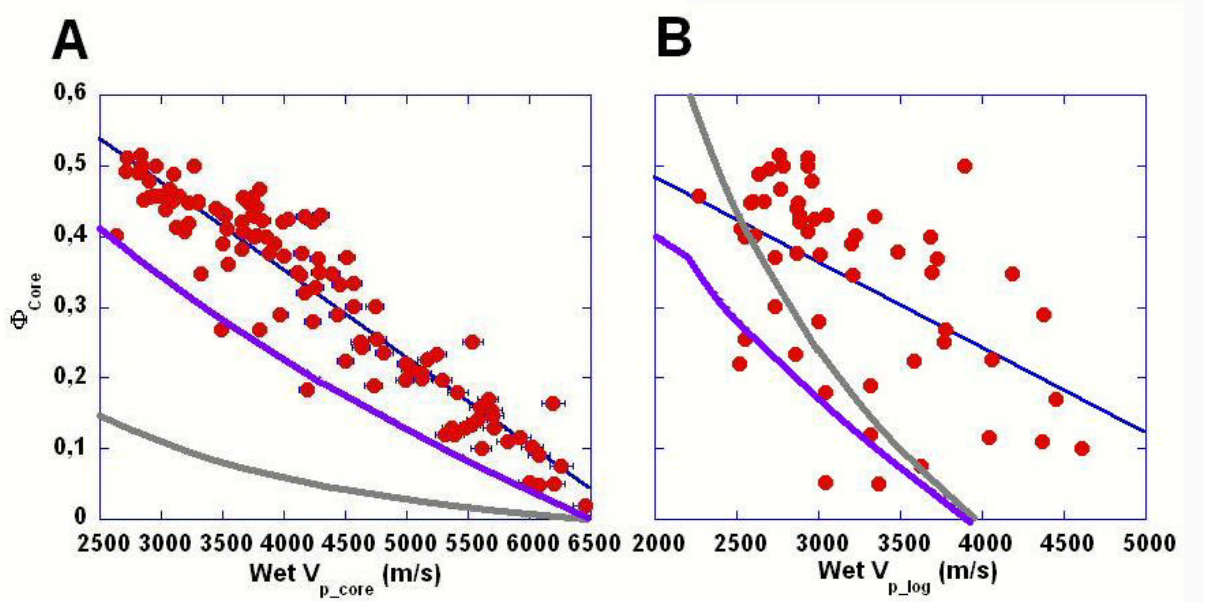

Figure P4- 6. Wyllie et al., 1956 (thick gray curve), and Raymer et al., 1980 (thick violet curve) F to V_p relations are indicated on the plots. (A) Core porosity F_{core} (113 plugs), vs. core sonic compressional velocity V_p in MC2 well; the medium blue linear best fit line equation is: y= 0,85 – 0,00012x, R^2= 0,87. (B) Crossplot of F_{core} (54 plugs) vs. V_p, with a medium blue best fit line of equation: y= 0.73 – 0.0081x, R^2= 0.27.

The plot of wet Φ_{core} vs. V_p (Fig. P4-6A) displays a good linear trend from 2 to 52% porosity. On this plot, it appears that zero porosity calcite has a wet compressional sound speed of 6524m/s in this formation and in the laboratory conditions. The following linear relation relating F_s and V_p could be used (Fig. P4-6A):

$\Phi_S = 0.85 - 0.00012\ V_p$ (20)

It can be seen on the plot that the relation is not exactly linear however ($R^2 = 0.87$), most probably due to the textural and lithological effects evocated in paragraph 3.3.2. The Wyllie time-average porosity equation (6) does not seem to apply in this case (this is in accordance to the remark made above, that the linear Wyllie relation is only satisfactory in the 10 to 25% porosity range); applying a correction factor to the Wyllie relation could however improve the data fit. This relation is not of the Raymer et al., 1980 type either, because, there is no visible inflexion point, and the Raymer et al. relation curve is to low compared to the data points.

4.3 Downhole logging tools

4.3.1 Neutron

It is possible to extract the following calibration relation from the comparison between Φ_{core} and the ratio SSNF/LSNF (F stands for filtered; filtering the SSN and LSN channels is a necessity, because of the low counting rate in this high porosity formation) from the neutron logging tool:

$F_N = - 0.015 + 0.034*SSNF/LSNF$ (22)

The comparison between Formulae (16) from the manufacturer and (22) from core measurements shows very close values of the multiplicative coefficient, but different additive coefficients (practically nil for our calibration).

Applying Formula (22) to the measured ratio SSNF/LSNF leads to Φ_N values in MC2 well, that are plotted vs. depth and compared to the core porosity values Φ_{core} on Fig. 6.

Large statistical variations of Φ_N are observed; in particular in subunit Ib, below 60mbgl, where Φ_{core} median value is 44%, with a standard deviation of 3.5%, ΦN median value is 36% with a standard deviation of 5.5%.

Only three of the mineralization zones (the lowest one) are surveyed by the neutron porosity tool. It is observed that in these zones, Φ_{core} does not go lower than 20%, and sometimes does not even move down. Since we have noted that in these zones, the content of dolomite is generally high, when it is nil in other places, we have to conclude that the change of lithology from calcite to dolomite increases the apparent Φ_N porosity (this is observed on neutron porosity charts supplied by the service oil and gas companies).

4.3.2 Sonic

Results of log compressional velocity V_p are displayed on Fig. P4-3 and are compared to core V_p measurements vs. depth on Fig. P4-6B. We observe a difference between log and core V_p. This is due to: different measuring frequencies, sample size, and measurement direction (most core plug are oriented horizontally, log measurements are oriented vertically). We also observe that the log seems a bit noisy.

4.3.2.1 Calibration in MC2 well

The plot of Φ_{core} vs. log V_p (Fig. P4-6B) does not display as good a linear trend as was observed for the core measurements (Fig. P4-6A). On this plot, it appears that zero porosity calcite has a wet compressional velocity of 3947m/s, quite different from the one obtained on the plugs (6524m/s). The following relationship is to be used for calibrating the log (Fig. P4-6B):

$Fs = 0.73 - 0.00012\ V_p$ (23)

a formula not very different from Equation (20) obtained for the core measurements.

The data plot far from both the Wyllie and the Raymer et al. curves.

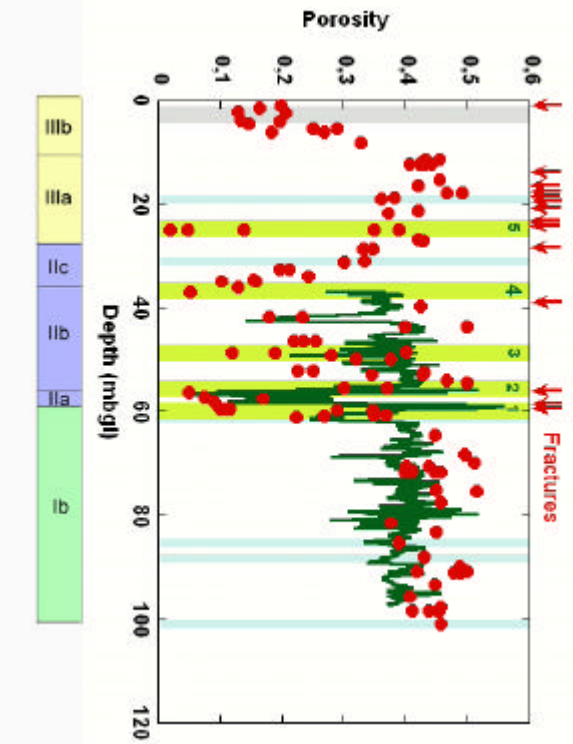

Figure P4- 7 Stratigraphic subunits are indicated on the left side of the figure. Sonic log calibrated porosity F_S medium green curve) compared to core porosity F_{core} (red full dots) from 116 plugs, vs. depth in MC2 well. Light blue, green, gray shadings, and red arrows as per Fig. P4-4.

It is interesting to compare the calibration plot of both acoustic measurements: from cores (Fig. P4-6A) and from log (Fig. P4-6B). The determination coefficient R^2 of the linear best fit is much higher for the cores than for the log (0.87 compared to 0.27), and more core measurements are used for the cores (113) than for the log (54). All other reasons for non linearity between direct porosity measurements and acoustic porosity measurements being similar in both cases, it comes that the only difference between both crossplots is that the core to log depth correlation, although executed with the greatest care, is not perfect.

It is also interesting to compare the porosity calibration equations of neutron log SSNF/LSNF (Formula (22)) and acoustic log V_p (Formula (23)). Here, both R^2 are low (respectively 0.16 and 0.27), and they seem to be so in accordance with the number of plugs used for porosity calibration (respectively 40 and 54). This is a clear indication that the neutron measurement quality was not so bad, in spite of the excessive neutron statistical variations being observed.

Applying Formula (23) to the log V_p values leads to MC2 log Φ_S values, that are plotted vs. depth and compared to the core porosity values of Φ_S and Φ_T on Fig. P4-7. Note the overall good overlap of log Φs with core Φs and Φ_T, even though the log Φ_S curve appears a bit noisy. The three mineralization zones are well apparent.

4.3.2.2 Analysis in MC2 and other wells

We have also applied the calibration Formula (23) to the other wells of Ses Sitjoles, where the sonic logging tool has been run: MC1, MC3, MC5, MC8, MC9, MC10. Fig. P4-8A compares the measurements at the 5m scale (distances between wells) and Fig. P4-8B compares the measurements at the 100m scale. We can observe the low porosity zones (mineralization) on the 46-48mbgl and 56-60mbgl intervals. Note also how the 60-100mbgl (subunit Ib) interval displays porosity values that are well grouped around 40%, with variations of +/- 10%.

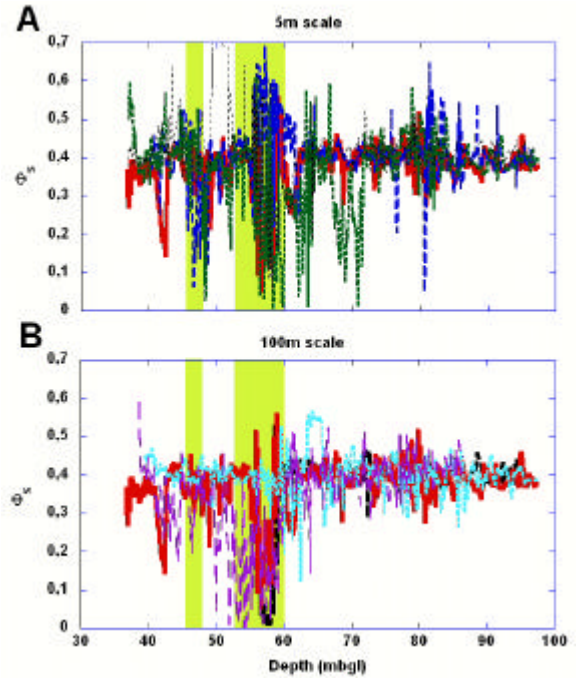

Figure P4- 8. Light green shadings: mineralization zones. Sonic porosity calibrated log in the Ses Sitjoles wells, at a 5m distance scale (A) in MC2 (red thick curve), MC8 (medium blue dashed curve), MC9 medium short dashed green curve) and MC10 (thin short dashed black curve) wells, and at a 100m scale (B) in MC1 (thick dashed black curve), MC2 (red thick curve), MC3 (medium short dashed pale blue curve) and MC5 (medium long dashed violet curve) wells.

4.3.3 Resistivity

The ELXG and DIL 45 formation resistivity and the water resistivity records from the MC2 well are displayed vs. depth on Fig. P4-3. Since porous formations resistivity depends both on the formation fluid resistivity and on the porosity of the formation, it is observed that: 1) in the zone below 78mbgl, of relatively constant water conductivity and porosity, the logs read a fairly constant value; 2) in the transition formation fluid interval, which is also a relatively constant porosity interval, an increasing upward resistive gradient is observed; 3) in the brackish formation water interval, where the formation water conductivity is relatively constant, but the porosity is widely varying (Fig. P4-6 and P4-7), the logs read a varying resistivity, with resistivity increasing when porosity decreases.

It is also observed that SN and LN channels overlap relatively well in the entire surveyed interval, while ILM and ILD overlap well in the sea water and the transition zones, but ILM is constantly lower than ILD in the brackish water interval.

Plugs measurements of resistivity $R_o = 1/\sigma_o$ have led to conclude that: 1) in the sea water and in the transition zones, the ELXG measurements read too high resistivity values, while the DIL 45 measurements are checking the lab measurements; 2) in the brackish water zone, the dispersion of the results is higher, and the ILD 45 readings are either constantly too low (ILM) or somewhat erratic (ILD either apparently correct or much too high), while the ELXG measurements seem both reading relatively correctly (with a tendency for their curves to have a bad vertical resolution).

As a consequence of these observations, it becomes clear that it is necessary to use in the MC2 well a combined final resistivity R_t, composed of a mixture of ILD for the low resistivities, and of SN for the high resistivities. The change between ILD and SN channel is operated when SN becomes larger than ILD; in the MC2 well, this change occurs for the value R_t= ILD= SN= 100Ohm.m.

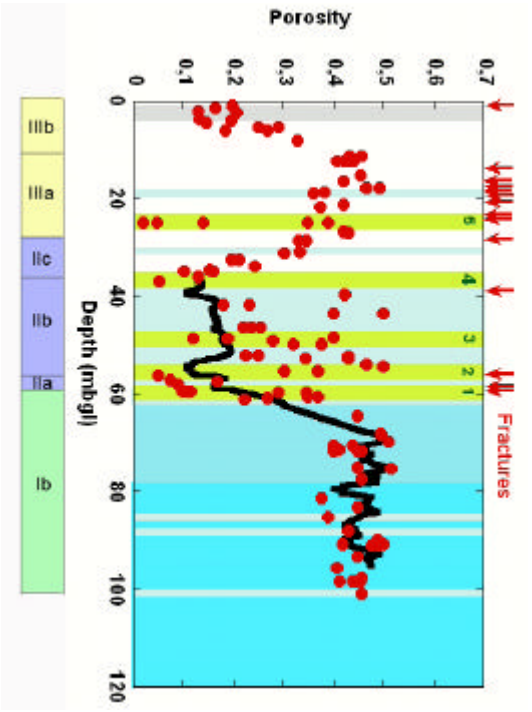

Figure P4- 9. Stratigraphic subunits are indicated on the left side of the figure. In MC2 well, plot vs. depth plug measured triple weight porosity F_{core} (116 plugs, full red dots), and computed and calibrated porosity from resistivity log value R_t, $F_{Rcal} = 0.92*(R_w/R_t)^{1/2.56}$, (thick black curve), 2.56 being the average of the m values measured on each plug. R_t is a mixture of ILD and SN log measurements, ILD for the low resistivity values, SN for the high resistivity values. Light blue, green, gray shadings, and red arrows as per Fig. P4-4.

We have seen that in this well σ_s is negligible compared to σ_w/F, except in the brackish water interval, where it is however lower at least by a factor of 3 (Maria-Sube et al., submitted b. If we neglect σ_s over the whole interval (because no downhole logging tool allows to measure σ_s), we can use Formula (15), in which σ_s is made equal to zero, to compute the porosity from log resistivity Φ_R. If computing Φ_R only at the corresponding depth of a plug, the core cementation factor m is available at that depth. However if computing Φ_R for continuous resistivity log values (Fig. P4-9), this requires the continuous knowledge of m, that we do not have; consequently, we will have to make an other approximation, by using a constant value for m, equal to the average of the plug measured values, i.e. 2.56 (Maria-Sube et al., submitted b).

Once calibrated in porosity, it is possible to display Φ_R vs. depth in the MC2 well (Fig. P4-9). We observe that the mineralization levels are identified on the Φ_R curve.

We have also applied the calibration formula to the other wells of Ses Sitjoles, where the DIL 45 and the ELXG tools have been run. Fig. P4-10A compares those measurements at the 5m (distances between wells) scale, and Fig. P4-10B compares them at the 100m scale. It becomes then apparent that: 1) there is a good agreement between the Φ_R from different wells in the sea water zone; 2) the top of the transition zone generally generate an abnormal porosity peak, similar to the one observed in MC2; 3) the agreement curves is not very good in the brackish water zone: spurious variations, incoherent measurements (even at the 5m scale) are observed in this interval.

It is also interesting to compare Fig. P4-10 to Fig. P4-7 (Sonic), to see that the Sonic porosity from log is of better reliability in the brackish and transition water zones, while in the sea water, the porosity from ILD is overly smoothed compared to the other porosity logs.

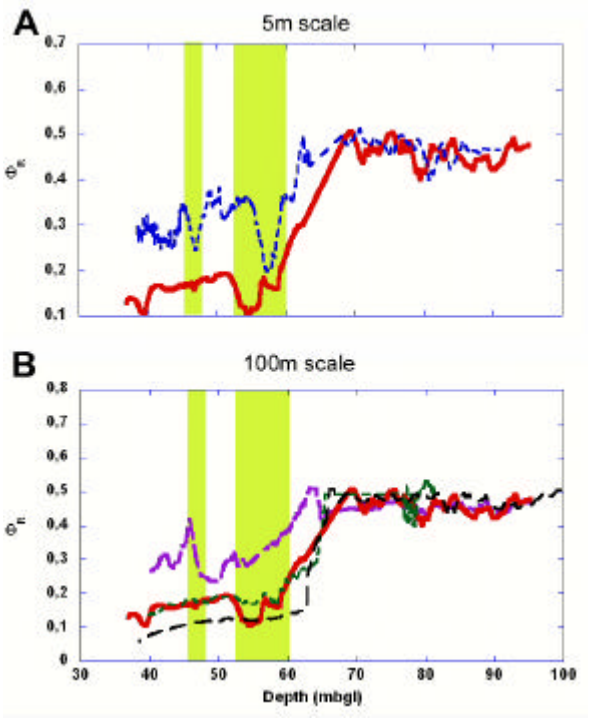

Figure P4- 10. Light Green shadings: mineralization zones. Porosity from resistivity calibrated log F_R vs. depth in the Ses Sitjoles wells, at a 5m distance scale (A) F_R for MC2 (thick red line) and MC8 (medium dashed blue curve) wells, and 100m scale. (B) F_R for MC1 (thick violet curve), MC2 (thick reed curve), MC3 medium short dashed green curve) and S17 (medium black curve) well.

4.3.4 Image log

Although the vuggy porosity extraction from borehole image logs method is supposed to be self-calibrated, due to perturbations from the drilling or coring operations, and also to different physical effects on the optical and acoustic images, it becomes necessary to apply a calibration, in order to have coherent macro porosity results from the three different methods, and also from the optical image in air and in water. We have applied a two points calibration method on the raw, unfiltered image porosities. The calibrated values have been determined from the image and caliper logs, checked with core lab photos, will be explained in Gaillot et al., in prep.

This calibration method uses only logs. In such a way, it is independent from the correlation core depth to log depth, and the inevitable dispersion of results that it generates. The core measured values are only used for control.

The processing of the image was performed on MC2, MC8, and MC9 image log. The acoustic image logs on MC8 and MC9 were of very bad quality (dark, very hard to visually analyze) compared to the one obtained on MC2; we note that the computer processing is not perturbed by this mediocre quality.

The comparison of the results obtained in the three 5m apart only MC2, MC8 and MC9 boreholes (Fig. P4-11) is interesting, because, obviously the caliper log shows differences (Fig. P4-11C) between wells: MC8 and MC9 holes are generally larger (bit size seems to be 12cm here) than MC2 hole (bit size 10cm), and present much larger caves, up to the maximum extension of the caliper (46cm). The bottom part of the boreholes (below 83mbgl) are not as smooth in MC8 and MC9 as they are in MC2. The explanation for this could be that MC2 has been continuously cored, with as a consequence a slower drilling operation, while MC8 and MC9 were drilled faster, without coring.

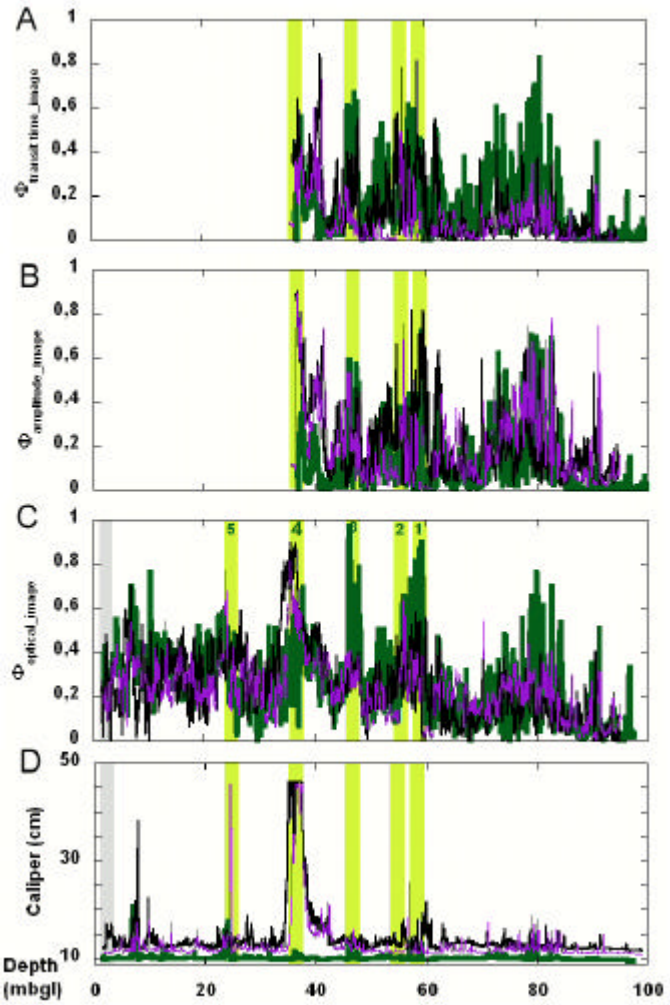

Figure P4- 11. MC2 (thick green curves), MC8 (medium black curves), and MC9 (thin violet curves) well logs vs. depth in air (optical image and caliper) and in water; light green shadings indicate mineralization zones, light gray shadings indicate cementation zone. (A) filtered and calibrated acoustic transit time porosity image. (B) filtered and calibrated acoustic amplitude porosity image. (C) filtered and calibrated optical porosity image. (D) Caliper. Light blue, green, gray shadings as per Fig. P4-4.

Only Φ_{image} from amplitude acoustic image in MC8 and MC9 (Fig. P4-11B) could use the same calibration values as for MC2. Φ_{image} from optical and transit time acoustic images had to be recalibrated. A larger gain has to be used for Φ_{image_TT}, while a smaller gain has to be used for Φ_{image_optic}, than for MC2.

After calibration, and taking into account the hole size specificity of each well, it is possible to say that there is good agreement between the image porosity of each hole. The mineralizations zones are clearly recognized on all Φi_{mage} log (Fig. P4-11A, P4-11B, P4-11C). The use of acoustic amplitude images, that are naturally insensitive to tool eccentralization, is a real advantage in respect of travel time and optical images. The proposed method allows detection and quantification of vugs. Additional methodological developments (inertia tensor computation) allow characterizing of the distribution and geometry of the vertical section of the detected vugs as well as their spatial anisotropy of distribution.

5 DISCUSSION

5.1 F_{core} vs F_{log}

The core petrophysical measurements, such as the triple weighting porosity measurement, are accurate, because they are performed in laboratory under the best instrumentation conditions, and using directly the definition principles. By definition, they are punctual measurements, hence discontinuous, they refer to a certain volume of sample, and to an individual core depth that is not always easy to relate to a continuous log depth.

5.1.1 F_{core}

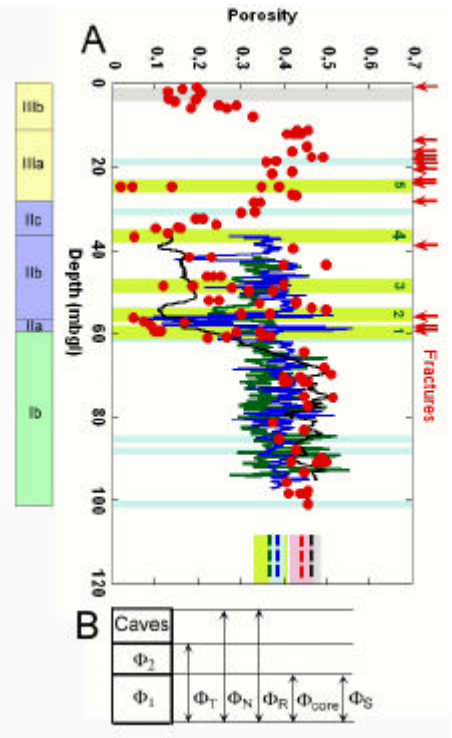

Figure P4- 12. Stratigraphic subunits are indicated on the left side of the figure. (A) In MC2 well, plot vs. depth of plug measured porosity F_{core} (116 plugs, full red dots), and F_N (thick green curve), F_S (medium blue curve), and F_R (thin black line), computed and calibrated porosities from log values At graph bottom, the median value in subunit Ib of each porosity value is indicated by a thick dashed segment, and the standard deviation around the median value is indicated in light colored shading. Light blue, green, gray shadings, and red arrows as per Fig. 4. (B) Sketch of log neutron porosity F_N, log resistivity porosity F_R, log sonic porosity F_S, and core porosity F_{core} readings relative to formation primary porosity F_1, secondary porosity F_2, total porosity F_T, and caves.

In this shallow depth unconsolidated carbonates, where different forms of diagenesis (mineralization, dolomitization, cementation) have occurred, the porosity range varies from 2 to 52%. Several relatively thin (about 70cm intervals), low porosity (<15%), zones of mineralization, mostly associated to dolomitization (Fig. P4-5), caused by sea water standstills (Maria-Sube et al., submitted b) have been identified. The bottom interval of MC2 (60-100mbgl), corresponding to subunit Ib, is characterized by an median porosity of 44%, with a moderate standard deviation of 3.5% (as compared to 13% on the whole interval), Fig. P4-12A.

5.1.2 F_N

No neutron measurement was performed in laboratory.

There is a linear relationship between Φ_N from log and the ratio SSN/LSN. The 11% offset communicated by the constructor appeared to be actually practically nil, while their gain seems correct. It is then possible to calibrate Φ_N in terms of SSN/LSN and to obtain a continuous log measurement (Fig. P4-7).
The neutron porosity is sensitive to every hydrogen molecule, and consequently, to the water included in all open porosity (including fractures and caves). In other words, Φ_N can be assimilated to the sum of Φ_T and the porosity filled by caves (Fig. P4-12B) in subunit Ib. The medium value of Φ_N is 36%, with a standard deviation of 5.3% (Fig; P4-12A).

5.1.3 F_S

The laboratory acoustic measurements, performed on the MC2 plugs, have provided a very interesting result: there is a linear relationship between Φ_s and the sound compressional velocity V_p; this linear relation is valid across the complete range of porosity (from 2 to 52%). In contrast, neither the Wyllie et al., 1956, nor the Raymer et al., 1980, equations are verified.
This result has been also verified on the log velocity measurements, although with a larger dispersion than on the plug measurements, due to the difficulty in conciliating core and plug depths. It is then possible to calibrate Φ_s in terms of V_p and obtain a continuous log measurement (Fig. P4-7).
Since the sound speed is much slower in water than inside a rock, it is considered that the sound wave first arrival is by-passing fractures and vugs. Consequently, Φ_s measurements exclude fracture porosity. This observation leads to the estimation that Φ_S measures approximately Φ_1 (Fig. P4-12B).
In subunit Ib, the median value of ΦS is 38%, with a standard deviation of 2.1% (Fig. P4-12A)

5.1.4 F_R

Laboratory electrical measurements provide values of m, F, σ_o, and σ_s. m measurements vary between 1.2 and 4.3, with an average of 2.56 and a standard deviation of 0.44, demonstrating how fallacious it is to consider m as a constant value in carbonates. There is however a loose tendency for m to be proportional to the porosity (in opposition to the Shell formula). Although the clay mineral content of the formation is generally low, the measurements are showing that in the brackish water interval of MC2 (36.4 to 62mbgl), the surface conductivity is not negligible compared to the volumetric conductivity.
When neglecting σ_s (but we have seen that this is only an approximation, and not a very good one in the brackish water interval), it is possible to compute Φ_R from the formation and from the formation water log measured resistivities, and to obtain a continuous measurement (Fig. P4-9); we have linearly calibrated this measurement from the core measurements. For doing this, we need to use an average value of m, which is in this very heterogeneous formation, a gross, but necessary, approximation. An other cause of uncertainty comes from the use of inappropriate resistivity logging tools in the brackish formation water interval (i.e. the lack of a focused resistivity logging tool in that interval). The last cause of uncertainty is the rapidly changing formation water resistivity in the transition interval, causing perturbations due to depth discrepancies between the different logging tools measuring σ_o and σ_w. For all the reasons that we just enumerated, the porosity measurement extracted from the resistivity logs Φ_R, is not a very accurate measurement, except in the sea water interval. It also suffers from a lack of vertical depth resolution of the resistivity logging tools in general, and consequently Φ_R provides a very smoothed curve, which is lacking character.

Φ_R can be, as Φ_N, assimilated to the sum of Φ_T and the porosity filled by caves (Fig. P4-12B). In MC2 subunit Ib, the median value of Φ_R is 46%, with a standard deviation of 2.3%.

5.1.5 F_T, F_N, F_S, F_R comparison

The comparison of the log measured Φ_N, Φ_S, and Φ_R curves and the plug measured Φ_T dots vs. depth (Fig. P4-12A) is revealing that: 1) Φ_R is much smoother than Φ_N and Φ_S, much probably because the vertical depth definition of the ILD 45 or the ELXG tools (around 1m) is not so small as for the neutron and the sonic tools (around 0.3m); the averaging of m value, is an other smoothing factor; 2) Φ_R is generally a bit larger than Φ_N and Φ_S in subunit Ib (sea and transition zone water) and corresponds rather well to the plug measured porosity; 3) Φ_R is much lower than Φ_N and Φ_S in Unit II (brackish water zone), most probably we see here the effect of neglecting σ_s in the log computation of σ_o (σ_o is too low in the brackish water zone, which means that Φ_R is too low in that same zone).
The three different log porosity measurements provide a continuous porosity in the wet zone of MC2 well (Fig. P4-12), with different characters: they all indicate the low porosity measurements that have been identified with the plug measurements (and no new one, i.e. we have not missed anyone of them in our choice of cores and plugs); Φ_R is smoother than Φ_N and especially Φ_S, these two last logs having a better vertical definition than the resistivity logs; the sharp variations of Φ_s, especially in the slope, reflect the detrital, laminated character of this formation, well observed on Cabo Blanco cliff outcrop (Fig. P4-4); Φ_R reads correctly in the sea water zone, and incorrectly in the brackish water zone.

5.1.6 Comparison of MC2 porosity and acoustic results with GBR and GBB coral reef results

5.1.6.1 Presentation of ODP legs 133 and 166

Two Ocean Drilling Program (ODP) legs have concerned carbonate complexes covering a Miocene to modern time window, respectively the Great Barrier Reef (GBR), leg 133 (Davies et al., 1990), and the Great Bahama Bank (GBB), leg 166 (Eberli et al., 1996; Eberli et al., 1996a), on which core and log porosity and acoustic data were obtained. The comparison of those data and those collected on the Ses Sitjoles Miocene carbonate complex might allow the confirmation of the Φ to Vp relation and of the slimhole sonic logging tool porosity calibration validity asserted for Ses Sitjoles. A similar comparison was used in Maria-Sube et al., submitted, for validating the use of the natural spectral gamma-ray slim-hole logging tool.
The GBR is the world's largest modern coral reef system, composed of roughly 3,000 individual reefs and 900 islands, that extend on about 2,600 kilometres, covering an area of approximately 344,400km². The reef is located in the Coral Sea, off the coast of Queensland in North-East Australia. The North-Eastern Australian margin was investigated from the GBR to the landward side of the Queensland Plateau. We have limited our investigation of ODP Leg 133's data (Davies et al., 1990), to sites 819A, 820B, 821A, and 822A, drilled on the Eastern side of the modern barrier reef, from 212 to 1010m below sea floor (mbsl), 10km offshore Cairns (Tables P4-2 and P4-3). This carbonate complex has developed from the late Miocene to modern time. Geochemistry has determined on the four sites, from 0 to 400mbsf minor amounts of dolomite and clays in a calcite, aragonite, quartz, and clay dominant mineralogy; the clay mineralogy is described on the near-by site 823C as being in average 60% montmorillonite, 25% kaolinite, 10% illite, 5% mixed layers and traces of chlorite (Davies et al., 1990).

Leg	Site	Number of samples	Sea floor depth (mbsl)	Depth interval (mbsf)	Age	V_p vs. Φ_D		Φ_D vs. V_p		Φ_D vs. ΔT	
						best fit line equation y=	R^2	best fit line equation y=	R^2	best fit curve equation y=	R^2
133 GBR	819A	2120	620	0- 73	Pleistocene	1774-411.8x	0.096	0.91-0.00023x	0.096	2.7-0.0087x+8.3 $10^{-6}x^2$	0.4
	820B	3820	340	0- 104	Pleistocene	1808-449.9x	0.25	1.4-0.00056x	0.25	4.3-0.014x+1.3 $10^{-5}x^2$	0.38
	821A	5200	**212**	0- 187	0-0.4m.a.	1888-593x	0.33	1.3-0.00055x	0.33	4.7-0.016x+1.5 $10^{-5}x^2$	0.47
	822A	3070	1010	0- 83	Pleistocene	1718-350.6x	0.074	0.84-0.00021x	0.074	1.9-0.0047x+4.1 $10^{-6}x^2$	0.10
166 GBB	1003A	1810	470	0- 100	Pleistocene	2295-1456x	0.12	0.59-7.7 10^{-5}x	0.11	0.84-0.002x+2.2 $10^{-6}x^2$	0.28
				100- 160	Late Pliocene						
	1005A	840	**350**	0- 51	Pleistocene	1772-392x	0.010	0.55-2.6 10^{-5}x	0.010	1.2-0027x+2.6 $10^{-6}x^2$	0.093
	1006A	4470	660	0- 100	Pleistocene	1799-455.1x	0.0069	0.51-1.5 10^{-5}x	0.0069	0.98-0.0021x+2.1 $10^{-6}x^2$	0.13
				100- 272	Late Pliocene						
	1007A	110	650	0- 5.9	Pleistocene	2982-2465x	0.093	0.58-3.8 10^{-5}x	0.093	0.94-0.002x+2.1 $10^{-6}x^2$	0.28
SS	MC2	113	-	0- 100	Miocene	6524-7073x	**0.87**	0.85-0.00012x	**0.87**	-0.94+0.0082x-1.2 $10^{-5}x^2$	**0.88**

Table P4- 2. Comparison of core porosity vs. acoustic velocity best fit curve equations between Ses Sitjoles MC2 well and wells in the GBR and GBB area.

Leg	Site	Number of samples	Sea floor depth (mbsl)	Depth interval (mbsf)	Age	V_p vs. Φ_D		Φ_D vs. V_p		Φ_D vs. ΔT	
						best fit line equation y=	R^2	best fit line equation y=	R^2	best fit curve equation y=	R^2
133 GBR	819A	1990	620	66- 366	Pleistocene	2411-1099x	0.077	0.57-7.1 10^{-5}x	0.078	0.067+0.00095x-4.7 $10^{-7}x^2$	0.13
	820B	2000	340	73- 380	Pleistocene	2611-1552x	0.024	0.43-1.6 10^{-5}x	0.024	0.32+0.00011x+1.1 $10^{-7}x^2$	0.088
	821A	2030	**212**	65- 140	0-0.5m.a.	2596-1456x	0.054	0.46-3.8 10^{-5}x	0.055	0.31+0.00012x+7.8 $10^{-8}x^2$	0.10
				140-375	0.5-1.8m.a.						
	822A	1550	1010	72-80	Pleistocene	1516+346.7x	0.015	0.67+4.8 10^{-5}x	0.016	0.7+0.00015x-1.1 $10^{-7}x^2$	0.027
				80-308	Pliocene						
166 GBB	1003D	6120	470	114-300	Pliocene	4753-4844	**0.71**	0.80-0.00015x	**0.71**	-0.35+0.0027x-1.8 $10^{-6}x^2$	**0.75**
				300-1050	Miocene						
	1005C	1910	**350**	386-400	Pliocene	4090-2793	0.31	0.55-0.00011x	0.31	-0.12+0.0018x-9.4 $10^{-7}x^2$	0.33
				400-678	Miocene						
	1006A	3920	660	102-450	Late Pliocene	4831-5952x	0.60	0.68-0.0001x	0.60	0.0062+0.0014x-9.3 $10^{-7}x^2$	0.62
				450-699	Miocene						
	1007C	6730	650	109-350	Pliocene	4355-3582x	0.071	0.46-2.0 10^{-5}x	0.071	-0.28+0.0027x-2.2 $10^{-6}x^2$	0.46
				350-1134	Miocene						
SS	MC2	54	-	0- 100	Miocene	3947-2239x	0.26	0.73-0.0081x	0.27	0.74+0.0013x	0.26

Table P4- 3. Comparison of log porosity vs. acoustic velocity best fit curve equations between Ses Sitjoles MC2 well and wells in the GBR and GBB area.

The Bahama Banks are the submerged carbonate platforms that form the basement of the modern Bahama Archipelago. The GBB is the carbonate bank that is located around Andros Island, extending on 600km from the Northwest to the Southeast. Four sites (1003D,1005C, 1006A, and 1007C), were drilled and logged in the North-West slope transect off the GBB, between Florida, Cuba and Andros Island, from the proximal to the drift, from 350 to 660mbsl water depth during the ODP Leg 166 (Eberli et al., 1996, Tables P4-2 and P4-3). The site is more than 200km away from the coasts of Florida, Cuba or Andros island; the biostratigraphic evidence suggests a depositional environment deeper than 200mbsl. The GBB is a carbonate system that developed from the Jurassic up to modern time. The drilled

formations range in ages from the Lower Miocene to the Pleistocene. Geochemistry has determined minor amounts of dolomite, aragonite (very abundant at shallow depth, from 0 to 250mbsf at most, minor below that depth), and very minor amounts of clays in a calcite dominant mineralogy. Free hydrocarbons, methane, H_2S, propane, isobutane, etc., are noted starting at depth of about 100 to 200mbsf, with increase in the concentration of heavy-weight hydrocarbons below 735mbsf in site 1003, below 74.3mbsf in site 1005, below 630.6mbsf, in site 1006, and below 540mbsf in site 1007. Traces of celestite evaporite (SrSO4) was observed in site 1003 between 200 and 500 msbf, and in site 1007; traces of pyrite (FeS2) in site 1007 and of glauconite mica were also observed in sites 1006 and 1007 (Eberli et al., 1996).

The ODP shipboard core measurements where recorded by the multisensor track (MST) device, which is a multiprocessor, multisensor data collection system that takes measurements on cores from several sensors simultaneously. The MST is designed to handle all sampling automatically. Of interest for this document are the density and the acoustic velocity measurements.

Gamma-ray attenuation (GRA) density is measured by determining the attenuation of gamma-rays that pass through the cores and is used to estimate bulk density ρ_b. The degree of attenuation is proportional to the electron density in the gamma path. Gamma attenuation coefficients vary as a function of atomic number, but, as most earth-forming mineral have similar and low atomic numbers, the correlation between gamma density and bulk density is generally very good. A value of porosity $\Phi_{Dcalcite}$ is then calculated from ρ_b, assuming that the grain density ρ_{ma} is constant and equal to the density of calcite ρ_{ma}= 2.71g/cm^3, Serra, 1990; this is an approximation since we have seen that the mineralogy of each site is complex and varied along the borehole. The measurement spacing was 2.5 to 5cm. This measurement is very sensitive to core disturbance (Jarrard et al. 1993).

Shipboard core acoustic P-wave velocity measurements (PWL, for P-Wave logger) were undertaken in a Hamilton-Frame velocimeter; vertical compressional wave velocity was measured, using a pair of 500kHz transducers. The measurement spacing was 2.5cm. This measurement is very sensitive to cycle-skipping (Jarrard et al. 1993).

5.1.6.2 Core porosity vs. V_p relationship

Crossplots of core Φ_D vs. V_p and Φ_D vs. ΔT have been plotted for GBR (Fig. P4-13A), GBB (Fig. P4-13C) and are compared to similar plots obtained in MC2 well (Fig. 13E). Although the number of measurements is generally large (Table P4-2), the number of plotted data are generally more limited, for two reasons: 1) for quality control, we had to eliminate the data points where $\Phi_D < 0$, $\Phi_D > 0.8$; $V_p > 2100$m/s (GBR), and $V_p > 4000$m/s (GBB), these large V_p data corresponding to nearly constant porosities; 2) for depth correspondence, some Φ_D measurements where without corresponding V_p measurements at the same depth, or the contrary.

The GBR and GBB core depth intervals are in a similar range (0- 272mbsf) as the MC2 cores (0-100mbgl), Table P4-2. The core Φ_D porosity range, however, for both the GBR and GBB is of 0.25-0.8, compared to 0.02-.052 for MC2, thus indicating a shift toward the larger porosity values. It appears that for the GBR and GBB, the phenomenon of mineralization encountered in the Ses Sitjoles data was absent, but a larger carbonate dissolution process than in Ses Sitjoles was at work. The age of the GBR and GBB studied cores varies from modern to Pliocene, whereas the age of the MC2 plugs is Miocene (Table P4-2). It is then probable that this younger age in the GBR and GBB sediments yields a less developed cementation than in Ses Sitjoles, and hence larger porosities at shallow depths than in MC2 well.

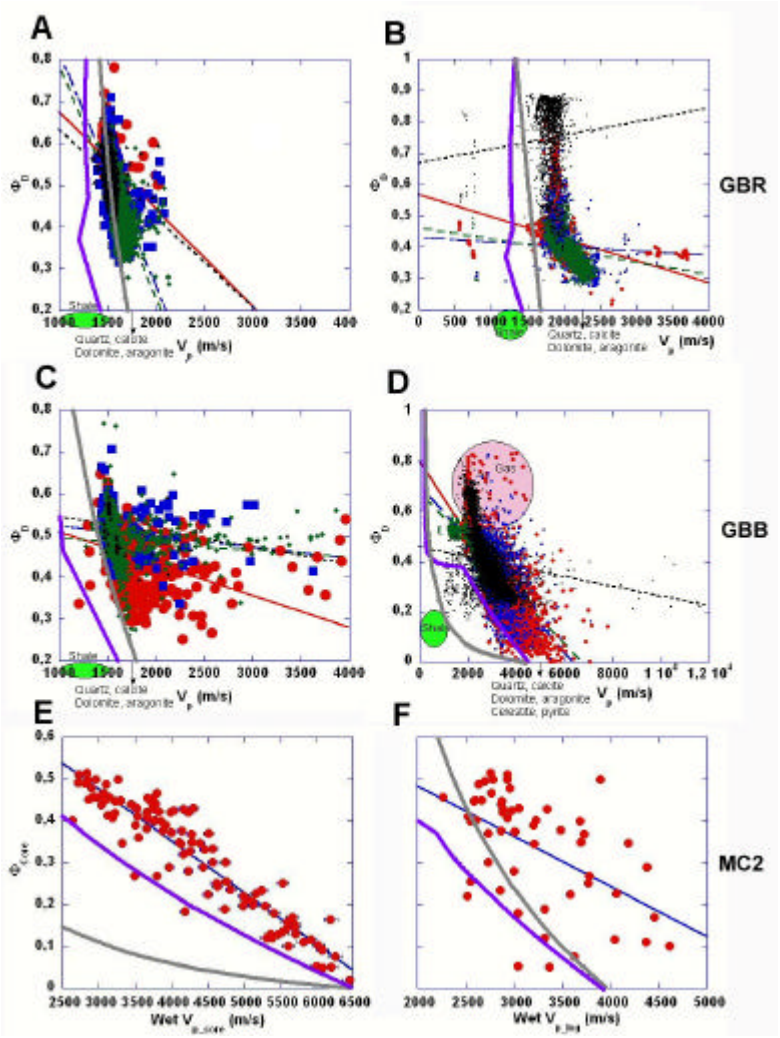

Figure P4- 13. Crossplots of core and log measurements Φ vs. wet velocity V_p (with linear best fit curves); Wyllie et al., 1956 (thick gray curve), and Raymer et al. 1980 (thick violet curve) Φ to V_p relations are indicated on the plots. Best fit curve equations are listed in Tables 13 and 14. (A) Great Barrier Reef (GBR) sites 819A (2120 measures, large red dots, red line best fit curve), 820B (3820 measures, large medium blue full squares, blue long dash best fit curve), 821A (5200 measures, small medium full green lozenges, green dash best fit curve), and 822A (3070 measures, small full black triangles, black dot best fit curve) core measurements porosity from density radioactive measurement Φ_D vs. V_p crossplot. (B) GBR sites 819A (1990 measures, small red dots, red line best fit curve), 820B (2000 measures, small blue full squares, blue long dash best fit curve), 821A (2030 measures, small full green lozenges, green dash best fit curve), and 822A (1550 measures, small full black triangles, black dot best fit curve) log measurements porosity from radioactive density measurement Φ_D vs. V_p crossplot. (C) Great Bahama Bank (GBB) sites 1003A (1810 measures, large red dots, red line best fit curve), 1005A (840 measures, large medium blue full squares, blue long dash best fit curve), 1006A (4470 measures, small medium full green lozenges, green dash best fit curve), and 1007A (110 measures, small full black triangles, black dot best fit curve) core measurements Φ_D vs. V_p crossplot. (D) GBB sites 1003D (6120 measures, small red dots, red line best fit curve), 1005C (1910 measures, small blue full squares, blue long dash best fit curve), 1006A (3920 measures, small full green lozenges, green dash best fit curve), and 1007C (6730 measures, small full black triangles, black dot best fit curve) log measurements Φ_D vs. V_p crossplot. (E) and (F): refer to Fig. 5A and 5B respectively.

In GBR and GBR sites, V_p ranges from 1000 to 4000m/s, while in MC2 V_p ranges from 2500 to 6500m/s. It is also possible to compare the average V_{ma}'s of 1796m/s (GBR) and 2212m/s to the V_{ma} of 6524m/s for MC2; the distribution of the data on the plots suggests that the GBB data points where Vp> 2500m/s are erroneous (Fig. P4-13C), due to cycle skipping. This GBR and GBB velocity shift toward the low speeds is partially explained by the larger

minimum and maximum porosities in GBR and GBB than in MC2. Another explanation results from the differences in the measurement procedures and devices.
The best fit curve equations for three different core plots and for all the sites are listed in Table P4-2; although the V_p vs. Φ_D plot is not displayed in Fig. P4-13, the best fit line equation for this plot provides directly the values of the V_f, V_{ma}, (and hence ΔT_f, ΔT_{ma}) and the V_{37} and V_{47} parameters that are useful for calculating the Wyllie and Raymer et al. curves represented on the six plots of Fig. P4-13. The R^2 values are much closer to 1 for the MC2 cores than for the GBR or the GBB cores, thus reflecting the superior coherence and quality of the laboratory porosity and acoustic velocity measurements performed on the MC2 plugs; if the GBB data where Vp> 2500m/s had been eliminated, this would have improved R^2 for the GBB plots. The GBR data fit remarkably well to the Φ to V_p Wyllie relationship curve (Fig. P4-13A). The GBB data lie close to the Wyllie relationship curve (Fig. P4-13C), but not as well as the GBR data. In both cases, the Raymer et al. relation curve is much further off the data points than the Wyllie relation curve. For MC2 data, both Wyllie and Raymer et al. curves are off the data points, but Raymer et al. curve is closer than Wyllie curve (Fig. P4-13E).

5.1.6.3 Log porosity vs. V_p relationship

The log density ρ_b was recorded using a Schlumberger hothole lithodensity tool (HLDT), using the same measurement principles as the GRA device. Other provided measurements are: the mud-cake correction $\Delta\rho_b$ and the photo-electric effect PEF. $\Delta\rho_b$ provides a mud-cake correction and also provides a log quality control (it is considered that when $\Delta\rho_b$ exceeds +/- 0.15g/cm^3, the ρ_b measurement is doubtful). PEF is a good qualitative lithology indicator, as it is nearly independent of porosity. The measurements are recorded every 15cm.
The log acoustic traveltime was recorded using a Schlumberger long-spaced sonic (LSS) tool. This tool measures four compressional wave traveltimes over source-receiver spacing of 2.4, 3.0, 3.0, and 3.6m. Although traveltimes include the time for wave propagation both within the borehole and as a refracted wave along the borehole wall, the difference between traveltimes for different source-receiver spacings is a direct measure of the vertical velocity (inverse of traveltime) over a 0.61m interval of formation. Real-time Schlumberger processing yields two travel times logs: a short-spaced (3.0-2.4m) and a long-spaced (3.6-3.0m). In these generally shallow carbonate formations, we have privileged the long-spaced measurements, which allow to capture the traveltime arrival by the unaltered formation (Serra and Serra, 2000). The acoustic frequency can be varied from 5 to 18kHz. The measurements are recorded every 15cm.
The other logging tool recorded in GBR and GBB was the hothole natural gamma-ray sonde (HNGS); in GBB, a neutron hydrogen index tool was recorded, either of CNT (compensated neutron tool, 1007C site) or of APS (accelerator porosity sonde, 1003, 1005C and 1006A sites) type. The HNGS radioactive mineral analysis performed on Thorium vs. potassium (K) crossplots confirmed the GBR clay composition of montmorillonite, kaolinite, illite, chlorite, and indicated a possible GBB clay composition of montmorillonite, kaolinite, illite, and confirmed presence of glauconite as well in the GBB sites (Maria-Sube et al., submitted). Using the full set of logs, a series of mineralogy crossplots were analyzed: ρ_b vs. ΔT, ρ_b vs. K, PEF vs. ρ_b, and PEF vs. K, in GBB and GBR, and ρ_b vs. Φ_N, ΔT vs. Φ_N in GBB. This confirmed the geochemistry results indicated above (and notably the presence of gas in the GBB sites, clearly evidenced on the ρ_b vs. Φ_N crossplot), but more importantly, allowed to position the clay, and other minerals on Fig. P4-13B and P4-13D, and by extension on Fig. P4-13A and P4-13C, and the gas on Fig. P4-13D.
The data characteristics are listed in Table P4-3. Note that log data where acquired on GBB sites 1003D and 1005C, instead of sites 1003A and 1005A for the core data; sites 1003D and

1005C are sidetracked from respectively sites 1003A and 1005A, have a common part and are deeper. Generally the log data of both GBR and GBB sites are deeper than the core data, and consequently, the deepest part is older. This is even more true for the GBB sites which could reach in their lowest parts sediments of Miocene age, comparable to the age of the MC2 sediments. The GBR sites have a log depth interval from about 70 to 360mbsf; their porosity range is from 0.2 to 0.88 (Fig. 13B), quite cP4-omparable to the porosity range measured on cores (Fig. P4-13A), the slightly higher minimum porosity measured on cores being explained by the difference in maximum depth between cores and logs. The GBB sites have a log depth interval from about 100 to 700 or 1200mbsf; their porosity range is from 0 to 0.82 (Fig. P4-13D). This is very different from the porosity range measured on cores (Fig. P4-13C), notably the lower porosity range 0-0.25 is absent on the cores. This can be explained by the difference in maximum depth between cores and logs. The difference in maximum log Φ_D (at shallow depth) between GBR and GBB sites could be due to the presence of dolomite (ρ_b= 2.86g/cm^3), aragonite (ρ_b= 2.9g/cm^3) and also of traces of heavy elements celestite (ρ_b= 3.79g/cm^3), and pyrite (ρ_b= 4.99g/cm^3), (Serra, 1990) in the GBB sites, which pull $\Phi_{Dcalcite}$ artificially toward the low porosity values. The presence of gas has exactly the reverse effect, but concentration of gas is low at shallow depth in the GBB sites. The comparison of the GBR and GBB sites' log porosity range (Fig. P4-13B and P4-13D) with the MC2 well log porosity range (Fig. P4-13F) indicates that only when the carbonate sediments reach the Miocene age (as in GBB and MC2), porosities between 0 and 0.20 can be observed.

In GBR sites, V_p log ranges from 500 to 4000m/s, with an average V_{ma}=1796m/s. In GBB sites, V_p ranges from 1000 to 12000m/s, with an average V_{ma}= 4507m/s, in MC2, V_p ranges from 2500 to 5000m/s, with V_{ma}= 3947m/s (Table P4-3). The distribution of the data on the plots suggests that for GBR sites, the data points which exhibit V_p> 2800m/s are erroneous, due to cycle skipping; it is also possible that the data which exhibit V_p< 1000m/s are wrong. For GBB sites, the data points which exhibit V_p> 7000m/s are erroneous due to cycle skipping. Although the V_{ma} values found for both core and log GBR sites are remarkably close, they are quite different for the GBB sites and for the MC2 well.

The best fit curve equation for three different log plots and for all the sites are listed in Table 3, in a similar way as was done for the core plots in Table P4-2. This time, the highest R^2 values are obtained for the plots of the GBB sites, notably for sites 1003D and 1006A, the lowest R^2 values being observed in the GBR sites. These low R^2 values in the GBR sites illustrate the difficulty of V_p log measurements in non consolidated shallow formations. None of the plots of Fig. P4-13 exhibit data fitting well with either the Willie or the Raymer et al. curves.

5.1.6.4 Core and log porosity and acoustic results discussion

The GBR and GBB core and log measurements use a $\Phi_{Dcalcite}$ porosity measurement derived from a radioactive density measurement, and calibrated for a pure calcite mineralogy associated to water fluid filling the pores. This results in a poor quality total porosity measurement, affected by mineralogy and fluid (GBB logs) perturbations. For the cores, core disturbance affects the measures. For the logs, hole perturbations due to invasion and hole size further affect the measurements despite the mudcake correction, in case of excessive mudcake, or irregular hole.

The GBR and GBB core and log measurements use an acoustic compressional wave velocity measurement that are both affected by cycle skipping problems. There are differences from core to log measurement in sample size and operative frequency.

The GBR and GBB core depth correspondence between GRA and PWL measurements is only approximate; this is one of the main cause for low R^2 for the best fit curves (Table P4-2). The GBR and GBB log depth correspondence between Schlumberger HLDT and LSS

measurement is perfect since the log are recorded in one single run of a combined tool, and all curves are depth corrected automatically to one reference curve by software. This explains the relatively high R^2 in GBB; The low R^2 in GBR is in turn explained by the excessive cycle skipping observed on Fig. P4-13C.
In comparison with the ODP measurements, the MC2 core porosity and acoustic velocity measurements are of excellent quality, due to the used methodology; their depth correspondence is perfect, since they are performed on exactly the same plug. This quality results in the good concentration of the data points on Fig. P4-13E.
The same quality cannot be observed for the MC2 core porosity vs. log acoustic data of Fig. P4-13F, due to the problem of plug to log depth correspondence.
A noticeable difference in the V_{ma} core measurements (from 1796m/s in GBR, to 6524m/s in MC2) and in the V_{ma} log measurements (from 1796 m/s in GBR, to 4507m/s in GBB) is noted and is attributed to the different methods of measurements.
Even with data of good quality and concentration (MC2 plugs, GBB site logs), the Wyllie or Raymer et al. Φ to acoustic velocity relation are not verified; it is therefore necessary in carbonate reef sediments to calibrate the acoustic velocity to porosity on a case by case method.

5.2 F_{image}

The image porosity can be extracted by processing of the borehole image logs (optical, and acoustic amplitude and transit time). The acoustic amplitude log provides the most reliable results, the optical log provides the least reliable results, but results are available over the whole interval, including the vadose zone. Calibration of each method is necessary, to get coherent results. We have used a two points calibration based on minimum (close to zero, verified on image log) and maximum (in caves, the exact value being verified on image log) macro porosity. This calibration method has the advantage of not necessitating core measurements (although we have used them, but only for verification purposes); only image and caliper logs are used.
This method of image porosity extraction from image logs obtains coherent results from the three image data sources; the drilling or coring effects are minimized. The resulting quantitative and continuous macro porosity is thus a combination of vug porosity and cave effect; the caving effect in this kind of formation can be due to drilling action if the sediments are soft (such as shale in subunit IIIb), or to karst.

5.3 Comparison of F_{core} and F_{image}

Caves are clearly identified by high macro porosity zones (Fig. P4-14B and P4-14C); however, in the vadose zone where only the optical image tool is available, caution must be taken, especially in the upper part (subunit IIIb) where clay is present, that dark clay is not mistaken for cave; for this reason, the caliper tool record is a must.
The comparison of macro porosity computed from optical image log and of total porosity in MC2 well (Fig. P4-14C) reveals that: 1) because of the relation $\Phi_{image} = \Phi_2 + \Phi_{caves}$ (Fig. P4-14D), we observe that $\Phi_{image} < \Phi_{core}$, except where Φ_{cave} is large; 2) the caliper indicates the cave's lateral depth (Fig. P4-14B), while the borehole images indicate the cave's percentage of horizontal 360°, and area (Fig. 14A); 3) the proximal slope (subunit Ib), which looked smooth in terms of core porosity, is far from being smooth in terms of macro porosity (and as well in terms of continuous porosity logs (Fig. P4-5, P4-14)). This is confirmed by the outcrop of Cabo Blanco cliff (Fig. P4-4).

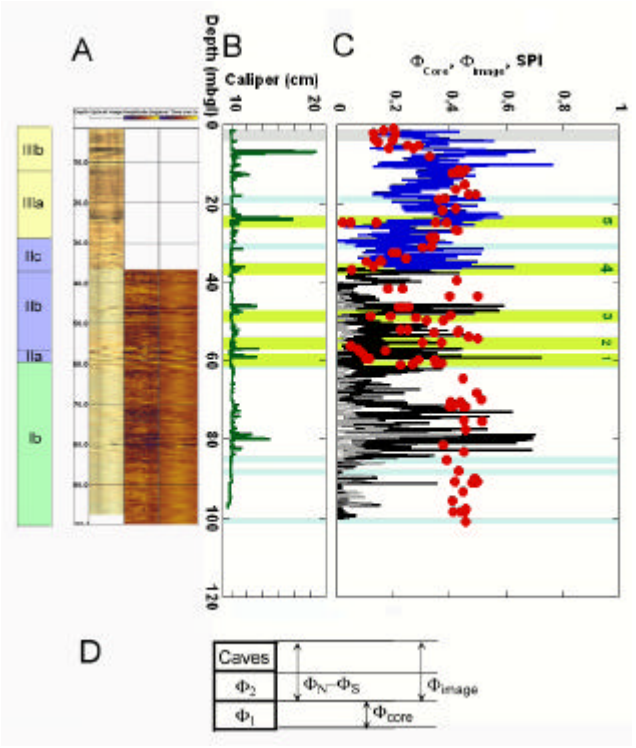

Figure P4- 14. Stratigraphic subunits are indicated on the left side of the figure. In MC2 well, plots vs. depth of, (A) from left to right, optical, acoustic amplitude and transit time image logs; (B) caliper log; (C) calibrated image porosity computed from optical image log, in air (thick blue curve) and acoustic amplitude (thick black) image log in water, compared with triple weighting total porosity F_T (full red dots) from 116 core plugs, and secondary porosity index SPI computed from SPI= F_N - F_S (thin gray curve). (D) Sketch of log neutron porosity F_N minus log sonic porosity F_S, core porosity F_{core}, and porosity from borehole images F_{image} readings relative to formation primary porosity F_1, secondary porosity F_2, and caves.

The secondary porosity index (SPI= Φ_T- Φ_s, that we can approximate by Φ_N- Φ_S), is an indication of secondary porosity presence, since we have seen above that Φ_N is close to Φ_T, and Φ_s is close to Φ_2. The good correlation of the SPI and of Φ_{image} (represented by Φ_{image_amp}) (Fig. P4-14C), is an independent confirmation that the performed image processing has a true geological meaning; it is also a validation of the neutron and sonic calibration in porosity.
The three Φ_{image} calibrated results in the MC2 well are displayed vs. depth on Fig. P4-15A. We remark (Fig. P4-15A) that there is an apparent drift of the calibrated Φ_{image} from optical image tool, compared to Φ_{image} from acoustic image tool in the upper part of the water zone (above 65mbgl). This makes the results of Φ_{image} from the optical image tool in the vadose zone slightly suspect.

5.4 Mineralizations

All mineralization zones (Fig. P4-15A) appear as low vuggy porosity (as well as they have been identified by low total porosity). They form horizontal flat zones over MC2, MC8 and MC9 (Fig. P4-11A, B and C), as well as the other wells of Ses Sitjoles, an observation indicating that these zones correspond to either present or past sea level standstills (Maria-Sube, submitted b).

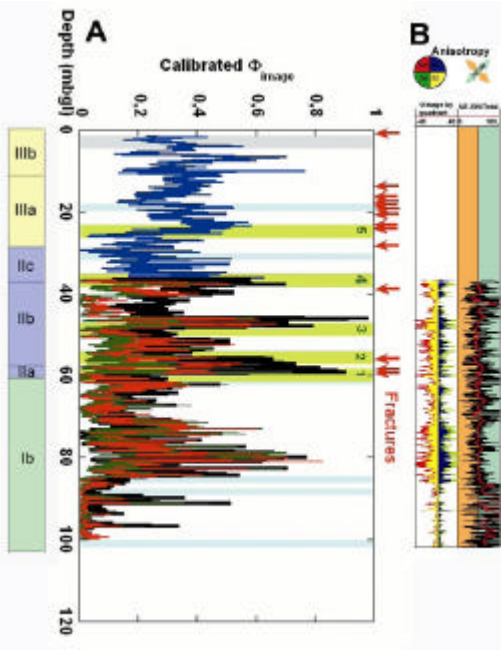

Figure P4- 15. Stratigraphic subunits are indicated on the left side of the figure. In MC2 well, plots vs. depth of: (A) calibrated image porosity computed from optical image log in air (thick blue curve), and in water (medium black curve), and acoustic image log (amplitude, thin green curve, and transit time thin red curve); (B) azimuthal distribution of vugs from image acoustic amplitude log; left, vuggy porosity by quadrant: NE blue, SE yellow, SW green, NW red; right: NE-SW/ total, ochre 0-50%, green 50-100%. Light blue, green, gray shadings, and red arrows as per Fig. P4-4.

5.5 Azimuthal distribution of vugs

The analysis of the azimuthal distribution of vugs using the results deriving from the processing of the acoustic amplitude image shows (Fig. P4-15B) that the anisotropy is minor when macro-scale porosity is high. Indeed, to get a high macro-scale porosity, a major portion of the borehole circumference must be detected as vug or karst, leading to unpreferential quadrant distribution of the vugs/karst. On the contrary, when macro-scale porosity is about 3 to 10% and may play a major role in present transport properties, a contribution of the NE-SW direction, compatible with the NE-SW faulting direction (Maria-Sube, submitted a) in the SE Majorca reef complex, is evidenced (Fig. P4-15B). This result is interesting, because, contrarily to the Φ_{image} results, it cannot be even approached by a visual estimation of the cores or of the image logs apparent vugs, or from Φ_{core} measurements. However, a comparable result had been obtained from the fracture image processing on the 12 wells of the Ses Sitjoles site (Maria-Sube et al., submitted) and on the 25 wells of the entire SE Majorca reef complex (Maria-Sube et al. submitted a).

5.6 The reef slope

We have seen above that both Φ_N and Φ_s indicate that the detrital proximal slope (subunit Ib, 60-100mbgl interval) is a laminated interval (Fig. P4-14 and P4-4). Furthermore, the zone below 83mbgl is a very low vuggy porosity zone (Fig. P4-15A). We have however demonstrated, in Maria-Sube, submitted a, that this zone is not geologically belonging to the distal slope, and is still part of the proximal slope, like all sediments below 60mbgl of MC2. In MC2, like in every well of Ses Sitjoles, the distal slope is to be found below 100mbgl, and has been found in well S17 to be located from 100 to 128mbgl, as indicated by this well core report (available down to 266mbgl). The proximal slope is receiving debris from the overlaying reef, in relation with the waves and storms, and possibly earth tremors. This

change of macro porosity distribution along the proximal slope may be attributed to the change of bathymetry (and possibly as well of a change of talus slope), which corresponds for the sediments to a lower deposition energy in the lower part of the proximal slope.

Conclusions and perspectives

The Φ_{core} discrete measurements have been used to calibrate in porosity the neutron, sonic and resistivity logs to obtain the continuous log porosities Φ_N, Φ_S, and Φ_R, respectively.

The good quality and coherence of the core porosity and acoustic compressional velocity measurements allow to obtain a reliable core Φ_{core} to V_p relation, notably different from the Wyllie and Raymer et al. classical relations. This relation is different from the Wyllie and Raymer et al. relations for the ODP carbonate GBR and GBB site Φ_D and V_p core and log data and also from the MC2 core and log data, therefore demonstrating that is has to be determined on a case by case approach in carbonate reef sediments.

The log porosities, available only in the wet zone of the wells, confirm that no low porosity measurement has been missed by the cores. Φ_N and Φ_S sharp variations in subunit Ib reflect the detrital, laminated nature of this formation. Φ_R presents a very smoothed curve, due to the poor vertical resolution of the resistivity logs; its quality is good in the sea water zone, and mediocre in the salinity transition and brackish water zones.

A macro porosity can be extracted from the high quality image logs processing. Each image log processing has to be calibrated by a two point calibration method, using the borehole image and the caliper logs.

The comparison Φ_{core} and Φ_{image} demonstrates that $\Phi_{image} < \Phi_{core}$, except when the caliper indicates caves.

The analysis of the azimuthal distribution of vugs shows a major contribution of the NE-SW direction, compatible with the NE-SW faulting direction in the SE Majorca reef complex. This preferential direction had also been found from the fracture image processing of the 25 surveyed wells of the reef complex.

The smooth trend observed on Φ_{image} in the lower part of the slope of subunit Ib (below 83mbgl) of MC2 does not correspond to a change from proximal slope to distal slope. It reflects more probably a mere change of bathymetry and deposition energy.

Acknowledgements

We are grateful for funding from the European Union Advanced Logging Investigations of Aquifer iN Coastal Environment (ALIANCE) project EKV-2001-0039 a three and half years duration program (2002-2005)

The authors wish to thanks specially Gilles Henry and Pierre Azaïs, Université Montpellier II, Institut des Sciences de la Terre, de l'Eau et de l'Espace de Montpellier (ISTEEM) France; Gilles Henry carried out most of the downhole logging on the well-site and maintenance of the downhole equipment, although several other persons participated as well; Pierre Azaïs was very instrumental in providing technical help for the laboratory petrophysical measurements.

ISES-Industry, an associated European project based in Amsterdam, provided help in the form of data originating from the Vrieje Universiteit (V.U.), Amsterdam (The Netherlands).

The Ses Sitjoles log data are available on http://hplus.ore.fr Internet site.

The ODP Legs 133 and 166 log data were collected on-line from the Columbia Lamond Doherty Earth Observatory Internet site.

We also want to acknowledge the help provided by the Direccio General de Régim Hydraulic, from the Balearic Government, especially by hydro-geologists Concha and Alfredo Baron,

who, among other things, proposed the drilling site of Ses Sitjoles and smoothed relations with the Majorcan authorities.

References

Archie G.E., 1942.The electrical resistivity log as aid in determining some reservoir characteristics, Trans. Americ. Inst. Mineral. Met.

Bonnier, B. (2005) Etude sédimentologique et géochimique des récifs Miocènes de Majorque (Baléares, Espagne). Influence des caractéristiques diagénétiques sur les propriétés physiques des roches carbonatées. Ms. Thesis, 31p. (unpublished), *Université Paul Cézanne, CEREGE, Aix-en-Provence.*

Brachert T.C., Hultz N., Knoerich A.C., Krauworst U.M.R., Stückrad OM, 2001. Climatic signatures in shallow water carbonates: high resolution stratigraphic markers in structurally controlled carbonate buildups (Late Miocene, Southern Spain), Palaeogeog. Palaeoclimatol. Palaeoecol. 175, 211-237.

Brie A., Johnson, D. Murphy, B., Plona T., Anderson R, 1985. Sound propagation in rocks, The Technical Review, 33, 1, pp. 53-68, Schlumberger.

Cunningham K. J., Carlson I. J., Hurley F. N., 2004. New method for quantification of vuggy porosity from digital optical borehole images as applied to the karstic P leistocene limestone of the Biscayne aquifer, southeastern Florida. Journal of Applied Geophysics, Vol. 55, Issue 1-2, p. 61-76.

Davies, P.J., McKenzie, J.A., Palmer-Julson, A.A. et al. (1990) Northeast Australian Margin. Proc. ODP, Sci. Results, Leg 133, 810p.

Ellis, D.V., 1987. Well logging for earth scientists, Elsevier, Amsterdam.

Eberli, G., Swart, P.K., and shipboard scientific party, (1996) Bahamas Transect, Init. Rep. ODP, vol. 166. 849p.

Eberli, G., Swart, P.K., and shipboard scientific party, (1996a) Bahamas Transect, Sci. Results, ODP, 166. 213p.

Esteban, M., Calvet, F., Dabrio, C., Baron, A., Giner, J., Pomar, L., Salas, R., & Permannyer, A., 1978. Aberrant features of the Messinian coral reefs, Spain. Acta geol.Hisp., 13, 20-22.

Esteban, M., 1979. Significance of the Upper Miocene reefs of the Western Mediterranean. Paleogeog. Paleoclimatol. Paleoecol. 29, 169-188.

Focke, J.W., Munn D., 1987. Cementation exponents in Middle Eastern carbonate reservoirs, SPE Form. Eval. 2, pp 155-167

Gaillot, P., Maria-Sube, Y., Pezard, P.A., 2005. Quantification of meso-scale porosity from borehole wall images: a comparative study – Example from the ALAINCE Campos experimental site, Mallorca, Spain. SPWLA. The 11th Formation Evaluation Symposium of Japan.

Glover P.W.J., Meredith G.P., Sammonds P.R., Murrell S.A.F., 1994. Ionic surface conductivity in sandstone, Journal of Geophysical Research, Vol. 99, No B11, Pages 21,635-21,650, November 10.

Hilchie D.W., 1989, Advanced Well Log Interpretation, Boulder Co D.W. Hichie Inc.

Homand F., Duffaud P., 2000. Manuel de mécanique des roches, Tome 1, Fondements, Ecole des Mines de Paris.

Jaeggi, D. (2006) Multiscalar porosity structure of a Miocene reefal carbonate complex. *PhD thesis*, Diss ETH nb. 16519.

Jarrard, R.D., Jackson, P.D., Kasschau, M., Ladd, J.W., 1993. Velocity and density of carbonate-rich sediments from northeastern Australian margin: integration of core and log data, Proc. ODP, Sci. Results, Leg 133, pp. 633-647.

Jenkyns, H.C., Sellwood B.W., Pomar L. (1973) A field incursion guide to the island of Mallorca: Geologists' Association guide, London, the Geologists' Association, 93 p.

Maria-Sube Y., Camoin G., Pezard P., Löw S., Jaeggi D., Montoto M., Mateos F., submitted. Multi-scalar study of depositional environment and heterogeneity in a Miocene reef sequence, Sedimentology, Blackwell.

Maria-Sube Y., Camoin G., Pezard P., Jaeggi D., Braaksma H., Verwert K., submitted a. Depositional environment and structure in a Miocene reef complex, Majorca, Spain. AAPG.

Maria-Sube Y., Pezard P., Loggia D., Camoin G., Braaksma H., Montoto M., Mateos F., Jaeggi D., Löw S., submitted b. Core petrophysical properties of a Miocene coral reef, Campos site, Majorca, Spain. Tectonophysics, Elsevier.

Mateos F., Montoto M. et al. (in press). Pore space structure with hydraulic significance.

Pomar, L., 1991. Reef geometries, erosion surfaces and high frequency sea-level changes, upper Miocene reef complex, Mallorca, Spain, Sedimentology, 38, 2, 243-269.

Pomar L., Ward W.C., 1994. Response of a late Miocene Mediterranean reef platform to high-frequency eustasy, Geology, 2, 131-134.

Pomar L., Ward W.C., 1995. Sea-level changes, carbonate production and platform architecture: the Llucmajor platform, Mallorca, Spain, in Sequence stratigraphy and depositional response to eustatic, tectonic and climatic forcing, 87-112, B.U. Haq Kluwer Academic Publishers.

Pomar L., Ward W.C., Green D.G., 1996. Upper Miocene reef complex of the Llucmajor area, Majorca, Spain, SEPM Concepts in Sedimentology and Paleontology, 1-56576-033-6, 191-225.

Pomar L., Ward W.C., 1999. Reservoir-scale heterogeneity in depositional packages and diagenetic patterns on a reef-rimmed platform, Upper Miocene, Mallorca, Spain, AAPG, 83, 1759-1773.

Raymer L.L, Hunt E.R., Gardner J.S., 1980. an improved sonic transit time to porosity transform, Transactions of the SPWLA, 21 st Annual Logging Symposium.

Sarmiento, R., 1961. Geological factors influencing porosity estimates from velocity logs. Bull. Amer. Assoc. Petroleum Geol., 45, 5.

Serra O., 1990. Element Mineral Rock Catalog. Schlumberger.

Serra O., Serra L., 2000. *Diagraphies*, Serralog.

Tittman, J., 1986. Geophysical well logging. Academic Press, Inc., London.

Waxman M. H., Smits L.J.M., 1968. Electrical conductivity in oil-bearing shaly sands. SPE.

Wyllie, M.R.J., Gregory, A.R., Gardner L.W, 1956. Elastic velocities in heterogeneous and porous media. Geophysics, 21, 1.

5 Hydrogéologie et biseau salé sur le complexe récifal Miocène du Sud-Est de Majorque

Dans ce chapitre , les résultats obtenus à l'aide des diagraphies d'hydrogéologies sont présentés.

5.1 Site de Ses Sitjoles

Pour l'étude qui suit, qui utilise des enregistrements de diagraphies sur les douze forages du site de Ses Sitjoles (c'est-à-dire sur un carré de 100m de côté), mais aussi des diagraphies de la même sorte répétées plusieurs fois sur le même puit, il est encore plus essentiel que le calage en profondeur de toutes les diagraphies enregistrées sur les puits soit effectué au préalable avec méthode et soin (Voir Annexe 2).

5.1.1 Colonnes d'eau

On constate (à l'aide des diagraphies Idronaut, et à défaut électriques) les colonnes d'eau suivantes sur les différents puits de Ses Sitjoles, à la date (année/mois/jour) indiquée (Tab. 4).

Fluide	MC1 (mbgl) 03/06/09	MC2 (mbgl) 03/06/09	MC3 (mbgl) 03/06/06	MC4 (mbgl) 03/08/20	MC5 (mbgl) 03/06/07	MC6 (mbgl) 04/07/11	MC7 (mbgl) 03/08/27	MC8 (mbgl) 04/07/10	MC9 (mbgl) 04.07/08	S17 (mbgl) 03/06/09
Eau douce	36,35-64,8	36,9 - 62,3	39,6 – 66,7	38,96-61,0	38,92-63,4	38,96	38,96-61,6	36,9-61,4	36,9-61,9	39,83-66,8
Transition	64,8-79,5	62,3-78,0	66,7-85,0	61,0-77,5	63,4-82,2	-	61,6-77,3	61,4-77,8	61,9-78,4	66,8-81,4
Eau de mer	79,5-99,0	78,0-100,9	85,0-98,0	77,5-96,6	82,9-99,0	-	77,3-100,7	77,8-100,14	78,4-100,0	81,4-99,0

Tableau 4. Zones d'eau observées sur les différents puits de Campos.

On peut en déduire la hauteur des colonnes d'eau douce et de transition (Tab. 5). Les hauteurs des colonnes d'eau de mer n'a pas été calculé, car dépendant de la topographie, et parce que le point bas de la colonne est difficile à établir.

Fluide	MC1 (m) 03/06/09	MC2 (m) 03/06/09	MC3 (m) 03/06/06	MC4 (m) 03/08/20	MC5 (m) 03/06/07	MC6 (m) 04/07/11	MC7 (m) 03/08/27	MC8 (m) 04/07/10	MC9 (m) 04.07/08	S17 (m) 03/06/09
Colonne d'eau douce	28,45	25,4	27,1	22,04	24,48	-	22,64	24,5	25,0	26,97
Colonne d'eau de transition	14,7	15,7	18,3	16,5	16,8	-	15,7	16,4	16,5	14,6
Somme des deux colonnes	43,15	41,1	45,4	38,54	41,28	-	38,34	40,9	41,5	41,57

Tableau 5. Hauteurs de colonnes d'eau douce et de transition sur le champ de Campos, observées sur les diagraphies de base, et somme des deux colonnes. La moyenne de cette somme sur les puits considérés est de 41,3m.

On peut voire que même en considérant les puits où les diagraphies Idraunaut ont été enregistrées à la même date (MC1 et MC2), il n'est pas simple de trouver une relation entre les colonnes d'eau.

5.1.2 Hauteur du plan d'eau

La Figure 16 montre le schéma des zones d'eau douce et d'eau salée à proximité d'une zone côtière. Ici on a supposé que l'interface eau douce- eau salée est abrupte (hypothèse de Badon Ghyben (1889) et Herzberg (1901)), et que le biseau salé est statique.

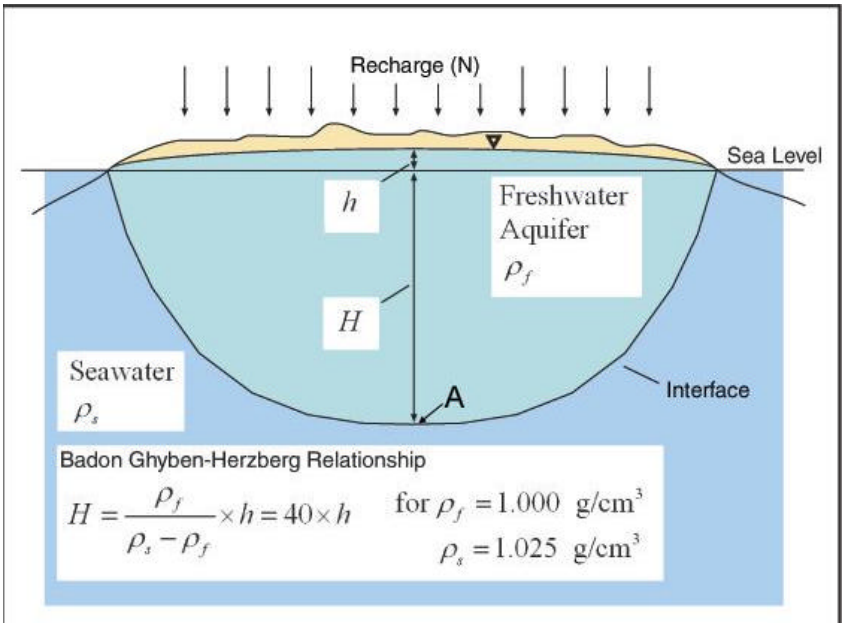

Figure 16. Dans ce schéma on considère une petite île avec un aquifère d'eau douce en forme de lentille surmontant un aquifère d'eau de mer ; l'interface eau douce – eau de mer est statique. C'est la relation de Ghyben- Herzberg

Si l'on considère un point A sur cette interface, H est la profondeur de A en dessous du niveau de l'eau de mer, h est l'élévation du niveau d'eau douce au dessus du niveau d'eau de mer à la verticale de A. Pour que A soit en équilibre hydrostatique, il faut égaliser les poids d'eau douce [ρ_f (h+H)] en A et d'eau de mer [ρ_s H] à la même profondeur que A ; on obtient ainsi :

$$H = \frac{r_f}{r_s - r_f} h \approx 40h \qquad (1)$$

en effet, ρ_f (densité de l'eau douce) est proche de 1g/cm^3, et ρ_s (densité de l'eau salée) est proche de 1,025g/cm^3.

Le Tableau 5 montre que h + H ~ 41,3m (2) si on considère que l'interface eau douce-eau de mer est au niveau de l'interface eau de transition- eau de mer sur le site de Ses Sitjoles, et donc, en résolvant le système d'équations (1) et (2), on trouve h ~ 1m.

Le Tableau 6 montre le calcul de h en fonction de l'élévation des têtes de puit et de la profondeur du sommet de zone vadose observée sur chaque puit du champ de Campos. On voit que la relation (1) n'est pas tout-à-fait observée. Sans doute faut-il tenir compte des variations saisonnières du sommet de zone vadose (environ 60cm), et aussi des erreurs de mesure de profondeur. Mais en fait, les hypothèses de départ de la relation (1) (interface eau douce- eau salée abrupte, biseau salé statique) sont trop simples.

Dans les années 1960, Henry et Cooper ont jeté les bases de notre présente compréhension des intrusions d'eau salée en zone côtière. Essentiellement, l'interface entre eau douce et eau salée n'est pas abrupte. Au contraire, les puits côtiers habituellement montrent une zone de

transition où l'eau salée se diffuse, qui peut atteindre plusieurs mètres (souvent plusieurs dizaines de mètres) d'épaisseur.
On trouve ainsi une explication de la zone de transition observée (Tableaux 4 et 5).
Ceci implique que l'eau de mer se mélange à l'eau douce. La salinité coule vers le haut et vers la zone de transition, jusqu'à ce que les pressions s'équilibrent. Pour remplacer ce débit de salinité, l'eau de mer doit s'écouler vers la terre, ce qui entraîne une cellule de conversion (eau de mer entrant en profondeur et sortant près de la surface, comme sur la Figure 17).

Elevation	MC1 (m)	MC2 (m)	MC3 (m)	MC4 (m)	MC5 (m)	MC6 (m)	MC7 (m)	MC8 (m)	MC9 (m)	S17 (m)
Elevation de la tête de puit : z	37,77	38,32	41,02	40,37	40,34	40,38	40,38	38,32	38,32	41,25
Profondeur du plan d'eau: z - h	36,1	36,43	38,67	38,5	38,51	38,5	38,55	36,34	36,72	40,0
Elevation duplan d'eau: h	1,89	1,89	1,89	1,89	1,89	1,89	1,89	1,89	1,89	1,89

Tableau 6. Tableau montrant le calcul de h pour chaque puit du champ de Campos, après correction de profondeur pour se ramener sur la hauteur du plan d'eau observée sur l'imagerie optique du puit MC2.

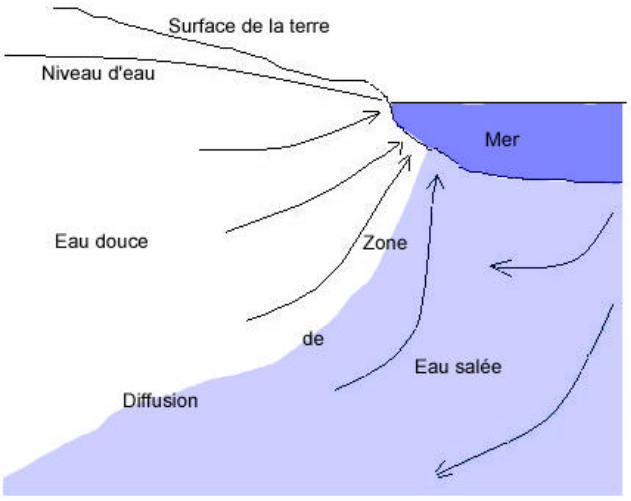

Figure 17. Schéma de la zone de mélange et des flux d'eau le long de la zone de mélange. Noter que la salinité est emmenée horizontalement vers la terre par un flux souterrain d'eau de mer et, après mélange, s'écoule vers le haut et vers la mer.

Le résultat est que l'eau de mer perd de son énergie, de telle façon que l'interface (en fait, la zone de mélange) est quelque peu déplacée vers la mer comparé à la prédiction de Ghyben-Herzberg.

5.1.3 Variations saisonnières

5.1.3.1 Conductivité du fluide, MC2

Quatre diagraphies Idronaut ont été enregistrées sur MC2 à ce jour. Le tableau ci-dessous résume l'interprétation de la conductivité de fluide qu'on peut en faire :

Date	Profondeur du plan d'eau (mbgl)	Profondeur de la séparation eau douce-eau salée (mbgl)	Profondeur de la séparation eau salée-eau de mer (mbgl)	Conductivité eau douce à 55mbgl (mS/cm) @ T°C	Conductivité eau de mer à 95mbgl (mS/cm) @ T°C	Salinité eau douce à 55mbgl (ppm)	Salinité eau de mer à 95mbgl (ppm)
9 juin 2003	36,43	61,73	77,53	4,215 @ 23,964	55,830 @ 25,078	2500	38000
28 octobre 2003	35,15	57,85	74,45	4,268 @ 23,934	55,872 @ 25,142	2500	38000
6 juillet 2004	36,43	61,73	76,00	4,193 @ 23,952	55,386 @ 25,087	2500	38000
17 avril 2005	36,774	62,06	76,99	3,925 @ 23,915	53,191@ 25,069	2500	38000

Tableau 7. Interprétation de quatre enregistrements de l'Idronaut sur MC2 sur une période d'un an.

Voici quelques conclusions que l'on peut tirer de l'examen des chiffres du Tableau 7 :

1. **Salinité eau douce à 55m** : on est à 2500ppm tout au long de l'année. Ceci correspond à une eau légèrement salée déjà (l'eau douce a une salinité maximum de 1000ppm, l'eau potable de 800ppm), donc en fait saumâtre. La conversion conductivité et température est faite à l'aide de l'abaque Gen-9 de Schlumberger. Celle-ci n'a pas une résolution permettant d'évaluer des différences de salinité dans ces conditions.
2. **Salinité eau de mer à 95m** : on est à 38000ppm, soit la valeur de l'eau de la Méditerranée. Là aussi, pas de possibilité d'apprécier des différences de salinité avec l'abaque Gen-9.
3. On observe des variations saisonnières de colonnes d'eau d'une amplitude surprenante (voir Fig. 18). On voit que l'abondance des pluies à l'automne 2003 (28 octobre) a entraîné une remontée du niveau du plan d'eau douce, et que les frontières eau douce-eau de transition et eau de transition- eau de mer sont également remontées.

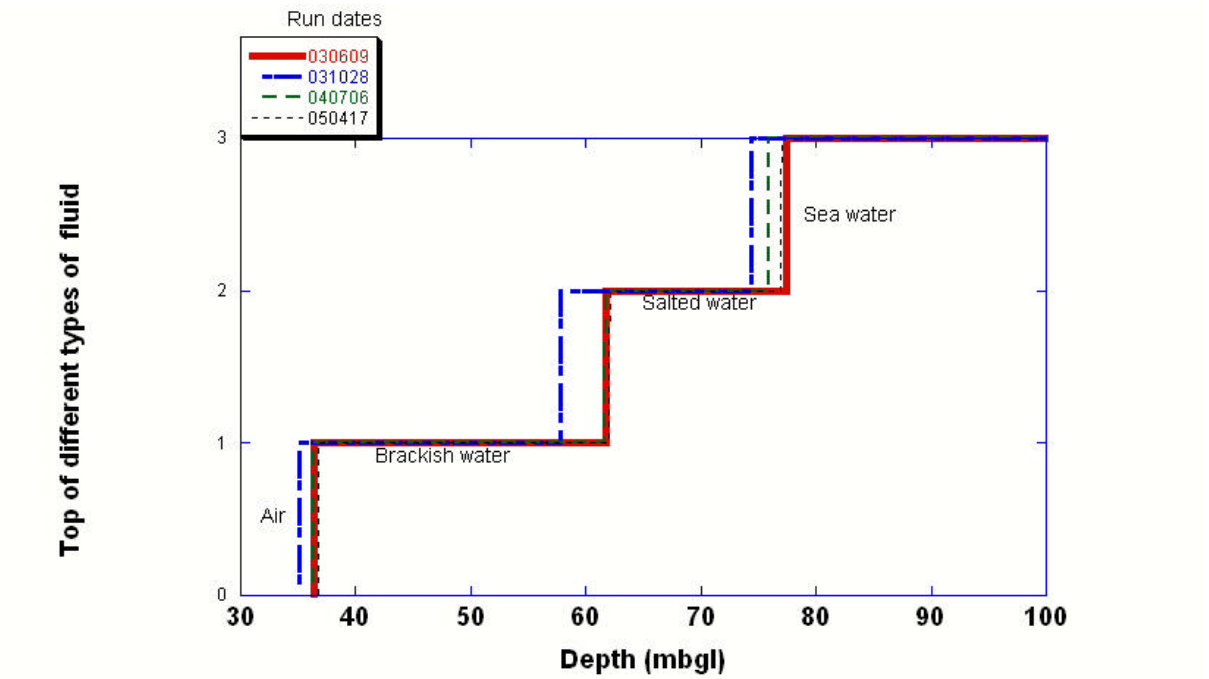

Figure 18. Représentation graphique des variations saisonnières de hauteur de colonnes d'eau sur MC2 en fonctions des résultats du Tableau 7.

5.1.3.2 Hydrochimie

L'Idronaut permet également du mesurer le pH (acidité, ou caractère basique) et l'Eh (coefficient réducteur ou oxydant, ou Redox) du fluide.
Le pH est pratiquement constant et égal à 7 (sauf en haut de S17 le 02/06/09, Tab. 8).
L'évolution de l'Eh est plus intéressante (on sait que lorsque Eh> 0, le fluide est oxydant, tandis que lorsque Eh< 0, le fluide est réducteur, Tab. 8) :
Les conditions réductrices se produisent :

- Dans le fond du puit, là où le fluide est le moins oxygéné, sauf pour S17 le 02/06/09, où une anomalie se produit aussi sur le pH en haut du plan d'eau.
- Dans l'eau salée, ou encore plus, dans l'eau de mer
- Au printemps ou en été, jamais en automne (un seul log enregistré en automne, pas un seul en hiver).

Puit	Date (AA/MM/JJ)	Profondeur du plan d'eau (mbgl)	Profondeur de la séparation eau fraîche-eau salée	Profondeur de la séparation eau salée-eau de mer	Redox eau douce (mV)		Redox eau salée (mV)		Redox eau de mer (mV)		Remarque
					En haut	En bas	En haut	En bas	En haut	En bas	
MC1	030609	35,88	64,33	79,03	131,9	18,9	83,2	91,6	79,3	48,6	Log de base
	040707	35,88	63,00	84,20	101	111	162	35	35	35	
MC2	030609	36,43	61,73	77,53	114,5	118,5	121,5	122	120	-147	Log de base
	031028	35,15	57,85	74,45	82	78,4	83,7	64,1	59,4	35,2	Seul log en automne
	040706	36,43	61,73	76,00	88,9	122,4	124,6	118,7	113,5	-221,5	
MC3	030606	39,13	66,23	84,53	97,8	112,1	126,2	93,3	91,6	-132,9	Seul log Idronaut
MC5	030607	38,45	62,97	79,73	59,6	87,4	70	-215	-224	-247,5	Log de base
	030820	38,35	-	-	153,3	154,4	-	-	-	-	Log ne descend pas en dessous de 62,5mbgl
MC6	040711	38,49	-	-	-	41,9	89,6				Seul log Idronaut, TD= 58,0
MC7	030827	38,49	61,13	76,83	114,3	61,1	61,9	152,4	152,4	129,2	Seul log Idronaut
MC8	040710	36,43	60,93	77,33	73,9	105,2	108,2	75,7	67,8	21,7	Seul log Idronaut
MC9	040708	36,43	61,43	77,97	72,2	64,7	67,6	69,8	68,7	-43	Seul log Idronaut
S17	020513	37,70	65,20	82,90	37,4	52,8	86	-162	-171	-265	Pb. sur conductivité, limites copiées sur log 020516
	020516	37,70	65,10	82,80	66,1	109,9	127,0	-19	-42	-172	
	020609	37,70	64,72	80,35	-197	35,8	52	-141	-168	-208	Sous le plan d'eau, pH= 10 !
	030609	39,36	66,33	80,93	125,7	125,3	138,7	-141,7	-164,6	-193,8	Log de base
	030821	39,36	66,56	79,16	129,0	135,0	161	59	-77	-208	
	030827	39,36	66,66	79,26	130,0	137,2	156,6	128	-58	-228	
	040705	39,36	66,56	80,36	109,0	116,0	127,0	-91	-172	-271	
	050418	39,63	66,95	83,24	18,4	34,77	32,93	29,76	29,22	30,30	

Tableau 8. Evolution saisonnière hydrostatique et redox sur le site de Ses Sitjoles. L'ombrage brun dénote une diagraphie enregistrée au printemps 2002, l'ombrage jaune dénote un diagraphie enregistrée au printemps 2003, l'ombrage rose saumon dénote une diagraphie enregistrée en automne 2003, l'ombrage vert dénote une diagraphie enregistrée en été 2003, l'ombrage bleu dénote une diagraphie enregistrée en été 2004, l'ombrage turquoise clair dénote une diagraphie enregistrée au printemps 2005. L'ombrage rose dénote un redox négatif.

5.1.3.3 Niveaux hydrostatiques MC1, S17

S17 offre la particularité que c'est le puit sur lequel le plus grand nombre d'Idronauts a été enregistré, et aussi celui sur lequel les enregistrements ont commencé le plus tôt (en fait à une époque où les autres puits n'avaient pas encore été forés, en 2002). Il est donc intéressant à ces titres.

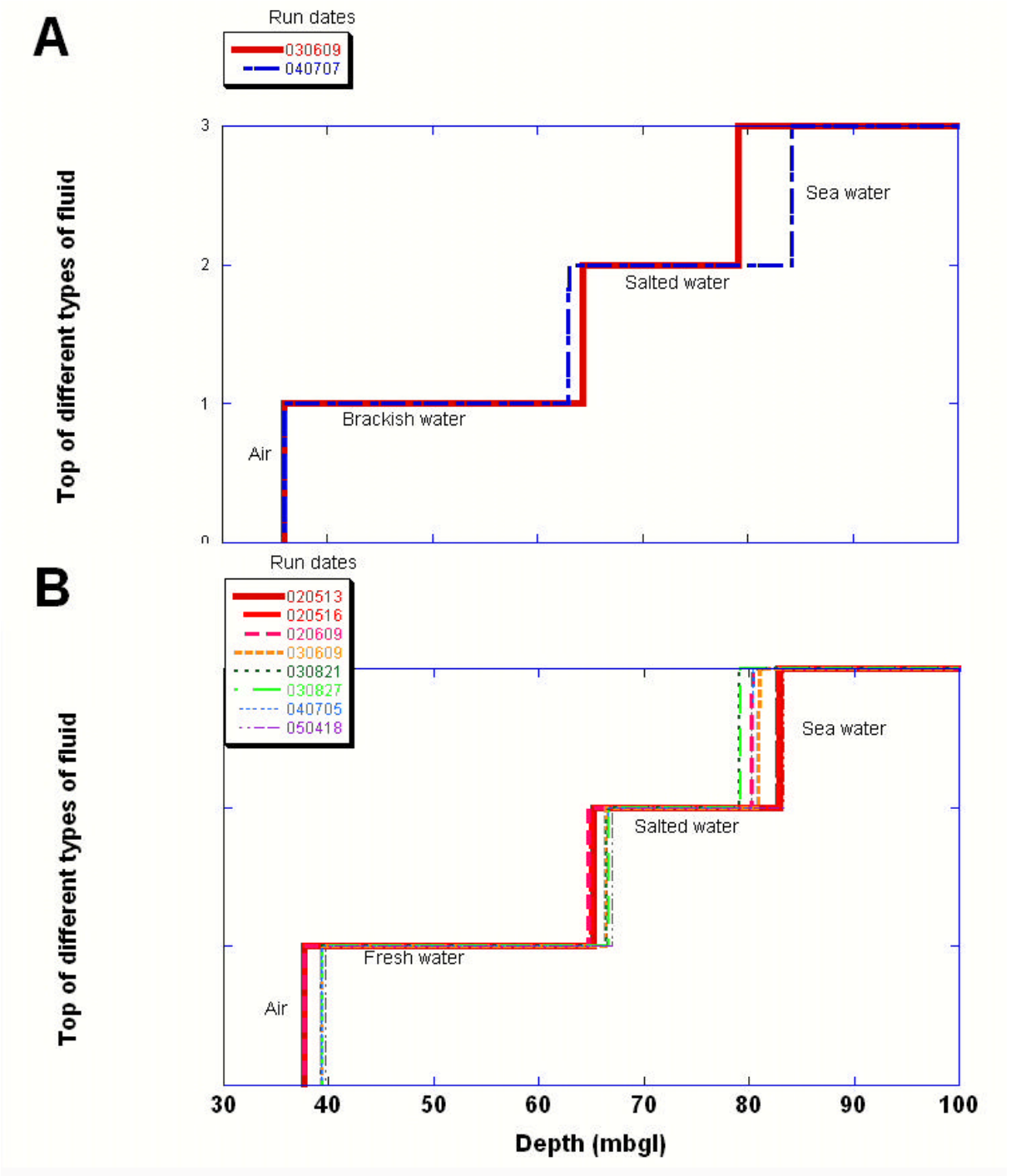

Figure 19. Représentation graphique des variations saisonnières de hauteur de colonnes d'eau sur les puits MC1 (A) et S17 (B) en fonctions des résultats du Tableau 8.

On constate sur les profondeurs de plan eau douce- eau salée- eau de mer suivant les saisons sur le même puit :

- Les variations du plan d'eau sont relativement faibles (maximum : 1,66m entre mai-juin 2002_ point haut_ et juin-août 2003 ou juillet 2004_ point bas_ sur S17, Fig. 19B)
- Les variations de niveau eau douce-eau salée peuvent atteindre jusqu'à 3,88m (MC2 entre juin 2003 ou juillet 2004_ point bas et octobre 2003_ point haut, Fig. 18) tandis que les variations de niveau eau salée- eau de mer peuvent atteindre jusqu'à 5,17m (MC1 entre juin 2003_ point haut et juillet 2004_ point bas, Fig. 19A)

- Il est intéressant de noter qu'un point haut sur le niveau eau douce-eau salée s'accompagne également d'un point haut sur le niveau eau salée-eau de mer sur MC2, Fig. 18, alors que pour MC1 et S17, un point haut sur le niveau eau douce-eau salée s'accompagne d'un point bas sur le niveau eau salée-eau de mer, Fig. 19.

5.1.4 Débitmètre sur MC2

5.1.4.1 Débitmètre

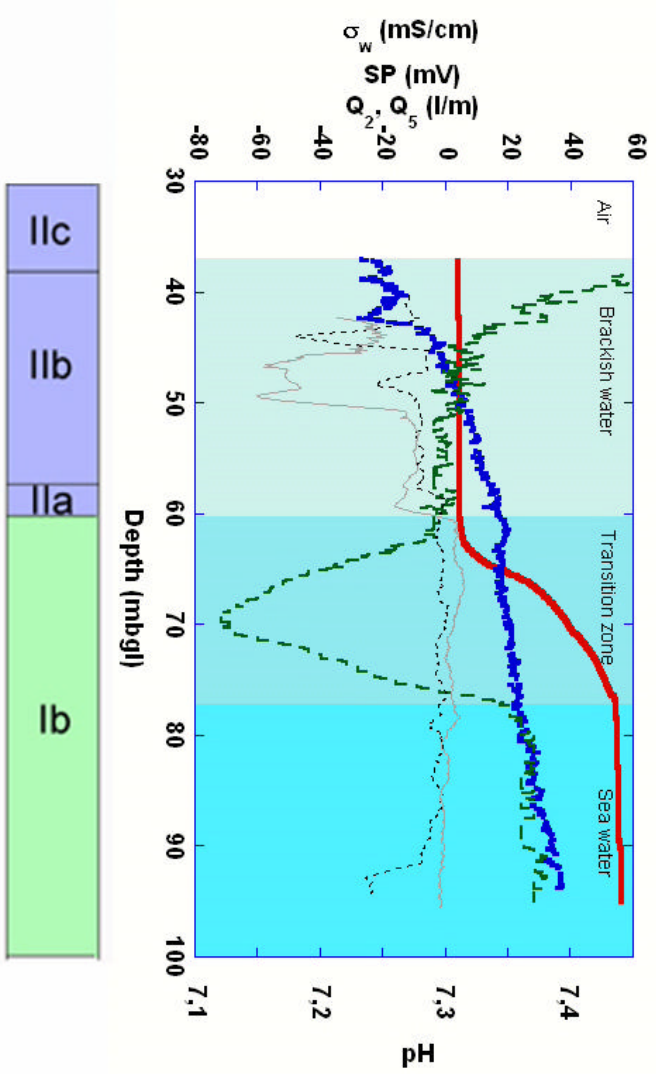

Figure 20. Les sous-unités stratigraphiques de MC2 sont indiquées sur la gauche. Comparaison de la SP (trait long tirets épais bleu) et de la conductivité de l'eau s_w (trait rouge continu épais) enregistrés par l'outil Muset avec les débits Q2 (en descendant, trait fin continu gris) et Q5 (en montant, trait fin hachuré noir) enregistrés par le débitmètre à hélice sur MC2. L'enregistrement pH est indiqué par un trait moyen, avec des tirets moyens vert).

Trois descentes et trois montées à des vitesses différentes du débitmètre IMPF ont été enregistrées sur MC2 le 19 avril 2005. Le débitmètre est calibré en débit dans les zones où la vitesse de l'hélice est la plus constante, en utilisant les données de vitesse du câble, vitesse de l'hélice, et diamétreur, et la méthode exposée dans Schlumberger, 1973. Nous conservons deux débits calculés, Q2 (en descendant) et Q5 (en montant), Fig. 19. On voit qu'il y a un décalage d'environ 3m de profondeur entre Q2 et Q5, Q2 étant plus bas que Q5 ; ce décalage est vraisemblablement dû à la géométrie de l'outil et à des phénomènes de dynamique des fluides, et d'inertie mécanique, les débits mesurés étant très faibles (de l'ordre de la dizaine de

ml/m). Nous prendrons comme référence de profondeur Q2, les vitesses d'hélice étant légèrement plus importantes dans ce cas. Par convention, lorsque le débit est positif, le fluide monte. On voit qu'entre 100 et 60mbgl, il n'y a aucun débit, entre 60 et 50mbgl, il y a un débit de 12l/m de fluide qui descend, entre 50 et 46m il y a un débit plus important 44l/m de fluide qui descend, entre 46 et 40mbgl, le débit redescend à 20l/m (Fig. 20 et Tab. 9).

5.1.4.2 Muset

L'outil MuSET (Multiple Sensor Electrical Tool), qui a été enregistré le même jour que le débitmètre sur MC2, est un Idronaut modifié avec une électrode SP au Pb/ PbCl2 non-polarisable supplémentaire. Il fait partie des nouveaux outils de faible diamètre qui ont été conçus, essayés et mis en œuvre dans le cadre du programme ALIANCE.
La Fig. 20 montre qu'entre 100 et 77mbgl, le fluide est de l'eau de mer, entre 77 et 60mbgl, le fluide est de l'eau de transition, entre 60 et 37mbgl, le fluide est de l'eau saumâtre.
Une différence de potentiel sur la SP peut apparaître pour trois différentes raisons dans ce type de forage :

- Un potentiel de membrane dû à la présence de minéraux argileux ; ce n'est pas le cas dans cette zone du puit (Maria-Sube et al., sous presse)
- Un gradient de salinité ; c'est le cas sur toute la zone de transition
- Un potentiel cinétique dû à un mouvement de fluide : c'est le cas, on l'a vu plus haut, sur l'intervalle 60 à 40mbgl.

Ainsi (Fig. 20 et Tab. 9), de 100 à 77mbgl, aucune de ces raisons n'est présente, la SP est une ligne droite de pente 0,94mV/m constante, due à la chute ohmique par unité de longueur dans les formations traversées par le courant de mesure (Serra, 2000).
De 77 à 60mbgl, il y a un gradient de salinité, et on voit que la SP présente une forme d'arc faible dont la concavité est tournée vers le haut.
De 60 à 50mbgl, il n'y a plus de gradient de salinité, mais on observe un débit de fluide vers le bas de 12ml/m, et, simultanément, la SP redevient une ligne droite, mais avec une pente accrue de 1,6mV/m.
De 50 à 46mbgl, le débit de fluide vers le bas est accru à 44ml/mn, et simultanément celle de la SP est accrue à 3ml/mn.

Intervalle (mbgl)	Potentiel de membrane	Gradient de salinité	Potentiel cinétique	Débit de fluide vers le bas (ml/mn)	Pente SP (mV/m)
94- 77	Non	Non	Non	0	0,94
77- 60	Non	Oui	Non	0	Arc faible vers le haut
60- 50	Non	Non	Oui	12	1,6
50- 46	Non	Non	Oui	44	3
46- 43	Non	Non	Oui	Inconnu, en raison de turbulences	Arc important vers le bas
43- 37	Non	Non	Probablement non	Inconnu, parce que débitmètre non enregistré	Arc important vers le haut

Tableau 9. Causes de variations sur la SP, débit mesuré par le débitmètre à hélice et pente de la SP suivant la profondeur sur MC2, mesurés le 19 avril 2005.

De 46 à 43mbgl, de fortes turbulences ne permettent pas d'avoir une mesure du débit avec le débitmètre à hélice, on observe sur la SP un arc important vers le bas. Il semblerait donc que cette perturbation du débitmètre à hélice soit due à la source du débit vers le bas jusque là observée.

De 43 à 37mbgl, le débitmètre n'est pas enregistré, et on observe sur la SP d'abord un arc en sens inverse du précédent (de 43 à 37mbgl), puis un alignement avec la droite de pente 3mV/m déjà observée sur l'intervalle 50- 46mbgl. En l'absence de débitmètre sur cet intervalle, il est plus difficile d'interpréter la mesure SP ; on peut néanmoins estimer que le point de rebroussement observé à 43mbgl correspond au point ou le débit vers le bas devient nul, ce qui permet à la SP de rejoindre sa droite de variation normale.
On peut donc conclure de cet essai que, sous certaines conditions, l'outil Muset peut être utilisé comme un débitmètre électrique pour mesurer les faibles débits.
D'autre part, on voit que dans la zone de transition de salinité se produit une légère acidification (de pH= 7,3 à pH= 7,1) due aux effets ioniques ayant lieu dans cette zone.

5.2 Complexe récifal

Nous présentons maintenant les résultats des diagraphies hydrogéologiques sur l'ensemble des 25 puits considérés du complexe récifal.

5.2.1 Zones d'eau

On constate (à l'aide des diagraphies électriques) les zones d'eau suivantes sur les différents puits de la plate forme récifale Miocène du Sud-Est de Majorque (hors Campos) : Tab. 10 (les puits sont géographiquement localisés dans Maria-Sube[1] et al. sous presse).

Fluide	CBC (mbgl)	S14 (mbgl)	S15 (mbgl)	S16 (mbgl)	S18 (mbgl)	S19 (mbgl)	S20 (mbgl)	S21 (mbgl)	S22 (mbgl)	S23 (mbgl)	S24 (mbgl)
Eau douce	81,47	81,5-145	122,2-137,9	86,00-129,0	119-170,6	60,2	71,3	61,87-71,00	41,0-47,0	5,75-9,42	47,59-69,76
Transition				129,0-175,0	170,6-173,0			71,00-79,37	47,0-65,0	9,42-14,14	69,76-82,47
Eau de mer		145		175,0-202	173,0-178,77			79,37-163,14	65,0-105,0	14,14-86	82,47-114

Tableau 10. Zones d'eau observées sur les différents puits de Cap blanc, Llucmajor, Campos, Ses Salines.

D'autre part, connaissant l'élévation de chaque tête de puit (au niveau du sol) au-dessus du niveau de la mer, et la profondeur mesurée de chaque plan d'eau au-dessous du niveau du sol, on peut en déduire l'élévation h de chaque plan d'eau au-dessus du niveau de la mer (Tab. 11). On voit que, en-dehors des erreurs de mesure, h est une fonction de la distance du puit à la côte.

Elevation	S16 (m)	S18 (m)	CBA (m)	CBB (m)	CBC (m)	S14 (m)	S15 (m)	S16 (m)	S18 (m)	S19 (m)	S20 (m)	S21 (m)	S22 (m)	S23 (mbgl)	S24 (mbgl)
Elévation de la tête de puit au-dessus du niveau de la mer : z	88,14	121,30	94,25	94,04	83,23	82,54	125,42	86,16	118,86	61,35	74,84	63,87	42,09	5,92	48,13
Profondeur du plan d'eau en dessous du niveau du sol: z - h	86,16	118,85	-	-	81,47	81,5	122,2	86,00	119	60,2	71,3	61,87	41,0	5,75	47,59
Elévation du plan d'eau au-dessus du niveau de la mer: h	1,98	2,45	-	-	1,76	1,04	3,22	0,16	-0,14	1,15	3,54	2,0	1,09	0,17	0,54

Tableau 11. Tableau montrant le calcul de h (élévation du plan d'eau au dessus du niveau de la mer) pour chaque puit des sites de Cap blanc, Llucmajor, Campos, Ses Salines.

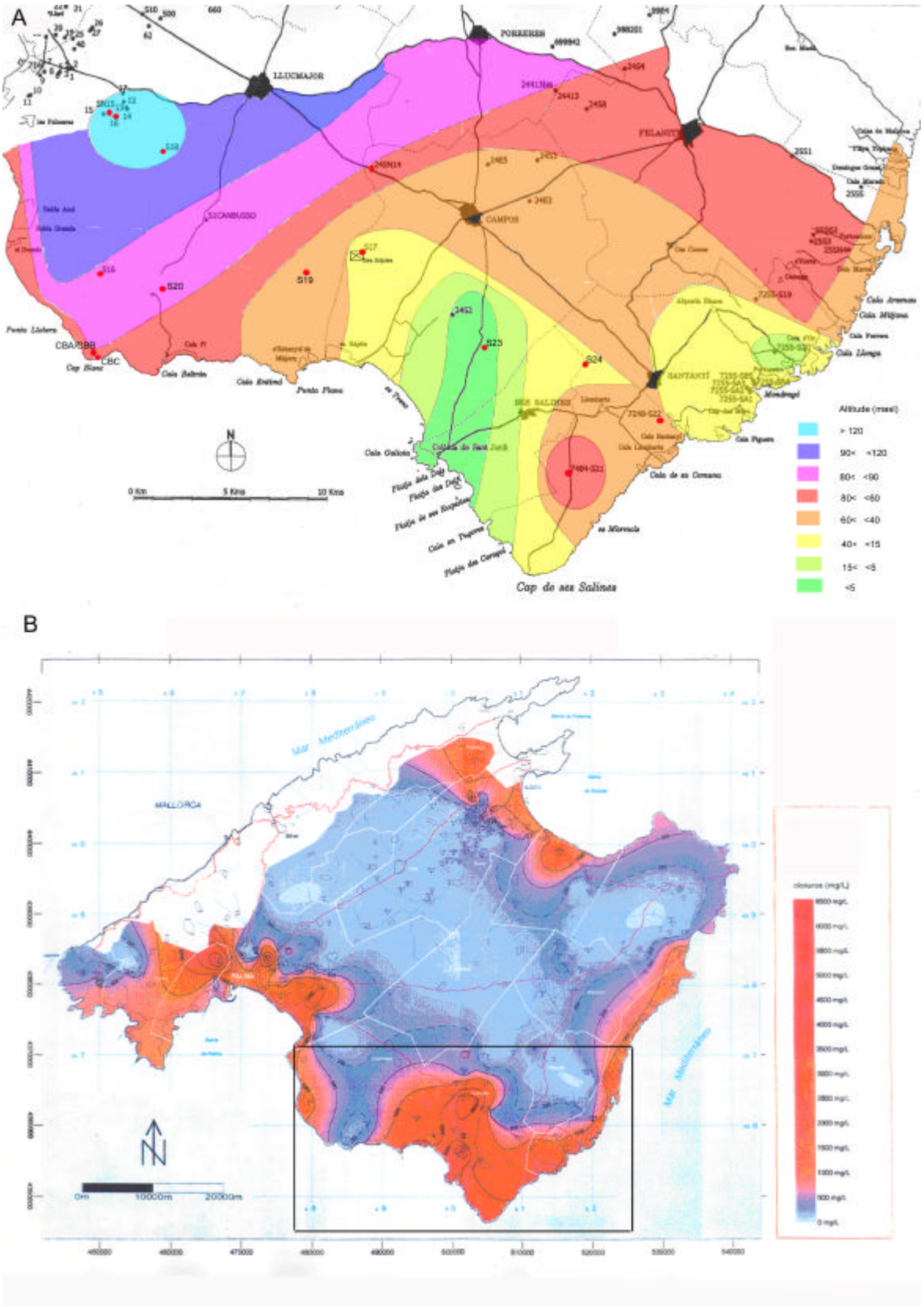

Figure 21. (A) Différents niveaux d'altitude à la tête de puit, (carte modifiée et données altimétriques du Gouvernement des îles Baléares). (B) Carte des isoclorures, au sommet de la nappe phréatique ; bleu de 0 à 500 mg/l, rouge de 500 à 6500 mg/l, (modifiée d'après carte du Gouvernement des Iles Baléares), le rectangle noir correspond à l'aire représentée sur la Fig. 21A.

La Fig. 21A et le Tab. 12 représente une étude de l'influence de l'altitude. Sur la salinité de l'eau de surface mesurée à l'intérieur des différents puits du complexe récifal Miocène du Sud-Est de Majorque.
La Fig. 21B visualise la carte des isochlorures dans les bassins sédimentaires de Majorque. On voit que les régions de Cap blanc et Llucmajor sont des régions à eau douce, tandis que Ses Salines est la région à plus forte intrusion d'eau salée. On voit également la limite Nord de pénétration du biseau salé.
Ainsi, la salinité de l'eau douce varie de 400ppm (dans S18, où l'élévation de la tête de puit est la plus élevée_ 121m_,et loin de la mer_ 10 km) à 4500ppm (dans S21, moyennement élevé_ 64m, mais surtout le puit le plus proche de la mer_ 4km_ parmi ceux observés), tandis que la salinité de l'eau de mer varie de 35000ppm à 40000ppm (Tab. 12). Elle est la plus importante à S23, situé à côté des Salines de Levante, et le puit le plus bas_ 6m d'altitude. A noter que l'eau de mer recueillie à Colonia de Sant Jordi a une salinité mesurée de 38000ppm, et un Ph de 8,22 à 20,2°C mesuré en laboratoire.

Puit	Date (AAMMJJ)	Température eau douce (°C)	Conductivité eau douce (mS/cm)	Conductivité eau de mer (mS/cm)	Température eau de mer (°C)	pH	Altitude tête de puit au-dessus niveau de la mer (m)
S17	020513	22	2,52	7,074 ?	24		41
	020516	22	3,763	54,912	24,8		
	030609	23,333	3,306	54,681	24,806		
	030821	22,875	3,589	54,560	24,608		
	030827	22,524	3,755	54,772	24,895		
	040705	22,921	3,344	54,268	24,889	7,06	
S16	050420	22,878	1,542	61,965	27,013	7,67	88
S18	050420	22,348	0,844	35,278 (transition)	23,656	7,37	121
S21	050422	19,987	7,44	61,889	22,433	7,25	64
S22	050707	22,0	2,94	49,502	22,5	9	42
S23	050422	19,350	5,203	61,965	26,744	7,13	6
S24	050421	20,731	2,311	61,787	22,576	7,4	48
MP1	020905	18,8	1,24	-	-	7,2	-

Tableau 12. Données d'hydrogéologie relevées à l'Idronaut sur différents puits à travers la plate-forme récifale de Majorque. A titre de comparaison, MP1 (Pollenca) situé au Nord dans la Sierra Norte, présente une eau douce. On voit que la douceur de l'eau est assez dépendante de l'altitude et de la proximité des montagnes (voir Fig. 20).

L'eau distillée équilibrée en calcaire de Campos présente un pH= 9,34 @ 19,1°C, mesuré en laboratoire. Ceci qui laisse supposer que l'outil Idronaut utilisé sur tout les puits lit trop bas en pH ; noter qu'un outil Muset a été enregistré à S22 à la place de l'Idronaut, et que cet outil lit un pH de 9 (Tab. 12).

5.2.2 Failles actives

On remarque à S23 une rapide élévation de la température de 19 à 26°C entre 10 et 15mbgl de profondeur, à l'entrée dans la zone d'eau saumâtre (Fig. 22A). Simultanément, on voit qu'on passe d'une eau de mer à une eau saumâtre, et que le pH varie de –200 à +100, indiquant une brusque oxygénation. Ceci est interprété comme une faille active facilitant l'arrivée d'eau chaude venant des profondeurs. S23 est situé à côté de bains thermaux (à Banos de San Juan) (Fig. 21A).
On voit sur les Fig. 22B et 22C un enregistrement de température et de conductivité sur S2, situé non loin de S23 (Fig. 21A), qui montre aussi une anomalie de température à l'entrée

dans la zone d'eau saumâtre, à 40mbgl, bien qu'avec une amplitude moindre qu'à S23. Il y a donc deux failles actives parallèles de direction NE-SO, l'une passant par S2, l'autre par S3.

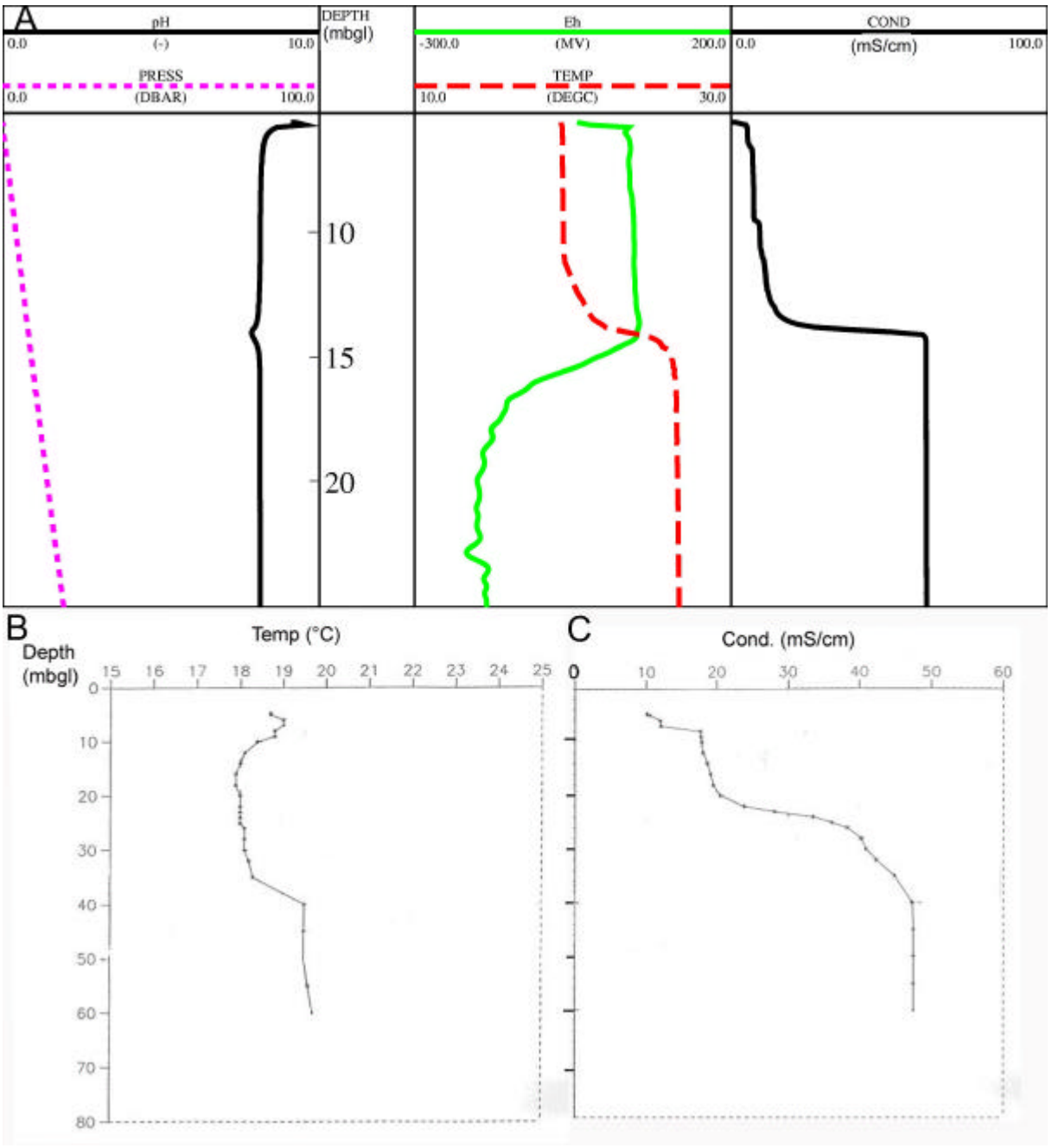

Figure 22. (A) Idronaut à S23, montrant une anomalie de température à partir de 15mbgl de profondeur. Température (B) et conductivité (C) sur S2 (modifié d'après enregistrement Gouvernement des Baléares).

6 Synthèse, conclusion et perspectives

Nous allons d'abord considérer les résultats obtenus sur la structure du réservoir formé par le complexe récifal du Sud-Est de Majorque, puis ceux obtenus en hydrogéologie.

6.1 Réservoir

6.1.1 Le développement du complexe récifal du Sud-Est de Majorque au Miocène

Le complexe récifal du Sud-Est de Majorque a une histoire géologique qui s'étend du début à la fin du Miocène. Elle peut se résumer comme suit (Fig. 13) :

- A l'**Aquitanien**, début de la progradation du récif à partir du Nord-Est. La température est chaude, le niveau de la Méditerranée est haut, environ 100m plus haut qu'aujourd'hui ; l'orogénèse alpine n'a pas encore commencée ; ceci implique que les coraux se développent autour des collines existantes, les vallées étant inondées ; c'est l'age du talus de Ses Sitjoles. Les communications Est-Ouest sont bonnes, tant avec l'Océan atlantique qu'avec l'Océan Indien, impliquant une salinité normale, favorable à la diversité des genres de Madréporaires. Le talus de Ses Sitjoles date de l'Aquitanien inférieur.
- Au début du **Burdigalien**, début de l'orogénèse alpine, le niveau marin étant globalement constant autour de +100m ; ceci favorise la progradation des coraux vers le Sud-Est, les anciennes plaines inondées acquerrant progressivement une bathymétrie favorable à la croissance de coraux. La température est toujours chaude. Au Burdigalien Supérieur, une régression se produit, émergeant certains coraux, mais permettant la colonisation de certaines plaines ; tandis que l'Océan Indien ne communique plus avec la Méditerranée, entraînant une augmentation progressive de la salinité de la Méditerranée, et une raréfaction des genres de Madréporaires aux seuls genres capables de supporter une salinité élevée ; c'est aussi l'age des coraux de Ses Sitjoles (17m.a.), où seul le genre *Porites*, avec la seule morphologie massive, sont observés. Ceci implique que : 1) les coraux sont établis dans une structure plate-forme à faible profondeur ; 2) le niveau eustatique est généralement constant pendant la période de construction récifale.
- Au **Langhien**, la température est toujours élevée, la salinité de la Méditerranée croît, le genre *Porites* résistant aux salinités importantes devient dominant. A la fin du Langhien, une autre régression se produit.
- Au **Serravallien** Moyen se produisent à la fois la fin de l'orogénèse alpine et un refroidissement qui stoppe la croissance des coraux en Méditerranée ; on observe un hiatus au Serravalien à Ses Sitjoles. Une régression globale a lieu du début à la fin du Serravallien, le maximum de la régression étant atteint à la frontière Serravallien-Tortonien. En même temps, la température augmente.
- Au **Tortonien** Inférieur, une transgression s'amorce, qui atteindra son maximum au Messinien moyen. C'est l'explosion de la construction récifale, avec faible diversité de genre de madréporaires. A partir du Tortonien Moyen, la température décroît. Le talus de Cap Blanc date du Tortonien Moyen.
- Au **Messinien**, la température décroît. Une transgression se produit au Messinien Moyen, entraînant une croissance récifale modérée ; c'est l'age des coraux et du lagon de Cap Blanc, ainsi que du lagon de Ses Sitjoles. Puis, au Messinien Supérieur, se produit la MSC, causant d'abord la fin des coraux de la Méditerranée par excès de salinité, puis le TCC observable sur les quatre sites explorés du complexe récifal

Miocène du Sud-Est de Majorque. On remarquera que les roches correspondant au TCC a été daté à environ 6m.a. aussi bien à Cap Blanc qu'à Ses Sitjoles, laissant supposer que le TCC est bien coéval sur l'ensemble du récif.

6.1.2 Classification des récifs coralliens Miocène de Majorque

En reprenant la classification de Saint Martin, 1990, (paragraphe 2.2.4 ci-dessus), il semble clair que compte tenu de la présence très importante de *Porites* et d'algues rouges, et moins importante de *Tarbellastraea* et d'*Haliméda* notée dans les coraux Miocène de Majorque (Pomar et al., 1994 ; Pomar et Ward, 1995 ; Pomar et al., 1996 ; Pomar, et Ward, 1999 ; Pomar, 2001, Jaeggi, 2006, Maria-Sube et al., Maria-sube[1] et al., sous presse), il faille classer ces coraux dans les groupes 3 (récifs de plate-forme en général peu développés) et 4 (récifs monogénériques à *Porites* présentant des phénomènes de progradation).

6.1.3 Tectonique

La tectonique du Sud-Est de Majorque à partir du Miocène Inférieur, doit tenir compte de la phase compressive de l'orogénèse alpine du Burdigalien Inférieur au Serravallien Moyen (Fig. 11A et 13), qui a créé la Sierra Tramuntana et les Sierres de Llevante orientée NE-SE (Fig. 11B), mais aussi de la phase extensive du début du Pléistocène qui a créé le Bassin de Campos, avec les failles normales qui y sont associées (Maria-Sube[1] et al., sous presse). Cependant, nous avons vu (Maria-Sube[1] et al., sous presse), que pendant la période Pliocène Inférieur à aujourd'hui, des mouvements compressifs ont dû également se produire, puisque au moins une faille inverse a été détectée.

6.2 Hydrogéologie

Les enregistrements de diagraphies hydrogéologiques ont démontré :

- La présence d'un biseau salée d'eau de mer pénétrant jusqu'à au moins 20km à l'intérieur des terres
- Ce biseau salé est surmonté d'unbiseau d'eau soit saumâtre, soit douce, en fonction de la proximité ou non de zones de collines
- La présence d'anomalies de température d'eau sur les puits permet de détecter la présence de faille actives

La méthode multi-scalaire et multi-disciplinaire utilisée s'est révélée adéquate pour étudier ces formations calcaires complexes et a permis d'extraire un grand nombre de conclusions importantes.

6.3 Perspectives

A la suite du projet ALIANCE, dont cette thèse relate une partie des résultats, divers projets soit peuvent se mettre en place, soit sont déjà en cours de mise en œuvre à Majorque.

6.3.1 Extension et origine du complexe récifal Miocène de Majorque

Il serait intéressant d'effectuer des datations sur des coraux au Nord-Est de Santanyi dans le complexe récifal.

Il serait aussi intéressant de forer des puits près de S21 et S22, avec prélèvement de carottes et enregistrement de diagraphies afin de vérifier : 1) la datation du Calcaire de Santanyi, et des coraux ; 2) l'existence d'une faille inverse (par enregistrement et interprétation de diagraphie d'imagerie de la paroi du puit) ; 3) la séquence sédimentaire à cet endroit.

Enfin des puits de 300m de profondeur permettraient d'étudier :

- le «Off Reef Open Shelf (OROS) », les calcaires à Heterostegina (Pomar et Ward, 1996)
- l'évolution du contenu d'uranium en dessous de 100m et en dessous de 200m (dans la zone aphotique.
- Les zones de minéralisation correspondant aux période de glaciation du Pléistocène.

6.3.2 Etude de l'hétérogénéité

Etude de l'hétérogénéité à différentes échelles entre 10 et 100m du site de Ses Sitjoles, de l'existence de cavités.

6.3.3 Etude de la diagenèse

Etude de la diagenèse sur le site de Ses Sitjoles, des phénomènes chimico-électriques dans la zone de transition de salinité.

6.3.4 Projet Girelle

Le projet GIRELLE a pour but la mise en place d'une stratégie de pilotage et donc de gestion des aquifères côtiers, par le développement de "sites pilote" avec instrumentation autonome du sous-sol et modélisation des flux en vue de rétroaction sur la ressource. GIRELLE est plus particulièrement focalisé sur les risques associés à la salinisation, progressive ou accidentelle, des nappes phréatiques côtières en zone urbaine.
La partie scientifique de GIRELLE a été initiée dans le cadre du projet ALIANCE, qui a permit la mise en place d'un premier observatoire in-situ à Maguelone en juin 2004. Cet observatoire est doté d'un fonctionnement autonome depuis avril 2006. Cependant, situé hors contexte urbain et loin de tout intérêt patrimonial et économique ce site ne pourra servir que de base instrumentale au projet GIRELLE.
D'un point de vue fondamental, on poursuivra les travaux en cours permettant de mieux comprendre la dispersion des polluants dans les milieux poreux hétérogènes, aussi bien d'un point de vue expérimental que dans la mise au point de d'instruments et de modèles permettant d'en rendre compte de façon pertinente.
De façon appliquée, le projet prévoit le développement de "sites pilotes" pertinents vis à vis de la thématique et centrés sur des problématiques urbaines et hydrogéologiques différentes. Deux sites en Languedoc-Roussillon et trois sites à Majorque (Baléares) permettront respectivement de surveiller un processus de salinisation naissant dans des nappes profondes et de suivre un processus de réhabilitation de nappes polluées par les chlorures

6.3.5 Géothermie et faille active

Les résultats d'enregistrements d'hydrogéologie obtenus sur le puit ancien S23 ont démontré la présence d'une faille active.
Un nouveau forage à proximité de S23, avec la gamme complète de carottage et de mesures permettra de mieux étudier les phénomènes géochimiques qui accompagnent les failles actives.

7 Références

Alvaro M., Barnolas A., del Olmo P., Ramirez del Pozo J., Simo A., 1984. El Neogeno de Mallorca: caracterization sedimentologica y bioestratigrafica; Boletin Geologico y Minero, v. 95, p. 3-25.

Bizon G., Bizon J.J., Bourrouilh R., Massa D., 1973. Présence aux îles Baléares (Méditerranée Occidentale) de sédiments « messiniens » déposés dans une mer ouverte à salinité normale : Paris, Comptes rendus des séances de l'Académie des Sciences, v. 277, p. 985-988.

Bonnier, B., 2005. Etude sédimentologique et géochimique des récifs Miocènes de Majorque (Baléares, Espagne). Influence des caractéristiques diagénétiques sur les propriétés physiques des roches carbonatées. Ms Thesis, 31p. (non publiée), Université de Marseille-Aix-en-Provence, Centre Européen de Recherche et d'Enseignement des Géosciences de l'Environnement (CEREGE) France.

Bourbié, T., Coussy, O., Zinszner B., 1986. Acoustique des milieux poreux, Edition Technip, 334 p.

Brachert T.C., Hultzsch N., Knoerich A., Krauworst U.M.R., Stückrad O.M., 2001. Climatic signatures in shallow-water carbonates: high resolution stratigraphic markers in structurally controlled carbonate buildups (Late Miocene, southern Spain), Elsevier Science. Palaeogeog. Palaeoclimatol. Palaeoecol. 175, 211-237.

Braga J.C., Aguirre, J., 2001. Coralline algal assemblages in upper Neogene reef and temperate carbonates in Southern Spain. Palaeogeog. Palaeoclimatol. Palaeoecol. 175 27-41.

Brown B., Morgan M., 1990. The Miracle Panet, Gallery Books.

Camoin G.F., Ebren P., Eisenhauer A., Bard E., Faure G., 2001. A 300,000-yr coral reef record of sea level changes, Mururoa atoll (Tuamotu archipelago, French Polynesia). Palaeogeog. Palaeoclimatol. Palaeoecol. 175 325-341.

Camoin G.F., Iryu Y., McInroy D.B., and the Expedition 310 Scientists, 2005, Tahiti Sea Level, Proceedings of the Integrated Ocean Drilling Program, V. 310 Expedition reports.

Chamley, H., 1987, Sédimentologie, Dunod.

Chevalier J.P., 1977. A glimpse of the Neogene corallian fauna, Second Symposium international sur les coraux et récifs coralliens fossiles, Paris, , BRGM Orléans France, 1977, p. 359-366, Mem. BRGM n° 89.

Cornée J.J, Roger S., Münch P., Saint Martin J.P., Féraud G., Conesa G., Pestrea- Saint Martin S., 2002. Messinian events: new constraints from sedimentological investigation and new AR40/AR39 ages in the Melilla-Nador Basin (Morocco), Sedimentary Geology 151 127-147.

Cunningham, K.J., Farr M.R., Rakid-El Bied K., 1994. EPSL, vol. 127, Issues 1-4, p. 77-93.

Daly, R.A., 1915. The glacial control theory of coral reefs. Proc Am Acad Arts Sci, 51: 157-251.

Darwin C., 1842. The structure and distribution of coral reefs, Smith Elder and Co., London.

Davies, P., J., J.A. McKenzie, A. Palmer-Julson, et al., 1990. Proceed. *ODP*, Sci. Rep., 133, 810p

Duggen S., Hoernie K., Van den Bogaard P., Rüpke L., Phipps M.J., 2003. Deep roots of the Messinian salinity crisis, Nature , 422, 602.

Dunham R.J., 1962. Classification of Carbonate Rocks according to Depositional Texture, AAPG. Mem.: p.108-121.

Eberli, G., Swart, P., and shipboard scientific party, 1996. Init. Rep., ODP, 166.

Embry A.F, Klovan J.E., 1971. A Late Devonian reef tract on nertheastern Banks Islands Northwest Territories. Bull. Can. Petr. Geol., v. 19, p 730-781.

Esteban M.,1979. Significance of the upper Miocene coral reefs of the Western Mediterraneann, Palaeogeog. Palaeoclimatol. Palaeoecol. 29, 169-188.

Fornos J.J., Pomar L., 1983. Mioceno Superior de Mallorca: Unidad Calizas de Santanyi ("Complejo Terminal"), Itinerio E. en: El Terciaro de las Baleares. Guia de las excursions des X Congreso Nacional de Sedimentologia. Menorca, 26-30 de Septiembre.

Freiwald, A., 2003. Les coraux des profondeurs, Pour la science, Juil.

Haq, Bilal U., Hardenbol J., Vail, P.R., 1987. Chronology of fluctuating sea levels since the Triassic, Science, v. 235, p. 1156-1167.

Hassan M., Hossin A.: Contribution à l'étude des comportements du thorium et du potassium dans les roches sédimentaires. C. R. Académie des Sciences (Paris) , 280, 1975.

Hsü, K.J., Ryan, W.B. F., Cita, M.B., 1973. Late Miocene desiccation of the Mediterranean . Nature 242, 240-244.

Hsü K.J., Montadert, L., Bernouilli D., Cita M.B., Erikson A., Garrison R.E., Kidd R.G., Mélières F. Müller, C., Wright, R.,1977. History of the Messinian salinity crisis, Nature 267, 399-403.

Jaeggi D., 2006. Multiscalar porosity structure of a Miocene reefal carbonate complex, thesis, Diss ETH nb. 16519.

Jenkyns, H.C., Sellwood B.W., Pomar L., 1973. A field incursion guide to the island of Mallorca: Geologists' Association guide, London, the Geologists' Association, 93 p.

Krijgsman W., Hilgen F.J., Raffi I., Sierro F.J., Wilson D.S.,1999. Chronology, causes and progression of the Messinian crisis, Nature, Volume 400.

Lieske, E., Myers, R.F., 2004. Coral reef guide; Red Sea London, HarperCollins.

Lyells C., 1830. Principles of geology, John Murray.

Maria-Sube Y., Camoin G., Pezard P., Löw S., Jaeggi D., Montoto M., Mateos F., submitted. Multi-scalar study of depositional environment and heterogeneity in a Miocene reef sequence, Sedimentology.

Maria-Sube[1] Y., Camoin G., Pezard P., Jaeggi D., Braaksma H., Verwert K., submitted. Depositional environment and structure in a Miocene reef complex, Majorca, Spain. AAPG.

Maria-Sube[2] Y., Pezard P., Loggia D., Camoin G., Braaksma H., Montoto M., Mateos F., Jaeggi D., Löw S., submitted. Core petrophysical properties of a Miocene coral reef, Campos site, Majorca, Spain. Tectonophysics.

Maria-Sube[3] Y., Pezard P., Loggia D., Braaksma H., Gaillot P., Montoto M., Mateos F., Jaeggi D., Löw S., Camoin G., submitted. Porosity structure of a Miocene coral reef, Ses Sitjoles site, Majorca, Spain. Geophysics, Geochemistry, Geosystems.

Mateos F., Montoto M., sous presse. Pore space structure with hydraulic significance from MC2 cores.

Mattauer, M., 2001. L'autonomie (géologique) de la Corse. Pour la Science, n° 286, août.

Mauffret A., 1976. Etude géodynamique de la marge des îles Baléares. Th. Doct. Univ. P. et M. Curie. CNRS, n° 12305, 145 p.

Pellant C., Blackburn R., Blackburn R., Booth B., Brewer D., Collinson J., Gould J., Headland R., Kemp T., Latham J., Lewis R., Peel D., Reynolds J., Tarling D., Vago G., 1985. Earthscope , Salamander books.

Pomar, L., Esteban, M., Calvet F., Barón, A., 1983. La unidad arrecifal del Mioceno superior de Mallorca, El terciaro de la Baleares (Mallorca- Menorca). Guia de las excursions del X Cong. Nac. Sedimentologia (Ed. by L. Pomar, A. Obrador, J. Fornos & A. Rodriguez-Perea), pp. 139-175. Inst. Est. Balearics and Universidad de Palma de Mallorca, 256.

Pomar, L., 1991. Reef geometries, erosion surfaces and high frequency sea-level changes, upper Miocene reef complex, Mallorca, Spain, Sedimentology, vol. 38, n° 2, pp. 243-269.

Pomar L., Ward W.C., 1994. Response of a late Miocene Mediterranean reef platform to high-frequency eustasy, Geology, 2, 131-134.

Pomar L., Ward W.C., 1995. Sea-level changes, carbonate production and platform architecture: the Llucmajor platform, Mallorca, Spain, in Sequence stratigraphy and depositional response to eustatic, tectonic and climatic forcing, 87-112, B.U. Haq, Kluwer Academic Publishers.

Pomar L., Ward W.C., Green D.G., 1996. Upper Miocene reef complex of the Llucmajor area, Majorca, Spain, SEPM Concepts in Sedimentology and Paleontology, 1-56576-033-6, 191-225.

Pomar L., Ward W.C., 1999. Reservoir-scale heterogeneity in depositional packages and diagenetic patterns on a reef-rimmed platform, Upper Miocene, Mallorca, Spain, AAPG, 83, 1759-1773.

Pomar L., 2001. Ecological control of sedimentary accomodation: evolution from a carbonate ramp to rimmed shelf, Upper Miocene, Balearic Islands, Palaeogeog. Palaeoclimatol. Palaeoecol. 175 249-272.

Riba y Arderiu O., 1983. Las islas Baleares en el marco geologico de la cuenca Mediterranea occidental durante el Terciario. El Terciario de las Baleares, Guia de los excursiones del X congreso nacional de sedimentologia. Menorca, 26-30 sept.

Riding R., Martin J.M., Braga J.C., 1991. Coral-stromatolite reef framework, Upper Miocene, Almerie, Spain, Sedimentology, 38, 799-818.

Riding R., Braga J.C., Martin J.M., Sanchez-Almazo I.M., 1998. Mediterranean Messinian Salinity Crisis: constraints from a coeval marginal basin, Sorbas, southeastern Spain, Marine Geology, 146, 1-20.

Rouchy J.M., Saint Martin J.P., 1992. Late Miocene events in the Mediterranean as recorded by carbonate-evaporite relations, Geology, V. 20, 629-632.

Saint Martin J.P., 1990. Les formations récifales coralliennes du Miocène supérieur d'Algérie et du Maroc, Mémoire du Muséum National d'Histoire Naturelle.

Saint Martin J.P. 2003 La Recherche Hors Série, N° 11, Avril

Scholle P.A., Bebour D.G., Moore C.H. , 1983. Carbonate Depositional Environments, AAPG.

Schlumberger, 1973. Production log interpretation.

Serra O. : Fundamental of well-log interpretation 2. The interprétation of logging data. Elsevier, Amsterdam, Development in Petroleum Science 15B, 1986

Serra O., Serra L., 2000. Diagraphies, Serralog

Smith A.G., Woodcock N.H., 1982. Tectonic synthesis of the Alpine- Mediterranean region. A review. Geodynamic series n° 7:15-38. Geol. Soc. Am.

Sun Q.S., Esteban M., 1994. Paleoclimatic controls on sedimentation, diagenesis and reservoir quality: Lessons from Miocene carbonates, AAPG Bulletin, V 78, N° 4, pp. 519-545.

Veizer, J., Ala, D., Azmy, K., Bruckschen, P., Buhl, D., Bruhn, F., Carden, G.A.F., Diener, A., Ebneth, S., Godderis, Y., Jasper, T., Korte, C., Pawellek, F., Podlaha, O., Strauss, H., 1999. 87Sr/86Sr, d13C and d18O evolution of Phanerozoic seawater. Chemical Geology 161, 59-88.

Wright V.P., 1982. A revised classification of limestones. Sedimentary Geology, 76, 177-185.

Annexes

Trois annexes sont présentées : 1) Le protocoles de mesures pétrophysiques sur bouchons de carottes ; 2) Le calage en profondeur des diagraphies de Ses Sitjoles ; 3) L'étalonnage des outils de diagraphies.

A1 Protocole de mesures pétrophysiques sur bouchons de carottes

1 Découpe des échantillons dans la carotte

1.1Découpe d'un cylindre

On utilise une perceuse à levier munie d'un outil (scie trépan ou carotteur) à découpe cylindrique.

1.2Découpe des fonds de cylindre

Un touret munie d'une lame de scie tournante permet de découper les fonds parallèles du cylindre.

2 Séchage

Un four permet de sécher les échantillon à 56 °C, pendant au moins trois jours pour les roches poreuses, au moins sept jours pour les roches non poreuses, telles que les granites, jusqu'à stabilisation de leur masse.

3 Mesure des dimensions extérieures de l'échantillon

Mesure au pied à coulisse de :

- Longueur : ~22mm,
- Diamètre : ~25mm,

du cylindre, ce qui, à supposer que l'échantillon a la forme régulière d'un cylindre, permet de calculer son volume.

4 Pesée des échantillon secs

Les pesées se font sur une balance de précision électronique Precisa 410 AM-FR, qui, jusqu'à 100 g fournit 4 digits après la virgule.

On mesure :

- la masse de l'échantillon sec
- la masse de l'échantillon sec entouré sur son flanc d'un ruban téflon entouré de téflon (ceci indique le poids du ruban de téflon, qui reste alors sur l'échantillon pour toute la suite du protocole ; ce ruban de téflon permet de canaliser le fluide qui sera plus tard injecté dans l'échantillon pour les mesures de perméabilité ; il est aussi utile pour éviter l'évaporation du fluide au bord de son flanc, lors des mesures de conductivité, et également pour éviter qu'une pellicule d'eau sur les flancs de l'échantillon ne perturbe la pesée de l'échantillon immergé_ voir Paragraphe 7.2).

5 Dégazage

Jusqu'à maintenant, les mesures sur échantillon se sont faites sur des échantillons secs (après passage au four). A partir de maintenant, les mesures sur échantillons vont se faire sur échantillons immergés dans de l'eau. On va utiliser le type d'eau qui va endommager l'échantillon le moins possible (en vue des mesures de porosité et de perméabilité), afin de minimiser les interactions fluide- roche, et similaire autant que possible au fluide in-situ.

5.1 Cas des roches volcaniques

Ces mesures peuvent se faire à l'eau distillée douce ou salée qui n'a pas d'effet sur les roches volcaniques.

5.2 Cas des grès argileux

Dans le cas des grès argileux, il est important de commencer les mesures avec de l'eau salée, car l'eau douce va produire un gonflement des argiles.

5.3 Cas des carbonates

Les carbonates sont solubles dans l'acide, mais aussi dans l'eau distillée (Blackburn, 1985 ; Hall, 1988 ; Morel, 1983, Zim, 1957). En particulier, l'eau distillée employée pour préparer des solutions à différentes concentrations de NaCl, indispensables pour les mesures électriques, est très corrosive sur les carbonates, et perturbe donc les mesures de perméabilité. Il faut alors utiliser une eau dite «équilibrée », préparée un mois à l'avance à l'aide d'eau distillée dans laquelle une poudre des carbonates à étudier et mélangée après broyage de débris d'échantillons.

Le fluide utilisé est filtré à 0,2 µm (afin d'éliminer les bactéries les plus petites). Ensuite, on ajoute quelques gouttes de formol, pour se débarrasser durablement des bactéries, qui pourraient perturber les mesures de perméabilité.

Avant d'immerger les échantillons dans le fluide de mesure, il faut commencer par dégazer l'échantillon, dans un appareillage schématisé sur la Figure A1-1.

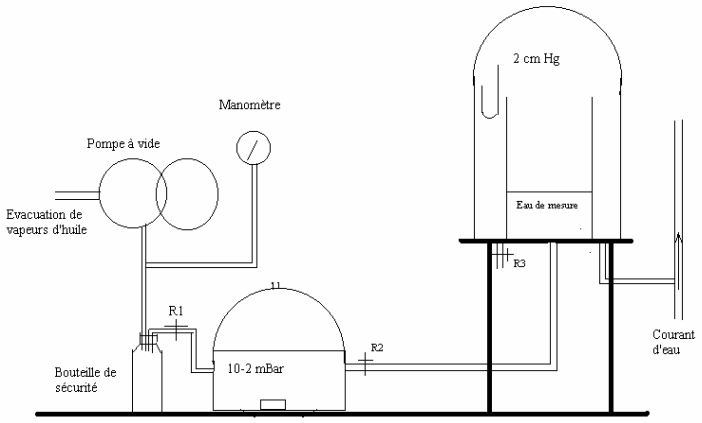

Figure A1- 1. Montage de dégazage.

La pompe à vide (pompe sèche BOC Edwards XDS 5, 4,86 M3h-1) permet d'établir une dépression de 0,07 mBar dans le récipient de gauche, à l'intérieur duquel est placé le ou les

échantillon(s) sec(s) jusqu'à ce que la pression atteigne cette valeur, le robinet R1 étant ouvert et le robinet R2 étant fermé. Ceci permet d'extraire toute l'eau qui était restée dans les pores.
Lorsque la dépression est atteinte, le récipient surélevé de droite est rempli d'eau de mesure, avec les robinets R2 et R3 fermés. La cloche sur ce récipient établit une étanchéité sur le plateau. On établit un courant d'eau dans le tube pour établir une dépression de 2cm de mercure (= différence entre les deux colonnes de mercure, environ 0,3 bars) sous la cloche ; ceci constitue un premier circuit de dégazage.
Quand l'eau du récipient de droite est dégazée (environ 1 heure, jusqu'à ce qu'il n'y ait plus de bulles dans l'eau) R1 est fermé, la pompe à vide est arrêtée, on arrête le courant d'air, R2 puis R3_ pour laisser entrer l'air dans le récipient de gauche_ sont ouverts : l'eau de mesure dégazée imbibe le ou les échantillons, qui se dégazent (pendant un jour).

6 Pesées des échantillons saturés et immergés

Ceci va compléter la méthode de « triple pesée » (échantillons secs, saturés et immergés) commencée avec les échantillons secs. On pèse l'échantillon saturé dans de l'eau:

- masse saturée Msat. Cette mesure se fait avec l'échantillon posé dans un récipient rempli d'eau placé sur le plateau de la balance. Le récipient est rempli d'eau sans échantillon et taré avant la pesée. Bien égoutter et sécher la bande de téflon avant la pesée, ne pas sécher les faces planes, en faisant rouler rapidement l'échantillon sur du papier absorbant sec. Ce protocole de mesure permet d'éviter les erreurs dues à l'évaporation du fluide si on posait simplement l'échantillon saturé d'eau sur la balance. On déduit ensuite la masse du téflon de la masse de l'échantillon saturé entouré de téflon. Faire trois mesures et prendre la moyenne.
- masse de l'échantillon immergé dans l'eau (Figure A1-2) Mim. Ne pas sécher l'échantillon.Tarer avec l'échantillon dans le bac, pour éviter l'erreur produite par la levée du liquide au moment de l'introduction de l'échantillon dans l'eau. On mesure Mim apparent, sans déduire la masse du téflon. Faire trois mesures et prendre la moyenne.

Ces pesées servent de référence, pour vérifier si l'échantillon a varié de poids entre les différentes pesées.
Ces pesées permettront de déduire la porosité et la densité de grain de l'échantillon, son volume ayant été mesuré et calculé au paragraphe 3 ci-dessus, par deux méthodes différentes, qui vont être détaillées ci-dessous.
La définition de la porosité totale ϕ d'une roche poreuse est :

$$\phi = V_{pores} / V_{total} \quad (1)$$

avec V_{pores} = volume des pores de l'échantillon
V_{total} = Volume total de l'échantillon

D'autre part , on connaît la définition de la masse volumique ρ d'un solide :

$$\rho = M / V \quad (2)$$

avec M = masse du solide
V = Volume du solide.

6.1Porosité calculée par la méthode de double pesée

En utilisant la Formule (2) pour l'eau contenue dans les pores de l'échantillon :

$$\rho_{eau} = M(\text{eau des pores}) / V_{pores} = (M_{sat} - M_{sec}) / V_{pores} \quad (3)$$

avec M_{sat} = Masse de l'échantillon saturé d'eau (g)
M_{sec} = masse de l'échantillon sec (g)

ρ_{eau} = densité de l'eau utilisée (g/cm^3).
En reportant cette valeur de V_{pores} (Formule 3) dans la Formule (1), on trouve

$$\phi = (M_{sat} - M_{sec}) / (\rho_{eau} * V_{total}) \quad (4)$$

Les échantillons étant séchés plusieurs jours au four à 56°C, la différence ($M_{sat} - M_{sec}$) est bien la masse de l'eau des pores, y compris l'eau liée aux argiles. On mesure donc bien avec la formule (4) une porosité totale (Ramamoorthy, 2000).
La formule (4) permet à partir des pesées effectuée au § 5 et 7, et des mesures de longueur effectuées au § 3, et de la valeur de la densité de l'eau ρeau à la concentration considérée de trouver la valeur de la porosité totale de la roche à la profondeur de l'échantillon considéré.
ρ_{eau} est mesurée en utilisant la Formule (2), un récipient gradué à Veau = 200ml à 20°C, et deux pesées : m_1 = récipient vide , et m_2 = récipient rempli de 200ml d'eau.
ρ_{eau} mesurée à 25,5°C pour une eau de concentration 2M/l = 1,0655g/cm^3.

6.1.1 Précision de la mesure

$$\Delta\phi / \phi \subseteq [(\Delta M_{sat} + \Delta M_{sec}) / (M_{sat} - M_{sec})] + (\Delta\rho_{eau} / \rho_{eau}) + (\Delta V_{total} / V_{total}) \quad (5)$$

Avec des échantillons de carbonate de longueur l = 2,18cm et de diamètre D = 2,48cm, on trouve les ordres de grandeur suivants :
M_{sat} # 20g
M_{sec} # 15g
ρ_{eau} # 1g/cm^3
V_{total} # 10cm^3
l # 2cm
D # 2,5cm
$\Delta M_{sat} = \Delta M_{sec} = \Delta m_1 = \Delta m_2 = 0,0005$g
$\Delta V_{eau} = 0,01$ml
$\Delta l = \Delta D = 0,005$cm
D'autre part, on a :

$$\Delta\rho_{eau} / \rho_{eau} = \Delta M_{eau} / M_{eau} + \Delta V_{eau} / V_{eau} \quad (6)$$

$$\Delta\rho_{eau} / \rho_{eau} = \Delta(m_2 - m_1) / (m_2 - m_1) + \Delta V_{eau} / V_{eau} \quad (7)$$

Et on a aussi :

$$\Delta V_{total} / V_{total} = (2\Delta D / D + \Delta l / l) \quad (8)$$

En reportant les Formules (7) et (8) dans la Formule (5), avec les valeurs définies plus haut, on obtient :
$\Delta\phi / \phi \leq 0,001 / 5 + 0,001 / 200 + 0,01 / 200 + (0,01 / 2,5 + 0,005 / 2)$
$\Delta\phi / \phi \leq 0,0065$ ou 0,65 %.
On voit que c'est l'erreur de mesure sur le volume (qui est susceptible d'être même supérieure à celle estimée, qui suppose que le cylindre formé par l'échantillon est régulier) qui est la plus importante, et qui dégrade la précision des autres mesures.

6.1.2 Mesure de la densité de grain

Dans un échantillon poreux, on a la relation suivante :

$$M_{total} = M_{solide} + M_{pores} \quad (9)$$

Avec M_{solide} = masse de la partie solide de la roche (« matrice »).
En appliquant les Formules (1), (2) et (9), on obtient :

$$\rho_{sat} = \phi * \rho_{eau} + (1 - \phi) * \rho_{ma} \quad (10)$$

où ρ_{sat}= densité de l'échantillon imbibé d'eau
ρma = densité de grain ou densité de la « matrice » de la roche

La Formule (2), fournit également la relation :

$\rho_{sat} = M_{sat} / V_{total}$ (11)

En négligeant le poids immergé du téflon, on peut écrire (Figure 3):

$A = [\rho_{eau} * V_{total}]*g$ (12)

$P = (M_{sat})*g$ (13)

Avec A = poussée d'Archimède

P = poids de l'échantillon lorsqu'il est immergé

g = accélération de la pesanteur.

D'où :

$P - A = M_{im}*g = [M_{sat} – (\rho_{eau} * V_{total})]*g$ (14)

Avec M_{im} = Masse de l'échantillon immergé (g)

En utilisant les formule (2), (11) et (14), on obtient finalement :

$\rho_{ma} = (\{[M_{sat}/(M_{sat} – M_{im})– \Phi]*\rho_{eau}]\} / (1 - \phi)$ (15)

M_{im} étant la masse de l'échantillon pesée au cours de l'immersion de l'échantillon.

L'erreur sur ρ_{ma} est telle que :

$$\frac{\Delta r_{ma}}{r_{ma}} \leq \frac{\frac{\Delta M_{sat}}{M_{sat}-M_{im}} + \frac{\Delta M_{sat}+\Delta M_{im}}{\left(\Delta M_{sat}-\Delta M_{im}\right)^2}\left(\Delta M_{sat}\right)+\Delta f}{\frac{M_{sat}}{M_{sat}-M_{im}} f} + \frac{\Delta r_{eau}}{r_{eau}} + \frac{\Delta r}{1-f} \quad (16)$$

Avec les ordres de grandeur additionnels suivants :

M_{im} # 10g

ΔM_{im} # 0,0005g

$\Delta\phi = 0{,}003$ (avec $\phi < 0{,}50$)

$\Delta\rho_{ma} / \rho_{ma} \leq [(0{,}0005/ 10) + \{([0{,}001/ 100)/ (100)]*20 + 0{,}003]/ (2 – 1)+ 0{,}001/200 + 0{,}0065$

$\Delta\rho_{ma} / \rho_{ma} \leq 0{,}0095$

Cette fois-ci, c'est l'erreur sur la mesure de porosité qui est prépondérante.

6.2Porosité calculée par la méthode de la triple pesée

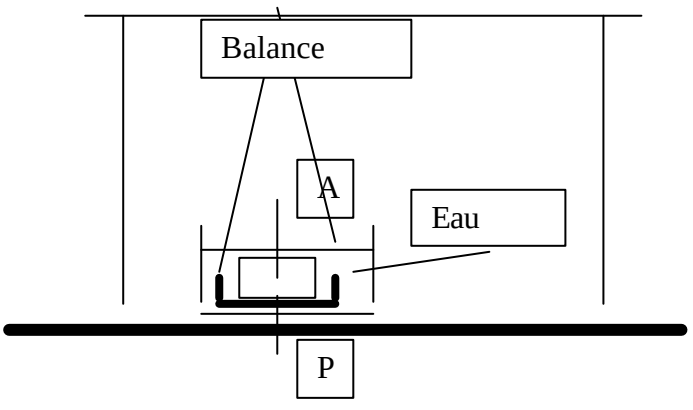

Figure A1- 2. Schéma montrant l'échantillon au cours de la pesée immergée, et les forces qui s'y appliquent.

Reprenons les Formules (12) à (14) en ne négligeant pas cette fois le poids du téflon immergé. On peut écrire que :

$A = [\rho_{eau} (V_{total} + V_{téf})]g$ (17)

$P = [M_{sat} + M_{téf}]g$ (18)

Avec $M_{téf}$: masse de la bande téflon enrobant le flanc de l'échantillon (g)
$V_{téf}$ = volume de téflon utilisé.
D'où :
$P - A = M_{im}*g = (M_{sat} + M_{téf})*g - (\rho_{eau} * [V_{total} + (V_{téf})]g$ (19)
Avec $\rho_{téf}$ = masse volumique du téflon utilisé (g/cm^3)
En utilisant les Formules (1), (3), et (19) on obtient :

$$f = \frac{M_{sat} - M_{sec}}{M_{sat} - M_{im} + M_{téf} - r_{eau} V_{téf}} \quad (20)$$

6.2.1 Précision de la mesure

$\Delta\phi/\phi \leq [(\Delta M_{sat} + \Delta M_{sec}) / [(M_{sat} - M_{sec}) +$
$\{[\Delta M_{sat} + \Delta M_{im} + \Delta M_{téf} + V_{téf}.\Delta\rho_{eau} + \rho_{eau}.\Delta V_{téf}] / (M_{sat} - M_{im} + M_{téf} + \rho_{eau}.V_{téf})\}$ (21)
Avec les ordres de grandeurs additionnels suivants :
$M_{téf}$ # 0,1g
$\rho_{téf}$ # $0,3 g/cm^3$
$V_{téf}$ # $0,3 cm^3$
$\Delta M_{téf}$ = 0,0005g
$\Delta\rho_{eau}$ = $0,00005 g/cm^3$
$\Delta V_{téf}$ # $V_{téf}$.(erreur relative sur la mesure de l'épaisseur du téflon) = 0,3*0,5 = $0,15 cm^3$
On trouve ainsi :
$\Delta\phi/\phi = 0,0005/5 + [0,0015 + (0,00005 \times 0,3) + (0,15 \times 1)]$
$\Delta\phi/\phi = 0,015$
Cette fois-ci, c'est la mesure de Vtéf qui grève la précision de la mesure ; il est donc indispensable de l'effectuer avec précaution. Dans ce cas, on obtient une précision qui est deux fois moins bonne que dans le cas de la méthode de double pesée, expliquée au § 7.1. A remarquer cependant que le poids du téflon avait été négligé dans le calcul de la méthode de double pesée. Si l'on ne tient pas compte du poids du téflon, la précision de la méthode de triple pesée est bien meilleure. C'est donc la méthode de la triple pesée qui sera retenue, la méthode de double pesée étant gardée pour comparaison et vérification.

6.2.2 Mesure de la densité de grain

La Formule (2), appliquée à la densité de la « matrice » de la roche fournit la formule suivante :
$\rho_{ma} = M_{sec} / V_{solide} = [M_{sec} / (V_{total} - V_{pores})]$ (22)

Dans la Formule (22), on a de plus utilisé la formule :
$V_{total} = V_{solide} + V_{pores}$ (23)
Avec V_{solide} = volume de la partie solide de la roche « matrice »
En utilisant la formule (1), la Formule (22) devient :
$\rho_{ma} = M_{sec} / [V_{total} (1-\Phi)]$ (24)
La Formule (19), fournit l'expression de V_{total}, qui est alors reportée dans la Formule (24), pour devenir :

$$r_{ma} = \frac{r_{eau} M_{sec}}{(1-f)(M_{sat} - M_{im} + M_{téf} - r_{eau}.V_{téf})} \quad (25)$$

on a $\Delta\rho_{ma}/\rho_{ma} \leq \Delta M_{sec}/M_{sec} + \Delta\phi/\phi + \Delta\rho_{eau}/\rho_{eau} + \{[\Delta M_{sat} + \Delta M_{im} + \Delta M_{téf} + V_{téf}.\Delta\rho_{eau} + \rho eau.\Delta V_{téf}] / (M_{sat} - M_{im} + M_{téf} + \rho_{eau}.V_{téf})\}$ (26)

soit, $\Delta\rho_{ma}/\rho_{ma} = 0{,}0005/15 + 0{,}015 + 0{,}00005 + 0{,}015 = 0{,}03$

Soit une précision relative de l'ordre de 3%, assez inférieure à celle de la méthode de mesure de volume, mais encore une fois, nous n'avions pas tenu compte dans la méthode des volume du poids du téflon, qui représente l'essentiel des erreurs.

Malgré la grande précision de la balance utilisée, les mesures d'échantillons ne répètent pas en raison de :

- M_{sec}, M_{sat} et M_{im} : pertes de matière des échantillons friables
- M_{sat}, M_{im} : difficulté à déterminer (malgré la bande de téflon) la couche d'eau attachée à l'échantillon, l'évaporation, le séchage.

Vérifier que l'eau distillée n'a pas attaqué l'échantillon au point de modifier la porosité d'une manière sensible.

7 Mesures de perméabilité et de potentiel zéta

On utilise la loi de Darcy :

$Q/S = - k/\mu * \Delta p/l$ (27)

Termes	Définition des termes	Unités historiques	Unités SI
Q	Débit	Cm3/sec	M3/sec
k	Perméabilité	Darcy (D)	M2
μ	Viscosité	Cp	Pa.sec
S	Aire	Cm2	M2
l	Longueur	Cm	M
ΔP	Pression différentielle	Atmosphère	Pascal (Pa)

Conversions d'unités :

1 atm. = 1,01325 bar

1 bar = 105 Pa

1 D = 0,987 10-12 m2

1 Cp = 10-3 Pa.sec

La viscosité de l'eau salée est donnée dans l'abaque FW-2 de Schlumberger (Figure A1-3), dont on déduit le Tableau A1-1 :

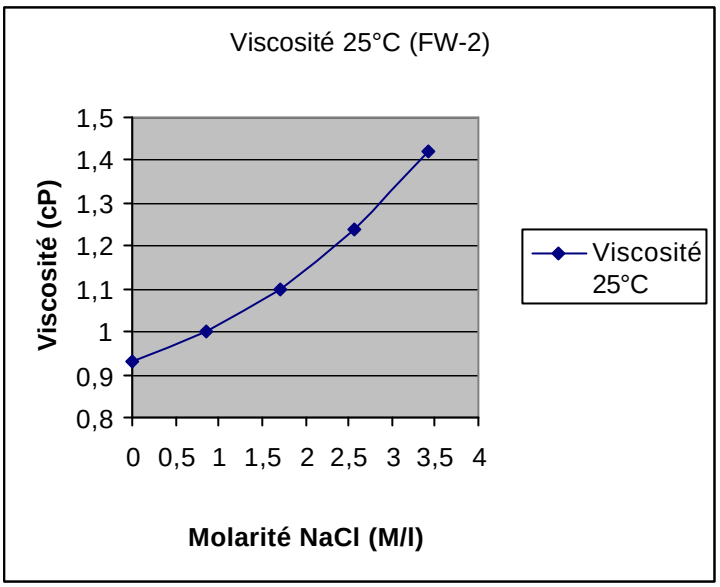

Figure A1- 3. Viscosité de l'eau salée à 25°C en fonction de la molarité. (D'après document Schlumberger, Chart FW-2, sachant qu'une Mole de NaCl = 58,45g/l)

Mole de NaCl	Viscosité (cP) à 25°C
2	1,14
1	1,01
0,5	0,97
0,1	0,94
0,05	0,93
0,01	0,93
0,005	0,93
0,001	0,93
0,0005	0,93
0,0001	0,93

Tableau A1- 1. Viscosité de l'eau salée en fonction de la molarité, pour les concentrations utilisées.

La Figure A1-3, le Tableau A1-1 et la Formule 26 montrent que lorsqu'on utilise pour la mesure de la perméabilité différentes eaux à salinité décroissante, la viscosité du fluide va diminuer, et donc la perméabilité mesurée de l'échantillon devrait diminuer d'environ 21%, toute choses étant égales.

Les échantillons sont placés dans une cellule Sonorex Bondelin RK 510S de nettoyage par ultra sons, pendant un quart d'heure, sur le flanc, dans des récipients en verre remplis d'eau équilibrée, et entouré d'eau ordinaire (pour la transmission des ultras sons).

L'échantillon saturé dans l'eau équilibrée filtrée est installé dans une cellule de mesure (Figure A1-5), qui est elle-même insérée dans l'appareillage de mesure de la Figure A1-4. Le fluide de mesure est récupéré, mais nécessite un nouveau filtrage avant de pouvoir être réutilisé.

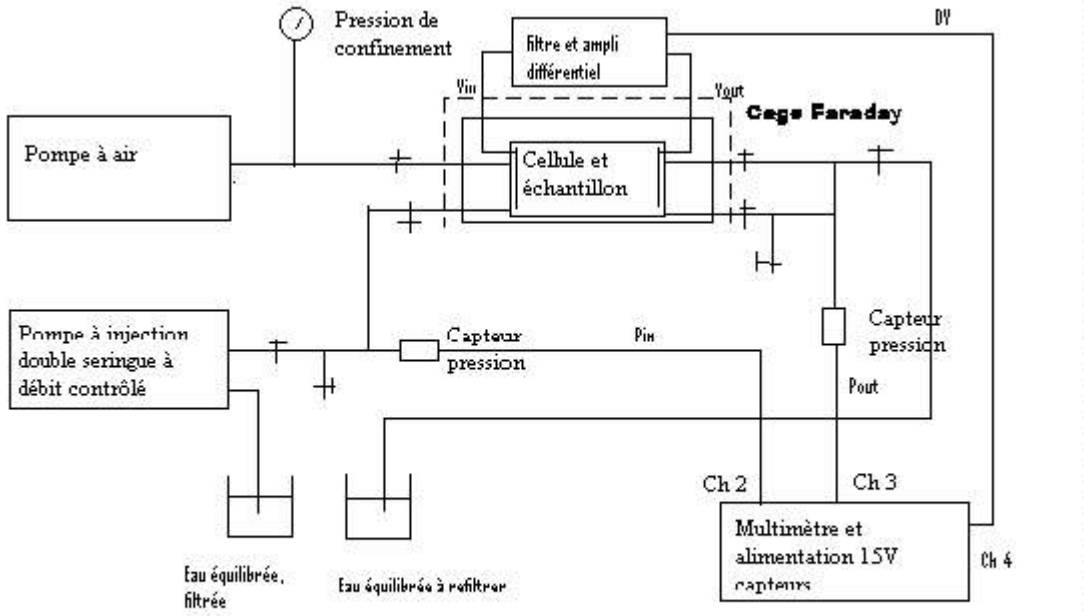

Figure A1- 4. Schéma de l'appareillage de mesure de perméabilité et de potentiel Zéta utilisé. Le channel 5 est ouvert. Pompe à injection Pharmacia Biotech Pump P-500. Capteurs de pression Keller max de pression 10 bars.

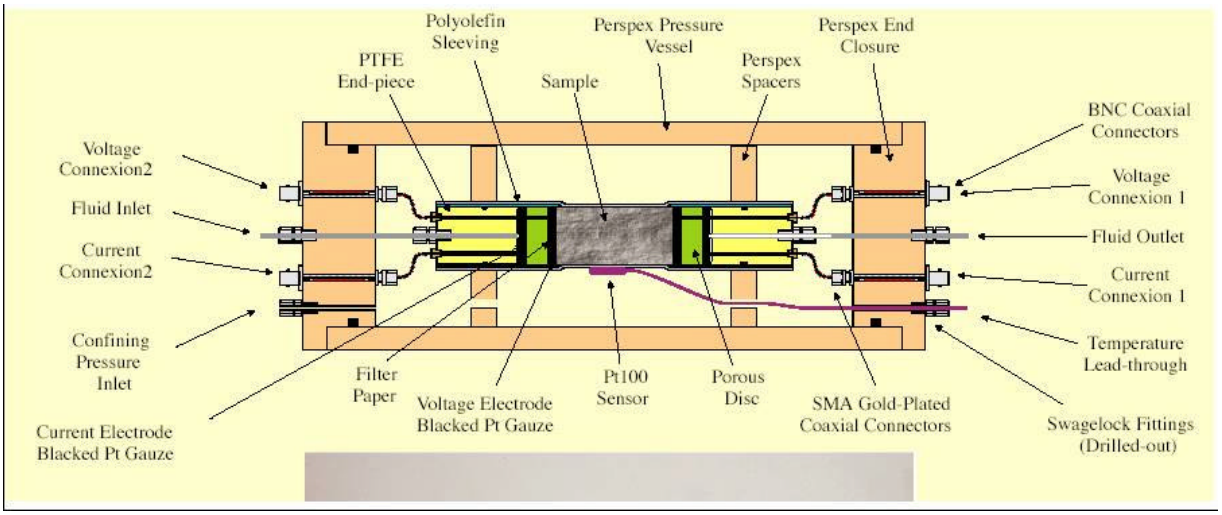

Figure A1- 5. Cellule de mesure de perméabilité et de potentiel Zéta.

La pompe Pharmacia a un débit minimum de 1ml/heure et maximum de 499ml/heure. Les capteurs de pression Keller ont une pression maximum de 10Bars. La pression de confinement utilisée est de 4Bars.
Le multimètre est un multimètre Kethley 2001 avec cartes d'acquisition pression et voltage.

7.1Mise de l'échantillon en cellule

De chaque côté de l'échantillon une grille platine et un filtre papier sont installés. Les fils d'électrode sont étalés sous le filtre papier. Le manchon entonnoir en téflon rétractable à la chaleur est enfilé sur l'échantillon, rajouter de l'eau.

Les tubes sont saturés d'eau avec une seringue. On pompe l'eau sous pression de confinement pour évacuer l'air.
Les embouts sont fixés de chaque côté. Brancher les tuyaux d'eau et les contacts électriques. Passer dans l'enceinte cylindrique et enfoncer les deux embouts.
L'enceinte est installée dans une boite en bois qui maintient les embouts en place. Une plaque en lace est placée par-dessus pour solidifier la boite en bois qui va supporter la pression de confinement qui pousse sur les embouts de la cellule.

7.2 Insertion de la cellule dans l'appareillage de mesure

La boite est placée sur le banc d'essai sous une vitrine. Connecter de chaque côté à l'impédance- mètre. Connecter l'eau à la pompe.
Pompe péristatique : Run pour démarrer la pompe. Une pression est réglée sur la pompe à 0,5 bar.
Brancher le gaz (air du compresseur) à moins de 10 bars (5 bars) : c'est la pression de confinement, qui permet de comprimer le manchon rétractable, pour étanchéité.
Fermer la sortie du gaz de confinement.
Mesurer la pression du liquide de sortie.
En sortie, on mesure soit la pression du gaz , soit la pression du liquide (enregistrée sur carte d'acquisition (NI). 1 volt = 2 bars. On utilise un programme Labview (Electrokinetics3.vi). Les constantes CH2 (1,891491bar/V) et CH3 (1,826996bar/V) sont entrées. Vatm (CH2 en bar) et Vatm (CH3 en bar) qui dépendent de la pression atmosphérique du jour doivent être mesurées tous les jours (Figure A1-6).
Entrer :

- Sample length (m)
- Fluid viscosity (cP)
- Sample diam. (m)
- Attente (ms)
- Débit (cm3/hr)
- Pression confinement (bar)

On mesure :

- P_in CH2 (bar)
- P_out CH3 (bar)
- Le résultat : K (mDa)
- ΔV CH4

Quatre schémas en fonction du temps apparaissent sur l'écran : Amplitude débit, Amplitude PCH2 et PCH3, KmDa, CH4 (ΔV).

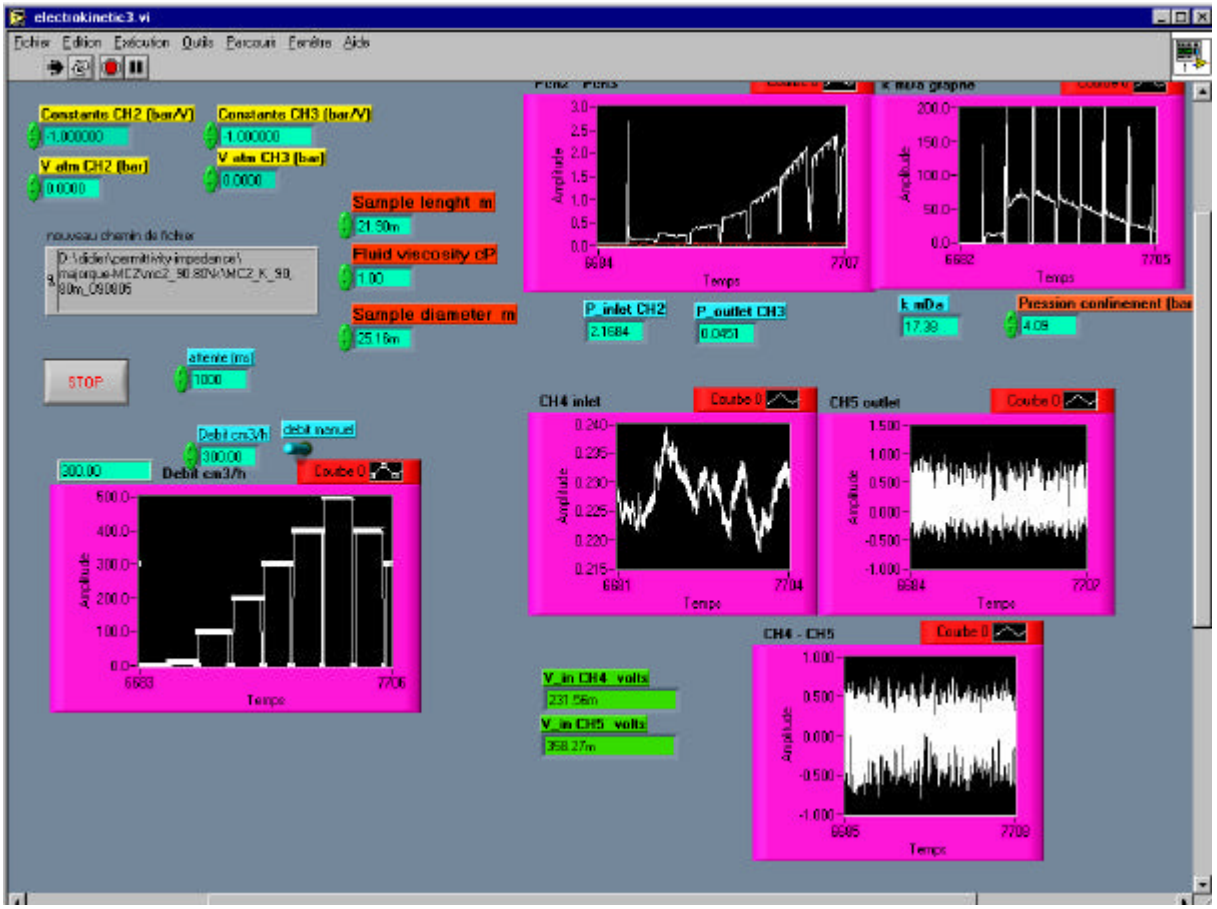

Figure A1- 6. Ecran du logiciel Electrokinetics3.vi. CH5 est ouvert : les écrans CH5 et CH4 -CH5 n'ont pas de signification pour cette expérience. Mesures de perméabilité et de Coefficient de couplage

7.3 Mesure de perméabilité

Les débits sont variés par palier croissants puis décroissants de 10 à 499ml/hr.

7.3.1 Précision de la mesure

La Formule 27 peut s'écrire :

$k = - Q*\mu*l / \Delta P*S$ (28)

d'où :

$\Delta k/k = \Delta Q/Q + \Delta\mu/\mu + \Delta l/l + \Delta(\Delta P)/\Delta P + \Delta S/S$ (29)

avec $\Delta S/S = 2\Delta D/D$

D étant le diamètre de l'échantillon.

$\Delta Q = 0{,}1$ ml/hr

$10 < Q < 499$ ml/hr

$\Delta\mu = 0{,}01$ cp

$\mu \# 1$cp

$\Delta l = \Delta D = 0{,}005$cm

$l \# 2$ cm

$D \# 2{,}5$ cm

$\Delta(\Delta P) = \Delta(Pin - Pout) = \Delta Pin + \Delta Pout = 2\,\Delta P = 2*0{,}0002 * P$

$0{,}1 < P < 4$ bars

$Pout \# 0$ ➔ $Pin - Pout \# P$

$\Delta k/k \leq 0{,}01 + 0{,}01 + 0{,}002 + 0{,}0002 + 0{,}004$

$\Delta k/k \leq 0{,}02$ ou 2%

0,06 < k < 3100mD

7.4 Mesure de potentiel Zéta

Quand un fluide est forcé à percoler à travers une roche perméable, un courant électrique apparaît. Ce courant est appelé le courant de convection. Il est proportionnel au gradient de pression, (Pinettes, 2001) :

$$\vec{j}_{conv} = \frac{e \times V}{\mu} \times \vec{\nabla}(P) = C \times s \times \vec{\nabla}(P) \quad (30)$$

Jconv : courant de convection (A)
ε : Constante diélectrique du fluide (F/m) ; $\varepsilon = \varepsilon_r * \varepsilon_o$; ε_o (air, vide)= 8,854187 10^{-12} (F/m) ; ε_r (eau douce)= 80 ; ε_r eau salée = 56.
ζ : Potentiel zéta de l'interface fluide/ roche (un potentiel qui mesure la capacité de l'interface fluide/ roche à être chargée potentiellement) (V)
μ : Viscosité dynamique du fluide (Pa.sec)
P : Pression (Pa)
C : coefficient de streaming potential (potentiel de courant) (au laboratoire, avec de l'eau distillée, C est habituellement de l'ordre de 100 mV/Mpa # 10 mV/bar, Ishido, 1981) Unité SI : V/pa
σ : conductivité électrique du fluide (S/m).

Un tel courant électrique crée un potentiel V, qui à son tour crée un second courant électrique, le courant de conduction, qui est proportionnel au gradient de potentiel

$$\vec{j}_{cond} = -s \times \vec{\nabla}(V) \quad (31)$$

et qui tend à annuler le courant de convection. La charge électrique totale est invariable, de sorte que lorsque le régime permanent est atteint, et en l'absence d'aucune autre source de courrant électrique, la divergence du courant total est égale à zéro :

$$\vec{\nabla}[s \times \vec{\nabla}(V)] = \vec{\nabla}[\frac{e \times z}{m} \times \vec{\nabla}(P)] = \vec{\nabla}[C \times s \times \vec{\nabla}(P)] \quad (32)$$

En régime permanent, la Formule (32) devient :

$$\Delta V = (\varepsilon\zeta/\sigma\mu) * \Delta P = C\Delta P \quad (33)$$

Ce qui donne accès à la mesure en laboratoire de :

$$\zeta = \sigma\mu\Delta V / \varepsilon\Delta P \quad (34)$$

ζ est exprimé en volts.

$$C = \Delta V / \Delta P = \varepsilon\zeta/\sigma\mu \quad (35)$$

La Formule (35) montre que C est un coefficient de couplage entre le débit hydraulique et électrique. D'autre part, C est proportionnel au coefficient ζ, qui peut être considéré comme une fonction linéaire du pH, en première approximation (Revil, 1999).
On mesure directement la conductivité de fluide avec le conductivimètre CDM 210 et une jauge (laisser tremper les échantillons une semaine dans chaque fluide salé), ΔV et ΔP sont mesurés sur l'appareillage des Figures A1-5 et A1-6.
Pour les valeurs de μ, utiliser le Tableau A1-1.
On utilise le même montage que pour les mesures de perméabilité (Figures A1-5 et A1-6).

Des électrodes en fil d'argent 1mm de diamètre ont reçu une couche d'AgCl par électrolyse de HCl 0.1M/l, avec un courant de 1A pendant 1 heure.
Pour cette mesure, l'électrode est branchée directement sur la carotte, sans filtre papier ni grille platine.
Deux capteurs de pression (amont et aval 10Bars ou Bar) et un filtre et amplificateur différentiel 1000GOhm sont nécessaires. Le voltmètre Keithley 2001 10 Mohm. Une adaptation d'impédance 50Ohm par un oscilloscope Tektronix est branchée entre le l'amplificateur et le voltmètre.
Pour tenir compte des polarisation d'électrode éventuelles, des mesures sans débit sont faites entre chaque palier de débit. Si besoin les valeur de ΔV à débit 0 sont retranchées des valeurs ΔV à débit non nul.
Des fils blindés sont utilisés partout où possible pour relier les capteurs. Une cage Faraday entoure le boîtier de la cellule de mesure.
La température, la conductivité et le pH du fluide de mesure sont mesurés avant chaque série de mesure pour vérifier les conditions de mesure.

7.4.1 Précision de la mesure

7.4.1.1 Coefficient de couplage

$$\Delta C/C = \Delta(\Delta V)/\Delta V + \Delta(\Delta P)/\Delta P \quad (36)$$

$\Delta(\Delta V)/\Delta V$ # 0,001

$\Delta C/C \leq 0{,}001 + 0{,}0002$

$\Delta C/C \leq 0{,}001$ ou 0,1%

Avec $-176 < C < 518$mV/bar

7.4.1.2. Potentiel zéta

$$\Delta\zeta/\zeta = \Delta C/C + \Delta\varepsilon/\varepsilon + \Delta\sigma/\sigma + \Delta\mu/\mu \quad (37)$$

$\Delta\sigma/\sigma = 0{,}0001$

$\Delta\varepsilon/\varepsilon = 0{,}0001$

$\Delta\zeta/\zeta \leq 0{,}001 + 0{,}0001 + 0{,}0001 + 0{,}01$

$\Delta\zeta/\zeta \leq 0{,}01$ ou 1%

Avec $-89 < \zeta < 236$mV

8 Mesures électriques à différentes salinités

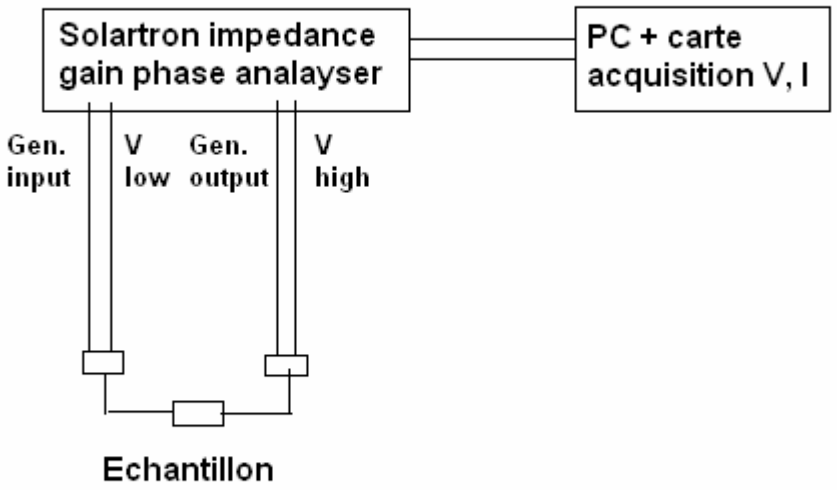

Figure A1- 7. Montage utilisé pour les mesures électriques.

Dans cette mesure, la salinité de l'eau va être variée : concentration d'abord de 2 Moles/ litre (= 117g/l), puis dix autres concentrations décroissantes jusqu'à 10^{-4} mole/ l (2 ; 1 ; 0,5 ; 0,1 ; 0,05 ;0,01 ; 0,005 ; 0,001 ; 0,0005 ; 0,0001M/l), avec des conductivités variant de 12,5 à 0,005S/m.

L'échantillon saturé est placé dans une pince qui comporte deux électrodes, avec un appareil de mesure Solartron SI 1260 (Schlumberger) : impedance / gain phase analyser et Solartron 1294 Impedance interface. Les mesures de voltage et d'intensité sont effectuées sur une carte d'acquisition National Instruments enfichée dans un PC (Figure A1-7).

Dix points de mesure (un pour chaque conductivité de solution) par décade de fréquence (7 décades : 1 ; 10 ; 100 ; 1000 ; 10^4 ; 10^5 ; 10^6Hz).

Le Solartron est branché sur les électrodes.

On utilise les logiciels LabView Zview2 (graphiques) et Zplot (contrôle de la mesure). Démarrage : « Sweepfrequency » (Control S). « Autoscale all graphs » permet d'ajuster les échelles automatiquement. Durée : 2'30'' par échantillon. Polarisation : DC POT 0V ; AC ampl. 100mV, Applied E.

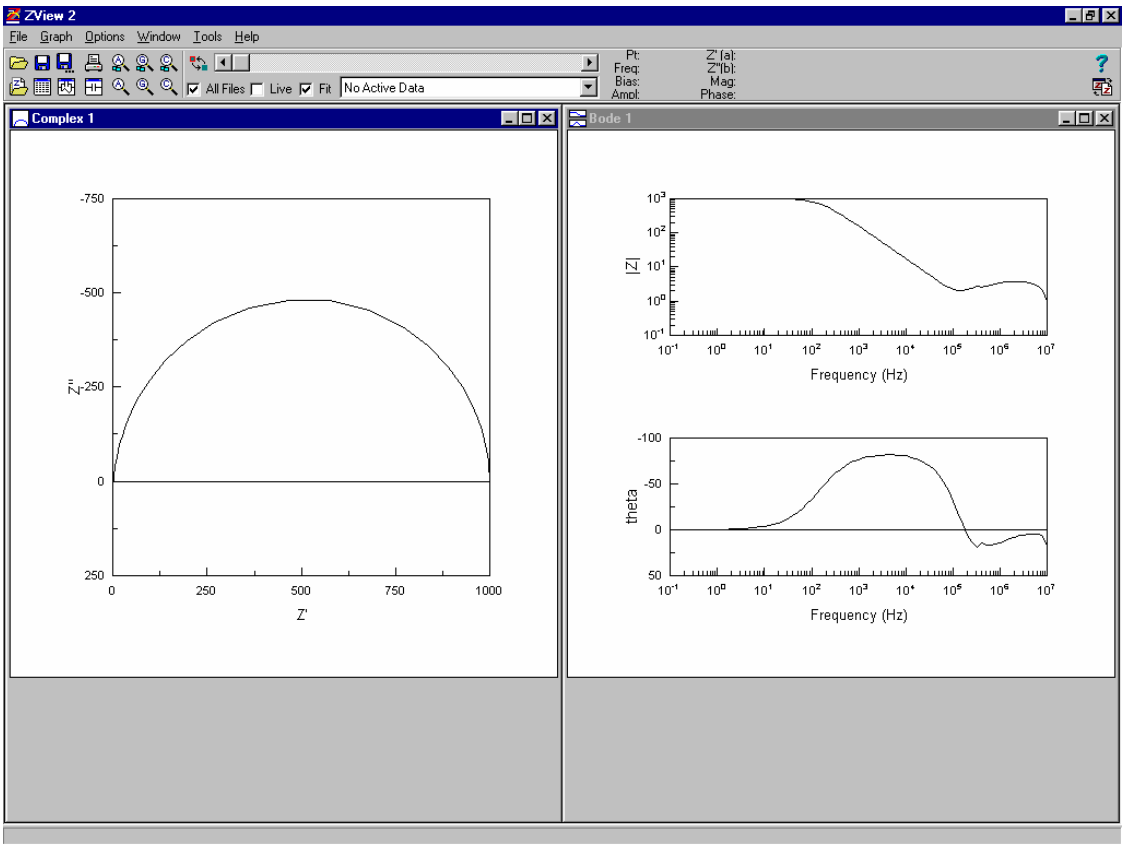

Figure A1- 8. Ecran du logiciel Zview2 dans le cas de la mesure de conductivité d'une résistance pure en parallèle avec une capacité. Cette manipulation sert de vérification de la bonne marche de la mesure.

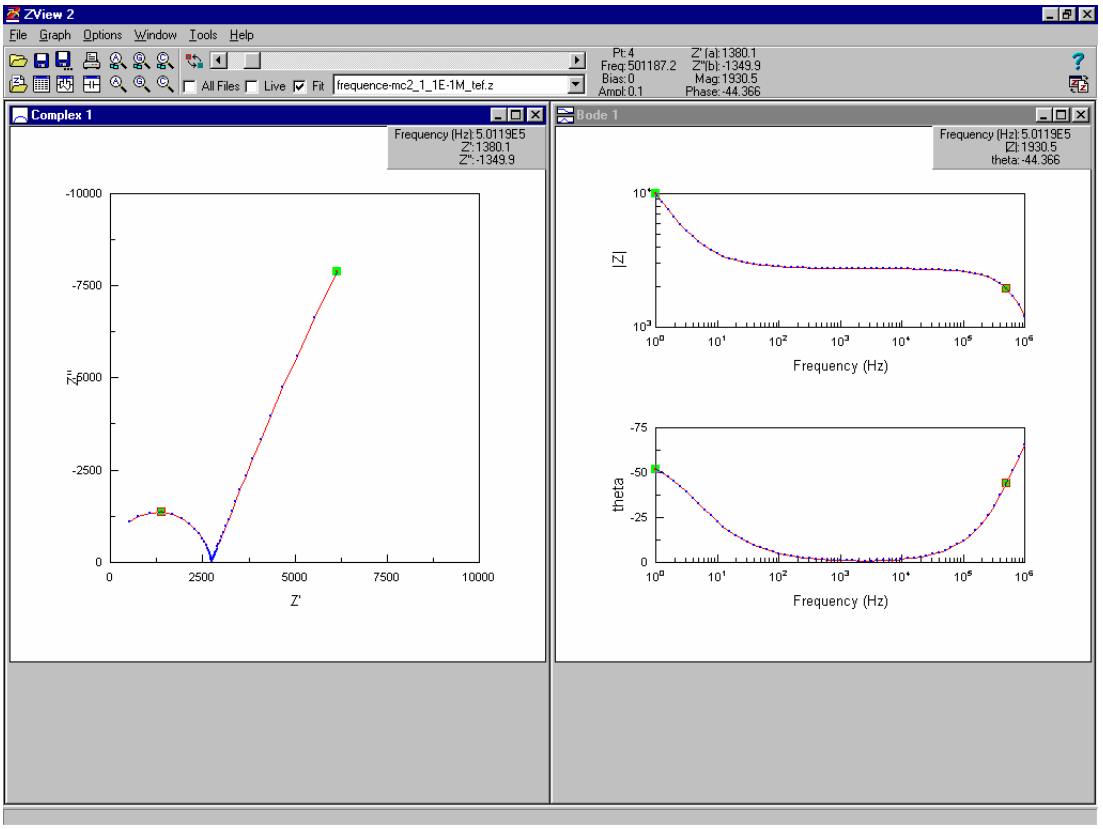

Figure A1- 9. Ecran de Zview 2 pour la mesure de la conductivité de l'échantillon MC2 1,1mm, avec une eau de salinité 1E-1/l, montrant |Z|, et téta en fonction de la fréquence.

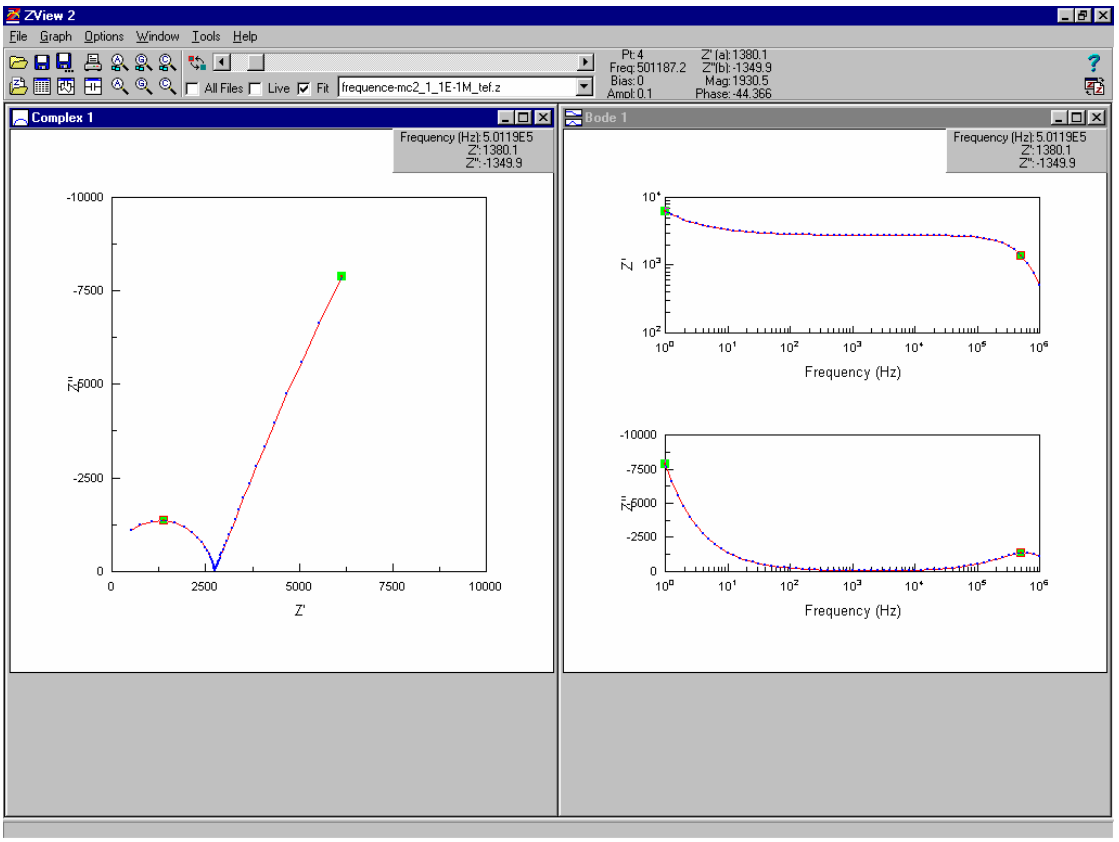

Figure A1- 10. Ecran de Zview 2 pour la mesure de la conductivité de l'échantillon MC2 1,0m, avec une eau de salinité 1E-1M/l. Z' et Z'' en fonction de la fréquence.

8.1 Mesure d'impédance

La loi d'Ohm :

$J = \sigma E = I/S = \sigma * U/L$ (38)

E champ électrique

σ conductivité (S/m)

I intensité (A)

J densité de courant

S surface (m^2)

U différence de potentiel (V)

L longueur (m)

$\sigma = L/S * I/U$ (39)

$\sigma = L/S * 1/Z$ (40)

L'impédance Z=U/I a une partie réelle Z' et imaginaire Z'' : $Z = Z' + iZ''$ (41)

$Z = |Z| e^{i\theta}$ (42)

La Figure A1-7 à gauche représente la partie complexe de Z, lorsque la fréquence varie de 1 Hz à 106 Hz, pour la mesure d'une résistance pure en parallèle avec une capacité, tandis que la Figure A1-9 à gauche représente le même résultat pour la mesure d'un échantillon poreux saturé d'eau de salinité connue.

Le module |Z| et l'argument θ de Z peuvent être représentés en fonction de la fréquence comme sur les Figures A1-7 et A1-8 à droite, respectivement pour une résistance pure et un échantillon poreux saturé d'eau de salinité connue.

On peut aussi représenter à droite Z' et Z'' en fonction de la fréquence, comme sur la Figure A1-10

Sur la Fig. A1-8, à gauche, on voit le demi cercle représentant la fonction d'impédance complexe Z = R – i/C?, avec ?= 2pf, f étant la fréquence en Hertz. L'origine correspond à f= ∞, tandis que l'autre point de rencontre du demi-cercle avec l'axe des Z' correspond à f= 0. Le diamètre du cercle est égal à R. Au point haut du demi cercle, on est en quadrature de phase (?= 45°), et à son maximum, tout comme –Z'' ; |Z| et Z' ont un point d'inflexion (Fig. 8 à droite). La partie droite de la Fig. A1-8 est déformée en raison des phénomènes diélectriques.
Sur les Fig. A1-9 et A1-10, on voit un peu les mêmes phénomènes, une carotte pouvant être assimilée électriquement à une résistance en série avec une capacité. Cependant, les phénomènes de polarisation sont plus importants en basse fréquence (ligne droite montant vers le Nord-Est sur le diagramme Z', Z'', déformations aux fréquences < 1000Hz (100Hz sur la Fig. A1-10) sur les diagrammes |Z|, ?, Z' et Z''.

8.2 Conductivité

A partir des mesures du paragraphe 8.1, on déduit la conductivité σ_o= L/S*1/|Z| (Formule 43) d'une roche saturée en eau de conductivité σw.
|Z| est mesuré à 1000Hz. On choisit une fréquence de 1000Hz, pour laquelle l'argument de Z est généralement le plus proche de zéro, tandis que le module de Z est stationnaire (Figure A1-10), tandis qu'en-dessous, l'argument de l'impédance croît en raison de phénomènes de polarisation, et qu'au-dessus, un déphasage se crée dû à un phénomène diélectrique. Les outils diagraphiques de mesures de résistivité opèrent généralement autour de cette fréquence, probablement pour les mêmes raisons.
On mesure directement la conductivité de fluide σ_w avec le conductivimètre Mlab cond level 2 et une jauge (laisser tremper les échantillons une semaine (ou deux pour les faibles porosités) dans chaque fluide salé).
σ_o en fonction de σ_w est représenté sur la Figure A1-11.

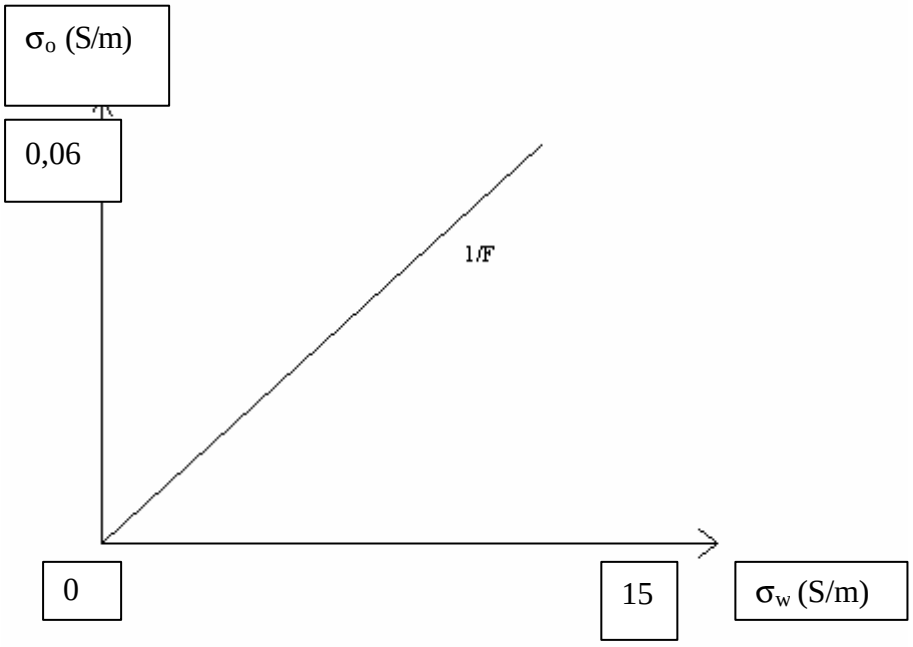

Figure A1- 11. Conductivité de la roche saturée en fonction de la conductivité du fluide la saturant.

Waxman, 1968 a énoncé la formule :

$$\sigma_o = \sigma_w/F + \sigma_s \qquad (44)$$

où le terme σ_w/F est un terme volumétrique de fluide , tandis que le terme σ_s est un terme de conductivité de surface.
L'équation (44) est une formule linéaire de σ_o en fonction de σ_s. Le terme σ_s représente l'ordonnée du point où la droite coupe l'axe vertical. Cette valeur est généralement très faible, de l'ordre du millième ou du dix millième de Siemens par mètre. Il est donc difficile de mesurer graphiquement cette valeur si l'on reste en coordonnées linéaires.
On observe deux domaines :

8.2.1 Haute salinité

Si l'on se borne aux quatre points de salinité la plus forte, on obtient la Figure 10, qui permet d'évaluer la pente 1/F de l'expression (44). Comme σ_s a une valeur très faible, il est difficile de l'observer sur la Figure A1-11. Dans ce domaine, l'équation (44) se réduit à :

$$\sigma_o = \sigma_w/F \quad (45)$$

F est le Facteur de Formation (Archie, 1942)
F>1 (tortuosité $T = F*\Phi$)

8.2.1.1 Précision de la mesure de F

$$\Delta F/F = \Delta\sigma_w/\sigma_w + \Delta\sigma_o/\sigma_o \quad (46)$$

On a vu que σ_w est mesuré directement avec un conductivimètre à fluide.
$\Delta\sigma_w/\sigma_w \leq 0{,}001$, avec
$0{,}005 < \sigma_w < 12{,}5$S/m
Suivant la formule (39), on a :

$$\Delta\sigma_o/\sigma_o = \Delta L/L + \Delta S/S + \Delta I/I + \Delta U/U \quad (47)$$

$\Delta L/L = 0{,}005/2 = 0{,}0025$
$\Delta S/S = 2\Delta D/D = 2*0{,}005/2{,}5 = 0{,}004$
$\Delta U/U = \Delta I/I \# 0{,}001$
$\Delta F/F \leq 0{,}001 + 0{,}0025 + 0{,}004 + 0{,}001 + 0{,}001$
$\Delta F/F \leq 0{,}0095$ ou environ 1%
avec $4{,}7 < F < 1111$

8.2.1 Basse salinité (cas des argiles)

Dans le cas des argiles, σ_s a une valeur plus importante. On utilise alors des coordonnées logarithmiques, et on obtient la Figure A1-12, qui permet de définir σ_s.
Waxman, 1968, et Clavier, 1977 ont défini σ_s de la façon suivante :

$$\sigma_s = \mu*Qv/F \quad (48)$$

Avec :

$$Qv = CEC*\rho_m*(1-\Phi)/\Phi \quad (49)$$

μ : mobilité des cations dans la partie externe de la double couche
Qv : Concentration des argiles en ions d'équilibre par unité de volume des pores (meq/cm3)
CEC : Capacité d'échange des cations (meq/g)
ρm : masse volumique de grain (g/cm3)
F : Facteur de formation
Φ : porosité

8.2.2.1 Précision de la mesure de σs

Pour la précision de la mesure, la formule (48) s'applique à σ_s, de sorte que l'on a :
$\Delta\sigma_s/\sigma_s \leq 0{,}0025 + 0{,}004 + 0{,}001 + 0{,}001$
$\Delta\sigma_s/\sigma_s \leq 0{,}0085$ ou 0,85%
Avec $1{,}00E^{-12} < \sigma_s < 0{,}001$S/m
Johnson, 1986, Revil, 1998, Wildenschild, 2000 ont donné des expressions plus précises de σ_s.

8.2.2 Cas des carbonates

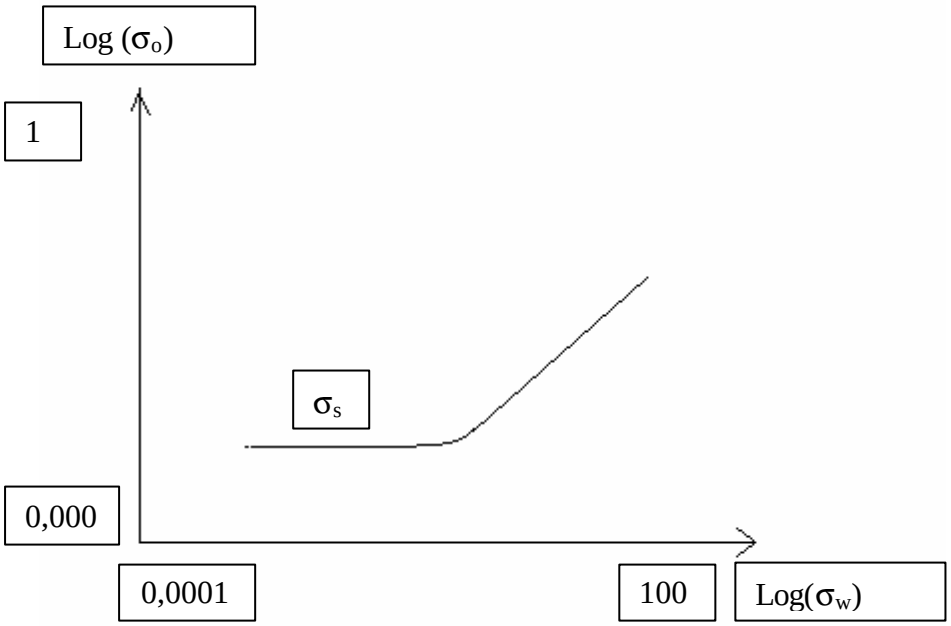

Figure A1- 12. Conductivité s_o d'une roche saturée en eau de conductivité s_w à 1000 Hz, coordonnées logarithmiques, faisant apparaître la conductivité de surface ss.

Dans les carbonates, $F = \Phi^{-m}$ (50)

Avec m # 2

$\sigma_o = \sigma_w / \Phi^{-m} + \sigma_s$ (51)

$\sigma_w = h(\sigma_s, \Phi, \sigma_o)$ (52)

8.2.3 Facteur de formation

8.2.4.1 Facteur de formation global

La Figure A1-13 permet de trouver le coefficient m de la loi d'Archie pour une certaine formation. On mesure $F= \sigma_o/\sigma_w$ pour les hautes salinités.

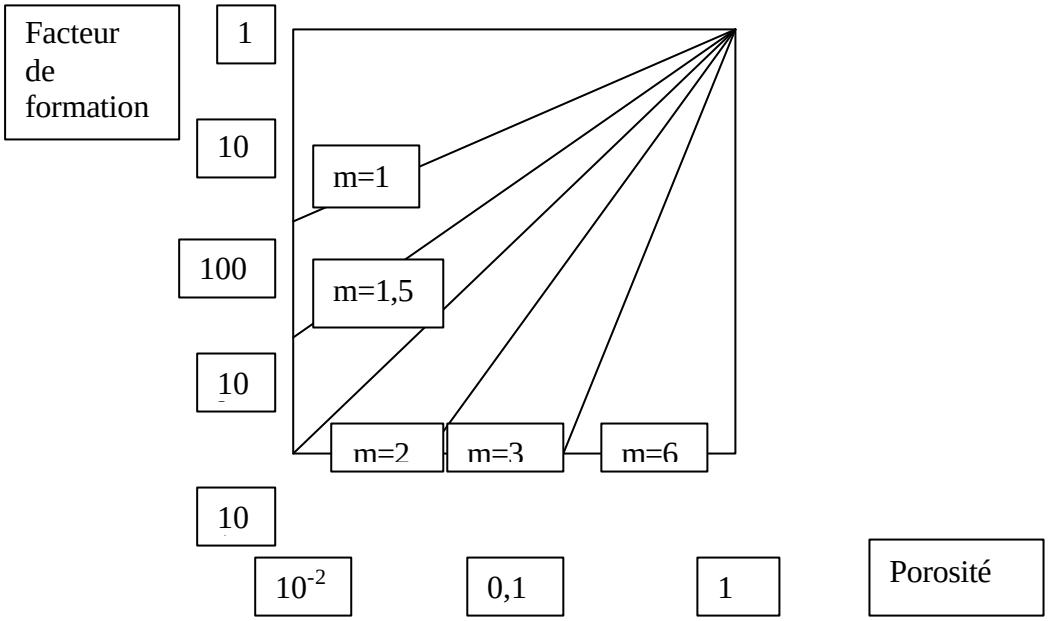

Figure A1- 13. Courbe F = s_w/s_o en fonction de la porosité en coordonnées logarithmiques.

8.2.4.2 Facteur de formation ponctuel

Archie : $\sigma_o = \sigma_w/\Phi^{-m}$ (53)

Soit: $m = -\text{LogF}/\text{Log}\Phi$ (54)

8.2.4.2.1 Précision de la mesure

En partant de la formule (54), on obtient :

$\Delta m/m = \Delta(\text{LogF})/\text{LogF} + \Delta(\text{Log}\Phi)/|\text{Log}\Phi|$

$\Delta m/m = \Delta F/F\text{LogF} + \Delta\Phi/\Phi|\text{Log}\Phi|$

$\Delta m/m = (1/\text{LogF})^* \Delta F/F + |1/\text{Log}\Phi|^* \Delta\Phi/\Phi$ (55)

En reprenant les formules (5) et (46), on obtient :

$\Delta m/m \leq (1/\text{LogF})^*0{,}0095 + |1/\text{Log}\Phi|^*0{,}0065$

Avec $1{,}63 < m < 3{,}05$

$4{,}7 < F < 1111$ $0{,}67 < \text{LogF} < 3{,}05$ $0{,}33 < 1/\text{LogF} < 1{,}49$

$0{,}02 < \Phi < 0{,}50$ $0{,}30 < \text{Log}\Phi < 1{,}70$ $0{,}59 < |1/\text{Log}\Phi| < 3{,}33$

$\Delta m/m \leq 0{,}014 + 0{,}022$

$\Delta m/m \leq 0{,}036$ soit 3,6%

9 Mesures acoustiques

9.1 Mesure des vitesses acoustiques, échantillons secs

Les échantillons sont remis dans l'étuve pendant une semaine (§ 2 Séchage). La Figure A1-14 schématise l'appareillage de mesure.

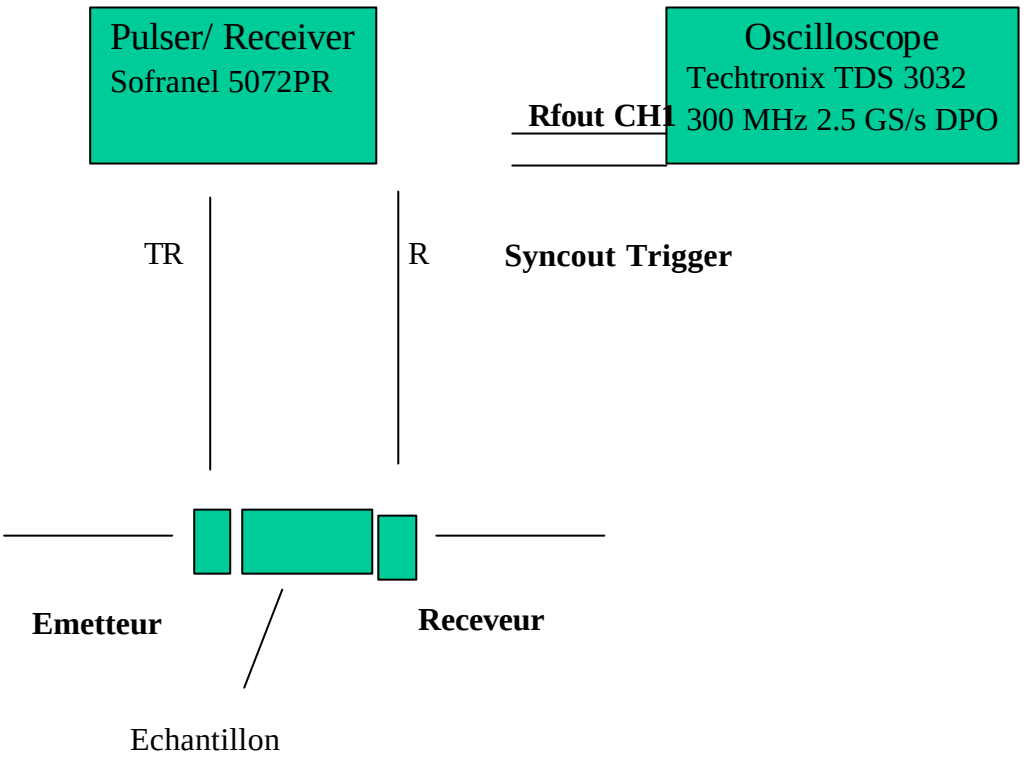

Figure A1-14. Appareillage de mesure des vitesses acoustiques.

On mesure le temps de parcours de l'onde acoustique envoyée par l'émetteur à travers l'échantillon.
Le pulser/ receiver est réglé à : PFR= 1KHz, Energy= 1, Damping= 3 (50?), gain= 1db (5), Mode= 2, HPF out (1MHz), LPF Full BW (10MHz).
Le temps est mesuré sur l'écran d'oscilloscope, qui visualise l'onde envoyée par l'émetteur ainsi que le train d'onde reçu sur le récepteur. L'oscilloscope est réglé (Menu rapide) à: Couplage CC impédance 1M? , Bande pas. Pleine, Déclan rap Normal. Mode Moy. 5.2, Curseur dés Bar H (Bar V).

Appuyer sur le bouton Delay (voyant éteint); régler T= 0 (sur l'écran) avec potentiomètre position H.
Réappuyer sur le bouton Delay (voyant allumé) ; régler avec potentiomètre position H de façon à lire le début de l'arrivée du signal sur le croisillon. Lecture su T.
Le contact acoustique entre émetteur, échantillon et receveur est réalisé par application d'un gel (UCA Ely Chemical pour onde p, et miel pour onde S) et pression de la pince. Ceci est la raison pour laquelle les mesures acoustiques sont faites en dernier (afin d'éviter la perturbation des autres mesures, notamment des mesures de pesée et de perméabilité) ; d'autre

part, pour les échantillons fragiles et saturés, il y a un risque de destruction des échantillons en appliquant dessus une pression excessive.
Emetteurs et récepteurs Valpey Fisher 500kHz. Il y a un jeu émetteur-récepteur pour les ondes compressionnelles (CSO) et un autre pour les ondes transversales (SSO) ; l'émetteur d'onde transversale émet une vrai onde transversale, contrairement à l'outil de terrain qui baigne dans l'eau (les ondes transversales ne se propagent pas dans l'eau). La longueur d'onde doit être de l'ordre de la taille de l'échantillon . $\lambda = v/f$, soir $\lambda = (6000m/s)./ 500000Hz = 1,2$ cm, on a donc λ de l'ordre de 2 fois la longueur de l'échantillon (2cm).

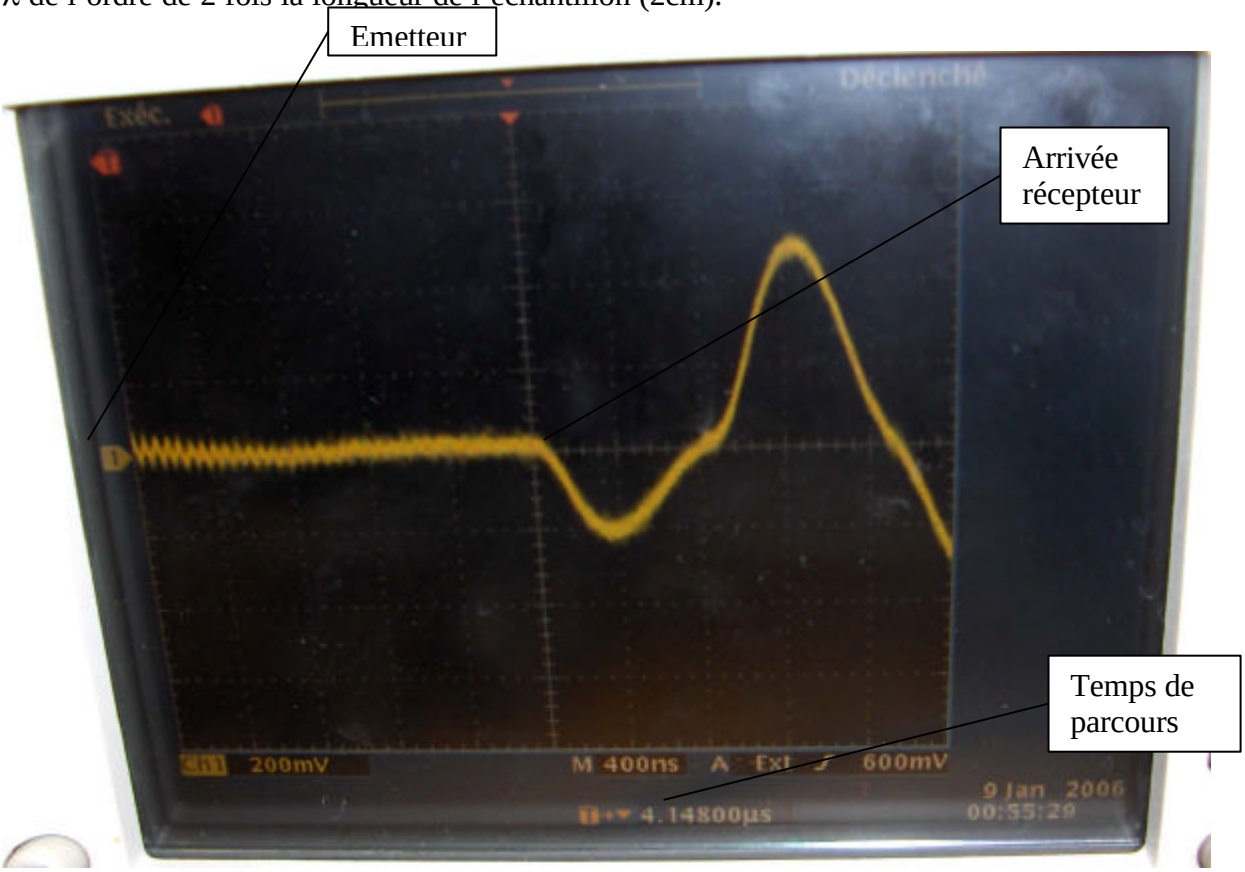

Figure A1- 15. Ecran de l'oscilloscope Tektronix. Lecture méthode T_o Delay, V_p avec CSO.

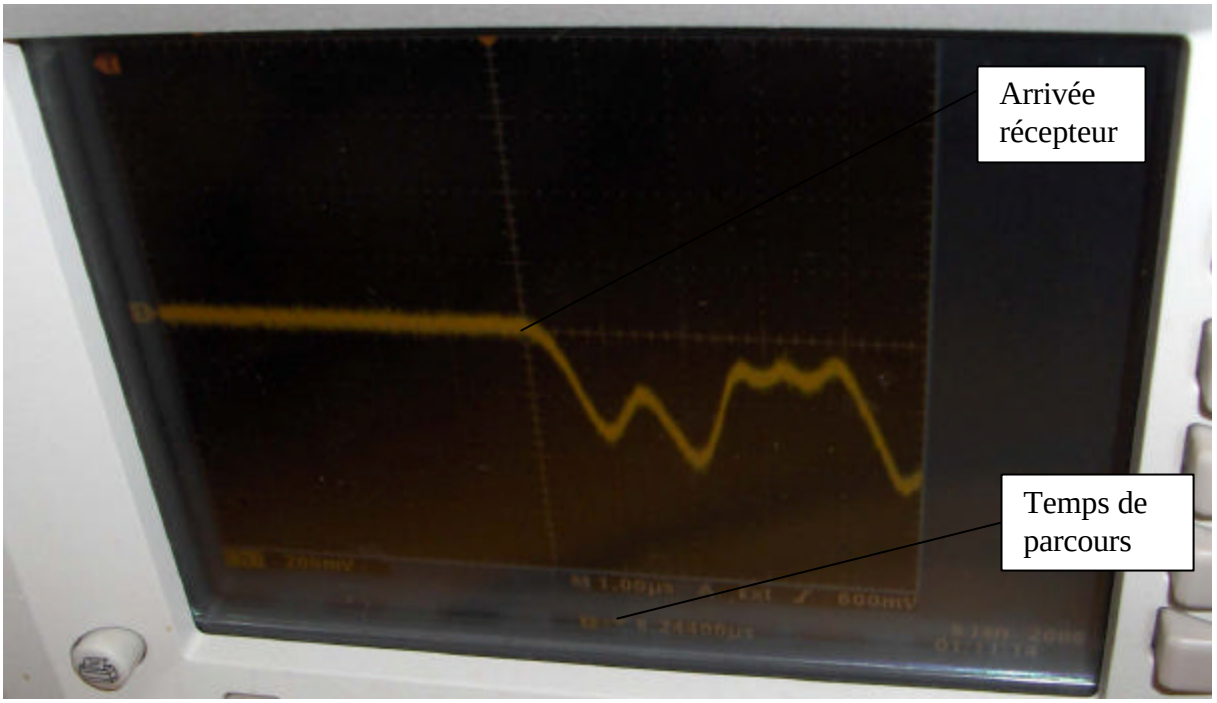

Figure A1- 16. Ecran de l'oscilloscope Tektronix. Lecture méthode T_o Delay, V_p avec SSO.

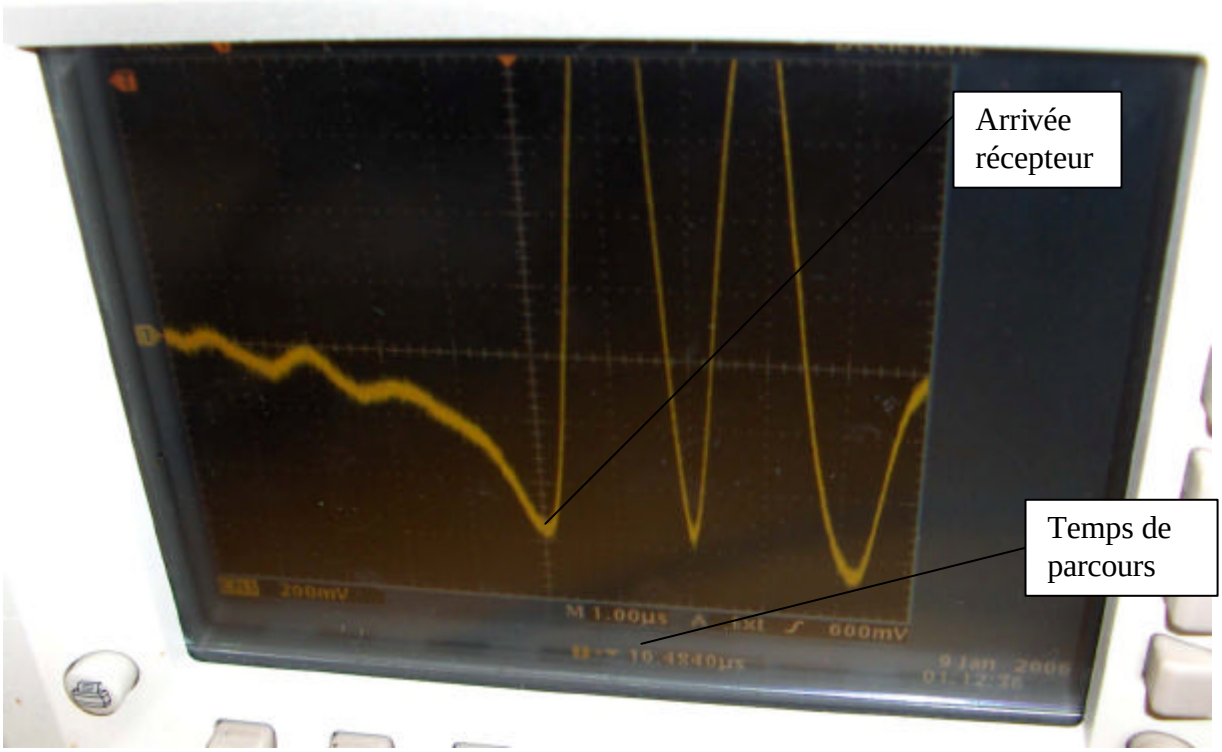

Figure A1- 17. Ecran de l'oscilloscope Tektronix. Lecture méthode To Delay, V_s avec SSO. Les capteurs SSO sont optimisés pour la création et la réception d'une onde S. Dès que le départ de l'onde S est noté, on considère que cela correspond à la première arrivée S.

Connaissant la longueur de l'échantillon (mesurée au § 3), on peut donc ainsi mesurer :

- V_p, vitesse de l'onde longitudinale
- V_s, vitesse de l'onde transversale.

L'onde de cisaillement est plus lente que l'onde compressionnelle. Elle ne se transmet pas dans les liquides. L'amplitude des ondes de cisaillement est plus grande que celle de l'onde de compression.
L'onde de Stoneley est une onde de surface circulant à l'interface liquide-solide. La vitesse de l'onde de Stoneley est inférieure à celle de l'onde de cisaillement, elles ont généralement une grande amplitude.
Une vérification des mesures se fait en mesurant V_p et V_s sur trois blocs d'aluminium de dimensions 25, 50 et 75mm (V_p et V_s pour l'aluminium sont connus). On peut aussi faire une vérification avec l'émetteur jointif au récepteur (pas d'échantillon).
V_p = 1000*L/(t –temps_retard)

10 Mesure des vitesses acoustiques, échantillons saturés

On reprend le même appareillage que pour la Figure A1-1. On mesure cette fois des vitesses dans les échantillon saturés d'eau équilibrée en calcite. Ces mesures sont effectuée en dernier, car elles peuvent être destructives (en raison de la pression exercée sur l'échantillon pour effectuer le contact acoustique). Pour les échantillons non consolidés, on commence les mesures d'abord avec les échantillons les moins poreux, et on choisit des échantillons de plus en plus poreux, tant que les échantillons ne sont pas détruits au cours de la mesure.
On compare les vitesses obtenues sur échantillons secs avec les vitesses obtenues sur échantillons saturés : On a $V_{psec} < V_{psat}$, et $V_{ssec} > V_{ssat}$, et $V_p/V_{ssat} > V_p/V_{ssec}$.
La formule (47) (Wyllie, 1956) relie la porosité mesurée par la diagraphie «sonic » Φ_S au temps de propagation de l'onde compressionnelle dans la formation (Δt_{sat}), dans le fluide (Δt_f) et dans la matrice (Δt_{mat}), similaire à la formule (10), qui relie Φ_D et la densité :

$$\Phi_S = (\Delta t_{sat} - \Delta t_{ma}) / (\Delta t_f - \Delta t_{ma}) \quad (56)$$

La formule (56) est appelée « équation de la moyenne des temps » (time average equation). Cette formule linéaire est à peu près satisfaisante dans les valeurs de porosité habituellement rencontrées dans les formations (entre 10 et 25 unités de porosité) et pour les porosités correspondant à des grains à peu près sphériques. La difficulté est dans le choix des paramètres de fluide et de matrice (Tableau A1-2). On a d'autre part

$$\Delta t_{sat}\ (\mu s/ft) = (1 / V_{psat}\ (m/s)) * (106 / 3{,}28) \quad (57)$$

Minéral (composition chimique)	Δt_c (µs/ft)	Δt_s (µs/ft)	V_p/V_s	V_p (Km/s) (Homand, 2000, d'après Belikov, 1967)	Vitesse V_s (Km/s) (Guéguen, 1992)	ν (Homand, 2000, d'après Belikov, 1967)	E (Gpa) (Homand, 2000, d'après Belikov, 1967)
Quartz (SiO_2)	56			6,050	4,11	0,08	96,4
Calcite ($CaCO_3$)	49	88,4	1,8	6,320	3,45	0,28	84
Aragonite ($Ca\,CO_3$)	47						
Dolomie ($CaCO_3MgCO_3$)	44.1	72	1,63	7,9	3,99		
Ankérite ($Ca(Mg,Fe),(CO_3)_2$)	44 ?	84,9	1,93				
Kaolinite ($Al_4Si_4O_{10}(OH)_8$)							
Montmorillonite ($(Ca,Na)_7(Al,Mg,Fe)_4(Si,Al)_6O_{20}(H_2O)_9$)							
Illite ($K1\text{-}1{,}5A_{14}(Si_{7\text{-}6{,}5},Al_{1\text{-}1{,}5})O_{20}(OH)_4$)							
Chlorite ($(Mg, Fe, Al)_6(Si,Al)_4O_{10}(OH)_8$							
Feldspath Alcali	69				3,06		
Rhodolite (silicate de magnésium et aluminium)							
Certains évaporites légers (halite, NaCl)	67						
Charbon (C, lignite)	160						
Eau douce	189	∞					
Eau salée	165-180	∞					
Halite				4,320	2,66		36
Gypse				5,200			
Muscovite				5,880		0,25	80
Biotite				5,360		0,30	67
Orthose				5,680		0,29	63
Plagioclase				6,220		0,29	77
Anhydrite					3,11		

Tableau A1- 2. D**tma et** D**tf observés dans différents minéraux, porosité nulle (Serra, 2000).**

Raymer, 1980 propose une autre relation reliant le temps de parcours à la porosité, qui convient en général mieux.

Calcaire à 15% porosité ; Δt= 210 µs/m ; v_t= 4760m/s

Roche	Vitesse V_p (Km/s) (Guéguen, 1992)	Vitesse V_p (Km/s) (Bourbié, 1986)	Vitesse V_p (Km/s) (Mavko, 1998)	Vitesse V_s (Km/s) (Bourbié, 1986)
Calcaire	4-7	3,5-6,0	3,5-6,4	2,2-3,3
Grès	2-5,5	2-3,5	1,5-6,0	0,8-1,8
Dolomites	5-7,5	3,5-6,5	4,5-7,1	1,9-3,6
Anhydrites	5-6,5	4,0-5,5	4,6-7,4	2,2-3,1
Shales	1,8-4,0		1,5-5,0	
Argiles	1,8-2,4	1,1-2,5		0,2-0,8
Sel	4,5	4,5-5,5		2,5-3,1

Tableau A1- 3. Données V_p et V_s pour les roches sédimentaires saturées usuelles.

Roche	V_p/V_s	ν
Calcaires	1,83-2	0,31
Calcite	1,93	0,29-3,3
Dolomite	1,85	0,29
Grès	1,59-1,75	0,16-0,25
Quartz	1,46	0,08
Sel	1,73	
Anhydrite	1,81	
Siderite	1,94	
Pyrite	1,55	

Tableau A1- 4. Données n **et V_p/V_s pour les roches sédimentaires usuelles (Guéguen, 1992).**

$$n = \frac{0{,}5\left(\frac{V_p}{V_s}\right)^2 - 1}{\left(\frac{V_p}{V_s}\right)^2 - 1} \qquad 0 < \nu < 0{,}5$$

Références

9 Archie G.E., 1942. The electrical resistivity log as aid in determining some reservoir characteristics, Trans. Americ. Inst. Mineral. Met.

10 Blackburn R. et al., 1985. Earthscope , Salamander books.

11 Bourbié T., Coussy O., Zinszner B., 1986. Acoustique des milieux poreux, Ed. Technip, IFP.

12 Clavier C., Coates G., Dumanoir J., 1977. The theoretical and experimental bases for "Dual water" model for the interpretation of shaly sands. SPE 52nd annual fall Tech. Conf. and Exhibition Denver.

13 Glover P.W.J., Meredith G.P., Sammonds P.R., Murrell S.A.F., 1994. Ionic surface conductivity in sandstone, Journal of Geophysical Research, Vol. 99, No B11, Pages 21,635-21,650, November 10.

14 Guéguen Yves, Palciauskas V., 1992: Introduction à la physique des roches, Hermann.

15 Hall Ray, Rawson P.F., 1988. The Illustrated Encyclopaedia of the Earth's resources, Marshal Cavendish.

16 Homand F., Duffaud P., 2000. Manuel de mécanique des roches, Tome 1, Fondements, Ecole des Mines de Paris.

17 Ishido, T. , Mizutani, H., 1981. Experimental and theoretical basis of electro-kinetic phenomena in rock- water systems and its application to geophysics, J. Geophys. Res., 86, 1763-1775.

18 Johnson D.L., Koplik J., Swart M. L., 1986. New pore-size parameter characterising transport in porous media, The American Physical Society.

19 Katz A. J., Thompson A. H., 1985. Fractal sandstone pores : implications for conductivity and pore formation, The American Physical Society.

20 Mavko G., Mukerji T., Dvorkin J., 1998. The rock physics handbook, Tools for seismic analysis in porous media, Cambridge University Press.

21 Morel, F.M.M., 1983. Principles of Aquatic Chemistry, Willy ans sons, N.Y.

22 Pinettes, P., Bernard P., Cornet F., Hovhannissian G., Jouniaux L., Pozzi J.-P., Barthès V., 20001. On the difficulty of detecting streaming potentials generated at depth, Pure and Applied Geophysics.

23 Ramamoorthy R., 2000., Paper J, SPWLA Annual Symposium.

24 Raymer L.L., Hunt E.R., Gardner J.S., 1980. An improved sonic transit time to porosity transform, Transactions of the SPWLA 21st Annual Logging Symposium.

25 Revil A., Cathles III L.M., Losh S., Nunn J.A., 1998. : Electrical conductivity in shaly sands with geophysical applications, Journal of geophysical research, Vol. 103, No B10, pages 23925-23936, October 10.

26 Revil A., Pezard P.A., Glover, P.W.J., 1999. Streaming potential in porous media, Theory of the Zeta Potential. J. Geophys. 104; 20, 021-20,031.

27 Waxman M. H., Smits L.J.M., 1968. Electrical conductivities in oil-bearing shaly sands. SPE.

28 Wildenschild D., Roberts J.J., Carlberg D.E., 2000. On the relationship between microstructure and electrical and hydraulic properties of sand-clay mixtures, Geophysical research letters, October.

29 Wyllie M.R.J., Gregory A.R, Gardner L.W., 1956. Elastic wave velocities in heterogeneous and porous media, Geophysics.

30 Zim H., Shaffer P., 1957. Roches et minéraux, Hachette.

A2 Calage en profondeur des diagraphies de Ses Sitjoles

1 Plan de corrélation des logs de Ses Sitjoles

Puits MC1, MC2, MC3, MC4, MC5, MC6, MC7, MC8, MC9, et S17
Coordonnées verticales fournies par ETH sur tous les puits sauf MC7, MC8, MC9, où elles ont été calculées approximativement par rapport aux puits adjacents.

1.1 Pourquoi une corrélation des logs ?

La mesure de profondeur des logs se fait grâce à un odomètre qui mesure le déroulement du câble de logging. Bien entendu, comme toute mesure, la mesure de profondeur faite de cette façon est susceptible d'erreurs. Celles-ci ont deux sources principales :

- La roue d'entraînement de l'odomètre s'use par le frottement du câble, et donc le périmètre de cette roue varie et le rapport de conversion de la mesure avec lui
- Le câble glisse sur la roue d'entraînement de l'odomètre

Dans les systèmes d'enregistrements pétroliers, différents dispositifs de corrections sont appliqués :

- Une vis micrométrique permet d'ajuster le diamètre de la roue d'entraînement de l'odomètre
- Un marquage magnétique du câble de logging tous les cinquante mètres est effectué en atelier sous une tension de câble fixe (1000lbs en général) maintenue par un système de contrepoids (« dead man »
- Ces marques sont détectées pendant l'enregistrement, et si un glissement est observé, une correction de profondeur est effectuée manuellement
- Des logs de corrélation (SP ou mieux GR) sont enregistrés simultanément à chaque log ; chaque log est enregistré de façon à ce que chacun soit en profondeur avec le premier log enregistré, dit log de base. Pour cela une section répétée au fond du puit est enregistrée préalablement au log principal, et sert à se recaler sur le log de base.
- Sur les enregistrements modernes, une cartouche de télémétrie permet d'enregistrer simultanément tous les logs en un seul voyage, et donc tous les logs sont automatiquement en profondeur les uns avec les autres, le décalage en profondeur des capteurs étant entrés comme paramètres dans le logiciel d'enregistrement.

Sur les puits à eau, les outils de faible diamètre utilisés par l'équipe de subsurface et les équipements d'enregistrement associés, n'ont aucune des possibilités décrites ci-dessus. Bien que les puits considérés à Campos ne présentent qu'une profondeur maximum de 100m (comparée à plusieurs milliers de mètres pour les puits pétroliers), des erreurs de corrélations pouvant aller jusqu'à 3m ont été observées. Il est donc nécessaire de recorréler les logs après enregistrement.
De plus, dans les champs pétroliers, il est rarissime d'avoir des puits distants de quelques mètres seulement, comme à Campos.
Une corrélation sur le même puit d'un outil à un autre est relativement facile. Sur le champ de Campos, du fait de la proximité des puits, il est également indispensable de corréler les logs entre des puits différents, de façon à obtenir un ensemble cohérent sur tout le champ.

1.2 Base de profondeur

Principe:

1. Pour chaque puit : log d'imagerie optique, si disponible, sinon, GR
2. De puit à puit : Idronaut, si disponible, sinon, log électrique

1.3 Méthode pratique proposée

Ordre	Tâche
1	Relever les dates d'imagerie optique Relever la côte du plan d'eau suivant imagerie optique En déduire les corrections (+/- x,yz m) à faire pour chaque imagerie optique pour que le plan d'eau soit plan (base MC2)
2	Caler les imageries optiques sur un même plan d'eau (suivant corrections de Tâche 1)
3	Relever les correction à faire sur les images acoustiques pour les mettre au niveau des images optique
4	Caler les images optiques suivant correction relevées en 3
5	Considérer les Idronauts de la même date (à une semaine près) que l'imagerie du même puit. Relever la côte plan d'eau sur Idronaut (visible sur Press_ peut être extrapolé_ EH, PH, COND)
6	Caler les Idronauts sur imagerie optique
7	Caler l'ELXG (SN) sur COND de l'Idronaut
8	Caler les autres logs sur l'ELXG : SGR sur GR de ELXG DIL sur SN de ELXG PNN sur SN et GR de ELXG

Tableau A2- 1. Méthode pratique proposée

1.4 Critique de la méthode pratique

1. **Point fort** : le plan d'eau est clairement visible sur l'imagerie et sur l'Idronaut, ce qui ne serait pas le cas de tout autre événement géologique fixe tel que cave ou changement de porosité. L'Idronaut permet de remonter de log à log aux autres logs sur un même puit par l'intermédiaire de l'ELXG, qui a le gros avantage d'enregistrer un log GR simultanément à un log électrique (et c'est malheureusement le seul des outils de l'équipe subsurface qui enregistre un log de corrélation simultanément à sa mesure principale).
2. **Point faible** : le plan d'eau subit des variation saisonnières d'amplitude verticale environ 50cm. Tous les logs sur tous les puits n'ont pas été enregistrés le même jour, le même mois, ni la même année. Partant de ce constat, il est difficile de déterminer un plan horizontal de limite air-eau à partir des logs de différent puits.

2 Tache 1 : Côte du plan d'eau suivant imagerie optique et idronaut

Les logs d'imagerie ne sont enregistrés qu'en montant.

Puit	Date imagerie optique Année/mois/jour	Côte du plan d'eau sur imagerie optique (mbgl)	Côte du plan d'eau sur Idronaut (non ajusté) (mbgl)	Date Idronaut Année/mois/jour
MC1	-	Pas visible sur optique, qui démarre plus bas	36,1	03/06/09
MC2	03/03/04	38,43	36,9	03/06/09
MC3	03/03/06	38,67	39,6	03/06/06
MC4	03/08/19, 0-36m seulement	-	38,5	03/08/20, ELXG seulement
MC5	03/06/07	38,51	38,7	03/06/07
MC6	-	-	38,5	04/07/11
MC7	03/08/21	38,55	39,0	03/08/27
MC8	04/07/10	38,34	36,5	04/07/10
MC9	04/07/09	36,72	37,0	04/07/08
S17	-	-	40,0	03/06/09

Tableau A2- 2. Côtes du plan d'eau sur imagerie optique et sur Idronaut

Elevation (m)	MC1 (mbgl)	**MC2 (mbgl)**	MC3 (mbgl)	MC4 (mbgl)	MC5 (mbgl)	MC6 (mbgl)	MC7 (mbgl)	MC8 (mbgl)	MC9 (mbgl)	S17 (mbgl)
Elevation de la tête de puit (base= msl) : z	37,77	38,32	41,02	40,37	40,34	40,38	40,38	38,32	38,32	41,25
Profondeur du plan d'eau sur imagerie optique: z-h	36,1	36,43	38,67	38,5	38,51	38,5	38,55	36,34	36,72	40,0
Elevation duplan d'eau: h	1,67	**1,89**	2,35	1,87	1,83	1,88	1,83	1,98	1,6	1,25
Correction à faire sur imagerie optique	-0,22	0	+0,46	-0,02	-0,06	-0,01	-0,06	+0,09	-0,29	-0,64

Tableau A2- 3. Côtes de plan d'eau et correction à faire sur les imageries optique (base = MC2), afin que le plan d'eau soit effectivement plan : élévation du plan d'eau puit x - correction = élévation du plan d'eau MC2= 36,43m.

Les puits MC1, MC4, MC6 et S17 n'ont pas d'imagerie optique ; les côtes de plan d'eau du Tableau A2-2 sont donc prises directement à partir du log de remplacement : ELXG pour MC4 et Idronaut pour MC6. En fait le puit MC1 a une imagerie optique, mais seulement de 53 à 97mbgl.

Après correction, on trouve ainsi une élévation h du plan d'eau par rapport au niveau de la mer de 1,89m pour le puit MC2 (qui n'est pas très loin de la moyenne sur les dix puits : 1,815m), que nous choisissons comme référence de base.

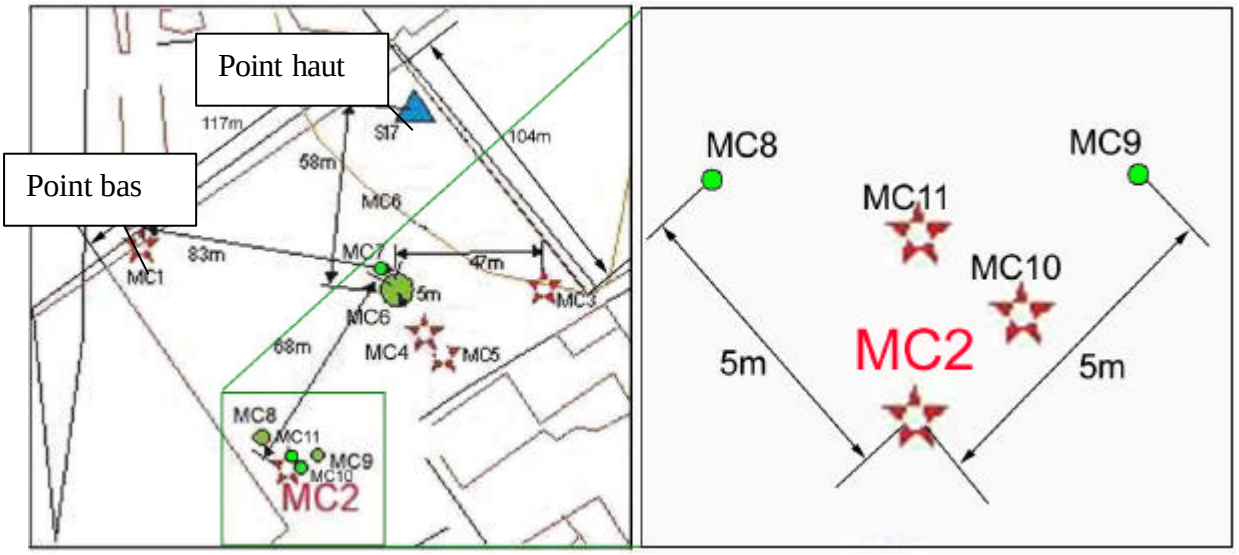

Figure A2- 1. Plan du site de Ses Sitjoles (à gauche), et détail des puits groupés autour de MC2 (à droite).

3 Tache 3 Corrections à faire sur imagerie acoustique

Elevation (m)	MC1 (mbgl)	**MC2 (mbgl)**	MC3 (mbgl)	MC4 (mbgl)	MC5 (mbgl)	MC6 (mbgl)	MC7 (mbgl)	MC8 (mbgl)	MC9 (mbgl)	S17 (mbgl)
Profondeur du plan d'eau sur imagerie optique avant correction	36,1	36,43	38,67	38,5	38,51	38,5	38,55	36,34	36,72	40,0
Correction à faire sur imagerie optique	-0,11	0	+0,46	-0,02	-0,06	-0,01	-0,06	+0,09	-0,29	-0,64
Profondeur o du plan d'eau sur imagerie optique après correction : o	(35,88)	36,43	39,13	(38,48)	38,45	(38,49)	38,49	36,43	36,43	39,36
Profondeur a du plan d'eau sur imagerie acoustique avant correction : a	(36,1) (en fait, le plan d'eau n'est pas visible, mais optique et acoustique sont à la même profondeur)	36,69	39,62	Pas d'acoustique	38,6	Pas d'acoustique	36,75	36,34	36,48	Pas d'acoustique
Correction à faire sur imagerie acoustique : o - a	-0,22	-0,26	-0,49	-	-0,15	-	+1,74	+0,09	-0,05	-

Tableau A2- 4. Corrections à faire sur imagerie acoustique par rapport à l'imagerie optique

4 Tache 6 : Calage des Idronauts sur imagerie optique

4.1 Calage des Idronauts de base

Puit	Côte du plan d'eau sur imagerie optique (non ajusté) (mbgl)	Côte du plan d'eau sur Idronaut (non ajusté) (mbgl)	Différence imagerie – Idronaut (m)	Côte du plan d'eau sur imagerie optique ajusté (Tableau A2-3) (mbgl)	Correction pour Idronaut (m)= correction Tableau A2-3 + différence Tableau A2-5
MC1	-	36,1	-	-	-0,22
MC2	36,43	36,9	-0,47	36,43	-0,47
MC3	38,67	39,6	-0,93	39,13	-0,47
MC4	-	38,5, ELXG	-	-	-0,02
MC5	38,51	38,7	-0,19	38,45	-0,25
MC6	-	38,5	-	-	-0,01
MC7	38,55	39,0	-0,45	38,49	-0,51
MC8	36,34	36,5	-0,16	36,43	-0,07
MC9	36,72	37,0	-0,28	36,43	-0,57
S17	-	40,0	-	-	-0,64

Tableau A2- 5. Corrections à faire sur Idronauts de base.

Les Idronauts sont toujours enregistrés en descendant (pour éviter de perturber les mesures de fluide dans le trou en montant).

4.2 Calage des Idronauts répétés

4.2.1 En utilisant les ELXG

Voir paragraphe 5.2, pour les explications sur la méthode.

Puit	Côte du plan d'eau sur ELXG répété ajusté (mbgl) Tableau 8	Date ELXG répété	Côte du plan d'eau sur Idronaut répété (non ajusté) (mbgl)	Date Idronaut AAMMJJ	Correction pour Idronaut (m)= Différence ELXG - Idronaut
MC2	35,15	031028	36,7	031028	-1,55
S17	37,7	020609	39,92	020609	-2,22

Tableau A2- 6. Corrections à faire sur Idronauts répétés.

4.2.2 En utilisant les Idronauts déjà calés et le plan d'eau

Les Idronauts non calés sont corrigés en profondeur de façon à ce que, par rapport aux Idronauts calés et enregistrés sensiblement à la même date sur les autres puits, ils fassent apparaître le plan d'eau comme étant effectivement plan.

Puit	Date Idronaut AAMMJJ	Profondeur plan d'eau (mbgl) Ironaut non corrigé	Elévation tête de puit (masl)	Elévation plan d'eau (m) 03/06/09	Elévation plan d'eau (m) 03/08/20	Elévation plan d'eau (m) 04/07/06	Elévation plan d'eau (m) 02/06/09 et 03/10/28	Correction à appliquer (m)
MC1	**030609**	**35,88**	**37,77**	**1,89**				**0**
	040707	36,110				1,67		-0,22
MC2	**030609**	**36,43**	**38,32**	**1,89**				**0**
	031028	**35,15**					**1,17**	**0**
	040706	36,70				1,62		-0,27
MC3	**030606**	**39,13**	**41,02**	**1,89**				**0**
MC5	**030607**	**38,45**	**40,34**	**1,89**				**0**
	030820	38,50			1,84			-0,05
MC6	**040711**	**38,49**	**40,38**			**1,89**		**0**
MC7	**030827**	**38,49**	**40,38**		**1,89**			**0**
MC8	**040710**	**36,43**	**38,32**			**1,89**		**0**
MC9	**040708**	**36,43**	**38,32**			**1,89**		**0**
S17	020513	39,80	**41,25**				1,45	-2,10
	020516	39,90					1,35	-2,20
	020609	**37,70**					**3,55**	**0**
	030609	**39,36**		**1,89**				**0**
	030821	39,60			1,65			-0,24
	030821	39,70			1,55			-0,34
	040705	40,00				1,25		-0,64

Tableau A2- 7. Les Idronauts déjà calés sont indiqués en caractères gras. Les Idronauts enregistrés sensiblement à la même date sont indiqués avec une trame de la même couleur.

5 Tache 8 : Calage ELXG (SN) sur COND de l'Idronaut

5.1 Calage des ELXG de base

Puit	Côte du plan d'eau sur imagerie optique ajustée (et sur Idronaut ajusté) (mbgl)	Date Idronaut (Année/ Mois/ jour)	Côte du plan d'eau sur ELXG_ UP (mbgl)	Date de l'ELXG (Année/ Mois/ jour)	Correction à faire sur ELXG_UP (m) (idronaut-ELXG)	Remarques
MC1	(35,88)	030609	35,40	030609	+0,48	Pas d'imagerie optique à hauteur du plan d'eau
MC2	36,43	030609	39,40	030609	-2,97	
MC3	39,13	030606	38,77	030607	+0,36	
MC4	(38,48)	-	38,10	030820	+0,38	Pas d'imagerie ni d'Idronaut
MC5	38,45	030607	38,00	030608	+0,45	
MC6	(38,49)	040711	-	-	-	Pas d'imagerie ni d'ELXG
MC7	38,49	030827	35,47	031027	+3,02	
MC8	36,43	040710	33,50	031026	+2,93	
MC9	36,43	040708	-	-	-	Pas d'ELXG
S17	(39,36)	030609	40,63	030609	-1,27	Pas d'imagerie

Tableau A2- 8. Corrections à faire sur ELXG_UP de base. Les lectures ELXG pour une résistivité < 20 Ohm.m ne sont pas correctes.

Seuls les logs ELXG_UP sont corrélés.
Le sommet du plan d'eau est détecté sur ELXG_UP au saut de résistivité des courbes SPR (de 200 vers 60000 Ohm) et SN (de 1000 vers 60000Ohm.mètre). La Long Normal est ignorée pour cette tâche, car on sait qu'elle souffre d'un décalage en profondeur non constant (voir Serra, 2000).
Le puit MC4 présente un cas spécial : sur ce puit, il n'y a ni log d'imagerie ni Idronaut. Dans les tableaux A2-3 et Q2-4, la profondeur de (38,96)mbgl du plan d'eau avait été déterminée sur l'ELXG_DW (par erreur). Il faut donc prendre 38,10mbgl comme profondeur du plan d'eau sur ce puit, et non 38,96mbgl.

5.2 Calage des Idronauts répétés

Nous allons maintenant caler sur les ELXG de base (c'est-à-dire ceux qui ont été enregistrés, dans la mesure du possible quasiment à la même date, que les logs d'imagerie optique), en calant sur le canal GR (le seul qui soit insensible aux variations de niveaux de fluides) de l'ELXG de base. Ceci nous permet de repérer la profondeur du plan d'eau à cette date, et de caler en profondeur (en utilisant le canal Pression) les Idronauts qui ont été enregistrés quasiment le même jour sur le même puit (voir ci-dessus, paragraphe 4.2).

Puit	Côte du plan d'eau sur imagerie optique ajusté (et sur ELXG de base ajusté) (mbgl)	Date log de base (imagerie optique ou à défaut (Idronaut, ou ELXG))	Côte du plan d'eau sur ELXG_UP répété ajusté (mbgl)	Date de l'ELXG répété (Année/ Mois/ jour)	Correction à faire sur ELXG_UP répété (m) / ELXG de base	Variation du plan d'eau/ log de base (m)
MC1	(35,88)	(030609)	35,62	030306	+0,0	-0,26
			34,84	031027	+2,0	-1,04
MC2	36,43	030304	36,37	030304	+0,2	-0,06
			35,15	031027	+1,55	-1,28
MC3	39,13	030306	37,79	031027	+1,47	-1,34
MC5	38,45	030607	38,9	031026	+0,45	-0,45
S17	(39,36)	(030609)	37,7	020609	-4,5	+1,66

Tableau A2- 9. Corrections en profondeur à faire pour ELXG_UP répétés (sauf S17, ELXG_DW, car UP n'a pas été enregistré sur ce puit.

5.3 Variations de niveau d'eau saisonnières

5.3.1 Variations observées sur les enregistrements ELXG

Ceci amène, pour vérification, à considérer les variations sur la même période du plan d'eau sur des puits différents de Campos (qui en principe devraient être les mêmes) :

Période	Puit	Variation du plan d'eau (m)
Mars- juin 2003	MC1	- 0,26
Mars- octobre 2003	MC1	-1,30
	MC2	-1,28
	MC3	-1,34
Juin- octobre 2003	MC1	-1,04
	MC5	-0,45
Juin 2002- juin 2003	S17	+1,66

Tableau A2- 10. Variation saisonnières du plan d'eau d'un puit à l'autre, et constatation qu'elles varient très peu d'un puit à l'autre sur la même période.

On observe que de mars à juin, les variations du plan d'eau sont faibles : -26cm, mais de mars à octobre elles sont de –1,30m en moyenne, tandis que de juin à octobre, elles sont de –75cm en moyenne. Il est donc difficile considérer que le niveau d'eau ne varie pas au cours de l'année, comme nous l'avons fait dans notre méthode (voir paragraphe 1.3).
Toutes les variations saisonnières du plan d'eau ont été réalisées sur l'année 2003.

5.3.2 Mesures de pression enregistrées sur le site Ses Sitjoles par ETH

ETH a enregistré les variations de pression d'eau et d'air sur le site de Ses Sitjoles avec une fréquence minimum de 30 secondes et maximum de deux heures, sur de longues périodes (plusieurs mois).
La Fig. A2-2 montre qu'il est nécessaire de corriger les lectures de pression d'eau par la pression d'air enregistrée afin d'avoir une mesure de variation verticale du plan d'eau.
C'est ce qui a été fait sur les Fig. A2-4 à A2-5 et A2-7 à A2-9. Cependant, la Fig. A2-3 montre que sur les puits de pompage, cette correction n'est pas nécessaire, parce qu'incorporée dans l'appareil de mesure.

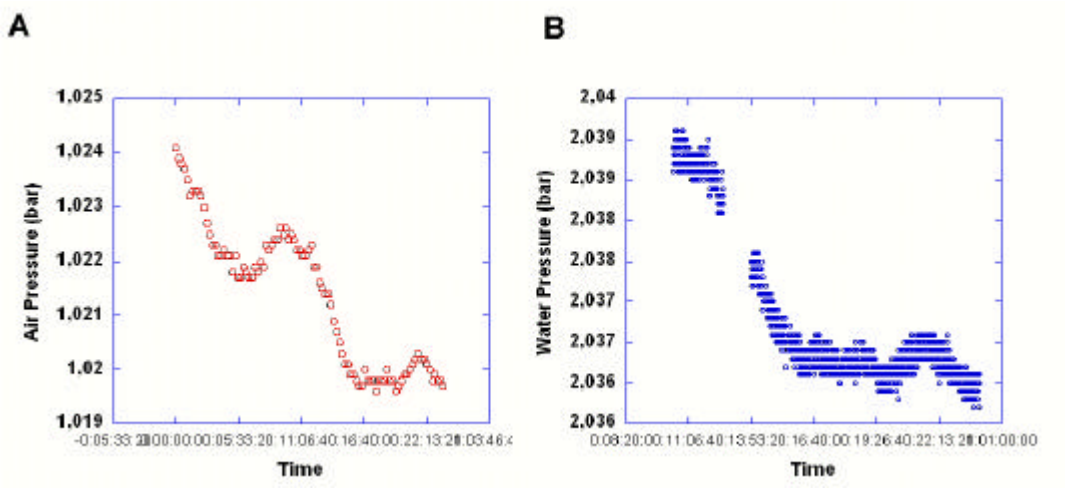

Figure A2- 2. Comparaison des variations de pressions d'air (A) et de pression d'eau enregistrée dans le puit S17 (B) au cours de la même journée du 4 mars 2004. On voit qu'il y a une similitude des courbes et que les variations de pression d'air sont du même ordre de grandeur que les variations de pression d'eau : pour la mesure du niveau d'eau dans un puit, il est donc nécessaire de retrancher la pression d'air à la pression d'eau.

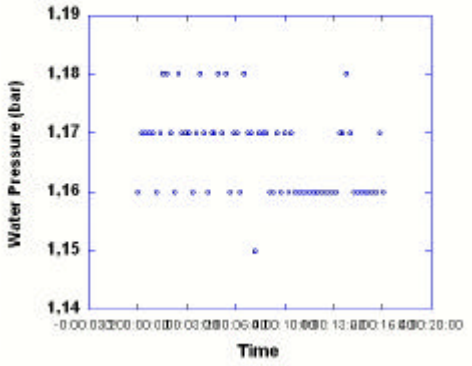

Figure A2- 3. Pression d'eau dans le puit Nord, le même jour. On voit que sur cet appareil de mesure de la pression d'eau, il y a une correction de pression d'air incorporée.

Nous constatons sur les Fig. A2-4A et A2-5A une pression de 1,424bar au 4 mars 2003 et une pression de 1,445 bar au 8 septembre 2003. Le niveau d'eau est donc plus élevé de 21cm en septembre qu'en mars. Cependant, nous n'avons plus d'enregistrements après le 8 septembre, et nous ne savons donc pas quel est le niveau d'eau au 27 octobre 2003 : ceci nous empêche de vérifier les résultats du tableau A2-10.

La Figure A2-4A montre aussi qu'entre décembre 2002 et mars 2003, nous constatons des variations de niveau pouvant aller jusqu'à 22 cm (période des eaux les plus basses: 31 janvier ; période des eaux les plus abondantes : 24 mars) sur le puit S17, tandis qu'entre le 12 juillet et le 8 septembre (Fig. A2-5A), les variations ne dépassent pas 8cm.

La Figure A2-4B montre que sur le puit de pompage Nord (situé seulement à 33m du puit S17, Fig. A2-1),

- les variations de pression sont d'une amplitude beaucoup plus grande que sur S17
- Les oscillations de pression du puit Nord sont suivies, avec une plus faible amplitude sur S17, sauf du 8 au 23 mars, où elles semblent inversées.

Sur la Fig. A2-5B, on observe les mêmes évènements, sauf qu'il n'y a pas d'inversion d'oscillation entre S17 et le puit de pompage Nord.

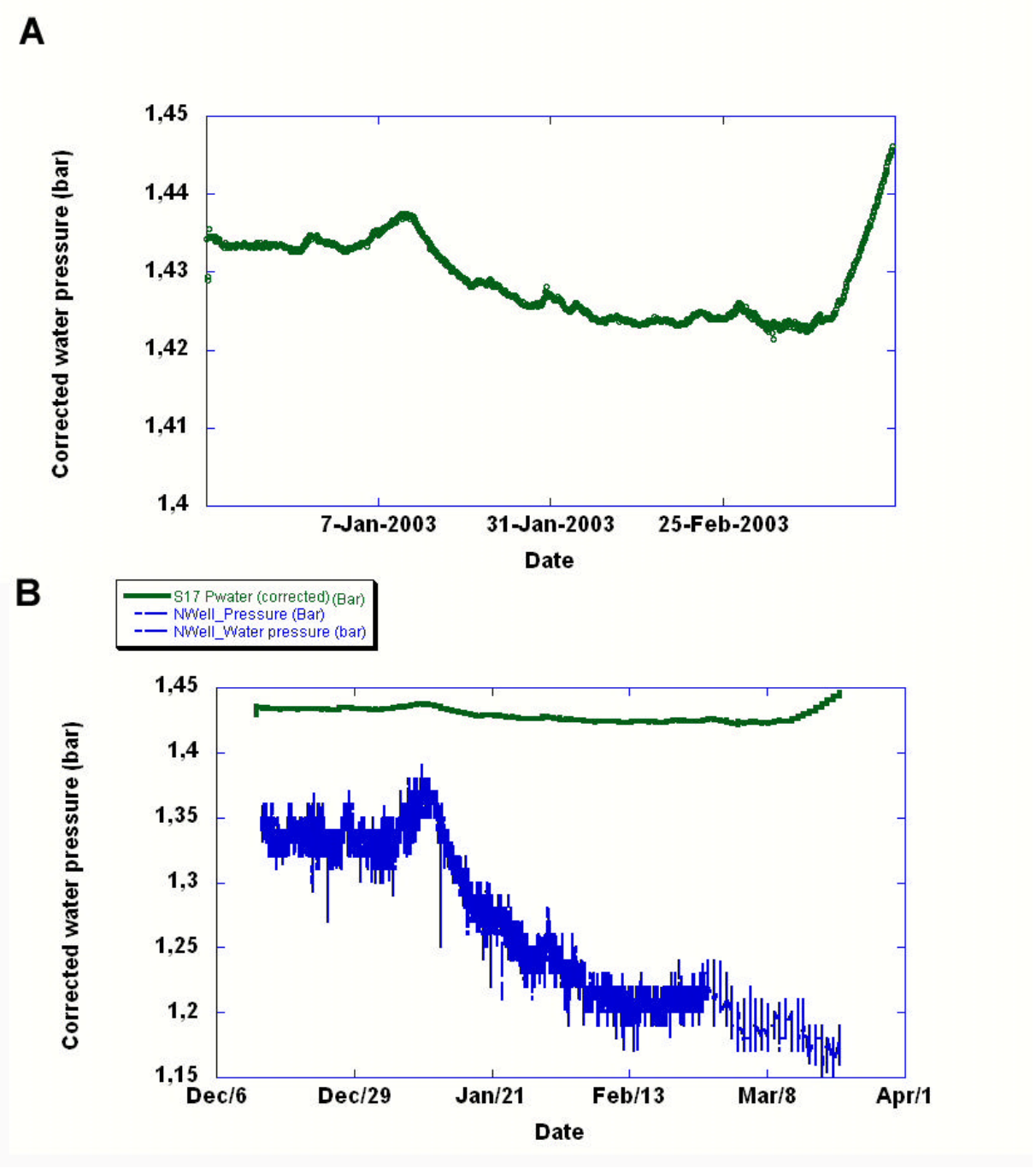

Figure A2- 4. (A) Variations de pression d'eau dans S17 entre le 13 décembre 2002 et le 23 mars 2003. Pression en bar (une différence de 1 bar de pression correspond à environ 10 mètres de variation de niveau d'eau), corrigée par la valeur de pression d'air enregistrée simultanément. Variation maximum de niveau d'eau : 30 cm. Le niveau d'eau augmente rapidement en mars. (B) Pression d'eau enregistrée dans S17 entre le 13 décembre 2002 et le 23 mars 2003, comparée à la pression d'eau sur le puit Nord de pompage pendant la même période. Les périodes de pompage les plus intenses sont janvier à mars.

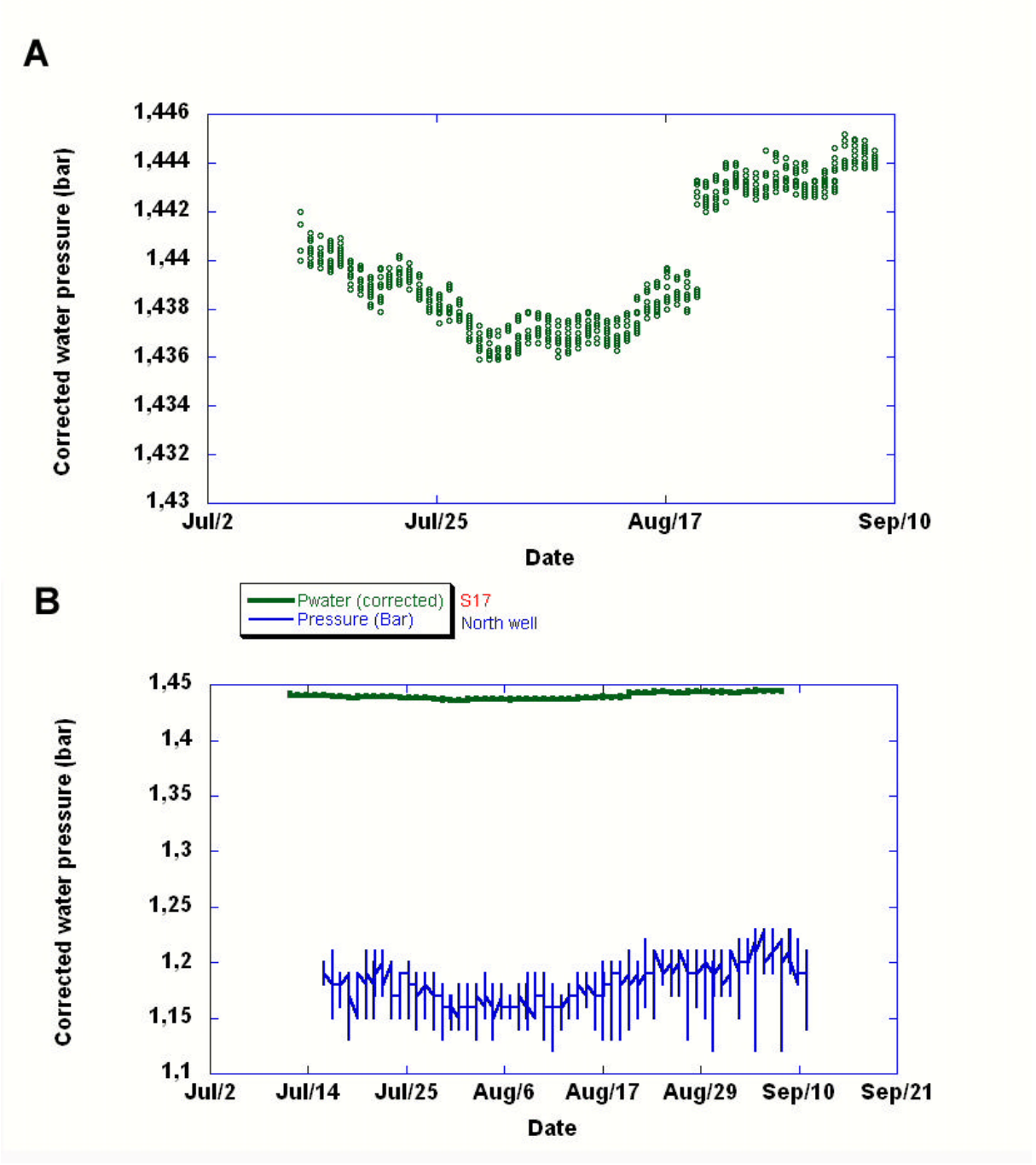

Figure A2 - 5. (A) Variations de pression d'eau sur S17 entre le 12 juillet et le 8 septembre 2003. Pression en bar (soi environ 10 mètres de variation de niveau d'eau), corrigée par la valeur de pression d'ai enregistrée simultanément. Variation maximum de niveau d'eau : 8 cm. Le niveau d'eau augmente en septembre. Le saut observé en août est probablement dû à un variation accidentelle du niveau du capteur de pression. (B) Pression d'eau enregistrée sur S17 entre le 12 juillet et le 8 septembre 2003, comparée à la pression d'eau sur le puit Nord de pompage pendant la même période. Les périodes de pompage les plus intenses sont juillet et la première moitié d'août.

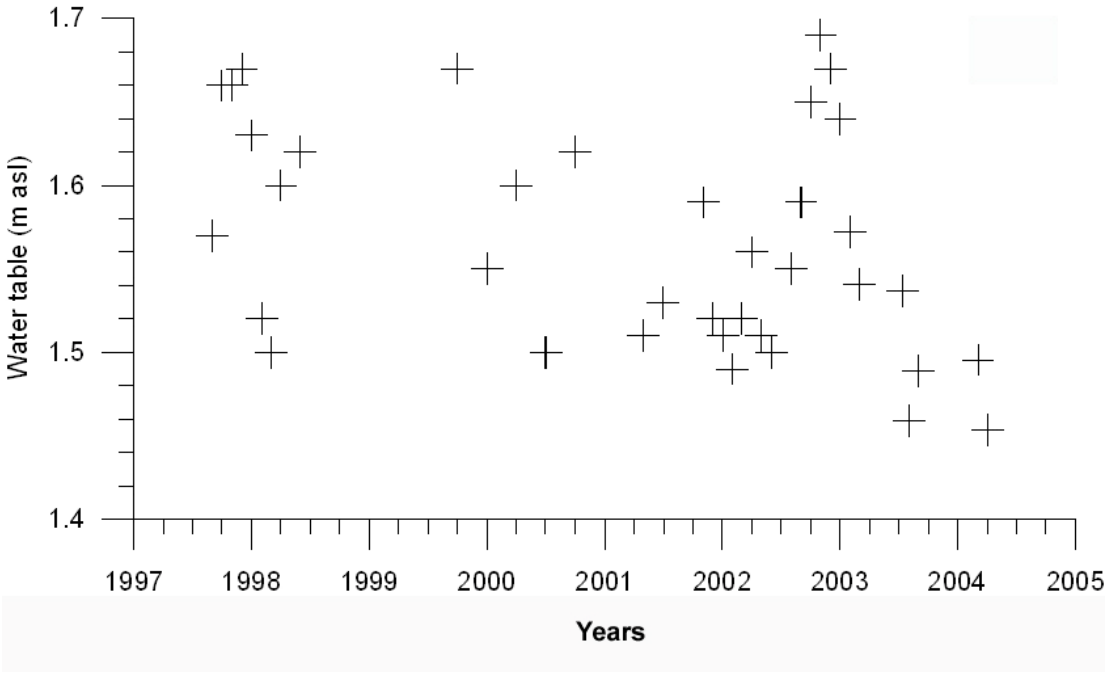

Figure A2- 6. Variations de pression hydrostatiques à long terme sur S17 (données ETH).

La Fig. A2-6 montre des variations de pression hydrostatiques à long terme sur S17. On voit que l'amplitude des variations peut tout de même atteindre plus de 2m.
Il faut donc revenir en arrière et faire des corrections de la manière suivante : MC2 étant le puit de base, nous conservons son log de base inchangé (imagerie optique enregistrée le 03/03/04); les autres logs sont corrigés de la manière suivante :

Puit	Date log de base (année mois jour)	Correction par rapport à 03/03/04	Profondeur du plan d'eau avant correction (mbgl)	Profondeur du plan d'eau après correction (mbgl)
MC1	030609	-0,26	35,88	35,62
MC2	030304	0	36,43	36,43
MC3	030306	0	39,13	39,13
MC4	030820	?	38,48	?
MC5	030607	-0,26	38,45	38,19
MC6	040711	?	38,49	?
MC7	030821	?	38,49	?
MC8	040710	?	36,43	?
MC9	040708	?	36,43	?
S17	030609	-0,26	39,36	39,10

Tableau A2- 11. Corrections de variation saisonnières du plan d'eau.

Nous constatons qu'aucun log de base n'a été enregistré en octobre 2003 (Fig. A2-4, A2-5, A2-7, A2-8). Nous ne connaissons pas les variations saisonnières correspondant à juillet 2004 ou août 2003 (voir cependant Fig. A2-8A et B), bien que ce soient à priori des périodes sèches, donc de basses eaux. En conséquence, la seule corrections connue est pour les puits dont le log de base a été enregistré en juin 2003 (MC1, MC5 et S17), et elle est faible (-0,26m). Nous allons donc négliger la correction de variation saisonnière sur tous les puits.
On observe sur les ELXG calés en profondeur que la courbe SN subit des variations de profondeur sur le même puit suivant la saison, suivant en cela les variations saisonnières de niveau de fluide liquide (eau douce, eau de transition, eau de mer) ; ceci laisse peser un doute sur les calages en profondeur de log en fonction de la courbe SN (voir ci-dessous, DIL, et PNN).

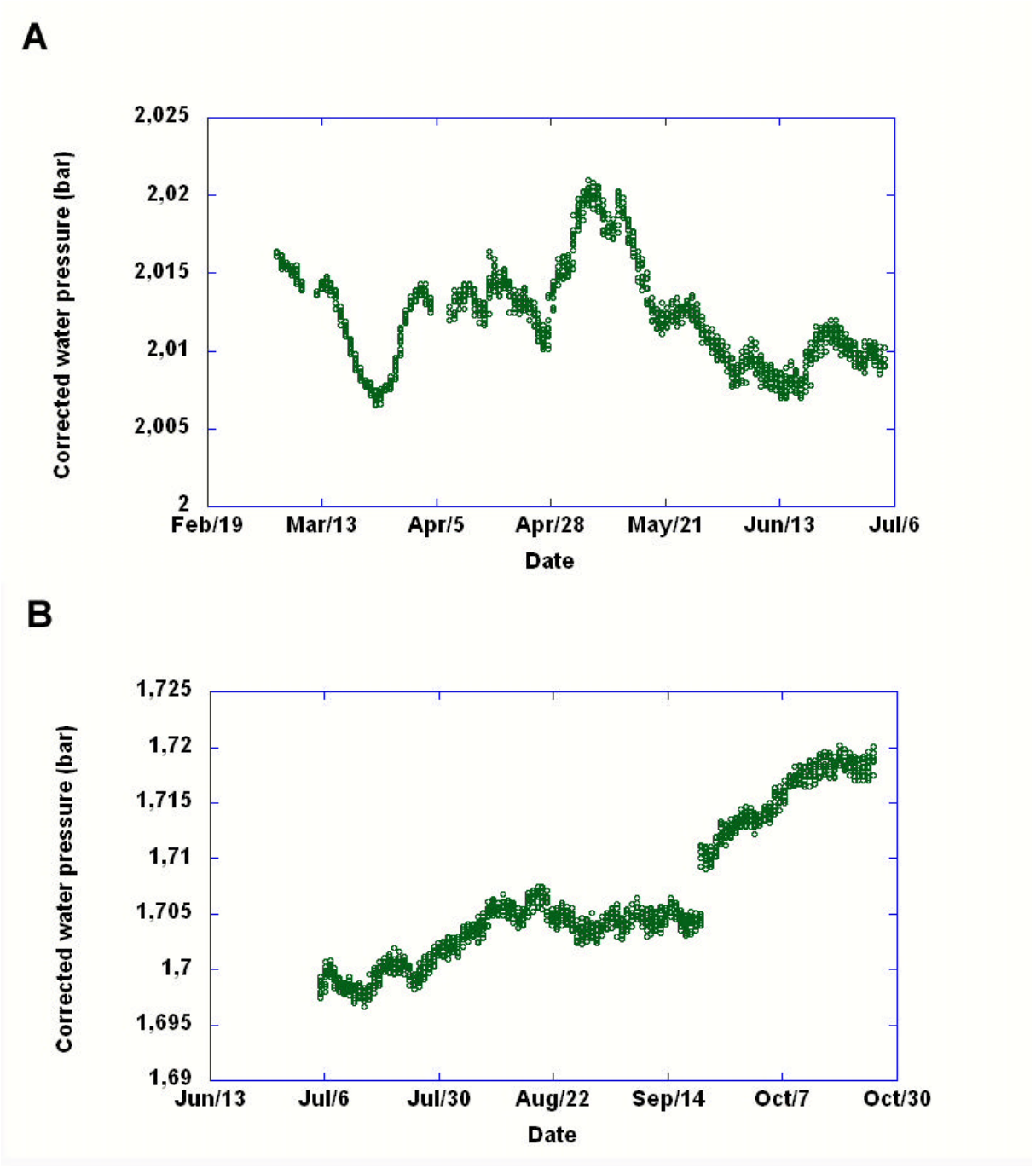

Figure A2- 7. (A) Variations de pression d'eau sur S17 entre le 3 mars et le 7 juillet 2004. Variations maximales de niveau d'eau : 25 cm. Le niveau d'eau augmente en mai. (B) Variations de pression d'eau sur S17 entre le 7 juillet et le26 octobre 2004. Variations maximales de niveau d'eau : 25 cm. On note une tendance à l'augmentation de pression (donc du niveau d'eau) de juillet à octobre. Le niveau d'eau augmente en octobre.

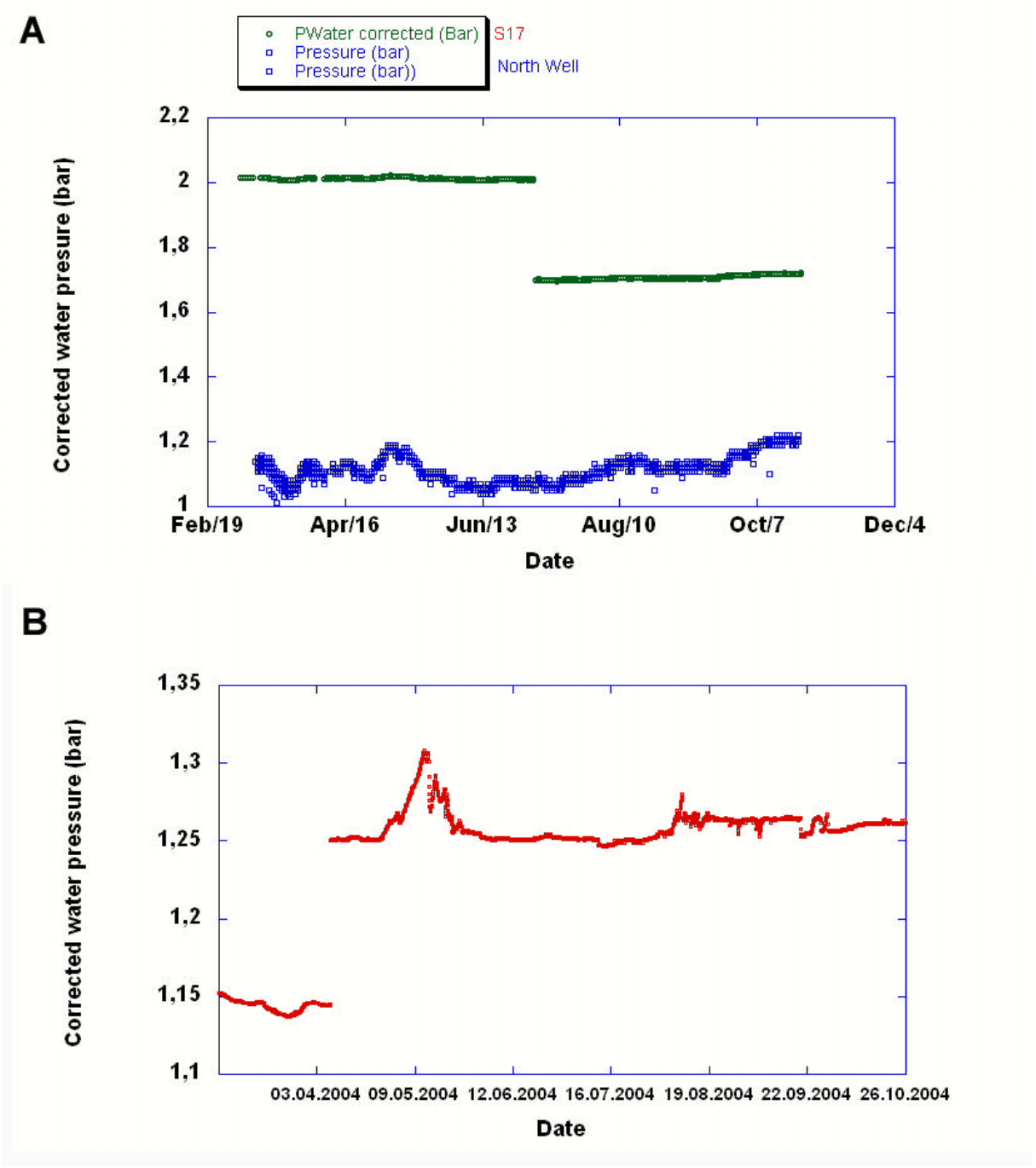

Figure A2- 8. (A) Variations de pression d'eau sur S17 entre le 3 mars et le26 octobre 2004 comparée à la pression d'eau sur le puit Nord de pompage pendant la même période. On remarque des évènements analogues à ceux observés en 2003 sur le même puit (Fig. 7 et 9). Les périodes de pompage les plus intenses semblent être mars et juin-juillet. (B) Variations de pression d'eau sur MC6 entre le 29 février et le27 octobre 2004. Variations maximales de niveau d'eau : 1m. Le niveau d'eau augmente en mai. Le saut en avril est dû à un changement de niveau du capteur de pression.

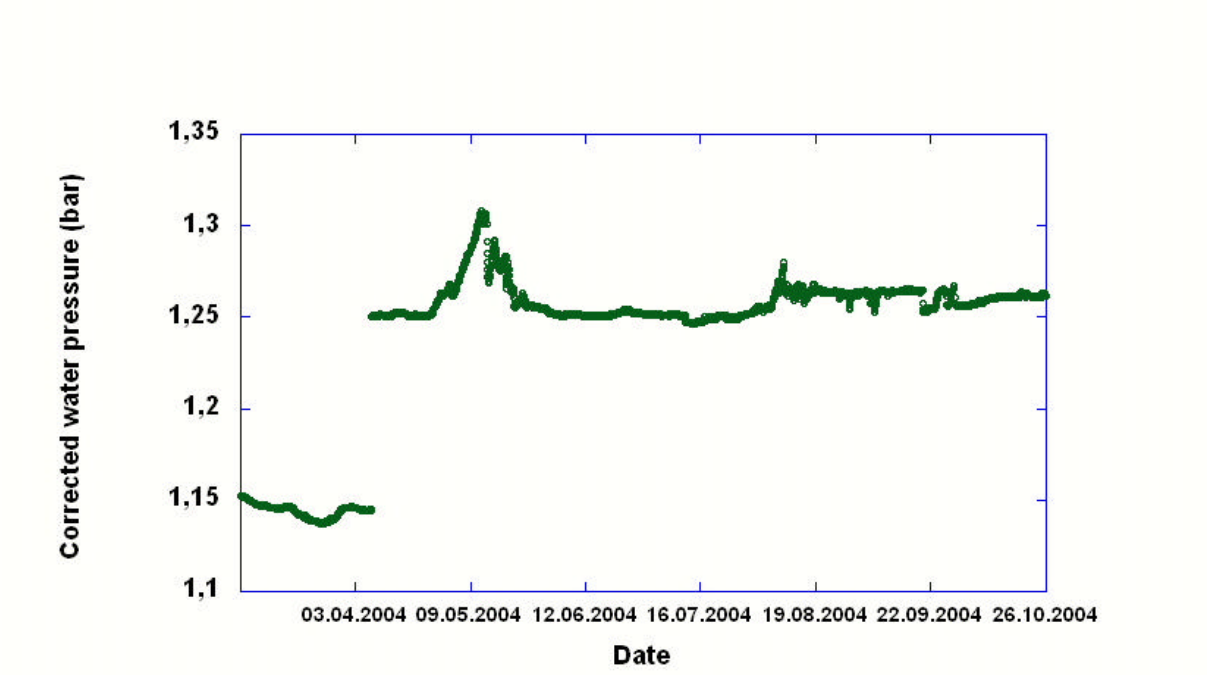

Figure A2- 9. Comparaison entre les variations saisonnières de MC6 et S17. Curieusement, les variations saisonnières sont plus importantes sur MC6 que sur S17. Les sauts sont dus à des changements de niveau du capteur de pression.

5.3.3 Pluviosité en 2002

Janvier	Février	Mars	Avril	Mai	Juin	Juillet	Août	Sept.	Oct.	Nov.	Déc.
99.2	3.0	70.3	59.9	64.6	31.8	10.7	59.0	35.5	60.5	88.7	45.8

Tableau A2- 12. Tableau de précipitations en mm d'eau, 2002 à Campos (Service Météo de Majorque).

Le Tableau A2-12 permet de voir qu'en 2002, le maximum de pluie a eu lieu au cours des mois de janvier et novembre, tandis que le minimum a eu lieu en février et juillet.

6 Tache 9 : Calage des autres logs sur ELXG

Caler :

- DIL sur SN de ELXG
- SGR sur GR de ELXG
- PNN sur SN et GR de ELXG
- Sonic sur SN et GR de ELXG, vérification avec PNN
- Caliper sur imagerie optique et acoustique

Les puits MC6 et MC9 n'ont pas eu d'enregistrement ELXG effectué. Il ne sera donc pas possible pour ces puits de caler les autres logs sur le GR ou la courbe SN de l'ELXG.
Pour MC9, on essayera de trouver la côte du plan d'eau su,43r le DIL (en comparant avec les puits où à la fois ELXG et DIL sont disponibles), et ensuite de caler le SGR et le Neutron sur DIL.
Le puit MC6 est un cas désespéré : les seuls logs enregistrés ont été : Idronaut (sur mon insistance) et SGR. Il est hors de question de caler le SGR sur quelque plan d'eau que ce soit. Il n'est donc pas possible de caler le SGR sur ce puit, et il faudra donc prendre le SGR_UP tel quel.
Seuls les logs enregistrés en montant sont corrélés (nous n'avons pas d'information sur la direction d'enregistrement pour les logs enregistrés par les autres Universités que Montpellier II: DIL 38, Sonic, Caliper).

6.1 Calage DIL

Puit	Côte du plan d'eau sur imagerie optique ajusté (et sur Idronaut ajusté) (mbgl)	Date de l'ELXG, (Année/ Mois/ jour)	Date DIL (Année/ Mois/ jour) DIL 38/ DIL 45	Correction à faire sur DIL 38/ DIL 45 (m)	Remarques
MC1	(35,88)	030609	031203/040707	-2,0/ -2,2	
MC2	36,43	030609	310304/040706	-2,1/ -2,2	
MC3	39,13	030607	031213/ 040707	-1,0/ -1,9	
MC4	(38,48)	030820	-	-	Pas de DIL
MC5	38,45	030608	031203/040707	-1,4/+0,5	
MC6	(38,49)	-	-	-	Pas de ELXG/ DIL
MC7	38,49	031027	031207/-	+1,83/-	
MC8	36,43	031026	-/040709	-/+0,2	
MC9	36,43	-	-/040708	-/-0,5	
S17	(39,36)	030609	-/040705	-/-0,2	

Tableau A2- 13. Calage du DIL sur l'ELXG. Les DIL45 ont été recalibrés, suivant la formule ILDcor=2,835ILD - 0,598 ; ILMcor= 2,253ILM – 1,035. DIL 38 limité en résistivité > 20 Ohm.m

6.2 Calage SGR

Puit	Côte du plan d'eau sur imagerie optique ajusté (et sur Idronaut ajusté) (mbgl)	Date de l'ELXG, (Année/ Mois/ jour)	Date SGR (Année/ Mois/ jour)	Correction à faire sur SGR (m)	Remarques
MC1	(35,88)	030609	030609	-2,4	Fortes variations statistiques
MC2	36,43	030609	040706	-2,3	
MC3	39,13	030607	030607	-2,5	Fortes variations statistiques
MC4	(38,48)	030820	030819	-2,03	Fortes variations statistiques
MC5	38,45	030608	030609	-2,5	Fortes variations statistiques
MC6	(38,49)	-	030819	0,5	Pas de ELXG, fortes variations statistiques, calage du SGR impossible
MC7	38,49	031027	030826	-0,87	Fortes variations statistiques
MC8	36,43	031026	040709	+0,2	Doute sur ajustement raie potassium
MC9	36,43	-	040708	-1,5	Correction/ DIL 45
S17	(39,36)	030609	030609	-3,7	Fortes variations statistiques

Tableau A2- 14. Calage du SGR sur ELXG

6.3 Calage PNN

Puit	Côte du plan d'eau sur imagerie optique ajusté (et sur Idronaut ajusté) (mbgl)	Date de l'ELXG, (Année/ Mois/ jour)	Date PNN (Année/ Mois/ jour)	Correction à faire sur PNN (m)	Remarques
MC1	(35,88)	030609	040707	-0,2	
MC2	36,43	030609	040706	-2,2	
MC3	39,13	030607	040708	+1,3	
MC4	(38,48)	030820	-	-	Pas de PNN
MC5	38,45	030608	040708	-2,2	
MC6	(38,49)	-	-	-	Pas de PNN
MC7	38,49	-	-	-	Pas de PNN
MC8	36,43	031026	040710	+0,0	
MC9	36,43	-	040708	-2,5	Correction/ DIL 45
S17	(39,36)	030609	040705	+0,0	Correction/ DIL 45

Tableau A2- 15. Calage du PNN sur ELXG. Tous les PNN ont été recalibrés suivant la formule : NPHI= 0,034405*(SSNF/LSNF).

6.4 Calage Sonic

Puit	Côte du plan d'eau sur imagerie optique ajusté (et sur Idronaut ajusté) (mbgl)	Date de l'ELXG, (Année/ Mois/ jour)	Date Sonic (Année/ Mois/ jour)	Correction à faire sur Sonic (m)	Remarques
MC2	36,9	030609	03	-2,5	
MC3	39,6	030607	03	+0,33	

Tableau A2- 16. Calage Sonic sur ELXG

6.5 Calage caliper

Puit	Côte du plan d'eau sur imagerie optique ajusté (et sur Idronaut ajusté) (m)	Date de Imagerie optique, (Année/ Mois/ jour)	Date Caliper (Année/ Mois/ jour)	Correction à faire sur Caliper (m)	Remarques
MC2	36,9	03/04/04	03	0,0	
MC3	39,6	03/06/06	03	-0,3	

Tableau A2- 17. Calage Caliper sur Imagerie optique

7 Mesures de hauteur de plan d'eau à l'aide du « piézo » en avril 2005

Un ruban gradué en longueur muni d'une sonde « piézo » permet d'obtenir un signal lumineux et sonore dés que la sonde atteint le niveau d'eau, et ainsi de mesurer la profondeur du plan d'eau.

Elevation (m)	MC1 (mbgl)	MC2 (mbgl)	MC3 (mbgl)	MC4 (mbgl)	MC5 (mbgl)	MC6 (mbgl)	MC7 (mbgl)	MC8 (mbgl)	MC9 (mbgl)	S17 (mbgl)
Elevation de la tête de puit (base= msl) : z	37,77	38,32	41,02	40,37	40,34	40,38	40,38	38,32	38,32	41,25
Profondeur du plan d'eau piézo: z-h	36,29 (17)	36,77 (17)	36,59 (22)	36,25 (18) 38,74 (22)	38,28 (17) 38,28 (22)	38,69 (18)	38,85 (18) 38,69 (22)	36,80 (17)	36,87 (17)	39,63 (18)
Elevation duplan d'eau: h	1,48	1,55	**2,43**	**2,12** **1,93**	**2,06** **2,06**	1,69	1,53 1,69	1,52	1,45	1,62

Tableau A2- 18. Elevation de la tête de puit, profondeur du plan d'eau mesurée au piézo (date de la mesure entre parenthèses), et élévation du plan d'eau h.

On voit que h est sensiblement égal à 1,50m pour l'ensemble des puits de Ses Sitjoles, sauf pour les puits MC3, MC4 et MC5, où h est égal à environ 2,15m.

8 Calage SGR de 2005

Plusieurs SGR ont été refaits en avril 2005, pour améliorer la qualité (variations statistiques, calage de la raie du potassium) des SGR faits précédemment. Ces nouveaux SGR sont alors calés sur les anciens SGR.

Puit	Date ancien SGR (Année/ Mois/ jour)	Date nouveau SGR (Année/ Mois/ jour)	Correction à faire sur nouveau SGR (m)	Remarques
MC1	030609	050419	-2,55	Corrigé Th et K (mauvais calage raie K)
MC2	040706	-	-	Ancien SGR OK
MC3	030607	050422	-2,2	Corrigé Th et K (mauvais calage raie K)
MC4	030819	050422	-2,0	
MC5	030609	050422	-1,8	
MC6	030819	050422	0	
MC7	030826	050422	-0,4	
MC8	040709	050417	+0,25	
MC9	040708	-	-	Ancien SGR OK
S17	030609	050418	-3,6	

Tableau A2- 19. Calage des nouveaux SGR sur les anciens.

9 Calage SGR de 2006

Puit	Date ancien SGR (Année/ Mois/ jour)	Date nouveau SGR (Année/ Mois/ jour)	Correction à faire sur nouveau SGR (m)	Remarques
MC1	030609	060501	-2,5	SGR 512
MC10	040706	060430	-2,5	SGR 512

Tableau A2- 20. Calage des SGR enregistrés en 2006.

MC10 OBI 060430 DC=0 WT= 36,71m
MC10 Caliper 060502 DC=0

A3 Etalonnage d'outils de diagraphie

Cette annexe est un complément à Maria-Sube[3] et al., soumis. La partie décrivant l'étalonnage de l'outil Sonic, est suffisamment complète dans le document, et ne sera donc pas reprise ci-dessous.

1 Neutron

L'analyse des Fig. A3-1A et A3-1B démontre que les détecteurs proches et éloignés de l'outil Neutron enregistré à MC2 sont affectés de grandes variations statistiques. Elles sont dues à : grandes porosités et un ensemble vitesse d'enregistrement- pas d'acquisition inadéquate (6m/mn, trop rapide, et 5cm, trop court). Ceci implique qu'il est nécessaire de filtrer les données (filtre Gaussien à 21 pas), avant de calculer le rapport SSNF/LSNF des données filtrées du détecteur proche et du détecteur éloigné (Fig. 3A-1C) ; même après filtrage de chacune des données, la courbe du rapport en fonction de la profondeur apparaît bruitée.

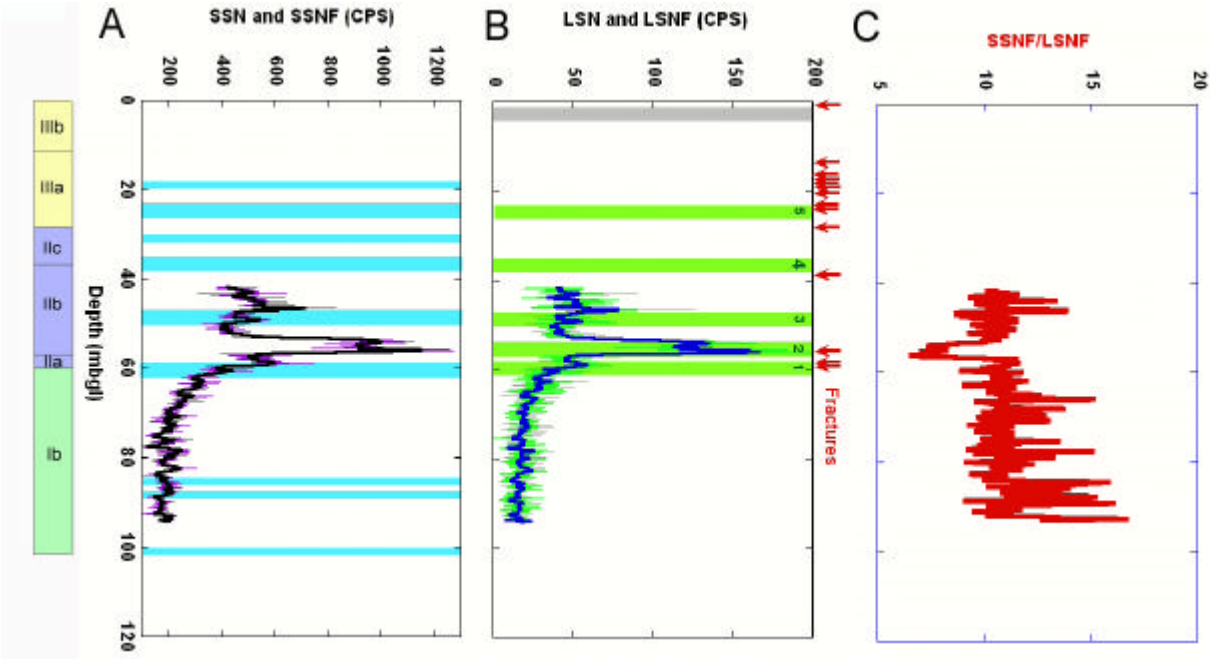

Figure A3- 1. Les sous-unités stratigraphiques sont indiquées sur la partie gauche de la figure. Les ombrages bleu pâle indiquent les zones de dolomitization, l'ombrage gris pâle indique une zone de cimentation, les ombrages vert pâle indiques les zones de minéralisation, et les flèches rouges indiquent les fractures reconnues d'après l'imagerie de la paroi du puit (Maria-Sube et al., soumis). Dans le puit MC2, diagraphie Neutron en fonction de la profondeur. (A) Données du détecteur proche non-filtré (SSN, courbe violette mince) et filtré (SSNF, courbe noire épaisse). (B) Données du détecteur distant non-filtré (lSN, courbe verte mince) et filtré (LSNF, courbe bleue épaisse). (C) Rapport SSNF/LSNF.

1.1 Etalonnage dans le puit MC2

La Fig. A3-2 montre le graphe d'étalonnage de la porosité carotte Φ_{core} en fonction du rapport SSNF/LSNF. Seulement 40 bouchons sont disponibles dans la zone humide enregistrée (l'alimentation de l'outil Neutron doit être coupée 5m en-dessous du plan d'eau, pour des raisons de sécurité). On observe que la linéarité de Φ en fonction de SSNF/LSNF est faible (R^2= 0.16), probablement dû à différents effets, comme : la minéralogie roche et fluide, le diamètre du puit, l'excentralisation de l'outil, des variations statistiques excessives, la

corrélation de profondeur entre carotte et enregistrement diagraphique, la différence de taille d'échantillon entre carotte et diagraphie. Il est cependant possible d'extraire la relation d'étalonnage suivante de la Fig. A3-2 :

$F_N = - 0.015 + 0.034 * SSNF/LSNF$ (1)

La comparaison entre la Formule (1) et la formule procurée par le constructeur (Maria-Sube[3] et al., soumis, montre des valuers très proches pour le coefficient multiplicateur, mais des coefficients additifs très différents (pratiquement nul pour notre étalonnage).

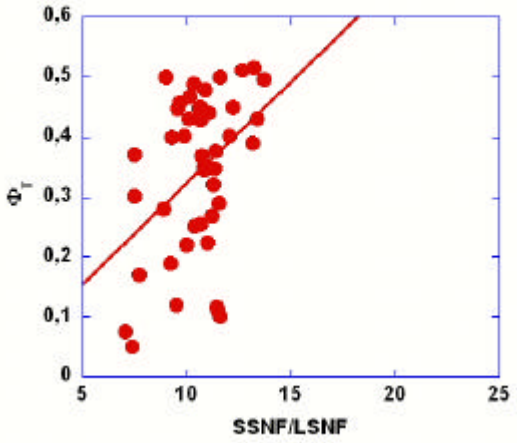

Figure A3- 2. Porosité de carotte F_{core} (ici assimilée à la porosité totale F_T) en fonction du rapport SSNF/LSNF amenant à l'étalonnage de la porosité Neutron par l'équation de la ligne de régression d'équation y= -0.015 + 0,034x, R^2= 0.16, dans le puit MC2.

1.2 Analysis in MC2 and other wells

Nous avons aussi appliqué la Formule (1) aux autres puits de Ses Sitjoles, où le PNN a été enregistré : MC1 (vitesse d'enregistrement 4,6m/mn), MC3 (vitesse d'enregistrement 3,5m/mn), MC5 (vitesse d'enregistrement 3,33m/mn), MC8 (vitesse d'enregistrement 4,66m/mn), MC9 (vitesse d'enregistrement 3,33m/mn), S17 (vitesse d'enregistrement 4,6m/mn),. La Fig. A3-3A compare ces enregistrements à l'échelle 5m (pour la distance entre les puits), et la Fig. A3-3B les compare à l'échelle 100m. Il devient donc apparent qu'il y a généralement une bonne superposition, plus spécialement à l'échelle 5m où les zones de minéralisation à faible porosité (intervalles 46-48 et 56-60m) sont particulièrement notable. Les sommets de grande porosité (certains autour de 70%) sont uniquement apparents dans les diagraphies qui ont été enregistrées trop rapidement (MC1, S17) ; les courbes les plus lissées s'observent sur les diagraphies dont la vitesse d'enregistrement était seulement de 3,33m/mn (MC5 et MC9). Nous notons aussi que généralement dans la sous-unité Ib, la porosité moyenne est de 40%, ce qui correspond à la porosité carotte de MC2 dans cette sous-unité.

Dans cette formation, un pas d'acquisition de 15cm avec une vitesse d'enregistrement de moins de 3,3m/mn aurait été une meilleure sélection, mais l'outil n'a pas été malheureusement disponible suffisamment longtemps pour que ce problème puisse être corrigé.

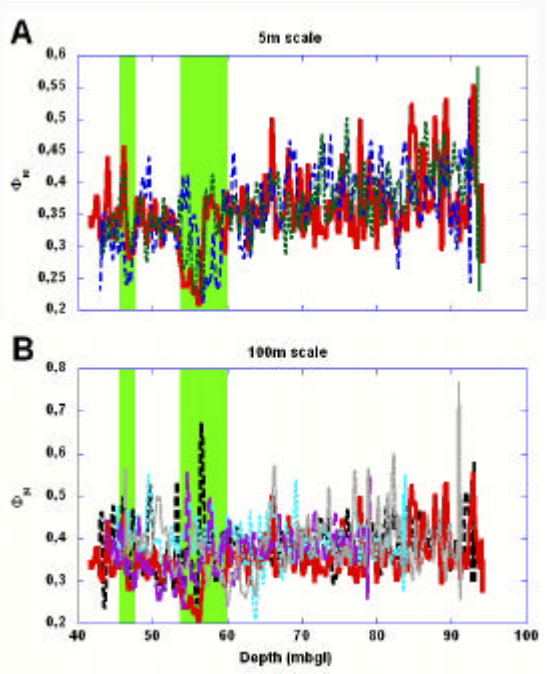

Figure A3- 3. Les ombrages verts représentent les zones de minéralisation. Neutron étalonné dans les puits de Ses Sitjoles, à une échelle 5m (A) pour les puits MC2 (courbe épaisse rouge continue), MC8 (courbe moyenne bleue, tirets), et MC9 (courbe verte moyenne pointillés) ; (B) pour les puits MC1 (courbe noire épaisse, tirets), MC2 (courbe épaisse rouge continue), MC3 (courbe moyenne bleu pâle pointillés), MC5 (courbe épaisse violette longs tirets), et S17 (courbe moyenne grise long tirets).

2 Résistivité

L'outil ELXG est fourni avec un système d'étalonnage composé d'une résistance e précision. L'outil DIL 45 est fourni avec une boucle d'induction externe ; la procédure d 'étalonnage doit être effectuée en surface dans un lieu aussi dépourvu de sources électromagnétiques que possible.

Pour l'outil DIL 45, ALT fournit des abaques de correction environnementale pour les données ILM et ILD. Des corrections sont proposées pour quatre décades de valeurs de résistivité de la boue R_{mud} (entre 0,1 Ohm.m et 100 Ohm.m). Dans le cas des puits à eau de Majorque, la résistivité de la boue est la même que celle de l'eau de formation R_w et varie entre 0,179 (eau de mer) et 2,35Ohm.m (eau saumâtre). Dans l'eau saumâtre, les corrections à appliquer sont négligeables pour la gamme complète des résistivités mesurables (0,2-200Ohm.m). Dans l'intervalle d'eau de mer, ces deux mesures sont inférieures à ces deux valeurs, sauf sur un court intervalle de seulement 1m de long. En conclusion, ce n'est pas nécessaire d'appliquer les corrections d'environnement pour le DIL 45 dans le puit MC2, et donc dans tous les puits de Ses Sitjoles.

Les mesures de laboratoire de la résistivité de bouchon saturé $R_o = 1/\sigma_o$ déduites de la formule d'Archie $\sigma_o = \sigma_w/F$ (F à partir des mesures électriques, Maria-Sube[2] et al., soumis, et σ_w à partir des mesures Idronaut sur le puit), sont utilisées pour vérifier les mesures des diagraphies de résistivité (Fig. A3-4). L'outil ILD 45 présente moins de dispersion (Fig. A3-5C) que l'ELXG (Fig. A3-5A), les données ILM et SN étant les moins dispersées pour chacun des outils ($R^2 = 0.498$ et $R^2 = 0.24$, respectivement). Les données SN présentent (Fig. A3-5A une droite de régression avec une pente très proche de 1 (1,01), la seconde pente la plus proche de 1 étant pour les données ILD (0,62). Cette bonne impression de SN est détruite par les Fig. A3-4 et A3-5B, qui montrent (comme déjà observé sur la fig. A3-5A) qu'à la fois LN et SN lisent trop haut dans les basses valeurs de résistivité (ils lisent environ 10Ohm.m, alors qu'ils devraient lire 1Ohm.m). Cette trop haute résistivité montre que l'outil ELXG n'est pas un bon

outil dans une formation de si haute salinité, dans la zone en dessous de 78m (les courants de mesure, n'étant pas focalisés, tendent à suivre le chemin du fluide à faible résistivité dans le trou, et à éviter le chemin plus résistif de la formation). L'outil ELXG ne peut simplement pas lire une résistivité inférieure à 10Ohm.m. Les deux canaux de l'ELXG sont plus à l'aise pour lire les résistivités supérieures à 50Ohm.m, mais avec cependant une large dispersion, et une tendance à lire une résistivité trop haute (Fig. A3-5B).

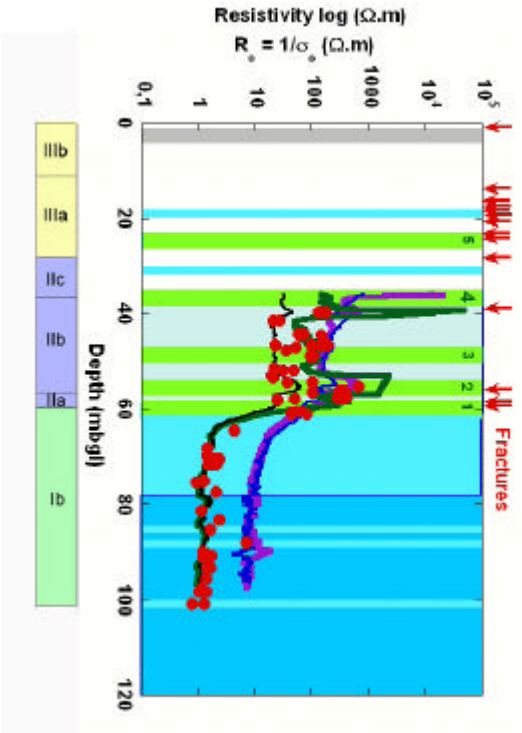

Figure A3- 4. Les sous-unités stratigraphiques sont indiquées sur la partie gauche de la figure. Ombrages des fluides : air : blanc ; eau saumâtre (s_w~4mS/cm) : bleu pale ; zone de transition : bleu ; eau de mer (s_w~55mS/cm) : bleu foncé. Diagraphies de résistivité dans la zone à eau : diagraphie électrique ELXG (SN : courbe violète épaisse, et LN, courbe bleue épaisse), et dagraphie dual induction DIL 45 (ILM, courbe noire moyenne, et ILD, courbe verte épaisse), comparées aux résistivités de bouchon $R_o = 1/\sigma_o$ (61 bouchons, larges points rouges), en fonction de la profondeur dans le puit MC2. Ombrages bleus, verts, et gris, et flèches rouges comme sur la Fig. A3-1.

Les données ILM (Fig. A3-5C et A3-5D) ont un coefficient de dispersion relativement bas, mais lisent systématiquement trop bas (probablement parce qu'elles sont trop influencées par le volume de fluide dans l'anneau situé entre l'outil et la formation : ce fluide est moins résistif que la formation imbibée d'eau elle-même). Les données ILD lisent bien dans les valeurs de faible résistivité (en-dessous de 10Ohm.m avec une légère tendance à lire trop bas) mais dans les hautes valeurs de résistivité, nous avons vu (Fig. A3-4) que les lectures étaient erratiques par endroit.

La fig. A3-6 montre que la relation Φ_T en fontion de Φ_R est relativement linéaire (avec une haute dispersion, $R^2 = 0{,}51$, mais rien d'extraordinaire pour une comparaison carotte en fonction de mesures de diagraphie), et que un facteur détalonnage de 0,92 doit être utilisée pour Φ_R. Un tel facteur d'étalonnage doit être utilisé pour compenser la lecture trop élevée de SN (Fig. A3-5B). Cependant, ceci a pour conséquence des distorsions des valeurs de Φ_{Rcal} (Fig. A3-6) que ce soit dans les basses ou les hautes valeurs. Au contraire, nous pensons que les lectures σ_w données par l'outil Idronaut sont correctes, parce que les mesures de conductivité « eau de mer » (en-dessous de 62m) ont été vérifiées par les mesures en

laboratoire des échantillons d'eau de mer (prélevés sur la côte du Sud-Est de Majorque) ; nous avons trouvé une salinité de 38g/l dans chaque cas.

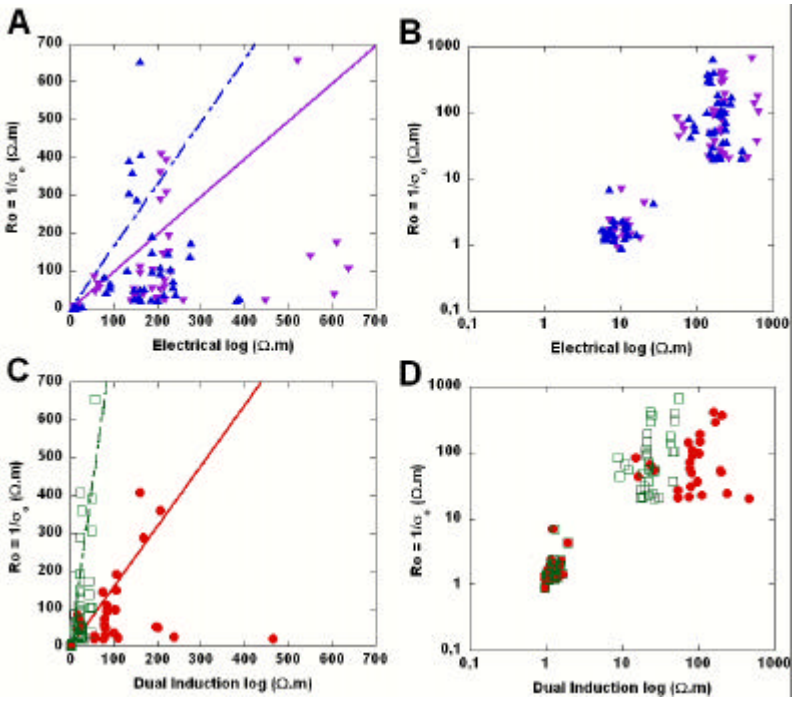

Figure A3- 5. Diagrammes de données croisées pour 61 bouchons de résistivité $R_o = 1/s_o$ en fonction des valeurs de résistivité de diagraphies dans le puit MC2. (A) R_o en fonction des données ELXG SN (triangle violet plein, pointe en haut) et LN (triangle bleu plein pointe en haut), échelles linéaires, avec lignes de régression, SN : SN: y= 1.0x, R^2= 0.24; LN: y= 0.61x, R^2= 0.11. (B) R_o en fonction des données ELXG SN et LN, échelles logarithmiques, mêmes symboles que pour la Fig. A3-5A. (C) R_o en fonction des données DIL 45, ILD (points rouges) et ILM (carrés verts vides), échelles linéaires, avec lignes de régression, y= 0.62x, R^2= 0.20; ILM: y= 0.12x, R^2= 0.44. (D) R_o en fonction des données DIL 45 ILS et ILM, échelles logarithmiques, même symboles que pour la Fig. A3-5C.

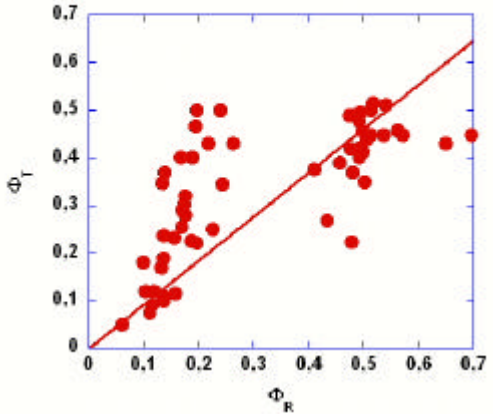

Figure A3- 6. Dans le puit MC2, diagramme de données croisées de 61 bouchons, de la porosité carotte F_{core} (assimilée ici à la porosité totale F_T), en fonction de la valeur de résistivité diagraphie R_t à la même profondeur de carotte $F_R = (R_w/R_t)^{1/m}$. m est mesuré sur chaque bouchon, par des mesures électriques, R_t est un mélange des données de diagraphies ILD et SN, ILD pour les basses valeurs de résistivité, SN pour les hautes valeurs de résistivité. La ligne rouge de régression a pour équation : y=0.92, R^2= 0.51.

3 Images de la paroi du trou

L'enregistrement des images de la paroi du trou dans le puit MC2 (Fig. A3-7) démontre que l'image la plus contrastée est celle de l'amplitude acoustique, tandis que l'image optique est la moins contrastée.

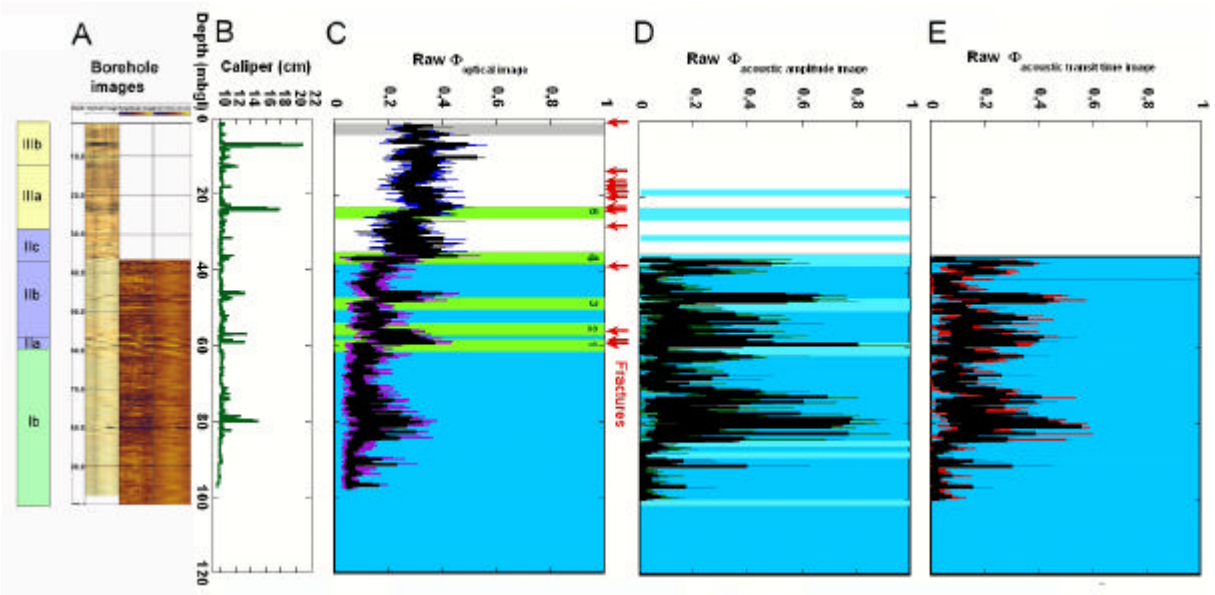

Figure A3- 7. Les sous-unités stratigraphiques sont indiquées sur le côté gauche de la figure. Dans le puit MC2, diagrammes en fonction de la profondeurde, (A) de gauche à droite, images de la paroi du trou optique, amplitude et temps de parcours acoustiques ; (B) diagraphie diamétreur ; (C) Porosité image F_{image} brute (courbe mince bleue dans l'air, mince violette dans l'eau) et filtrée courbe épaisse noire) calculée à partir des images optiques dans l'air et dans l'eau ; (D) F_{image} brute (courbe verte mince) et filtrée (courbe noire épaisse) calculée à partir des images amplitude acoustique dans l'eau ; (E) F_{image} brute (courbe rouge mince) et filtrée (courbe noire épaisse) calculée à partir des images temps de parcours acoustique dans l'eau. Ombrages bleu, vert et gris comme sur la Fig. A3-1; ombrages blanc dans l'air, bleu dans l'eau.

Les résultats de Φ_{image} (porosité dérivée des images de la paroi du trou), traités à partir des images optiques et acoustiques de MC2 (Maria-Sube[3] et al., soumis), sont représentés en fonction de la profondeur sur les figures A3-7C à A3-7E. Le pas d'acquisition était de 1mm, mais nous l'avons réduit à 2mm, en raison de limitations du logiciel de représentation graphique. Il apparaît qu'il devient nécessaire de lisser les résultats à des fins graphiques, en utilisant 50 échantillons au-dessus et en-dessous du point milieu, soit un lissage sur un intervalle glissant de 20cm.

La macro porosité due aux vacuoles ou aux fractures est appelée Φ_{vug}, la macro-porosité due aux caves est appelée Φ_{cave}, et la macro porosité artificiellement causée par le forage est appelée $\Phi_{drilling}$. On a alors la relation :

$$F_{image} = F_{vug} + F_{cave} + F_{drilling} \quad (2)$$

Nous ne sommes pas du tout intéressé par $\Phi_{drilling}$, mais les images de la paroi du trou enregistrent nécessairement $\Phi_{drilling}$. Notre intérêt est dans la macro-porosité de la formation $\Phi_{formation\text{-}macro}$ qui peut être définie par :

$$\Phi_{formation\_macro} = \Phi_{vug} + \Phi_{cave} \quad (3)$$

Les niveaux de minéralisation sont bien apparents comme des zones de faible porosité vacuolaires, tandis que le diamétreur (Fig. A3-7B) indique que les caves correspondent à des

zones de forte porosité. C'est aussi une bonne indication de trouver une zone de faible Φ_{image} en-dessous de 83m (Fig. A3-7C à A3-7F).

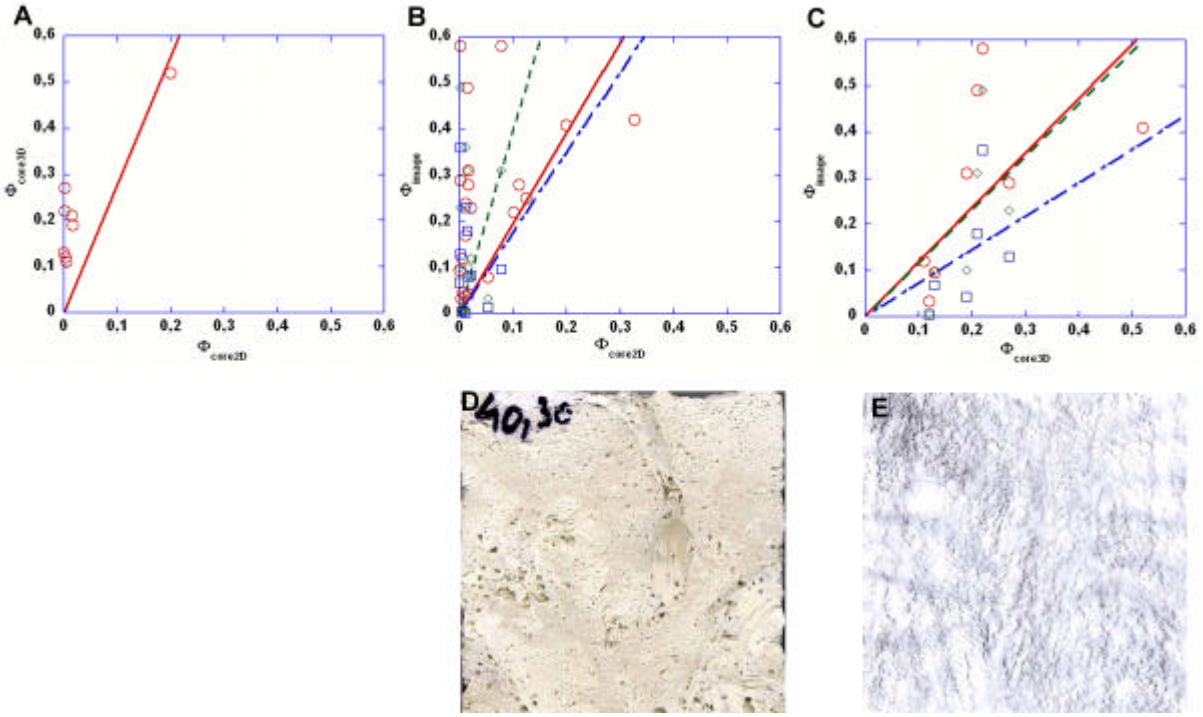

Figure A3 - 8. Dans le puit MC2, les mesures de porosité de la face plane de carotte sciée (F_{core2D}) et de la face courbe (F_{core3D}) sont comparées entre elles et avec les porosités de cavité étalonnées et filtrées à partir des trois diagraphies image (F_{image} optique, amplitude et temps de parcours acoustiques). (A) F_{core3D} en fonction de F_{core2D}, (8 carottes), ligne de régression linéaire d'équation : y= 2.8x, R^2= 0.83. (B) F_{image} en fonction de F_{core2D}, (20 carottes) ; F_{image} optique grand point rouge vide, ligne de régression linéaire rouge d'équation : y= 2x, R^2= 0.12; F_{image} amplitude acoustique carré bleu vide de moyenne taille, ligne de régression linéaire bleue d'équation : y= 1.7x, R^2= 0.035; F_{image} temps de parcours petit lozange vert, ligne de régression linéaire verte d'équation : y= 3.9x, R^2= 0.0029. (C) F_{image} en fonction de F_{core3D}, (8 carottes); F_{image} optique grand point rouge, ligne de régression linéaire rouge d'équation : y= 1.2x, R^2= 0.27; F_{image} amplitude acoustique carré bleu vide de taille moyenne, ligne de régression linéaire bleue longs tirets d'équation : y= 0.73x, R^2= 0.31; F_{image} temps de parcours petit losange vert, ligne de régression linéaire verte avec tirets d'équation : y= 1.1x, R^2= 0.43. (D) Photo de la face plane de la moitié de carotte MC2 à 40.30m, utilisée pour le comptage de F_{core2D} (Tableau A3-2). (E) Décalque de la face courbe de la carotte à 40,30m, utilisé pour le comptage de F_{core3D}. (Tableau A3-2).

Nous avons appliqué une méthode d'étalonnage à deux points (appelés Zéro et Plus) sur les données brutes, non filtrées des porosités image. Les valeurs étalonnées (Z_{cal} et P_{cal}) et mesurées (Z_{meas} et P_{meas}) sont listées dans le Tableau A3-1, avec les profondeurs utilisées et le gain et l'« offset », à utiliser. Les valeurs de mesure ont été choisies pour Z_{meas} dans les faibles valeurs de Φ_{vug} et Φ_{cave} du fond de talus (dans la zone à eau), et pour P_{meas} dans les caves indiquées par le diamétreur. Noter que les valeurs de Z_{meas} and the P_{meas} sont faciles à trouver, puisqu'elles représentent respectivement le minimum et le maximum des valeurs mesurées de porosité image. Les valeurs étalonnées ont été déterminées à partir des images et du diamétreur, et vérifiées avec les photos de carotte (Fig. A3-8).

Cette méthode d'étalonnage utilise seulement des diagraphies. De cette façon, elle est indépendante des corrélations de profondeur entre carotte et diagraphie, et de l'inévitable dispersion des résultats qu'elle génère. Les valeurs mesurées sur carotte sont seulement utilisées pour contrôle.

Fluide dans le puit Type d'image	Profondeur (mbgl)	Zcal (S/S)	Pcal (S/S)	Zmeas (S/S)	Pmeas (S/S)	Gain	Offset (S/S)
Air	29.532	0		0.15082		2.068	-0.31
Optique	6.766		0.7		0.48927		
Eau	94.696	0		0.044336		2.79	-0.12
Optique	59.254		0.9		0.36623		
Eau	90.226	0		0.0027778		1.50	-0.0042
Acoustique temps de parcours	82.700		0.9		0.60278		
Eau	90.226	0		0		0.90	0.00
Acoustique amplitude	59.254		0.9		100.00		

Tableau A3-1. Etalonnage deux-points de la macro-porosité calculée à partir de l'imagerie, dans le puit MC2, avec gain= (Pcal- Zcal)/ (Pmeas- Zmeas), et offset= Zcal –gain (Zmeas).

Ainsi (Tableau A3-1), la porosité dérivée des images d'amplitude acoustique nécessite les plus faibles corrections d'offset et de gain, tandis que la porosité dérivée des images optiques nécessite les plus fortes corrections d'offset et de gain (avec différents corrections dans l'ai et dans l'eau). Cette dernière porosité d'image n'est sans doute pas celle présentant la meilleure qualité, mais elle a le mérite par rapport à la porosité dérivée des images acoustiques d'être disponible même dans la zone sèche.

Φ_{vug} peut être mesuré ponctuellement en laboratoire à partir des faces planes de carottes (Fig. A3-8D). On peut alors exprimer directement F_{vug} en fonction de F_{core2D}, la porosité dérivée par le comptage d'image de la face plane de la carotte (en supposant que la porosité de vacuole le long d'un plan axial de carotte est égale à la porosité de vacuole le long de la périphérie de la carotte à la même profondeur) :

$$F_{vug} = F_{core2D} \quad (4)$$

Des photos de la face plane de moitiés de carottes (Fig. A3-8D), et des dessins de la face courbe de carottes obtenus par décalquage (Fig. A3-8E) ont été utilisés pour mesurer la porosité de vacuole (respectivement Φ_{core2D} et F_{core3D}) avec le logiciel de comptage d'image ImageJ du NIH (National Health Institute, disponible sur Internet). Les résultats sont listés sur le Tableau A3-2 ; noter que seulement 8 mesures de Φ_{core3D}, comparées à 21 mesures de Φ_{core2D} sont fournies. Les résultats correspondants de Φ_{image} sont aussi fournis dans le Tableau A3-2. Si la macro-porosité due à l'action du carottage is appelée F_{coring}, nous pouvons compléter la Relation (4) par :

$$F_{core3D} = F_{vug} + F_{coring} \quad (5)$$

Cette dernière relation, en supposant que les effets parasites sont ou bien négligeables ou équivalents (c'est-à-dire que $\Phi_{coring} \sim \Phi_{drilling}$), montre que, quand le diamétreur est ou bien plat ou égal au diamètre du trépan (ou quand les conditions de «bon trou » sont établies), il est possible d'écrire :

$$F_{image} \sim F_{core3D} \quad (6)$$

La Relation (5) est confirmée par les mesures du Tableau A3-2 (qui bien sur sont faites sur des carottes où l'effet de cave est absent, puisque par définition, il n'y a pas de carotte dans une cave), utilisée dans la Fig. A3-8C, qui montre que :

$$F_{image} \sim 1.02\, F_{core3D} \quad (7)$$

La Fig. A3-8A montre que:

$$F_{core3D} \sim 2.77\, F_{core2D} \quad (8)$$

La Fig. A3-8B montre que:

$F_{image} \sim 2.55\, F_{core2D}$ (9)

Les relations (8) et (9) démontrent que l'effet parasitique de respectivement Φ_{coring} (en prenant en compte les relations (4) et (5), et $\Phi_{drilling}$ (en prenant en compte les Relations (2), (4) et (6)), a été éliminé. Elles montrent aussi que Φ_{coring} est ou bien légèrement plus grande que $\Phi_{drilling}$, ou, plus probablement, à peu près égale.

Profondeur de carotte (mbgl)	Profondeur de diagraphie (mbgl)	Φ_{core2D} (S/S)	Φ_{core3D} (S/S)	Φ_{opt_cal} (S/S)	Φ_{amp_cal} (S/S)	Φ_{TT_cal} (S/S)	Φ_{core} (V/V)
2.08	0.58	0.0076	-	-	-	-	0.158
17.41	15.91	0.33	-	0.42	-	-	0.43
19.34	17.84	0.012	-	0.17	-	-	0.421
21.43	19.93	0.11	-	0.28	-	-	0.322
30.9	30.891	0.0048	0.11	0.12	-	-	0.334
33.41	33.40	0.13	-	0.25	-	-	0.228
34.41	34.40	0.10	-	0.22	-	-	0.155
34.9	34.89	0.20	0.52	0.41	-	-	0.159
39.7	37.7	0.0021	0.22	0.58	0.36	0.49	0.424
40.0	38.0	0.015	0.21	0.49	0.18	0.31	0.40
40.3	38.3	0.017	0.19	0.31	0.043	0.10	0.424
42.22	40.22	0.012	-	0.24	0.23	0.36	0.214
50.59	48.59	0.021	-	0.23	0.083	0.12	0.418
52.8	51.9	0.002	0.27	0.29	0.13	0.23	0.429
56.69	55.79	0.079	-	0.58	0.097	0.31	0.12
60.85	60.85	0.017	-	0.28	0.080	0.082	0.283
69.94	69.94	0.054	-	0.079	0.014	0.033	0.419
85.50	85.5	0.0073	-	0.047	0.0061	0.012	0.422
86.1	86.1	0.000706	0.13	0.095	0.068	0.098	0.41
89.00	89.0	0.012	-	0.039	0.0027	0.0074	0.417
91.7	91.7	0.0037	0.12	0.033	0.0032	0.0051	0.47

Tableau A3- 2. Comparaison des porosités de surface comptées sur la face plane de moitié de carottes (F_{core2D}), et sur la face courbe (F_{core3D}), calculées et étalonnées (par la méthode de deux points) sur les images de la paroi du trou à partir des enregistrements optique (F_{opt_cal}), amplitude acoustique (F_{amp_cal}), et temps de parcours acoustique (F_{TT_cal}), comparées avec la porosité de triple pesée mesurée sur bouchons F_{core}.

En comparant les Relations (2) et (7), et sachant que les carotees utilisées pour mesurer Φ_{core3D} ne sont pas cavées, on montre que notre étalonnage de Φ_{image} a pratiquement éliminé l'effet de $\Phi_{drilling}$, et on peut alors dire que pour des besoins pratiques :

$F_{image\_calibrated} = F_{vug} + F_{cave}$ (10)

On sait qu'on a entre la porosité totale Φ_T, la porosité primaire Φ_1 et la porosité secondaire Φ_2 la relation :

$\Phi_T = \Phi_1 + \Phi_2$ (11)

En raison de la relation (11), dans laquelle $\Phi 2 = \Phi vug$, nous avons $\Phi_{vug} \leq \Phi_T$. Mais en raison de la Relation (10), nous n'avons pas nécessairement $\Phi_{image\_calibrated} \leq \Phi_T$ (ainssi qu'on peut le voir dans le Tableau A3-2).

Les Tableaux A3-3 et A3-4 indiquent les valeurs de gain et d'offset qui ont été trouvées pour les puits MC8 et MC9, respectivement.

Fluide dans le puit Type d'image	Profondeur (mbgl)	Zcal (S/S)	Pcal (S/S)	Zmeas (S/S)	Pmeas (S/S)	Gain	Offset (S/S)
Air Optique	10.0	0		0.18		1.91	-0.34
	36.0		0.9		0.65		
Eau Optique	76.0	0		0.09		1.61	-0.14
	36.5		0.9		0.65		
Eau temps de parcours acoustique	90.226	0		0.0027778		4.24	-0.0042
	58.0		0.9		0.60278		
Eau Amplitude acoustique	90.226	0		0		0.90	0.00
	59.254		0.9		100.00		

Tableau A3- 3. Etalonnage de la porosité de vacuole à partir des images de la paroi du puit dans le puit MC8, avec gain= (Pcal- Zcal)/ (Pmeas- Zmeas), et offset= Zcal –gain (Zmeas).

Fluide dans le puit Type d'image	Profondeur (mbgl)	Zcal (S/S)	Pcal (S/S)	Zmeas (S/S)	Pmeas (S/S)	Gain	Offset (S/S)
Air Optique	6.5	0		0.15		1.6	-0.24
	36.0		0.8		0.65		
Eau Optique	60.0	0		0.02		1.27	-0.25
	36.5		0.9		0.65		
Eau temps de parcours acoustique	90.226	0		0.0027778		2.67	-0.0042
	56.0		0.9		0.60278		
Eau Amplitude acoustique	90.226	0		0		0.90	0.00
	59.254		0.9		100.00		

Tableau A3- 4. . Etalonnage de la porosité de vacuole à partir des images de la paroi du puit dans le puit MC9, avec gain= (Pcal- Zcal)/ (Pmeas- Zmeas), et offset= Zcal –gain (Zmeas).

Résumé
Les intrusions d'eau salée en zone côtière constituent une menace pour la population. Celles-ci sont particulièrement dommageables en contexte carbonaté.
Nous avons étudié le récif corallien Miocène du sud-est de Majorque afin de comprendre la relation entre structure géologique et intrusion. Pour cela nous avons utilisé des méthodes multi-scalaires et multi-disciplinaires. Les mesures dans 25 forages sur l'ensemble de la plate-forme corallienne ont permis de préciser la structure stratigraphique et certains éléments de la tectonique régionale. Le récif progade dans la direction NE-SO, en partant de l'Aquitanien pour aboutir au Messinien. La Crise de Salinité Messinienne entraîne une disparition des coraux méditerranéens et se traduit par un Complexe Carbonaté Terminal qui s'étend sur une grande partie des coraux autrefois vivants de Majorque.
A l'échelle du site expérimental, l'étude de la composition minérale, de la texture et de la diagenèse ont permis de caractériser l'hétérogénéité de la séquence carbonatée. Des couches de minéralisation accompagnées de dolomitisation et de faible porosité correspondent à différents niveaux eustatiques post-dépositionnels. Les causes de l'existence et de l'orientation des fractures sont étudiées. La relation de perméabilité à porosité est précisée. La structure de porosité est étudiée par comparaison entre la porosité primaire et la porosité secondaire.
Cette étude contribue à la connaissance du site le mieux documenté au monde pour l'évolution des réservoirs carbonatés récifaux, avec applications pour les intrusions d'eau salée et l'extraction des hydrocarbures.

Structure and heterogeneity of a Miocene reefal platform (Majorca); implication for the saline wedge in coastal aquifers

Abstract
The coastal intrusion of brine threatens populations. This is particularly prejudicial in carbonate environments.
We have studied the Miocene coral reef of S-E Majorca for better understanding the relation between geological structure and intrusion. For that purpose, we have used multi-scalar and multi-disciplinary methods. The measurements in 25 boreholes over the whole coral platform have allowed defining the stratigraphic structure and some elements of the regional tectonic. The reef progrades in the NE-SW direction, starting from the Aquitanian to terminates at the Messinian. The Messinian Salinity Crisis involves a disappearance of the Mediterranean corals and results in a Terminal Carbonate Complex which overlays a great part of the previously living corals of Majorca.
At the experimental site scale, the study of the mineral composition, the texture, and the diagenesis have allowed characterization of the carbonate sequence heterogeneity. Layers of mineralization accompanied by dolomitization and low porosity correspond to post-depositional eustatic levels. The causes for the existence and the orientation of fractures are studied. The permeability to porosity relation is approached. The porosity structure is studied by comparison between primary and secondary porosity.
This study contributes to the knowledge of the world best documented site for the evolution of carbonate reef reservoirs, with applications for brine intrusion and for hydrocarbon extraction.